



NAVAL POSTGRADUATE SCHOOL

MONTEREY, CALIFORNIA

DISSERTATION

COORDINATED CONTROL OF A
PLANAR DUAL-CRANE
NON-FULLY RESTRAINED
SYSTEM

by

Frank A. Leban

December 2008

Dissertation Supervisor:

Fotis Papoulias

Approved for public release; distribution is unlimited

THIS PAGE INTENTIONALLY LEFT BLANK

REPORT DOCUMENTATION PAGE			Form Approved OMB No. 0704-0188
<p>Public reporting burden for this collection of information is estimated to average 1 hour per response, including the time for reviewing instruction, searching existing data sources, gathering and maintaining the data needed, and completing and reviewing the collection of information. Send comments regarding this burden estimate or any other aspect of this collection of information, including suggestions for reducing this burden, to Washington headquarters Services, Directorate for Information Operations and Reports, 1215 Jefferson Davis Highway, Suite 1204, Arlington, VA 22202-4302, and to the Office of Management and Budget, Paperwork Reduction Project (0704-0188) Washington DC 20503.</p>			
1. AGENCY USE ONLY (Leave blank)	2. REPORT DATE December 2008	1. AGENCY USE ONLY (Leave blank) Dissertation	
4. TITLE AND SUBTITLE: Coordinated Control of a Planar Dual Crane Non-Fully Restrained System		5. FUNDING NUMBERS	
6. AUTHOR(S) Frank A. Leban			
7. PERFORMING ORGANIZATION NAME(S) AND ADDRESS(ES) Naval Postgraduate School Monterey, CA 93943-5000		8. PERFORMING ORGANIZATION REPORT NUMBER	
9. SPONSORING / MONITORING AGENCY NAME(S) AND ADDRESS(ES) N/A		10. SPONSORING / MONITORING AGENCY REPORT NUMBER	
11. SUPPLEMENTARY NOTES The views expressed in this thesis are those of the author and do not reflect the official policy or position of the Department of Defense or the U.S. Government.			
12a. DISTRIBUTION / AVAILABILITY STATEMENT Approved for public release; distribution is unlimited		12b. DISTRIBUTION CODE	
13. ABSTRACT (maximum 200 words) In this dissertation a control scheme that would provide motion compensation for a ship-based two-crane system suspending a single payload was developed. Historical experience during the conflict in Vietnam, along with the introduction of standard containerized packaging have steered military sustainment logistics towards a reliance on commercially developed cranes for discharge of containers - even for instream lightering operations. With the inclusion of Seabasing as one of the Navy's pillars, there has been a resurgence in interest in cargo transfer technology. While several approaches to the movement of individual containers have been pursued, there has not been a similar focus on the handling of outsize cargo in the military logistics-over-the-shore (LOTS) operating environment. In the body of this work is an algorithm for the coordinated control of two cranes to facilitate the movement of cargo. The use of multiple cranes may be required by either the geometric extent or the weight of the cargo. The kinematic chain is developed for the incompletely-restrained cable-suspended system that describes this system. With the inclusion of the dynamics of the system to fully describe the force and moment constraints, the equations of motion can be inverted to yield expressions that relate desired payload motion to crane control inputs. The presence of seaway induced motions on the ship platform introduces disturbances that must be accounted for in the kinematics of the ship-attached crane reference frame and be compensated for by the dual-crane system. Without this motion compensation, the operational capability is limited by the environment. With this system the payload is isolated from the ship motion and held fixed in inertial space. The weighted-norm method used to derive the solution allows for distribution of the actuation effort of the system, which could be useful in actual operations of the cranes onboard a vessel and provides an opportunity for optimization by judicious selection of the weighting matrix. Future development of coordinated control for dual-crane systems may also employ trajectory planning to automate the movement of large payloads. Results from a MATLAB/Simulink simulation and selected results from a 1/32nd-scale model are presented to illustrate the concepts developed.			
14. SUBJECT TERMS Shipboard Cranes, Motion Compensation, Inverse Kinematic Control, Minimum Norm Solution, Logistical Operations		15. NUMBER OF PAGES 415	
16. PRICE CODE			
17. SECURITY CLASSIFICATION OF REPORT Unclassified	18. SECURITY CLASSIFICATION OF THIS PAGE Unclassified	17. SECURITY CLASSIFICATION OF REPORT Unclassified	18. SECURITY CLASSIFICATION OF THIS PAGE UU

THIS PAGE INTENTIONALLY LEFT BLANK

Approved for public release; distribution is unlimited

COORDINATED CONTROL OF A PLANAR DUAL CRANE NON-FULLY RESTRAINED SYSTEM

Frank A. Leban
CIV, Naval Surface Warfare Center
B.S.A&AE, Purdue University, 1982
M.S.A&AE, Purdue University, 1990
M.S. Applied Physics, Johns Hopkins University, 1996

Submitted in partial fulfillment of the
requirements for the degree of

**DOCTOR OF PHILOSOPHY IN
MECHANICAL ENGINEERING**
from the

NAVAL POSTGRADUATE SCHOOL
December 2008

Author: _____
Frank A. Leban

Approved by:

Fotis Papoulias
Professor of Mechanical &
Astronautical Engineering
Dissertation Supervisor

Healey Anthony
Professor of Mechanical &
Astronautical Engineering
Dissertation Committee Chair

Roberto Cristi
Professor of Electrical Engineering

Morris Driels
Professor of M&AE

Isaac Kaminer
Professor of M&AE

Wei Kang
Professor of Applied Math

Approved by:
Knox Millsaps, Chair, Department of M&AE

Approved by:
Doug Moses, Associate Provost for Academic Affairs

THIS PAGE INTENTIONALLY LEFT BLANK

ABSTRACT

In this dissertation a control scheme that provides motion compensation for a ship-based two-crane system suspending a single payload is developed. Historical experience during the conflict in Vietnam, along with the introduction of standard containerized packaging have steered military sustainment logistics towards a reliance on commercially developed cranes for discharge of containers - even for instream lightering operations. With the inclusion of Seabasing as one of the Navys pillars, there has been a resurgence in interest in cargo transfer technology. While several approaches to the movement of individual containers have been pursued, there has not been a similar focus on the handling of outsize cargo in the military logistics-over-the-shore (LOTS) operating environment. In the body of this work is an algorithm for the coordinated control of two cranes to facilitate the movement of cargo. The use of multiple cranes may be required by either the geometric extent or the weight of the cargo. The kinematic chain is developed for the incompletely-restrained cable-suspended system that describes this system. With the inclusion of the dynamics of the system to fully describe the force and moment constraints, the equations of motion can be inverted to yield expressions that relate desired payload motion to crane control inputs. The presence of seaway induced motions on the ship platform introduces disturbances that must be accounted for in the kinematics of the ship-attached crane reference frame and be compensated for by the dual-crane system. Without this motion compensation, the operational capability is limited by the environment. With this system the payload is isolated from the ship motion and held fixed in inertial space. The weighted-norm method used to derive the solution allows for distribution of the actuation effort of the system, which could be useful in actual operations of the cranes onboard a vessel and provides an opportunity for optimization by judicious selection of the weighting matrix. Future development of coordinated control for dual-crane systems may also employ trajectory planning to automate the movement of large payloads.

Results from a MATLAB/Simulink simulation and selected results from a 1/32nd-scale model are presented to illustrate the concepts developed.

DISCLAIMER

The computer programs in the Appendix are supplied on an “as is” basis, with no warranties of any kind. The author bears no responsibility for any consequences of using these program.

THIS PAGE INTENTIONALLY LEFT BLANK

TABLE OF CONTENTS

I. INTRODUCTION	1
A. BACKGROUND - “SETTING THE STAGE, VIETNAM 1961-1968”	2
B. STATE-OF-THE-ART (VIETNAM TO THE PRESENT DAY)	15
C. RECENT INVESTIGATIONS AND PUBLICATIONS	22
II. DYNAMICS OF A PLANAR DUAL-CRANE SYSTEM	35
A. DERIVATION OF THE EQUATIONS OF MOTION	37
III. MODEL SIMULATION RESULTS	49
IV. INVERSE KINEMATIC CONTROL	85
A. FORCE CONSTRAINTS	86
B. KINEMATIC CONSTRAINTS	87
C. INVERSE KINEMATIC SOLUTION EXAMPLE	91
D. RESPONSE TO SINUSOIDAL SHIP MOTION WITH INVERSE KINEMATIC CONTROL	95
V. DERIVATION OF POWER EXPRESSIONS AND ALTERNA- TIVE WEIGHTING SCHEMES	125
A. TORQUE AND POWER RELATIONSHIPS APPLIED TO THE MINIMUM NORM SOLUTION	125
B. ALTERNATIVE WEIGHTING SCHEMES	132
1. Actuation Selectivity	132
2. Other Operational Considerations	160
VI. SUMMARY OF SIMULATION RESULTS	171
A. PERFORMANCE METRIC COMPARISON	171
VII. PHYSICAL SCALE-MODEL RESULTS	185
VIII. CONCLUSIONS & FUTURE WORK	235
A. CONCLUSIONS	235
B. CONTRIBUTION	236
C. FUTURE WORK	236

APPENDIX A. PLANAR DUAL-CRANE DYNAMIC MODEL	
RESULTS	239
A. TIME HISTORY DATA FOR PLANAR DUAL-CRANE SYSTEM	239
1. Surge Motion - 0.1 meter amplitude, 8.05 second period	239
2. Surge Motion - 0.1 meter amplitude, 8.75 second period	271
APPENDIX B. MINIMUM NORM SOLUTION	291
A. DERIVATION	291
APPENDIX C. INVERSE KINEMATIC CONTROL MODEL	
RESULTS	293
A. TIME HISTORY DATA FOR INVERSE-KINEMATIC SHIP MOTION COMPENSATOR	293
1. Power-based Weighting	293
APPENDIX D. INVERSE KINEMATIC CONTROL ALGORITHM - MATLAB CODE	317
A. INVERSE KINEMATIC CONTROL ALGORITHM- MATLAB M-FILE	317
APPENDIX E. DEVELOPMENT OF THE PHYSICAL CRANE MODEL	329
A. CRANE DESIGN REPORT	329
B. PURPOSE	331
C. BACKGROUND	331
D. ASSEMBLY OVERVIEW	331
1. Crane Structure	332
2. Winch & Motor Housing	332
E. DYNAMIC SCALING	334
1. Motor Drive Characteristics	334
2. Characterization of Crane Winches	335
F. SOFTWARE	336
1. LabVIEW	338
G. APPENDIX: PARTS LIST	341
H. APPENDIX: INTERFACE CONNECTIONS	342
I. APPENDIX: ALUMINUM PARTS DRAWINGS	343
APPENDIX F. DEVELOPMENT OF THE MOTION PLATFORM APPARATUS	345
A. MOTION PLATFORM DESIGN REPORT	345
B. PURPOSE	347
C. BACKGROUND	347
1. Structure	348
2. Components	348

3.	Kinematic	349
D.	SOFTWARE	352
1.	Motion Base Simulation in Processing	352
2.	LabVIEW	353
E.	APPENDIX: PARTS LIST	356
LIST OF REFERENCES		357
INITIAL DISTRIBUTION LIST		363

THIS PAGE INTENTIONALLY LEFT BLANK

LIST OF FIGURES

Figure 1. Comparison of World War II Pacific Fleet and Vietnam Pacific Service Force supply requirements. Only in the category of ship fuel does the WW II level exceed that of Vietnam. (From Figure 1 of [1], Courtesy of the Naval Historical Center, Department of the Navy)	3
Figure 2. Components of the standard yard and stay rigging from the Seaman course NAVEDTRA 14067 [2]	4
Figure 3. The light cargo ship USS Mark loads in Saigon's port for delivery of material to naval support bases in the Mekong delta. (Figure 5-14 in [3])	5
Figure 4. Cam Ranh Bay, 1965, before development as a logistical complex. (From [4] courtesy of the Naval Historical Center, Department of the Navy.)	6
Figure 5. Aerial view of Naval Support Facility, Cam Ranh Bay, 1969. (Figure 12 in [5] courtesy of the Naval Historical Center, Department of the Navy.)	7
Figure 6. Pontoon piers at the Naval Support Facility, Cam Ranh Bay, 1969. To the far right is a small floating drydock. (Figure 14 in [5] courtesy of the Naval Historical Center, Department of the Navy.)	8
Figure 7. Growth in port capability of Naval Support Activity, Danang. (Figure 25 in [6] courtesy of the Naval Historical Center, Department of the Navy.)	9
Figure 8. Observation Point, Danang, March 1965. (Figure 15 in [3] courtesy of the Naval Historical Center, Department of the Navy.)	9
Figure 9. Observation Point, Danang, November 1966. (Figure 16 in [3] courtesy of the Naval Historical Center, Department of the Navy.)	10
Figure 10. Landing craft - utility (LCU) 1476 offloads at Danang's Red Beach in March 1965 under direction of Naval Beach Group ONE personnel. (p. 528, [7])	11
Figure 11. Aerial view of the deep water piers in the Danang Harbor. The DeLong pier can be seen on the right. (Figure 21 in [6])	12
Figure 12. Map drawing of Danang area facilities. (p. 99, [4])	13
Figure 13. Cargo trailers at deep water pier site, Danang, 1969. (Figure 17 in [5] courtesy of the Naval Historical Center, Department of the Navy.)	13

Figure 14. Growth in port capability of naval support activity, Danang.	14
Figure 15. Typical wire-luffing jib crane on a single pedestal foundation.	16
Figure 16. Luffing-jib crane degrees of freedom.	17
Figure 17. Illustration of the influence on the load by the tagline and liftline control of the Rider Block Tagline System (RBTS) [8].	19
Figure 18. Schematic of Rider Block Tagline System (RBTS) degrees of freedom.	20
Figure 19. Schematic illustration of Platform Motion Control (PMC) system as installed on S.S. Keystone State in 1984. (From [9])	21
Figure 20. Demonstrating cargo transfer at sea using PCS-controlled luffing-jib cranes on the SS Flickertail State in 2002.	23
Figure 21. Illustration of use of AUTOLOG for discharging cargo to lighterage [10].	24
Figure 22. Illustration of the HICASS crane concept as developed for the Office of Naval Research by Oceaneering International, Inc.	25
Figure 23. Photo of two luffing jib cranes mounted on a twin platform.	27
Figure 24. Sketch of two luffing jib cranes executing a team lift.	28
Figure 25. Photo of a sideport ramp of a Large Medium Speed Roll- on/Roll-off (LMSR) vessel being lifted into place by two luffing-jib crane-sets in twin mode.	29
Figure 26. Photo of a U.S. Army modular warping tug being lifted onto the deck of the S.S. Flickertail State by two luffing-jib crane-sets in twin mode during Operation Humanitarian Support Over-The-Shore (HSOTS) 2007 in Puerto Quetzal, Guatemala.	30
Figure 27. Reference frame and coordinate definitions. Numbered circles are used to denote points on the system for vector descriptions.	36
Figure 28. Free-body diagram of the payload.	37
Figure 29. Front view of model of the dual crane system with jibs at arbitrary slew angles. Note the vertical offset of the hoist falls char- acterized by the angle ρ_I	46
Figure 30. End view of model of the dual crane system with jibs at arbitrary slew angles. The jibs clearly do not lie in a common plane. The vertical offset of the hoist falls is still discernable.	47
Figure 31. Aligned view of model of the dual crane system with jibs at arbitrary slew angles. Looking along the line containing the tips of the jibs, the payload clearly appears to lie vertically in this plane. Note that there is no vertical offset of the hoist falls analogous to the angle ρ_I	48
Figure 32. Top-level block diagram of SIMULINK simulation.	49
Figure 33. Oscillation mode for dual crane in <i>X-Z</i> plane when $\rho = 0$	51
Figure 34. Oscillation mode for dual crane in <i>Z-Y</i> plane with $\rho_l = 10^\circ$	52
Figure 35. Variation in response with changes in hoist length for $\rho_l = 0^\circ$	53

Figure 36. Effect of ρ on response amplitude ratio with payload set at deck-level	54
Figure 37. Effect of ρ_I on response amplitude ratio with hoist length set to 25 meters	55
Figure 38. Plot of amplitude ratio versus inertial hoist fall angle.	56
Figure 39. Sum-squared amplitudes of the lateral, rotational, and total combined displacements.	57
Figure 40. Time history of the payload motion for a 0.1 meter, 8.05 second period surge motion excitation with initial $\rho = 0$ degrees. The blue trace is the ship motion and the payload response is shown in green. Note that the payload rotation, θ_p about its pitch axis is essentially zero.	64
Figure 41. Time history of the inertial hoist fall angles, ρ_{I1} and ρ_{I2} for a 0.1 meter, 8.05 second period surge motion excitation with initial $\rho = 0$ degrees. The peak ρ angle response is slightly more than 3.5 degrees for the given input.	65
Figure 42. Time history of the hoist cable tensions, F_1 and F_2 in metric tons for a 0.1 meter, 8.05 second period surge motion excitation with initial $\rho = 0$ degrees. The peak response is approximately 0.5 percent above the initial (static) tension.	66
Figure 43. Time history of the calculation of the displacement metrics for a 0.1 meter, 8.05 second period surge motion excitation with initial $\rho = 0$ degrees. Note that since the payload rotation is essentially zero, there is no difference between J_l and $J_{l+\theta}$ and the sum of J_l and J_θ	67
Figure 44. Time history of the payload motion for a 0.1 meter, 8.05 second period surge motion excitation with initial $\rho = 1.0$ degree. The blue trace is the ship motion and the payload response is shown in green. The maximum x and z displacements are reduced slightly. Note that the payload rotation, θ_p is small, but not zero as was the case for $\rho = 0$	68
Figure 45. Time history of the calculation of the displacement metrics for a 0.1 meter, 8.05 second period surge motion excitation with initial $\rho = 1.0$ degree. Note that since the payload rotation is no longer zero, J_θ is nonzero and there is a separation between J_l and $J_{l+\theta}$ and the sum of J_l and J_θ	69
Figure 46. Time history of the payload motion for a 0.1 meter, 8.05 second period surge motion excitation with initial $\rho = -1.0$ degree. The blue trace is the ship motion and the payload response is shown in green. The maximum x and z displacements are reduced slightly. Note that the payload rotation, θ_p is small, but not zero as was the case for $\rho = 0$	70

Figure 47. Time history of the calculation of the displacement metrics for a 0.1 meter, 8.05 second period surge motion excitation with initial $\rho = -1.0$ degree. Note that since the payload rotation is no longer zero, J_θ is nonzero and there is a separation between J_l and $J_{l+\theta}$ and the sum of J_l and J_θ	71
Figure 48. Time history of the inertial hoist fall angles, ρ_{I1} and ρ_{I2} for a 0.1 meter, 8.05 second period surge motion excitation with initial $\rho = -1$ degree. The peak ρ angle response is slightly more than 3.5 degrees for the given input.	72
Figure 49. Time history of the payload motion for a 0.1 meter, 8.05 second period surge motion excitation with initial $\rho = -10.0$ degree. The blue trace is the ship motion and the payload response is shown in green. The maximum x and z displacements are reduced slightly. The payload rotation, θ_p is no longer small.	73
Figure 50. Time history of the inertial hoist fall angles, ρ_{I1} and ρ_{I2} for a 0.1 meter, 8.05 second period surge motion excitation with initial $\rho = -10$ degrees. The peak ρ angle response is more than 20 degrees on either side of the initial offset.	74
Figure 51. Plot of frequency data versus the hoist-fall offset angle, ρ_I for a 8.05 second period surge motion excitation. The forcing frequency is shown along with the calculated natural frequency of the planar dual-crane system. For purposes of comparison, the natural frequency of a simple pendulum corresponding to the hoist cable length, L_h , is shown. Note that for $\rho = -10$ degrees the system would be predicted to be in resonance with the forcing function.	75
Figure 52. This plot summarizes the results of the simulation of the open loop system for a 8.05 second period surge motion excitation. Maximum values of x and z in meters and θ_p in degrees for each run are plotted versus the hoist-fall offset angle, ρ	76
Figure 53. This plot summarizes the results of the simulation of the open loop system for a 8.05 second period surge motion excitation. Values of the displacement metrics in meters for each run are plotted versus the hoist-fall offset angle, ρ . Note that the peak representing a resonance at $\rho = -10$ degrees has a large x contribution while the peak at $\rho = 35$ degrees has a large θ_p component.	77
Figure 54. Time history of the hoist cable tensions, F_1 and F_2 in metric tons for a 0.1 meter, 8.05 second period surge motion excitation with initial $\rho = 50$ degrees. The peak response is approximately 1.5 percent above the initial (static) tension.	78
Figure 55. Hoist cable tension increase as a function of the cable offset angle, ρ	79

Figure 56. This plot summarizes the results of the simulation of the open loop system for a 8.75 second period surge motion excitation. Maximum values of x and z in meters and θ_p in degrees for each run are plotted versus the hoist-fall offset angle, ρ	80
Figure 57. This plot summarizes the results of the simulation of the open loop system for a 8.75 second period surge motion excitation. Values of the displacement metrics in meters for each run are plotted versus the hoist-fall offset angle, ρ . Note that the peak representing a resonance at $\rho = 0$ degrees has a large x contribution while the peak at $\rho = 25$ degrees has a large θ_p component.	81
Figure 58. Plot of frequency data versus the hoist-fall offset angle, ρ_I for a 8.75 second period surge motion excitation. The forcing frequency is shown along with the calculated natural frequency of the planar dual-crane system. For purposes of comparison, the natural frequency of a simple pendulum corresponding to the hoist cable length, L_h , is shown. Note that for $\rho = 0$ degrees the system would be predicted to be in resonance with the forcing function.	82
Figure 59. SIMULINK block diagram of the simulation modified for inverse kinematic control.	92
Figure 60. Illustration of the initial two-crane configuration.	93
Figure 61. Ship motion time histories used in the simulation example. . .	94
Figure 62. Crane jib and hoist motions with the control on and off. . .	95
Figure 63. Inertial motion of the payload with the control on and off. .	96
Figure 64. Plot of x , z , and θ time histories for the inverse kinematic control case with the identity matrix used as the weights in the minimum norm solution. (Simulation parameters: $\rho = 0$ degrees, $\vec{P}_{8/1,z} = -5$ meters, with a sinusoidal forcing function of $\mathbf{x}_s = 0.5$ meter at a period of 8.75 seconds.)	98
Figure 65. Plots of β , $\dot{\beta}$, L_h , and \dot{L}_h time histories for the inverse kinematic control case with the identity matrix used as the weights in the minimum norm solution. (Simulation parameters: $\rho = 0$ degrees, $\vec{P}_{8/1,z} = -5$ meters, with a sinusoidal forcing function of $\mathbf{x}_s = 0.5$ meter at a period of 8.75 seconds.)	99
Figure 66. Plot of time histories for the inertial hoist-fall angle, ρ , for the inverse kinematic control case with the identity matrix used as the weights in the minimum norm solution. (Simulation parameters: $\rho = 0$ degrees, $\vec{P}_{8/1,z} = -5$ meters, with a sinusoidal forcing function of $\mathbf{x}_s = 0.5$ meter at a period of 8.75 seconds.)	100

Figure 67. Plot of hoist cable tensions, F_1 and F_2 , for the inverse kinematic control case with the identity matrix used as the weights in the minimum norm solution. (Simulation parameters: $\rho = 0$ degrees, $\vec{P}_{8/1,z} = -5$ meters, with a sinusoidal forcing function of $\mathbf{x}_s = 0.5$ meter at a period of 8.75 seconds.)	101
Figure 68. Plot of time histories for instantaneous power for the inverse kinematic control case with the identity matrix used as the weights in the minimum norm solution. (Simulation parameters: $\rho = 0$ degrees, $\vec{P}_{8/1,z} = -5$ meters, with a sinusoidal forcing function of $\mathbf{x}_s = 0.5$ meter at a period of 8.75 seconds.)	102
Figure 69. Plot of peak values of hoist cable tension and jib torque versus ship motion amplitude. (Simulation parameters: $\mathbf{W} = \mathbf{I}$, $\rho = 0$ degrees, $\vec{P}_{8/1,z} = 5$ meters, and $\mathbf{x}_s = [0.1, 0.25, 0.5, 1.0, 1.5]$ meter at a period of 8.75 seconds.)	103
Figure 70. Plot of peak values of actuation rates and the rate-based performance metric versus ship motion amplitude. (Simulation parameters: $\mathbf{W} = \mathbf{I}$, $\rho = 0$ degrees, $\vec{P}_{8/1,z} = 5$ meters, and $\mathbf{x}_s = [0.1, 0.25, 0.5, 1.0, 1.5]$ meter at a period of 8.75 seconds.)	104
Figure 71. Plot of peak values of instantaneous power and the power-based metric versus ship motion amplitude. (Simulation parameters: $\mathbf{W} = \mathbf{I}$, $\rho = 0$ degrees, $\vec{P}_{8/1,z} = 5$ meters, and $\mathbf{x}_s = [0.1, 0.25, 0.5, 1.0, 1.5]$ meter at a period of 8.75 seconds.)	105
Figure 72. Cross-plot of the two performance metrics for a range of ship motion amplitude. (Simulation parameters: $\mathbf{W} = \mathbf{I}$, $\rho = 0$ degrees, $\vec{P}_{8/1,z} = 5$ meters, and $\mathbf{x}_s = [0.1, 0.25, 0.5, 1.0, 1.5]$ meter at a period of 8.75 seconds.)	106
Figure 73. Three dimensional plot of the performance metrics for a range of ship motion amplitude. (Simulation parameters: $\mathbf{W} = \mathbf{I}$, $\rho = 0$ degrees, $\vec{P}_{8/1,z} = 5$ meters, and $\mathbf{x}_s = [0.1, 0.25, 0.5, 1.0, 1.5]$ meter at a period of 8.75 seconds.)	107
Figure 74. Plot of x , z , and θ time histories for the inverse kinematic control case with the identity matrix used as the weights in the minimum norm solution. (Simulation parameters: $\rho = 0$ degrees, $\vec{P}_{8/1,z} = -5$ meters, with a sinusoidal forcing function of $\mathbf{z}_s = 1.0$ meter at a period of 10.0 seconds.)	108
Figure 75. Plots of β , $\dot{\beta}$, L_h , and \dot{L}_h time histories for the inverse kinematic control case with the identity matrix used as the weights in the minimum norm solution. (Simulation parameters: $\rho = 0$ degrees, $\vec{P}_{8/1,z} = -5$ meters, with a sinusoidal forcing function of $\mathbf{z}_s = 1.0$ meter at a period of 10.0 seconds.)	109

Figure 76. Plot of time histories for the inertial hoist-fall angle, ρ , for the inverse kinematic control case with the identity matrix used as the weights in the minimum norm solution. (Simulation parameters: $\rho = 0$ degrees, $\vec{P}_{8/1,z} = -5$ meters, with a sinusoidal forcing function of $z_s = 1.0$ meter at a period of 10.0 seconds.)	110
Figure 77. Plot of hoist cable tensions, F_1 and F_2 , for the inverse kinematic control case with the identity matrix used as the weights in the minimum norm solution. (Simulation parameters: $\rho = 0$ degrees, $\vec{P}_{8/1,z} = -5$ meters, with a sinusoidal forcing function of $z_s = 1.0$ meter at a period of 10.0 seconds.)	111
Figure 78. Plot of time histories for instantaneous power for the inverse kinematic control case with the identity matrix used as the weights in the minimum norm solution. (Simulation parameters: $\rho = 0$ degrees, $\vec{P}_{8/1,z} = -5$ meters, with a sinusoidal forcing function of $z_s = 1.0$ meter at a period of 10.0 seconds.)	112
Figure 79. Plot of x , z , and θ time histories for the inverse kinematic control case with the identity matrix used as the weights in the minimum norm solution. (Simulation parameters: $\rho = 0$ degrees, $\vec{P}_{8/1,z} = -5$ meters, with a sinusoidal forcing function of $\theta_s = 5.0^\circ$ at a period of 7.0 seconds.)	113
Figure 80. Plots of β , $\dot{\beta}$, L_h , and \dot{L}_h time histories for the inverse kinematic control case with the identity matrix used as the weights in the minimum norm solution. (Simulation parameters: $\rho = 0$ degrees, $\vec{P}_{8/1,z} = -5$ meters, with a sinusoidal forcing function of $\theta_s = 5.0^\circ$ at a period of 7.0 seconds.)	114
Figure 81. Plot of time histories for the inertial hoist-fall angle, ρ , for the inverse kinematic control case with the identity matrix used as the weights in the minimum norm solution. (Simulation parameters: $\rho = 0$ degrees, $\vec{P}_{8/1,z} = -5$ meters, with a sinusoidal forcing function of $\theta_s = 5.0^\circ$ at a period of 7.0 seconds.)	115
Figure 82. Plot of hoist cable tensions, F_1 and F_2 , for the inverse kinematic control case with the identity matrix used as the weights in the minimum norm solution. (Simulation parameters: $\rho = 0$ degrees, $\vec{P}_{8/1,z} = -5$ meters, with a sinusoidal forcing function of $\theta_s = 5.0^\circ$ at a period of 7.0 seconds.)	116
Figure 83. Plot of time histories for instantaneous power for the inverse kinematic control case with the identity matrix used as the weights in the minimum norm solution. (Simulation parameters: $\rho = 0$ degrees, $\vec{P}_{8/1,z} = -5$ meters, with a sinusoidal forcing function of $\theta_s = 5.0^\circ$ at a period of 7.0 seconds.)	117

Figure 84. Plot of x , z , and θ time histories for the inverse kinematic control case with the identity matrix used as the weights in the minimum norm solution. (Simulation parameters: $\rho = 10$ degrees, $\vec{P}_{8/1,z} = -5$ meters, with a combined sinusoidal forcing function of $\mathbf{x}_s = 1$ meter at a period of 8.75 seconds, $\mathbf{z}_s = 1$ meter at a period of 10 seconds, and $\theta_s = 5^\circ$ at a period of 7.0 seconds.)	118
Figure 85. Plots of β , $\dot{\beta}$, L_h , and \dot{L}_h time histories for the inverse kinematic control case with the identity matrix used as the weights in the minimum norm solution. (Simulation parameters: $\rho = 10$ degrees, $\vec{P}_{8/1,z} = -5$ meters, with a combined sinusoidal forcing function of $\mathbf{x}_s = 1$ meter at a period of 8.75 seconds, $\mathbf{z}_s = 1$ meter at a period of 10 seconds, and $\theta_s = 5^\circ$ at a period of 7.0 seconds.)	119
Figure 86. Plot of time histories for the inertial hoist-fall angle, ρ , for the inverse kinematic control case with the identity matrix used as the weights in the minimum norm solution. (Simulation parameters: $\rho = 10$ degrees, $\vec{P}_{8/1,z} = -5$ meters, with a combined sinusoidal forcing function of $\mathbf{x}_s = 1$ meter at a period of 8.75 seconds, $\mathbf{z}_s = 1$ meter at a period of 10 seconds, and $\theta_s = 5^\circ$ at a period of 7.0 seconds.)	120
Figure 87. Plot of hoist cable tensions, F_1 and F_2 , for the inverse kinematic control case with the identity matrix used as the weights in the minimum norm solution. (Simulation parameters: $\rho = 10$ degrees, $\vec{P}_{8/1,z} = -5$ meters, with a combined sinusoidal forcing function of $\mathbf{x}_s = 1$ meter at a period of 8.75 seconds, $\mathbf{z}_s = 1$ meter at a period of 10 seconds, and $\theta_s = 5^\circ$ at a period of 7.0 seconds.)	121
Figure 88. Plot of time histories for instantaneous power for the inverse kinematic control case with the identity matrix used as the weights in the minimum norm solution. (Simulation parameters: $\rho = 10$ degrees, $\vec{P}_{8/1,z} = -5$ meters, with a combined sinusoidal forcing function of $\mathbf{x}_s = 1$ meter at a period of 8.75 seconds, $\mathbf{z}_s = 1$ meter at a period of 10 seconds, and $\theta_s = 5^\circ$ at a period of 7.0 seconds.)	122
Figure 89. Free-body diagram of the left-side jib for purposes of deriving the torque equations.	126
Figure 90. Plot of hoist cable tensions, F_1 and F_2 , for the inverse kinematic control case with dynamically changing torques and cable tension values used as the weights in the minimum norm solution. (Simulation parameters: $\rho = 10$ degrees, $\vec{P}_{8/1,z} = 5$ meters, and $\mathbf{x}_s = 1$ meter at a period of 8.75 seconds.)	130

Figure 91. Plot of x , z , and θ time histories for the inverse kinematic control case with constant torques and cable tension values used as the weights in the minimum norm solution. The constant values chosen were the maximums observed during a simulation of the same conditions using the identity matrix as the weighting elements. (Simulation parameters: $\rho = 10$ degrees, $\vec{P}_{8/1,z} = 5$ meters, and $\mathbf{x}_s = 1$ meter at a period of 8.75 seconds.)	131
Figure 92. Plot of time histories for the inertial hoist-fall angle, ρ , for the inverse kinematic control case with constant torques and cable tension values used as the weights in the minimum norm solution. The constant values chosen were the maximums observed during a simulation of the same conditions using the identity matrix as the weighting elements. (Simulation parameters: $\rho = 10$ degrees, $\vec{P}_{8/1,z} = 5$ meters, and $\mathbf{x}_s = 1$ meter at a period of 8.75 seconds.)	132
Figure 93. Plots of β , $\dot{\beta}$, L_h , and \dot{L}_h for the inverse kinematic control case with constant torques and cable tension values used as the weights in the minimum norm solution. The constant values chosen were the maximums observed during a simulation of the same conditions using the identity matrix as the weighting elements. (Simulation parameters: $\rho = 10$ degrees, $\vec{P}_{8/1,z} = 5$ meters, and $\mathbf{x}_s = 1$ meter at a period of 8.75 seconds.)	133
Figure 94. Plot of hoist cable tensions, F_1 and F_2 , for the inverse kinematic control case with constant torques and cable tension values used as the weights in the minimum norm solution. The constant values chosen were the maximums observed during a simulation of the same conditions using the identity matrix as the weighting elements. (Simulation parameters: $\rho = 10$ degrees, $\vec{P}_{8/1,z} = 5$ meters, and $\mathbf{x}_s = 1$ meter at a period of 8.75 seconds.)	134
Figure 95. Plot of instantaneous power for the inverse kinematic control case with constant torques and cable tension values used as the weights in the minimum norm solution. The constant values chosen were the maximums observed during a simulation of the same conditions using the identity matrix as the weighting elements. (Simulation parameters: $\rho = 10$ degrees, $\vec{P}_{8/1,z} = 5$ meters, and $\mathbf{x}_s = 1$ meter at a period of 8.75 seconds.)	135
Figure 96. Plot of x , z , and θ time histories for the inverse kinematic control case with the identity matrix used as the weights in the minimum norm solution. (Simulation parameters: $\rho = 10$ degrees, $\vec{P}_{8/1,z} = 5$ meters, and $\mathbf{x}_s = 1$ meter at a period of 8.75 seconds.)	136

Figure 97. Plot of time histories for the inertial hoist-fall angle, ρ , for the inverse kinematic control case with the identity matrix used as the weights in the minimum norm solution. (Simulation parameters: $\rho = 10$ degrees, $\vec{P}_{8/1,z} = 5$ meters, and $\mathbf{x}_s = 1$ meter at a period of 8.75 seconds.)	137
Figure 98. Plots of β , $\dot{\beta}$, L_h , and \dot{L}_h for the inverse kinematic control case with the identity matrix used as the weights in the minimum norm solution. (Simulation parameters: $\rho = 10$ degrees, $\vec{P}_{8/1,z} = 5$ meters, and $\mathbf{x}_s = 1$ meter at a period of 8.75 seconds.)	138
Figure 99. Plot of hoist cable tensions, F_1 and F_2 , for the inverse kinematic control case with the identity matrix used as the weights in the minimum norm solution. (Simulation parameters: $\rho = 10$ degrees, $\vec{P}_{8/1,z} = 5$ meters, and $\mathbf{x}_s = 1$ meter at a period of 8.75 seconds.)	139
Figure 100. Plot of instantaneous power for the inverse kinematic control case with the identity matrix used as the weights in the minimum norm solution. (Simulation parameters: $\rho = 10$ degrees, $\vec{P}_{8/1,z} = 5$ meters, and $\mathbf{x}_s = 1$ meter at a period of 8.75 seconds.)	140
Figure 101. Plot of x , z , and θ time histories for the inverse kinematic control case with the weighting on $\dot{\beta}_1$ set to $1.0e+06$ in the minimum norm solution. (Simulation parameters: $\rho = 10$ degrees, $\vec{P}_{8/1,z} = -5$ meters, with a combined sinusoidal forcing function of $\mathbf{x}_s = 1$ meter at a period of 8.75 seconds, $\mathbf{z}_s = 1$ meter at a period of 10 seconds, and $\theta_s = 5^\circ$ at a period of 7.0 seconds.)	141
Figure 102. Plots of β , $\dot{\beta}$, L_h , and \dot{L}_h time histories for the inverse kinematic control case with the weighting on $\dot{\beta}_1$ set to $1.0e+06$ in the minimum norm solution. (Simulation parameters: $\rho = 10$ degrees, $\vec{P}_{8/1,z} = -5$ meters, with a combined sinusoidal forcing function of $\mathbf{x}_s = 1$ meter at a period of 8.75 seconds, $\mathbf{z}_s = 1$ meter at a period of 10 seconds, and $\theta_s = 5^\circ$ at a period of 7.0 seconds.)	142
Figure 103. Plot of time histories for the inertial hoist-fall angle, ρ , for the inverse kinematic control case with the weighting on $\dot{\beta}_1$ set to $1.0e+06$ in the minimum norm solution. (Simulation parameters: $\rho = 10$ degrees, $\vec{P}_{8/1,z} = -5$ meters, with a combined sinusoidal forcing function of $\mathbf{x}_s = 1$ meter at a period of 8.75 seconds, $\mathbf{z}_s = 1$ meter at a period of 10 seconds, and $\theta_s = 5^\circ$ at a period of 7.0 seconds.)	143
Figure 104. Plot of hoist cable tensions, F_1 and F_2 , for the inverse kinematic control case with the weighting on $\dot{\beta}_1$ set to $1.0e+06$ in the minimum norm solution. (Simulation parameters: $\rho = 10$ degrees, $\vec{P}_{8/1,z} = -5$ meters, with a combined sinusoidal forcing function of $\mathbf{x}_s = 1$ meter at a period of 8.75 seconds, $\mathbf{z}_s = 1$ meter at a period of 10 seconds, and $\theta_s = 5^\circ$ at a period of 7.0 seconds.)	144

Figure 105. Plot of time histories for instantaneous power for the inverse kinematic control case with the weighting on $\dot{\beta}_1$ set to 1.0e+06 in the minimum norm solution. (Simulation parameters: $\rho = 10$ degrees, $\vec{P}_{8/1,z} = -5$ meters, with a combined sinusoidal forcing function of $\mathbf{x}_s = 1$ meter at a period of 8.75 seconds, $\mathbf{z}_s = 1$ meter at a period of 10 seconds, and $\theta_s = 5^\circ$ at a period of 7.0 seconds.)	145
Figure 106. Plot of x , z , and θ time histories for the inverse kinematic control case with the identity matrix used as the weights in the minimum norm solution. (Simulation parameters: $\rho = 10$ degrees, $\vec{P}_{8/1,z} = -5$ meters, with a combined sinusoidal forcing function of $\mathbf{x}_s = 1$ meter at a period of 8.75 seconds, $\mathbf{z}_s = 1$ meter at a period of 10 seconds, and $\theta_s = 5^\circ$ at a period of 7.0 seconds.)	146
Figure 107. Plots of β , $\dot{\beta}$, L_h , and \dot{L}_h time histories for the inverse kinematic control case with the identity matrix used as the weights in the minimum norm solution. (Simulation parameters: $\rho = 10$ degrees, $\vec{P}_{8/1,z} = -5$ meters, with a combined sinusoidal forcing function of $\mathbf{x}_s = 1$ meter at a period of 8.75 seconds, $\mathbf{z}_s = 1$ meter at a period of 10 seconds, and $\theta_s = 5^\circ$ at a period of 7.0 seconds.)	147
Figure 108. Plot of time histories for the inertial hoist-fall angle, ρ , for the inverse kinematic control case with the identity matrix used as the weights in the minimum norm solution. (Simulation parameters: $\rho = 10$ degrees, $\vec{P}_{8/1,z} = -5$ meters, with a combined sinusoidal forcing function of $\mathbf{x}_s = 1$ meter at a period of 8.75 seconds, $\mathbf{z}_s = 1$ meter at a period of 10 seconds, and $\theta_s = 5^\circ$ at a period of 7.0 seconds.)	148
Figure 109. Plot of hoist cable tensions, F_1 and F_2 , for the inverse kinematic control case with the identity matrix used as the weights in the minimum norm solution. (Simulation parameters: $\rho = 10$ degrees, $\vec{P}_{8/1,z} = -5$ meters, with a combined sinusoidal forcing function of $\mathbf{x}_s = 1$ meter at a period of 8.75 seconds, $\mathbf{z}_s = 1$ meter at a period of 10 seconds, and $\theta_s = 5^\circ$ at a period of 7.0 seconds.)	149
Figure 110. Plot of time histories for instantaneous power for the inverse kinematic control case with the identity matrix used as the weights in the minimum norm solution. (Simulation parameters: $\rho = 10$ degrees, $\vec{P}_{8/1,z} = -5$ meters, with a combined sinusoidal forcing function of $\mathbf{x}_s = 1$ meter at a period of 8.75 seconds, $\mathbf{z}_s = 1$ meter at a period of 10 seconds, and $\theta_s = 5^\circ$ at a period of 7.0 seconds.)	150
Figure 111. Plot of x , z , and θ time histories for the inverse kinematic control case with the weighting on $\dot{\beta}_2$ set to 1.0e+03 in the minimum norm solution. (Simulation parameters: $\rho = 10$ degrees, $\vec{P}_{8/1,z} = -5$ meters, with a combined sinusoidal forcing function of $\mathbf{x}_s = 1$ meter at a period of 8.75 seconds, $\mathbf{z}_s = 1$ meter at a period of 10 seconds, and $\theta_s = 5^\circ$ at a period of 7.0 seconds.)	151

Figure 112. Plots of β , $\dot{\beta}$, L_h , and \dot{L}_h time histories for the inverse kinematic control case with the weighting on $\dot{\beta}_2$ set to 1.0e+03 in the minimum norm solution. (Simulation parameters: $\rho = 10$ degrees, $\vec{P}_{8/1,z} = -5$ meters, with a combined sinusoidal forcing function of $\mathbf{x}_s = 1$ meter at a period of 8.75 seconds, $\mathbf{z}_s = 1$ meter at a period of 10 seconds, and $\theta_s = 5^\circ$ at a period of 7.0 seconds.)	152
Figure 113. Plot of hoist cable tensions, F_1 and F_2 , for the inverse kinematic control case with the weighting on $\dot{\beta}_2$ set to 1.0e+03 in the minimum norm solution. (Simulation parameters: $\rho = 10$ degrees, $\vec{P}_{8/1,z} = -5$ meters, with a combined sinusoidal forcing function of $\mathbf{x}_s = 1$ meter at a period of 8.75 seconds, $\mathbf{z}_s = 1$ meter at a period of 10 seconds, and $\theta_s = 5^\circ$ at a period of 7.0 seconds.)	153
Figure 114. Plot of time histories for instantaneous power for the inverse kinematic control case with the weighting on $\dot{\beta}_2$ set to 1.0e+03 in the minimum norm solution. (Simulation parameters: $\rho = 10$ degrees, $\vec{P}_{8/1,z} = -5$ meters, with a combined sinusoidal forcing function of $\mathbf{x}_s = 1$ meter at a period of 8.75 seconds, $\mathbf{z}_s = 1$ meter at a period of 10 seconds, and $\theta_s = 5^\circ$ at a period of 7.0 seconds.)	154
Figure 115. Plot of x , z , and θ time histories for the inverse kinematic control case with the weighting on \dot{L}_{h2} set to 1.0e+06 in the minimum norm solution. (Simulation parameters: $\rho = 10$ degrees, $\vec{P}_{8/1,z} = -5$ meters, with a combined sinusoidal forcing function of $\mathbf{x}_s = 1$ meter at a period of 8.75 seconds, $\mathbf{z}_s = 1$ meter at a period of 10 seconds, and $\theta_s = 5^\circ$ at a period of 7.0 seconds.)	155
Figure 116. Plots of β , $\dot{\beta}$, L_h , and \dot{L}_h time histories for the inverse kinematic control case with the weighting on \dot{L}_{h2} set to 1.0e+06 in the minimum norm solution. (Simulation parameters: $\rho = 10$ degrees, $\vec{P}_{8/1,z} = -5$ meters, with a combined sinusoidal forcing function of $\mathbf{x}_s = 1$ meter at a period of 8.75 seconds, $\mathbf{z}_s = 1$ meter at a period of 10 seconds, and $\theta_s = 5^\circ$ at a period of 7.0 seconds.)	156
Figure 117. Plot of time histories for the inertial hoist-fall angle, ρ , for the inverse kinematic control case with the weighting on \dot{L}_{h2} set to 1.0e+06 in the minimum norm solution. (Simulation parameters: $\rho = 10$ degrees, $\vec{P}_{8/1,z} = -5$ meters, with a combined sinusoidal forcing function of $\mathbf{x}_s = 1$ meter at a period of 8.75 seconds, $\mathbf{z}_s = 1$ meter at a period of 10 seconds, and $\theta_s = 5^\circ$ at a period of 7.0 seconds.)	157
Figure 118. Plot of hoist cable tensions, F_1 and F_2 , for the inverse kinematic control case with the weighting on \dot{L}_{h2} set to 1.0e+06 in the minimum norm solution. (Simulation parameters: $\rho = 10$ degrees, $\vec{P}_{8/1,z} = -5$ meters, with a combined sinusoidal forcing function of $\mathbf{x}_s = 1$ meter at a period of 8.75 seconds, $\mathbf{z}_s = 1$ meter at a period of 10 seconds, and $\theta_s = 5^\circ$ at a period of 7.0 seconds.)	158

Figure 119. Plot of time histories for instantaneous power for the inverse kinematic control case with the weighting on \dot{L}_{h2} set to 1.0e+06 in the minimum norm solution. (Simulation parameters: $\rho = 10$ degrees, $\vec{P}_{8/1,z} = -5$ meters, with a combined sinusoidal forcing function of $\mathbf{x}_s = 1$ meter at a period of 8.75 seconds, $\mathbf{z}_s = 1$ meter at a period of 10 seconds, and $\theta_s = 5^\circ$ at a period of 7.0 seconds.)	159
Figure 120. Plot of x , z , and θ time histories for the inverse kinematic control case using weights that match the units of the actuators in the minimum norm solution. (Simulation parameters: $\rho = 10$ degrees, $\vec{P}_{8/1,z} = -5$ meters, and $\mathbf{x}_s = 1$ meter at a period of 8.75 seconds.)	160
Figure 121. Plot of time histories for the inertial hoist-fall angle, ρ , for the inverse kinematic control case using weights that match the units of the actuators in the minimum norm solution. (Simulation parameters: $\rho = 10$ degrees, $\vec{P}_{8/1,z} = 5$ meters, and $\mathbf{x}_s = 1$ meter at a period of 8.75 seconds.)	161
Figure 122. Plots of β , $\dot{\beta}$, L_h , and \dot{L}_h for the inverse kinematic control case using weights that match the units of the actuators in the minimum norm solution. (Simulation parameters: $\rho = 10$ degrees, $\vec{P}_{8/1,z} = 5$ meters, and $\mathbf{x}_s = 1$ meter at a period of 8.75 seconds.)	162
Figure 123. Plot of hoist cable tensions, F_1 and F_2 , for the inverse kinematic control case using weights that match the units of the actuators in the minimum norm solution. (Simulation parameters: $\rho = 10$ degrees, $\vec{P}_{8/1,z} = 5$ meters, and $\mathbf{x}_s = 1$ meter at a period of 8.75 seconds.)	163
Figure 124. Plot of instantaneous power for the inverse kinematic control case using weights that match the units of the actuators in the minimum norm solution. (Simulation parameters: $\rho = 10$ degrees, $\vec{P}_{8/1,z} = 5$ meters, and $\mathbf{x}_s = 1$ meter at a period of 8.75 seconds.)	164
Figure 125. Plot of x , z , and θ time histories for the inverse kinematic control case using weights selected in accordance with the method of Franklin & Powell in the minimum norm solution. (Simulation parameters: $\rho = 10$ degrees, $\vec{P}_{8/1,z} = -5$ meters, with a combined sinusoidal forcing function of $\mathbf{x}_s = 1$ meter at a period of 8.75 seconds, $\mathbf{z}_s = 1$ meter at a period of 10 seconds, and $\theta_s = 5^\circ$ at a period of 7.0 seconds.)	165
Figure 126. Plot of time histories for the inertial hoist-fall angle, ρ , for the inverse kinematic control case using weights selected in accordance with the method of Franklin & Powell in the minimum norm solution. (Simulation parameters: $\rho = 10$ degrees, $\vec{P}_{8/1,z} = -5$ meters, with a combined sinusoidal forcing function of $\mathbf{x}_s = 1$ meter at a period of 8.75 seconds, $\mathbf{z}_s = 1$ meter at a period of 10 seconds, and $\theta_s = 5^\circ$ at a period of 7.0 seconds.)	166

Figure 127. Plots of β , $\dot{\beta}$, L_h , and \dot{L}_h for the inverse kinematic control case using weights selected in accordance with the method of Franklin & Powell in the minimum norm solution. (Simulation parameters: $\rho = 10$ degrees, $\vec{P}_{8/1,z} = -5$ meters, with a combined sinusoidal forcing function of $x_s = 1$ meter at a period of 8.75 seconds, $z_s = 1$ meter at a period of 10 seconds, and $\theta_s = 5^\circ$ at a period of 7.0 seconds.)	167
Figure 128. Plot of hoist cable tensions, F_1 and F_2 , for the inverse kinematic control case using weights selected in accordance with the method of Franklin & Powell in the minimum norm solution. (Simulation parameters: $\rho = 10$ degrees, $\vec{P}_{8/1,z} = -5$ meters, with a combined sinusoidal forcing function of $x_s = 1$ meter at a period of 8.75 seconds, $z_s = 1$ meter at a period of 10 seconds, and $\theta_s = 5^\circ$ at a period of 7.0 seconds.)	168
Figure 129. Plot of instantaneous power for the inverse kinematic control case using weights selected in accordance with the method of Franklin & Powell in the minimum norm solution. (Simulation parameters: $\rho = 10$ degrees, $\vec{P}_{8/1,z} = -5$ meters, with a combined sinusoidal forcing function of $x_s = 1$ meter at a period of 8.75 seconds, $z_s = 1$ meter at a period of 10 seconds, and $\theta_s = 5^\circ$ at a period of 7.0 seconds.)	169
Figure 130. Cross-plot of the performance metrics J_{rate} and J_{power} for a range of conditions. Conditions are identified by run number in Table 4.	172
Figure 131. 3-Dimensional plot of the performance metrics J_{rate} , J_{power} , and $J_{L+\theta}$ for simulation runs 03 through 08. The relative value of $J_{L+\theta}$ can be discerned from the vertical line projected down to the J_{rate} - J_{power} plane. Simulation conditions are identified by run number in Table 4.	177
Figure 132. Cross-plot of the performance metrics J_{rate} and J_{power} for simulation runs 12J through 30J. Simulation conditions are identified by run number in Table 4.	178
Figure 133. 3-Dimensional plot of the performance metrics J_{rate} , J_{power} , and $J_{L+\theta}$ for simulation runs 12J through 30J. The relative value of $J_{L+\theta}$ can be discerned from the vertical line projected down to the J_{rate} - J_{power} plane. Simulation conditions are identified by run number in Table 4.	179
Figure 134. Cross-plot of the performance metrics J_{rate} and J_{power} for simulation runs 31 through 38. Simulation conditions are identified by run number in Table 4.	180

Figure 135. 3-Dimensional plot of the performance metrics J_{rate} , J_{power} , and $J_{L+\theta}$ for simulation runs 31 through 38. The relative value of $J_{L+\theta}$ can be discerned from the vertical line projected down to the J_{rate} - J_{power} plane. Simulation conditions are identified by run number in Table 4.	181
Figure 136. Calibration curve relating surge input amplitude for a 8.75 second period sinusoidal input to the calculated displacement metric values, $J_{L+\theta}$	182
Figure 137. Photograph of the 1/32-scale dual-crane configuration mounted on the motion platform. Note the reference target on the payload for use with the motion capture system.	186
Figure 138. Photograph of the 1/32-scale dual-crane configuration mounted on the motion platform. Note the reference target on the payload for use with the motion capture system.	187
Figure 139. Digital Motion Analysis System-6 (DMAS6) brochure.	189
Figure 140. Motion capture system - camera brochure.	190
Figure 141. Digital Motion Analysis System-6 (DMAS6) Specification sheet.	191
Figure 142. Surge time histories for simulated, scale-model, and input data for the uncontrolled case. (Simulation parameters: $\rho = 0$ degrees, $\vec{P}_{8/1,z} = 12.7$ mm, with a sinusoidal forcing function of $x_s = 31.25$ mm at a period of 2.65 seconds.)	192
Figure 143. Heave time histories for simulated, scale-model, and input data for the uncontrolled case. (Simulation parameters: $\rho = 0$ degrees, $\vec{P}_{8/1,z} = 12.7$ mm, with a sinusoidal forcing function of $x_s = 31.25$ mm at a period of 2.65 seconds.)	193
Figure 144. Pitch angle time histories for simulated, scale-model, and input data for the uncontrolled case. (Simulation parameters: $\rho = 0$ degrees, $\vec{P}_{8/1,z} = 12.7$ mm, with a sinusoidal forcing function of $x_s = 31.25$ mm at a period of 2.65 seconds.)	194
Figure 145. Out-of-plane (sway) time histories for simulated, scale-model, and input data for the uncontrolled case. The magnitude of the out-of-plane motion is about 10% of the primary forced response in surge. (Simulation parameters: $\rho = 0$ degrees, $\vec{P}_{8/1,z} = 12.7$ mm, with a sinusoidal forcing function of $x_s = 31.25$ mm at a period of 2.65 seconds.)	195
Figure 146. Surge time histories for simulated, scale-model, and input data for the controlled case. (Simulation parameters: $\rho = 0$ degrees, $\vec{P}_{8/1,z} = 12.7$ mm, with a sinusoidal forcing function of $x_s = 31.25$ mm at a period of 2.65 seconds.)	196

Figure 147. Heave time histories for simulated, scale-model, and input data for the controlled case. (Simulation parameters: $\rho = 0$ degrees, $\vec{P}_{8/1,z} = 12.7$ mm, with a sinusoidal forcing function of $\mathbf{x}_s = 31.25$ mm at a period of 2.65 seconds.)	197
Figure 148. Pitch angle time histories for simulated, scale-model, and input data for the controlled case. (Simulation parameters: $\rho = 0$ degrees, $\vec{P}_{8/1,z} = 12.7$ mm, with a sinusoidal forcing function of $\mathbf{x}_s = 31.25$ mm at a period of 2.65 seconds.)	198
Figure 149. Out-of-plane (sway) time histories for simulated, scale-model, and input data for the controlled case. The magnitude of the peaks of the out-of-plane motion is about 20% of the primary forced response in surge. (Simulation parameters: $\rho = 0$ degrees, $\vec{P}_{8/1,z} = 12.7$ mm, with a sinusoidal forcing function of $\mathbf{x}_s = 31.25$ mm at a period of 2.65 seconds.)	199
Figure 150. Surge time histories for simulated, scale-model, and input data for the uncontrolled case. (Simulation parameters: $\rho = 10$ degrees, $\vec{P}_{8/1,z} = 12.7$ mm, with a sinusoidal forcing function of $\mathbf{x}_s = 31.25$ mm at a period of 2.65 seconds.)	200
Figure 151. Heave time histories for simulated, scale-model, and input data for the uncontrolled case. (Simulation parameters: $\rho = 10$ degrees, $\vec{P}_{8/1,z} = 12.7$ mm, with a sinusoidal forcing function of $\mathbf{x}_s = 31.25$ mm at a period of 2.65 seconds.)	201
Figure 152. Pitch angle time histories for simulated, scale-model, and input data for the uncontrolled case. (Simulation parameters: $\rho = 10$ degrees, $\vec{P}_{8/1,z} = 12.7$ mm, with a sinusoidal forcing function of $\mathbf{x}_s = 31.25$ mm at a period of 2.65 seconds.)	202
Figure 153. Out-of-plane (sway) time histories for simulated, scale-model, and input data for the uncontrolled case. The magnitude of the out-of-plane motion is about 5% of the primary forced response in surge. (Simulation parameters: $\rho = 10$ degrees, $\vec{P}_{8/1,z} = 12.7$ mm, with a sinusoidal forcing function of $\mathbf{x}_s = 31.25$ mm at a period of 2.65 seconds.)	203
Figure 154. Surge time histories for simulated, scale-model, and input data for the controlled case. (Simulation parameters: $\rho = 10$ degrees, $\vec{P}_{8/1,z} = 12.7$ mm, with a sinusoidal forcing function of $\mathbf{x}_s = 31.25$ mm at a period of 2.65 seconds.)	204
Figure 155. Heave time histories for simulated, scale-model, and input data for the controlled case. (Simulation parameters: $\rho = 10$ degrees, $\vec{P}_{8/1,z} = 12.7$ mm, with a sinusoidal forcing function of $\mathbf{x}_s = 31.25$ mm at a period of 2.65 seconds.)	205

Figure 156. Pitch angle time histories for simulated, scale-model, and input data for the controlled case. (Simulation parameters: $\rho = 10$ degrees, $\vec{P}_{8/1,z} = 12.7$ mm, with a sinusoidal forcing function of $\mathbf{x}_s = 31.25$ mm at a period of 2.65 seconds.)	206
Figure 157. Out-of-plane (sway) time histories for simulated, scale-model, and input data for the controlled case. The magnitude of the peaks of the out-of-plane motion is about 15% of the primary forced response in surge. (Simulation parameters: $\rho = 10$ degrees, $\vec{P}_{8/1,z} = 12.7$ mm, with a sinusoidal forcing function of $\mathbf{x}_s = 31.25$ mm at a period of 2.65 seconds.)	207
Figure 158. Surge time histories for simulated, scale-model, and input data for the uncontrolled case. (Simulation parameters: $\rho = 0$ degrees, $\vec{P}_{8/1,z} = 12.7$ mm, with a sinusoidal forcing function of $\mathbf{z}_s = 31.25$ mm at a period of 2.65 seconds.)	208
Figure 159. Heave time histories for simulated, scale-model, and input data for the uncontrolled case. (Simulation parameters: $\rho = 0$ degrees, $\vec{P}_{8/1,z} = 12.7$ mm, with a sinusoidal forcing function of $\mathbf{z}_s = 31.25$ mm at a period of 2.65 seconds.)	209
Figure 160. Pitch angle time histories for simulated, scale-model, and input data for the uncontrolled case. (Simulation parameters: $\rho = 0$ degrees, $\vec{P}_{8/1,z} = 12.7$ mm, with a sinusoidal forcing function of $\mathbf{x}_s = 31.25$ mm at a period of 2.65 seconds.)	210
Figure 161. Out-of-plane (sway) time histories for simulated, scale-model, and input data for the uncontrolled case. The magnitude of the out-of-plane motion is about 33% of the primary forced response in heave. (Simulation parameters: $\rho = 0$ degrees, $\vec{P}_{8/1,z} = 12.7$ mm, with a sinusoidal forcing function of $\mathbf{x}_s = 31.25$ mm at a period of 2.65 seconds.)	211
Figure 162. Surge time histories for simulated, scale-model, and input data for the controlled case. (Simulation parameters: $\rho = 0$ degrees, $\vec{P}_{8/1,z} = 12.7$ mm, with a sinusoidal forcing function of $\mathbf{z}_s = 31.25$ mm at a period of 2.65 seconds.)	212
Figure 163. Heave time histories for simulated, scale-model, and input data for the controlled case. (Simulation parameters: $\rho = 0$ degrees, $\vec{P}_{8/1,z} = 12.7$ mm, with a sinusoidal forcing function of $\mathbf{z}_s = 31.25$ mm at a period of 2.65 seconds.)	213
Figure 164. Pitch angle time histories for simulated, scale-model, and input data for the controlled case. (Simulation parameters: $\rho = 0$ degrees, $\vec{P}_{8/1,z} = 12.7$ mm, with a sinusoidal forcing function of $\mathbf{z}_s = 31.25$ mm at a period of 2.65 seconds.)	214

Figure 165. Out-of-plane (sway) time histories for simulated, scale-model, and input data for the controlled case. The magnitude of the peaks of the out-of-plane motion is about +/-10mm about 5 times the magnitude of the primary forced response in heave. (Simulation parameters: $\rho = 0$ degrees, $\vec{P}_{8/1,z} = 12.7$ mm, with a sinusoidal forcing function of $z_s = 31.25$ mm at a period of 2.65 seconds.)	215
Figure 166. Surge time histories for simulated, scale-model, and input data for the uncontrolled case. (Simulation parameters: $\rho = 0$ degrees, $\vec{P}_{8/1,z} = 12.7$ mm, with a sinusoidal forcing function of $\theta_s = 5^\circ$ at a period of 2.12 seconds.)	216
Figure 167. Heave time histories for simulated, scale-model, and input data for the uncontrolled case. (Simulation parameters: $\rho = 0$ degrees, $\vec{P}_{8/1,z} = 12.7$ mm, with a sinusoidal forcing function of $\theta_s = 5^\circ$ at a period of 2.12 seconds.)	217
Figure 168. Pitch angle time histories for simulated, scale-model, and input data for the uncontrolled case. (Simulation parameters: $\rho = 0$ degrees, $\vec{P}_{8/1,z} = 12.7$ mm, with a sinusoidal forcing function of $\theta_s = 5^\circ$ at a period of 2.12 seconds.)	218
Figure 169. Out-of-plane (sway) time histories for simulated, scale-model, and input data for the uncontrolled case. The magnitude of the out-of-plane motion is about +/-20 mm. (Simulation parameters: $\rho = 0$ degrees, $\vec{P}_{8/1,z} = 12.7$ mm, with a sinusoidal forcing function of $\theta_s = 5^\circ$ at a period of 2.12 seconds.)	219
Figure 170. Surge time histories for simulated, scale-model, and input data for the controlled case. (Simulation parameters: $\rho = 0$ degrees, $\vec{P}_{8/1,z} = 12.7$ mm, with a sinusoidal forcing function of $\theta_s = 5^\circ$ at a period of 2.12 seconds.)	220
Figure 171. Heave time histories for simulated, scale-model, and input data for the controlled case. (Simulation parameters: $\rho = 0$ degrees, $\vec{P}_{8/1,z} = 12.7$ mm, with a sinusoidal forcing function of $\theta_s = 5^\circ$ at a period of 2.12 seconds.)	221
Figure 172. Pitch angle time histories for simulated, scale-model, and input data for the controlled case. (Simulation parameters: $\rho = 0$ degrees, $\vec{P}_{8/1,z} = 12.7$ mm, with a sinusoidal forcing function of $\theta_s = 5^\circ$ at a period of 2.12 seconds.)	222
Figure 173. Out-of-plane (sway) time histories for simulated, scale-model, and input data for the controlled case. The magnitude of the peaks of the out-of-plane motion is about +/-40mm. (Simulation parameters: $\rho = 0$ degrees, $\vec{P}_{8/1,z} = 12.7$ mm, with a sinusoidal forcing function of $\theta_s = 5^\circ$ at a period of 2.12 seconds.)	223

Figure 174. Surge time histories for simulated, scale-model, and input data for the uncontrolled case. (Simulation parameters: $\rho = 0$ degrees, $\vec{P}_{8/1,z} = 12.7$ mm, with a sinusoidal forcing function of $x_s = 31.25$ mm at a period of 2.65 seconds, $z_s = 31.25$ mm at a period of 2.65 seconds, and $\theta_s = 5^\circ$ at a period of 2.12 seconds.)	224
Figure 175. Heave time histories for simulated, scale-model, and input data for the uncontrolled case. (Simulation parameters: $\rho = 0$ degrees, $\vec{P}_{8/1,z} = 12.7$ mm, with a sinusoidal forcing function of $x_s = 31.25$ mm at a period of 2.65 seconds, $z_s = 31.25$ mm at a period of 2.65 seconds, and $\theta_s = 5^\circ$ at a period of 2.12 seconds.)	225
Figure 176. Pitch angle time histories for simulated, scale-model, and input data for the uncontrolled case. (Simulation parameters: $\rho = 0$ degrees, $\vec{P}_{8/1,z} = 12.7$ mm, with a sinusoidal forcing function of $x_s = 31.25$ mm at a period of 2.65 seconds, $z_s = 31.25$ mm at a period of 2.65 seconds, and $\theta_s = 5^\circ$ at a period of 2.12 seconds.)	226
Figure 177. Out-of-plane (sway) time histories for simulated, scale-model, and input data for the uncontrolled case. The magnitude of the out-of-plane motion is about +/-20 mm. (Simulation parameters: $\rho = 0$ degrees, $\vec{P}_{8/1,z} = 12.7$ mm, with a sinusoidal forcing function of $x_s = 31.25$ mm at a period of 2.65 seconds, $z_s = 31.25$ mm at a period of 2.65 seconds, and $\theta_s = 5^\circ$ at a period of 2.12 seconds.)	227
Figure 178. Surge time histories for simulated, scale-model, and input data for the controlled case. (Simulation parameters: $\rho = 0$ degrees, $\vec{P}_{8/1,z} = 12.7$ mm, with a sinusoidal forcing function of $x_s = 31.25$ mm at a period of 2.65 seconds, $z_s = 31.25$ mm at a period of 2.65 seconds, and $\theta_s = 5^\circ$ at a period of 2.12 seconds.)	228
Figure 179. Heave time histories for simulated, scale-model, and input data for the controlled case. (Simulation parameters: $\rho = 0$ degrees, $\vec{P}_{8/1,z} = 12.7$ mm, with a sinusoidal forcing function of $x_s = 31.25$ mm at a period of 2.65 seconds, $z_s = 31.25$ mm at a period of 2.65 seconds, and $\theta_s = 5^\circ$ at a period of 2.12 seconds.)	229
Figure 180. Pitch angle time histories for simulated, scale-model, and input data for the controlled case. (Simulation parameters: $\rho = 0$ degrees, $\vec{P}_{8/1,z} = 12.7$ mm, with a sinusoidal forcing function of $x_s = 31.25$ mm at a period of 2.65 seconds, $z_s = 31.25$ mm at a period of 2.65 seconds, and $\theta_s = 5^\circ$ at a period of 2.12 seconds.)	230

Figure 181. Out-of-plane (sway) time histories for simulated, scale-model, and input data for the controlled case. The magnitude of the peaks of the out-of-plane motion is about +/-40mm. (Simulation parameters: $\rho = 0$ degrees, $\vec{P}_{8/1,z} = 12.7$ mm, with a sinusoidal forcing function of $x_s = 31.25$ mm at a period of 2.65 seconds, $z_s = 31.25$ mm at a period of 2.65 seconds, and $\theta_s = 5^\circ$ at a period of 2.12 seconds.)	231
Figure 182. Photograph of jib top of scale crane model showing warping. This warping may produce out-of-plane motion during controlled cases with significant luffing and hoisting motion.	232
Figure 183. Time history of the payload motion for a 0.1 meter, 8.05 second period surge motion excitation with initial $\rho = -10.0$ degree. The blue trace is the ship motion and the payload response is shown in green. The maximum x and z displacements are reduced slightly. The payload rotation, θ_p is no longer small.	240
Figure 184. Time history of the inertial hoist fall angles, ρ_{I1} and ρ_{I2} for a 0.1 meter, 8.05 second period surge motion excitation with initial $\rho = -10$ degrees. The peak ρ angle response is more than 20 degrees on either side of the initial offset.	240
Figure 185. Time history of the calculation of the displacement metrics for a 0.1 meter, 8.05 second period surge motion excitation with initial $\rho = -10.0$ degree. Note that payload rotation is no longer zero, so J_θ is nonzero and there is a separation between J_l and $J_{l+\theta}$ and the sum of J_l and J_θ	241
Figure 186. Time history of the payload motion for a 0.1 meter, 8.05 second period surge motion excitation with initial $\rho = -7.5$ degree. The blue trace is the ship motion and the payload response is shown in green.	241
Figure 187. Time history of the inertial hoist fall angles, ρ_{I1} and ρ_{I2} for a 0.1 meter, 8.05 second period surge motion excitation with initial $\rho = -7.5$ degrees.	242
Figure 188. Time history of the hoist cable tensions, F_1 and F_2 in metric tons for a 0.1 meter, 8.05 second period surge motion excitation with initial $\rho = -7.5$ degrees.	242
Figure 189. Time history of the calculation of the displacement metrics for a 0.1 meter, 8.05 second period surge motion excitation with initial $\rho = -7.5$ degree. Note that payload rotation is no longer zero, so J_θ is nonzero and there is a separation between J_l and $J_{l+\theta}$ and the sum of J_l and J_θ	243
Figure 190. Time history of the payload motion for a 0.1 meter, 8.05 second period surge motion excitation with initial $\rho = -5.0$ degree. The blue trace is the ship motion and the payload response is shown in green.	243

Figure 191. Time history of the inertial hoist fall angles, ρ_{I1} and ρ_{I2} for a 0.1 meter, 8.05 second period surge motion excitation with initial $\rho = -5.0$ degrees.	244
Figure 192. Time history of the hoist cable tensions, F_1 and F_2 in metric tons for a 0.1 meter, 8.05 second period surge motion excitation with initial $\rho = -5.0$ degrees.	244
Figure 193. Time history of the calculation of the displacement metrics for a 0.1 meter, 8.05 second period surge motion excitation with initial $\rho = -5.0$ degree. Note that payload rotation is no longer zero, so J_θ is nonzero and there is a separation between J_l and $J_{l+\theta}$ and the sum of J_l and J_θ	245
Figure 194. Time history of the payload motion for a 0.1 meter, 8.05 second period surge motion excitation with initial $\rho = -2.5$ degree. The blue trace is the ship motion and the payload response is shown in green.	246
Figure 195. Time history of the inertial hoist fall angles, ρ_{I1} and ρ_{I2} for a 0.1 meter, 8.05 second period surge motion excitation with initial $\rho = -2.5$ degrees.	247
Figure 196. Time history of the calculation of the displacement metrics for a 0.1 meter, 8.05 second period surge motion excitation with initial $\rho = -5.0$ degree. Note that payload rotation is no longer zero, so J_θ is nonzero and there is a separation between J_l and $J_{l+\theta}$ and the sum of J_l and J_θ	247
Figure 197. Time history of the payload motion for a 0.1 meter, 8.05 second period surge motion excitation with initial $\rho = -1.0$ degree. The blue trace is the ship motion and the payload response is shown in green. The maximum x and z displacements are reduced slightly. Note that the payload rotation, θ_p is small, but not zero as was the case for $\rho = 0$	248
Figure 198. Time history of the inertial hoist fall angles, ρ_{I1} and ρ_{I2} for a 0.1 meter, 8.05 second period surge motion excitation with initial $\rho = -1$ degree. The peak ρ angle response is slightly more than 3.5 degrees for the given input.	248
Figure 199. Time history of the calculation of the displacement metrics for a 0.1 meter, 8.05 second period surge motion excitation with initial $\rho = -1.0$ degree. Note that since the payload rotation is no longer zero, J_θ is nonzero and there is a separation between J_l and $J_{l+\theta}$ and the sum of J_l and J_θ	249

Figure 200. Time history of the payload motion for a 0.1 meter, 8.05 second period surge motion excitation with initial $\rho = 0$ degrees. The blue trace is the ship motion and the payload response is shown in green. Note that the payload rotation, θ_p about its pitch axis is essentially zero.	250
Figure 201. Time history of the inertial hoist fall angles, ρ_{I1} and ρ_{I2} for a 0.1 meter, 8.05 second period surge motion excitation with initial $\rho = 0$ degrees. The peak ρ angle response is slightly more than 3.5 degrees for the given input.	251
Figure 202. Time history of the hoist cable tensions, F_1 and F_2 in metric tons for a 0.1 meter, 8.05 second period surge motion excitation with initial $\rho = 0$ degrees. The peak response is approximately 0.5 percent above the initial (static) tension.	251
Figure 203. Time history of the calculation of the displacement metrics for a 0.1 meter, 8.05 second period surge motion excitation with initial $\rho = 0$ degrees. Note that since the payload rotation is essentially zero, there is no difference between J_l and $J_{l+\theta}$ and the sum of J_l and J_θ	252
Figure 204. Time history of the payload motion for a 0.1 meter, 8.05 second period surge motion excitation with initial $\rho = 1.0$ degree. The blue trace is the ship motion and the payload response is shown in green. The maximum x and z displacements are reduced slightly. Note that the payload rotation, θ_p is small, but not zero as was the case for $\rho = 0$	253
Figure 205. Time history of the inertial hoist fall angles, ρ_{I1} and ρ_{I2} for a 0.1 meter, 8.05 second period surge motion excitation with initial $\rho = 1.0$ degrees.	254
Figure 206. Time history of the calculation of the displacement metrics for a 0.1 meter, 8.05 second period surge motion excitation with initial $\rho = 1.0$ degree. Note that since the payload rotation is no longer zero, J_θ is nonzero and there is a separation between J_l and $J_{l+\theta}$ and the sum of J_l and J_θ	254
Figure 207. Time history of the payload motion for a 0.1 meter, 8.05 second period surge motion excitation with initial $\rho = 2.5$ degree. The blue trace is the ship motion and the payload response is shown in green.	255
Figure 208. Time history of the calculation of the displacement metrics for a 0.1 meter, 8.05 second period surge motion excitation with initial $\rho = 2.5$ degree. Note that payload rotation is no longer zero, so J_θ is nonzero and there is a separation between J_l and $J_{l+\theta}$ and the sum of J_l and J_θ	255

Figure 209. Time history of the payload motion for a 0.1 meter, 8.05 second period surge motion excitation with initial $\rho = 5.0$ degree. The blue trace is the ship motion and the payload response is shown in green.	256
Figure 210. Time history of the inertial hoist fall angles, ρ_{I1} and ρ_{I2} for a 0.1 meter, 8.05 second period surge motion excitation with initial $\rho = 5.0$ degrees.	256
Figure 211. Time history of the hoist cable tensions, F_1 and F_2 in metric tons for a 0.1 meter, 8.05 second period surge motion excitation with initial $\rho = 5.0$ degrees.	257
Figure 212. Time history of the calculation of the displacement metrics for a 0.1 meter, 8.05 second period surge motion excitation with initial $\rho = -5.0$ degree. Note that payload rotation is no longer zero, so J_θ is nonzero and there is a separation between J_l and $J_{l+\theta}$ and the sum of J_l and J_θ	257
Figure 213. Time history of the payload motion for a 0.1 meter, 8.05 second period surge motion excitation with initial $\rho = 10.0$ degree. The blue trace is the ship motion and the payload response is shown in green.	258
Figure 214. Time history of the inertial hoist fall angles, ρ_{I1} and ρ_{I2} for a 0.1 meter, 8.05 second period surge motion excitation with initial $\rho = 10.0$ degrees.	258
Figure 215. Time history of the hoist cable tensions, F_1 and F_2 in metric tons for a 0.1 meter, 8.05 second period surge motion excitation with initial $\rho = 10.0$ degrees.	259
Figure 216. Time history of the calculation of the displacement metrics for a 0.1 meter, 8.05 second period surge motion excitation with initial $\rho = 10.0$ degree. Note that payload rotation is no longer zero, so J_θ is nonzero and there is a separation between J_l and $J_{l+\theta}$ and the sum of J_l and J_θ	259
Figure 217. Time history of the payload motion for a 0.1 meter, 8.05 second period surge motion excitation with initial $\rho = 15.0$ degree. The blue trace is the ship motion and the payload response is shown in green.	260
Figure 218. Time history of the inertial hoist fall angles, ρ_{I1} and ρ_{I2} for a 0.1 meter, 8.05 second period surge motion excitation with initial $\rho = 15.0$ degrees.	261
Figure 219. Time history of the hoist cable tensions, F_1 and F_2 in metric tons for a 0.1 meter, 8.05 second period surge motion excitation with initial $\rho = 15.0$ degrees.	262

Figure 220. Time history of the calculation of the displacement metrics for a 0.1 meter, 8.05 second period surge motion excitation with initial $\rho = 15.0$ degree. Note that payload rotation is no longer zero, so J_θ is nonzero and there is a separation between J_l and $J_{l+\theta}$ and the sum of J_l and J_θ	262
Figure 221. Time history of the payload motion for a 0.1 meter, 8.05 second period surge motion excitation with initial $\rho = 20.0$ degree. The blue trace is the ship motion and the payload response is shown in green.	263
Figure 222. Time history of the inertial hoist fall angles, ρ_{I1} and ρ_{I2} for a 0.1 meter, 8.05 second period surge motion excitation with initial $\rho = 20.0$ degrees.	263
Figure 223. Time history of the hoist cable tensions, F_1 and F_2 in metric tons for a 0.1 meter, 8.05 second period surge motion excitation with initial $\rho = 20.0$ degrees.	264
Figure 224. Time history of the calculation of the displacement metrics for a 0.1 meter, 8.05 second period surge motion excitation with initial $\rho = 20.0$ degree. Note that payload rotation is no longer zero, so J_θ is nonzero and there is a separation between J_l and $J_{l+\theta}$ and the sum of J_l and J_θ	264
Figure 225. Time history of the payload motion for a 0.1 meter, 8.05 second period surge motion excitation with initial $\rho = 25.0$ degree. The blue trace is the ship motion and the payload response is shown in green.	265
Figure 226. Time history of the inertial hoist fall angles, ρ_{I1} and ρ_{I2} for a 0.1 meter, 8.05 second period surge motion excitation with initial $\rho = 25.0$ degrees.	265
Figure 227. Time history of the hoist cable tensions, F_1 and F_2 in metric tons for a 0.1 meter, 8.05 second period surge motion excitation with initial $\rho = 25.0$ degrees.	266
Figure 228. Time history of the calculation of the displacement metrics for a 0.1 meter, 8.05 second period surge motion excitation with initial $\rho = 25.0$ degree. Note that payload rotation is no longer zero, so J_θ is nonzero and there is a separation between J_l and $J_{l+\theta}$ and the sum of J_l and J_θ	266
Figure 229. Time history of the payload motion for a 0.1 meter, 8.05 second period surge motion excitation with initial $\rho = 30.0$ degree. The blue trace is the ship motion and the payload response is shown in green.	267
Figure 230. Time history of the inertial hoist fall angles, ρ_{I1} and ρ_{I2} for a 0.1 meter, 8.05 second period surge motion excitation with initial $\rho = 30.0$ degrees.	267

Figure 231. Time history of the hoist cable tensions, F_1 and F_2 in metric tons for a 0.1 meter, 8.05 second period surge motion excitation with initial $\rho = 30.0$ degrees.	268
Figure 232. Time history of the calculation of the displacement metrics for a 0.1 meter, 8.05 second period surge motion excitation with initial $\rho = 30.0$ degree. Note that payload rotation is no longer zero, so J_θ is nonzero and there is a separation between J_l and $J_{l+\theta}$ and the sum of J_l and J_θ	268
Figure 233. Time history of the payload motion for a 0.1 meter, 8.05 second period surge motion excitation with initial $\rho = 35.0$ degree. The blue trace is the ship motion and the payload response is shown in green.	269
Figure 234. Time history of the inertial hoist fall angles, ρ_{I1} and ρ_{I2} for a 0.1 meter, 8.05 second period surge motion excitation with initial $\rho = 35.0$ degrees.	269
Figure 235. Time history of the hoist cable tensions, F_1 and F_2 in metric tons for a 0.1 meter, 8.05 second period surge motion excitation with initial $\rho = 35.0$ degrees.	270
Figure 236. Time history of the calculation of the displacement metrics for a 0.1 meter, 8.05 second period surge motion excitation with initial $\rho = 35.0$ degree. Note that payload rotation is no longer zero, so J_θ is nonzero and there is a separation between J_l and $J_{l+\theta}$ and the sum of J_l and J_θ	271
Figure 237. Time history of the payload motion for a 0.1 meter, 8.05 second period surge motion excitation with initial $\rho = 40.0$ degree. The blue trace is the ship motion and the payload response is shown in green.	272
Figure 238. Time history of the inertial hoist fall angles, ρ_{I1} and ρ_{I2} for a 0.1 meter, 8.05 second period surge motion excitation with initial $\rho = 40.0$ degrees.	272
Figure 239. Time history of the hoist cable tensions, F_1 and F_2 in metric tons for a 0.1 meter, 8.05 second period surge motion excitation with initial $\rho = 40.0$ degrees.	273
Figure 240. Time history of the calculation of the displacement metrics for a 0.1 meter, 8.05 second period surge motion excitation with initial $\rho = 40.0$ degree. Note that payload rotation is no longer zero, so J_θ is nonzero and there is a separation between J_l and $J_{l+\theta}$ and the sum of J_l and J_θ	273
Figure 241. Time history of the payload motion for a 0.1 meter, 8.05 second period surge motion excitation with initial $\rho = 45.0$ degree. The blue trace is the ship motion and the payload response is shown in green.	274

Figure 242. Time history of the inertial hoist fall angles, ρ_{I1} and ρ_{I2} for a 0.1 meter, 8.05 second period surge motion excitation with initial $\rho = 45.0$ degrees.	274
Figure 243. Time history of the hoist cable tensions, F_1 and F_2 in metric tons for a 0.1 meter, 8.05 second period surge motion excitation with initial $\rho = 45.0$ degrees.	275
Figure 244. Time history of the calculation of the displacement metrics for a 0.1 meter, 8.05 second period surge motion excitation with initial $\rho = 30.0$ degree. Note that payload rotation is no longer zero, so J_θ is nonzero and there is a separation between J_l and $J_{l+\theta}$ and the sum of J_l and J_θ	275
Figure 245. Time history of the payload motion for a 0.1 meter, 8.05 second period surge motion excitation with initial $\rho = 50.0$ degree. The blue trace is the ship motion and the payload response is shown in green.	276
Figure 246. Time history of the hoist cable tensions, F_1 and F_2 in metric tons for a 0.1 meter, 8.05 second period surge motion excitation with initial $\rho = 50$ degrees. The peak response is approximately 1.5 percent above the initial (static) tension.	276
Figure 247. Time history of the payload motion for a 0.1 meter, 8.75 second period surge motion excitation with initial $\rho = -15.0$ degree. The blue trace is the ship motion and the payload response is shown in green.	277
Figure 248. Time history of the inertial hoist fall angles, ρ_{I1} and ρ_{I2} for a 0.1 meter, 8.75 second period surge motion excitation with initial $\rho = -15.0$ degrees.	277
Figure 249. Time history of the hoist cable tensions, F_1 and F_2 in metric tons for a 0.1 meter, 8.75 second period surge motion excitation with initial $\rho = -15.0$ degrees.	278
Figure 250. Time history of the calculation of the displacement metrics for a 0.1 meter, 8.75 second period surge motion excitation with initial $\rho = -15.0$ degree. Note that payload rotation is no longer zero, so J_θ is nonzero and there is a separation between J_l and $J_{l+\theta}$ and the sum of J_l and J_θ	278
Figure 251. Time history of the payload motion for a 0.1 meter, 8.75 second period surge motion excitation with initial $\rho = -10.0$ degree. The blue trace is the ship motion and the payload response is shown in green.	279
Figure 252. Time history of the inertial hoist fall angles, ρ_{I1} and ρ_{I2} for a 0.1 meter, 8.75 second period surge motion excitation with initial $\rho = -10.0$ degrees.	279

Figure 253. Time history of the calculation of the displacement metrics for a 0.1 meter, 8.75 second period surge motion excitation with initial $\rho = -10.0$ degree. Note that payload rotation is no longer zero, so J_θ is nonzero and there is a separation between J_l and $J_{l+\theta}$ and the sum of J_l and J_θ	280
Figure 254. Time history of the payload motion for a 0.1 meter, 8.75 second period surge motion excitation with initial $\rho = -5.0$ degree. The blue trace is the ship motion and the payload response is shown in green.	281
Figure 255. Time history of the inertial hoist fall angles, ρ_{I1} and ρ_{I2} for a 0.1 meter, 8.75 second period surge motion excitation with initial $\rho = -5.0$ degrees.	282
Figure 256. Time history of the calculation of the displacement metrics for a 0.1 meter, 8.75 second period surge motion excitation with initial $\rho = -5.0$ degree. Note that payload rotation is no longer zero, so J_θ is nonzero and there is a separation between J_l and $J_{l+\theta}$ and the sum of J_l and J_θ	282
Figure 257. Time history of the payload motion for a 0.1 meter, 8.75 second period surge motion excitation with initial $\rho = 0.0$ degree. The blue trace is the ship motion and the payload response is shown in green.	283
Figure 258. Time history of the inertial hoist fall angles, ρ_{I1} and ρ_{I2} for a 0.1 meter, 8.75 second period surge motion excitation with initial $\rho = 0.0$ degrees.	283
Figure 259. Time history of the hoist cable tensions, F_1 and F_2 in metric tons for a 0.1 meter, 8.75 second period surge motion excitation with initial $\rho = 0.0$ degrees.	284
Figure 260. Time history of the calculation of the displacement metrics for a 0.1 meter, 8.75 second period surge motion excitation with initial $\rho = 0.0$ degree. Note that payload rotation is no longer zero, so J_θ is nonzero and there is a separation between J_l and $J_{l+\theta}$ and the sum of J_l and J_θ	284
Figure 261. Time history of the payload motion for a 0.1 meter, 8.75 second period surge motion excitation with initial $\rho = 5.0$ degree. The blue trace is the ship motion and the payload response is shown in green.	285
Figure 262. Time history of the inertial hoist fall angles, ρ_{I1} and ρ_{I2} for a 0.1 meter, 8.75 second period surge motion excitation with initial $\rho = 5.0$ degrees.	285

Figure 263. Time history of the calculation of the displacement metrics for a 0.1 meter, 8.75 second period surge motion excitation with initial $\rho = 5.0$ degree. Note that payload rotation is no longer zero, so J_θ is nonzero and there is a separation between J_l and $J_{l+\theta}$ and the sum of J_l and J_θ	286
Figure 264. Time history of the payload motion for a 0.1 meter, 8.75 second period surge motion excitation with initial $\rho = 10.0$ degree. The blue trace is the ship motion and the payload response is shown in green.	286
Figure 265. Time history of the inertial hoist fall angles, ρ_{I1} and ρ_{I2} for a 0.1 meter, 8.75 second period surge motion excitation with initial $\rho = 10.0$ degrees.	287
Figure 266. Time history of the calculation of the displacement metrics for a 0.1 meter, 8.75 second period surge motion excitation with initial $\rho = 10.0$ degree. Note that payload rotation is no longer zero, so J_θ is nonzero and there is a separation between J_l and $J_{l+\theta}$ and the sum of J_l and J_θ	287
Figure 267. Time history of the payload motion for a 0.1 meter, 8.75 second period surge motion excitation with initial $\rho = 15.0$ degree. The blue trace is the ship motion and the payload response is shown in green.	288
Figure 268. Time history of the inertial hoist fall angles, ρ_{I1} and ρ_{I2} for a 0.1 meter, 8.75 second period surge motion excitation with initial $\rho = 15.0$ degrees.	288
Figure 269. Time history of the hoist cable tensions, F_1 and F_2 in metric tons for a 0.1 meter, 8.75 second period surge motion excitation with initial $\rho = 15.0$ degrees.	289
Figure 270. Time history of the calculation of the displacement metrics for a 0.1 meter, 8.75 second period surge motion excitation with initial $\rho = 15.0$ degree. Note that payload rotation is no longer zero, so J_θ is nonzero and there is a separation between J_l and $J_{l+\theta}$ and the sum of J_l and J_θ	289
Figure 271. Plot of hoist cable tensions, F_1 and F_2 , for the inverse kinematic control case with dynamically changing torques and cable tension values used as the weights in the minimum norm solution. (Simulation parameters: $\rho = 10$ degrees, $\vec{P}_{8/1,z} = 5$ meters, and $\dot{x}_s = 1$ meter at a period of 8.75 seconds.)	294

Figure 272. Plot of x , z , and θ time histories for the inverse kinematic control case with constant torques and cable tension values used as the weights in the minimum norm solution. The constant values chosen were the maximums observed during a simulation of the same conditions using the identity matrix as the weighting elements. (Simulation parameters: $\rho = 10$ degrees, $\vec{P}_{8/1,z} = 5$ meters, and $\dot{x}_s = 1$ meter at a period of 8.75 seconds.)	295
Figure 273. Plot of time histories for the inertial hoist-fall angle, ρ , for the inverse kinematic control case with constant torques and cable tension values used as the weights in the minimum norm solution. The constant values chosen were the maximums observed during a simulation of the same conditions using the identity matrix as the weighting elements. (Simulation parameters: $\rho = 10$ degrees, $\vec{P}_{8/1,z} = 5$ meters, and $\dot{x}_s = 1$ meter at a period of 8.75 seconds.)	296
Figure 274. Plots of β , $\dot{\beta}$, L_h , and \dot{L}_h for the inverse kinematic control case with constant torques and cable tension values used as the weights in the minimum norm solution. The constant values chosen were the maximums observed during a simulation of the same conditions using the identity matrix as the weighting elements. (Simulation parameters: $\rho = 10$ degrees, $\vec{P}_{8/1,z} = 5$ meters, and $\dot{x}_s = 1$ meter at a period of 8.75 seconds.)	297
Figure 275. Plot of hoist cable tensions, F_1 and F_2 , for the inverse kinematic control case with constant torques and cable tension values used as the weights in the minimum norm solution. The constant values chosen were the maximums observed during a simulation of the same conditions using the identity matrix as the weighting elements. (Simulation parameters: $\rho = 10$ degrees, $\vec{P}_{8/1,z} = 5$ meters, and $\dot{x}_s = 1$ meter at a period of 8.75 seconds.)	298
Figure 276. Plot of instantaneous power for the inverse kinematic control case with constant torques and cable tension values used as the weights in the minimum norm solution. The constant values chosen were the maximums observed during a simulation of the same conditions using the identity matrix as the weighting elements. (Simulation parameters: $\rho = 10$ degrees, $\vec{P}_{8/1,z} = 5$ meters, and $\dot{x}_s = 1$ meter at a period of 8.75 seconds.)	299
Figure 277. Plot of x , z , and θ time histories for the inverse kinematic control case with constant torques and cable tension values used as the weights in the minimum norm solution. The constant values chosen were the maximums observed during a simulation of the same conditions using the identity matrix as the weighting elements. (Simulation parameters: $\rho = 10$ degrees, $\vec{P}_{8/1,z} = 5$ meters, and $\dot{z}_s = 1$ meter at a period of 10.0 seconds.)	300

Figure 278. Plot of time histories for the inertial hoist-fall angle, ρ , for the inverse kinematic control case with constant torques and cable tension values used as the weights in the minimum norm solution. The constant values chosen were the maximums observed during a simulation of the same conditions using the identity matrix as the weighting elements. (Simulation parameters: $\rho = 10$ degrees, $\vec{P}_{8/1,z} = 5$ meters, and $\dot{z}_s = 1$ meter at a period of 10.0 seconds.)	301
Figure 279. Plots of β , $\dot{\beta}$, L_h , and \dot{L}_h for the inverse kinematic control case with constant torques and cable tension values used as the weights in the minimum norm solution. The constant values chosen were the maximums observed during a simulation of the same conditions using the identity matrix as the weighting elements. (Simulation parameters: $\rho = 10$ degrees, $\vec{P}_{8/1,z} = 5$ meters, and $\dot{z}_s = 1$ meter at a period of 10 seconds.)	302
Figure 280. Plot of hoist cable tensions, F_1 and F_2 , for the inverse kinematic control case with constant torques and cable tension values used as the weights in the minimum norm solution. The constant values chosen were the maximums observed during a simulation of the same conditions using the identity matrix as the weighting elements. (Simulation parameters: $\rho = 10$ degrees, $\vec{P}_{8/1,z} = 5$ meters, and $\dot{z}_s = 1$ meter at a period of 10.0 seconds.)	303
Figure 281. Plot of instantaneous power for the inverse kinematic control case with constant torques and cable tension values used as the weights in the minimum norm solution. The constant values chosen were the maximums observed during a simulation of the same conditions using the identity matrix as the weighting elements. (Simulation parameters: $\rho = 10$ degrees, $\vec{P}_{8/1,z} = 5$ meters, and $\dot{z}_s = 1$ meter at a period of 10.0 seconds.)	304
Figure 282. Plot of x , z , and θ time histories for the inverse kinematic control case with constant torques and cable tension values used as the weights in the minimum norm solution.. (Simulation parameters: $\rho = 10$ degrees, $\vec{P}_{8/1,z} = 5$ meters, and $\theta_s = 5$ degrees at a period of 12 seconds.)	305
Figure 283. Plot of time histories for the inertial hoist-fall angle, ρ , for the inverse kinematic control case with constant torques and cable tension values used as the weights in the minimum norm solution. (Simulation parameters: $\rho = 10$ degrees, $\vec{P}_{8/1,z} = 5$ meters, and $\theta_s = 5$ degrees at a period of 12 seconds.)	305
Figure 284. Plots of β , $\dot{\beta}$, L_h , and \dot{L}_h for the inverse kinematic control case with constant torques and cable tension values used as the weights in the minimum norm solution. (Simulation parameters: $\rho = 10$ degrees, $\vec{P}_{8/1,z} = 5$ meters, and $\theta_s = 5$ degrees at a period of 12 seconds.)	306

Figure 285. Plot of hoist cable tensions, F_1 and F_2 , for the inverse kinematic control case with constant torques and cable tension values used as the weights in the minimum norm solution. (Simulation parameters: $\rho = 10$ degrees, $\vec{P}_{8/1,z} = 5$ meters, and $\theta_s = 5$ degrees at a period of 12 seconds.)	306
Figure 286. Plot of instantaneous power for the inverse kinematic control case with constant torques and cable tension values used as the weights in the minimum norm solution. (Simulation parameters: $\rho = 10$ degrees, $\vec{P}_{8/1,z} = 5$ meters, and $\theta_s = 5$ degrees at a period of 12 seconds.)	307
Figure 287. Plot of x , z , and θ time histories for the inverse kinematic control case with the identity matrix used as the weights in the minimum norm solution. (Simulation parameters: $\rho = 10$ degrees, $\vec{P}_{8/1,z} = 5$ meters, and $\dot{x}_s = 1$ meter at a period of 8.75 seconds.)	308
Figure 288. Plot of time histories for the inertial hoist-fall angle, ρ , for the inverse kinematic control case with the identity matrix used as the weights in the minimum norm solution. (Simulation parameters: $\rho = 10$ degrees, $\vec{P}_{8/1,z} = 5$ meters, and $\dot{x}_s = 1$ meter at a period of 8.75 seconds.)	309
Figure 289. Plots of β , $\dot{\beta}$, L_h , and \dot{L}_h for the inverse kinematic control case with the identity matrix used as the weights in the minimum norm solution. (Simulation parameters: $\rho = 10$ degrees, $\vec{P}_{8/1,z} = 5$ meters, and $\dot{x}_s = 1$ meter at a period of 8.75 seconds.)	309
Figure 290. Plot of hoist cable tensions, F_1 and F_2 , for the inverse kinematic control case with the identity matrix used as the weights in the minimum norm solution. (Simulation parameters: $\rho = 10$ degrees, $\vec{P}_{8/1,z} = 5$ meters, and $\dot{x}_s = 1$ meter at a period of 8.75 seconds.)	310
Figure 291. Plot of instantaneous power for the inverse kinematic control case with the identity matrix used as the weights in the minimum norm solution. (Simulation parameters: $\rho = 10$ degrees, $\vec{P}_{8/1,z} = 5$ meters, and $\dot{x}_s = 1$ meter at a period of 8.75 seconds.)	310
Figure 292. Plot of x , z , and θ time histories for the inverse kinematic control case with the identity matrix used as the weights in the minimum norm solution. (Simulation parameters: $\rho = 0$ degrees, $\vec{P}_{8/1,z} = 5$ meters, and $\dot{x}_s = 1$ meter at a period of 8.75 seconds.)	311
Figure 293. Plot of time histories for the inertial hoist-fall angle, ρ , for the inverse kinematic control case with the identity matrix used as the weights in the minimum norm solution. (Simulation parameters: $\rho = 0$ degrees, $\vec{P}_{8/1,z} = 5$ meters, and $\dot{x}_s = 1$ meter at a period of 8.75 seconds.)	311

Figure 294. Plots of β , $\dot{\beta}$, L_h , and \dot{L}_h for the inverse kinematic control case with the identity matrix used as the weights in the minimum norm solution. (Simulation parameters: $\rho = 0$ degrees, $\vec{P}_{8/1,z} = 5$ meters, and $\dot{x}_s = 1$ meter at a period of 8.75 seconds.)	312
Figure 295. Plot of hoist cable tensions, F_1 and F_2 , for the inverse kinematic control case with the identity matrix used as the weights in the minimum norm solution. (Simulation parameters: $\rho = 0$ degrees, $\vec{P}_{8/1,z} = 5$ meters, and $\dot{x}_s = 1$ meter at a period of 8.75 seconds.)	312
Figure 296. Plot of instantaneous power for the inverse kinematic control case with the identity matrix used as the weights in the minimum norm solution. (Simulation parameters: $\rho = 10$ degrees, $\vec{P}_{8/1,z} = 5$ meters, and $\dot{x}_s = 1$ meter at a period of 8.75 seconds.)	313
Figure 297. Plot of x , z , and θ time histories for the inverse kinematic control case with the jib length used as the weights on the luffing rates and unity on the hoist rates so that the actuation rates are in equivalent units of m/s. (Simulation parameters: $\rho = 10$ degrees, $\vec{P}_{8/1,z} = 5$ meters, and $\dot{x}_s = 1$ meter at a period of 8.75 seconds.)	313
Figure 298. Plot of time histories for the inertial hoist-fall angle, ρ , for the inverse kinematic control case with the jib length used as the weights on the luffing rates and unity on the hoist rates so that the actuation rates are in equivalent units of m/s. (Simulation parameters: $\rho = 10$ degrees, $\vec{P}_{8/1,z} = 5$ meters, and $\dot{x}_s = 1$ meter at a period of 8.75 seconds.)	314
Figure 299. Plots of β , $\dot{\beta}$, L_h , and \dot{L}_h for the inverse kinematic control case with the jib length used as the weights on the luffing rates and unity on the hoist rates so that the actuation rates are in equivalent units of m/s. (Simulation parameters: $\rho = 10$ degrees, $\vec{P}_{8/1,z} = 5$ meters, and $\dot{x}_s = 1$ meter at a period of 8.75 seconds.)	314
Figure 300. Plot of hoist cable tensions, F_1 and F_2 , for the inverse kinematic control case with the jib length used as the weights on the luffing rates and unity on the hoist rates so that the actuation rates are in equivalent units of m/s. (Simulation parameters: $\rho = 10$ degrees, $\vec{P}_{8/1,z} = 5$ meters, and $\dot{x}_s = 1$ meter at a period of 8.75 seconds.)	315
Figure 301. Plot of instantaneous power for the inverse kinematic control case with the jib length used as the weights on the luffing rates and unity on the hoist rates so that the actuation rates are in equivalent units of m/s. (Simulation parameters: $\rho = 10$ degrees, $\vec{P}_{8/1,z} = 5$ meters, and $\dot{x}_s = 1$ meter at a period of 8.75 seconds.)	315
Figure 302. Drawing of crane model provided by Craft Engineering.	332
Figure 303. Drawing of the motor and winch bracket design.	333
Figure 304. Side view of crane model, motor/winch structure and rotary table.	334
Figure 305. Graph plotting encoder counts versus boom angle for crane 1.	336

Figure 306. Graph plotting encoder counts versus hoist displacement for crane 1.	337
Figure 307. Graph plotting encoder counts versus boom angle for crane 2.	337
Figure 308. Graph plotting encoder counts versus hoist displacement for crane 2.	338
Figure 309. Acquiring joystick inputs for controlling luff, hoist and slew axes.	339
Figure 310. Axes of motion being configured and given velocity commands.	339
Figure 311. 3D Drawing of Motor Mounting Bracket Dimensions (in inches).	343
Figure 312. 3D Drawing of Winch Motor Bracket Dimensions (in inches).	344
Figure 313. CAD Drawing of Winch Adapter Plate Dimensions (in inches).	344
Figure 314. Exploded view of three main motion base components.	349
Figure 315. Base-fixed coordinate system.	350
Figure 316. Example DAT file containing 6-DOF data for motion base simulation.	351
Figure 317. Screenshot of Processing motion base simulator.	352
Figure 318. Project Explorer window showing Local and Networked files.	354

THIS PAGE INTENTIONALLY LEFT BLANK

LIST OF TABLES

Table 1. Military Population of I Corps Tactical Zone on 01 July of the Fiscal Year, 1966-1968. Data compiled from [11], [3], [6].	3
Table 2. Summary table of simulation results for the forced response of the planar dual-crane system.	83
Table 3. Performance metric values, peak actuation rates, and peak instantaneous power for two simulation runs using different minimum norm solution weighting schemes.	131
Table 4. Summary table of simulation results for the forced response of the planar dual-crane system.	183
Table 5. Continuation of Table 4, summary of simulation results for the forced response of the planar dual-crane system.	184
Table 6. Comparison of simulated and scale-model results using the displacement metric, $J_{L+\theta}$	233
Table 7. Electro-mechanical Parts List	335
Table 8. Parts list of all significant components to build a single scale crane model.	341
Table 9. Motion Command and Feedback Connections.	342
Table 10. Electro-mechanical Parts List	356

THIS PAGE INTENTIONALLY LEFT BLANK

ACKNOWLEDGMENTS

First and foremost I have to give credit to my family, for without their constant support, patience, and sacrifice I never would have been able to sustain this effort over the years. To my wife, Karen, for her incredible patience and understanding and motivation to see this through to completion - I hope to make it up to you from now on.

To my daughter, Katelyn, for the use of her grammatical and vocabulary skills and to my son, Matthew, for his assistance with video production and editing used in my defense presentation.

I wish to thank my committee for their support and perseverance in staying around long enough for me to finish, particularly my advisor Prof. Anthony Healey and Prof. Fotis Papoulis who have been instrumental in working out the final details.

While not formally a part of my committee, I cannot overstate the role that Prof. Gordon Parker of Michigan Technological University has had in keeping me moving forward to this day. His optimism and confidence that I could achieve this milestone have been greatly appreciated. Along with Prof. Parker, I have to recognize one of his graduate students - James Diaz-Gonzalez for all the LaTeX and MATLAB tricks he has shared and for his invaluable assistance in assembling the dissertation.

Dr. W. Thomas Zhao and Joey Darrah of BMT Designers and Planners played a vital role in supporting the development of the scale-crane and motion platform apparatus and were always available when called upon.

Also, my gratitude to Prof. Hanspeter Schaub of the University of Colorado at Boulder for his support and modification of his CraneSim to facilitate the visualization of the simulation results, the staff of the Naval Historical Center at the Washington Navy Yard for access to their archive of operations reporting, and to Prof. Louis Whitcomb of the Johns Hopkins University for early on giving me a place to get away from the distractions of the office and access to the university library, which allowed me to search the literature and define my topic.

I would like to acknowledge the role of Dr. J. Dexter Bird, III as a pioneer in the development of practical crane control systems and his ongoing collaboration with the naval research and development community in this area.

There are truly many others who have made contributions that have enabled me to get to this point - too many to mention individually, but everyone significant.

For my parents, Frank and Marie Leban.

I. INTRODUCTION

“Logistics sets the campaign’s operational limits.”

- -Joint Pub 1: Joint Warfare of the Armed Forces of the United States

“A sound logistics plan is the foundation upon which a war operation should be based. If the necessary minimum of logistics support cannot be given to the combatant forces involved, the operation may fail, or at best be only partially successful.”

- -ADM Raymond A. Spruance

“Amateurs talk about tactics, but professionals study logistics.”

- -Gen. Robert H. Barrow, USMC (Commandant of the Marine Corps) noted in 1980

“I don’t know what the hell this ‘logistics’ is that Marshall is always talking about, but I want some of it.”

-Fleet ADM E. J. King: To a staff officer. (1942)

(Quotes from “The Navy Supply Corps Newsletter,” May-June 2003)

A. BACKGROUND - “SETTING THE STAGE, VIETNAM 1961-1968”

As the preceding quotes indicate, the role of logistics in warfare can not be over emphasized. This is particularly true in naval and expeditionary operations. Setting the stage for much of the current interest in expeditionary logistical operations and the SeaBase leg of the United States Navy’s operating concept is the experience gained during the Vietnam conflict in Southeast Asia. Significant logistical operations began in December 1961 with the arrival of the vessel USS Core in Saigon and the establishment of the U.S. Military Assistance Command Vietnam (MACV) in February 1962, with a steady building of forces through the period until 1966 [7]. On 1 July 1962, the Headquarters Support Activity, Saigon (HSAS) was established to manage the growing responsibilities of sustaining the military assistance effort. All of the United States forces supplies during this time were unloaded at the port of Saigon for further distribution [7]. Viet Cong actions threatened land transport, so forward movement of supply was accomplished by sea or air [7]. Eventually the volume of supply required the establishment of additional port facilities capable of receiving shipments directly from the United States. What had started as a force of several thousand in 1962, quickly became an order of magnitude larger. The number of military personnel involved in the conflict increased much more rapidly than had been planned. As highlighted in the following quote from [4] referring to the establishment of the Naval Support Activity, Danang, supporting the forces in the I Corps Tactical Zone - ”Initial planning had been on the basis of an estimated military population of 48,000.” This greatly underestimated the actual number onboard in 1966 as listed in Table 1 for that year.

Even at the projected personnel levels the required port capacity was 60,000 measurement tons per month ¹. It might seem that after the experience gained

¹The definition of measurement ton is 40 cubic feet of break bulk cargo. Thus, a 4 foot by 4 foot pallet stacked 5 feet high comprised 80 cubic feet or 2 measurement tons (M/T) [12].

Fiscal Year (FY)	Population
1966	88,000
1967	137,000
1968	198,000

Table 1. Military Population of I Corps Tactical Zone on 01 July of the Fiscal Year, 1966-1968. Data compiled from [11], [3], [6].

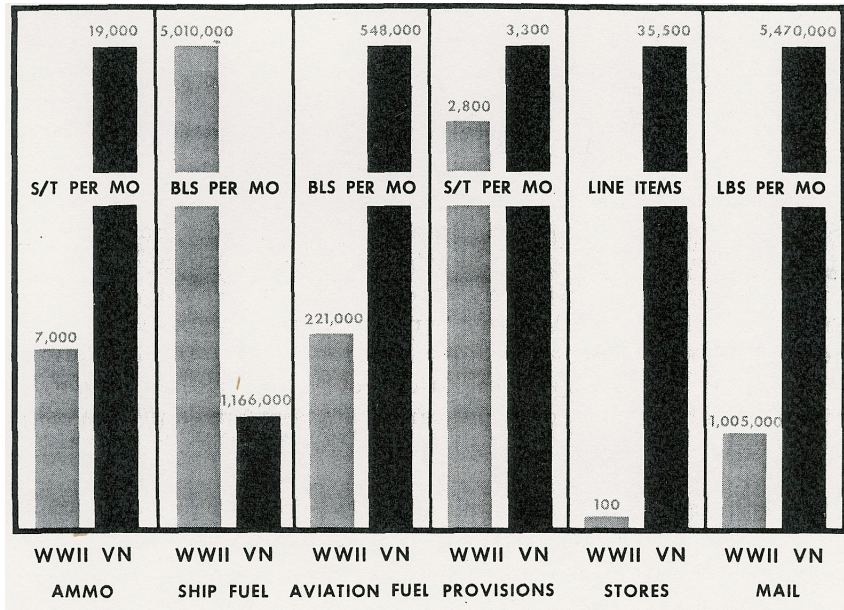


Figure 1. Comparison of World War II Pacific Fleet and Vietnam Pacific Service Force supply requirements. Only in the category of ship fuel does the WW II level exceed that of Vietnam. (From Figure 1 of [1], Courtesy of the Naval Historical Center, Department of the Navy)

from logistical operations in World War II, that the logistical requirements of the Vietnam conflict would not be overly taxing. This was not true on several accounts. On a category-by-category basis, the monthly supply requirements for the Vietnam conflict were much larger in all regards except for fuel for ships, as shown in Figure 1.

As a case in point, the nuclear powered carrier USS Enterprise in Vietnam was expending air-to-ground munitions at a rate of up to 4,478 tons per month while her World War II predecessor only expended 2,000 tons of bombs during the entire

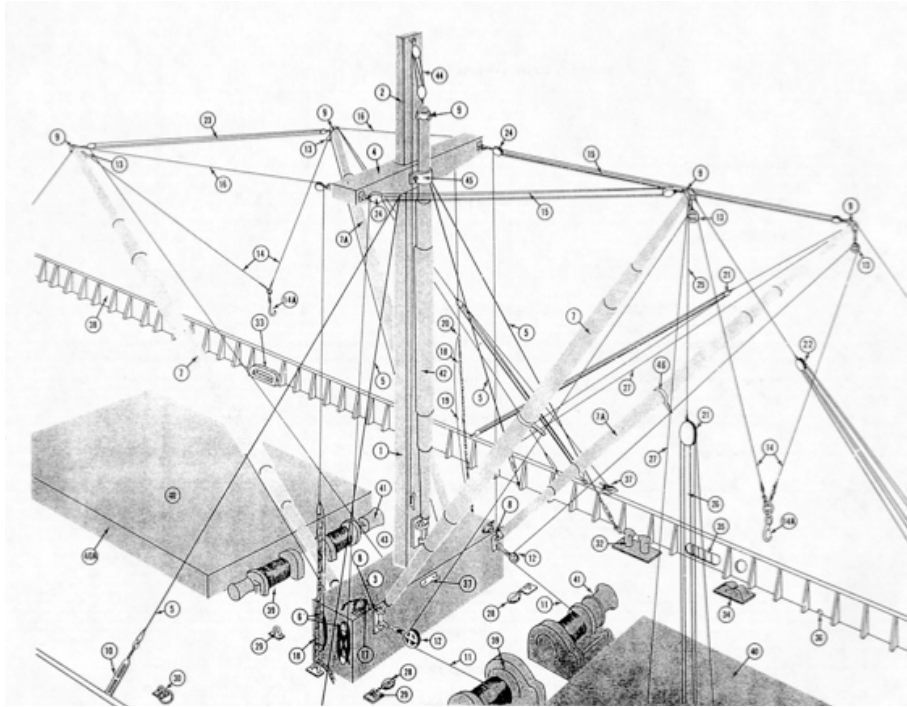


Figure 2. Components of the standard yard and stay rigging from the Seaman course NAVEDTRA 14067 [2] .

war [4]. Secondly, along with fewer ships consuming fuel, there were also fewer ships and personnel available to deliver the necessary commodities. The third factor in the struggle to keep pace with the flow of logistics was the state-of-the-art of cargo handling technology. From 1962 through 1967 virtually all of the cargo was break-bulk, meaning that pallets were assembled and lifted with shipboard yard and stay² rigging as shown in Figure 2.

Figure 3 shows yard and stays rigs in use for cargo operations at the pier facilities in the port of Saigon. Conducting cargo operations at the forward ports, such as Danang and Cam Ranh Bay were more difficult until suitable facilities such as deep draft piers could be constructed.

²The Cape J class of break-bulk ammunition ships use yard and stay rigs to lift palletized ammunition out of their holds for Vertical Replenishment (VERTREP) and Standard Alongside Method (STREAM) replenishment operations and are currently in service with the Ready Reserve Fleet of the U.S. Maritime Administration(reference [13]).



Figure 3. The light cargo ship USS Mark loads in Saigon's port for delivery of material to naval support bases in the Mekong delta. (Figure 5-14 in [3])

Figure 4 shows Cam Ranh Bay as it appeared in 1965 prior to the establishment of the Naval Support Activity. Because of its well-protected deep-water port and proximity to the II Corps Tactical Zone, Cam Ranh Bay became the site of a major Air Force airfield and Army logistic complex. The Navy occupied a smaller area on the point at the northern side of the harbor entrance [4].

By 01 September 1967, the detachment at Cam Ranh Bay was redesignated as a Naval Support Facility under the command of Commander Naval Support Activity, Saigon and by 1969 had been developed to the extent shown in Figure 5 [5]. Figure 6 shows the piers at Naval Support Facility, Cam Ranh Bay in 1969.

Port facilities were established at Danang and Cam Ranh Bay that became significant logistical hubs during the considerable build-up of forces and expansion that occurred from 1966 to 1969. Figure 7 shows cargo movement through the Danang facility growing from slightly more than 50,000 short tons (stons) per month in 1966 to almost 300,000 stons midway through 1968.



Figure 4. Cam Ranh Bay, 1965, before development as a logistical complex. (From [4] courtesy of the Naval Historical Center, Department of the Navy.)

Illustrative of the rapid development of facilities to keep pace with the demands for logistical support are two photographs of the Observation Point area of Danang. The first photograph, 8, shows a view of the area in March 1965. The second photograph, 9, shows the same area in November 1966. Not only have three deep water piers been constructed, but a 1,600 foot quay wall spans the natural mouth of the harbor. The entire tidal area of the harbor behind the quay wall has been filled in to facilitate cargo movement from the piers to the marshalling areas [4].

Aside from the harassment from the Viet Cong, the two significant hindrances to logistics throughput were the climate and the infrastructure. All operations at the Danang site were conducted by logistics-over-the-shore (LOTS) to a bare beach as shown in Figure 10 prior to the construction of two deepwater piers in October 1966 ([4]).



Figure 5. Aerial view of Naval Support Facility, Cam Ranh Bay, 1969. (Figure 12 in [5] courtesy of the Naval Historical Center, Department of the Navy.)

A quote from the FY1967 annual report of the Pacific Service Force of which the Danang port operations were a part, summarizes the situation prior to the construction of the piers: “Ships had to be offloaded in an open roadstead exposed to the seas of the Northeast Monsoon, at times mounting to above 8 feet, and accompanied by deluges of rain. It was often necessary to suspend all cargo offloading from deep draft ships (once for as long as five days) in the unprotected roadstead of Danang which is completely open to the Northeast Monsoon. “Lighterage was scanty; offloading sites insufficient. Yet through good planning and scheduling, ingenuity and hard work, the planned throughput was exceeded the first month and the backlog greatly reduced by the end of the calendar year.” A third floating pier of the DeLong³ type

³The DeLong pier was a floating pier design patented by the DeLong Corporation. Piers could



Figure 6. Pontoon piers at the Naval Support Facility, Cam Ranh Bay, 1969. To the far right is a small floating drydock. (Figure 14 in [5] courtesy of the Naval Historical Center, Department of the Navy.)

was completed by January 1967. An aerial view of the completed deepwater piers at Danang are shown in Figure 11.

However, the presence of piers could not overcome the obstacles associated with the fall-winter monsoon season that occurred every year. Severe tropical storms often accompanied the monsoons and could produce significant damage. On 05 September 1968, tropical storm BESS, backed by 65 knot winds, deposited 11 inches of rain at Danang causing considerable damage to structures and vessels in port. It took 10 days to restore operations and required 7,450 man-days of work for repairs [5]. The throughput capability of the port did not recover completely to the pre-BESS levels until January 1969 as shown in Figure 14. Even without Typhoons,

be configured in many combinations of floating and 6-foot diameter steel-pile-supported sections of dimension 90 x 300 foot (reference [14]).

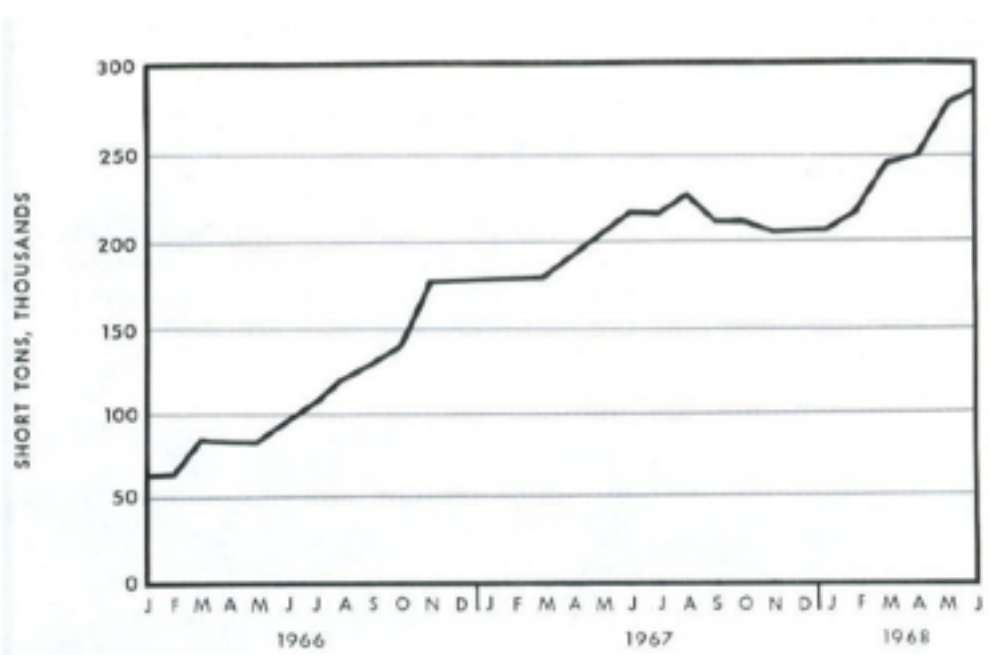


Figure 7. Growth in port capability of Naval Support Activity, Danang. (Figure 25 in [6] courtesy of the Naval Historical Center, Department of the Navy.)



Figure 8. Observation Point, Danang, March 1965. (Figure 15 in [3] courtesy of the Naval Historical Center, Department of the Navy.)



Figure 9. Observation Point, Danang, November 1966. (Figure 16 in [3] courtesy of the Naval Historical Center, Department of the Navy.)

operating in monsoon season conditions was difficult. In November 1966, lighterage operations had to be suspended for a total of 169 hours as a result of wind and sea conditions. Swell conditions even effected operations at the deep water piers in Danang that were the mainstay of port throughput. Vessels had to remain in the anchorage and resupply to coastal bases was suspended 98 times for periods up to four days [3]. Nevertheless, sixty-three of the seventy-two ships that arrived in November were offloaded. It should not be overlooked that a significant amount of material and repairable equipment was being back-loaded onto vessels at these ports. Figure 12 depicts the facilities in the Danang area after the construction of deep water piers at Observation Point.

By June 1967 the monthly volume of cargo offloaded and backloaded at Danang (228,212 short tons) was matching the largest port in South Vietnam, Saigon (229,375 short tons) [3]. This level of throughput was necessary to accommodate the logistical



Figure 10. Landing craft - utility (LCU) 1476 offloads at Danang's Red Beach in March 1965 under direction of Naval Beach Group ONE personnel. (p. 528, [7])

requirements of a military population that had doubled in size over the previous twelve months. Cargo throughput requirements at these levels, were stretching the limits of the port operations personnel. Already civilian stevedores from Vietnam and Korea were augmenting the military workforce. With a limited number of piers and lighterage the solution was to increase the productivity of each vessel offload operation. As early as 1957 the National Academy of Sciences released a study as part of the Liberty Ship Modernization Program that indicated shipboard cranes were superior to boom and winch (yard and stay) for cargo handling [15]. On 01 August 1967, the SS BIENVILLE arrived at Danang with its cargo packages in 228 containers. This was the first use of containerized cargo in Vietnam [6]. Naval Support Activity Danang personnel operating the ships cranes and placing the offloaded containers directly onto truck trailers on the pier were able to discharge 7,221 measurement tons in 18 hours. Trucks began delivering the containers within a half-hour of the

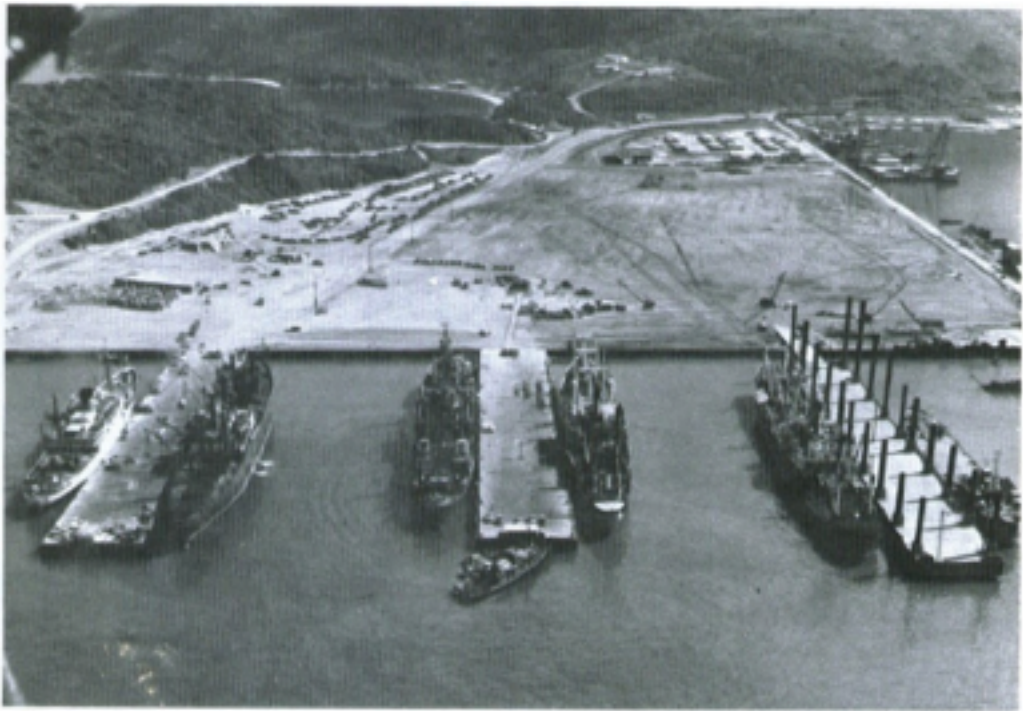


Figure 11. Aerial view of the deep water piers in the Danang Harbor. The DeLong pier can be seen on the right. (Figure 21 in [6])

first container being offloaded from the BIENVILLE. Recalling that a nominal pallet was approximately two measurement tons, the movement of these 228 containers was equivalent to 3,610 pallet lifts in 18 hours at a rate of over three pallets per minute. The efficiency of containerized cargo was quickly recognized and containerships began arriving at Danang about every 15 days with 226 containers of which 60 would be refrigerated units for an equivalent of 18,000 measurement tons per month [6]. With the caveat that correlation does not establish causality, it is possible to speculate that the efficiency of unloading containerized cargo using truck trailers such as those shown in Figure 13 vice break-bulk contributed to the increase in port capability seen in Figure 14 in early 1969.

The year 1969 would see the peak of logistical operations in the I Corps tactical area. Subsequent to that period the "Vietnamization" program transferred many responsibilities and assets including ships to the Vietnam government and the military's

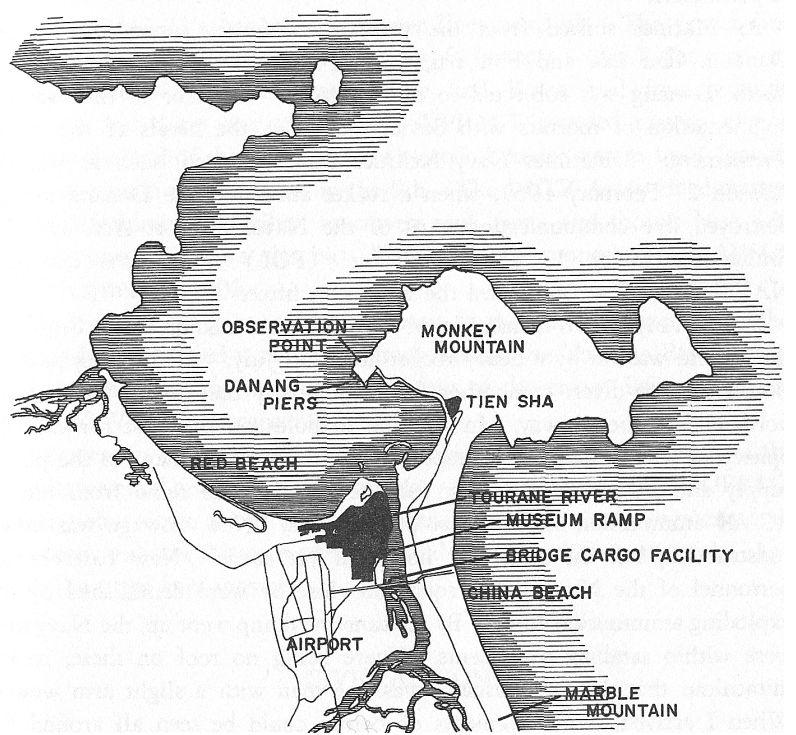


Figure 12. Map drawing of Danang area facilities. (p. 99, [4])



Figure 13. Cargo trailers at deep water pier site, Danang, 1969. (Figure 17 in [5] courtesy of the Naval Historical Center, Department of the Navy.)

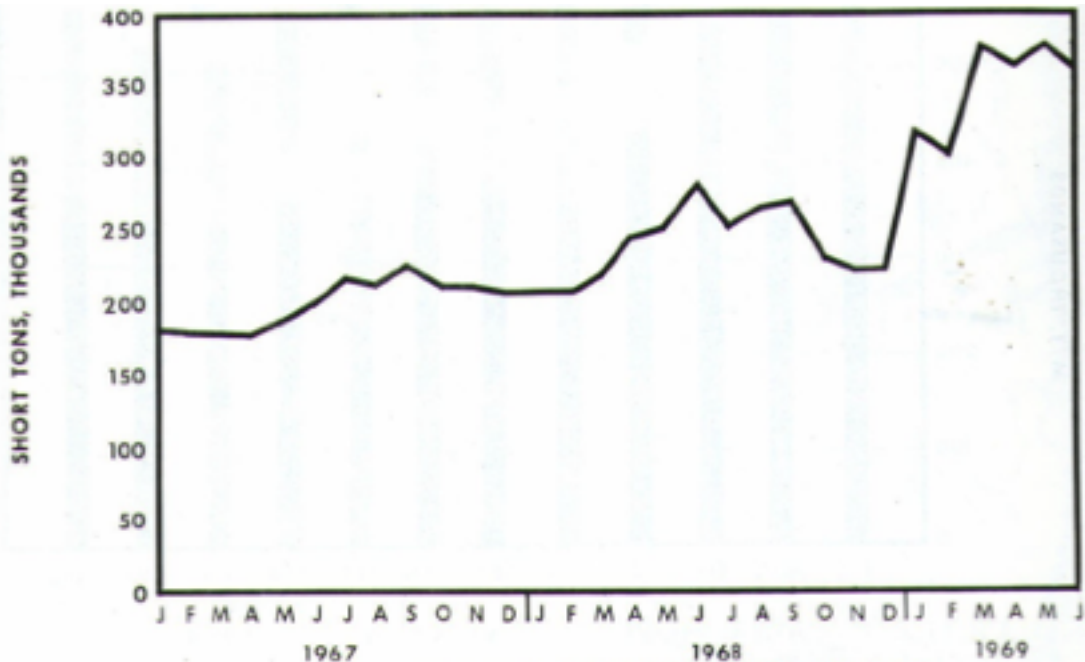


Figure 14. Growth in port capability of naval support activity, Danang.

role shifted to providing training and assistance rather than conducting operations.

The experience in Vietnam had shown that the logistical requirements for the conflict were initially grossly underestimated - presumably in part from the continual buildup of forces and partly because of the increased complexity of the systems required to support those forces. Driven by the need to offload more vessels in shorter time and with fewer personnel the greater efficiencies of containerized cargo operations were recognized and embraced.

One of the significant realizations from Vietnam was the risk associated with operating from a limited number of ports in a tropical climate subject to seasonal monsoons. With the inherent efficiencies of containerized cargo, there was the hope that in the post-Vietnam era significant throughput capability could be attained in a LOTS environment.

B. STATE-OF-THE-ART (VIETNAM TO THE PRESENT DAY)

The United States military services experience with the discharge of cargo from the Vietnam War demonstrated that vessels could languish for days while awaiting the availability of port facilities [9]. This immediately led to the joint Army/Navy/Marine Corps exercises in 1970 and 1972 referred to as Off-shore Discharge of Containership (OSDOC) I and II [16]. OSDOC II was conducted in the vicinity of Fort Story, Virginia in 1972 and the observed sea conditions varied from sea state 1 (1-foot significant wave height)⁴ to sea state 3 (3.5-5 foot significant wave height) [18] [19]. Not surprisingly, uncontrolled swinging (pendulation) caused by seaway disturbances to the ship or barge-mounted cranes resulted in a hazardous working environment and reduced productivity in the placement of containers onto lighters for transport to shore. Technical innovations such as a guide for container spotting onto truck trailers [20] and operational procedures [21] explored in the intervening years since OSDOC I were demonstrated in OSDOC II with limited success. However, the overall efficiency of working with containerized cargo rather than the traditional methods of offloading pallets remained the motivation for resolving the cargo pendulation problem. This problem became the focus of many crane-related developments over the next thirty-five years.

Perhaps it attests to the utility of cranes aboard ships that so many varieties are found; from the basic yard and stay configuration to gantry-types and one of the most common, the wire-luffing jib crane as shown in Figure 15. The basic luffing-jib crane has three degrees freedom for control of the load as shown in Figure 16. Luffing the jib up moves the load inwards toward the pedestal, while luffing down moves the load outward. Slewing the jib left or right moves the load along an arc in those directions and hoisting the moves the load vertically up or down.

⁴Significant wave height is calculated as the average of the highest one-third of the wave peaks recorded over a given duration. As reported in [17] significant wave height was found to correlate well with human observers estimate of wave height.

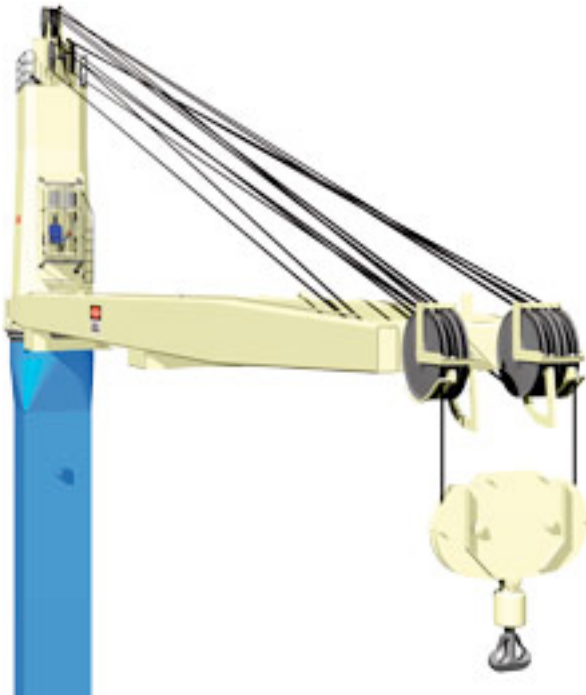


Figure 15. Typical wire-luffing jib crane on a single pedestal foundation.

This design is particularly versatile, capable of handling containerized cargo as well as vehicles and other outsized objects. A single jib crane, with a lifting capacity of 35 to 40 tons, is sufficient for moving containers. By combining several cranes larger loads can be accommodated. One characteristic of luffing-jib cranes is that the length of the hoisting cables, or hoist-falls, can be very long when the load is positioned close to the base of the crane or when over the side of the ship and near the surface of the water. As will be shown later, long hoist cable lengths have an oscillation period in the same range as the seaway-induced motion of the ship resulting in a resonance condition. Various methods have been implemented to suppress pendulation either by (1) removing the mechanism causing the motion or (2) altering the dynamic response of the system. Input shaping techniques, to filter pendulation inducing frequency components from the operator commands as described by Agostini [22] et al. and Singer and Seering[23] reside within the former category.

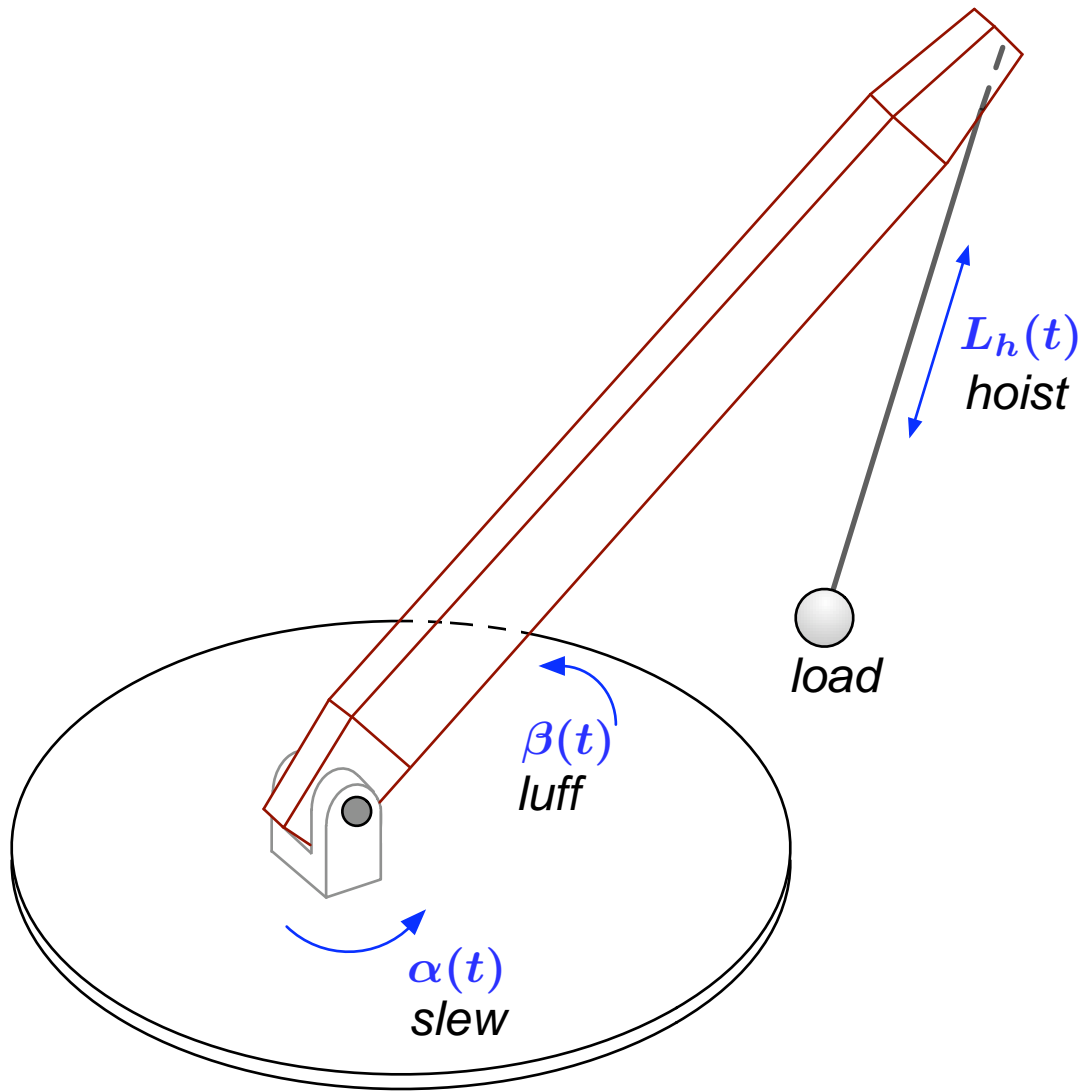
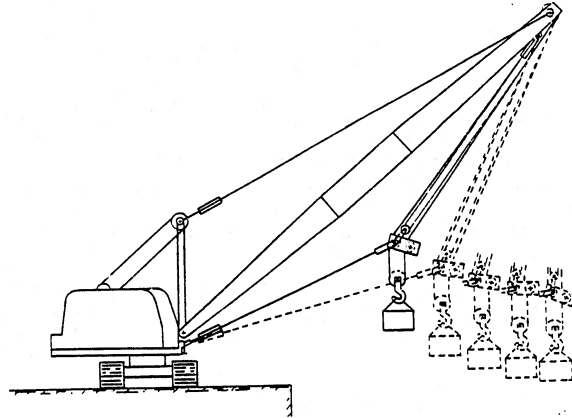


Figure 16. Luffing-jib crane degrees of freedom.

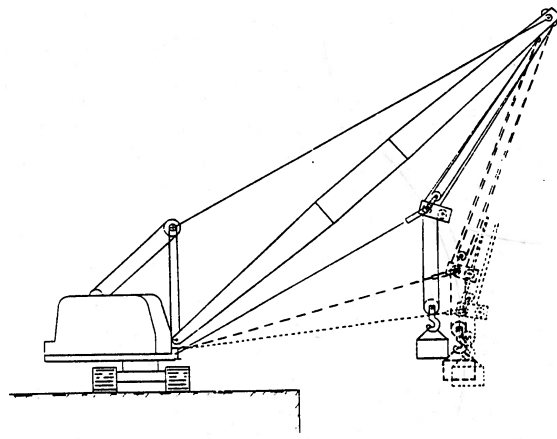
One of the first efforts to alter the dynamics of the pendulum itself was the development of the Rider Block Tagline System (RBTS), shown in Figure 17. The development of the RBTS was a response to the outcome of the OSDOC test/evaluation exercises as described in Bonde and Dillon [24]. Bird [25] further developed the concept. Figure 18 shows schematically a luffing jib crane with the RBTS and the additional degrees of freedom introduced by the liftline and taglines.

The intent of the Rider Block Tagline System (RBTS) was to reduce the pendulation that hindered operations as well as introduced lateral forces on the jib. The RBTS used wire-rope taglines attached to a moveable block through which the load hoist lines are reeved and hence “rides” along. The taglines provide lateral restraint to the rider block, which also determines the pivot point for load pendulation. The shortened pendulum is effectively detuned from the longer period ship motions. The RBTS includes winches for repositioning the rider block, but is essentially a passive method for pendulation control of the load. The RBTS was successfully demonstrated in 1977 [8] and the design was subsequently incorporated into the auxiliary crane ships (T-ACS) procured by the U.S. Navy in the mid-1980s [26]. The S.S. Keystone State (T-ACS 1) participated in the JLOTS II exercise off Fort Story, Virginia in 1984 and as seen in the following excerpt from [27] limitations in the operation of the RBTS were identified: "The T-ACS demonstrated the capability to move containers in SS 3⁵ as long as the sea conditions consisted of small period waves, i.e. wave/chop rather than long period ground swells. ...Whenever the T-ACS became exposed to ground swells on her beam she would begin to roll slightly, about 1 degree, which induced spreader bar pendulation. The controls for the RBTS were difficult to use and have

⁵The term sea state referring to the distribution of wave heights and periods observed during operations can be quantified differently depending on the standard selected. In the context of JLOTS operations, the sea state is defined in accordance with a wave height distribution proposed for use by Pierson and Moskowitz [28]. The sea state scale based on the Pierson-Moskowitz spectrum correlates well with fully developed wind-driven waves. Sea conditions dominated by swells are not explicitly considered. Other commonly used standards are the NATO-STANAG (Standardization Agreement) 4194 [29] and the Beaufort scale[30].



Tagline Control



Rider Block Line Control

Figure 17. Illustration of the influence on the load by the tagline and liftline control of the Rider Block Tagline System (RBTS) [8].

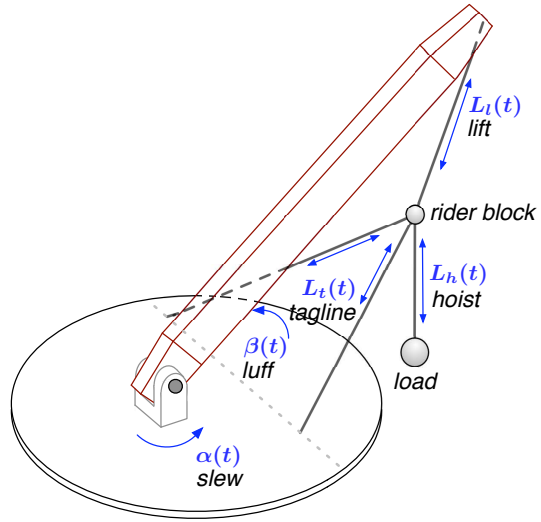


Figure 18. Schematic of Rider Block Tagline System (RBTS) degrees of freedom.

an unacceptable time lag of 6 seconds in transitioning from raising the rider block to tensioning the taglines... As such, the crane and RBTS are not integrated and lack the control characteristics and functions needed for the operator to control the hook at all times so that load pendulation cannot start." Operation of the RBTS lift-line and tag-line winches that had previously required simultaneous control of foot-pedals was developed by Bird [31] et al. and referred to as the Integrated-RBTS (IRBTS). The IRBTS synchronized the lift-line and tagline winches with the luffing and hoisting motions of the crane with a single button push, yet did not provide any active motion compensation. The Platform Motion Compensation (PMC) system was installed on the S. S. Keystone State (T-ACS 1) in 1984 to investigate active control of payload heave motion induced by pitch and roll of the craneship [32]. Whereas one end of the payload hoist cable is normally dead-ended to the jib of the crane, the PMC concept wrapped the cable end on a winch separate from the standard hoist. Thus, the cable was pulled from both ends. Figure 19 shows a schematic of the PMC system.

One winch responded to the operator's hoist commands and the other was

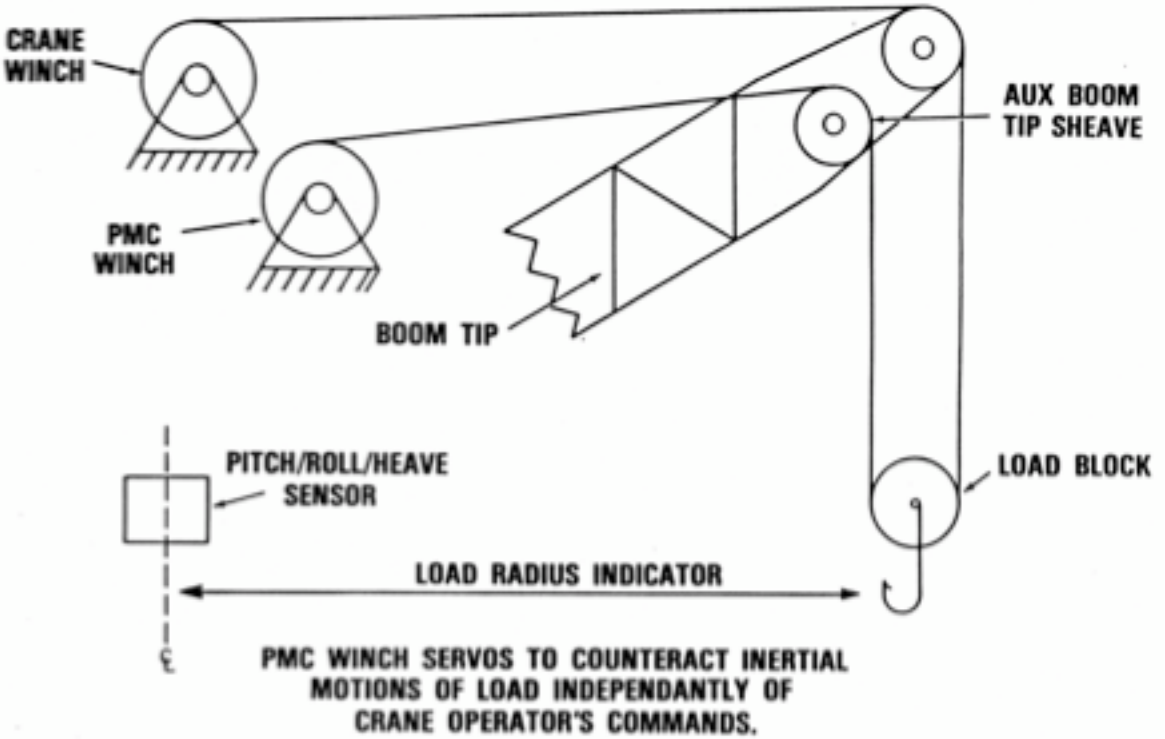


Figure 19. Schematic illustration of Platform Motion Control (PMC) system as installed on S.S. Keystone State in 1984. (From [9])

slaved to a control system driven by the ship motion. The PMC was operationally tested during a 1984 Joint Logistics Over-The-Shore (JLOTS) exercise and was found to be effective [32]. However; given the mechanical and electrical complexity of the implementation at that time, it was deemed too costly to support and it was removed from T-ACS 1 and no additional installations were planned. A very powerful technique that also falls into this category is the application of inverse kinematic feedforward control. This technique has been used in the robotics community with comparatively rigid end-effectors and has been adapted for incompletely restrained systems by several researchers including Yamamoto et al [33] and Henry et al [34]. In 1996 the Office of Naval Research (ONR) began funding both basic and applied research into the pendulation behavior of shipboard cranes, in particular its char-

acterization as a nonlinear system [35], [36], [37], [38], [39]. Several years of applied research came to fruition with the first U.S. Navy implementation of active shipboard-crane control of pendulation. Sandia National Laboratory developed a 'Swing-Free Controller' for the Naval Surface Warfare Center, Carderock Division as part of the Office of Naval Research Advanced Technology Demonstration (ATD) program [40]. The end product of the ATD was the Pendulation Control System (PCS) that was demonstrated aboard the S.S. Flickertail State (T-ACS 5) in 2001-2002 (Figure 20). The PCS used the basic crane actuation capabilities of luffing, slewing, and hoisting much like a robotic manipulator, to eliminate or reduce the pendulation response to ship motion by maintaining the suspension point over the center-of-gravity of the payload. Agostini [22] et al. describes the interaction of the three methods employed to eliminate payload pendulation; namely command shaping for suppressing operator induced oscillation, feedforward inverse kinematics for ship motion compensation, and feedback of pendulation to damp residual motions. The successful ATD was followed by an installation of PCS aboard the Large Medium-Speed Roll-on/Roll-off (LMSR) vessel, USNS Red Cloud (T-AKR 313) in 2005 as part of an at-sea demonstration program.

C. RECENT INVESTIGATIONS AND PUBLICATIONS

While PCS is representative of the state-of-the-art of one type of pendulation control there are other approaches. Pendulation control can also result from mechanical restraint such as through a solid arm or multiple cable suspension rather than a single cable suspension point. A simple example of a multiple cable suspension method is the yard and stay rigging described earlier and also known as the Burtoning or Double-Burtoning method used since the days of sail to transfer items between ships [41]. Relative motions between the ships required coordinated hoisting at both ends of the rig to keep the payload out of the water while not over-tensioning the rigging. With the advent of computer controlled winches making coordination of mul-



Figure 20. Demonstrating cargo transfer at sea using PCS-controlled luffing-jib cranes on the SS Flickertail State in 2002.

tiple cables feasible, there have been recent developments in this type of pendulation control. One example is the AUTOLOG described in reference [10]. Several U.S. patents have been issued for this concept, which is similar to yard and stay arrangement where the payload is suspended from four winch-controlled cables supported by fixed masts. Conceptual sketches of the AUTOLOG show the potential for the system to be employed intra-ship, inter-ship, as a port crane, or to lighterage within a port as illustrated in Figure 21.

In Shiang ([42]), et al., the dynamic model underlying the AUTOLOG concept is derived using a Lagrangian formulation. Four cables over-constrain the motion of the point mass representing the load, so a decoupling transformation is applied to produce a system of three variables and a kinematic constraint related to the cable lengths. An inverse dynamics analysis is performed to determine generalized forces required to generate specified kinematic responses. As this could result in cables generating compressive forces or unrealistically high tensile forces, an optimization using constrained linear programming is applied. Two different objective functions were constructed; one minimizing the total tension of all cables and a second maxi-



Figure 21. Illustration of use of AUTOLOG for discharging cargo to lighterage [10].

mizing the tension in the longest cables. A numerical simulation of two sets of results obtained with the different objective functions produced almost identical results for a representative trajectory. The authors mentioned that future research areas may address the cables as flexible, rather than rigid members, and include the presence of ship motions as a disturbance. Experimental results for a scale-model of the AUTOLOG were presented by Gorman, Jablokow, and Cannon [43].

Additional cargo transfer solutions currently under investigation are the National Institute of Standards and Technology’s (NIST) RoboCrane of references [44] and [45], the High-Capacity Alongside Sea Base Sustainment (HiCASS) crane of reference [46] (see Figure 22, and the Automated Rider Block Tagline System (ARBTS) of reference [47]. The RoboCrane suspends the load with six tension members in

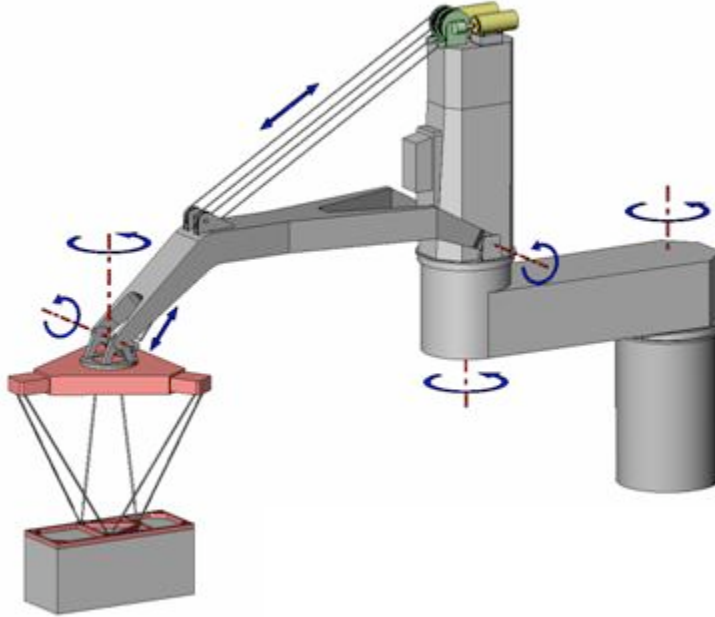


Figure 22. Illustration of the HICASS crane concept as developed for the Office of Naval Research by Oceaneering International, Inc.

a hexapod configuration and so is also referred to as an inverted Stewart-platform. Other multi-legged configurations include the seven-wire FALCON (Kawamura, et al. [48]) and the eight-wire WARP (Maeda, et al. [49]). The FALCON and the WARP configurations have the advantage that the forces restraining the motion are not limited by the weight of the load.

Many of the aforementioned methods have been applied to single jib-cranes, but the literature is sparse on the topic of multiple crane systems. Previously, it was stated that it is common practice to use several cranes together to lift heavy or unwieldy loads. In some cases two cranes can be installed on a common base called a 'twin platform' as shown in Figure 23 and by slaving one crane motion to the other, they can be operated as a single unit with double capacity. The additional lifting capacity does not bring any additional means of control and typically the

twin platform has a reduced maximum slewing rate compared to a single crane. Another configuration for a multiple crane lift uses two single or twinned jib cranes on separate pedestal lifting a single load as shown in Figure 24. However, these 'team lifts' are performed manually and require the coordinated efforts of several individual operators. For the Large Medium Speed Roll-on/Roll-off (LMSR) vessels owned by the Military Sealift Command (MSC), this type of lift is required to deploy the sideport ramp. The LMSRs normally use the stern ramp, but the sideport ramp provides additional vehicle access capability for rapid loading or unloading of the ship.

For shipboard cranes, these operations can be successfully conducted only with experienced operators and in very benign environmental conditions as shown in Figures 25 and 26. They would not be attempted when significant ship motions were present. While coordinated robotic maneuvers have been investigated in the literature, the scenario of having base motion, and an underactuated load, has not. For example, the paper by Smith, Starr, Lumia, and Wood [50] presented an approach for developing swing-free motion trajectories for a dual-arm manipulator, but only in the context of a manufacturing environment where base motion disturbances are not present. The paper references previous research on single manipulator systems and goes on to develop an approach for dual manipulator systems. The authors constrained the end effectors to remain at a constant separation distance equal to the extent of the payload. The authors identify the three vibrational modes of the system by inspection and then generate linearized equations of motion for each mode. Using the method of Singer and Seering [23], trajectories with zero residual vibration (to first order) were generated. Numerical simulation showed that the trajectories reduced residual vibration, but nonlinearities including time-varying natural frequencies resulted in non-zero residual motions. In cases where the input trajectory is consistent with the linearization assumptions, the results reproduce the theoretical prediction.

The paper by McDonald, et al [51], describes the use of virtual environments



Figure 23. Photo of two luffing jib cranes mounted on a twin platform.

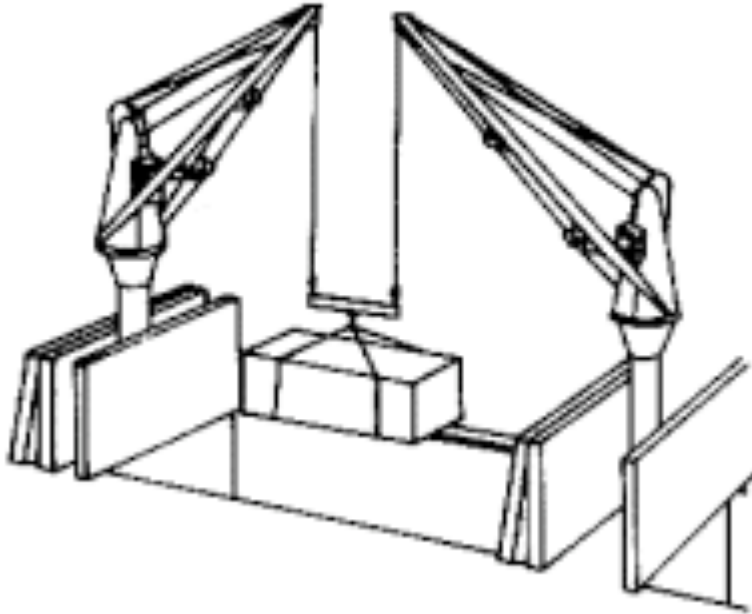


Figure 24. Sketch of two luffing jib cranes executing a team lift.

that have been used for collaborative visualization and engineering design as a tool for path planning and decision making for networked control systems. A collaborative graphical programming interface and a supervisory control program, coordinate the various operator input to the actuating robotic system. While it appears that this approach could be applied to the manipulation of objects in near-real time, its primary relevance may be in a predefined manufacturing setting. Another possible approach is described in Wilson, Robinett, and Eisler [52], which discusses a method of generating optimal paths for single robotic manipulators using Discrete Dynamic Programming (DDP). A linear optimal control problem is posed that incorporates the dynamics of the flexible manipulator as well as various control objectives such as minimal effort, minimal effort with bounded actuators, minimal time, and minimum torque-rate (power). For each case the DDP solution had to be obtained offline using a recursive equation algorithm. The trajectory was discretized into 200 steps ($N=201$)



Figure 25. Photo of a sideport ramp of a Large Medium Speed Roll-on/Roll-off (LMSR) vessel being lifted into place by two luffing-jib crane-sets in twin mode.

for all cases. It does not appear that the method is applicable to real-time on-the-fly calculation of trajectories at the current state of development. Galicki [53], describes a method for on-line generation of end-effector trajectories. In the context of this paper a redundant manipulator refers to a multilink effector, not multiple effectors, although its possible that case could be admitted. Also, the dynamic environment refers to moving obstacles within the workspace of the effector and not base motion disturbances. The solution of the path generation and the end-effector commands are generated simultaneously and include obstacle avoidance via an exterior penalty function. Because of the dynamic nature of the command generation the stability of the system is determined by Lyapunov methods. The on-line nature of the method for path generation is attractive, but this paper does not offer any insights into operation on a moving platform. Another advantage is that the command generation does not



Figure 26. Photo of a U.S. Army modular warping tug being lifted onto the deck of the S.S. Flickertail State by two luffing-jib crane-sets in twin mode during Operation Humanitarian Support Over-The-Shore (HSOTS) 2007 in Puerto Quetzal, Guatemala.

require the construction an inverse of the Jacobian, but rather the transpose only. It is noted that the effector performance resulting from the commands generated by the method were considered too conservative and that the results from the numerical simulation were used to adjust the gains of the system. Another development with relevance to path planning is described in Agirrebeitia, et al [54]. This method uses the inverse of the Jacobian to generate the effector commands. In the paper the effector structure being manipulated is a highly redundant Variable Geometry Truss (VGT) and the coordinates of the truss nodes are calculated in relation to potential functions representing obstacles. The optimal configuration minimizes the value of the potential function. In treating the crane lift as a multi-effector systems it is intriguing to consider the application of techniques for multiagent systems such as those described in Ogren, Egerstedt, and Hu [55], using the principle of Control Lyapunov Functions (CLF) a method is developed to coordinate the response of an arbitrary number of dynamic systems, provided that each subsystem also is governed by a CLF. Various properties of a Formation Function are derived to establish error bounds and asymptotic behavior of the formation. While there are numerous topics on the movement of effectors, it was found that that they were exclusively relating to an environment where no disturbances were introduced through base motion. So, acknowledging that trajectory planning may have to be part of a practical system, it appears that in regard to the control and dynamics of the crane payload there is a paucity of information. One paper that does offer a very good treatment in this area is the one by Yamamoto, Yanai, and Mohri [33]. This paper offers insights into the multiple wire suspension of a load. The suspension arrangement is similar, but not the precise arrangement of the dual crane system. The authors were primarily concerned with multiple independent overhead trolleys. The environment was industrial, so there was not the discussion of base motion disturbances as would be encountered on a waterborne vessel. The author cites numerous studies of multiple wire suspension of an end-effector and states that the completely restrained case is the main topic of

interest. The authors present a characterization of the general wire suspended effector mechanism by first separating the completely restrained-type of mechanism whereby the suspended objects position and orientation can be completely determined by the inverse kinematic relationships and the incompletely restrained-type of mechanism, which can swing and thus requires additional dynamic information to determine the position. In a previous paper by Yamamoto and Mohri [56] the authors showed that a minimum of three wires are required to completely determine the six degrees of freedom of the suspended rigid body. So for three or more wires, there is an inverse that determines the solution of the wire tensions. In the case of wire-suspension type mechanisms with fixed wire supports, i.e. the winch or fairlead sheave is fixed in an inertial reference frame, then another dynamics equation can be written for wire tensions and directions that generates the body trajectory. The authors then define that a mechanism is completely restrained when the dynamic equation has a unique solution in which all the wire tensions are positive, or there exist redundant solutions of which one results in positive wire tensions. The definition of incompletely restrained mechanisms therefore applies when the solution of the dynamic equation does not exist, or if a unique solution exists the wire tensions are not all positive, or if redundant solutions exist none have all-positive wire tensions. While it is obvious that the two-wire case that fits the dual-crane configuration falls within the incompletely restrained category, it is not clear whether the proposed criterion would apply since the jib tops do not represent fixed wire supports. The more general relation described previously can be used, but it is clear that because of the incomplete restraint by the suspension wires the total solution must consider all the forces on the object including gravity. The remainder of the paper discusses the application of feedback control to the incompletely-restrained mechanism to address outer-loop control of pendulation caused by unmodeled errors and disturbances. The concept proposed is to linearize the system using the inverse dynamics calculation. In other words, the control input for state feedback is derived from the observed linear and angular accel-

eration of the suspended object, which is then fed through the solution of the inverse problem to generate the wire tensions. These values are input to the dynamics of the suspended system to generate a linearized version of the object accelerations which can be integrated to obtain the object state.

The focus of this dissertation is to investigate the dynamic behavior of team lift crane operations and develop a control scheme that keeps the payload swing low in the presence of base motion disturbances. The research approach starts by considering a planar two-crane scenario. This can be used to investigate inherent benefits of using multiple cranes to decouple the pendulum dynamics from the base motion excitation. In addition, it can be used to develop baseline control strategies. The remainder of this document describes a planar, two-crane model, simulation results both open and closed loop, and comparison to some results obtained from a physical model. At the end of the document suggestions for future work are presented.

THIS PAGE INTENTIONALLY LEFT BLANK

II. DYNAMICS OF A PLANAR DUAL-CRANE SYSTEM

To begin the investigation of the dynamics of the team-lift crane operations introduced in the previous section, consider the planar, two crane system of Figure 27. The figure can be interpreted in the context of the side of a ship as viewed from the portside with the bow pointing to the left. The jibs lie in a plane defined by the X and Z axes. The configuration chosen is illustrative of the conditions likely to be encountered on an operational vessel, yet it would be straightforward to generalize the selection of the location of the origin of the ship-fixed reference frame and the orientation relative to the ship's centerline. The two jibs (segments 2-4 and 3-5) of length L_{b1} and L_{b2} , support a single rigid body payload (segment 6-8-7) suspended by cables 4-6 and 5-7 with lengths L_{h1} and L_{h2} respectively. The jibs are attached to the moving base (segment 2-1-3) which can translate and rotate relative to the inertial frame denoted $\{I\}$.

The origin of the ship-fixed reference frame, denoted as $\{s\}$, is at point 1, which is at a distance d_{s1} from point 2 and a distance d_{s2} from point 3, the hinge points of the crane jibs. The length of the jib or boom, L_b , is generally the same for both cranes, but here is allowed to differ for the sake of generality. For each crane, the angle of the jib relative to the deck is denoted by β_i where $i = 1$ is the left crane and $i = 2$ is the right crane. Items that refer to characteristics of the payload will be denoted by the subscript $()_p$ as in the mass of the payload m_p . In general, the payload does not have a uniform mass distribution, thus point 8, the center of mass does not have to be at the midpoint of the segment 6-8-7.

The notation follows the conventions used in Craig [57]. The inertial reference frame in the plane is defined by the fixed axes \hat{Z} and \hat{X} . The position vector with respect to the inertial of the point denoted "8" is given by \vec{P}_8 . Relative position vectors such as the one shown between points "1" and "8" use the notation $\vec{P}_{8/1}$. The

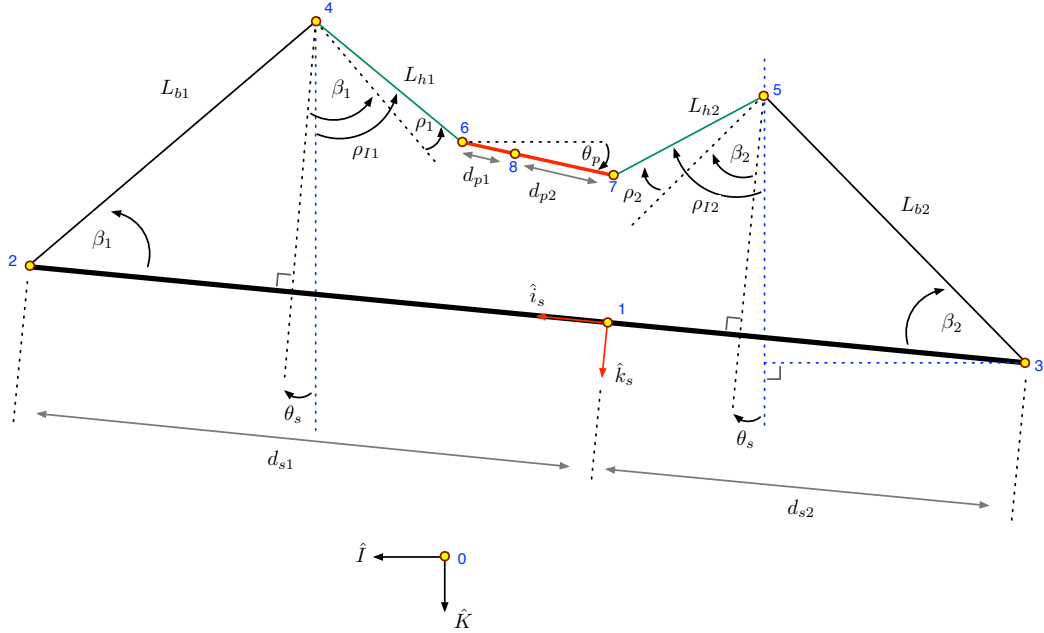


Figure 27. Reference frame and coordinate definitions. Numbered circles are used to denote points on the system for vector descriptions.

ship-fixed reference frame $\{s\}$ is defined by the unit vectors \vec{i}_s and \vec{k}_s . In addition to translating in the plane the ship can rotate relative to the inertial frame as defined by the angle θ_s . Similarly, the unit vectors \hat{i}_p and \hat{k}_p are fixed to the payload center of mass and define the payload-fixed reference frame $\{p\}$. The rotation of $\{p\}$ relative to $\{I\}$ is denoted θ_p and is the payload's absolute rotation angle.

The coordinates remaining to be defined are the offset angles ρ_{I1} and ρ_{I2} that result when the jib angles β_i are set to a value that places the tips of the jibs offset from a vertical line extending from the ends of the payload. The angle relative to the jib is denoted by ρ_i and the angle relative to the inertial frame is denoted by ρ_{Ii} . When both ρ_{Ii} are positive, then the jib ends do not lie over the payload as is the case shown in Figure 27. It is possible for the ρ_{Ii} to take on negative values. It will be shown later that in these cases the response of the payload differs significantly from positive angles of the same magnitude.

One feature to note is that although the payload is shown above the height of the deck connecting the two jibs, in practice for the payload to reach the surface of the water or to a low freeboard vessel, the length of the hoist lines may extend below the deck to an extent comparable to the height of the jibs above the deck.

A. DERIVATION OF THE EQUATIONS OF MOTION

The formulation of the equations of motion is developed using Newton's 2nd Law of Motion with the goal of creating a numerical simulation. Three generalized coordinates will be used; the \hat{i} and \hat{k} components of the relative position vector $\vec{p}_{8/1}$ and the absolute payload rotation angle θ_p . Using the assumption that the hoist cables are inextensible results in two constraint equations that will be applied to reduce the system to a single degree of freedom.

The free-body diagram of the payload is shown in Figure 28.

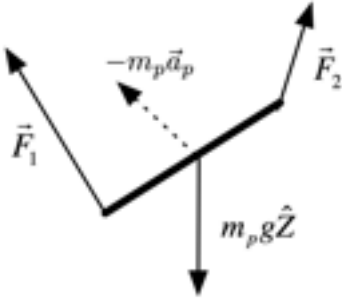


Figure 28. Free-body diagram of the payload.

The forces acting on the payload are the two cable tensions, \vec{F}_1 and \vec{F}_2 , and the weight of the payload, $m_p \vec{g}$, where \vec{g} is the gravitational acceleration vector. The absolute acceleration of the center of mass is denoted as \vec{a}_p . Applying Newton's 2nd law to the free body diagram of Figure 28 gives Eq. (II.1).

$$\vec{F} = m_p \vec{a}_8 = m_p \vec{g} + \vec{F}_1 + \vec{F}_2 \quad (\text{II.1})$$

where

$$\vec{F}_1 = F_1 \hat{P}_{4/6} \quad (\text{II.2})$$

and

$$\vec{F}_2 = F_2 \hat{P}_{3/7} \quad (\text{II.3})$$

The absolute acceleration of the center of mass, \vec{a}_8 , is found by first defining its absolute position vector as

$$\vec{P}_8 = \vec{P}_1 + \vec{P}_{8/1} \quad (\text{II.4})$$

and then taking two absolute derivatives as shown in Eq. (II.5).

$$\begin{aligned} \vec{v}_s &= \vec{v}_1 + \dot{\vec{P}}_{8/1} + \vec{\omega}_s \times \vec{P}_{8/1} \\ \vec{a}_s &= \vec{a}_1 + \ddot{\vec{P}}_{8/1} + 2\vec{\omega}_s \times \dot{\vec{P}}_{8/1} + \vec{\omega}_s \times (\vec{\omega}_s \times \vec{P}_{8/1}) + \vec{\alpha}_s \times \vec{P}_{8/1} \end{aligned} \quad (\text{II.5})$$

where \vec{v}_1 and \vec{a}_1 are the absolute velocities and accelerations of the origin of $\{s\}$, $\vec{\omega}_s$ and $\vec{\alpha}_s$ are the absolute angular velocity and angular acceleration of $\{s\}$. The notation $\dot{\vec{P}}$ implies time derivatives of the components of the vector \vec{P} represented in a rotating coordinate frame. Euler's equation governs the rotational motion of the payload; relating the applied moments to the rotational acceleration of the rigid body. Since the system is planar, only the \vec{j} component is needed and thus, Euler's equation is given by Eq. (II.6).

$$\vec{M} \cdot \vec{j} = J_p \ddot{\theta}_p \quad (\text{II.6})$$

where J_p is the y-component of the mass moment of inertia of the payload about its center of mass. It should be noted that the use of \vec{j} in the dot product of Eq. (II.6) is

not ambiguous since all the frames used in Figure 27 have the same y-axis definition. The general expression for the externally applied moments can be written in terms of the applied cable forces, F_1 and F_2 , as shown in Eq.(II.7).

$$\vec{M} = \vec{P}_{6/8} \times \vec{F}_1 + \vec{P}_{7/8} \times \vec{F}_2 = \vec{F}_1 \left(\vec{P}_{6/8} \times \vec{P}_{4/6} \right) + \vec{F}_2 \left(\vec{P}_{7/8} \times \vec{P}_{5/7} \right) \quad (\text{II.7})$$

To summarize, the three dynamic equations, found by direct application of Newton's 2nd law and Euler's equation are given in Eq. (II.8) and Eq. (II.9).

$$m_p \left[\vec{a}_1 + \ddot{\vec{P}}_{8/1} + 2\vec{\omega}_s \times \dot{\vec{P}}_{8/1} + \vec{\omega}_s \times (\vec{\omega}_s \times \vec{P}_{8/1}) + \vec{\alpha}_s \times \vec{P}_{8/1} \right] = m_p \vec{g} + F_1 \hat{\vec{P}}_{4/6} + F_2 \hat{\vec{P}}_{5/7} \quad (\text{II.8})$$

$$J_p \ddot{\theta}_p = \left[\vec{P}_{6/8} \times \vec{F}_1 + \vec{P}_{7/8} \times \vec{F}_2 = F_1 \left(\vec{P}_{6/8} \times \vec{P}_{4/6} \right) + F_2 \left(\vec{P}_{7/8} \times \vec{P}_{5/7} \right) \right] \cdot \hat{j} \quad (\text{II.9})$$

It should be noted that all the quantities in Eq. (II.8) and Eq. (II.9) (e.g. \vec{a}_1 , $\vec{\omega}_s$, $\vec{\alpha}_s$) are known time histories, except the three generalized coordinates, $\vec{P}_{8/1}$ and θ_p , and the two line force amplitudes, F_1 and F_2 . Two independent constraint equations can be formed in a variety of ways, including those of Eq (II.10).

$$\begin{aligned} \left\| \vec{P}_{4/6} \right\|^2 &= L_1^2 \\ \left\| \vec{P}_{5/7} \right\|^2 &= L_2^2 \end{aligned} \quad (\text{II.10})$$

where

$$\begin{aligned} \vec{P}_{4/6} &= \vec{P}_{2/1} + \vec{P}_{4/2} - \vec{P}_{8/1} - \vec{P}_{6/8} \\ \vec{P}_{5/7} &= \vec{P}_{3/1} + \vec{P}_{5/3} - \vec{P}_{8/1} - \vec{P}_{7/8} \end{aligned} \quad (\text{II.11})$$

Casting this system into a numerical simulation requires the integration of the dynamic equations of Eq. (II.8) and Eq. (II.9).

Defining the states as

$$\begin{aligned}
x_1 &= P_{8/1,X} \\
x_2 &= P_{8/1,Z} \\
x_3 &= \theta_p \\
x_4 &= \dot{P}_{8/1,X} \\
x_5 &= \dot{P}_{8/1,Z} \\
x_6 &= \dot{\theta}_p
\end{aligned} \tag{II.12}$$

The time derivatives of the states are

$$\begin{aligned}
\dot{x}_1 &= x_4 \\
\dot{x}_2 &= x_5 \\
\dot{x}_3 &= x_6 \\
\dot{x}_4 &= \ddot{P}_{8/1,X} \\
\dot{x}_5 &= \ddot{P}_{8/1,Z} \\
\dot{x}_6 &= \ddot{\theta}_p
\end{aligned} \tag{II.13}$$

Thus, the 2nd derivatives of the three generalized coordinates are required at each integration time step. Since the dynamic equations of Eq. (II.8 and II.9) are functions of the line forces, F_1 and F_2 , these accelerations cannot be obtained by simply solving Eqns. II.8, II.9 alone. However, the set of 5 equations, formed by combining Eqns. II.8, II.9 and the second derivative of Eq. (II.10), can be solved simultaneously for the 5 unknowns $\ddot{\theta}_p$, $\ddot{P}_{8/1,Y}$, $\ddot{P}_{8/1,Z}$, F_1 , and F_2 . The accelerations can then be extracted from this solution to be used during integration. The forces are calculated as a by-product of the solution making it convenient to assess cable loads.

Consider the first derivative of the L_{h1} constraint of Eq. (II.10)

$$\frac{d}{dt} \left(\vec{P}_{4/6}^T \vec{P}_{4/6} \right) = 2 \vec{P}_{4/6}^T \dot{\vec{P}}_{4/6} = 2 L_{h1} \dot{L}_{h1} \quad (\text{II.14})$$

Differentiating again yields

$$\dot{\vec{P}}_{4/6}^T \dot{\vec{P}}_{4/6} + \vec{P}_{4/6}^T \ddot{\vec{P}}_{4/6} = \dot{L}_{h1}^2 + \ddot{L}_{h1} \quad (\text{II.15})$$

Taking two derivatives of Eq. (II.11) and substituting it into Eq. (II.15) introduces the $\ddot{\vec{P}}_{8/1}$ term into Eq. (II.15) which is needed for the simultaneous solution method described above. Noting that $\vec{P}_{4/1}$ can be written as

$$\vec{P}_{4/1} = \vec{P}_{8/1} + \vec{P}_{6/8} + \vec{P}_{4/6} \quad (\text{II.16})$$

Substituting this relation for $\vec{P}_{4/6}$, Eq. (II.15) can be expressed as shown in Eq. (II.17).

$$\dot{\vec{P}}_{4/6}^T \dot{\vec{P}}_{4/6} + \vec{P}_{4/6}^T \left(-\ddot{\vec{P}}_{8/1} + \ddot{\vec{P}}_{4/1} - \ddot{\vec{P}}_{6/8} \right) = \dot{L}_{h1}^2 + L_{h1} \ddot{L}_{h1} \quad (\text{II.17})$$

Additional attention must be given to the $\ddot{\vec{P}}_{6/8}$ term since it is a function of the generalized coordinate θ_p .

Up to this point the dynamic equations have been expressed without explicit mention of their frame of representation. Of course, eventually a frame must be selected to implement the equations into a simulation. From now on, all the vectors will be expressed in the $\{s\}$ frame since this strikes a balance in terms of the complexity of the expressions for kinematic quantities. To remove all ambiguity, a left superscript will be used to denote the frame of representation for a vector. Next, the issue of $\ddot{\vec{P}}_{6/8}$ will be addressed.

Consider the vector ${}^s \vec{P}_{6/8}$ in the Eq.(II.18)

$${}^s\vec{P}_{6/8} = \begin{Bmatrix} 0 \\ -\cos(\theta_p - \theta_s) \\ -\sin(\theta_p - \theta_s) \end{Bmatrix} d_p 1 \quad (\text{II.18})$$

Taking two derivatives of Eq. (II.18) gives

$${}^s\ddot{\vec{P}}_{6/8} = \begin{Bmatrix} 0 \\ \sin(\theta_p - \theta_s) \\ -\cos(\theta_p - \theta_s) \end{Bmatrix} d_p 1 \left(\ddot{\theta}_p - \ddot{\theta}_s \right) + \begin{Bmatrix} 0 \\ \cos(\theta_p - \theta_s) \\ \sin(\theta_p - \theta_s) \end{Bmatrix} d_p 1 \left(\dot{\theta}_p - \dot{\theta}_s \right)^2 \quad (\text{II.19})$$

Thus, Eq. (II.19) can be written as

$${}^s\ddot{\vec{P}}_{6/8} = {}^s\ddot{\vec{P}}_{6/8,A} + {}^s\vec{\Gamma}_{6/8}\ddot{\theta}_p \quad (\text{II.20})$$

where

$${}^s\ddot{\vec{P}}_{6/8,A} = -d_p 1 \begin{Bmatrix} 0 \\ \sin(\theta_p - \theta_s) \\ -\cos(\theta_p - \theta_s) \end{Bmatrix} \ddot{\theta}_s + \begin{Bmatrix} 0 \\ \cos(\theta_p - \theta_s) \\ \sin(\theta_p - \theta_s) \end{Bmatrix} d_5 \left(\dot{\theta}_p - \dot{\theta}_s \right)^2 \quad (\text{II.21})$$

and

$${}^s\vec{\Gamma}_{6/8}\ddot{\theta}_p = d_p 1 \begin{Bmatrix} 0 \\ \sin(\theta_p - \theta_s) \\ -\cos(\theta_p - \theta_s) \end{Bmatrix} \quad (\text{II.22})$$

Finally, Eq. (II.17) can now be expressed in a form where the accelerations, needed for the simulation, can be separated from the rest of the terms. Specifically, the L_{h1} constraint equation is

$${}^s\vec{P}_{4/6}^T {}^s\ddot{\vec{P}}_{8/1} + {}^s\vec{P}_{4/6}^T {}^s\vec{\Gamma}_{6/8}\ddot{\theta}_p = {}^s\dot{\vec{P}}_{4/6}^T {}^s\dot{\vec{P}}_{4/6} + {}^s\vec{P}_{4/6}^T \left({}^s\ddot{\vec{P}}_{4/1} - {}^s\ddot{\vec{P}}_{6/8,A} \right) - \dot{L}_{h1}^2 - L_{h1}\ddot{L}_{h1} \quad (\text{II.23})$$

Where the left-hand-side of the equation consists of coefficients of the desired accelerations. In a similar manner, the L_{h2} constraint equation can be manipulated to obtain the acceleration constraint equation of Eq. (II.24).

$${}^s\vec{P}_{5/7}^T {}^s\ddot{\vec{P}}_{8/1} + {}^s\vec{P}_{5/7}^T {}^s\vec{\Gamma}_{7/8}\ddot{\theta}_p = {}^s\dot{\vec{P}}_{5/7}^T {}^s\dot{\vec{P}}_{5/7} + {}^s\vec{P}_{5/7}^T \left({}^s\ddot{\vec{P}}_{5/1} - {}^s\ddot{\vec{P}}_{7/8,A} \right) - \dot{L}_{h2}^2 - L_{h2}\ddot{L}_{h2} \quad (\text{II.24})$$

The 5 equations (Eq. II.8 and Eq. II.9 gives 3 equations with the other two from Eq. (II.23) and Eq. (II.24)) can now be combined into a system of 5 simultaneous equations, in 5 unknowns as shown in Eq. (II.25).

$$\mathbf{A}\vec{V} = \vec{Y} \quad (\text{II.25})$$

where \mathbf{A} is a 5-by-5 matrix of the coefficients of the $\ddot{P}_{8/1,X}$, $\ddot{P}_{8/1,Z}$, $\ddot{\theta}_p$, F_1 , and F_2 terms of Eq. (II.8), Eq. (II.9), Eq. (II.23), and Eq. (II.24). The vector \vec{Y} is 5-by-1 and contains the remaining terms of Eq. (II.8), Eq. (II.9), Eq. (II.23), and Eq. (II.23). The unknowns are stored in \vec{V} as shown in Eq. (II.26).

$$\vec{V} = \begin{Bmatrix} \ddot{P}_{8/1,X} \\ \ddot{P}_{8/1,Z} \\ \ddot{\theta}_p \\ F_1 \\ F_2 \end{Bmatrix} \quad (\text{II.26})$$

The elements of the \mathbf{A} matrix are shown in Eq. (II.27).

$$\mathbf{A} = \begin{bmatrix} m_p & 0 & 0 & -\hat{\vec{P}}_{4/6,x} & -\hat{\vec{P}}_{5/7,x} \\ 0 & m_p & 0 & -\hat{\vec{P}}_{4/6,z} & -\hat{\vec{P}}_{5/7,z} \\ 0 & 0 & J_p & \left(-\vec{P}_{6/8} \times -\vec{P}_{4/6} \right)_{,y} & \left(-\vec{P}_{7/8} \times -\vec{P}_{5/7} \right)_{,y} \\ {}^s\vec{P}_{4/6,x} & {}^s\vec{P}_{4/6,z} & {}^s\vec{P}_{4/6}^T {}^s\vec{\Gamma}_{6/8} & 0 & 0 \\ {}^s\vec{P}_{5/7,x} & {}^s\vec{P}_{5/7,z} & {}^s\vec{P}_{5/7}^T {}^s\vec{\Gamma}_{7/8} & 0 & 0 \end{bmatrix} \quad (\text{II.27})$$

The elements of the vector \vec{Y} are shown in Eq. (II.28).

$$\vec{Y} = \left\{ \begin{array}{l} -m_p \left[\vec{a}_{1,x} + 2 \left(\vec{\omega}_s \times \dot{\vec{P}}_{8/1} \right)_{,x} + \left(\vec{\omega}_s \times \left(\vec{\omega}_s \times \vec{P}_{8/1} \right) \right)_{,x} + \left(\vec{\alpha}_s \times \vec{P}_{8/1} \right)_{,x} \right] \\ -m_p \left[\vec{a}_{1,z} + 2 \left(\vec{\omega}_s \times \dot{\vec{P}}_{8/1} \right)_{,z} + \left(\vec{\omega}_s \times \left(\vec{\omega}_s \times \vec{P}_{8/1} \right) \right)_{,z} + \left(\vec{\alpha}_s \times \vec{P}_{8/1} \right)_{,z} \right] \\ 0 \\ {}^s \dot{\vec{P}}_{4/6}^T {}^s \dot{\vec{P}}_{4/6} + {}^s \vec{P}_{4/6}^T \left({}^s \ddot{\vec{P}}_{4/1} - {}^s \ddot{\vec{P}}_{6/8,A} \right) - \dot{L}_{h1}^2 - L_{h1} \ddot{L}_{h1} \\ {}^s \dot{\vec{P}}_{5/7}^T {}^s \dot{\vec{P}}_{5/7} + {}^s \vec{P}_{5/7}^T \left({}^s \ddot{\vec{P}}_{5/1} - {}^s \ddot{\vec{P}}_{7/8,A} \right) - \dot{L}_{h2}^2 - L_{h2} \ddot{L}_{h2} \end{array} \right\} \quad (\text{II.28})$$

At each integration time step the \mathbf{A} matrix is inverted to solve for the unknowns of Eq. (II.26). It should be noted that a small amount of damping is added to each of the three generalized coordinate acceleration expressions in the simulation. The addition of a small amount of damping in the simulation closely approximates the natural energy loss mechanisms such as cable stretching and bending that occur in the physical crane system.

The discussion of the response of the non-fully restrained dual crane system is intentionally restricted to the X-Z planar model. This is justified not merely as a simplification necessary to make the analysis more tractable, it also arises from the character of the system. The hoist-fall offset angle ρ is the parameter that distinguishes the dual crane system from the simple pendulum, but ρ lies in the plane defined by the line connecting the tips of the two jibs and the inertial vertical direction. To demonstrate this, examine the following photographs of a physical model of the dual crane system with the jibs placed at an arbitrary orientation.

From the front view, Figure 29, the angle ρ formed by the hoist-falls from the vertical is apparent. The side view, Figure 30 shows clearly that the jibs do not lie in the same plane. The third photo, taken from a viewpoint aligned with the jib tops, Figure 31 clearly shows the payload lying in this plane. Thus, the parameter ρ in the planar system suffices to investigate the unique characteristics of this system and there is not an analogous offset angle that is introduced by considering the full three



Figure 29. Front view of model of the dual crane system with jibs at arbitrary slew angles. Note the vertical offset of the hoist falls characterized by the angle ρ_I .

dimensional model. It appears that the out-of-plane motion can be decoupled from the planar motion considered here and would be amenable to the solution methods for simple pendular motion.



Figure 30. End view of model of the dual crane system with jibs at arbitrary slew angles. The jibs clearly do not lie in a common plane. The vertical offset of the hoist falls is still discernable.

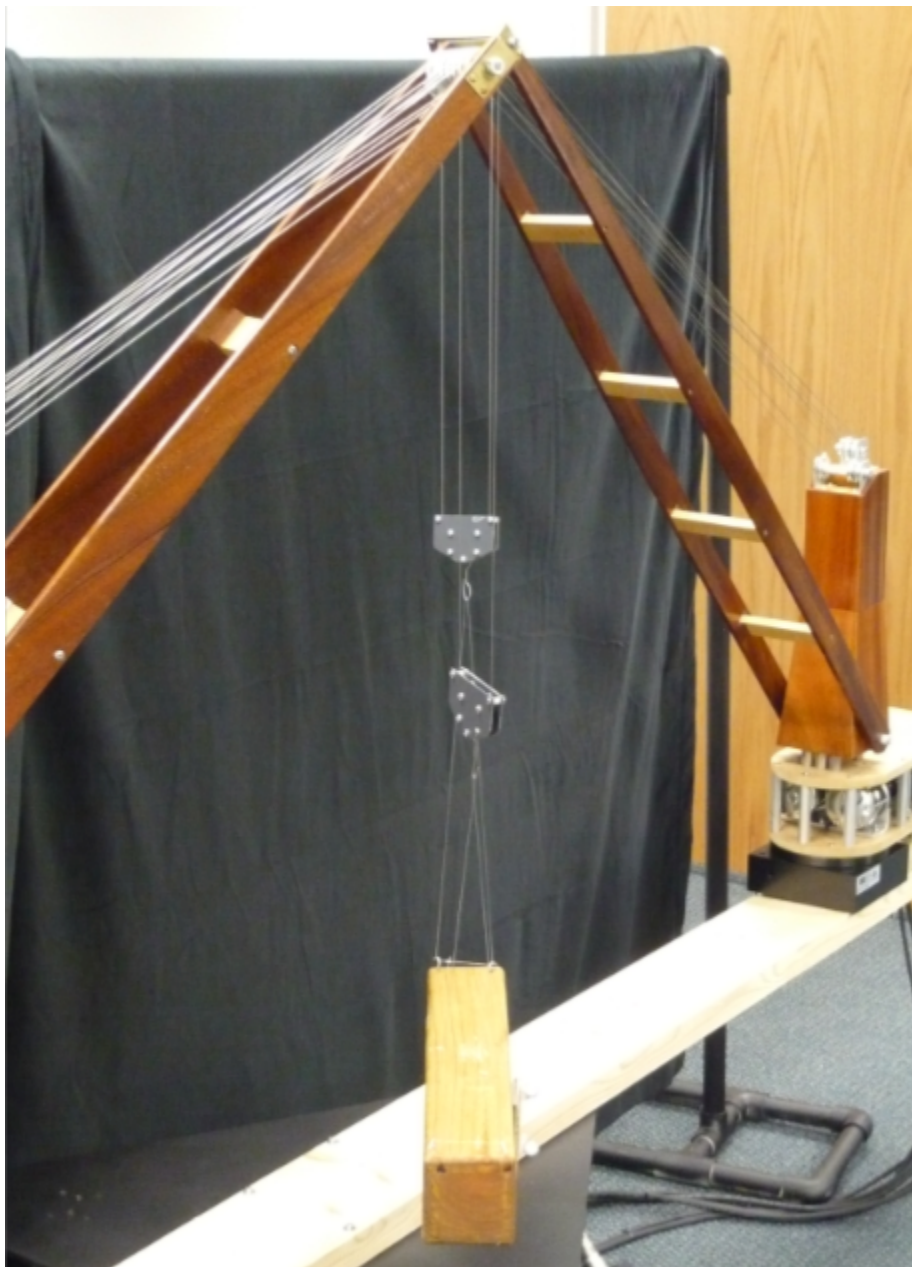


Figure 31. Aligned view of model of the dual crane system with jibs at arbitrary slew angles. Looking along the line containing the tips of the jibs, the payload clearly appears to lie vertically in this plane. Note that there is no vertical offset of the hoist falls analogous to the angle ρ_I .

III. MODEL SIMULATION RESULTS

The equations of motion developed in the previous section were implemented in a time domain simulation in the MATLAB Simulink environment. The top-level block diagram is shown in figure 32.

The block labeled ‘twocrndyn’ is a custom m-file S-function that calls m-files for the calculation of accelerations and forces using the approach described in the previous section. Internal to ‘twocrndyn’ is the function ‘CalcAccelnForce’ that implements equations II.8 through II.25. The inputs are the payload state, the ship state, and the crane state. The remaining blocks, ‘Make_Shp_States’ and ‘Make_Crn_States’ were developed using predefined Simulink primitives and use parameters from an external m-file to set the configuration and the initial state of the dual crane system. Several versions of the setup routine were used to generate specific configurations and initial conditions, but in all cases the following parameters (Eq. (III.1)) of crane location relative to the ship frame and the payload length and mass were held constant.

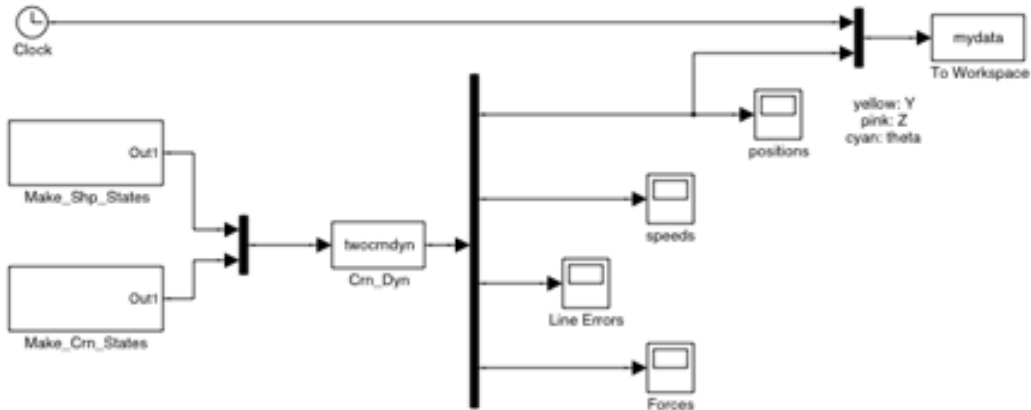


Figure 32. Top-level block diagram of SIMULINK simulation.

$$\begin{aligned}
ds1 &= ds2 = 36 \text{ m} \\
L_{b1} &= L_{b2} = 34 \text{ m} \\
d_{p1} &= d_{p2} = 12 \text{ m} \\
m_p &= 2000 \text{ kg} \\
J_p &= \frac{m_p}{12} (3 + (d_{p1} + d_{p2})^2) \text{ kg} \cdot \text{m}^2
\end{aligned} \tag{III.1}$$

Typically the payload height relative to the ship frame, the payload orientation, θ_p , and the angle of the hoist cables ('falls') relative to the inertial frame, ρ_I were selected with the values for hoist cable lengths, L_h and the jib luffing angles, β derived from those values using the geometric constraints of the kinematic chains. Referring to Figure 27 the following relationships (Eq. (III.2)) can be derived for the left-side jib.

$$\begin{aligned}
L_{b1} \sin \beta_1 - \vec{P}_{8/1,z} - d_{p1} \sin \theta_p &= L_{h1} \cos \rho_{I1} \\
L_{b1} \cos \beta_1 + L_{h1} \sin \rho_{I1} + d_{p1} \cos \theta_p &= d_{s1}
\end{aligned} \tag{III.2}$$

By squaring both equations and adding together the β dependency is eliminated, leaving the following quadratic expression in L_{h2} , Eq. (III.3).

$$\begin{aligned}
L_{h1}^2 + 2L_{h1} \left(\vec{P}_{8/1,z} \cos \rho_{I1} - d_{s1} \sin \rho_{I1} + d_{p1} \sin \rho_{I1} \cos \theta_p + d_{p1} \sin \theta_p \cos \rho_{I1} \right) + \\
\left(2\vec{P}_{8/1,z} d_{p1} \sin \theta_p + d_{p1}^2 + \vec{P}_{8/1,z}^2 + d_{s1}^2 - 2d_{s1} d_{p1} \cos \theta_p - L_{b1}^2 \right) = 0
\end{aligned} \tag{III.3}$$

The largest root is selected as the value for L_{h1} . L_{h2} is set to $L_{h1} + d_{p1} \sin \theta_p$. The initial jib angles (β) are calculated by noting the following trigonometric relationships, (Eq.(III.4)).

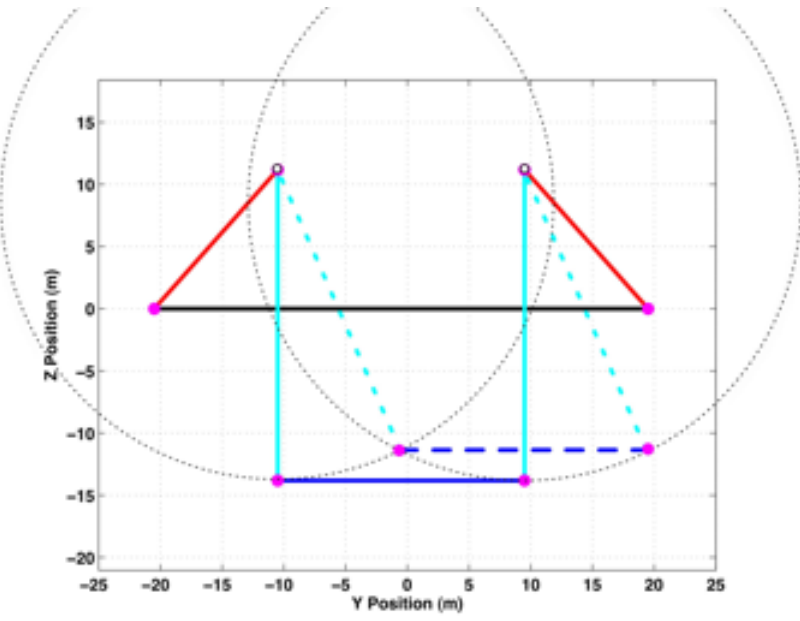


Figure 33. Oscillation mode for dual crane in X - Z plane when $\rho = 0$.

$$\begin{aligned} L_{b1} \sin \beta_1 &= \vec{P}_{8/1,z} + d_{p1} \sin \theta_p + L_{h1} \cos \rho_{I1} \\ L_{b1} \cos \beta_1 &= -L_{h1} \sin \rho_{I1} - d_{p1} \cos \theta_p + d_{s1} \end{aligned} \quad (\text{III.4})$$

Thus, β_1 can be obtained from Eq. (III.5).

$$\tan \beta_1 = \left(\vec{P}_{8/1,z} + d_{p1} \sin \theta_p + L_{h1} \cos \rho_{I1} \right) / (d_{s1} - d_{p1} \cos \theta_p - L_{h1} \sin \rho_{I1}) \quad (\text{III.5})$$

By generating a plot of the payload position at each timestep a simple animation of the dual-crane system is available to facilitate visualization of the oscillation mode. An annotated 'snapshot' of one such view is shown in figure 33.

The solid lines show the payload in the equilibrium (rest) position and the dotted lines indicate the displacement of the payload along a pair of circular arcs. With $\rho_l = 0$, the hoist lines supporting the payload remain parallel and no rotation

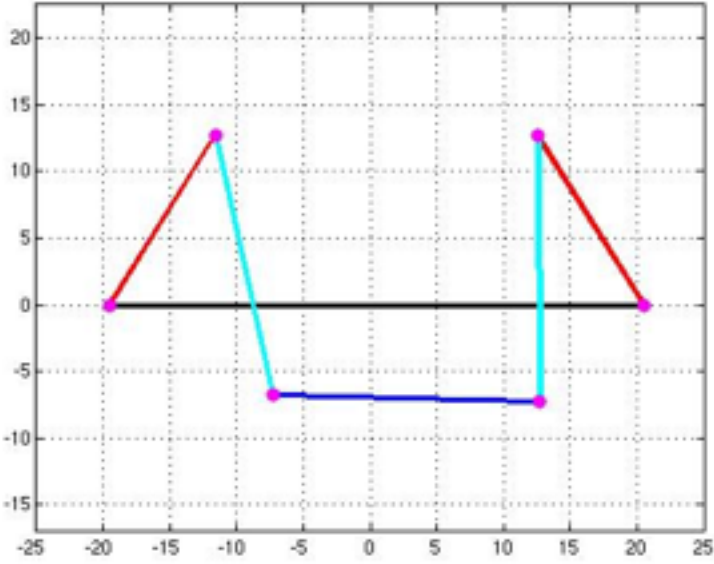


Figure 34. Oscillation mode for dual crane in Z-Y plane with $\rho_l = 10^0$.

occurs about the center of mass. When ρ_l is non-zero, the symmetry is broken and any lateral displacement will be accompanied by a body rotation. An example of an oscillation mode shape with $\rho_l = 10^0$ and hoist cable lengths of 20 meters is shown in Figure 34.

By varying the length of the crane hoist cables and the jib offset angle, ρ_l a set of simulations were generated. To simulate the base motion of the ship, which in the X - Z plane could be surge, heave, or pitch rotation, the ‘deck’ of the ship was oscillated in the x -direction at a frequency of 0.6 rad/sec and amplitude of 0.3 meters. The forcing frequency was selected so that the dual crane system appeared to be near a resonance condition when the hoist lengths were set to 25 meters. The variation in response amplitude ratio with hoist length for $\rho_I = 0$ degrees is shown in Figure 35.

This scenario is consistent with what is observed in practice when payloads are lowered to the ship’s waterline. The x and z linear displacements and the payload rotation angle, θ_p , generated during 1000 seconds of simulation runtime were post-

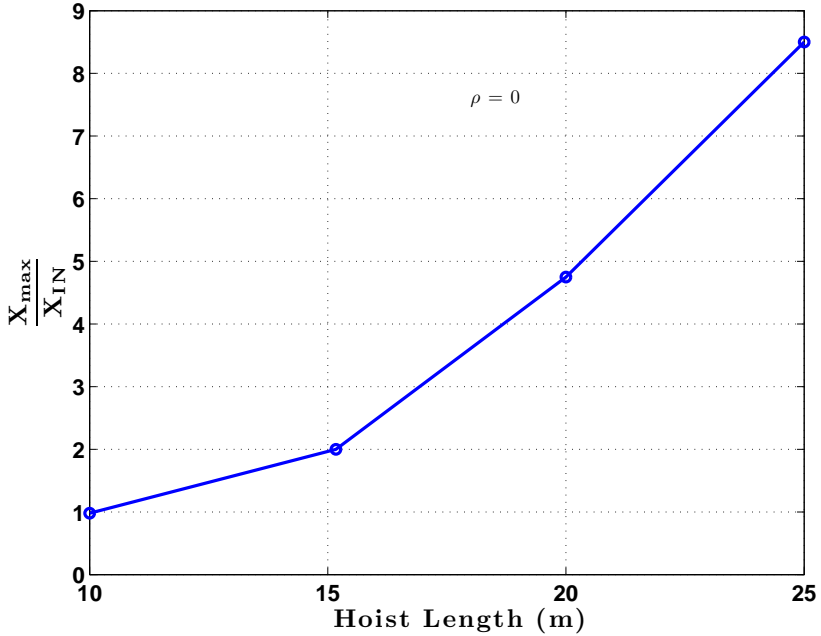


Figure 35. Variation in response with changes in hoist length for $\rho_l = 0^\circ$.

processed to extract the maximum displacements and calculate the sum of the squared amplitudes. To facilitate the comparison of the linear and angular quantities, the payload rotation angle, θ_p , was multiplied by the payload length, L_p , to produce an equivalent linear displacement. To further normalize the response, the quantity plotted in the figures is the ratio of the maximum displacement to the maximum forcing amplitude.

Prior to a further discussion of the system dependence on the parameter ρ_l , it is worth a brief sidebar on the interaction of this angle with another parameter; the length of the hoist cables, Lh_1 and Lh_2 . In the simulations that follow the length of the hoist cables are set equal, so that $Lh_1 = Lh_2 = L_H$. For a spherical pendulum there is a single mode of oscillation, which for small amplitudes is described by sinusoidal motion with a period given by $2\pi\sqrt{L/g}$, where L is the length of the pendulum. In the dual crane system there remains a strong dependence on L_H with some influence by the offset angle ρ_I . The efficacy of using ρ_I to modulate the response was found to

be dependent on the configuration of the dual crane system. To generate figure 36, the jib offset angle in the simulation was nominally set to 0, 10, and 20 degrees and then the hoist length L_H was adjusted to maintain the resting position of the payload at the height of the hinge point of the jibs, which in this case also corresponds to the ship's 'deck'. Over this range of conditions the amplitude of oscillation was relatively insensitive to changes in ρ_I .

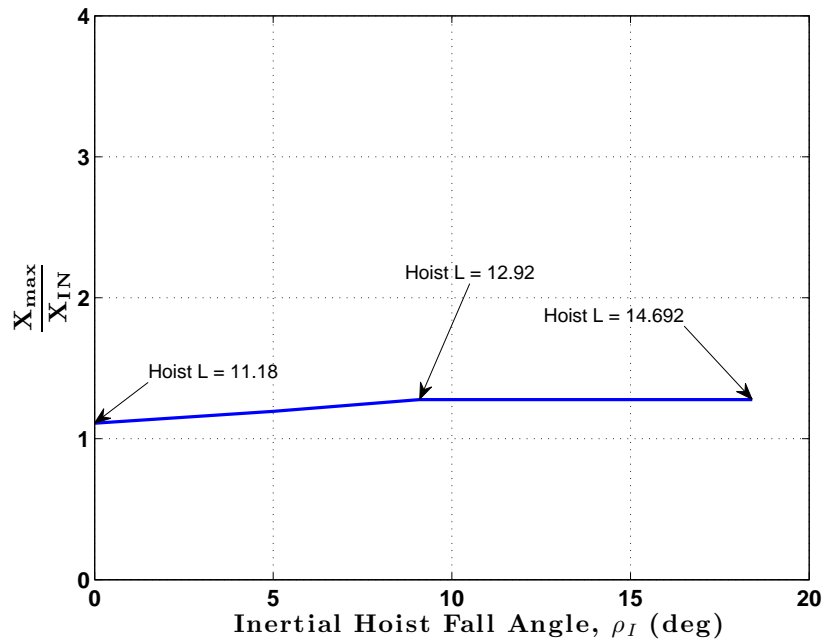


Figure 36. Effect of ρ on response amplitude ratio with payload set at deck-level.

However, for longer hoist lengths corresponding to the payload approaching the waterline, the offset angle had a significant influence on the system response as shown in figure 37.

Such a finding has a significant operational impact; whereas one of the critical phases of cargo transfer is the placement on the deck of a lighter or landing craft, use of a dual-crane would allow the system to be "detuned" to avoid large amplitude payload oscillations characteristic of resonant conditions. Figure 38 shows the amplitude response ratio of the system for a range of jib offset angles with the hoist length

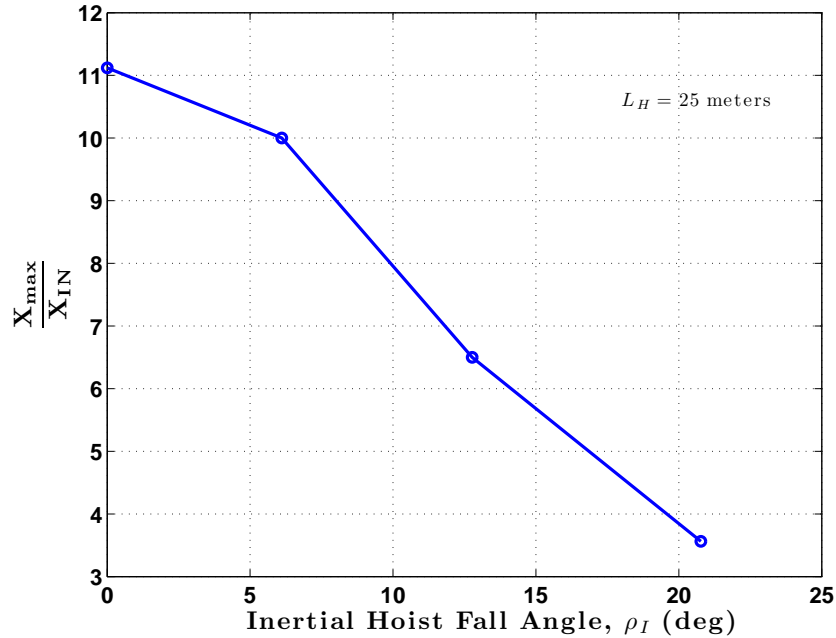


Figure 37. Effect of ρ_I on response amplitude ratio with hoist length set to 25 meters.

fixed at 20 meters. Here again the rotation of the load about its own pitch-axis is multiplied by the payload length to produce an equivalent linear displacement on the same scale as the surge motion. Note that based on the results shown in figure 37 we can expect that the effects would be more pronounced for longer hoist lengths.

It is apparent that the largest overall response occurs when $\rho_I = 0$, although as discussed previously there is no body rotational displacement in this case. Also examining the sum of the squared amplitude values of the response (Figure 39) it is apparent that $\rho_I = 0$ is the condition for maximum response. It is interesting to note that the dependence on ρ_I is not symmetrical; negative values appear to be trending towards a lesser detuning effect with a proportionally larger contribution from the body rotation, while the larger positive values of ρ_I show a continuation of the trend of displacement reduction.

Figures 37, 38, and 39 were produced with constant values of hoist length, L_H . The next series of results considered a constant height of the center of mass of the

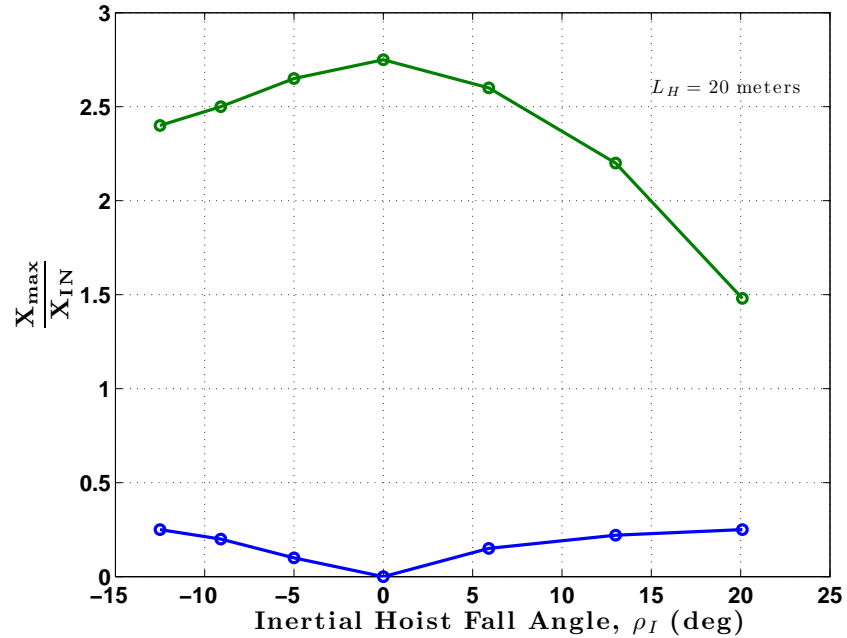


Figure 38. Plot of amplitude ratio versus inertial hoist fall angle.

load above the deck, denoted by $\vec{P}_{8/1,z}$. The height was fixed at 5 meters above the deck and the hoist lengths and jib angles calculated accordingly.

The presentation and interpretation of the results that follow uses a slightly different form than the metrics used previously. The sum of the squared amplitudes and amplitude ratio comparison is replaced by the displacement-based metrics, J_l , J_θ , and $J_{l+\theta}$. Graziano [58] used a similar metric form to compare the effectiveness of pendulation reduction methods for single cranes. The metrics are normalized by elapsed time to allow comparison between simulation runs of different duration. The metrics are defined as follows:

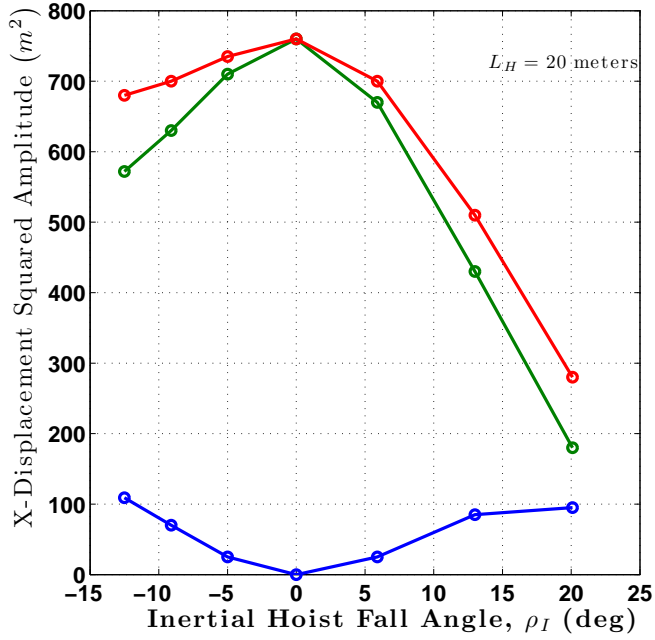


Figure 39. Sum-squared amplitudes of the lateral, rotational, and total combined displacements.

$$J_l = \frac{1}{t_f - t_0} \int_{t_0}^{t_f} \sqrt{\tilde{x}^2(t) + \tilde{z}^2(t)} dt \quad (\text{III.6})$$

$$\text{where } \tilde{x}(t) = x(t) - x(0)$$

$$\tilde{z}(t) = z(t) - z(0)$$

$$J_\theta = \frac{1}{t_f - t_0} \int_{t_0}^{t_f} \sqrt{(d_{p1} + d_{p2})^2 \tilde{\theta}_p^2(t)} dt \quad (\text{III.7})$$

where $\tilde{\theta}_p(t) = \theta_p(t) - \theta_p(0)$

$$J_{l+\theta} = \frac{1}{t_f - t_0} \int_{t_0}^{t_f} \sqrt{\tilde{x}^2(t) + \tilde{z}^2(t) (d_{p1} + d_{p2})^2 \tilde{\theta}_p^2(t)} dt \quad (\text{III.8})$$

In all cases, the continuous integrals are approximated by Euler integration of the simulation values.

To further investigate the influence of the parameter ρ on the response of the open-loop system to base motion, a series of simulations were generated with a single frequency sinusoidal input with an amplitude of 0.1 meters in the surge (x -axis) direction. For one set of simulations the period of the forcing function was set to 8.05 seconds, which corresponds to the resonant period for a simple pendulum with a length of 16.1 meters. Another set of results was generated for a surge period of 8.75 seconds, corresponding to a 19 meter pendulum length. This is precisely the length of the hoist falls for the $\rho = 0$ condition at the 5 meter payload height.

For each condition that was simulated, time histories of x , z , and θ_p referenced to the inertial frame were generated, along with the inertial hoist fall angles, ρ_{I1} , ρ_{I2} , the tensions F_1 , F_2 in the hoist cables, and the calculation of the metrics. Sample data are presented here along with plots that summarize the sets of results, while the complete set of data are resident in Appendix A.

To begin, examine a set of 200 second time histories of the payload for the 8.05 second period surge motion for $\rho = 0$. This is shown in Figure 200. The peak amplitude of the x -displacement is approximately 1.1 meter and the maximum z -displacement is less than 0.04 meters. In the figure, the forcing function is shown in blue. Because of the symmetry, the hoist cables move in parallel and there is no measurable rotation of the payload about its pitch axis as shown in the bottom plot of the figure. The next figure (Figure 201) shows the time history of the hoist fall angles referenced to the inertial frame ¹. The two angles, ρ_{I1} and ρ_{I2} appear to be completely symmetric about the $\rho = 0$ line. The final indication of the symmetry present in the $\rho = 0$ case is the hoist cable tensions shown in Figure 202. The plots of data for the two crane hoists, F_1 and F_2 , are identical. The calculation of the values

¹Since in all the simulations discussed in this section the ship frame was moving linearly in surge, the angular reference to the inertial frame is assumed to be understood in the remaining discussion.

of the previously defined displacement-based metrics, J_l , J_θ , and $J_{l+\theta}$ is plotted in Figure 203 along with the sum of J_l and J_θ . J_θ is essentially zero and so J_l and $J_{l+\theta}$ overlay each other along with the sum of J_l and J_θ .

Even with an initial offset in ρ of 1.0 degree, the symmetry is broken and the same forcing conditions produce different results, as seen in Figure 204. The differences are measurable as shown by the separation of the calculated metrics in Figure 206.

With $\rho = -1.0$, the results are very similar as shown in Figures 197 and 199. The peak of the ρ angle response as shown in Figure 198 is slightly over 4 degrees as compared to approximately 3.5 degrees for the $\rho = 0$ case.

It is apparent that the character of the response is affected by the different jib angles and hoist lengths required to satisfy the selected ρ offset while maintaining the 5 meter payload height initial condition. In general, the hoist lengths decrease as the ρ offset decreases through zero and goes negative. In practice the negative ρ offset would be limited by the length of the payload and the distance separating the crane pedestals.

For the 8.05 second surge period, the system is approaching resonance as the ρ offset approaches -10 degrees, which corresponds to a 16.1 meter length on the hoist cables. The time histories at this condition are shown in Figure 183 and 184. The maximum x -displacement is over 6 meters with over 5 degrees of payload rotation. The ρ angle excursion is over 20 degrees in either direction.

In a further attempt to characterize the influence of the offset in the hoist fall angles, it is possible to exploit the amplitude modulation or 'frequency beating' behavior exhibited in all the simulated responses. This results from the mixing of different frequencies, those frequencies being the forcing frequency and the natural response frequency of the dual crane pendulum. The relationship between the frequency components is given by III.9 or by III.10 in terms of periods [59]. The frequency of the beating phenomenon was estimated by observing the zero crossings

of the long period modulation. The forcing frequency (period) is prescribed from the setup of the simulation. Thus, the natural frequency (period) of the system can be calculated from these quantities for each set of simulation data generated.

The data used to generate the following plots, which summarize the influence of the parameter, ρ on the forced response of the planar dual crane system are tabulated in Table 2 at the end of this section. The column headings in the table are defined as follows: T_F is the surge period of the ship (specified forcing function), ρ is the inertial hoist-fall angle offset (specified parameter), L_h is the hoist cable length (calculated parameter), T_{beat} is the period of the beat phenomenon (estimated from generated time histories), T_n is the natural period of the system (calculated from relationship between forcing and beating frequencies), T_n (Based on L_h) is the period of a simple pendulum corresponding to the hoist cable length, X_{max} is the maximum absolute displacement in the X-direction, Z_{max} is the maximum absolute displacement in the Z-direction, $\theta_{p,max}$ is the maximum absolute payload rotational displacement, J_l is the value of the displacement metric based on X and Z displacements, J_θ is the value of the metric based on payload rotational displacement, and $J_{l+\theta}$ is the value of the metric based on the combination of X, Z, and θ_p displacements.

Figure 51 summarizes the relationship between the response frequencies and the parameter ρ . The blue triangles represent the beat frequency data estimated from examination of the simulation time histories. It can be seen from Equation III.9 that the beat frequency should fall to zero if the forcing frequency and natural frequency are equal. The red crosses show what the pendulum frequency would be for a simple pendulum with the same length of hoist cable, L_h and $\rho = 0$. The green circles represent the system natural frequency as calculated from the beat frequency data. Comparing the calculated natural frequencies with the frequencies based solely on hoist length and noting the separation in frequency as ρ is increased, it is apparent that ρ has a significant influence on the system response. An interpretation of the trends in the data is that there are two competing factors; the length and tension

of the hoist cables. For the same payload position the length of the hoist cables has to increase proportionally as the offset angle, ρ is increased - this factor tends to lower the natural frequency. The cable tension increases with ρ and the component in the x -direction acts as restoring force similar to a spring that increases in stiffness proportional to ρ , thereby increasing the natural frequency of the system. Analogous to a linear spring-mass system that has a natural frequency proportional to $\sqrt{\frac{K}{M}}$ [60] , where K is the spring constant (stiffness) and M is the mass - it would be expected that the increased hoist cable tension for non-zero ρ would result in a higher natural frequency. It appears that for the range of ρ from -15 to -10 degrees the natural frequency is being determined by the hoist length, while for the range from -10 to 35 degrees there is an interplay between the two factors, and for ρ between 35 and 50 degrees the cable tension seems to be the dominant factor affecting the natural frequency. For this case in which the resonant period occurs when $\rho = -10$ degrees there does not appear to any symmetry in regards to the expected system response about the $\rho = 0$ point. This supposition will be reinforced by examining the following two figures. The first plot (Figure 52) contains the maximum displacement data in x , z , and θ_p for each value of ρ that used in this set of simulations. The obvious features are the peaks that occur at $\rho = -10$ degrees and $\rho = 30$ degrees. The peak at $\rho = -10$ is a maximum x -displacement, which we corresponds to a resonance condition with the pendulum frequency. As the peak at $\rho = 30$ degrees is largest for θ_p it is possible that this is a resonance condition for the rotation of the payload; however, the frequency of 0.1242 Hz does not correspond to the frequency predicted in [60] for a pivoting beam. The maximum z -displacements are directly coupled to the x -displacements through the dual-pendulum geometry and are proportionally smaller. For ρ greater than 30 degrees the maximum values decrease rapidly.

The second plot (Figure 53) shows the values of the three metrics, J_l , J_θ , and $J_{l+\theta}$ for the same set of simulations. An advantage of interpreting the results based on the metrics is that all the metrics have the same units; i.e. displacement in meters.

The general trends are the same as the previous figure, but comparing the metric values it is even clearer that the peak at -10 degrees ρ represents a peak in x and z alone, while the peak around $\rho = 30$ degrees is the result of a combination of x , z , and θ_p .

Based on the figure, it would appear that setting the offset in ρ to either 10-15 degrees or greater than 45 degrees would result in reduced motion response to the forcing condition. A consideration for choosing which offset to use is the difference in hoist cable tension. Examining Figure 202, from the $\rho = 0$ condition, we see that the static (initial) hoist cable tension is slightly over 9.8 metric tons (9,800 N) with a maximum dynamic value resulting from the pendulation motion of slightly over 9.85 metric tons, a 0.5 percent change. Comparing that to Figure 246, the hoist cable tension is elevated to 15.26 metric tons (static) with a peak value of 15.49 MT (1.5 percent). The tension increase is as expected proportional to $\frac{1}{\cosine(\rho)}$ since this represents the vertical component of the hoist cable tension, which must satisfy static equilibrium with the weight of the payload. A plot of the tension increase factor versus ρ is shown in Figure 55. So, we can see that at $\rho = 50$ degrees the tension has increased by over 50 percent. Given that the values of the displacement metrics are comparable at $\rho = 15$ degrees and $\rho > 45$ degrees it would seem that taking into account the hoist cable tension, the $\rho = 15$ degrees condition is preferable.

To further clarify the interaction of the offset angle, ρ , with the resonance condition, another set of data was generated with the surge period set to 8.75 seconds. This meant that resonance would be expected to occur with $\rho = 0$ and a hoist length, L_h of 19 meters.

As expected then, the maximum values of x and z increase in proximity to $\rho = 0$ and θ_p goes to zero as shown in Figure 56. The values of the displacement metrics shown in Figure 57 show a similar trend. The trends for positive and negative ρ are not exactly symmetric, possibly because of the effect of another resonance as observed in Figure 51. This effect is more clearly seen in Figure 58, where it is seen

that for this case the second resonance condition occurs when ρ is between 25 and 30 degrees. For $\rho < 0$, the effect of the shortening hoist falls and the effect of the cable tension both tend to increase the natural frequency of the system. For $\rho > 0$, the lengthening hoist falls and the cable tension effects are in opposition, lessening the resulting frequency separation until the cable tension effect dominates for large values of ρ . It is worth recalling that this is single degree-of-freedom system. The combinations of x , z , and θ_p are variations of a single mode shape.

Additional investigations could be directed at characterizing the occurrences of resonance conditions as it appears that hoist length, ρ , and the forcing frequency (ship motion) all play a role in the system response. Frequency separation from resonance conditions as well as hoist cable tensions are both considerations for choosing an operating condition. Although only the planar model is being considered here, it is significant to note that the inclusion of a non-zero ρ also provides a separation in frequency, further decoupling the in-plane and out-of-plane dynamics. The out-of-plane motion should be governed strictly by the (effective) length of the hoist cables as in the classic case of a pendulum. The angle, ρ , is selectable by the crane-system operator and given measurements of the cranes (including geometry and cable tension) and ship motion it should be possible to develop look-up tables or some other method to adapt the selection of ρ to the environment and any preferred crane-system configuration.

This section described an investigation of using nonzero hoist-fall (cable) offset angles to facilitate detuning the systems natural response from the base motion of the ship. For a single lift line crane with hoist lengths of 16 to 25 meters, the natural periods of a pendulum are between 8 and 10 seconds, which are not unreasonable values for the roll period of a large cargo-carrying vessel. These periods are at the high end of the significant range for the Pierson-Moskowitz wind-driven sea spectrum [61] for sea state 3.5-4; however, swells can often be observed in this range of periods. This can result in large payload motion for small ship motion amplitudes. By changing

the crane geometry to generate an offset in the fall angle of the hoist cables, it appears that it is possible to manipulate the crane-system natural response away from the ship resonant condition, thus passively reducing payload motion. In the next section, an active means to reduce the crane response to the ship (base motion) excitation will be developed. Relationships for tension, torque and power of the dual-crane system will be developed and applied in the context of the active solution.

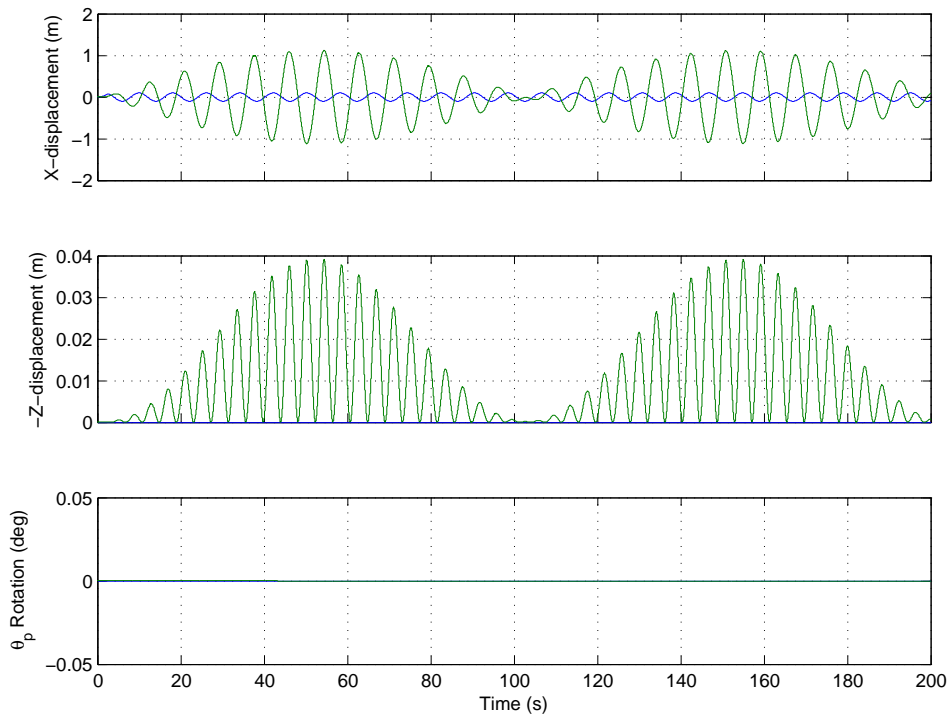


Figure 40. Time history of the payload motion for a 0.1 meter, 8.05 second period surge motion excitation with initial $\rho = 0$ degrees. The blue trace is the ship motion and the payload response is shown in green. Note that the payload rotation, θ_p about its pitch axis is essentially zero.

$$f_{beat} = f_{natural} - f_{force} \quad (\text{III.9})$$

$$\frac{1}{T_{beat}} = \frac{1}{T_{natural}} - \frac{1}{T_{force}} \quad (\text{III.10})$$

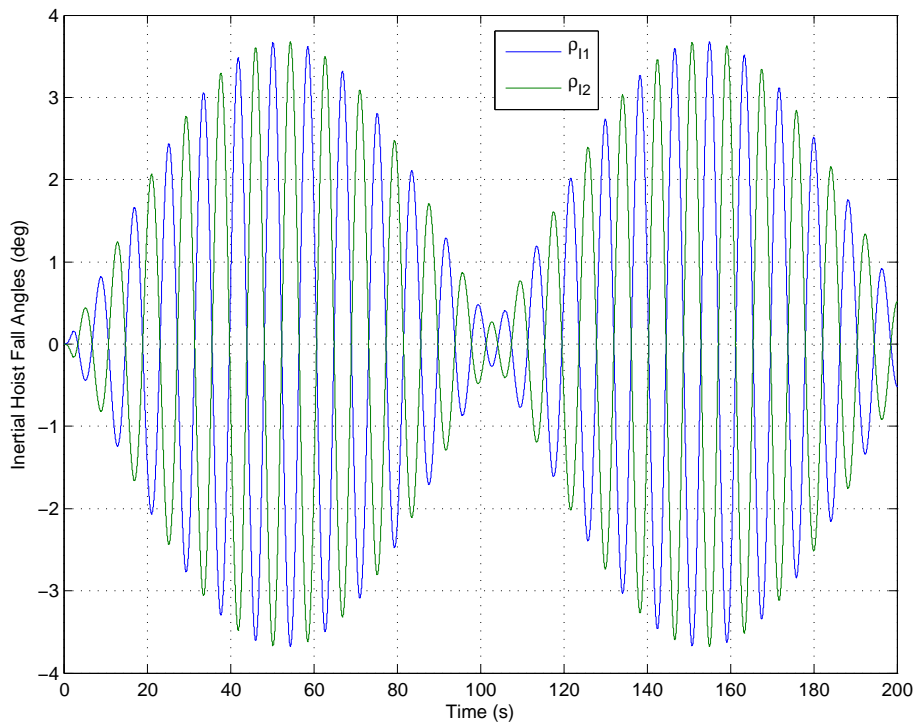


Figure 41. Time history of the inertial hoist fall angles, ρ_{I1} and ρ_{I2} for a 0.1 meter, 8.05 second period surge motion excitation with initial $\rho = 0$ degrees. The peak ρ angle response is slightly more than 3.5 degrees for the given input.

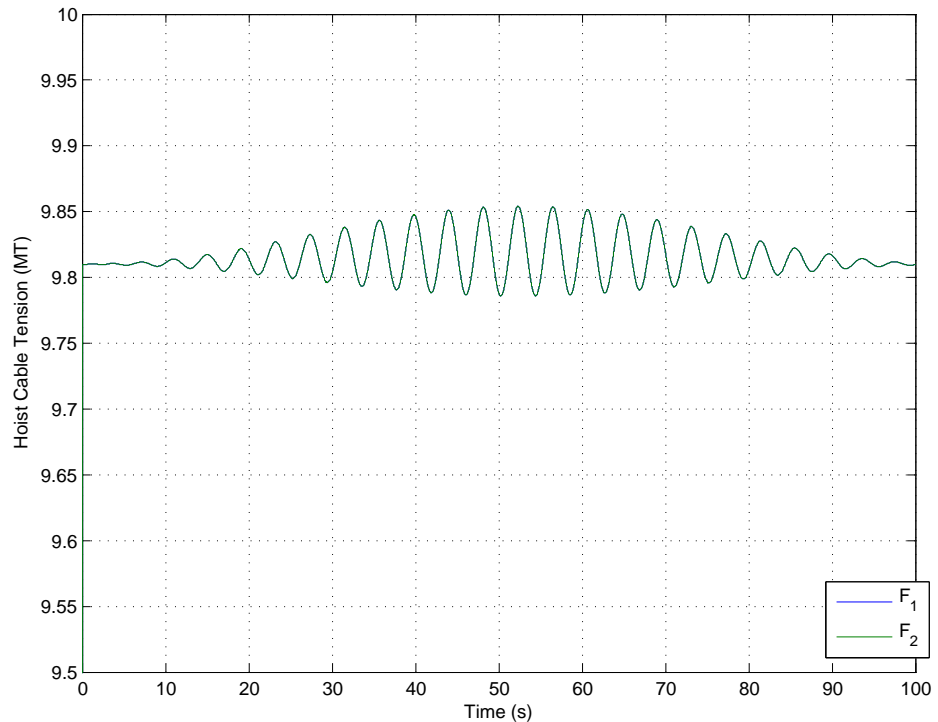


Figure 42. Time history of the hoist cable tensions, F_1 and F_2 in metric tons for a 0.1 meter, 8.05 second period surge motion excitation with initial $\rho = 0$ degrees. The peak response is approximately 0.5 percent above the initial (static) tension.

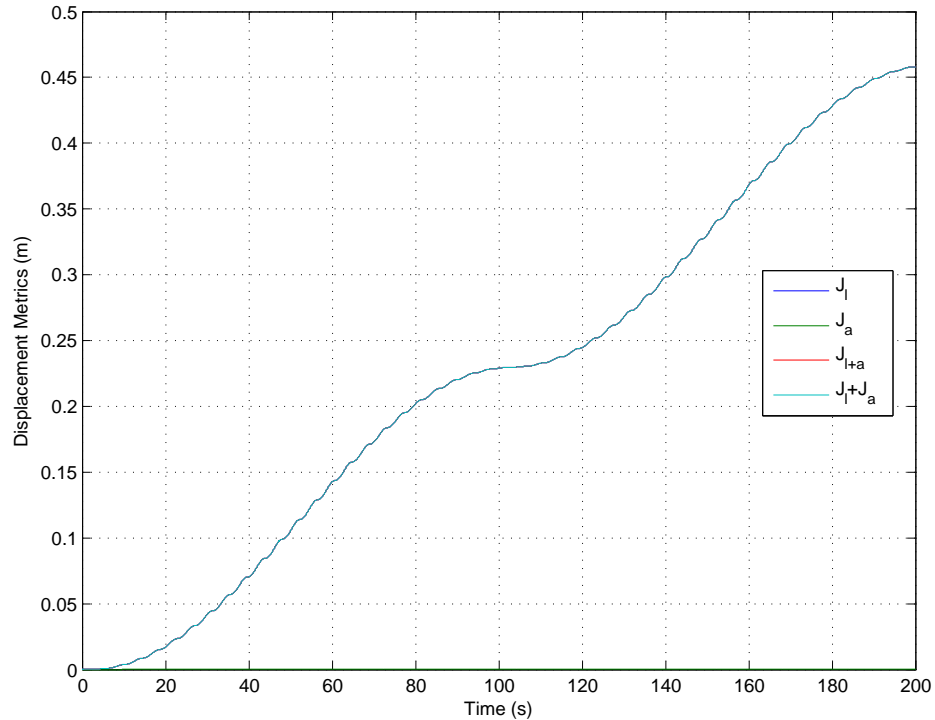


Figure 43. Time history of the calculation of the displacement metrics for a 0.1 meter, 8.05 second period surge motion excitation with initial $\rho = 0$ degrees. Note that since the payload rotation is essentially zero, there is no difference between J_l and $J_{l+\theta}$ and the sum of J_l and J_θ .

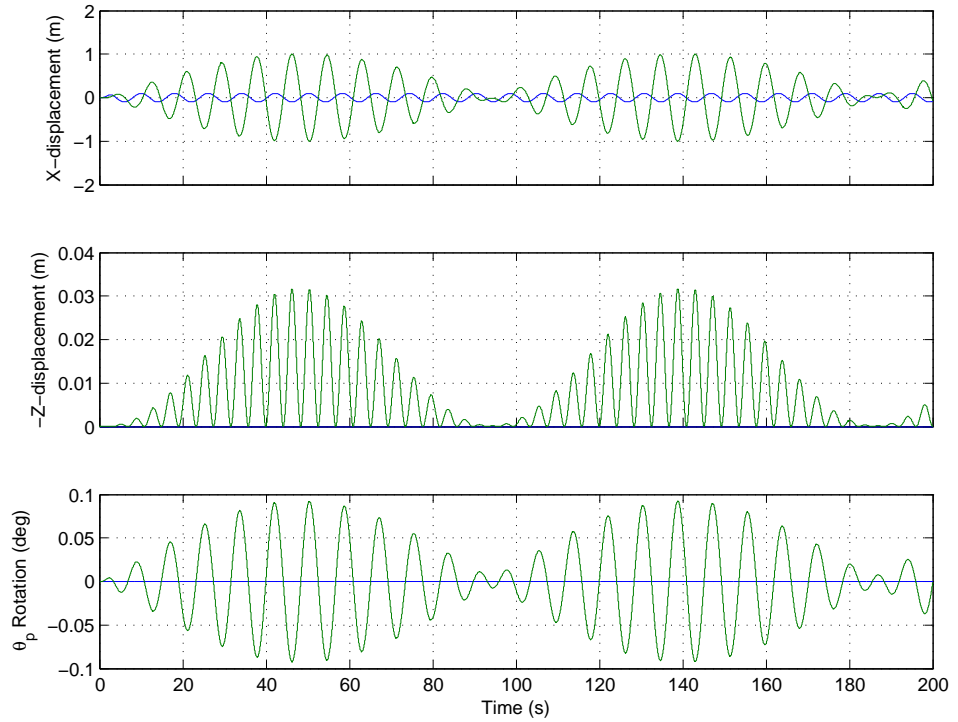


Figure 44. Time history of the payload motion for a 0.1 meter, 8.05 second period surge motion excitation with initial $\rho = 1.0$ degree. The blue trace is the ship motion and the payload response is shown in green. The maximum x and z displacements are reduced slightly. Note that the payload rotation, θ_p is small, but not zero as was the case for $\rho = 0$.

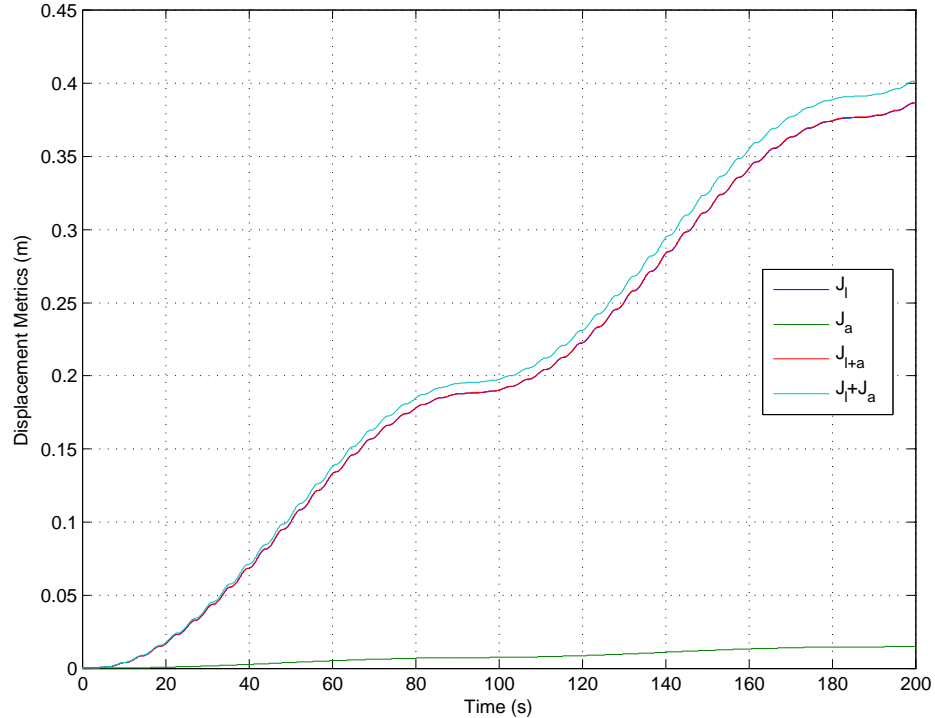


Figure 45. Time history of the calculation of the displacement metrics for a 0.1 meter, 8.05 second period surge motion excitation with initial $\rho = 1.0$ degree. Note that since the payload rotation is no longer zero, J_θ is nonzero and there is a separation between J_l and $J_{l+\theta}$ and the sum of J_l and J_θ .

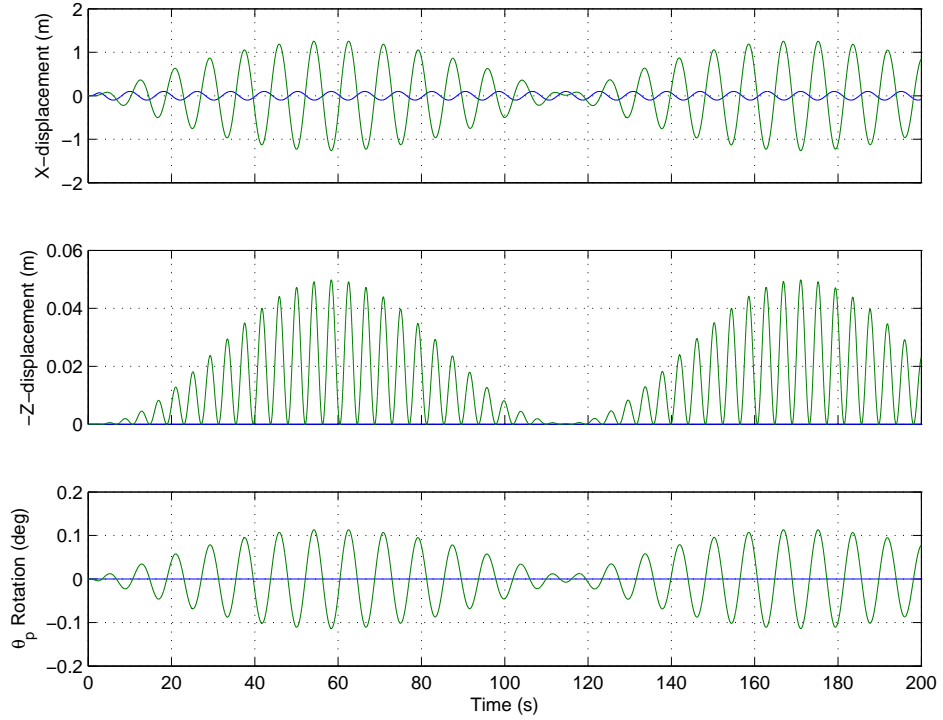


Figure 46. Time history of the payload motion for a 0.1 meter, 8.05 second period surge motion excitation with initial $\rho = -1.0$ degree. The blue trace is the ship motion and the payload response is shown in green. The maximum x and z displacements are reduced slightly. Note that the payload rotation, θ_p is small, but not zero as was the case for $\rho = 0$.

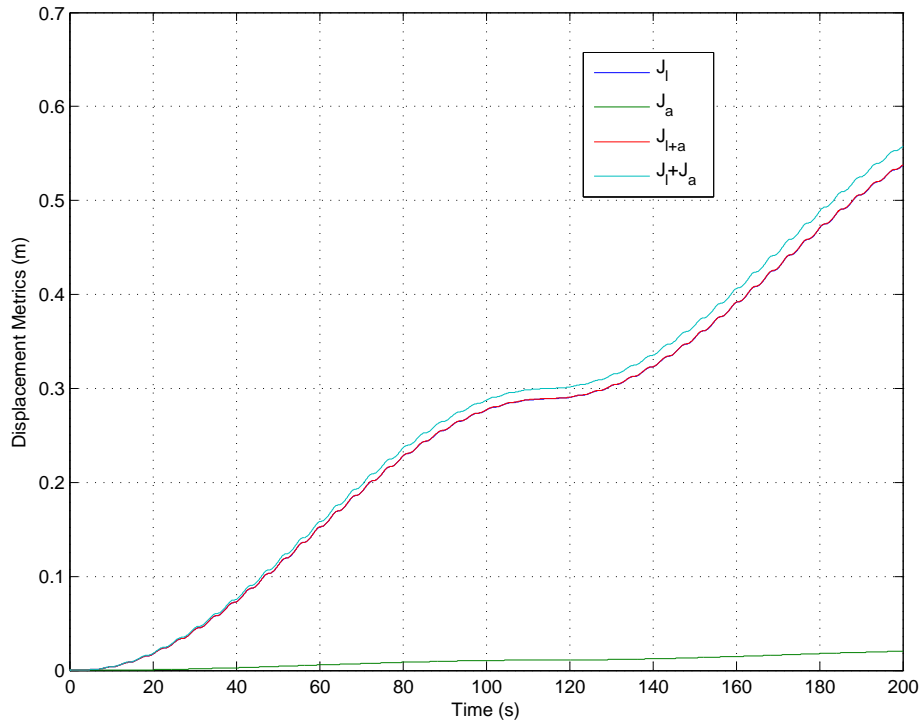


Figure 47. Time history of the calculation of the displacement metrics for a 0.1 meter, 8.05 second period surge motion excitation with initial $\rho = -1.0$ degree. Note that since the payload rotation is no longer zero, J_θ is nonzero and there is a separation between J_l and $J_{l+\theta}$ and the sum of J_l and J_θ .

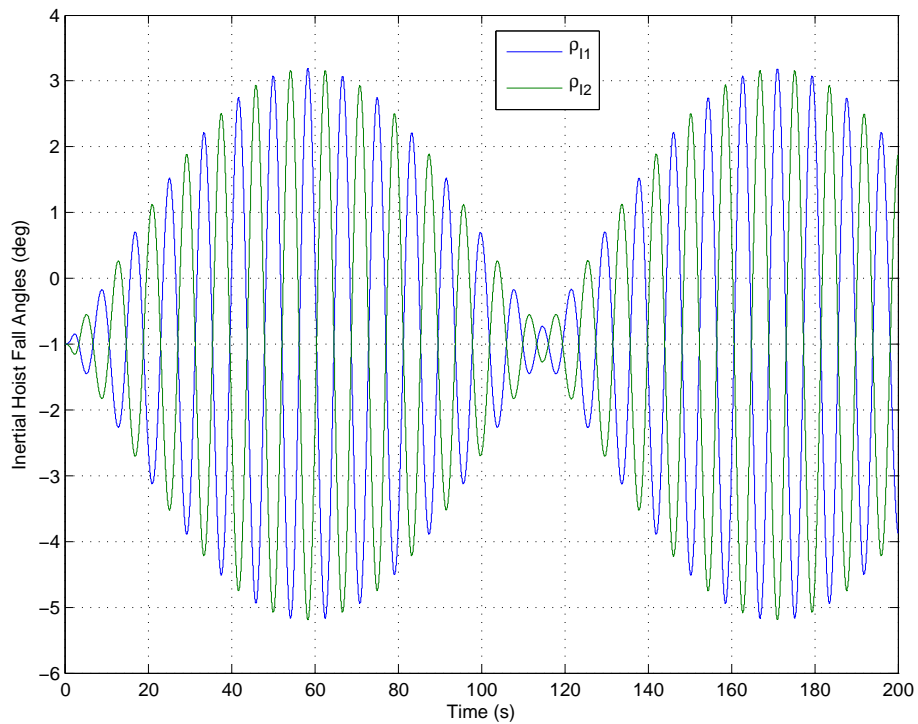


Figure 48. Time history of the inertial hoist fall angles, ρ_{I1} and ρ_{I2} for a 0.1 meter, 8.05 second period surge motion excitation with initial $\rho = -1$ degree. The peak ρ angle response is slightly more than 3.5 degrees for the given input.

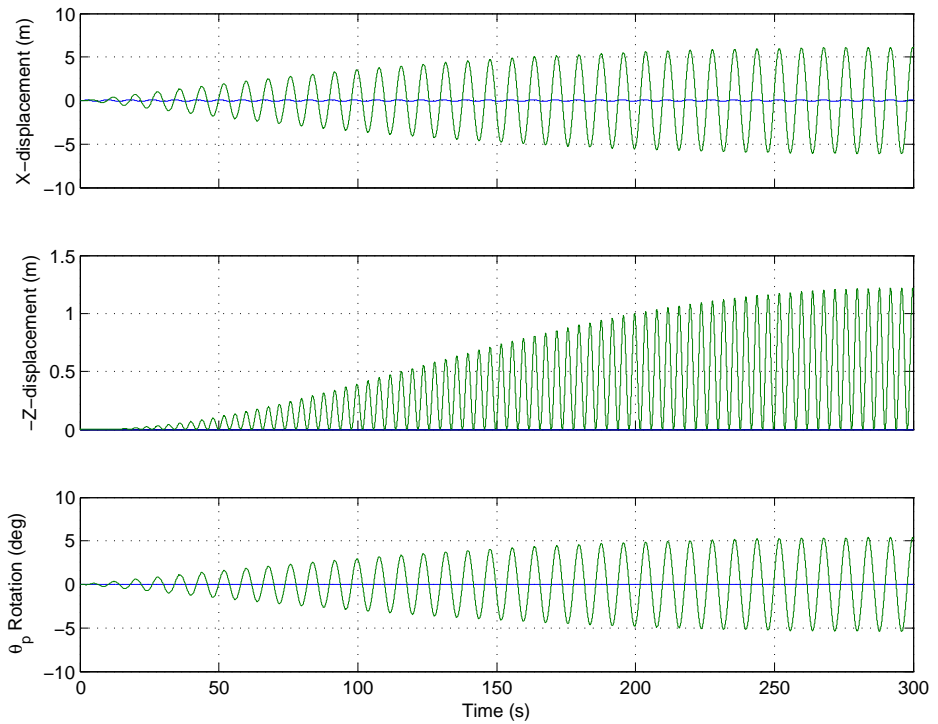


Figure 49. Time history of the payload motion for a 0.1 meter, 8.05 second period surge motion excitation with initial $\rho = -10.0$ degree. The blue trace is the ship motion and the payload response is shown in green. The maximum x and z displacements are reduced slightly. The payload rotation, θ_p is no longer small.

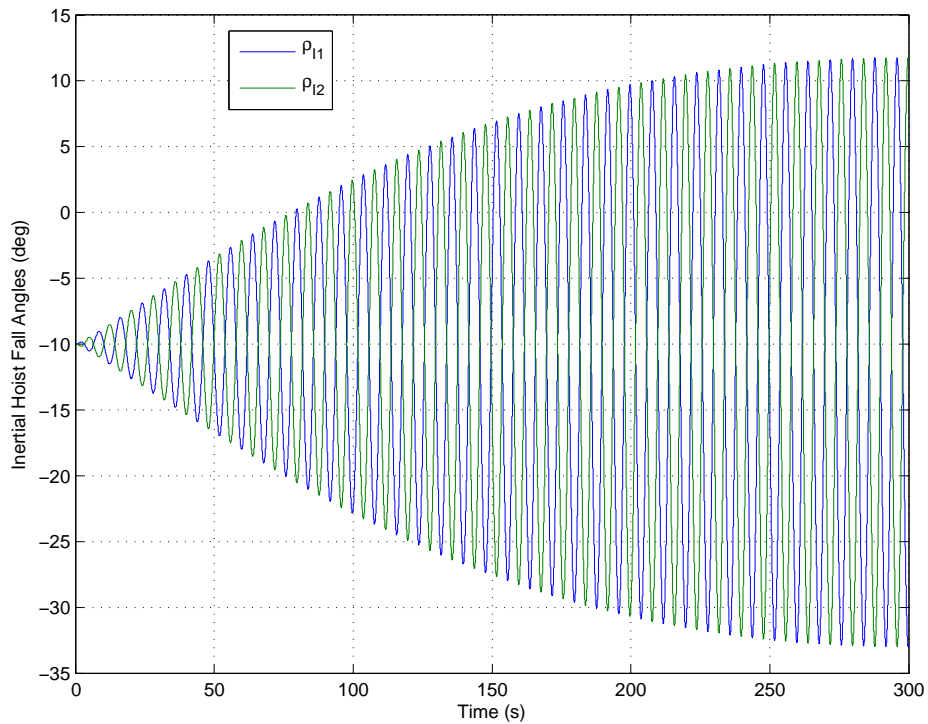


Figure 50. Time history of the inertial hoist fall angles, ρ_{I1} and ρ_{I2} for a 0.1 meter, 8.05 second period surge motion excitation with initial $\rho = -10$ degrees. The peak ρ angle response is more than 20 degrees on either side of the initial offset.

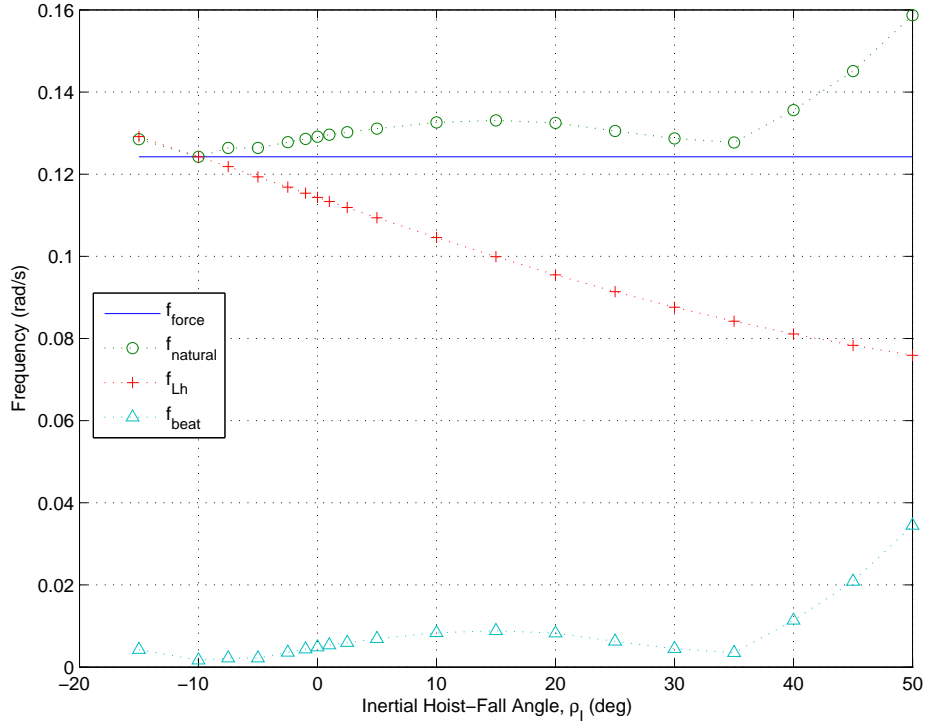


Figure 51. Plot of frequency data versus the hoist-fall offset angle, ρ_I for a 8.05 second period surge motion excitation. The forcing frequency is shown along with the calculated natural frequency of the planar dual-crane system. For purposes of comparison, the natural frequency of a simple pendulum corresponding to the hoist cable length, L_h , is shown. Note that for $\rho = -10$ degrees the system would be predicted to be in resonance with the forcing function.

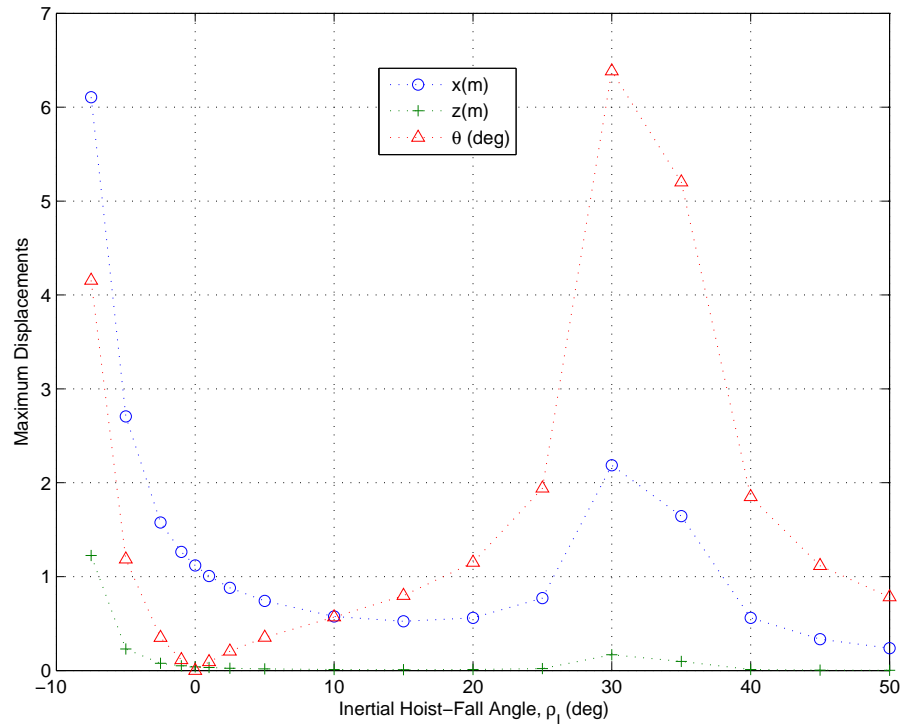


Figure 52. This plot summarizes the results of the simulation of the open loop system for a 8.05 second period surge motion excitation. Maximum values of x and z in meters and θ_p in degrees for each run are plotted versus the hoist-fall offset angle, ρ .

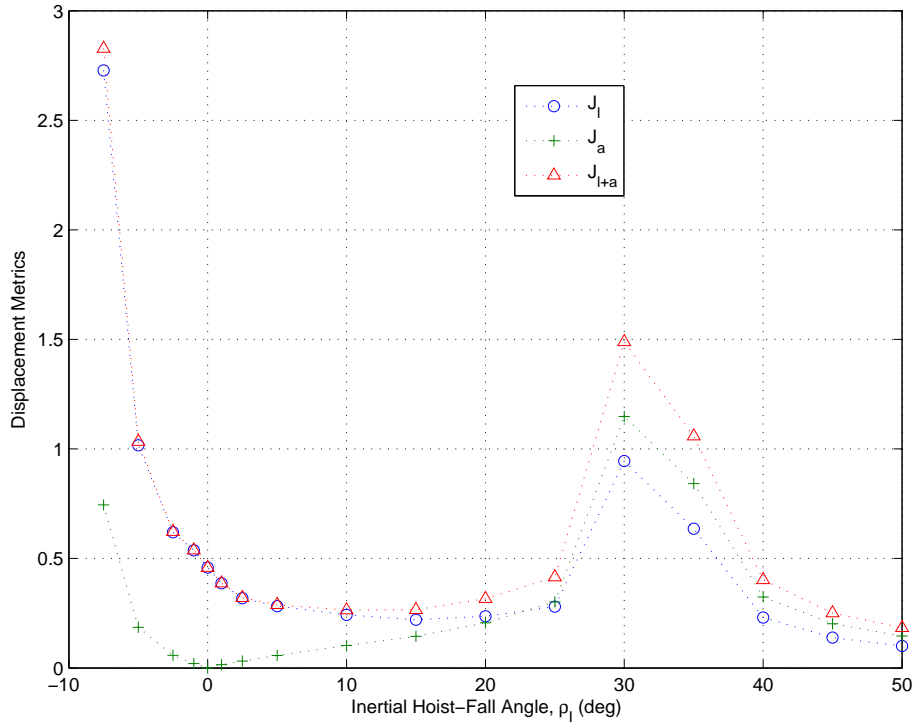


Figure 53. This plot summarizes the results of the simulation of the open loop system for a 8.05 second period surge motion excitation. Values of the displacement metrics in meters for each run are plotted versus the hoist-fall offset angle, ρ . Note that the peak representing a resonance at $\rho = -10$ degrees has a large x contribution while the peak at $\rho = 35$ degrees has a large θ_p component.

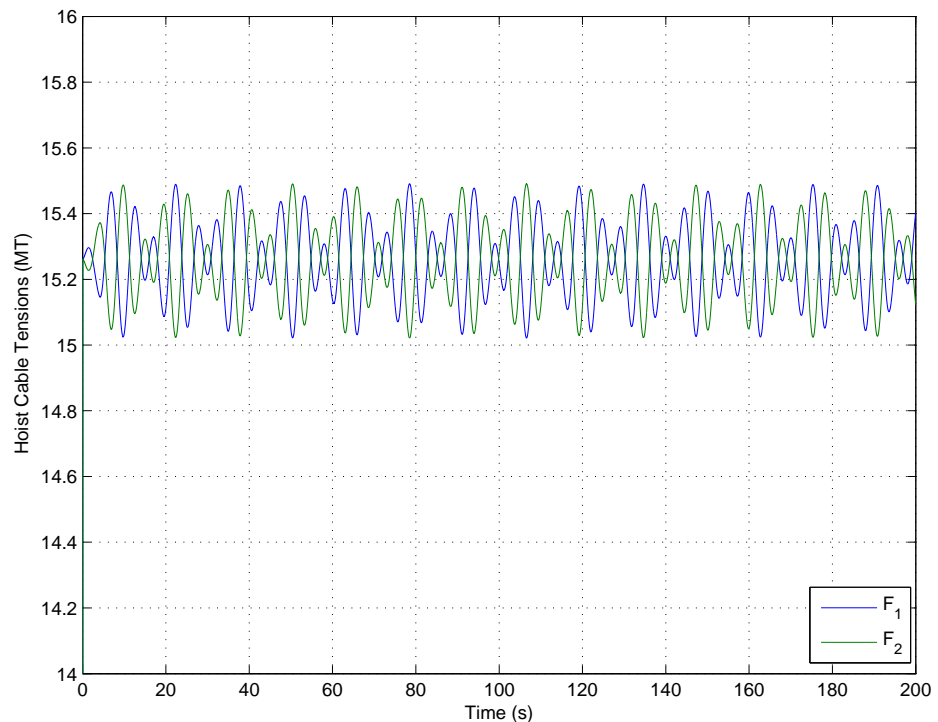


Figure 54. Time history of the hoist cable tensions, F_1 and F_2 in metric tons for a 0.1 meter, 8.05 second period surge motion excitation with initial $\rho = 50$ degrees. The peak response is approximately 1.5 percent above the initial (static) tension.

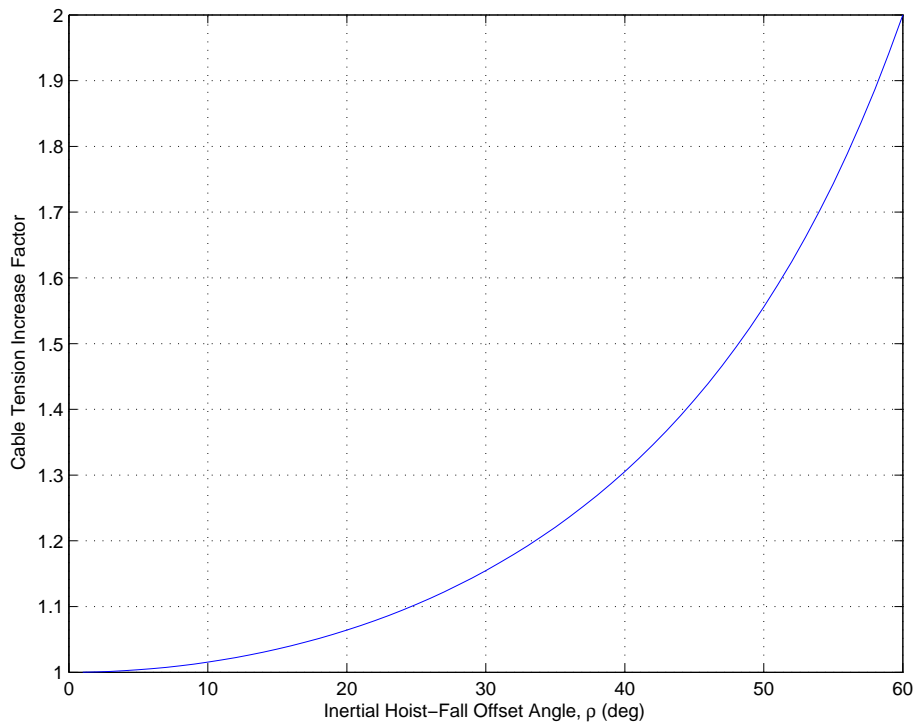


Figure 55. Hoist cable tension increase as a function of the cable offset angle, ρ .

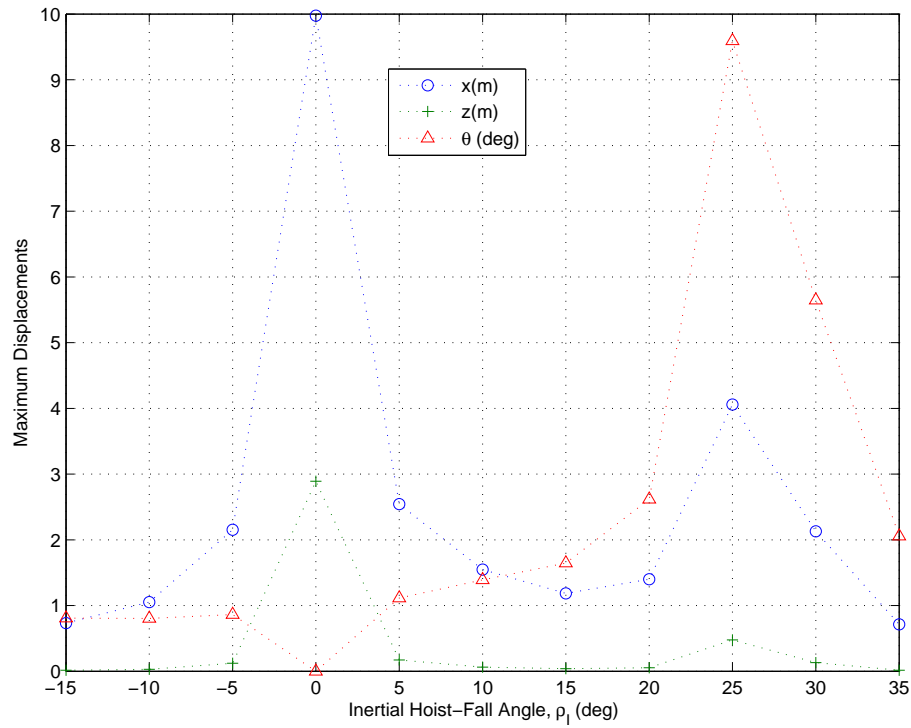


Figure 56. This plot summarizes the results of the simulation of the open loop system for a 8.75 second period surge motion excitation. Maximum values of x and z in meters and θ_p in degrees for each run are plotted versus the hoist-fall offset angle, ρ .

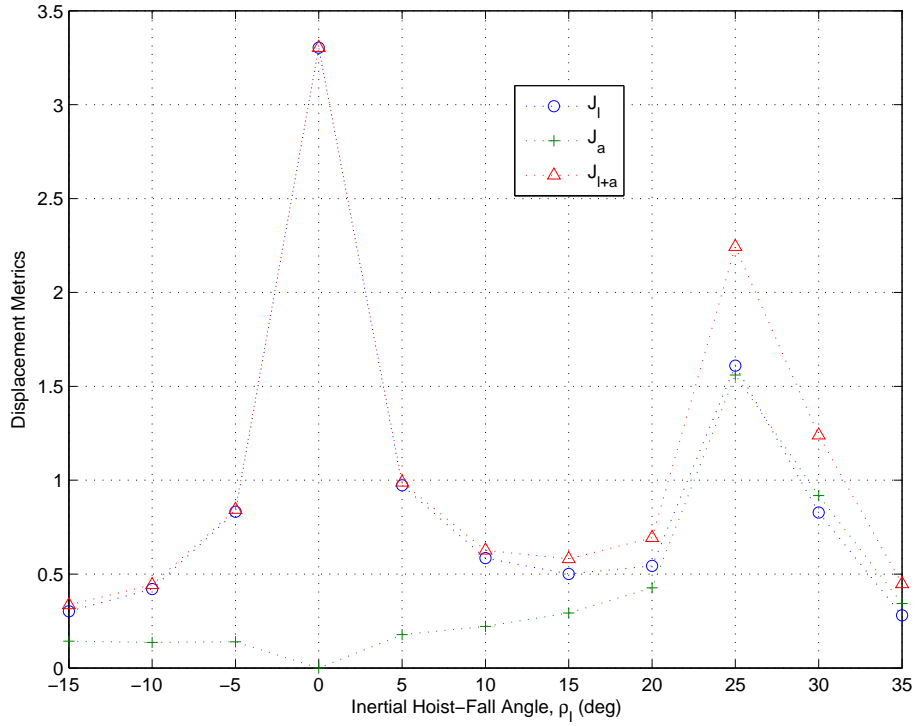


Figure 57. This plot summarizes the results of the simulation of the open loop system for a 8.75 second period surge motion excitation. Values of the displacement metrics in meters for each run are plotted versus the hoist-fall offset angle, ρ . Note that the peak representing a resonance at $\rho = 0$ degrees has a large x contribution while the peak at $\rho = 25$ degrees has a large θ_p component.

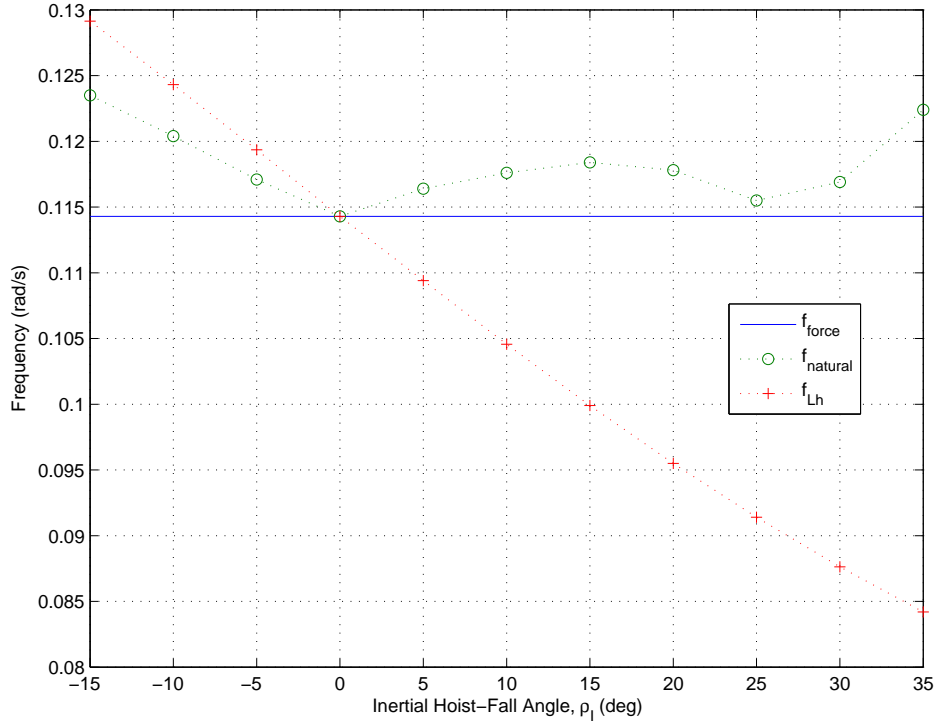


Figure 58. Plot of frequency data versus the hoist-fall offset angle, ρ_I for a 8.75 second period surge motion excitation. The forcing frequency is shown along with the calculated natural frequency of the planar dual-crane system. For purposes of comparison, the natural frequency of a simple pendulum corresponding to the hoist cable length, L_h , is shown. Note that for $\rho = 0$ degrees the system would be predicted to be in resonance with the forcing function.

T_F (s)	ρ (deg)	L_h (m)	T_{beat} (s)	T_n (Based on L_h)	T_n (s)	X_{max} (m)	Z_{max} (m)	$\theta_{p,max}$ (deg)	J_l	J_θ	$J_{l+\theta}$
8.75	-15.0	14.8992	109	8.0998	7.7433	0.7318	0.0146	0.8090	0.3019	0.1426	0.3361
8.75	-10.0	16.0810	163	8.3042	8.0445	1.0528	0.0294	0.8034	0.4203	0.1359	0.4430
8.75	-5.0	17.4431	360	8.5424	8.3783	2.1522	0.1224	0.8626	0.8320	0.1396	0.8440
8.75	0.0	19.0000	-	8.7500	8.7500	9.9762	2.8919	0	3.3036	0	3.3036
8.75	5.0	20.7613	470	8.5901	9.1406	2.5425	0.1710	1.1145	0.9726	0.1779	0.9891
8.75	10.0	22.7291	300	8.5020	9.5639	1.5465	0.0632	1.3915	0.5854	0.2215	0.6270
8.75	15.0	24.0000	241	8.4434	10.0095	1.1845	0.0381	1.6473	0.5004	0.2929	0.5814
8.05	-10.0	16.0810	600	7.9434	8.0445	6.1147	1.2200	5.3902	2.6866	0.9503	2.8500
8.05	-7.5	16.7385	462	7.9121	8.2074	6.1064	1.2244	4.1549	2.7274	0.7446	2.8275
8.05	-5.0	17.4431	456	7.9104	8.3783	2.7063	0.2297	1.1860	1.0166	0.1854	1.0337
8.05	-2.5	18.1964	280	7.8250	8.5573	1.5759	0.0776	0.3508	0.6197	0.0579	0.6226
8.05	-1.0	18.6725	228	7.7550	8.6685	1.2638	0.0499	0.1140	0.5373	0.0204	0.5377
8.05	0.0	19.0000	200	7.7385	8.7442	1.1187	0.0391	0.0000	0.4581	0.0000	0.4581
8.05	1.0	19.3357	187	7.7178	8.8212	1.0068	0.0317	0.0924	0.3867	0.0150	0.3870
8.05	2.5	19.8548	168	7.6819	8.9388	0.8814	0.0243	0.2048	0.3185	0.0315	0.3203
8.05	5.0	20.7613	145	7.6266	9.1406	0.7414	0.0173	0.3518	0.2824	0.0572	0.2888
8.05	10.0	22.7291	120	7.5439	9.5639	0.5755	0.0106	0.5690	0.2423	0.1025	0.2646
8.05	15.0	24.8961	113	7.5147	10.0095	0.5238	0.0090	0.7984	0.2207	0.1443	0.2659
8.05	20.0	27.2444	121	7.5478	10.4709	0.5614	0.0106	1.1502	0.2358	0.2066	0.3162
8.05	25.0	29.7461	160	7.6644	10.9411	0.7707	0.0203	1.9412	0.2803	0.3012	0.4150
8.05	30.0	32.3645	222	7.7683	11.4125	2.1866	0.1686	6.3839	0.9448	1.1481	1.4886
8.05	35.0	35.0573	286	7.8296	11.8778	1.6447	0.0970	5.2020	0.6359	0.8420	1.0582
8.05	40.0	37.7784	088	7.3753	12.3301	0.5612	0.0115	1.8494	0.2302	0.3242	0.4021
8.05	45.0	40.4813	048	6.8938	12.7636	0.3337	0.0042	1.1161	0.1386	0.2022	0.2507
8.05	50.0	43.1204	029	6.3009	13.1731	0.2376	0.0022	0.7834	0.1004	0.1462	0.1835

Table 2. Summary table of simulation results for the forced response of the planar dual-crane system.

THIS PAGE INTENTIONALLY LEFT BLANK

IV. INVERSE KINEMATIC CONTROL

In the previous section the response of the uncontrolled planar dual-crane system to a base-excitation environment similar to a ship in a seaway was explored. It was found that the crane hoist-fall angle offset, ρ , had a significant effect that could be potentially exploited to 'tune' the system away from frequencies that would cause resonance with the motion environment. This effect was observed for pure linear motion in the x-direction, but in-plane rotations and z-linear motions could not be influenced by strictly passive means.

This section develops an active method to decouple the payload from the base (ship) motion environment. The selected method uses an inverse kinematic approach such as described by Yamamoto in [56] and by Baillieul in [62]. One advantage to the selected approach is that it does not require sensing of the payload motion. In the author's experience with shipboard crane control system, including the Pendulation Control System, the sensing of payload motion can be problematic. In practice, sensing of ship motion is much more straightforward.

The goal of the inverse kinematic controller is to use the crane's actuation capability (L_{h1} , L_{h2} , β_1 and β_2) to keep the load fixed in inertial space. Thus, the load's center of mass coordinates in the x-z plane, and its absolute orientation should experience zero time rate of change even if $\{s\}$ has motion. A combination of kinematic and force constraints need to be satisfied, that results in three equations and 4 unknowns. The resulting linear system of undetermined equations has an infinite set of solutions. A weighted, minimum norm solution is used to illustrate one type of solution in this section and used in the simulation results that follow.

Based on experience with shipboard cargo movement, the overarching goal is to reduce payload motion to 1 meter or less.

A. FORCE CONSTRAINTS

Since the goal of the control strategy is to keep the load in static equilibrium, the sum of all external forces acting on the load must be zero. Force and moment balance equations are given in Eq. IV.1

$$\begin{aligned} -F_1 \cos \rho_{I1} - F_2 \cos \rho_{I2} + m_p g &= 0 \\ F_1 \sin \rho_{I1} - F_2 \sin \rho_{I2} &= 0 \\ d_{p1} F_1 \cos (\theta_p + \rho_{I1}) - d_{p2} F_2 \cos (\theta_p - \rho_{I2}) &= 0 \end{aligned} \quad (\text{IV.1})$$

Clearly, the unknown force amplitudes, F_1 and F_2 , can be resolved out of the first two expressions of Eq. IV.1, resulting in a single equation in θ_p , ρ_{I1} , and ρ_{I2} . Taking its derivative, and imposing the desired condition that $\dot{\theta}_p = 0$, results in an equation of the form shown in Eq. IV.2.

$$J_1(\rho_{I1}, \rho_{I2}, \theta_p) \cdot \dot{\rho}_{I1} + J_2(\rho_{I1}, \rho_{I2}, \theta_p) \cdot \dot{\rho}_{I2} = 0 \quad (\text{IV.2})$$

where J_1 and J_2 are the nonlinear functions shown in Eq. IV.3.

$$J_1 = \frac{Num_{J1}}{Den_{J1}} \quad \text{and} \quad J_2 = \frac{Num_{J2}}{Den_{J2}} \quad (\text{IV.3})$$

and,

$$\begin{aligned}
Num_{J1} = & mgd_2 \cos(-\theta_p + \rho_{I2}) (d_2 \cos(-\theta_p + \rho_{I2}) + \sin(\rho_{I1}) d_1 \sin(\theta_p + \rho_{I1}) \cos(\rho_{I2}) \\
& + \cos(\rho_{I1}) d_1 \cos(\theta_p + \rho_{I1}) \cos(\rho_{I2}) - d_1 \cos(\theta_p + \rho_{I1}) \sin(\rho_{I2}) \sin(\rho_{I1}) \\
& + d_1 \sin(\theta_p + \rho_{I1}) \sin(\rho_{I2}) \cos(\rho_{I1}))
\end{aligned}$$

$$\begin{aligned}
Den_{J1} = & \cos(\rho_{I1})^2 d_2^2 \cos(-\theta_p + \rho_{I2})^2 + d_1^2 \cos(\theta_p + \rho_{I1})^2 \cos(\rho_{I2})^2 \\
& + 2 \cos(\rho_{I1}) d_2 \cos(-\theta_p + \rho_{I2}) d_1 \cos(\theta_p + \rho_{I1}) \cos(\rho_{I2})
\end{aligned}$$

$$\begin{aligned}
Num_{J2} = & -mgd_1 \cos(\theta_p + \rho_{I1}) (d_2 \sin(-\theta_p + \rho_{I2}) \sin(\rho_{I1}) \cos(\rho_{I2}) - \\
& d_2 \cos(-\theta_p + \rho_{I2}) \sin(\rho_{I1}) \sin(\rho_{I2}) + \sin(\rho_{I2}) \cos(\rho_{I1}) d_2 \sin(-\theta_p + \rho_{I2}) \\
& + d_1 \cos(\theta_p + \rho_{I1}) + \cos(\rho_{I2}) \cos(\rho_{I1}) d_2 \cos(-\theta_p + \rho_{I2}))
\end{aligned}$$

$$\begin{aligned}
Den_{J2} = & \cos(\rho_{I1})^2 d_2^2 \cos(-\theta_p + \rho_{I2})^2 + d_1^2 \cos(\theta_p + \rho_{I1})^2 \cos(\rho_{I2})^2 \\
& + 2 \cos(\rho_{I1}) d_2 \cos(-\theta_p + \rho_{I2}) d_1 \cos(\theta_p + \rho_{I1}) \cos(\rho_{I2})
\end{aligned}$$

B. KINEMATIC CONSTRAINTS

Two vector loops can be formed that capture the kinematic constraints of the system and are given in Eq. IV.4

$$\begin{aligned}
\vec{p}_1 + \vec{p}_{2/1} + \vec{p}_{4/2} + \vec{p}_{6/4} + \vec{p}_{8/6} &= \vec{p}_8 \\
\vec{p}_1 + \vec{p}_{3/1} + \vec{p}_{5/3} + \vec{p}_{7/5} + \vec{p}_{8/7} &= \vec{p}_8
\end{aligned} \tag{IV.4}$$

Taking the x and z components of Eq. IV.4 gives 4 constraint equations given

in Eq. IV.5.

$$\begin{aligned}
(1) \quad & x_1 + d_{s1} \cos(\theta_s) - L_{b1} \cos(\beta_1 - \theta_s) - L_{h1} \sin(\rho_{I1}) - \\
& d_{p1} \cos(\theta_p) - x_8 = 0 \\
(2) \quad & z_1 - d_{s1} \sin(\theta_s) - L_{b1} \sin(\beta_1 - \theta_s) + L_{h1} \cos(\rho_{I1}) + \\
& d_{p1} \sin(\theta_p) - z_8 = 0 \\
(3) \quad & x_1 - d_{s2} \cos(\theta_s) + L_{b2} \cos(\beta_2 + \theta_s) + L_{h2} \sin(\rho_{I2}) + \\
& d_{p2} \cos(\theta_p) - x_8 = 0 \\
(4) \quad & z_1 + d_{s2} \sin(\theta_s) - L_{b2} \sin(\beta_2 + \theta_s) + L_{h2} \cos(\rho_{I2}) - \\
& d_{p2} \sin(\theta_p) - z_8 = 0
\end{aligned} \tag{IV.5}$$

Taking the time derivatives of the first and third equations of Eq. IV.5 and noting that $\dot{x}_1 = \dot{x}_s$, yields Eq. IV.6

$$\begin{aligned}
\frac{d}{dt} eq1 \quad : \quad & \dot{x}_s - d_{s1} \sin(\theta_s) \dot{\theta}_s - L_b \sin(-\beta_1 + \theta_s) \dot{\beta}_1 + L_b \sin(-\beta_1 + \theta_s) \dot{\theta}_s \\
& - \dot{L}_{h1} \sin(\rho_{I1}) - L_{h1} \cos(\rho_{I1}) \dot{\rho}_{I1} + d_{p1} \sin(\theta_p) \dot{\theta}_p - \dot{x}_8 = 0 \\
& \\
\frac{d}{dt} eq3 \quad : \quad & \dot{x}_s + d_{s2} \sin(\theta_s) \dot{\theta}_s - L_b \sin(\beta_2 + \theta) \dot{\beta}_2 - L_b \sin(\beta_2 + \theta_s) \dot{\theta}_s \\
& + \dot{L}_{h2} \sin(\rho_{I2}) + L_{h2} \cos(\rho_{I2}) \dot{\rho}_{I2} - d_{p2} \sin(\theta_p) \dot{\theta}_p - \dot{x}_8 = 0
\end{aligned} \tag{IV.6}$$

Solving the two expressions of Eq. IV.6 for $\dot{\rho}_{I1}$ and $\dot{\rho}_{I2}$, results in Eq. IV.7.

$$\begin{aligned}
\dot{\rho}_{I1} &= \frac{\dot{x}_s - d_{s1} \sin(\theta_s) \dot{\theta}_s + L_b \sin(\beta_1 - \theta_s) \dot{\beta}_1 - L_b \sin(\beta_1 - \theta_s) \dot{\theta}_s}{L_{h1} \cos(\rho_{I1})} \\
&+ \frac{-\dot{L}_{h1} \sin(\rho_{I1}) + d_{p1} \sin(\theta_p) \dot{\theta}_p - \dot{x}_8}{L_{h1} \cos(\rho_{I1})} \\
\dot{\rho}_{I2} &= \frac{-\dot{x}_s - d_{s2} \sin(\theta_s) \dot{\theta}_s + L_b \sin(\beta_2 + \theta_s) \dot{\beta}_2 + L_b \sin(\beta_2 + \theta_s) \dot{\theta}_s}{L_{h2} \cos(\rho_{I2})} \\
&- \frac{-\dot{L}_{h2} \sin(\rho_{I2}) + d_{p2} \sin(\theta_p) \dot{\theta}_p + \dot{x}_8}{L_{h2} \cos(\rho_{I2})}
\end{aligned} \tag{IV.7}$$

Substituting Eq. IV.7 into Eq. IV.2, and the derivatives of equations 2 and 4 of Eq. IV.5 yields three linear equations in the 4 unknowns, \dot{L}_{h1} , \dot{L}_{h2} , $\dot{\beta}_1$ and $\dot{\beta}_2$. These are shown in Eq. IV.8, where A is a 3×4 Jacobian with elements as shown in Eq. IV.9 and \vec{y} is a 3×1 vector of all the terms of the constraint equations that do not contain \dot{L}_{h1} , \dot{L}_{h2} , $\dot{\beta}_1$ and $\dot{\beta}_2$ as shown in Eq. IV.11. Note that the J_1 and J_2 in the elements of the Jacobian are the nonlinear functions defined in Eq. IV.3.

$$\vec{y} = A \begin{Bmatrix} \dot{\beta}_1 \\ \dot{\beta}_2 \\ \dot{L}_{h1} \\ \dot{L}_{h2} \end{Bmatrix} \quad (\text{IV.8})$$

$$A = \begin{bmatrix} -\frac{L_b \cos(-\theta - \rho_{I1} + \beta_2)}{\cos(\rho_{I1})} & 0 & \frac{1}{\cos(\rho_{I1})} & 0 \\ 0 & -\frac{L_b \cos(\theta - \rho_{I2} + \beta_2)}{\cos(\rho_{I2})} & 0 & \frac{1}{\cos(\rho_{I2})} \\ \frac{J_1 L_b \sin(\beta_2 - \theta)}{L_{h1} \cos(\rho_{I1})} & \frac{J_2 L_b \sin(\beta_2 + \theta)}{L_{h2} \cos(\rho_{I2})} & -\frac{J_1 \sin(\rho_{I1})}{L_{h1} \cos(\rho_{I1})} & -\frac{J_2 \sin(\rho_{I2})}{L_{h2} \cos(\rho_{I2})} \end{bmatrix} \quad (\text{IV.9})$$

$$\begin{aligned}
y(1) &= \frac{-\dot{z}_s \cos(\rho_{I1}) + d_{s1} \dot{\theta} \cos(\rho_{I1} + \theta) - L_b \dot{\theta} \cos(-\theta - \rho_{I1} + \beta_1) + \sin(\rho_{I1}) \dot{x}_s}{\cos(\rho_{I1})} \\
&\quad + \frac{-\sin(\rho_{I1}) \dot{x}_8 + \dot{z}_8 \cos(\rho_{I1}) - d_{p1} \dot{\theta}_d \cos(\theta_p + \rho_{I1})}{\cos(\rho_{I1})} \\
y(2) &= \frac{-\dot{z}_s \cos(\rho_{I2}) - d_{s2} \dot{\theta} \cos(\rho_{I2} - \theta) + L_b \dot{\theta} \cos(\theta - \rho_{I2} + \beta_2) - \sin(\rho_{I2}) \dot{x}_s}{\cos(\rho_{I2})} \\
&\quad + \frac{d_{p2} \dot{\theta}_p \cos(-\theta_p + \rho_{I2}) + \sin(\rho_{I2}) \dot{x}_8 + \dot{z}_8 \cos(\rho_{I2})}{\cos(\rho_{I1})} \\
y(3) &= \frac{1}{L_{h1} L_{h2} \cos(-\rho_{I1} + \rho_{I2}) + L_{h1} L_{h2} \cos(\rho_{I1} + \rho_{I2})} \left(-2 J_1 \dot{x}_s L_{h2} \cos(\rho_{I2}) \right. \\
&\quad + J_1 d_{s1} \dot{\theta} L_{h2} \sin((\rho_{I2} + \theta)) - J_1 d_{s1} \dot{\theta} L_{h2} \sin((\rho_{I2} - \theta)) \\
&\quad + J_1 L_b \dot{\theta} L_{h2} \sin((\rho_{I2} + \beta_1 - \theta)) + J_1 L_b \dot{\theta} L_{h2} \sin((- \rho_{I2} + \beta_1 - \theta)) \\
&\quad - J_1 d_{p1} \dot{\theta}_p L_{h2} \sin((\rho_{I2} + \theta_p)) + J_1 d_{p1} \dot{\theta}_p L_{h2} \sin((- \theta_p + \rho_{I2})) + 2 J_1 \dot{x}_8 L_{h2} \cos(\rho_{I2}) \\
&\quad + 2 J_2 \dot{x}_s L_{h1} \cos(\rho_{I1}) + J_2 d_{s2} \dot{\theta} L_{h1} \sin((\rho_{I1} + \theta)) - J_2 d_{s2} \dot{\theta} L_{h1} \sin((\rho_{I1} - \theta)) \\
&\quad - J_2 L_b \dot{\theta} L_{h1} \sin((\rho_{I1} + \beta_2 + \theta)) - J_2 L_b \dot{\theta} L_{h1} \sin((- \rho_{I1} + \beta_2 + \theta)) \\
&\quad \left. - J_2 d_{p2} \dot{\theta}_p L_{h1} \sin((\theta_p + \rho_{I1})) + J_2 d_{p2} \dot{\theta}_p L_{h1} \sin((\rho_{I1} - \theta_p)) - 2 J_2 \dot{x}_8 L_{h1} \cos(\rho_{I1}) \right)
\end{aligned} \tag{IV.10}$$

One objective of the inverse kinematic controller is to compute the rate commands, \dot{L}_{h1} , \dot{L}_{h2} , $\dot{\beta}_1$ and $\dot{\beta}_2$ such that the contribution of ship motion to \vec{P}_8 is zero. For this purpose we could explicitly set $\dot{x}_8 = 0$ and $\dot{z}_8 = 0$ in the elements of the y-vector; however, the controller must also permit the operator to issue commands to move the payload for which the rates are not zero. Thus, the \dot{x}_8 and \dot{z}_8 terms that remain represent the operator commanded rates.

The solution of the planar two-crane inverse kinematics problem is underdetermined when the hoist-fall angle is non-zero. Two kinematic chain relations in which the ρ dependency are captured and a third equation that captures the force balance were used to construct the Jacobian that relates to the four actuation rates.¹ Since

¹This same condition will occur in the nonplanar case where there are 5 kinematic constraint conditions (ignoring axial roll of the load) and 6 crane inputs (2 in luff, hoist and slew).

the Jacobian is not square, a unique inverse does not exist. To obtain a solution, a form using the weighted minimum norm is used. The development of the solution follows a technique as described by Junkins [63]. A short derivation of the form is included in Appendix B.

The resulting minimum norm solution for the crane rate commands is shown in Eq. IV.11.

$$\begin{Bmatrix} \dot{\beta}_1 \\ \dot{\beta}_2 \\ \dot{L}_{h1} \\ \dot{L}_{h2} \end{Bmatrix} = W^{-1}A^T(AW^{-1}A^T)^{-1}\vec{y} \quad (\text{IV.11})$$

where W is a 4×4 weighting matrix. Obviously, one of the conditions that must be satisfied for a solution to exist is that W is positive definite. Beyond that the weighting matrix can be constructed so as to manipulate the individual contributions of the \dot{L}_{h1} , \dot{L}_{h2} , $\dot{\beta}_1$ and $\dot{\beta}_2$ components in the inverse kinematic solution as will be investigated in the following sections. To summarize, the structure of the inverse kinematic motion compensator is a feedforward controller that uses sensed ship motion to generate actuator command signals by inverting a non-linear Jacobian by means of a weighted minimum norm solution technique.

C. INVERSE KINEMATIC SOLUTION EXAMPLE

To illustrate the approach developed in Section IV, a simulated example was created. The SIMULINK simulation used in Section II was modified to include an additional m-file block to encompass the inverse kinematic control calculations. The modified simulation structure is shown in Figure 59. The 'ik' block outputs the commanded actuator rates, $\dot{\beta}_1$, $\dot{\beta}_2$, \dot{L}_{h1} , and \dot{L}_{h2} that then feed through the actuator dynamics model. The actuators use a three-state variable model with a response equivalent to an overdamped second order system with a time constant of 0.002 seconds. The state space model used generically for all four actuation systems is

described by Eqn IV.12. The output of the actuator dynamics blocks are taken to be the current crane state. The two cranes were initialized in the configuration shown in Figure 60 where the distance between their jib pins was 72 meters. The jibs of both cranes were 33.94 meters, and their initial angles were set to 45° . Both hoist lengths were set to 12 meters, connected to the ends of the load which had a total length of 24 meters. This resulted in the origin of $\{s\}$ lying directly below the center of mass of the payload. The origin of $\{I\}$ was placed at the origin of $\{s\}$ initially.

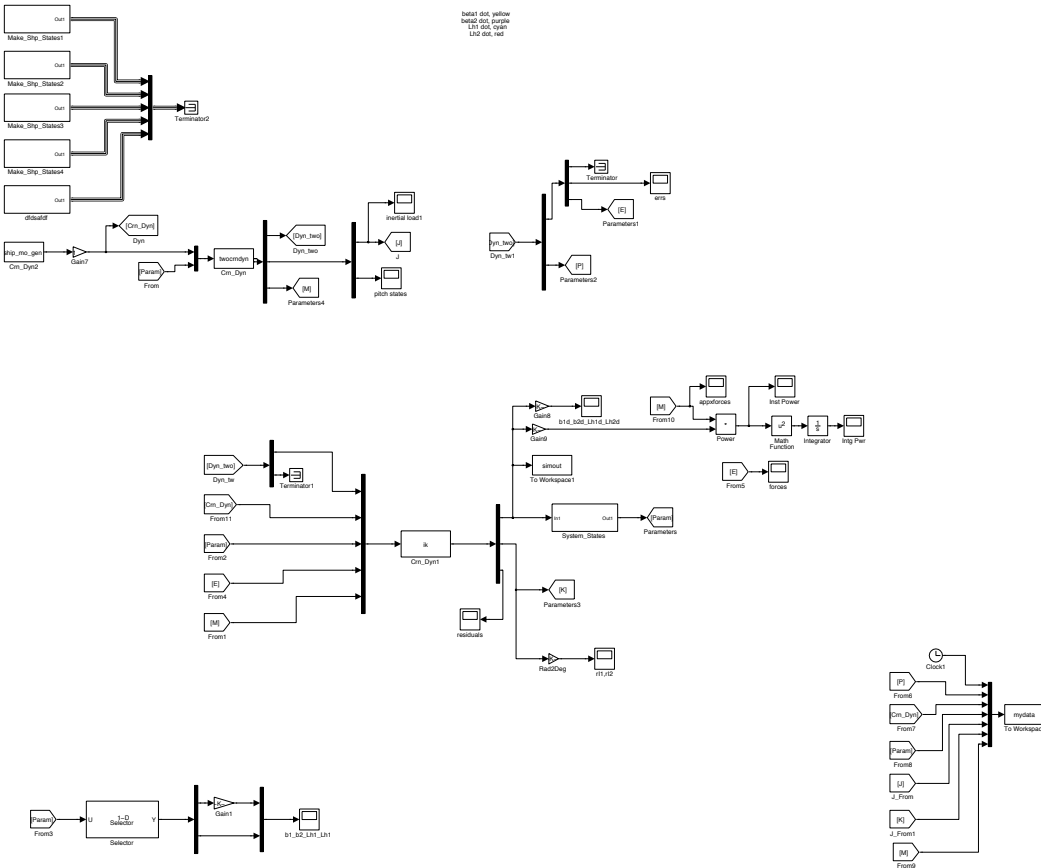


Figure 59. SIMULINK block diagram of the simulation modified for inverse kinematic control.

$$\begin{aligned}
A &= \begin{bmatrix} 0 & 1 & 0 \\ 0 & 0 & 1 \\ 0 & -2.5e + 05 & -1000 \end{bmatrix} & B &= \begin{bmatrix} 0 \\ 0 \\ 2.5e + 05 \end{bmatrix} \\
C &= \begin{bmatrix} 1 & 0 & 0 \\ 0 & 1 & 0 \\ 0 & 0 & 1 \end{bmatrix} & D &= \begin{bmatrix} 0 \\ 0 \\ 0 \end{bmatrix} \\
\text{Example : } x_{\beta_1} &= \begin{bmatrix} \beta_1 \\ \dot{\beta}_1 \\ \ddot{\beta}_1 \end{bmatrix}; & u_{\beta_1} &= \dot{\beta}_1
\end{aligned} \tag{IV.12}$$

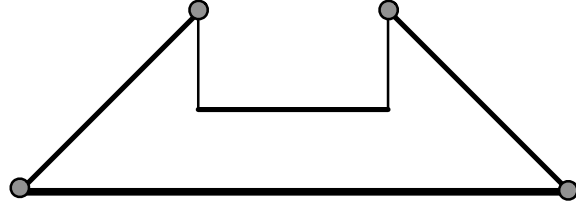


Figure 60. Illustration of the initial two-crane configuration.

Two cases were executed, using identical ship motion. The first, referred to as "control off" in the ensuing plots, did not send any commands to the crane's jib or hoist drives. The second, "control on," sent commands to the crane's jib and hoist drives using the strategy described in Section IV. A diagonal minimum norm weighting matrix was used for Eq. IV.11. The elements corresponding to the hoist were set to 1 and the elements corresponding to luff were set to 100. Selection of these values for the weights provided a rough balance between the hoist rates in units of meters per second and luff rates in radians per second computed by the minimum norm solution.

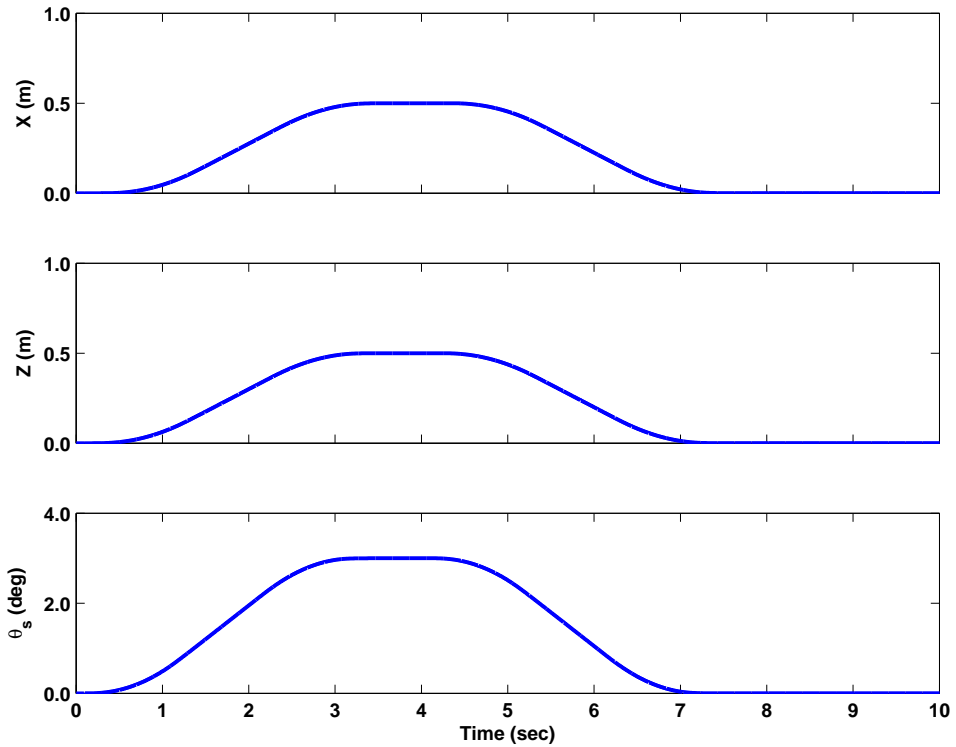


Figure 61. Ship motion time histories used in the simulation example.

The ship motion time history consisted of simultaneous surge, heave, and pitch motion as shown in Figure 61. The resulting crane jib and hoist motions are shown in Figure 62, and the resulting inertial load motion in Figure 63. Clearly, the load

was kept fixed in inertial space and thus there was no payload swing during, or after the maneuver. This is in contrast to the "control off" case where significant payload x motion persisted after the maneuver finished. This residual motion had no rotation component since the load endpoints were located directly below the boom tips.

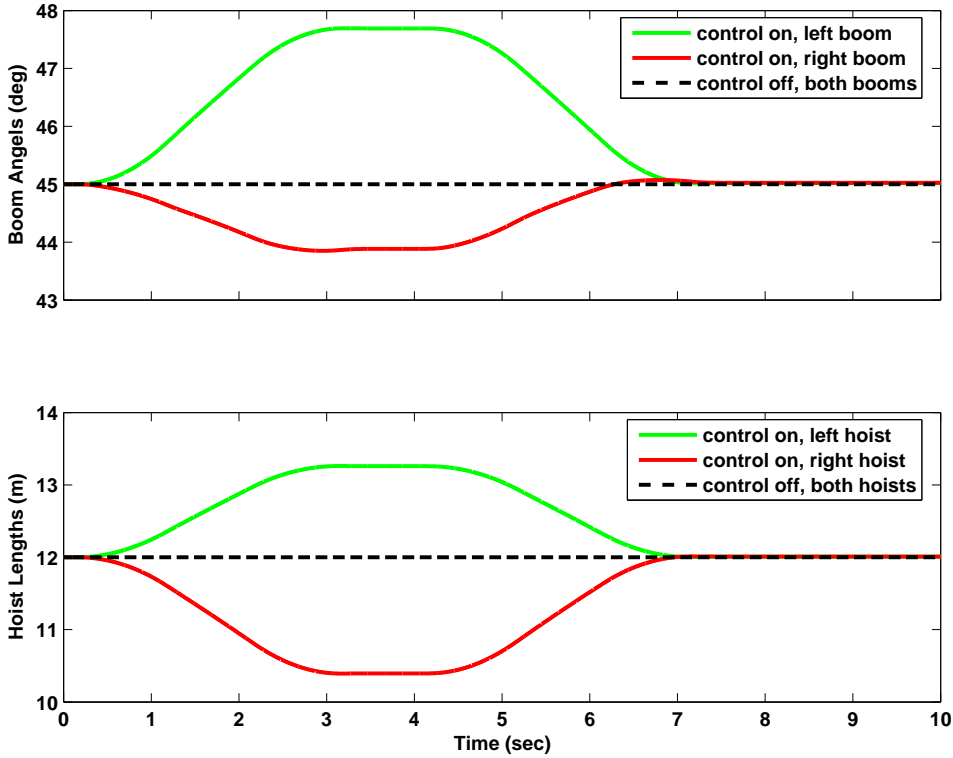


Figure 62. Crane jib and hoist motions with the control on and off.

D. RESPONSE TO SINUSOIDAL SHIP MOTION WITH INVERSE KINEMATIC CONTROL

A set of simulations was generated to explore the relationship between the ship motion conditions and the inverse kinematic control. One set isolated the affect of the magnitude of the ship motion by driving the system with sinusoidal surge motion with a period of 8.75 seconds and increasing amplitude of the motion from 0.1 to 0.25 to 0.5 to 1.0, and finally 1.5 meters.

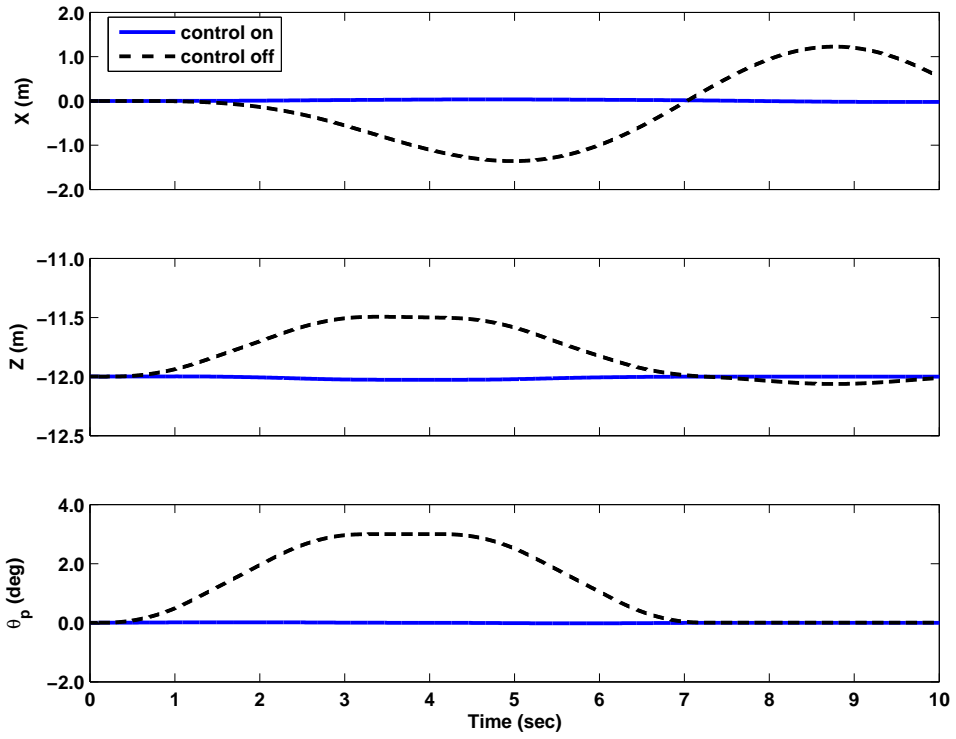


Figure 63. Inertial motion of the payload with the control on and off.

Performance metrics similar to those used in Section III will be introduced to facilitate an objective comparison between simulation cases. When interpreting results using the inverse kinematic motion compensation, the displacement metrics will be used to quantify the motion reduction performance relative to the uncontrolled system. The major purpose of the metrics will be to identify relative differences between simulated conditions rather than placing much emphasis placed on the absolute magnitude of the residual motion - recognizing that this simulation model may be overly optimistic.

That statement is based on the fact that other than the actuators being modeled as a very-responsive (time constant on the order of 0.002 seconds) system, there are no physical limits in the model to restrict its response, e.g. no rate saturation and no force or torque limitations.

The other performance metrics used to compare the response of the controlled (motion-compensated) system are based on the actuation rates and the consumed power. The metrics are defined in the following equations, IV.13 and IV.14 ².

$$J_{rate} = \frac{1}{t_f - t_0} \int_{t_0}^{t_f} \sqrt{\left((L_{B1} \cdot \dot{\beta}_1(t))^2 + (L_{B2} \cdot \dot{\beta}_2(t))^2 + \dot{L}_{h1}^2(t) + \dot{L}_{h2}^2(t) \right)} dt \quad (\text{IV.13})$$

$$J_{power} = \frac{1}{t_f - t_0} \int_{t_0}^{t_f} \sqrt{\left(\tau_1(t) \cdot \dot{\beta}_1(t) + \tau_2(t) \cdot \dot{\beta}_2(t) + F_1(t) \cdot \dot{L}_{h1}(t) + F_2(t) \cdot \dot{L}_{h2}(t) \right)^2} dt \quad (\text{IV.14})$$

To obtain a basic idea of the sensitivity of these metrics to various parameters a set of simulations were run for a sinusoidal surge motion with a range of input amplitudes from 0.1 meter to 1.5 meter. The minimum norm solution weighting was chosen to be the Identity matrix. Figures 64, 65, 66, 67, and 68 show the time histories for one of the cases with an input amplitude of 0.5 meter. Individual time histories for the remaining runs are found in Appendix C, but the results are summarized here as shown in Figures 69, 70, 71, and 72. In Figure 69 we see that the peak value of the tension in the hoist-falls is relatively insensitive to the change in forcing amplitude and that the peak torque at the jib increases linearly with the amplitude. Figure 70 shows that the peak actuation rates along with the rate metric are also linearly related to the forcing function amplitude. As expected, the peak instantaneous power and the power metric both have a quadratic relationship to the forcing amplitude as shown in Figure 71. Figure 72 shows the cross-plot of the rate metric, J_{rate} and the power metric, J_{power} for the range of input amplitudes, which again shows the quadratic increase in J_{power} while J_{rate} increases linearly. In a final look at this series of conditions, Figure 73 shows a three dimensional plot of the

²The expression for consumed power is derived in Section VI.

performance metrics, $J_{L+\theta}$, J_{rate} , and J_{power} . From this figure it is apparent that the displacement metric also increases quadratically as the input increases linearly.

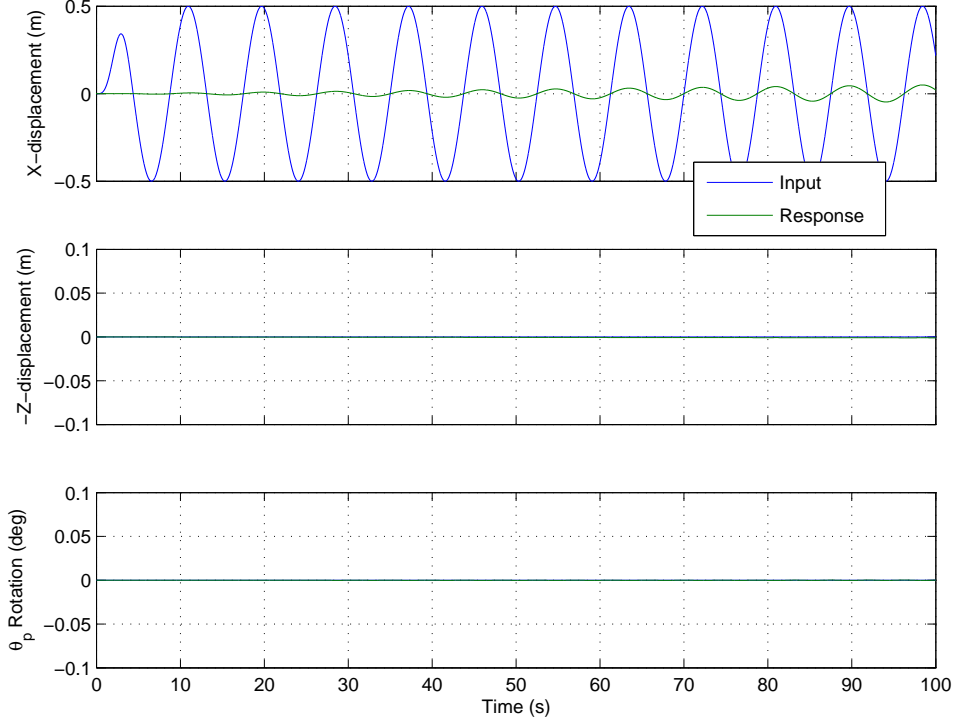


Figure 64. Plot of x , z , and θ time histories for the inverse kinematic control case with the identity matrix used as the weights in the minimum norm solution. (Simulation parameters: $\rho = 0$ degrees, $\vec{P}_{8/1,z} = -5$ meters, with a sinusoidal forcing function of $\mathbf{x}_s = 0.5$ meter at a period of 8.75 seconds.)

The other sinusoidal forcing conditions that were employed were pure heave, pure pitch, and a combination of surge, heave, and pitch with the same amplitude and periods as was used in the individual axis cases.

Figures 74, 75, 76, 77, and 78 are shown here as examples of the system response to a pure heave input with an amplitude of 1.0 meter at a period of 10.0 seconds. Two observations regarding the response to the heave input - one is the symmetry of the response, all the left-hand and right-hand side actuators have the

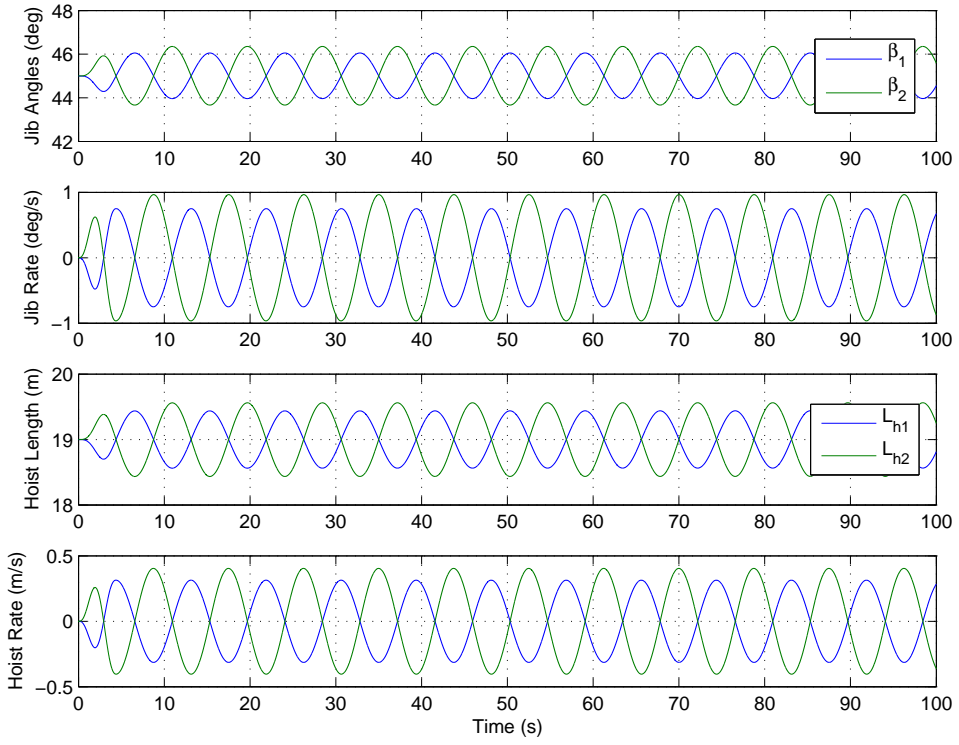


Figure 65. Plots of β , $\dot{\beta}$, L_h , and \dot{L}_h time histories for the inverse kinematic control case with the identity matrix used as the weights in the minimum norm solution. (Simulation parameters: $\rho = 0$ degrees, $\vec{P}_{8/1,z} = -5$ meters, with a sinusoidal forcing function of $x_s = 0.5$ meter at a period of 8.75 seconds.)

same time history and the second is the low actuation rates for both luffing and hoisting.

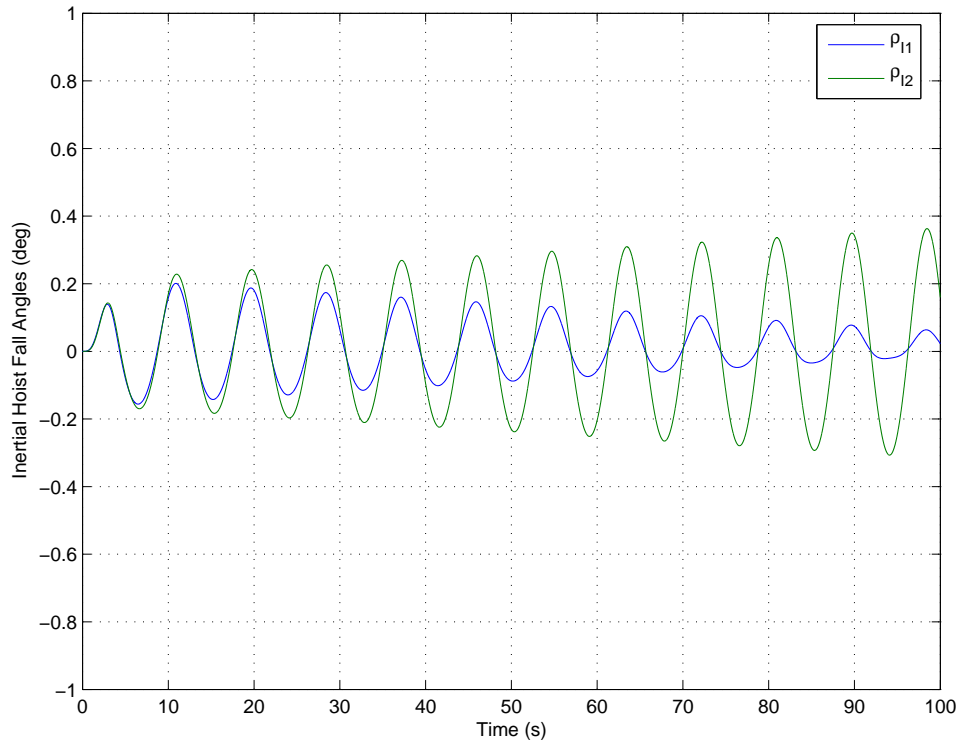


Figure 66. Plot of time histories for the inertial hoist-fall angle, ρ , for the inverse kinematic control case with the identity matrix used as the weights in the minimum norm solution. (Simulation parameters: $\rho = 0$ degrees, $\vec{P}_{8/1,z} = -5$ meters, with a sinusoidal forcing function of $x_s = 0.5$ meter at a period of 8.75 seconds.)

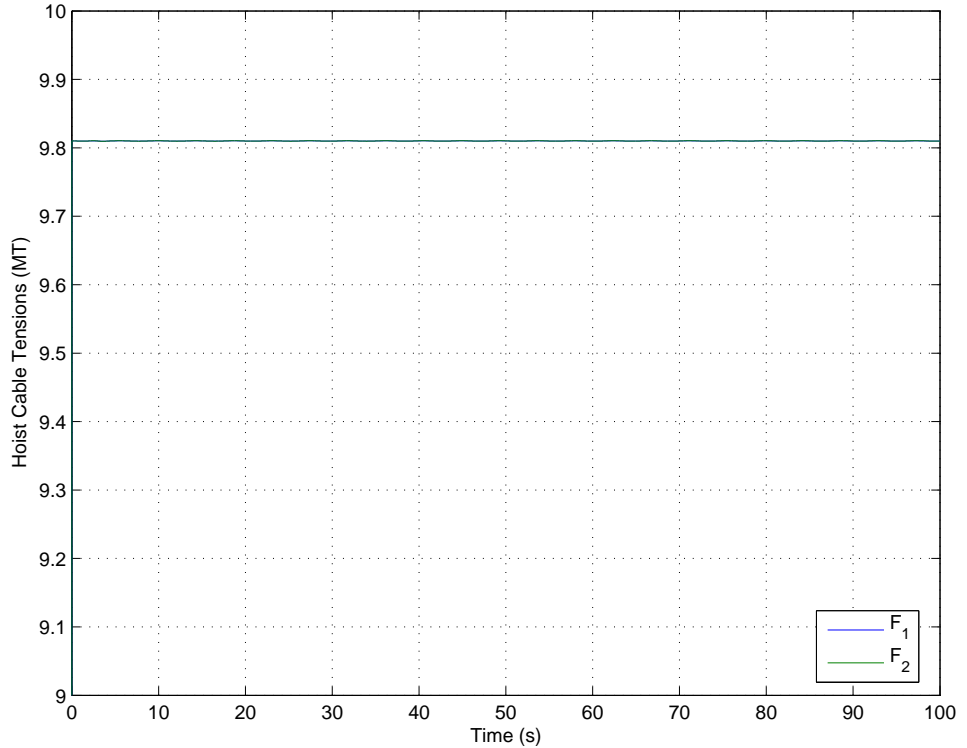


Figure 67. Plot of hoist cable tensions, F_1 and F_2 , for the inverse kinematic control case with the identity matrix used as the weights in the minimum norm solution. (Simulation parameters: $\rho = 0$ degrees, $\vec{P}_{8/1,z} = -5$ meters, with a sinusoidal forcing function of $x_s = 0.5$ meter at a period of 8.75 seconds.)

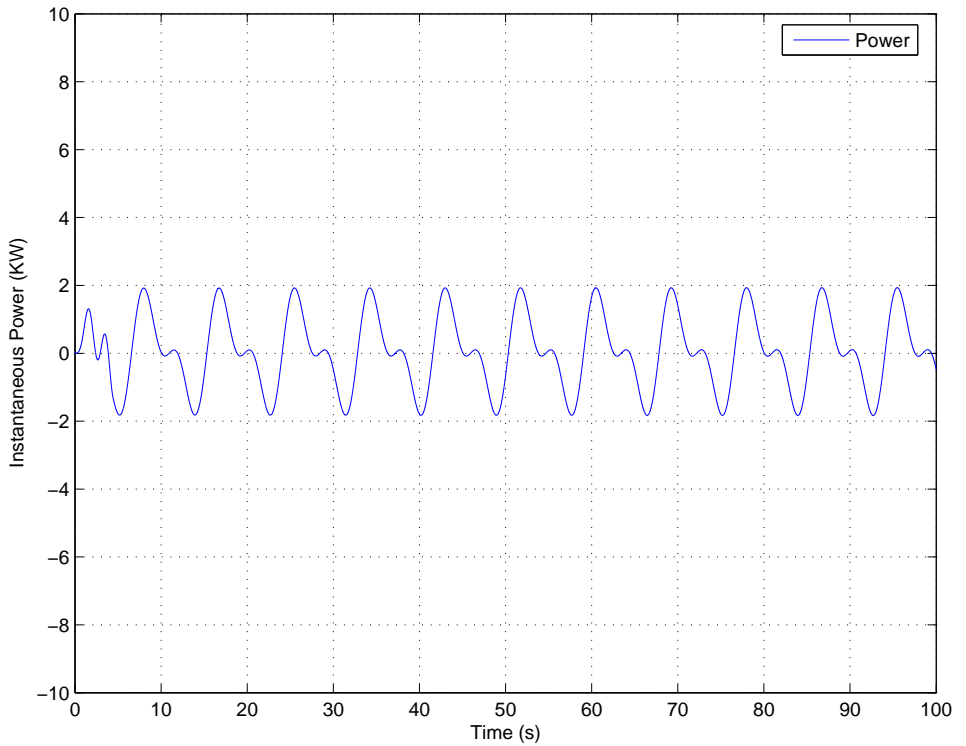


Figure 68. Plot of time histories for instantaneous power for the inverse kinematic control case with the identity matrix used as the weights in the minimum norm solution. (Simulation parameters: $\rho = 0$ degrees, $\vec{P}_{8/1,z} = -5$ meters, with a sinusoidal forcing function of $x_s = 0.5$ meter at a period of 8.75 seconds.)

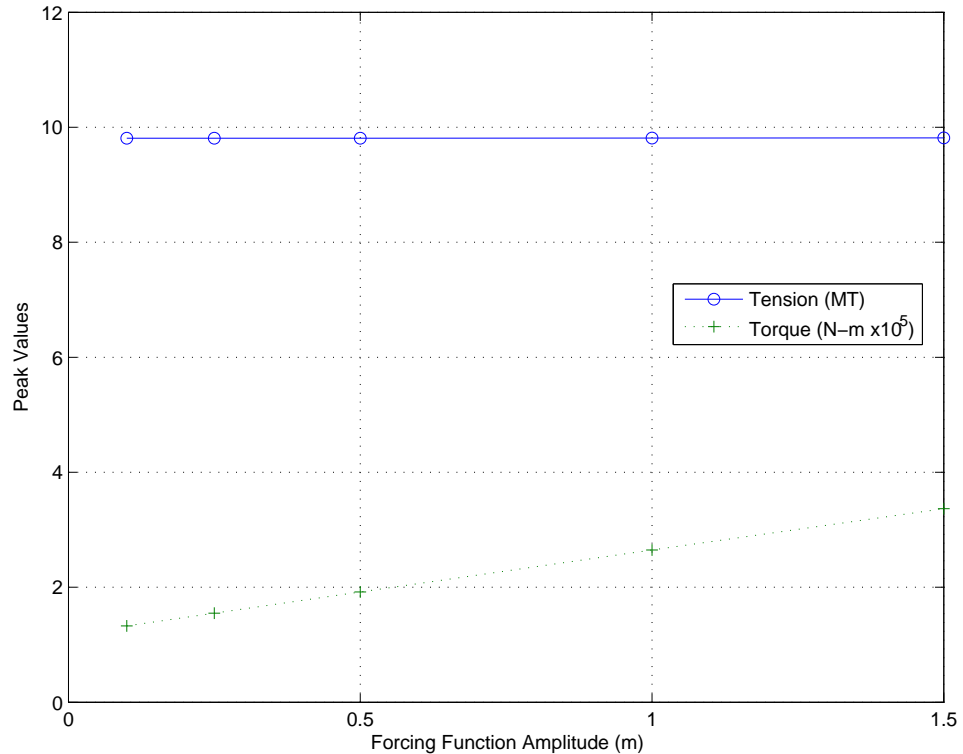


Figure 69. Plot of peak values of hoist cable tension and jib torque versus ship motion amplitude. (Simulation parameters: $\mathbf{W} = \mathbf{I}$, $\rho = 0$ degrees, $\vec{P}_{8/1,z} = 5$ meters, and $\mathbf{x}_s = [0.1, 0.25, 0.5, 1.0, 1.5]$ meter at a period of 8.75 seconds.)

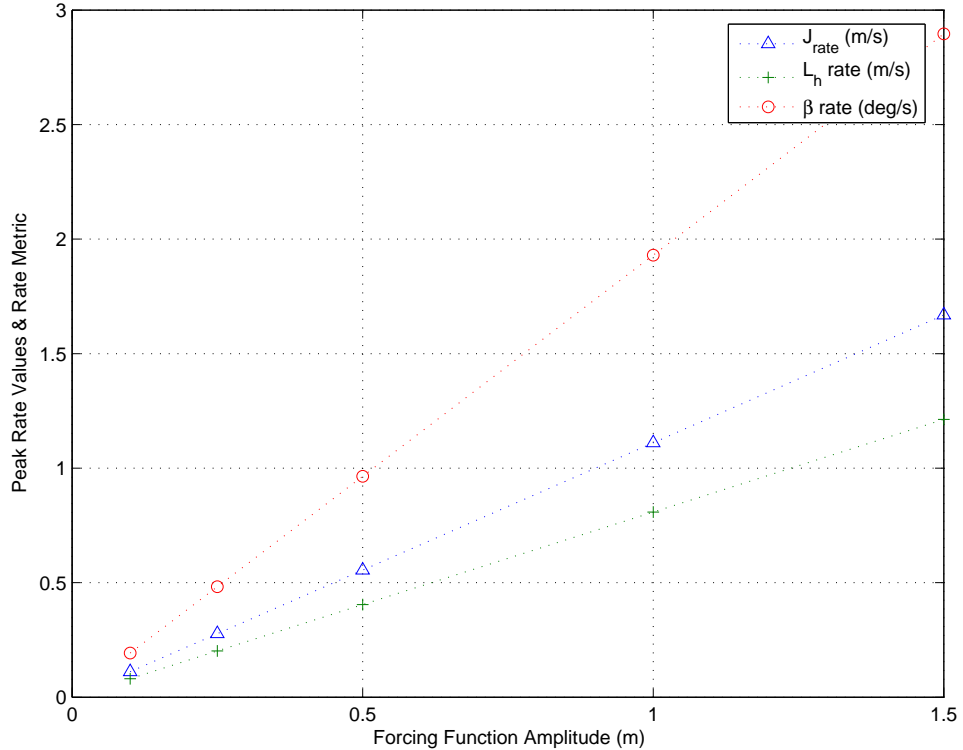


Figure 70. Plot of peak values of actuation rates and the rate-based performance metric versus ship motion amplitude. (Simulation parameters: $\mathbf{W} = \mathbf{I}$, $\rho = 0$ degrees, $\vec{P}_{8/1,z} = 5$ meters, and $\mathbf{x}_s = [0.1, 0.25, 0.5, 1.0, 1.5]$ meter at a period of 8.75 seconds.)

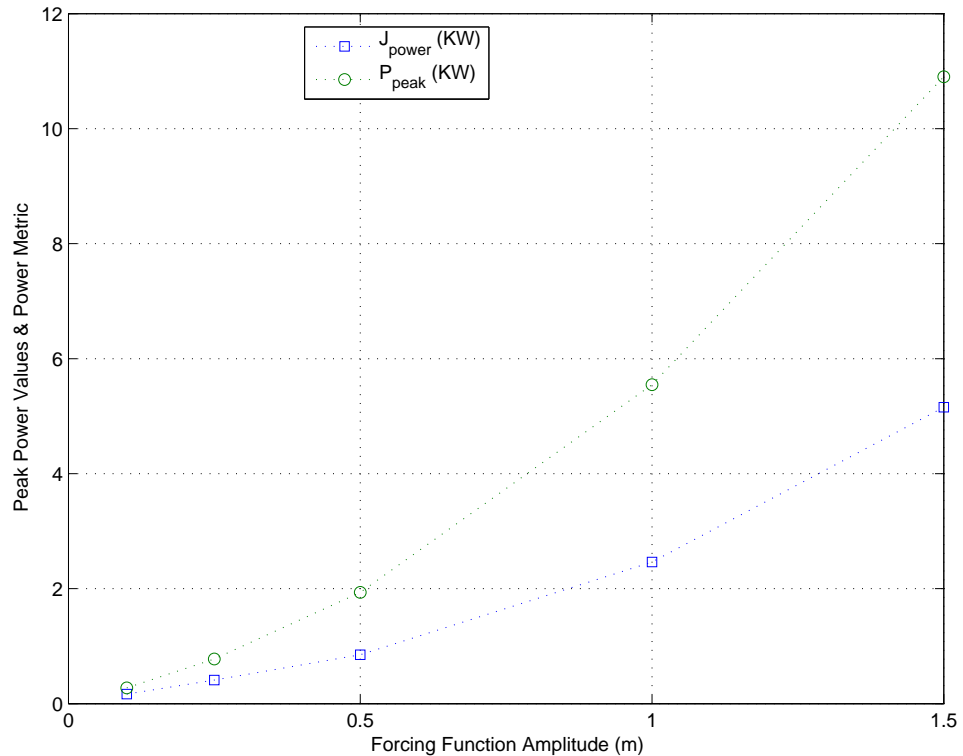


Figure 71. Plot of peak values of instantaneous power and the power-based metric versus ship motion amplitude. (Simulation parameters: $\mathbf{W} = \mathbf{I}$, $\rho = 0$ degrees, $\vec{P}_{8/1,z} = 5$ meters, and $\mathbf{x}_s = [0.1, 0.25, 0.5, 1.0, 1.5]$ meter at a period of 8.75 seconds.)

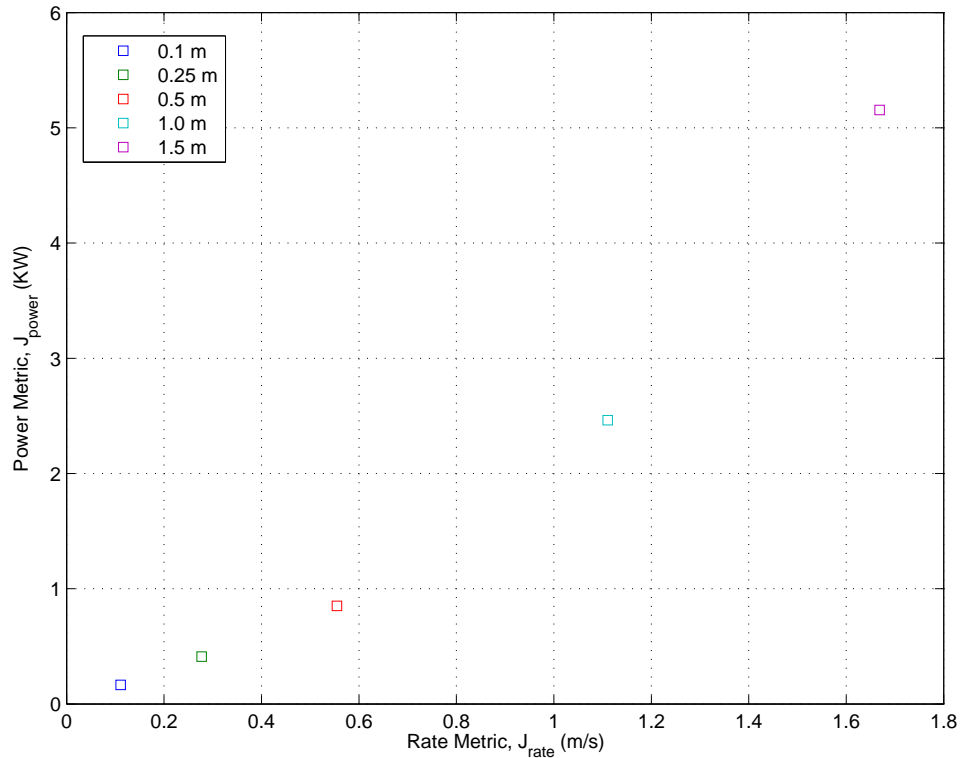


Figure 72. Cross-plot of the two performance metrics for a range of ship motion amplitude. (Simulation parameters: $\mathbf{W} = \mathbf{I}$, $\rho = 0$ degrees, $\vec{P}_{8/1,z} = 5$ meters, and $\mathbf{x}_s = [0.1, 0.25, 0.5, 1.0, 1.5]$ meter at a period of 8.75 seconds.)

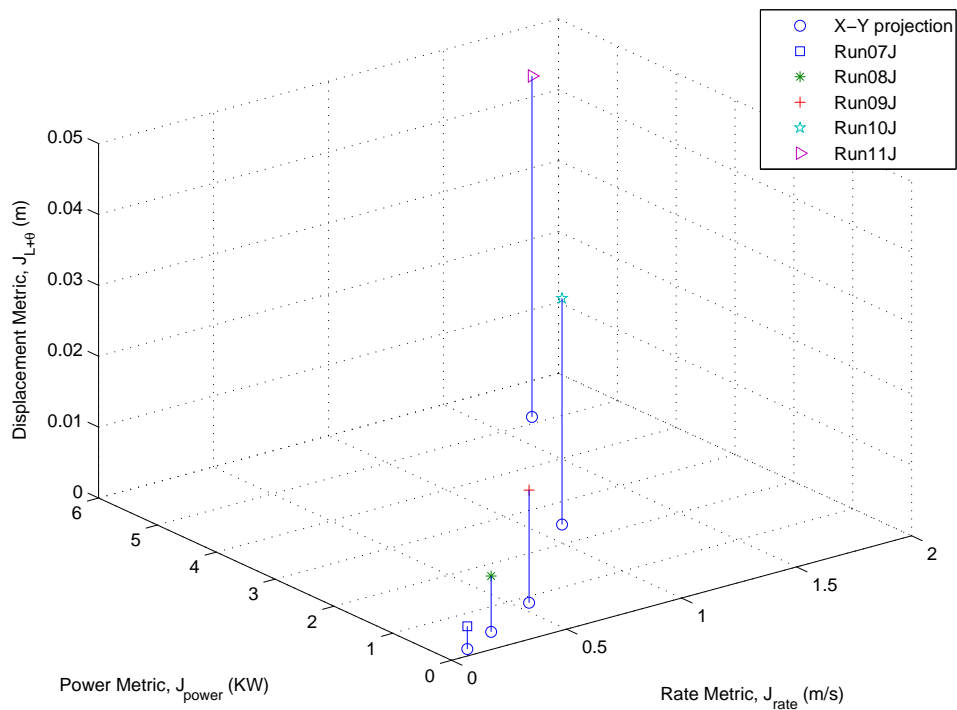


Figure 73. Three dimensional plot of the performance metrics for a range of ship motion amplitude. (Simulation parameters: $\mathbf{W} = \mathbf{I}$, $\rho = 0$ degrees, $\bar{P}_{8/1,z} = 5$ meters, and $\mathbf{x}_s = [0.1, 0.25, 0.5, 1.0, 1.5]$ meter at a period of 8.75 seconds.)

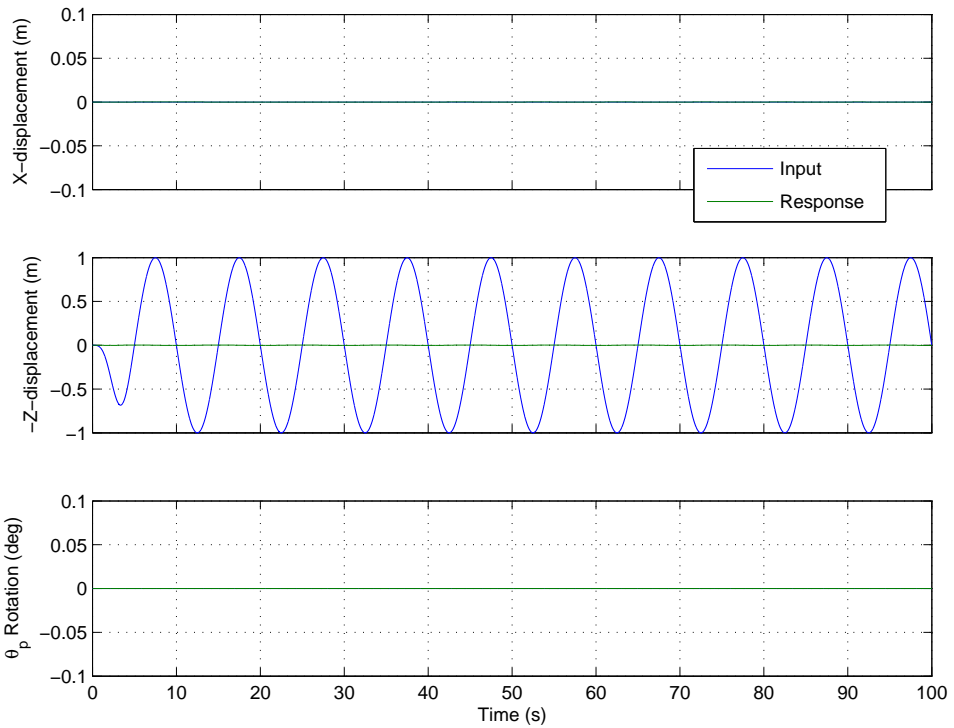


Figure 74. Plot of x , z , and θ time histories for the inverse kinematic control case with the identity matrix used as the weights in the minimum norm solution. (Simulation parameters: $\rho = 0$ degrees, $\vec{P}_{8/1,z} = -5$ meters, with a sinusoidal forcing function of $z_s = 1.0$ meter at a period of 10.0 seconds.)

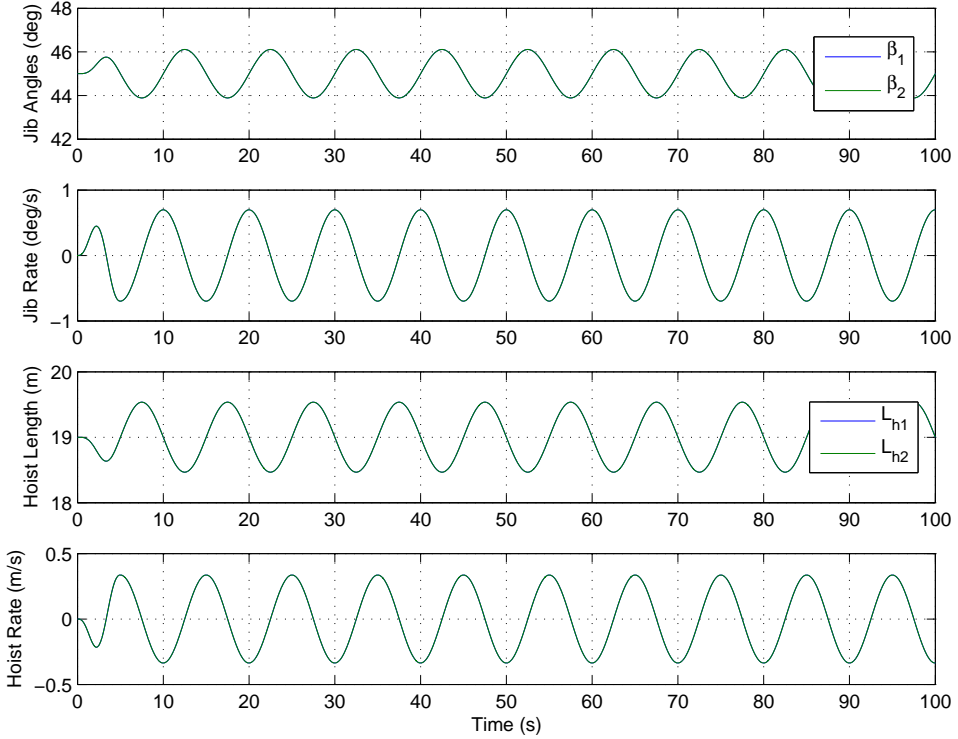


Figure 75. Plots of β , $\dot{\beta}$, L_h , and \dot{L}_h time histories for the inverse kinematic control case with the identity matrix used as the weights in the minimum norm solution. (Simulation parameters: $\rho = 0$ degrees, $\vec{P}_{8/1,z} = -5$ meters, with a sinusoidal forcing function of $z_s = 1.0$ meter at a period of 10.0 seconds.)

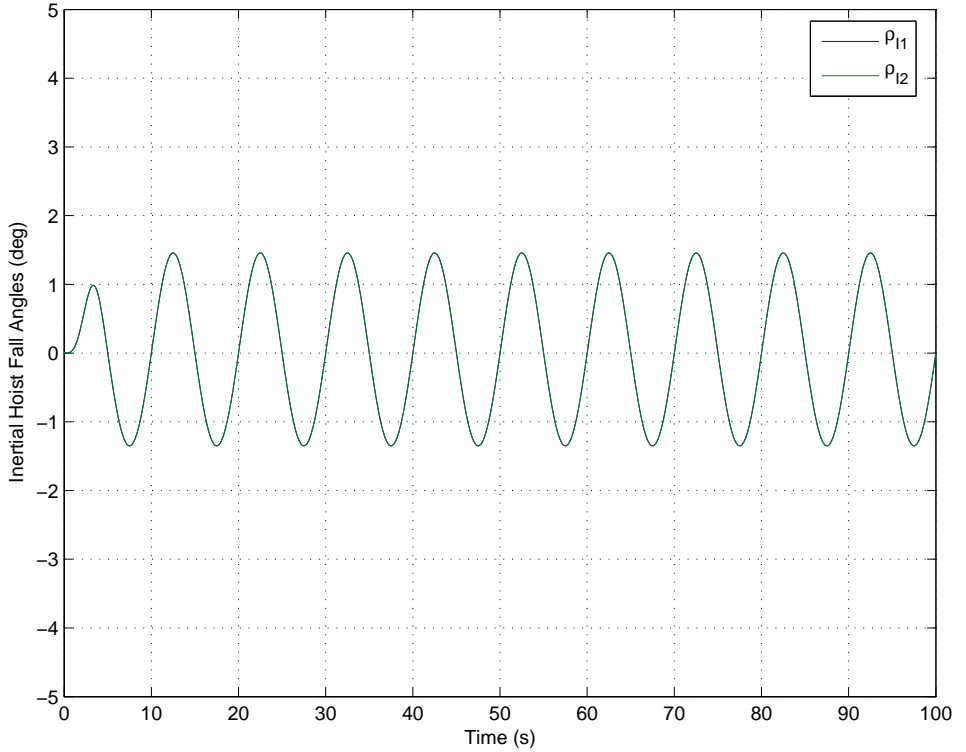


Figure 76. Plot of time histories for the inertial hoist-fall angle, ρ , for the inverse kinematic control case with the identity matrix used as the weights in the minimum norm solution. (Simulation parameters: $\rho = 0$ degrees, $\vec{P}_{8/1,z} = -5$ meters, with a sinusoidal forcing function of $z_s = 1.0$ meter at a period of 10.0 seconds.)

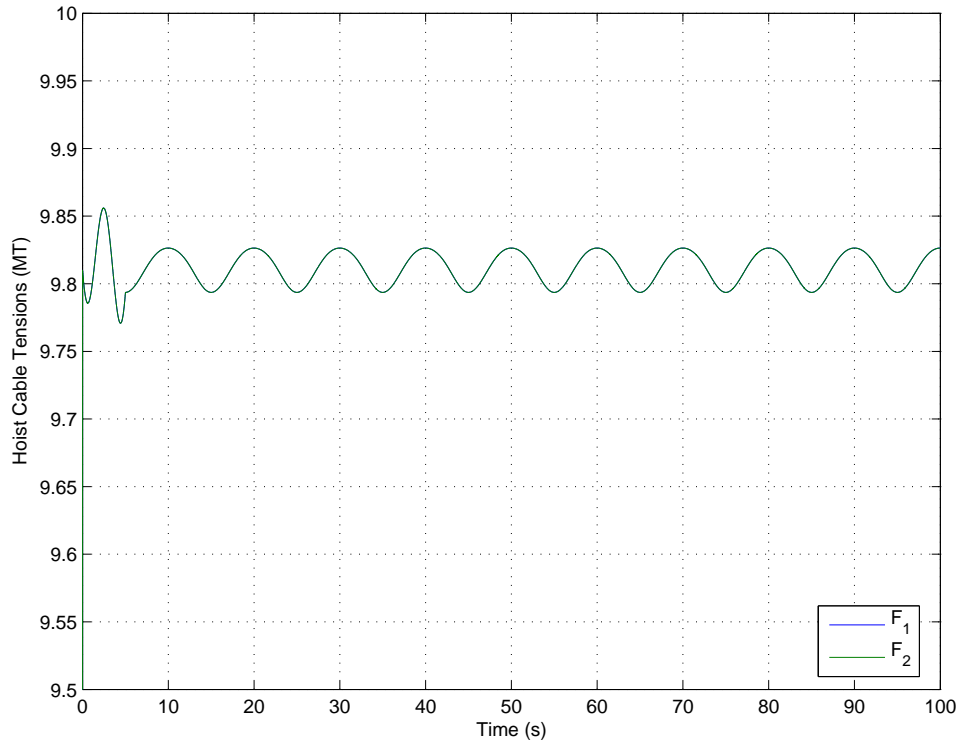


Figure 77. Plot of hoist cable tensions, F_1 and F_2 , for the inverse kinematic control case with the identity matrix used as the weights in the minimum norm solution. (Simulation parameters: $\rho = 0$ degrees, $\vec{P}_{8/1,z} = -5$ meters, with a sinusoidal forcing function of $z_s = 1.0$ meter at a period of 10.0 seconds.)

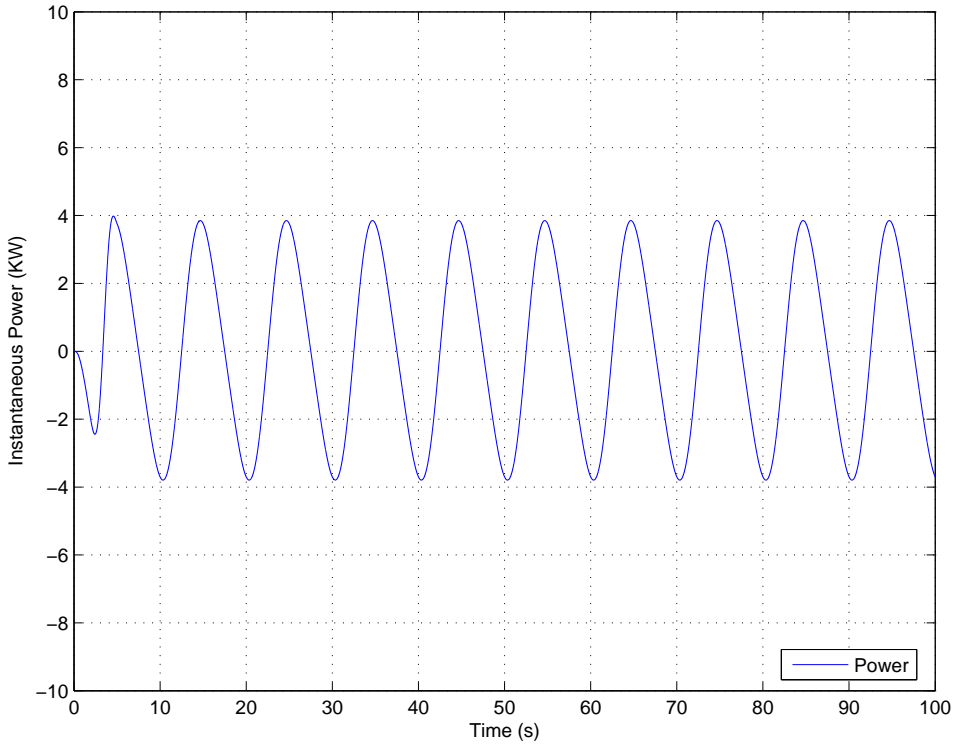


Figure 78. Plot of time histories for instantaneous power for the inverse kinematic control case with the identity matrix used as the weights in the minimum norm solution. (Simulation parameters: $\rho = 0$ degrees, $\vec{P}_{8/1,z} = -5$ meters, with a sinusoidal forcing function of $z_s = 1.0$ meter at a period of 10.0 seconds.)

Figures 79, 80, 81, 82, and 83 show a typical system response to pure pitch input with an amplitude of 5.0 degrees at a period of 7.0 seconds.

The final set of figures, ??, ??, ??, ??, and ?? show the time histories for the combined surge (1 m, 8.75 s), heave (1 m, 10.0 s), and pitch (5° , 7.0 s) input. Even in the presence of the combined motion input, the residual payload motion is less than 0.5 meters in surge or heave and less than 0.1 degree in pitch.

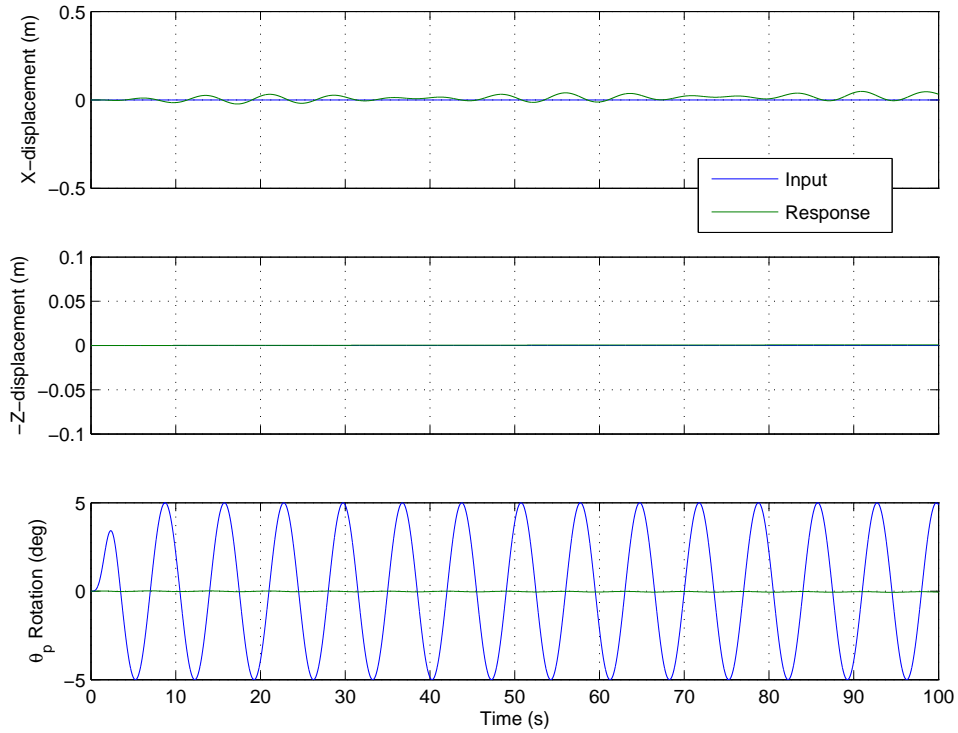


Figure 79. Plot of x , z , and θ time histories for the inverse kinematic control case with the identity matrix used as the weights in the minimum norm solution. (Simulation parameters: $\rho = 0$ degrees, $\vec{P}_{8/1,z} = -5$ meters, with a sinusoidal forcing function of $\theta_s = 5.0^\circ$ at a period of 7.0 seconds.)

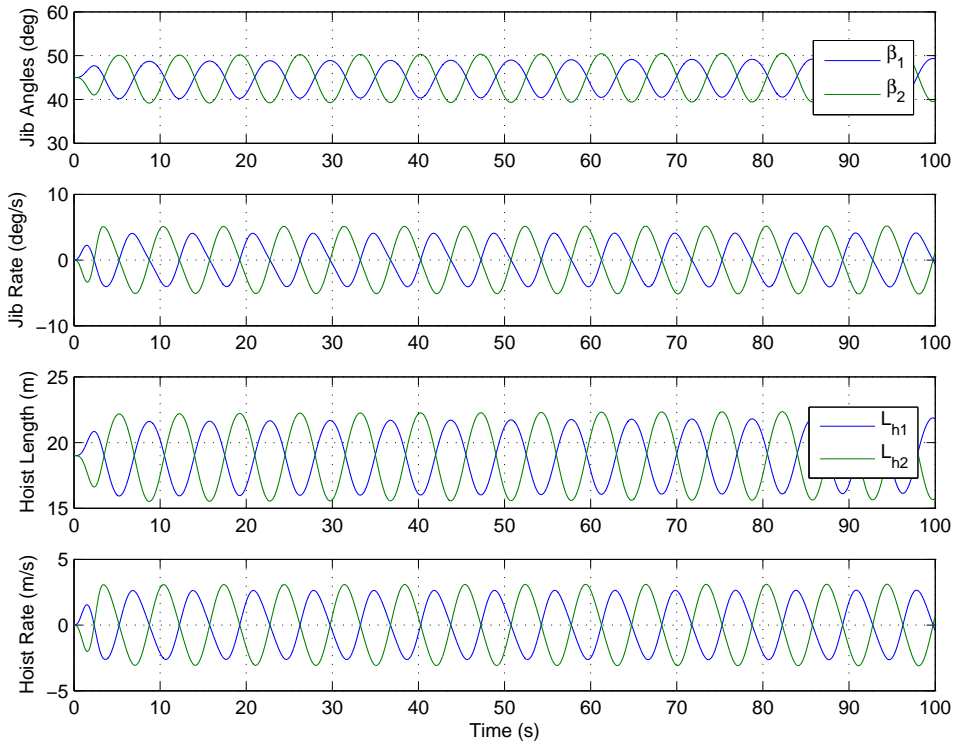


Figure 80. Plots of β , $\dot{\beta}$, L_h , and \dot{L}_h time histories for the inverse kinematic control case with the identity matrix used as the weights in the minimum norm solution. (Simulation parameters: $\rho = 0$ degrees, $\vec{P}_{8/1,z} = -5$ meters, with a sinusoidal forcing function of $\theta_s = 5.0^\circ$ at a period of 7.0 seconds.)

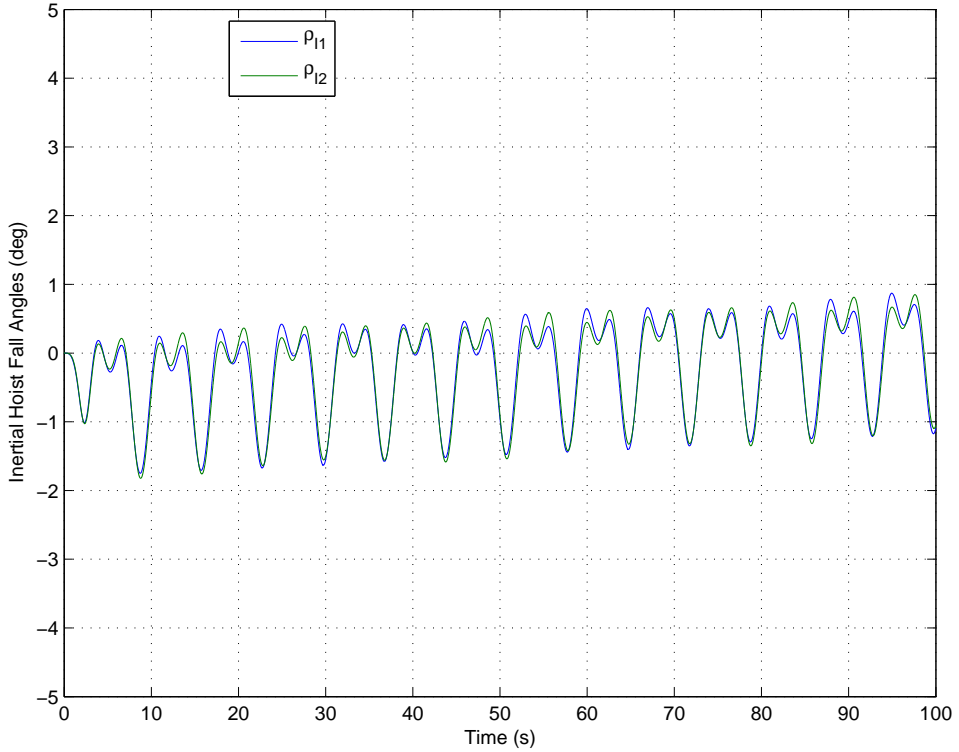


Figure 81. Plot of time histories for the inertial hoist-fall angle, ρ , for the inverse kinematic control case with the identity matrix used as the weights in the minimum norm solution. (Simulation parameters: $\rho = 0$ degrees, $\vec{P}_{8/1,z} = -5$ meters, with a sinusoidal forcing function of $\theta_s = 5.0^\circ$ at a period of 7.0 seconds.)

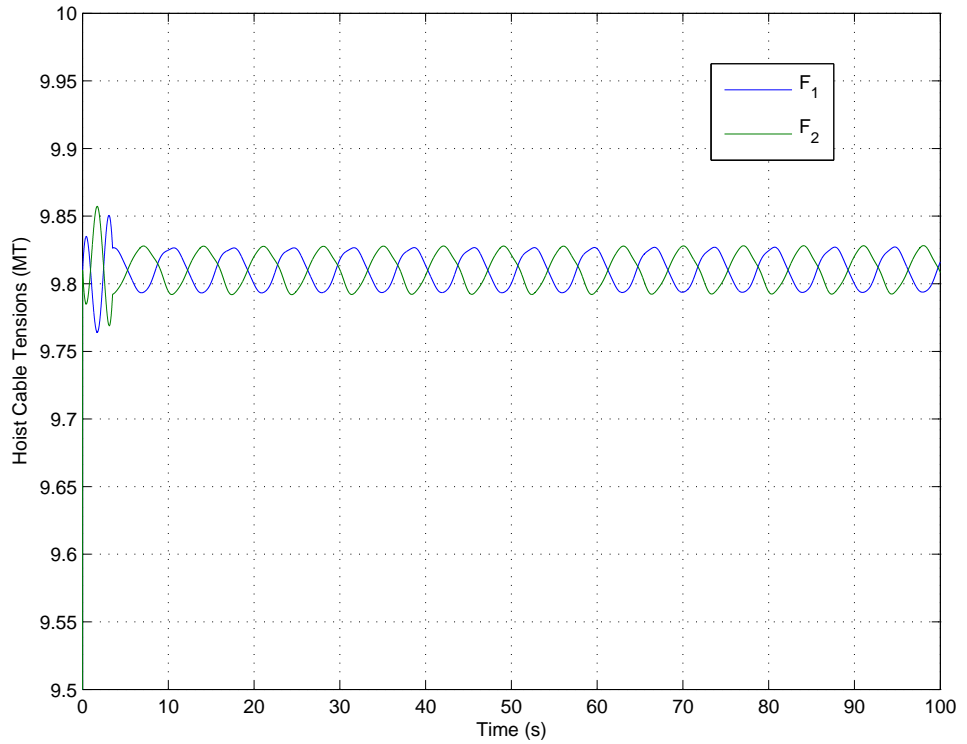


Figure 82. Plot of hoist cable tensions, F_1 and F_2 , for the inverse kinematic control case with the identity matrix used as the weights in the minimum norm solution. (Simulation parameters: $\rho = 0$ degrees, $\vec{P}_{8/1,z} = -5$ meters, with a sinusoidal forcing function of $\theta_s = 5.0^\circ$ at a period of 7.0 seconds.)

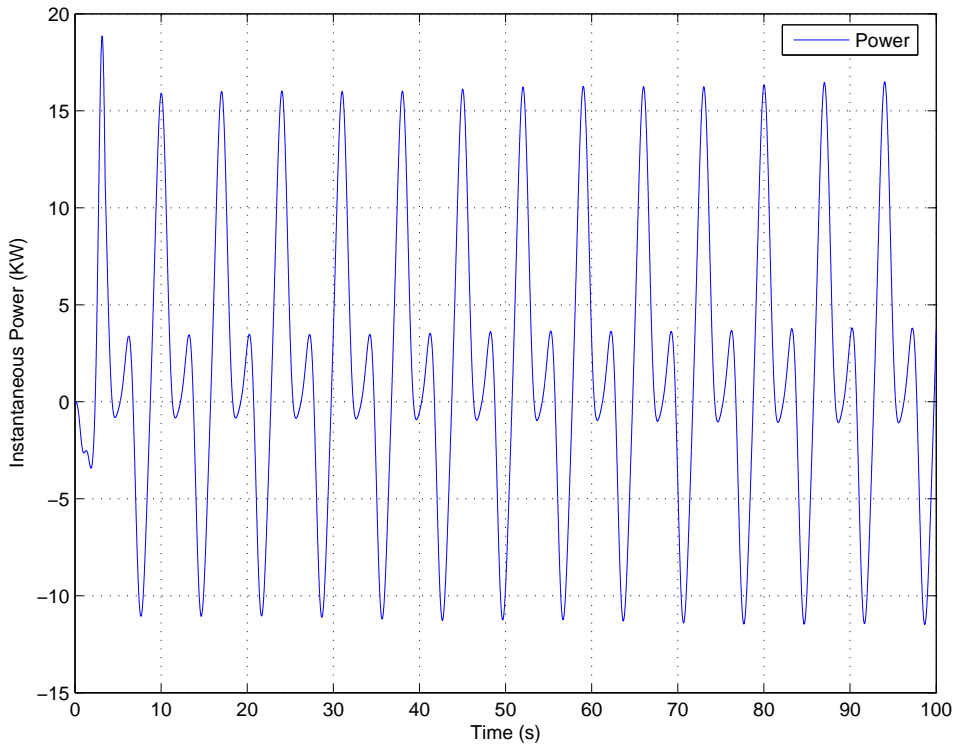


Figure 83. Plot of time histories for instantaneous power for the inverse kinematic control case with the identity matrix used as the weights in the minimum norm solution. (Simulation parameters: $\rho = 0$ degrees, $\vec{P}_{8/1,z} = -5$ meters, with a sinusoidal forcing function of $\theta_s = 5.0^\circ$ at a period of 7.0 seconds.)

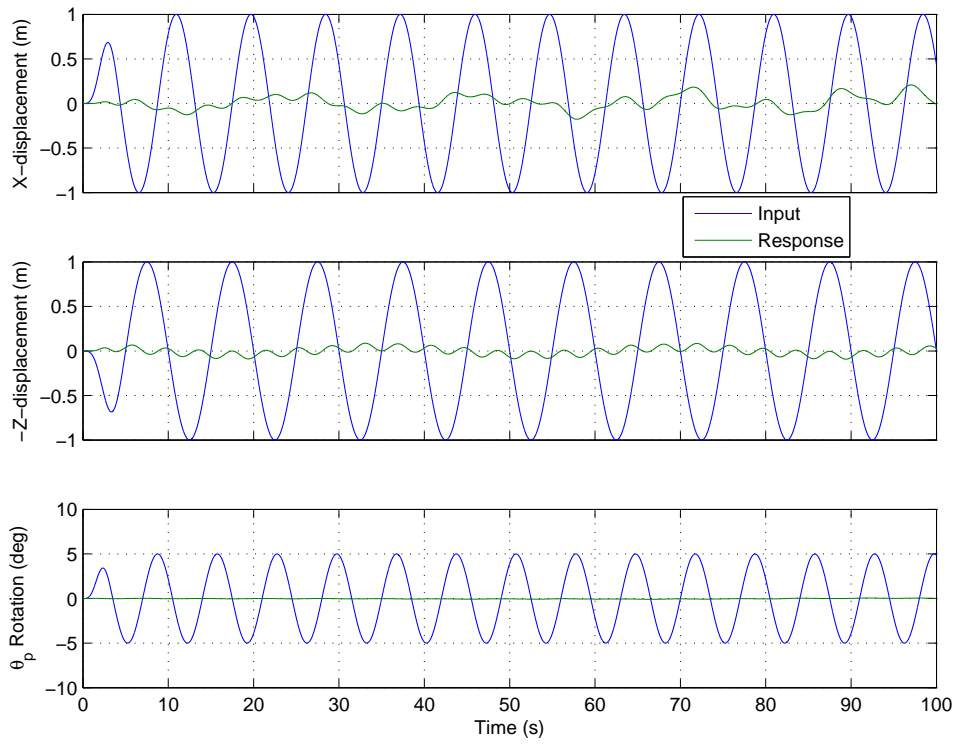


Figure 84. Plot of x , z , and θ time histories for the inverse kinematic control case with the identity matrix used as the weights in the minimum norm solution. (Simulation parameters: $\rho = 10$ degrees, $\vec{P}_{8/1,z} = -5$ meters, with a combined sinusoidal forcing function of $x_s = 1$ meter at a period of 8.75 seconds, $z_s = 1$ meter at a period of 10 seconds, and $\theta_s = 5^\circ$ at a period of 7.0 seconds.)

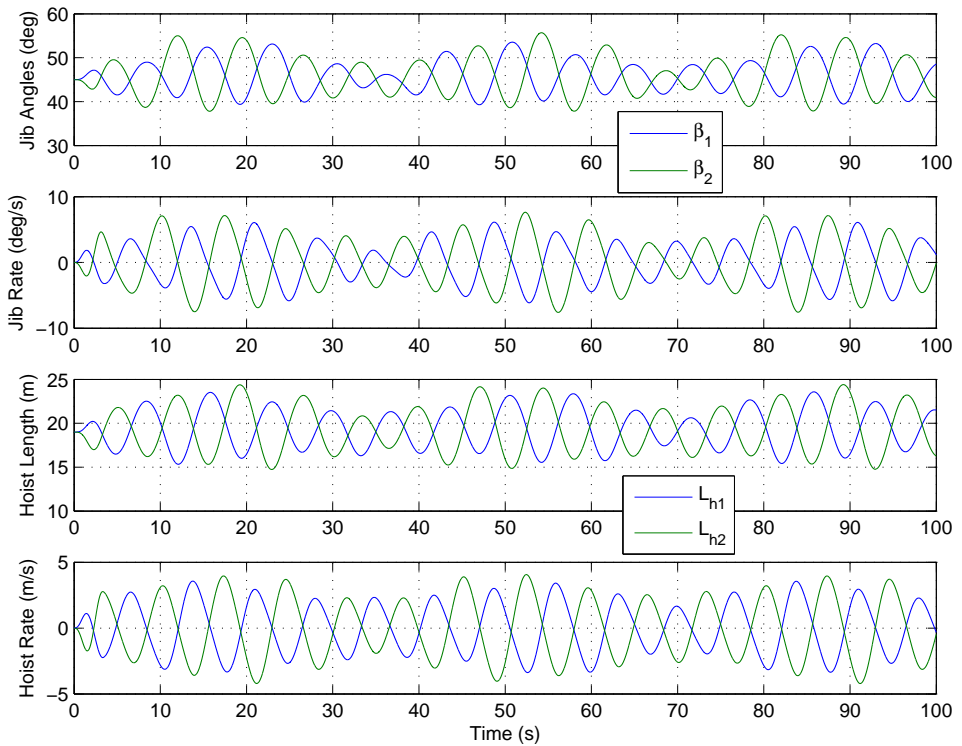


Figure 85. Plots of β , $\dot{\beta}$, L_h , and \dot{L}_h time histories for the inverse kinematic control case with the identity matrix used as the weights in the minimum norm solution. (Simulation parameters: $\rho = 10$ degrees, $\vec{P}_{8/1,z} = -5$ meters, with a combined sinusoidal forcing function of $x_s = 1$ meter at a period of 8.75 seconds, $z_s = 1$ meter at a period of 10 seconds, and $\theta_s = 5^\circ$ at a period of 7.0 seconds.)

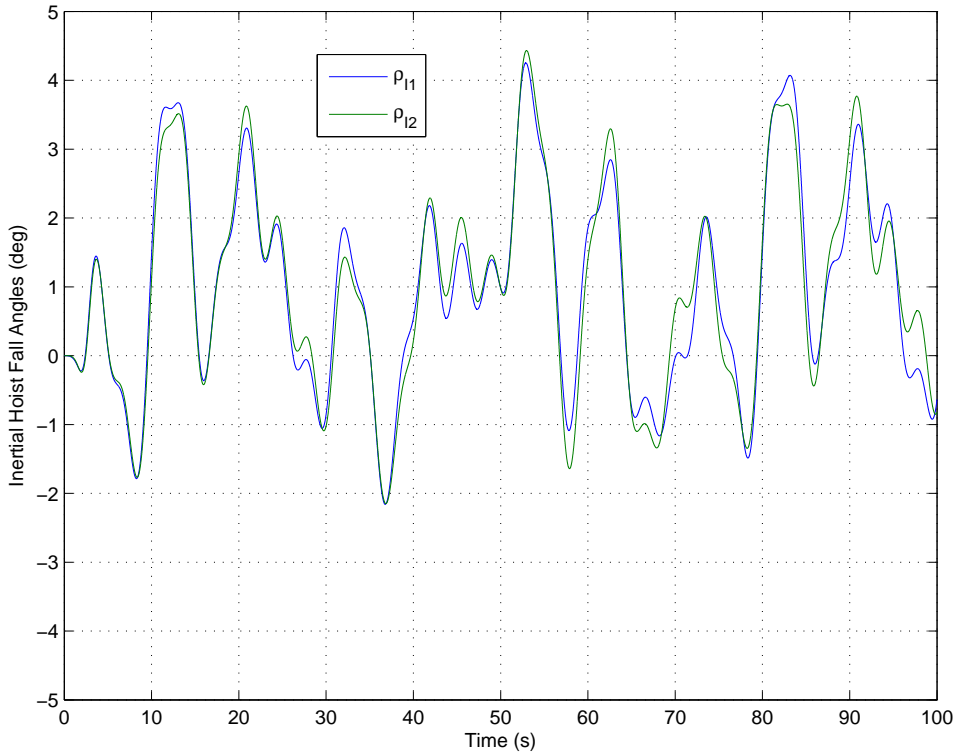


Figure 86. Plot of time histories for the inertial hoist-fall angle, ρ , for the inverse kinematic control case with the identity matrix used as the weights in the minimum norm solution. (Simulation parameters: $\rho = 10$ degrees, $\vec{P}_{8/1,z} = -5$ meters, with a combined sinusoidal forcing function of $\mathbf{x}_s = 1$ meter at a period of 8.75 seconds, $\mathbf{z}_s = 1$ meter at a period of 10 seconds, and $\theta_s = 5^\circ$ at a period of 7.0 seconds.)

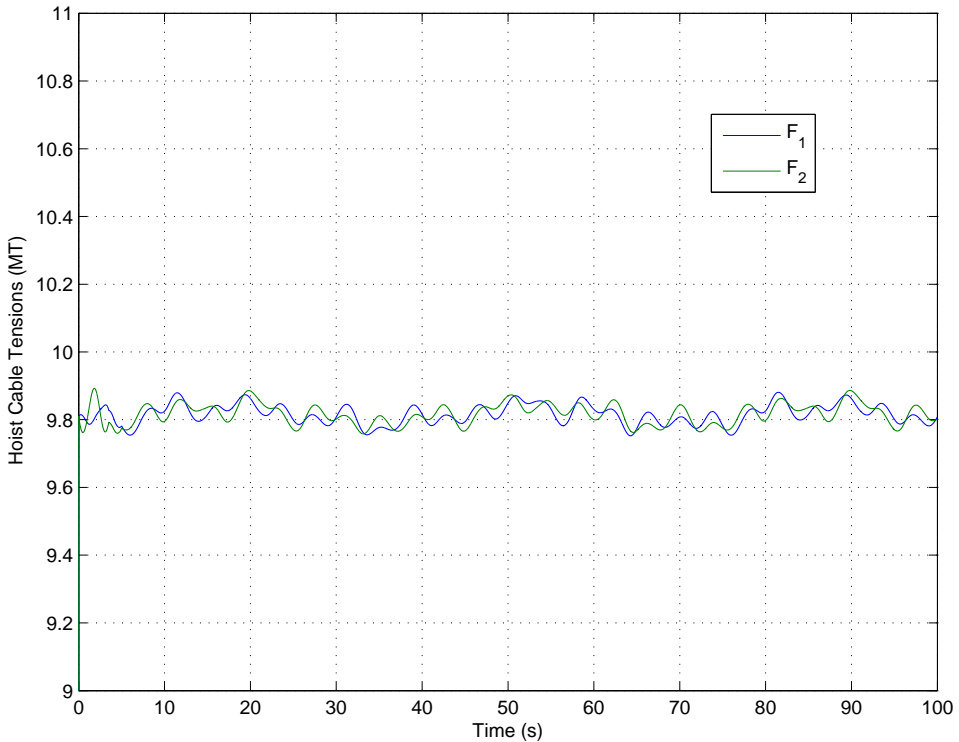


Figure 87. Plot of hoist cable tensions, F_1 and F_2 , for the inverse kinematic control case with the identity matrix used as the weights in the minimum norm solution. (Simulation parameters: $\rho = 10$ degrees, $\vec{P}_{8/1,z} = -5$ meters, with a combined sinusoidal forcing function of $x_s = 1$ meter at a period of 8.75 seconds, $z_s = 1$ meter at a period of 10 seconds, and $\theta_s = 5^\circ$ at a period of 7.0 seconds.)

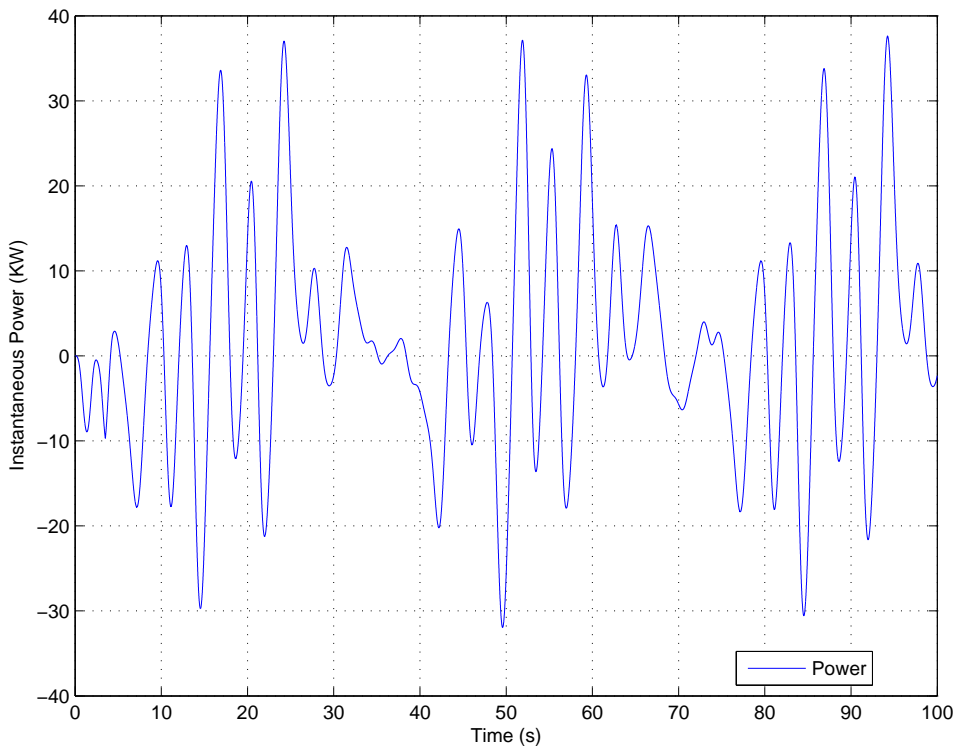


Figure 88. Plot of time histories for instantaneous power for the inverse kinematic control case with the identity matrix used as the weights in the minimum norm solution. (Simulation parameters: $\rho = 10$ degrees, $\vec{P}_{8/1,z} = -5$ meters, with a combined sinusoidal forcing function of $x_s = 1$ meter at a period of 8.75 seconds, $z_s = 1$ meter at a period of 10 seconds, and $\theta_s = 5^\circ$ at a period of 7.0 seconds.)

In Chapter VI that follows, expressions for the power required to implement the inverse kinematic control based on the hoist cable forces and jib torques are derived for use in the selection of appropriate weights for the minimum norm solution. Several other operationally meaningful weighting schemes are also identified for which simulation results are presented.

Following that, Chapter VI is dedicated to the comparison of all the simulation cases using the displacement-, rate-, and power-based performance metrics. Table 4 in this section lists the simulation conditions and identifies the cases by run number.

THIS PAGE INTENTIONALLY LEFT BLANK

V. DERIVATION OF POWER EXPRESSIONS AND ALTERNATIVE WEIGHTING SCHEMES

The previous section described the inverse kinematic control required to actively suppress the motion of the payload in the presence of ship motion. As the problem is over-determined a weighted norm solution is used. This introduces the ability to alter the solution based on the selection of the elements of the weighting matrix.

A. TORQUE AND POWER RELATIONSHIPS APPLIED TO THE MINIMUM NORM SOLUTION

In this section an attempt is made to select the appropriate weights of the minimum norm solution based on the power required to manipulate the jibs and hoist lines. For shipboard cranes, the power available is limited by the installed electrical generator sets. Certainly, for lifting heavy payloads a method of manipulating the power required could be useful for selecting an inverse kinematic control scheme that is in some sense optimal for a given operating condition. First we must derive the torque and power expressions for the dual-crane system. To begin, consider the free-body diagram of the left-side jib shown in Figure 89.

In general the right-side jib quantities such as the mass, luffing-angle, and the tension of the left-side jib need not be equal to the right-side. Writing Euler's equation about the center of mass of each jib separately results in the following pair of equations (Eqn V.1).

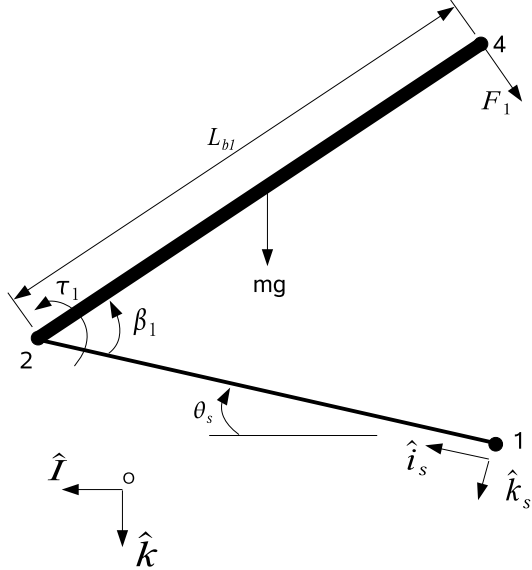


Figure 89. Free-body diagram of the left-side jib for purposes of deriving the torque equations.

$$\begin{aligned}\tau_1 - \frac{1}{2} L_{b1} \hat{P}_{4/2} \times \vec{F}_1 &= I_{b1} (\ddot{\theta}_s + \ddot{\beta}_1) \\ \tau_2 - \frac{1}{2} L_{b2} \hat{P}_{5/3} \times \vec{F}_2 &= I_{b2} (\ddot{\theta}_s + \ddot{\beta}_2)\end{aligned}\quad (\text{V.1})$$

Again noting that we are only dealing with the x - z plane, the axis of rotation of the ship frame and the crane frame are parallel.

The results we seek are expressions for the torque about the hinge-pin of the crane as this represents the effort required to resist the force exerted by the payload as well as the weight of the jib. We can solve the equations for the two torques, τ_1 and τ_2 , as the tensions, F_1 and F_2 in the hoist lines have been solved for previously (as discussed in section II) and the hoist line vectors are accessible through the simulation model as well (Eqn V.2).

$$\begin{aligned}\tau_1 &= \frac{1}{2} L_{b1} T_1 \hat{P}_{4/2} \times \hat{P}_{6/4} + I_{b1} (\ddot{\theta}_s + \ddot{\beta}_1) \\ \tau_2 &= \frac{1}{2} L_{b2} T_2 \hat{P}_{5/3} \times \hat{P}_{7/5} + I_{b2} (\ddot{\theta}_s + \ddot{\beta}_2)\end{aligned}\quad (\text{V.2})$$

Each jib has components of power attributed to the product of hoist cable tension and hoist line speed ($F \cdot \dot{L}_H$) and the product of luffing torque and luff-angular velocity ($\tau \cdot \dot{\beta}$). These relationships were developed by Graziano [58] for a single crane. Combining all the components into one expression, the power being absorbed by both jibs is expressed in the following equation (Eqn V.3).

$$Power = \tau_1 \dot{\beta}_1 + F_1 \dot{L}_{h1} + \tau_2 \dot{\beta}_2 + F_2 \dot{L}_{h2} \quad (\text{V.3})$$

which can also be written in the form of Equation V.4

$$Power = p'y \quad (\text{V.4})$$

where $p' = \begin{bmatrix} \tau_1 & \tau_2 & F_1 & F_2 \end{bmatrix}$ and

$$y = \begin{bmatrix} \dot{\beta}_1 \\ \dot{\beta}_2 \\ \dot{L}_{h1} \\ \dot{L}_{h2} \end{bmatrix}$$

Clearly the power is a function of the actuation rates, \dot{L}_{h1} , \dot{L}_{h2} , $\dot{\beta}_1$, and $\dot{\beta}_2$. Squaring this yields the following positive semi-definite ¹ expression that can be written compactly in quadratic form (Eqn V.5).

$$Power^2 = y' P y \quad (\text{V.5})$$

¹Because it is not guaranteed that the torque is strictly positive, it may be necessary to check if the torque passes through zero.

where

$$P = \begin{bmatrix} \tau_1^2 & \tau_1\tau_2 & \tau_1F_1 & \tau_1F_2 \\ \tau_1\tau_2 & \tau_2^2 & \tau_2F_1 & \tau_2F_2 \\ \tau_1F_1 & \tau_2F_1 & F_1^2 & F_1F_2 \\ \tau_1F_2 & \tau_2F_2 & F_1F_2 & F_2^2 \end{bmatrix}$$

It would appear that this form would lead to directly substituting the P matrix for the weighting matrix W in the minimum norm solution and thereby balance the actuation rates according to their weight in the power calculation. Unfortunately the structure of the P matrix makes it identically singular (which can be verified by computing the determinant), making it unsuitable for use in the minimum norm solution. Before giving up on this endeavor, consider that the magnitudes of the torques are generally much larger than the hoist cable tensions, so that by discarding elements that are torque-tension products the P matrix can be simplified to Eqn. V.6.

$$P_2 = \begin{bmatrix} \tau_1^2 & \tau_1\tau_2 & 0 & 0 \\ \tau_1\tau_2 & \tau_2^2 & 0 & 0 \\ 0 & 0 & T_1^2 & T_1T_2 \\ 0 & 0 & T_1T_2 & T_2^2 \end{bmatrix} \quad (\text{V.6})$$

In fact, using this form of P ² as the weighting matrix, W , is also infeasible because it is identically singular. Another possibility would be to take only the upper triangular elements of P ; however, the selected form of the minimum norm solution assumes that W is symmetric. The remaining option is for P to take the form shown in Eqn. V.7 where the torques and forces are the diagonal elements of P .

²The diagonal elements of the matrix were implemented with an additive term of unity to forstall the possibility of zero-valued elements

$$P_{diag} = \begin{bmatrix} \tau_1^2 & 0 & 0 & 0 \\ 0 & \tau_2^2 & 0 & 0 \\ 0 & 0 & T_1^2 & 0 \\ 0 & 0 & 0 & T_2^2 \end{bmatrix} \quad (V.7)$$

Note that here the values of torque and tension that populate the weighting matrix are dynamically changing.

The time histories of the displacements and even the actuation rates for this condition did not appear unusual; however, upon examination of the calculated hoist cable tensions as shown in Figure 90, it was apparent that there were problems with the numerical solution.

From equation V.2 we can see that the calculated torque is a function of the instantaneous values of the ship's pitch acceleration and the jib's angular acceleration. Because the weighting matrix, W influences the inverse kinematic solution that determines the actuation rates, $\dot{\beta}_{1,2}$ and $\dot{L}_{h1,2}$, this calculation has in effect introduced feedback from the jib angular acceleration. This is a phenomenon that is beyond the scope of this dissertation and could be the focus of a future effort. An approach to avoid this situation would be to use constant values to populate the W matrix. One set of values that could be selected are the maximum torques and tensions obtained from a previously executed simulation using the identity matrix as the weights. An example of the results obtained using this strategy is shown in Figures 91, 92, 93, 94, and 95. For comparison, the time histories for the response to the same condition with the minimum norm solution using the identity matrix for the weighting matrix are shown in Figures 96, 97, 98, 99, and 100.

It is difficult to assess from the time histories directly if the different weighting schemes used in the solution have any significant impact. The comparison between simulation runs using different minimum norm solution weighting schemes can be quantified using the calculated metrics shown in Table 3, along with the peak actuation rates and peak instantaneous power. The actuation-rate based metric values

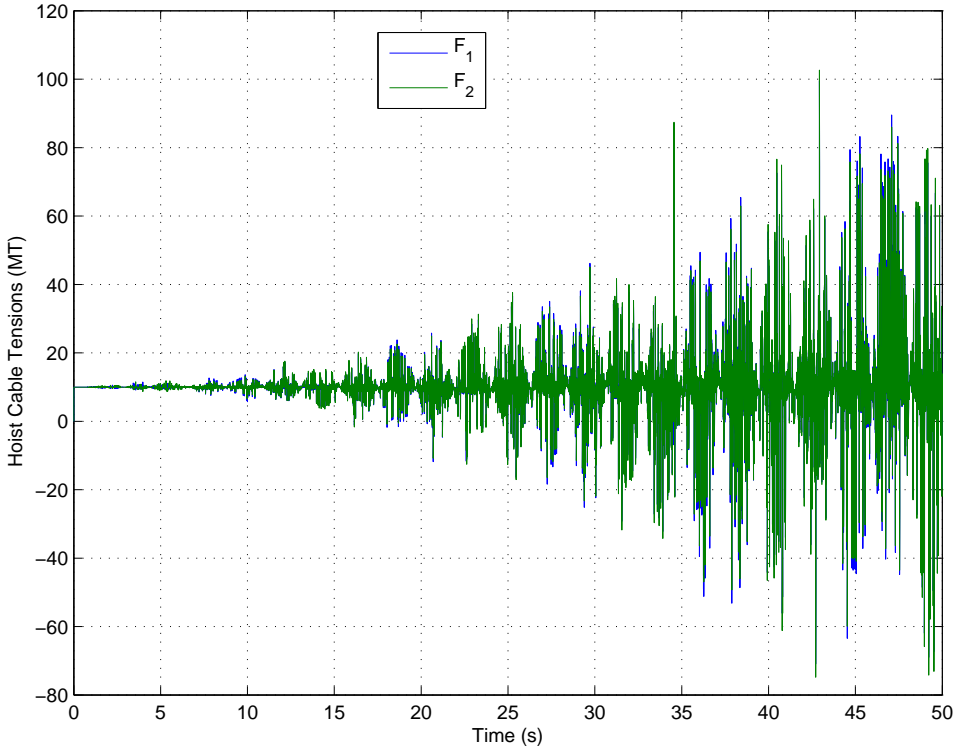


Figure 90. Plot of hoist cable tensions, F_1 and F_2 , for the inverse kinematic control case with dynamically changing torques and cable tension values used as the weights in the minimum norm solution. (Simulation parameters: $\rho = 10$ degrees, $\vec{P}_{8/1,z} = 5$ meters, and $x_s = 1$ meter at a period of 8.75 seconds.)

for the two cases are essentially equal, while the case that used the identity matrix weighting scheme actually has a lower (better) power-based metric value. As expected, the J_{rate} values seem to capture the same trend as the individual peak actuation rates, but in a more compact form, while the J_{power} value corresponds to the peak instantaneous power.

Based on this result, it appears that the intuitive connection between the power flow in the dual-crane system and the weighting scheme for the minimum norm solution does not exist, at least not in the straightforward method that it was implemented here.

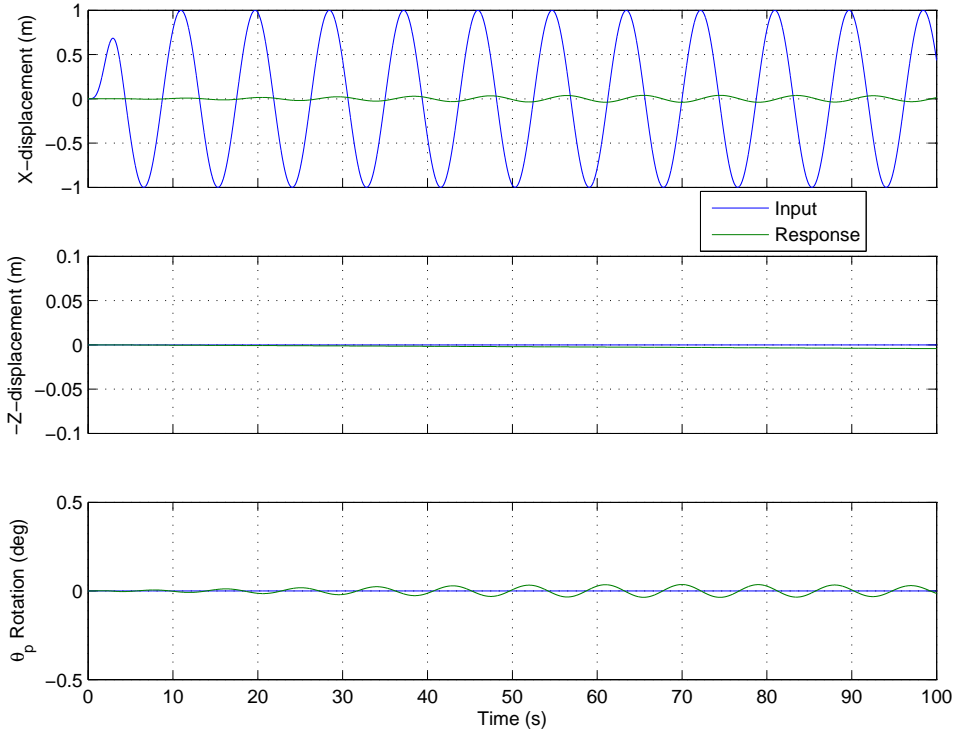


Figure 91. Plot of x , z , and θ time histories for the inverse kinematic control case with constant torques and cable tension values used as the weights in the minimum norm solution. The constant values chosen were the maximums observed during a simulation of the same conditions using the identity matrix as the weighting elements. (Simulation parameters: $\rho = 10$ degrees, $\vec{P}_{8/1,z} = 5$ meters, and $\mathbf{x}_s = 1$ meter at a period of 8.75 seconds.)

The next section will explore alternative forms of weighting schemes that may relate to other desirable operational features.

Weighting Scheme	$\dot{L}_{h,max}$ (m/s)	$\dot{\beta}_{max}$ (rad/s)	$Power_{inst,max}$ (KW)	J_{rate} (m/s)	J_{power} (KW)
Max. Torque,Tension	0.6144	1.7311	5.6329	1.0551	2.0520
Identity	0.6152	1.7360	5.3049	1.0553	1.7697

Table 3. Performance metric values, peak actuation rates, and peak instantaneous power for two simulation runs using different minimum norm solution weighting schemes.

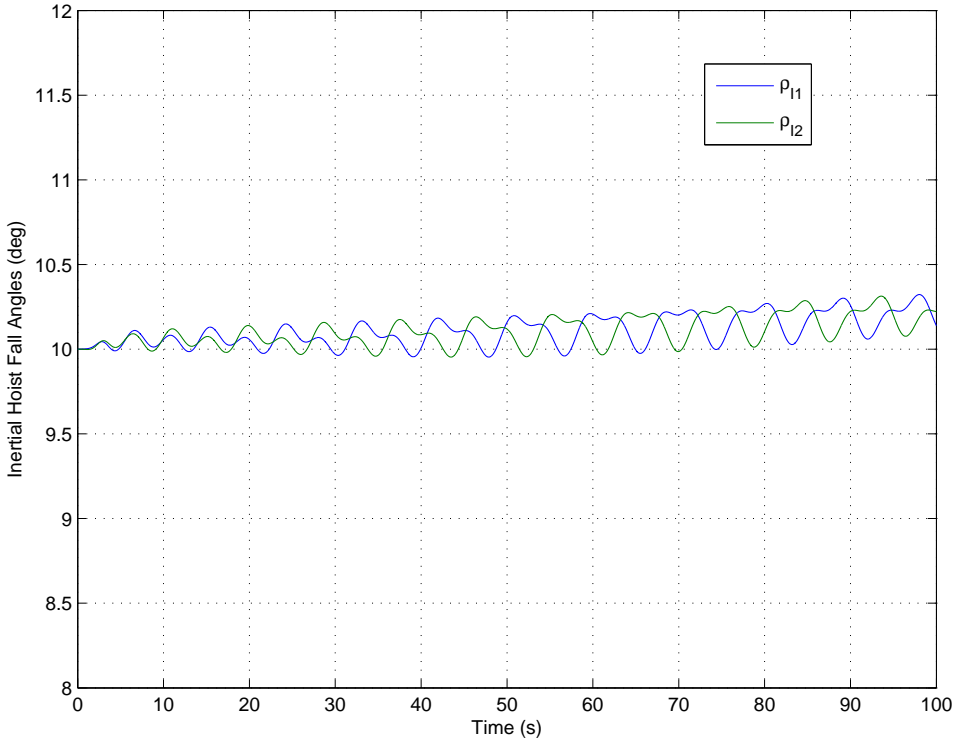


Figure 92. Plot of time histories for the inertial hoist-fall angle, ρ , for the inverse kinematic control case with constant torques and cable tension values used as the weights in the minimum norm solution. The constant values chosen were the maximums observed during a simulation of the same conditions using the identity matrix as the weighting elements. (Simulation parameters: $\rho = 10$ degrees, $\vec{P}_{8/1,z} = 5$ meters, and $x_s = 1$ meter at a period of 8.75 seconds.)

B. ALTERNATIVE WEIGHTING SCHEMES

In this section, several alternative schemes for manipulating the minimum norm solution will be investigated and relevance to operational scenarios established. Also, the various configurations and conditions simulated will be summarized using the previously defined performance metrics.

1. Actuation Selectivity

It may be operationally significant to have the capability to control the relative effort between the luffing and the hoisting degrees of freedom. Recognizing

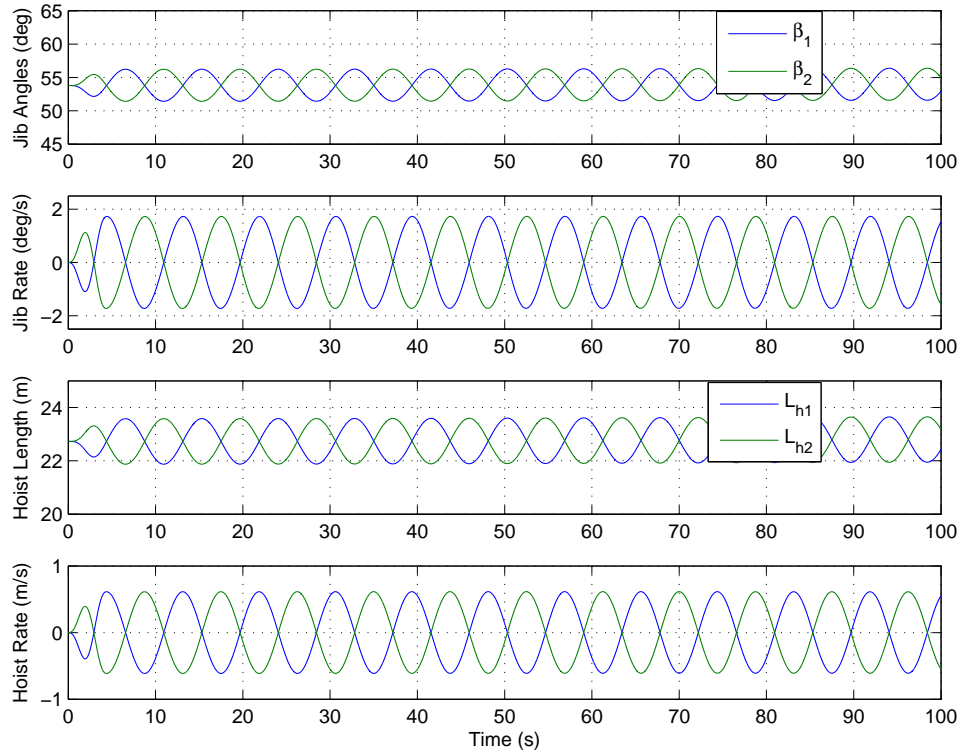


Figure 93. Plots of β , $\dot{\beta}$, L_h , and \dot{L}_h for the inverse kinematic control case with constant torques and cable tension values used as the weights in the minimum norm solution. The constant values chosen were the maximums observed during a simulation of the same conditions using the identity matrix as the weighting elements. (Simulation parameters: $\rho = 10$ degrees, $\vec{P}_{8/1,z} = 5$ meters, and $\mathbf{x}_s = 1$ meter at a period of 8.75 seconds.)

that choosing large values for some elements of \mathbf{W} relative to the others, will cause that actuation rate to be 'penalized' in the solution, this should be a means to selectively tailor the contribution of the four actuators in the inverse kinematic motion compensation. One application of this would be to reduce the contribution of an actuator when in proximity to a physical limit (e.g. minimum/maximum jib angle or minimum/maximum hoist length) to avoid driving the actuator into a condition that would cause the crane to be incapable of following the command signal. Another potential application of this feature would be fault tolerance. Coupled with a machinery

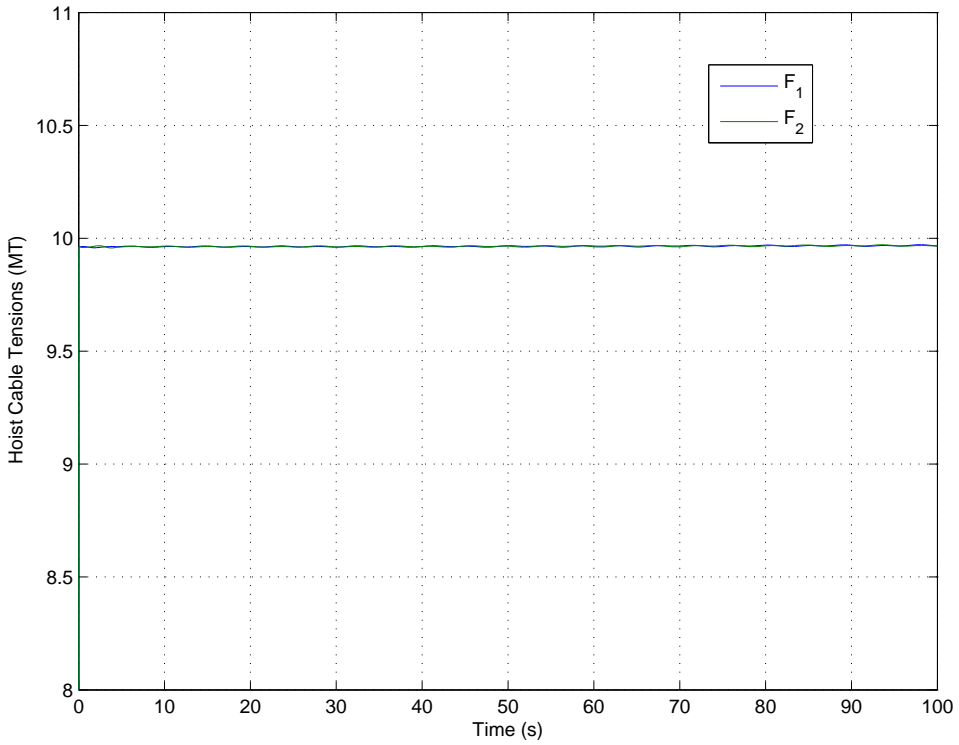


Figure 94. Plot of hoist cable tensions, F_1 and F_2 , for the inverse kinematic control case with constant torques and cable tension values used as the weights in the minimum norm solution. The constant values chosen were the maximums observed during a simulation of the same conditions using the identity matrix as the weighting elements. (Simulation parameters: $\rho = 10$ degrees, $\vec{P}_{8/1,z} = 5$ meters, and $x_s = 1$ meter at a period of 8.75 seconds.)

diagnostic system, the elements of the weighting matrix could be changed appropriately upon detection of a fault or reduced performance of one of the actuators so that crane operations would not be interrupted. Selecting the following forms of \mathbf{W} (Equation V.8) should introduce solutions with relative changes in the distribution of the actuation effort. The results are shown in Figures 101, 102, 103, 104, and 105. In this simulation all the ship motions (surge, heave, and pitch) are being excited and normally all actuators would be active. From Figure 101, it is apparent that the motion compensation is effective. The maximum surge amplitude is approximately

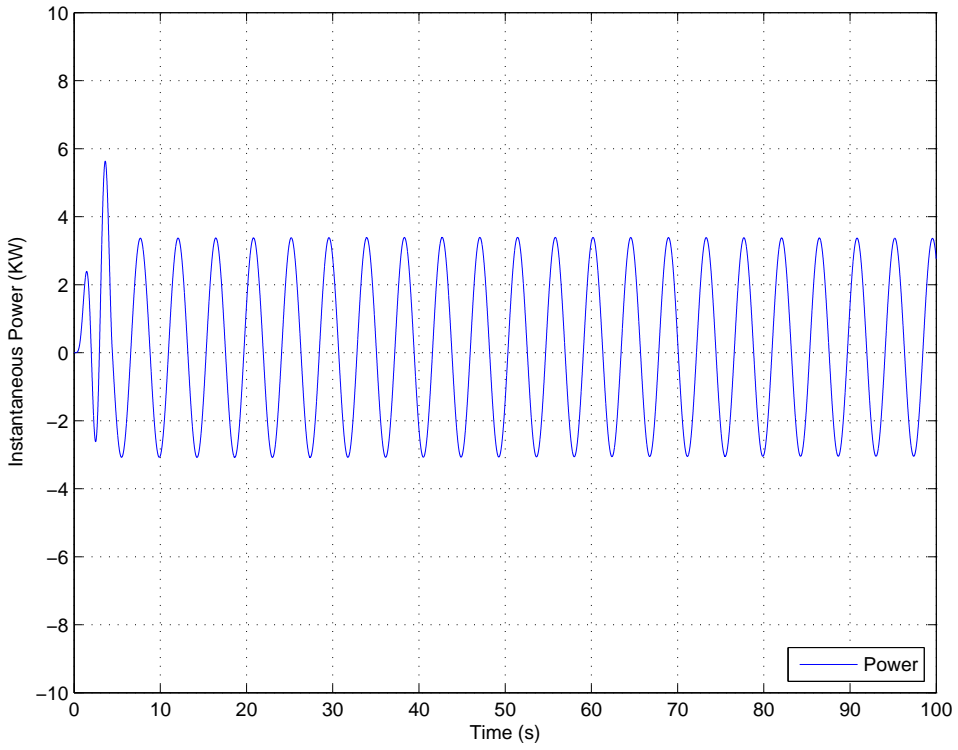


Figure 95. Plot of instantaneous power for the inverse kinematic control case with constant torques and cable tension values used as the weights in the minimum norm solution. The constant values chosen were the maximums observed during a simulation of the same conditions using the identity matrix as the weighting elements. (Simulation parameters: $\rho = 10$ degrees, $\vec{P}_{8/1,z} = 5$ meters, and $x_s = 1$ meter at a period of 8.75 seconds.)

0.2 meters - an 80% reduction relative to the 1.0 meter forcing function. More importantly, the uncontrolled system for this surge condition had a maximum response of over 1.5 meters to a 0.1 meter amplitude forcing function - an amplification factor of 15. So relative to the uncontrolled case the motion reduction is effectively 87% and well below the goal of <1 meter. Examination of Figure 102 reveals that this result is obtained with essentially no contribution from $\dot{\beta}_1$. Absent the contribution from $\dot{\beta}_1$, the peak rate on $\dot{\beta}_2$ has increased by only 20% relative to the same conditions simulated with equal weighting on all the actuators. Interestingly, the calculated J_{rate} is

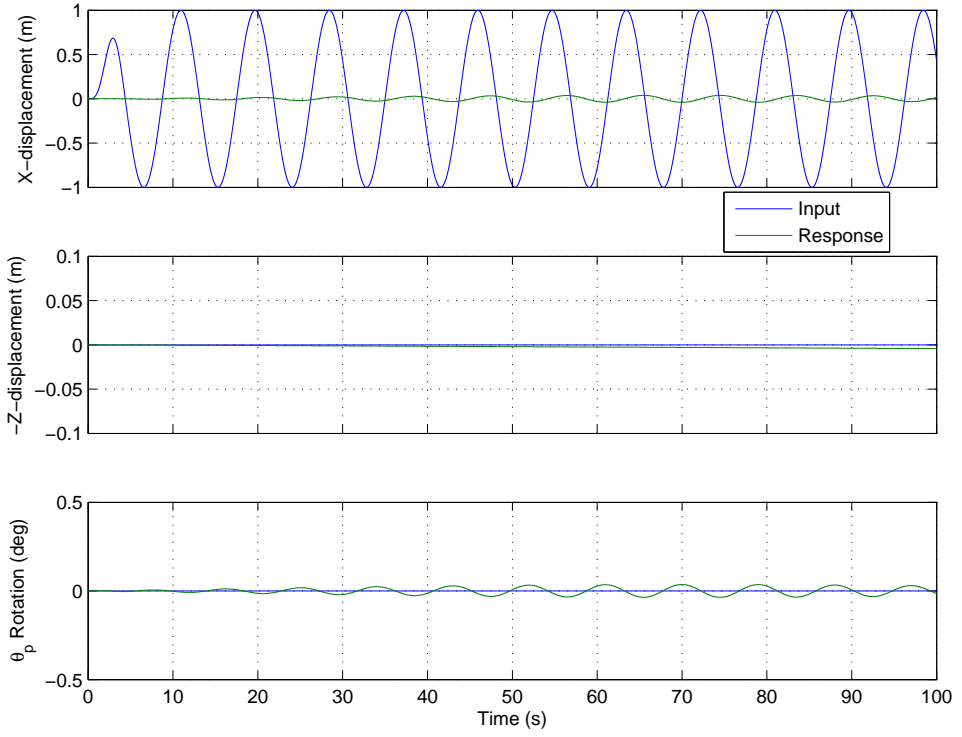


Figure 96. Plot of x , z , and θ time histories for the inverse kinematic control case with the identity matrix used as the weights in the minimum norm solution. (Simulation parameters: $\rho = 10$ degrees, $\vec{P}_{8/1,z} = 5$ meters, and $\mathbf{x}_s = 1$ meter at a period of 8.75 seconds.)

~ 3.5 m/s, which is less than the $J_{rate} \sim 4.5$ m/s calculated for the comparable conditions - as a result of the $\dot{\beta}_1$ contribution being essentially zero. Offsetting this positive result is the effect on J_{power} . Here we see that the calculated value of the metric has increased from 15.1 KW to 29.6 KW - almost doubling. Figures 103, 104 and 105 show the time histories of the hoist-fall angles, hoist cable tensions, and instantaneous power for the $\dot{\beta}_1 = 0$ simulation. For purposes of comparison, Figures 106, 107, 108, 109, and 110 show the corresponding time histories for the inverse kinematic control solution with $\mathbf{W} = \mathbf{I}$.

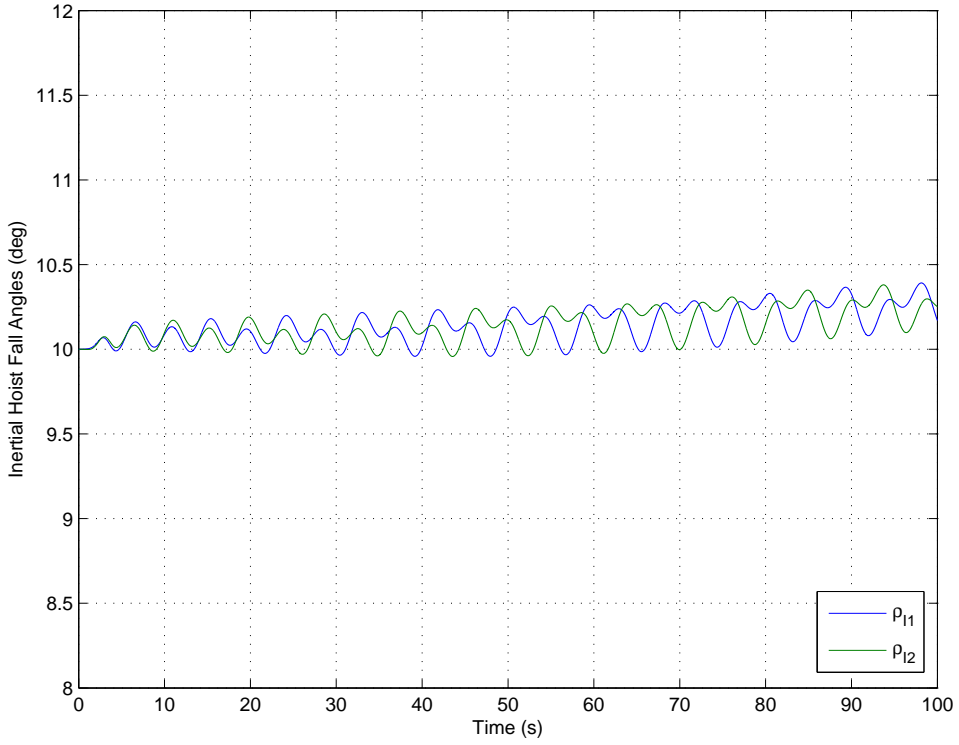


Figure 97. Plot of time histories for the inertial hoist-fall angle, ρ , for the inverse kinematic control case with the identity matrix used as the weights in the minimum norm solution. (Simulation parameters: $\rho = 10$ degrees, $\vec{P}_{8/1,z} = 5$ meters, and $\mathbf{x}_s = 1$ meter at a period of 8.75 seconds.)

$$W = \begin{bmatrix} 1.0e+06 & 0 & 0 & 0 \\ 0 & 1 & 0 & 0 \\ 0 & 0 & 1 & 0 \\ 0 & 0 & 0 & 1 \end{bmatrix} \quad (\text{V.8})$$

The selection of the values for \mathbf{W} lie on a continuum. In the previous example the selection of $1.0e+06$ was large enough to effectively shut-off the corresponding actuator. In the case that follows, \mathbf{W} was chosen to have the form shown in Eqn V.9. We should expect to see a reduction in the contribution from $\dot{\beta}_2$, while not shutting it down entirely. This is precisely the result seen in Figure 112. From Figure 111 we can

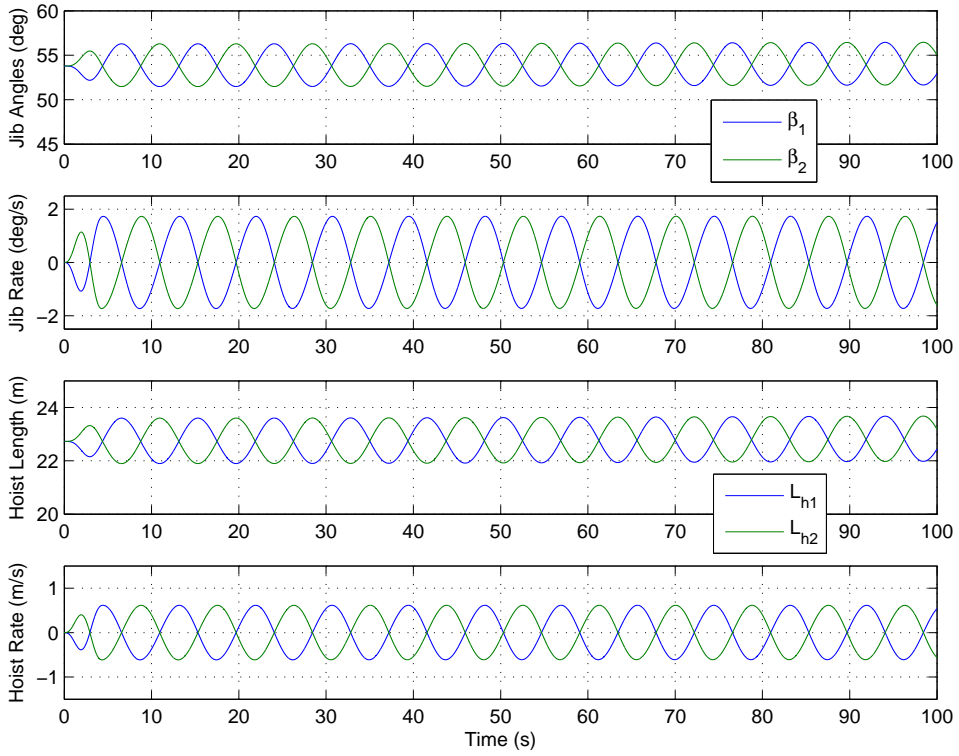


Figure 98. Plots of β , $\dot{\beta}$, L_h , and \dot{L}_h for the inverse kinematic control case with the identity matrix used as the weights in the minimum norm solution. (Simulation parameters: $\rho = 10$ degrees, $\vec{P}_{8/1,z} = 5$ meters, and $x_s = 1$ meter at a period of 8.75 seconds.)

verify that the inverse kinematic solution continues to be effective. The calculated metrics for this case are $J_{rate} = 4.7$ m/s and $J_{power} = 27.5$ KW which fall between the baseline case and the previous example. Changing the weight by a factor of 10^3 , resulted in a reduction in the peak value of $\dot{\beta}_2$ from 8.9 deg/sec to 5.1 deg/sec, or roughly 43%. For completeness, Figures 113 and 114 shows the hoist cable tensions and instantaneous power time histories.

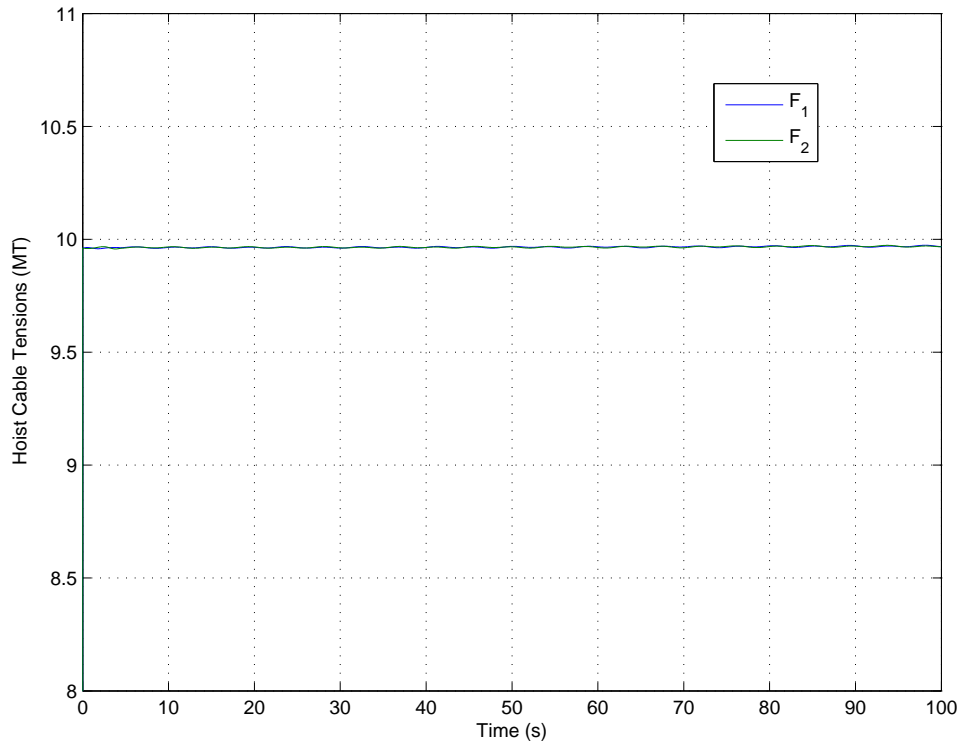


Figure 99. Plot of hoist cable tensions, F_1 and F_2 , for the inverse kinematic control case with the identity matrix used as the weights in the minimum norm solution. (Simulation parameters: $\rho = 10$ degrees, $\vec{P}_{8/1,z} = 5$ meters, and $\mathbf{x}_s = 1$ meter at a period of 8.75 seconds.)

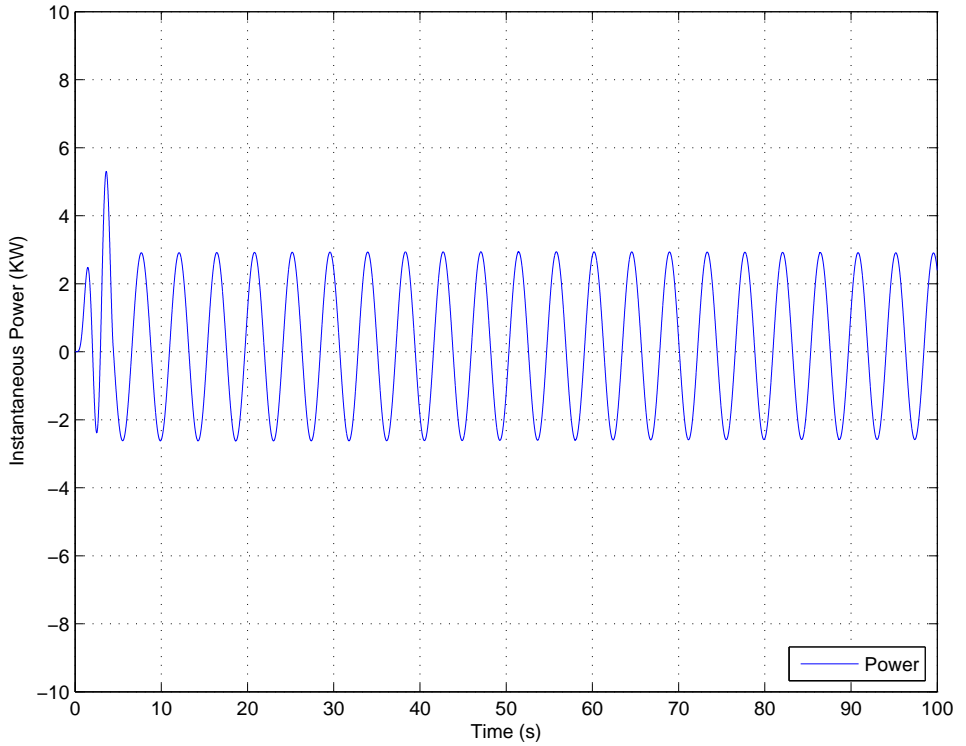


Figure 100. Plot of instantaneous power for the inverse kinematic control case with the identity matrix used as the weights in the minimum norm solution. (Simulation parameters: $\rho = 10$ degrees, $\vec{P}_{8/1,z} = 5$ meters, and $x_s = 1$ meter at a period of 8.75 seconds.)

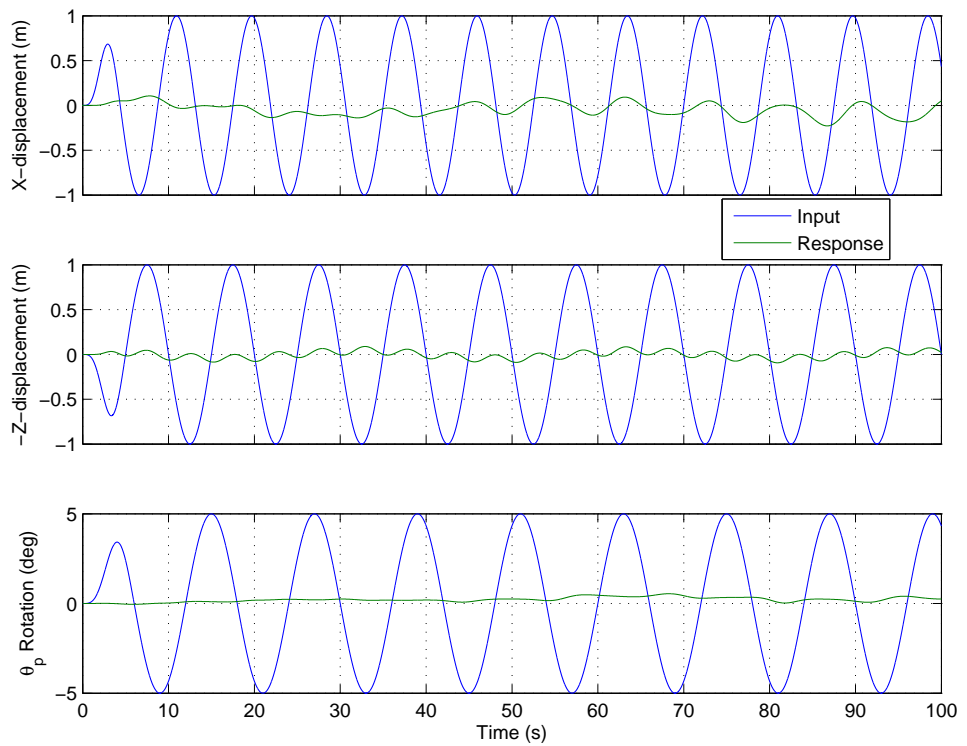


Figure 101. Plot of x , z , and θ time histories for the inverse kinematic control case with the weighting on $\dot{\beta}_1$ set to $1.0\text{e+}06$ in the minimum norm solution. (Simulation parameters: $\rho = 10$ degrees, $\vec{P}_{8/1,z} = -5$ meters, with a combined sinusoidal forcing function of $x_s = 1$ meter at a period of 8.75 seconds, $z_s = 1$ meter at a period of 10 seconds, and $\theta_s = 5^\circ$ at a period of 7.0 seconds.)

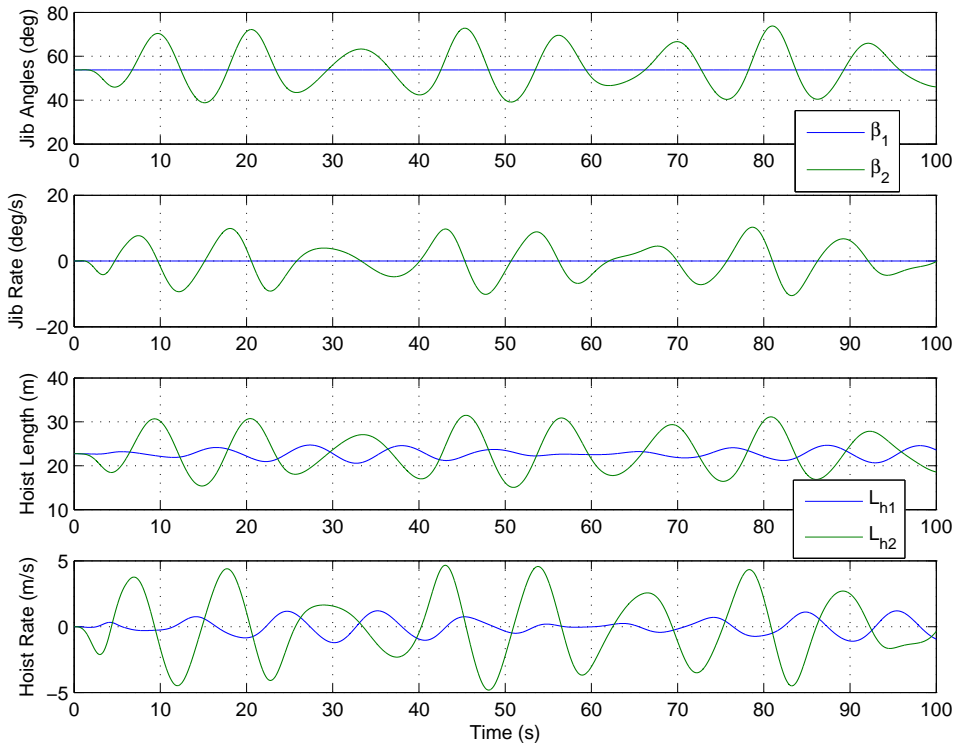


Figure 102. Plots of β , $\dot{\beta}$, L_h , and \dot{L}_h time histories for the inverse kinematic control case with the weighting on β_1 set to $1.0e+06$ in the minimum norm solution. (Simulation parameters: $\rho = 10$ degrees, $\vec{P}_{8/1,z} = -5$ meters, with a combined sinusoidal forcing function of $x_s = 1$ meter at a period of 8.75 seconds, $z_s = 1$ meter at a period of 10 seconds, and $\theta_s = 5^\circ$ at a period of 7.0 seconds.)

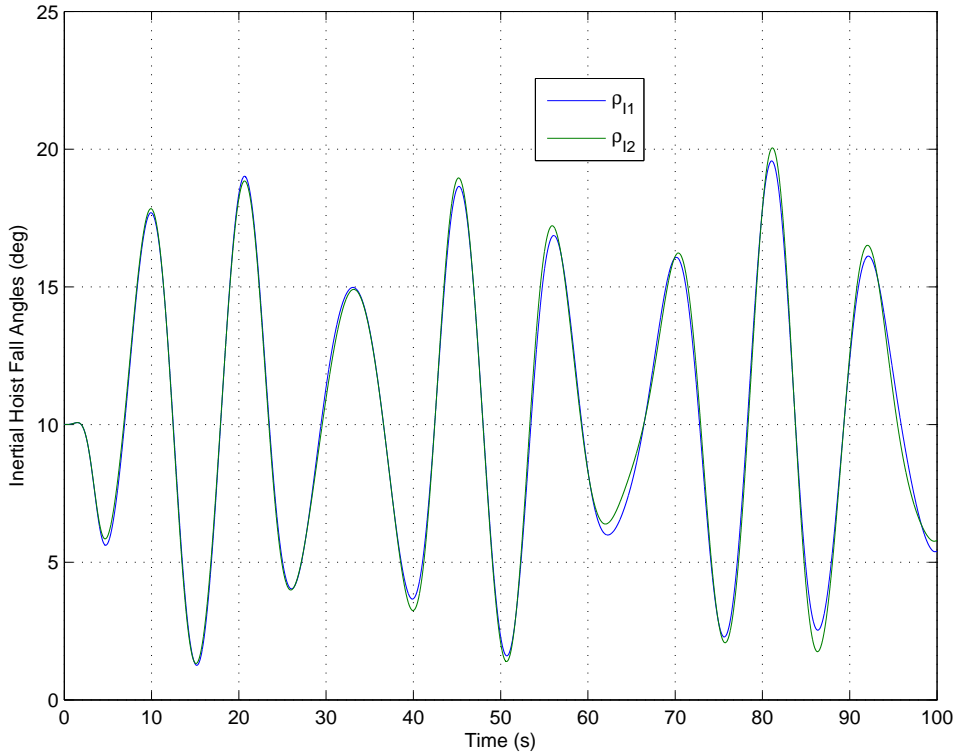


Figure 103. Plot of time histories for the inertial hoist-fall angle, ρ , for the inverse kinematic control case with the weighting on $\dot{\beta}_1$ set to $1.0\text{e+}06$ in the minimum norm solution. (Simulation parameters: $\rho = 10$ degrees, $\vec{P}_{8/1,z} = -5$ meters, with a combined sinusoidal forcing function of $\mathbf{x}_s = 1$ meter at a period of 8.75 seconds, $\mathbf{z}_s = 1$ meter at a period of 10 seconds, and $\theta_s = 5^\circ$ at a period of 7.0 seconds.)

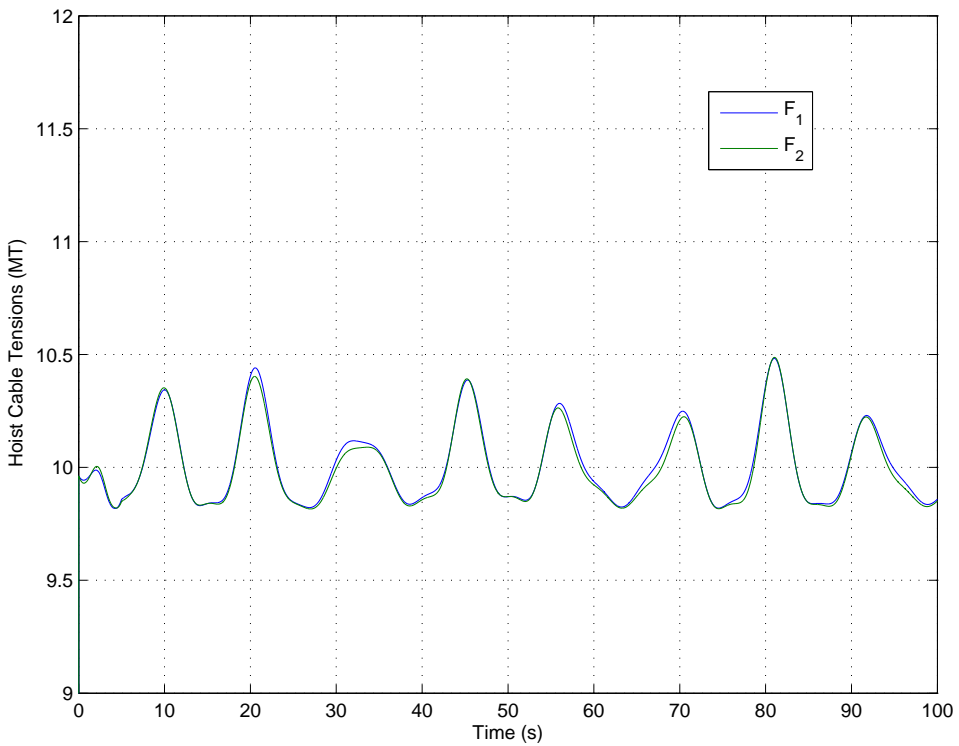


Figure 104. Plot of hoist cable tensions, F_1 and F_2 , for the inverse kinematic control case with the weighting on $\dot{\beta}_1$ set to $1.0\text{e}+06$ in the minimum norm solution. (Simulation parameters: $\rho = 10$ degrees, $\vec{P}_{8/1,z} = -5$ meters, with a combined sinusoidal forcing function of $x_s = 1$ meter at a period of 8.75 seconds, $z_s = 1$ meter at a period of 10 seconds, and $\theta_s = 5^\circ$ at a period of 7.0 seconds.)

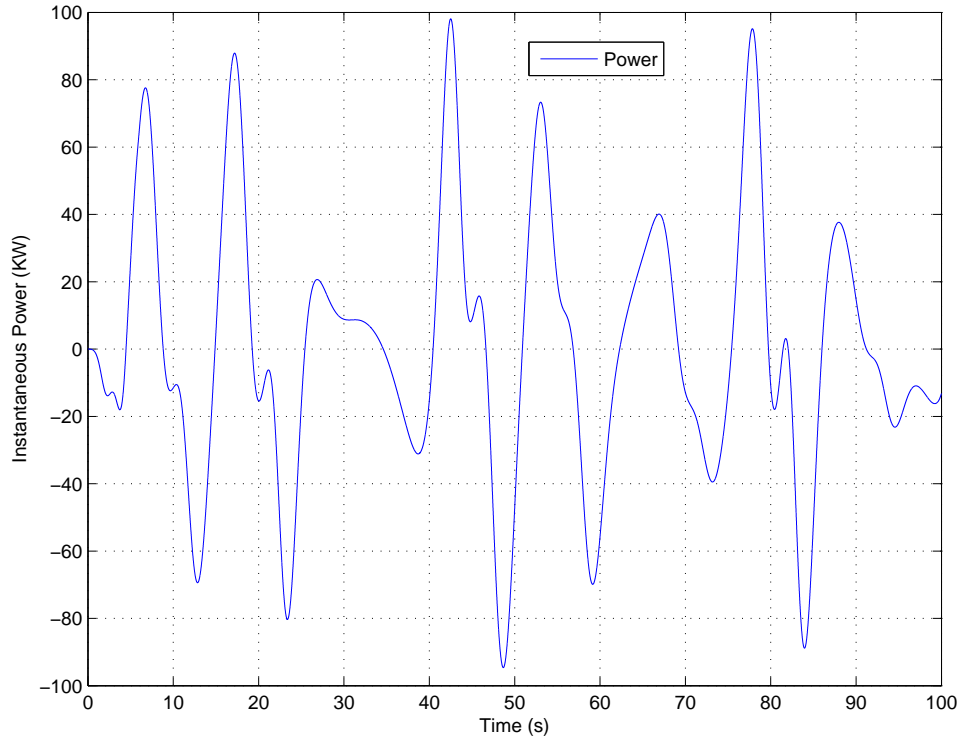


Figure 105. Plot of time histories for instantaneous power for the inverse kinematic control case with the weighting on $\dot{\beta}_1$ set to $1.0\text{e+}06$ in the minimum norm solution. (Simulation parameters: $\rho = 10$ degrees, $\bar{P}_{8/1,z} = -5$ meters, with a combined sinusoidal forcing function of $x_s = 1$ meter at a period of 8.75 seconds, $z_s = 1$ meter at a period of 10 seconds, and $\theta_s = 5^\circ$ at a period of 7.0 seconds.)

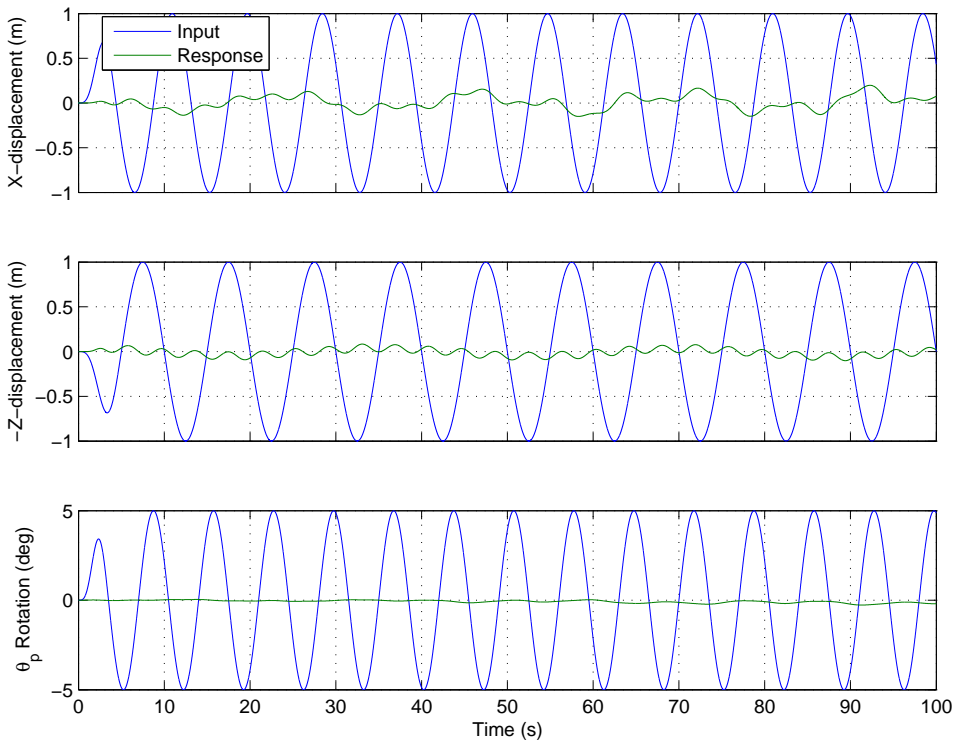


Figure 106. Plot of x , z , and θ time histories for the inverse kinematic control case with the identity matrix used as the weights in the minimum norm solution. (Simulation parameters: $\rho = 10$ degrees, $\vec{P}_{8/1,z} = -5$ meters, with a combined sinusoidal forcing function of $x_s = 1$ meter at a period of 8.75 seconds, $z_s = 1$ meter at a period of 10 seconds, and $\theta_s = 5^\circ$ at a period of 7.0 seconds.)

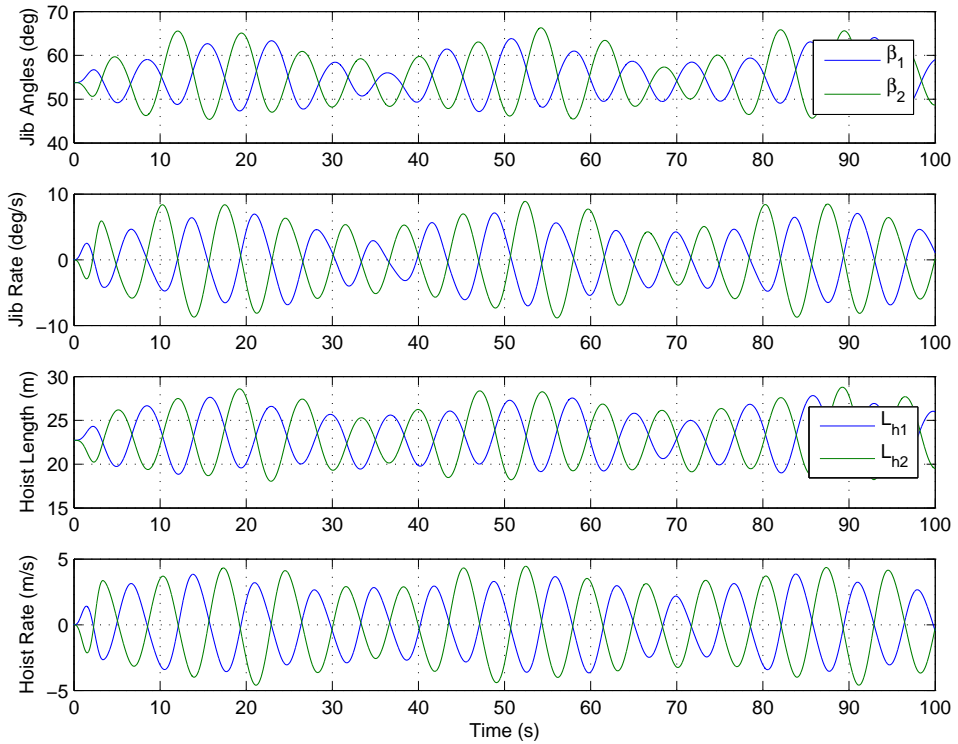


Figure 107. Plots of β , $\dot{\beta}$, L_h , and \dot{L}_h time histories for the inverse kinematic control case with the identity matrix used as the weights in the minimum norm solution. (Simulation parameters: $\rho = 10$ degrees, $\vec{P}_{8/1,z} = -5$ meters, with a combined sinusoidal forcing function of $x_s = 1$ meter at a period of 8.75 seconds, $z_s = 1$ meter at a period of 10 seconds, and $\theta_s = 5^\circ$ at a period of 7.0 seconds.)

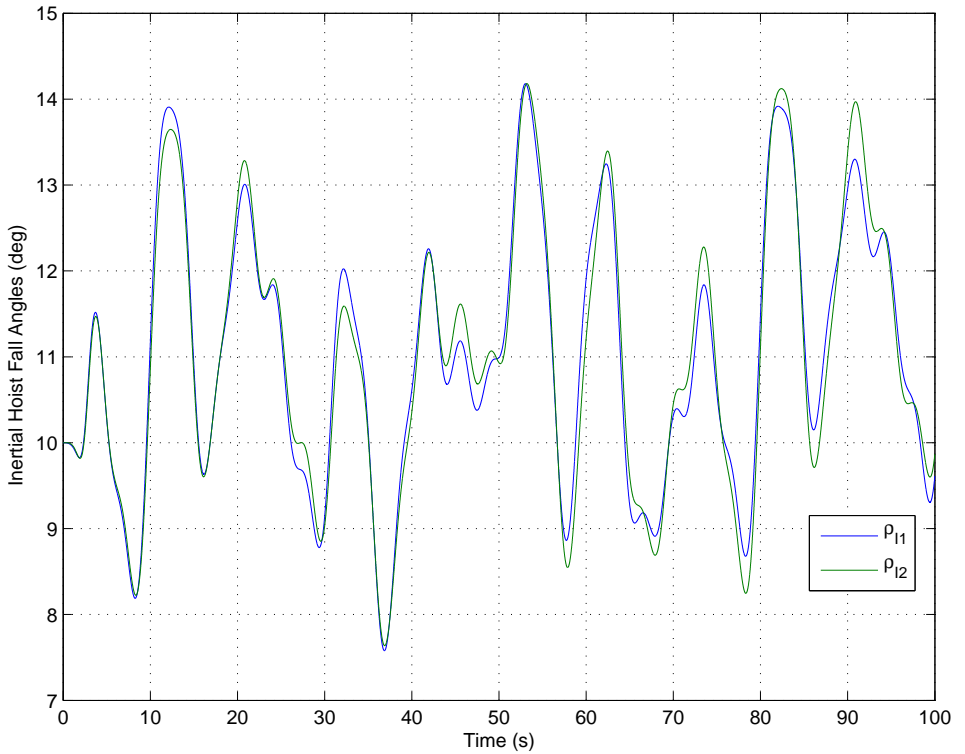


Figure 108. Plot of time histories for the inertial hoist-fall angle, ρ , for the inverse kinematic control case with the identity matrix used as the weights in the minimum norm solution. (Simulation parameters: $\rho = 10$ degrees, $\vec{P}_{8/1,z} = -5$ meters, with a combined sinusoidal forcing function of $x_s = 1$ meter at a period of 8.75 seconds, $z_s = 1$ meter at a period of 10 seconds, and $\theta_s = 5^\circ$ at a period of 7.0 seconds.)

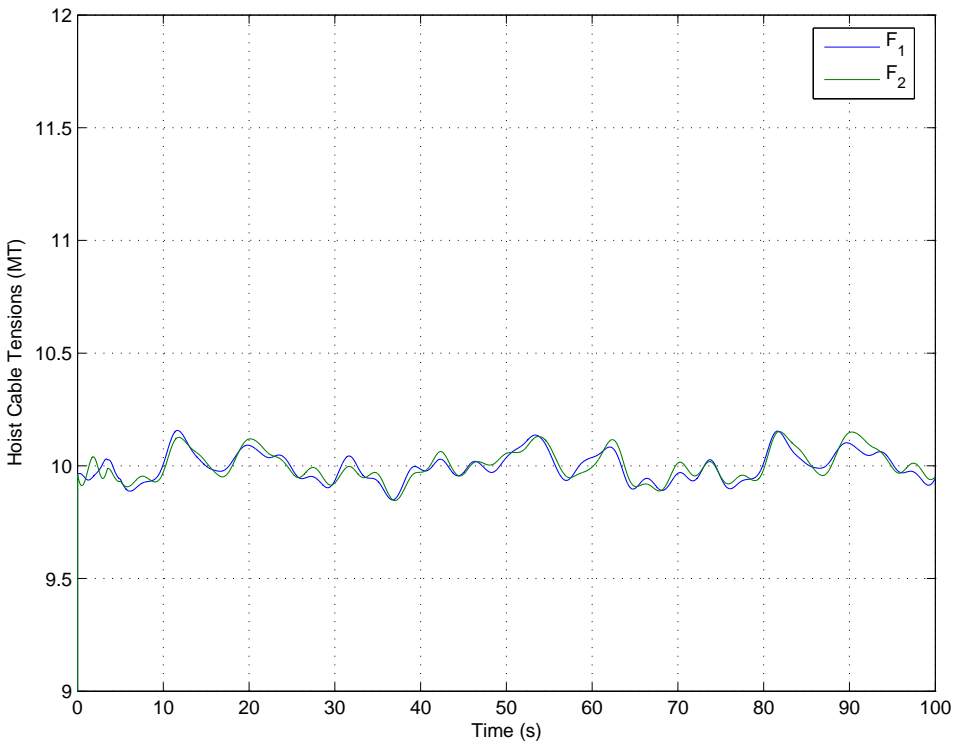


Figure 109. Plot of hoist cable tensions, F_1 and F_2 , for the inverse kinematic control case with the identity matrix used as the weights in the minimum norm solution. (Simulation parameters: $\rho = 10$ degrees, $\vec{P}_{8/1,z} = -5$ meters, with a combined sinusoidal forcing function of $x_s = 1$ meter at a period of 8.75 seconds, $z_s = 1$ meter at a period of 10 seconds, and $\theta_s = 5^\circ$ at a period of 7.0 seconds.)

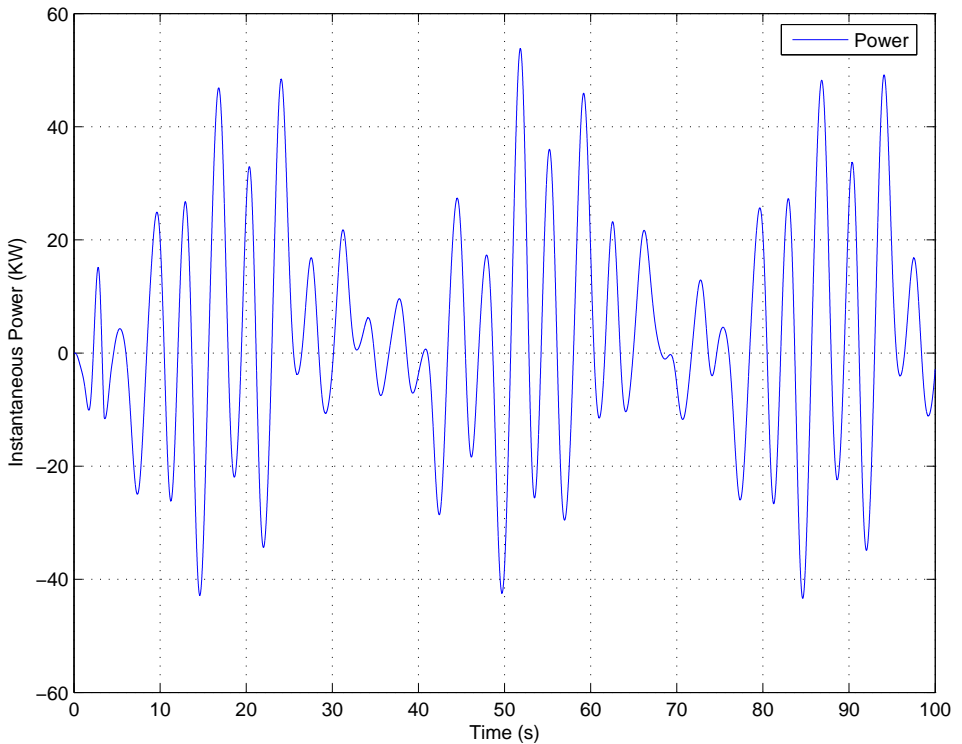


Figure 110. Plot of time histories for instantaneous power for the inverse kinematic control case with the identity matrix used as the weights in the minimum norm solution. (Simulation parameters: $\rho = 10$ degrees, $\vec{P}_{8/1,z} = -5$ meters, with a combined sinusoidal forcing function of $x_s = 1$ meter at a period of 8.75 seconds, $z_s = 1$ meter at a period of 10 seconds, and $\theta_s = 5^\circ$ at a period of 7.0 seconds.)

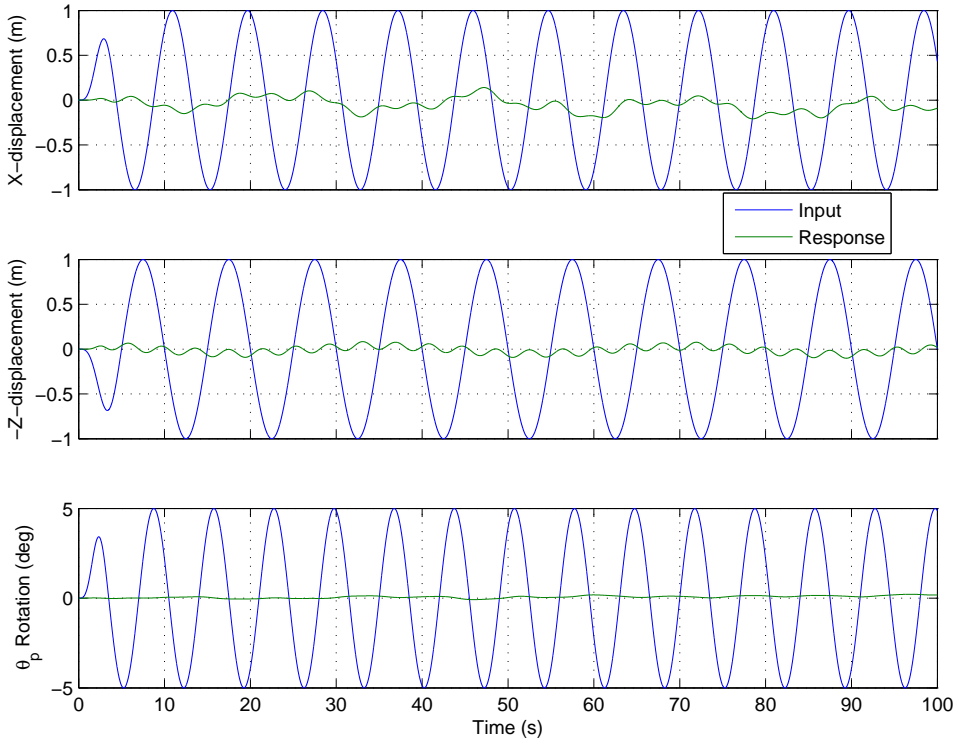


Figure 111. Plot of x , z , and θ time histories for the inverse kinematic control case with the weighting on β_2 set to $1.0e+03$ in the minimum norm solution. (Simulation parameters: $\rho = 10$ degrees, $\vec{P}_{8/1,z} = -5$ meters, with a combined sinusoidal forcing function of $x_s = 1$ meter at a period of 8.75 seconds, $z_s = 1$ meter at a period of 10 seconds, and $\theta_s = 5^\circ$ at a period of 7.0 seconds.)

Both of the previous two examples dealt with manipulation of the jib actuation contribution to the inverse kinematic solution. In the next example, we will see the impact of eliminating one of the hoists from the solution.

To do this, \mathbf{W} has the form shown in Eqn. V.10. The resulting time histories are shown in Figures 116, 115, 117, 118, and 119. From Fig. 116 it is apparent that \dot{L}_{h2} is essentially zero. The inverse kinematic solution continues to reduce the response to the combined motion input as shown in Fig. 115, although the residual motion in surge is ~ 0.3 meter, 0.1 meter in heave, and ~ 1.0 degree in pitch. The most significant impact of this weighting selection is seen in the instantaneous power

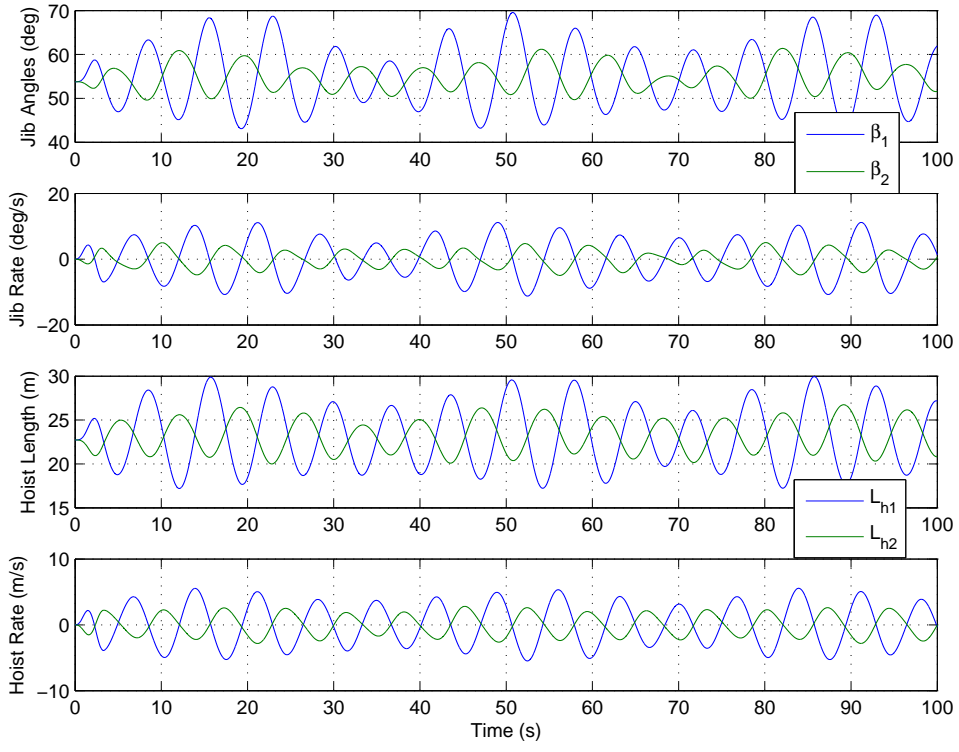


Figure 112. Plots of β , $\dot{\beta}$, L_h , and \dot{L}_h time histories for the inverse kinematic control case with the weighting on β_2 set to $1.0e+03$ in the minimum norm solution. (Simulation parameters: $\rho = 10$ degrees, $\vec{P}_{8/1,z} = -5$ meters, with a combined sinusoidal forcing function of $x_s = 1$ meter at a period of 8.75 seconds, $z_s = 1$ meter at a period of 10 seconds, and $\theta_s = 5^\circ$ at a period of 7.0 seconds.)

(Fig. 119). Compared to the baseline case, the peak power increased from 53.8 KW to 300KW. Correspondingly, the value of J_{power} increased from 15.1 KW to 92.8 KW. In contrast, the value of J_{rate} only increased to 6.7 m/s from 4.5 m/s. This result makes sense when considering that it is more efficient to lift the payload by pulling on the hoist cables, than by applying a torque to rotate the jib to produce the same motion.

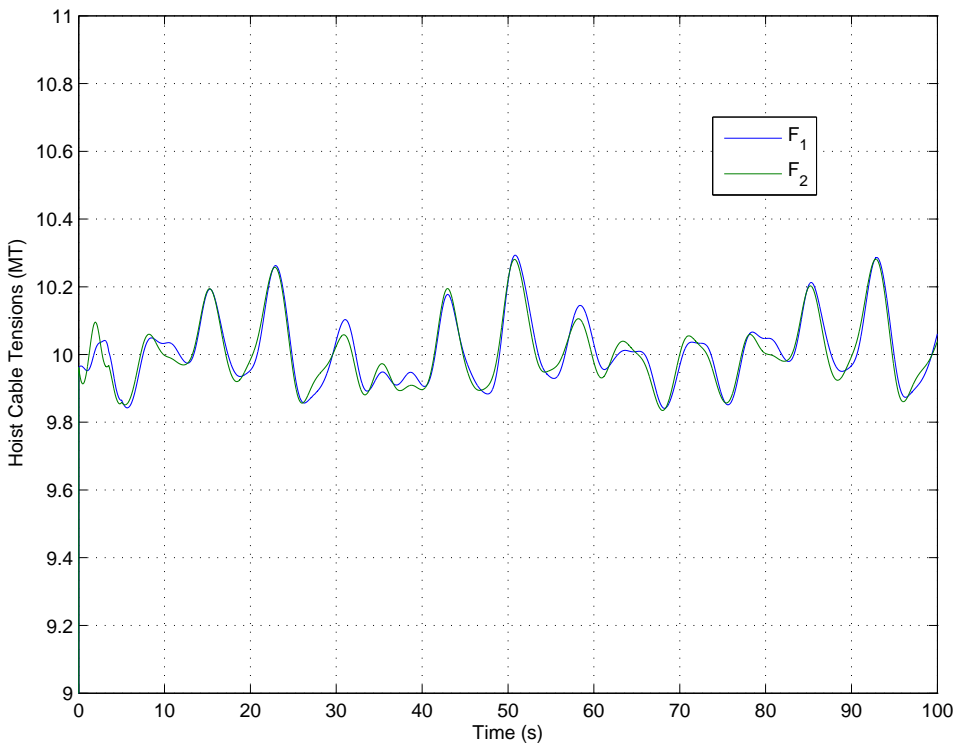


Figure 113. Plot of hoist cable tensions, F_1 and F_2 , for the inverse kinematic control case with the weighting on $\dot{\beta}_2$ set to $1.0\text{e}+03$ in the minimum norm solution. (Simulation parameters: $\rho = 10$ degrees, $\vec{P}_{8/1,z} = -5$ meters, with a combined sinusoidal forcing function of $x_s = 1$ meter at a period of 8.75 seconds, $z_s = 1$ meter at a period of 10 seconds, and $\theta_s = 5^\circ$ at a period of 7.0 seconds.)

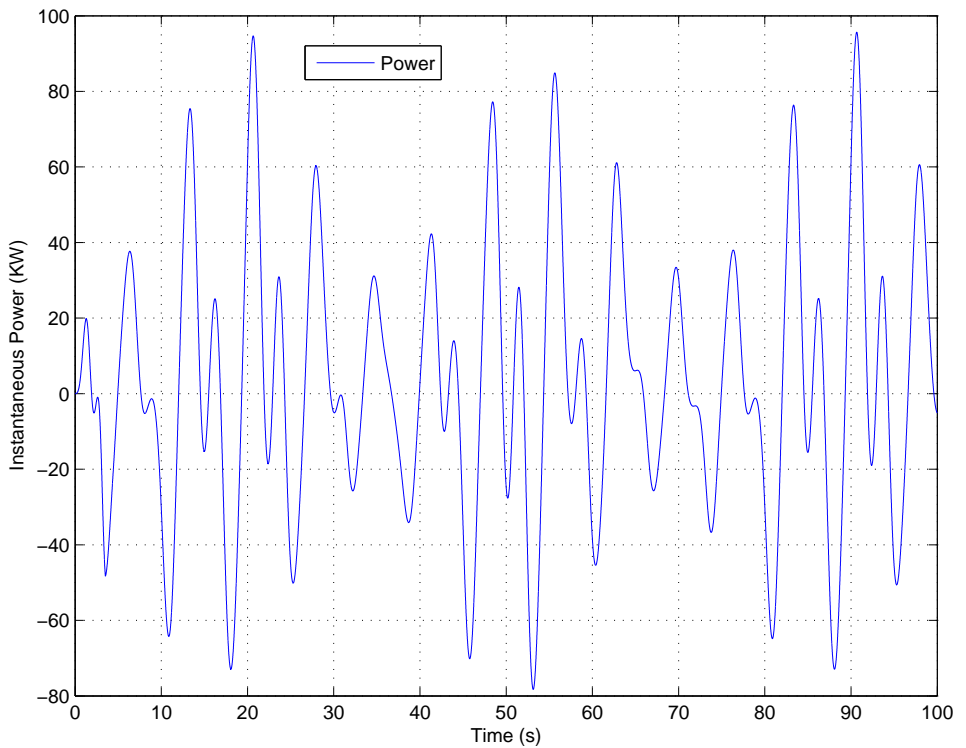


Figure 114. Plot of time histories for instantaneous power for the inverse kinematic control case with the weighting on $\dot{\beta}_2$ set to $1.0\text{e+}03$ in the minimum norm solution. (Simulation parameters: $\rho = 10$ degrees, $\vec{P}_{8/1,z} = -5$ meters, with a combined sinusoidal forcing function of $x_s = 1$ meter at a period of 8.75 seconds, $z_s = 1$ meter at a period of 10 seconds, and $\theta_s = 5^\circ$ at a period of 7.0 seconds.)

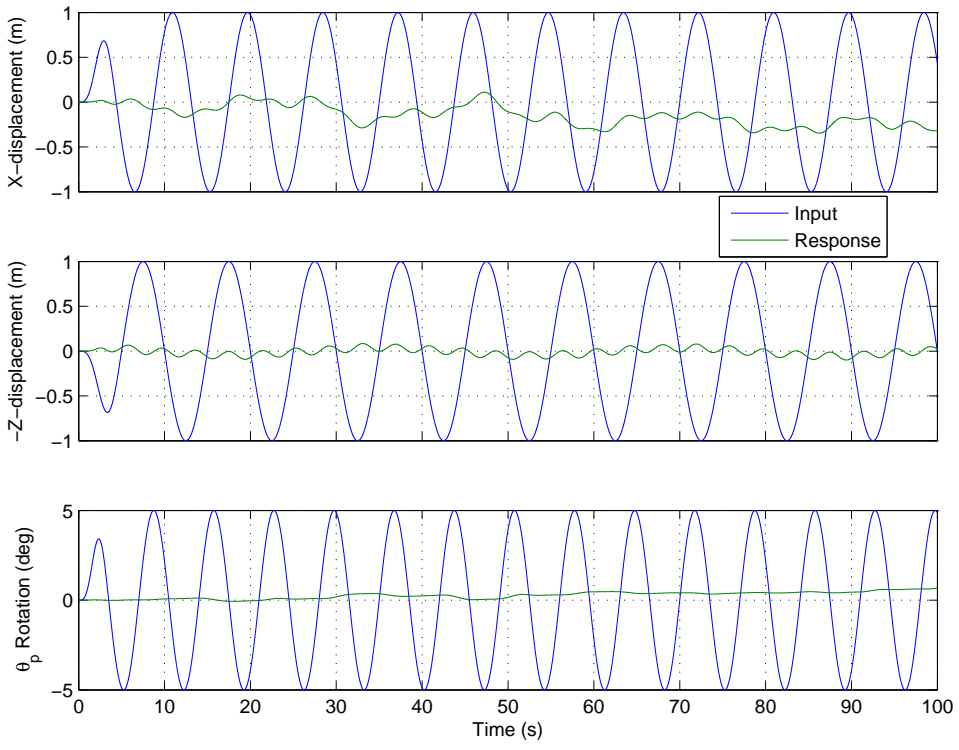


Figure 115. Plot of x , z , and θ time histories for the inverse kinematic control case with the weighting on \dot{L}_{h2} set to $1.0e+06$ in the minimum norm solution. (Simulation parameters: $\rho = 10$ degrees, $\vec{P}_{8/1,z} = -5$ meters, with a combined sinusoidal forcing function of $x_s = 1$ meter at a period of 8.75 seconds, $z_s = 1$ meter at a period of 10 seconds, and $\theta_s = 5^\circ$ at a period of 7.0 seconds.)

$$W = \begin{bmatrix} 1 & 0 & 0 & 0 \\ 0 & 1000 & 0 & 0 \\ 0 & 0 & 1 & 0 \\ 0 & 0 & 0 & 1 \end{bmatrix} \quad (\text{V.9})$$

$$W = \begin{bmatrix} 1 & 0 & 0 & 0 \\ 0 & 1 & 0 & 0 \\ 0 & 0 & 1 & 0 \\ 0 & 0 & 0 & 1.0e + 06 \end{bmatrix} \quad (\text{V.10})$$

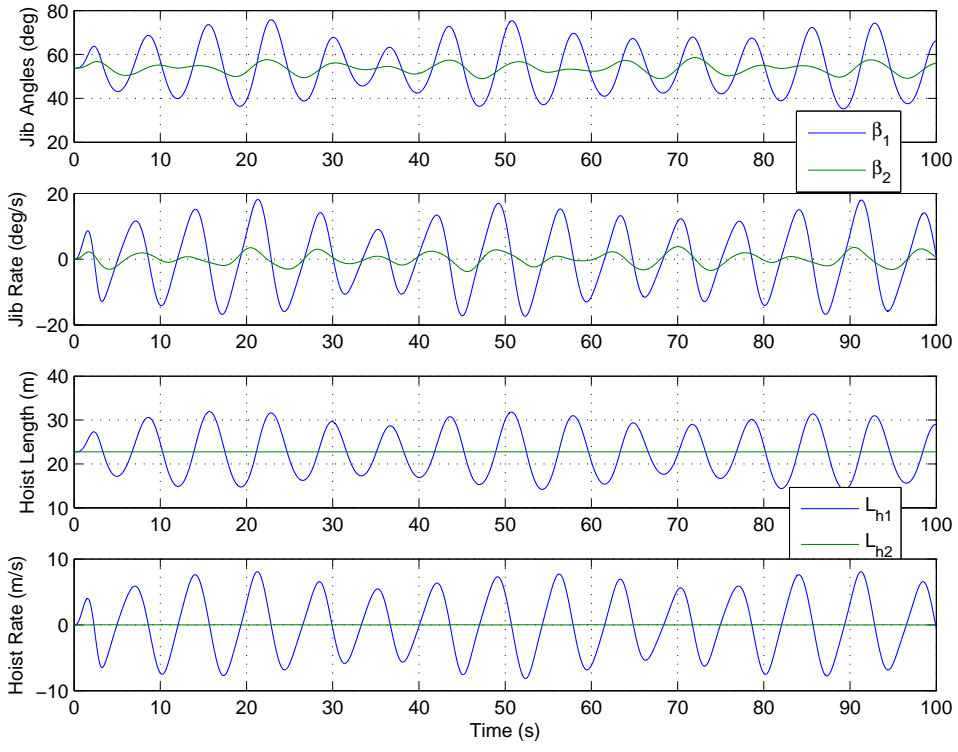


Figure 116. Plots of β , $\dot{\beta}$, L_h , and \dot{L}_h time histories for the inverse kinematic control case with the weighting on \dot{L}_{h2} set to $1.0e+06$ in the minimum norm solution. (Simulation parameters: $\rho = 10$ degrees, $\vec{P}_{8/1,z} = -5$ meters, with a combined sinusoidal forcing function of $x_s = 1$ meter at a period of 8.75 seconds, $z_s = 1$ meter at a period of 10 seconds, and $\theta_s = 5^\circ$ at a period of 7.0 seconds.)

It is apparent from the extreme cases presented above that the values of the weighting elements relative to each other influence the resulting contribution of the actuators to the inverse kinematic solution. It may be desirable to normalize or balance the actuator quantities. The jib luffing rates have the units of angular rate, rad/s (deg/s), while the hoisting rates are in m/s. Multiplying the luffing rate $\dot{\beta}$ in rad/s by the jib (boom) length, $L_b = 37$ m yields a quantity with the proper units of m/s in balance with the hoisting rates. The form of \mathbf{W} to achieve this balance is given by Eqn. V.11.

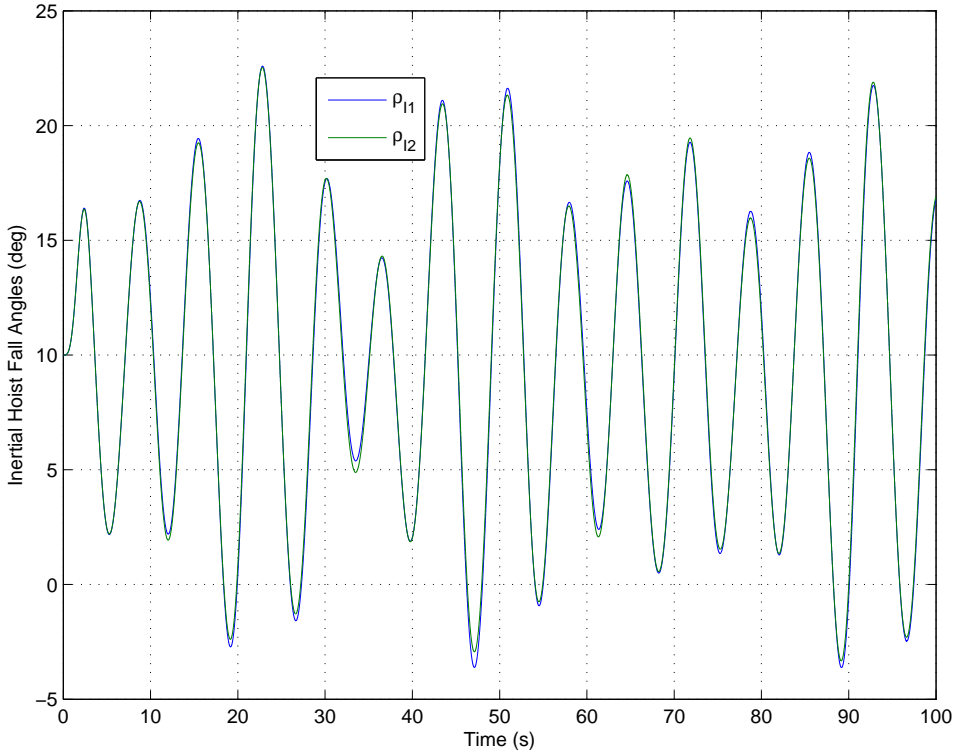


Figure 117. Plot of time histories for the inertial hoist-fall angle, ρ , for the inverse kinematic control case with the weighting on \dot{L}_{h2} set to $1.0e+06$ in the minimum norm solution. (Simulation parameters: $\rho = 10$ degrees, $\vec{P}_{8/1,z} = -5$ meters, with a combined sinusoidal forcing function of $\mathbf{x}_s = 1$ meter at a period of 8.75 seconds, $\mathbf{z}_s = 1$ meter at a period of 10 seconds, and $\theta_s = 5^\circ$ at a period of 7.0 seconds.)

$$W = \begin{bmatrix} L_b & 0 & 0 & 0 \\ 0 & L_b & 0 & 0 \\ 0 & 0 & 1 & 0 \\ 0 & 0 & 0 & 1 \end{bmatrix} \quad (\text{V.11})$$

A simulation of the system was run using this form of \mathbf{W} and the results are shown in Figures 297, 299, 298, 300, and 301. There are no significant differences when compared to a comparable set of results generated with $\mathbf{W} = \mathbf{I}$. The value of $J_{rate} = 1.0553$ is exactly the same and J_{power} increased slightly from 1.7697 to 1.7951.

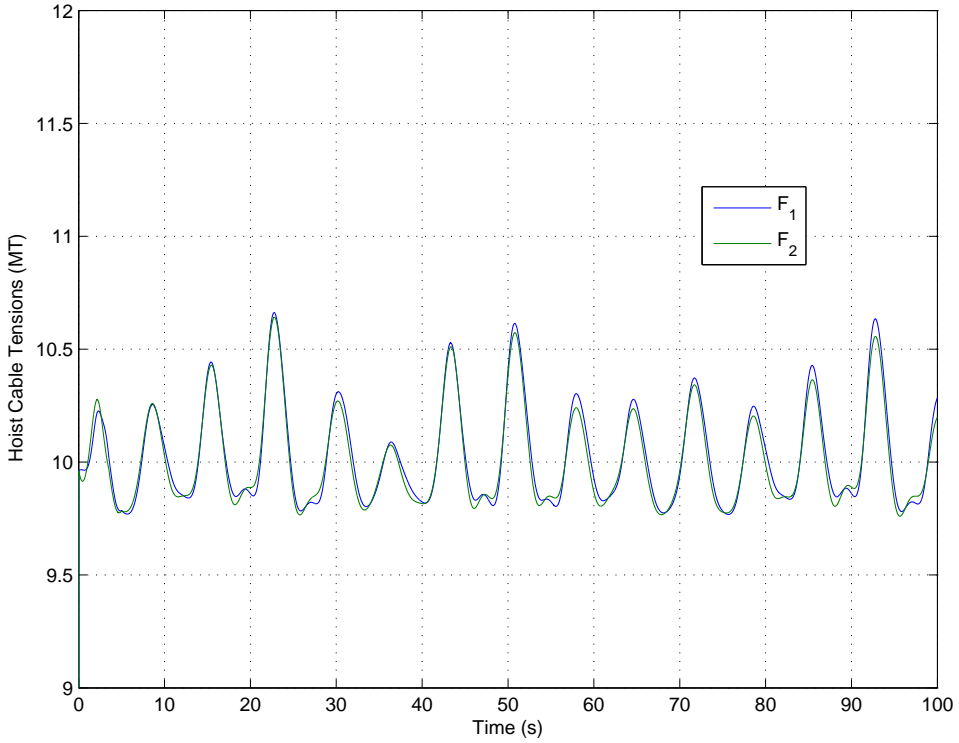


Figure 118. Plot of hoist cable tensions, F_1 and F_2 , for the inverse kinematic control case with the weighting on \dot{L}_{h2} set to $1.0e+06$ in the minimum norm solution. (Simulation parameters: $\rho = 10$ degrees, $\vec{P}_{8/1,z} = -5$ meters, with a combined sinusoidal forcing function of $x_s = 1$ meter at a period of 8.75 seconds, $z_s = 1$ meter at a period of 10 seconds, and $\theta_s = 5^\circ$ at a period of 7.0 seconds.)

The final rationale considered for selecting the elements of \mathbf{W} is based on an argument presented by Franklin & Powell ([64]) in their selection of weights for a optimal linear quadratic regulator (LQR) solution. Their goal was to balance the contribution of the quantities included in the state feedback. Their procedure was to observe the maximum excursion of a signal, which they referred to as m , and then apply $\frac{1}{m^2}$ as the corresponding element in the weighting matrix. Realizing that the minimum norm solution to generate the inverse kinematic control is not a LQR problem, using this weighting scheme may produce a useful result by substituting the maximum actuation rates for values of m . For the baseline we will use the results

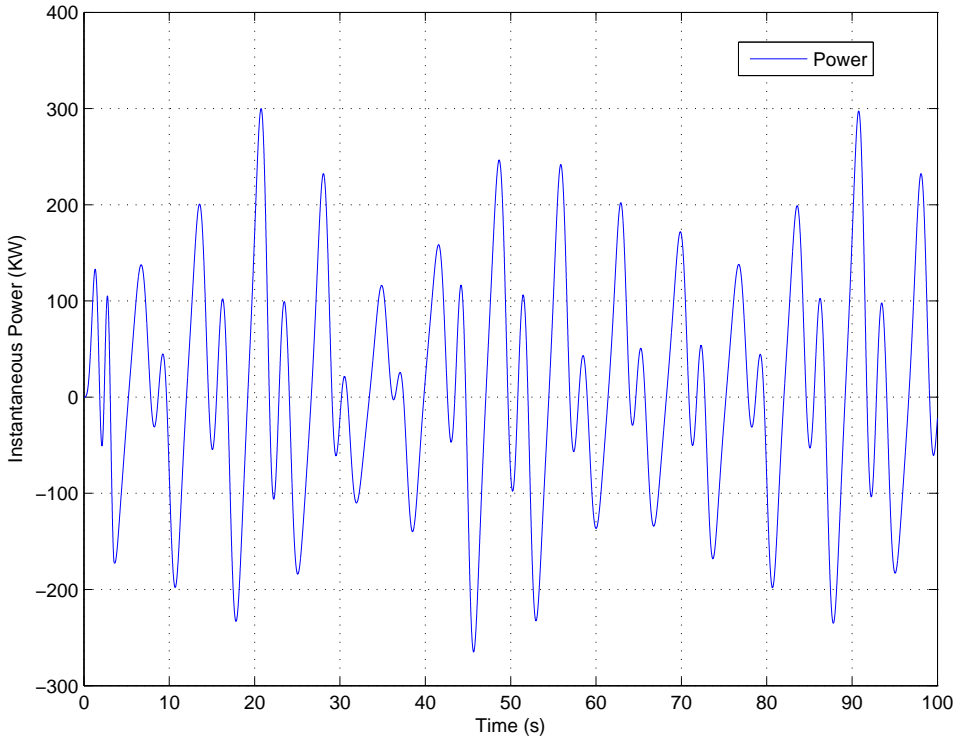


Figure 119. Plot of time histories for instantaneous power for the inverse kinematic control case with the weighting on \dot{L}_{h2} set to $1.0e+06$ in the minimum norm solution. (Simulation parameters: $\rho = 10$ degrees, $\vec{P}_{8/1,z} = -5$ meters, with a combined sinusoidal forcing function of $x_s = 1$ meter at a period of 8.75 seconds, $z_s = 1$ meter at a period of 10 seconds, and $\theta_s = 5^\circ$ at a period of 7.0 seconds.)

from a case with $\mathbf{W} = \mathbf{I}$, $\rho = 10^\circ$, $\vec{P}_{8/1,z} = -5$ m, and combined surge, heave, and pitch input. For this run the maximum values of actuation rates were: $\dot{\beta}_1 \sim 7$, $\dot{\beta}_2 \sim 9$, $\dot{L}_{h1} \sim 4$, and $\dot{L}_{h2} \sim 5$. Thus, \mathbf{W} had the form shown in Eqn. V.12. (Note that the L_b factor has been carried forward from the previous example.)

$$W = \begin{bmatrix} \frac{L_b}{7^2} & 0 & 0 & 0 \\ 0 & \frac{L_b}{9^2} & 0 & 0 \\ 0 & 0 & \frac{1}{4^2} & 0 \\ 0 & 0 & 0 & \frac{1}{5^2} \end{bmatrix} \quad (\text{V.12})$$

Using this \mathbf{W} in the simulation of the dual crane system, the results shown in

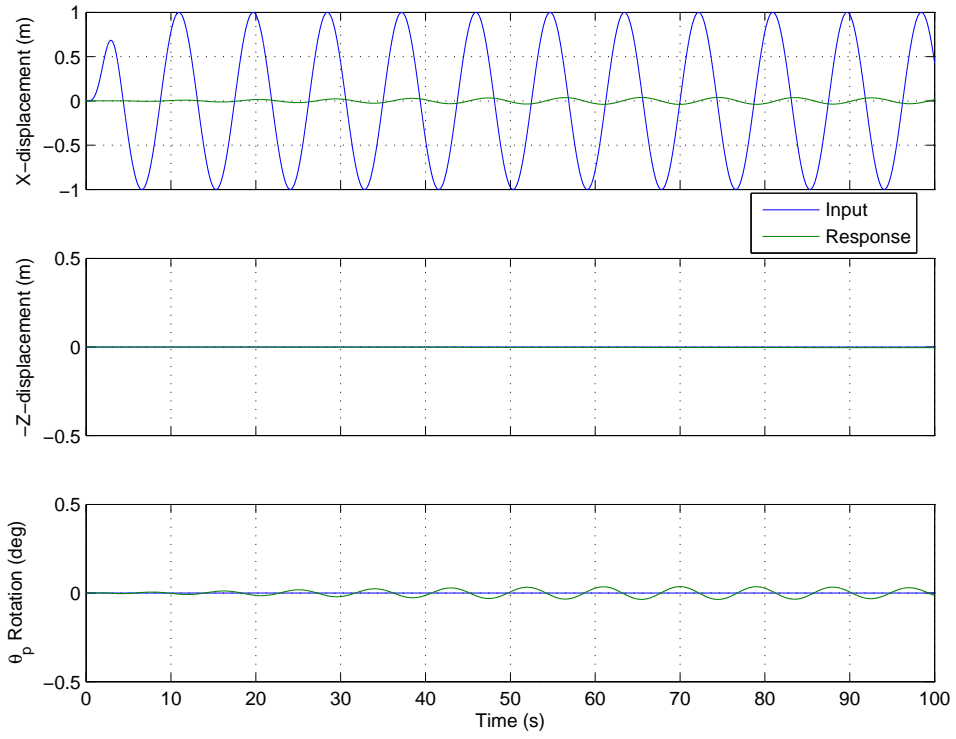


Figure 120. Plot of x , z , and θ time histories for the inverse kinematic control case using weights that match the units of the actuators in the minimum norm solution. (Simulation parameters: $\rho = 10$ degrees, $\vec{P}_{8/1,z} = -5$ meters, and $\mathbf{x}_s = 1$ meter at a period of 8.75 seconds.)

Figures 125, 127, 126, 128, and 129 were generated. Unfortunately, using a similar set of conditions, but with $\mathbf{W} = \mathbf{I}$ as a baseline, we see that this selection of \mathbf{W} has produced an unfavorable result. The peak rates for both luffing and hoisting actuators increased - luffing by 19% from 8.89 deg/s to 10.57 deg/s and hoisting by 8% from 4.60 m/s to 4.96 m/s. That resulted in a calculated $J_{rate} = 4.66$ m/s compared to the baseline J_{rate} of 4.46 m/s. The peak instantaneous power jumped from 53.8 KW to 73.2 KW and correspondingly J_{power} increased from 15.1 KW to 20.8 KW.

2. Other Operational Considerations

Many options exist for the selection of the weighting scheme that may be suitable for a particular scenario. The examples presented heretofore are only to

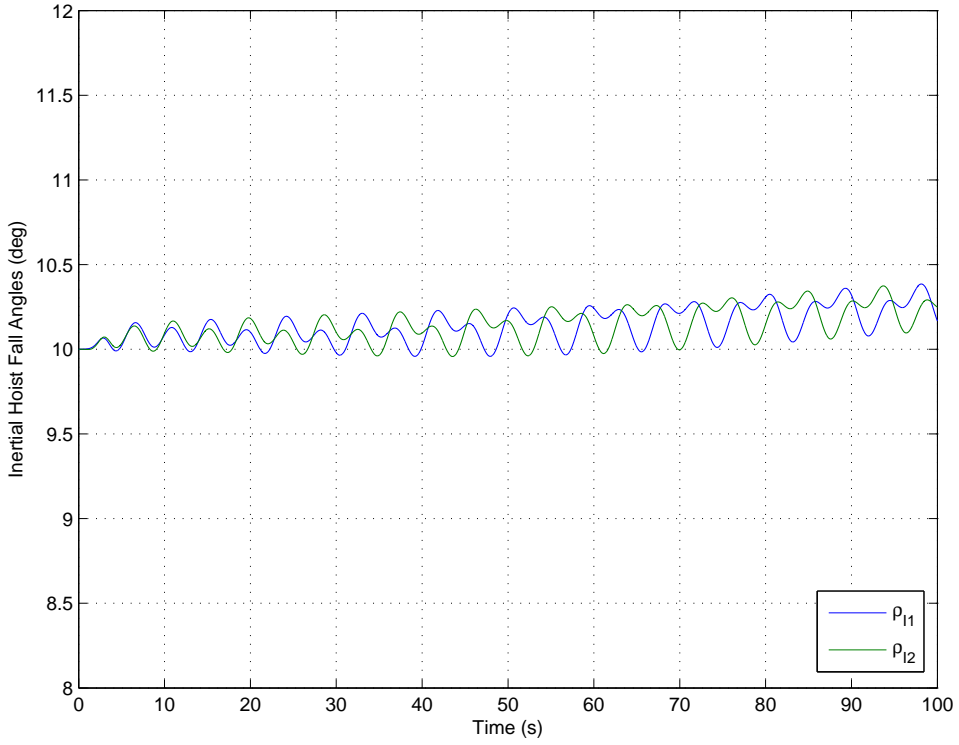


Figure 121. Plot of time histories for the inertial hoist-fall angle, ρ , for the inverse kinematic control case using weights that match the units of the actuators in the minimum norm solution. (Simulation parameters: $\rho = 10$ degrees, $\vec{P}_{8/1,z} = 5$ meters, and $x_s = 1$ meter at a period of 8.75 seconds.)

illustrate the potential for manipulating the form of the solution for the inverse kinematic controller. For several of these approaches, such as the actuator selectivity, the operational utility would be enhanced if there was a systematic way to adjust the weighting values 'on-the-fly' while maintaining performance and ensuring system stability. The importance of this was highlighted in the example that applied the dynamic torque and tension values in the weighting matrix. Offsetting the risk - the benefit to operation of a fielded system in terms of adapting to actuator performance limitations or failure would be significant.

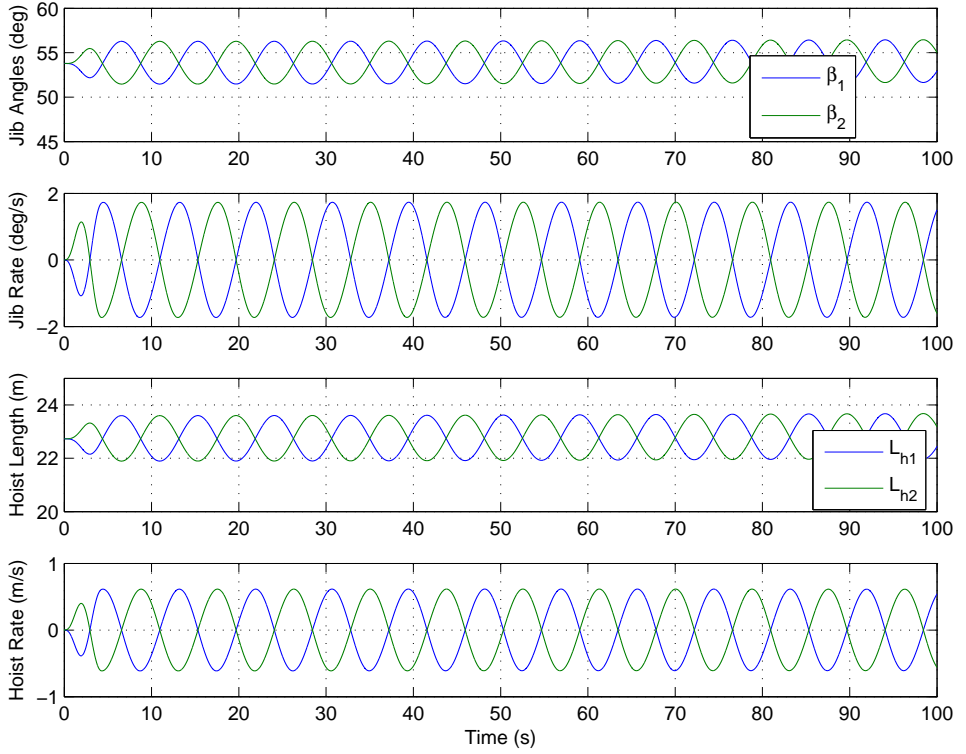


Figure 122. Plots of β , $\dot{\beta}$, L_h , and \dot{L}_h for the inverse kinematic control case using weights that match the units of the actuators in the minimum norm solution. (Simulation parameters: $\rho = 10$ degrees, $\vec{P}_{8/1,z} = 5$ meters, and $x_s = 1$ meter at a period of 8.75 seconds.)

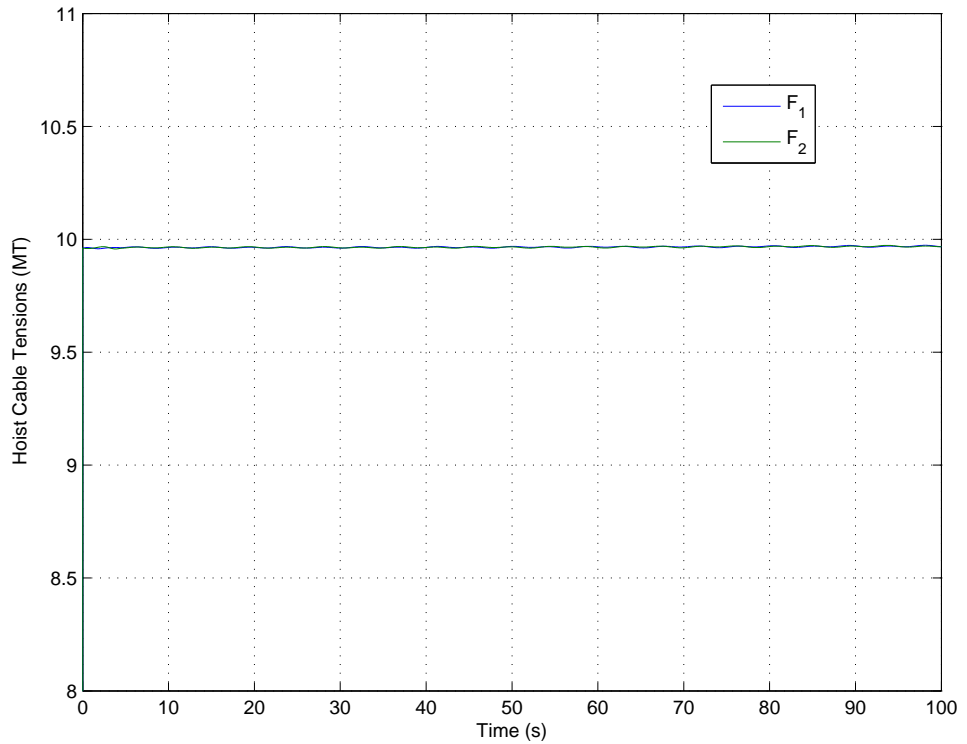


Figure 123. Plot of hoist cable tensions, F_1 and F_2 , for the inverse kinematic control case using weights that match the units of the actuators in the minimum norm solution. (Simulation parameters: $\rho = 10$ degrees, $\vec{P}_{8/1,z} = 5$ meters, and $\mathbf{x}_s = 1$ meter at a period of 8.75 seconds.)

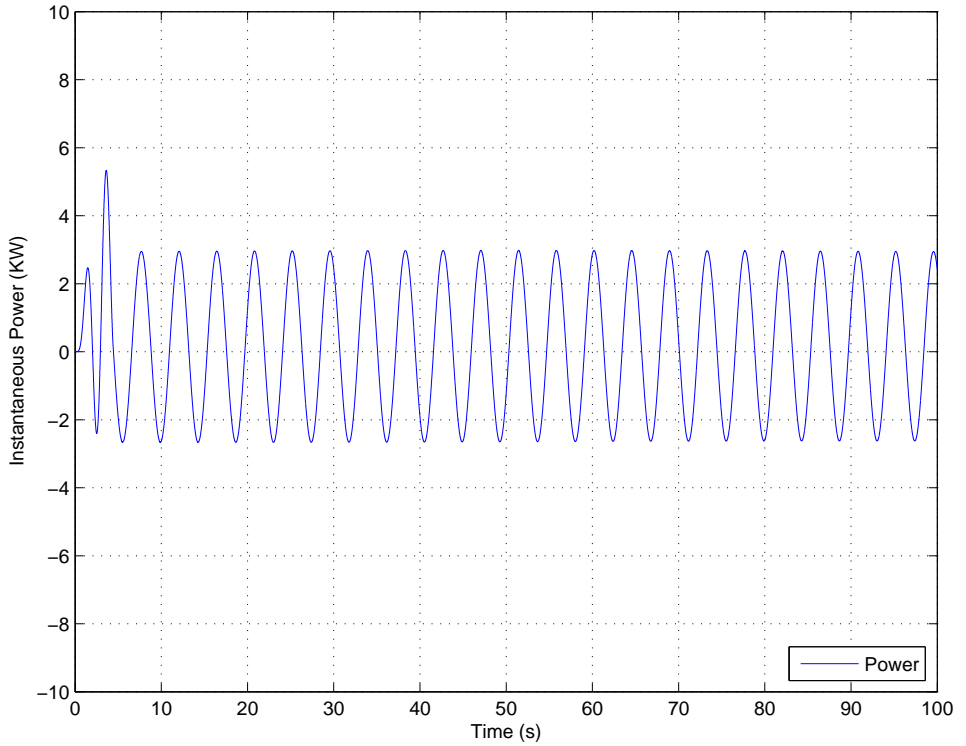


Figure 124. Plot of instantaneous power for the inverse kinematic control case using weights that match the units of the actuators in the minimum norm solution. (Simulation parameters: $\rho = 10$ degrees, $\vec{P}_{8/1,z} = 5$ meters, and $\mathbf{x}_s = 1$ meter at a period of 8.75 seconds.)

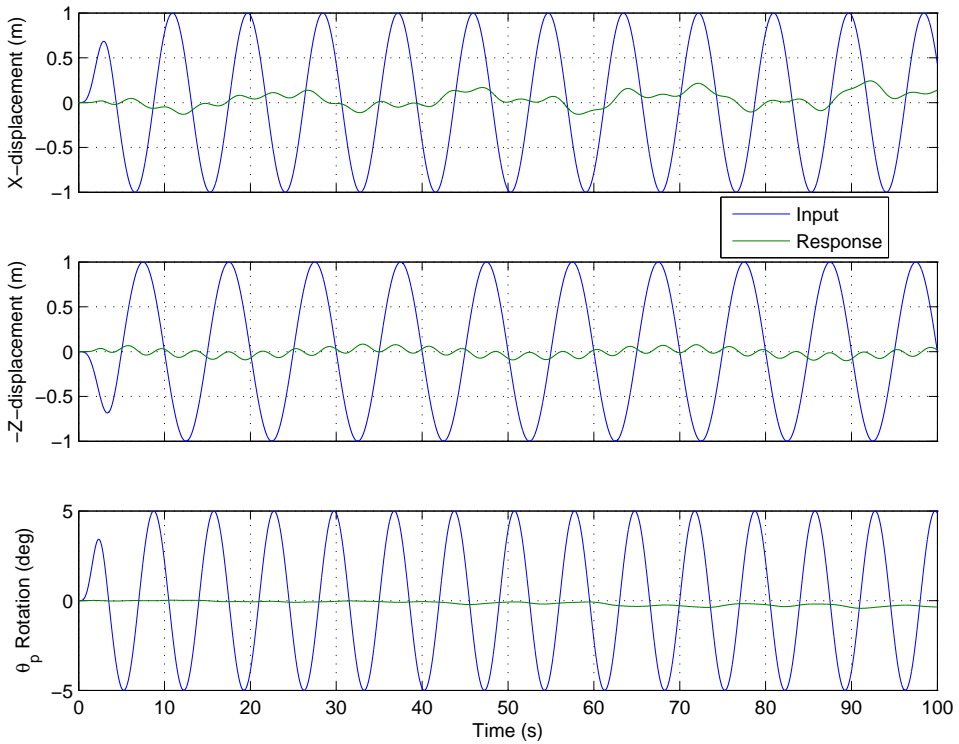


Figure 125. Plot of x , z , and θ time histories for the inverse kinematic control case using weights selected in accordance with the method of Franklin & Powell in the minimum norm solution. (Simulation parameters: $\rho = 10$ degrees, $\vec{P}_{8/1,z} = -5$ meters, with a combined sinusoidal forcing function of $\mathbf{x}_s = 1$ meter at a period of 8.75 seconds, $\mathbf{z}_s = 1$ meter at a period of 10 seconds, and $\theta_s = 5^\circ$ at a period of 7.0 seconds.)

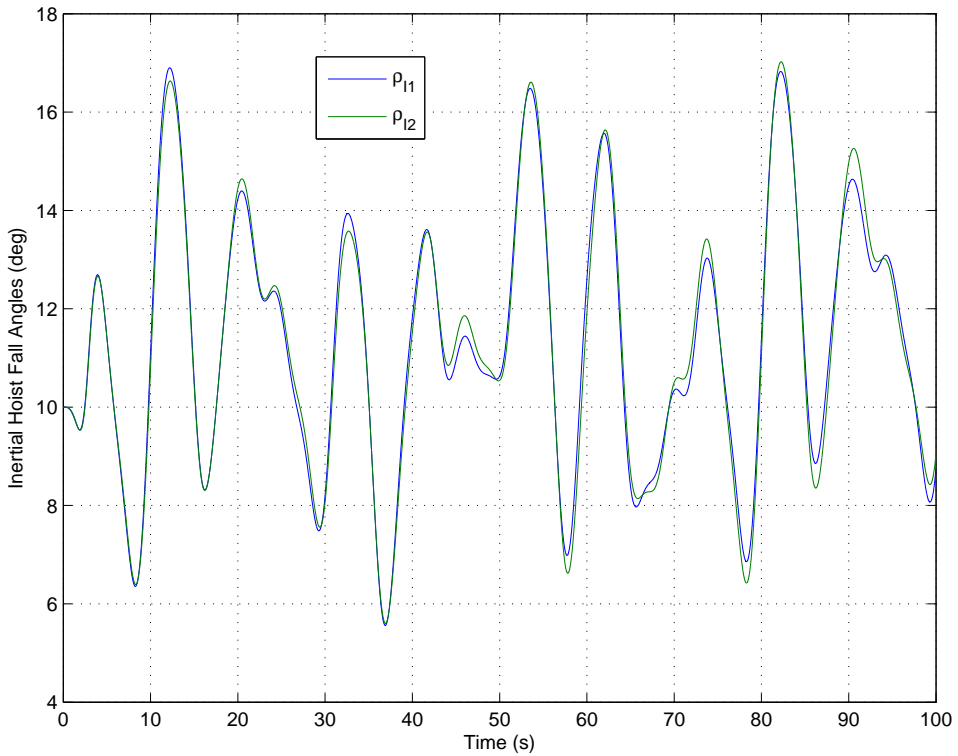


Figure 126. Plot of time histories for the inertial hoist-fall angle, ρ , for the inverse kinematic control case using weights selected in accordance with the method of Franklin & Powell in the minimum norm solution. (Simulation parameters: $\rho = 10$ degrees, $\vec{P}_{8/1,z} = -5$ meters, with a combined sinusoidal forcing function of $x_s = 1$ meter at a period of 8.75 seconds, $z_s = 1$ meter at a period of 10 seconds, and $\theta_s = 5^\circ$ at a period of 7.0 seconds.)

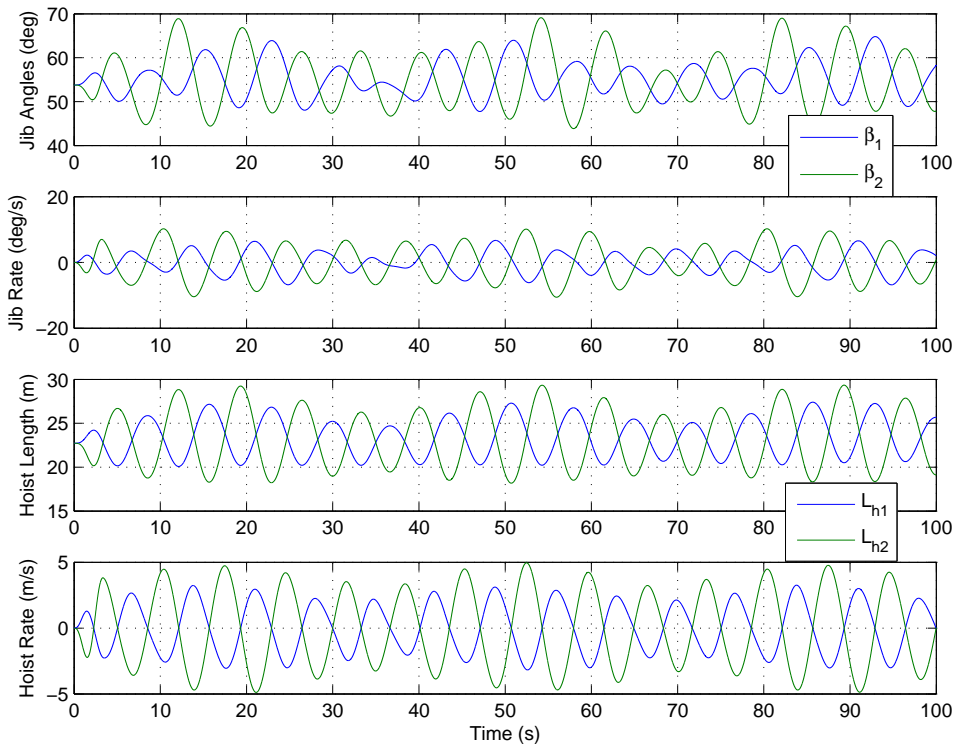


Figure 127. Plots of β , $\dot{\beta}$, L_h , and \dot{L}_h for the inverse kinematic control case using weights selected in accordance with the method of Franklin & Powell in the minimum norm solution. (Simulation parameters: $\rho = 10$ degrees, $\vec{P}_{8/1,z} = -5$ meters, with a combined sinusoidal forcing function of $x_s = 1$ meter at a period of 8.75 seconds, $z_s = 1$ meter at a period of 10 seconds, and $\theta_s = 5^\circ$ at a period of 7.0 seconds.)

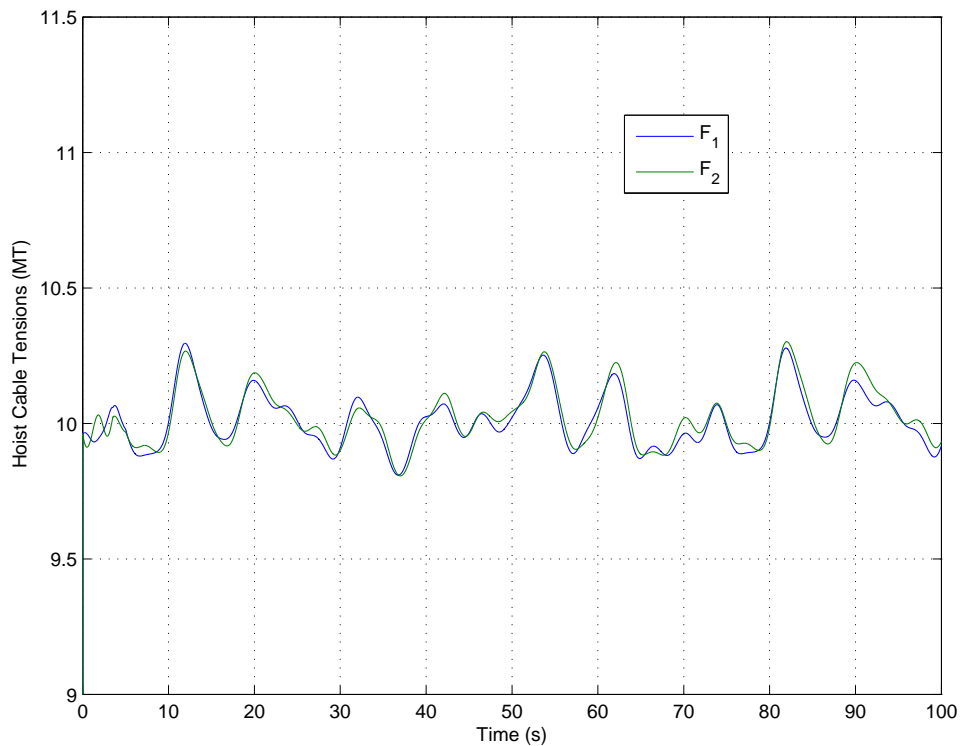


Figure 128. Plot of hoist cable tensions, F_1 and F_2 , for the inverse kinematic control case using weights selected in accordance with the method of Franklin & Powell in the minimum norm solution. (Simulation parameters: $\rho = 10$ degrees, $\vec{P}_{8/1,z} = -5$ meters, with a combined sinusoidal forcing function of $x_s = 1$ meter at a period of 8.75 seconds, $z_s = 1$ meter at a period of 10 seconds, and $\theta_s = 5^\circ$ at a period of 7.0 seconds.)

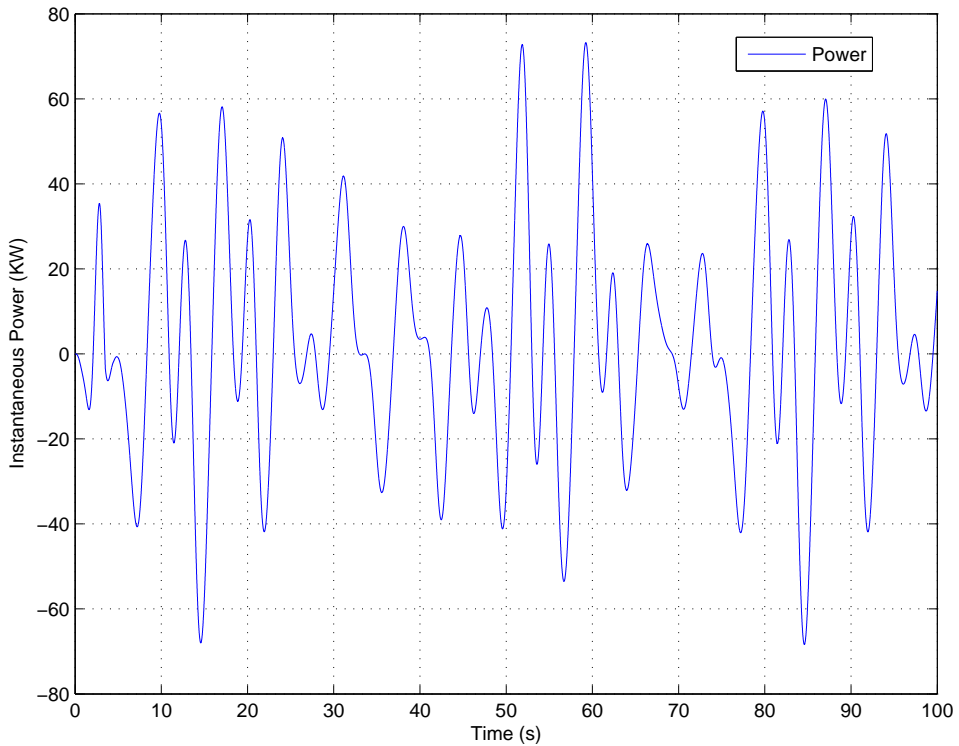


Figure 129. Plot of instantaneous power for the inverse kinematic control case using weights selected in accordance with the method of Franklin & Powell in the minimum norm solution. (Simulation parameters: $\rho = 10$ degrees, $\vec{P}_{8/1,z} = -5$ meters, with a combined sinusoidal forcing function of $x_s = 1$ meter at a period of 8.75 seconds, $z_s = 1$ meter at a period of 10 seconds, and $\theta_s = 5^\circ$ at a period of 7.0 seconds.)

THIS PAGE INTENTIONALLY LEFT BLANK

VI. SUMMARY OF SIMULATION RESULTS

The purpose of this chapter is to summarize the results of the simulation of the inverse-kinematic motion compensating controller for the planar dual-crane system. Earlier in Chapter , the J_{rate} and J_{power} metrics were introduced and some basic investigations were made into the response of the system to various inputs. In Chapter the power and torque relationships for the system were derived and an attempt made to establish a rationale for selecting the weighting matrix in the minimum norm solution. The results of both chapters are presented herein for purposes of comparison and identification of overall trends.

Table found at the end of this chapter lists the simulation cases that were generated to illustrate the performance of the inverse kinematic controller. The weighting schemes were previously defined and the modes of ship excitation are listed along with the amplitude and period of the sinusoidal forcing. For all of these cases the main instrument for defining performance will be the three metrics, $J_{L+\theta}$, J_{rate} , and J_{power} .

A. PERFORMANCE METRIC COMPARISON

The J_{rate} and J_{power} performance metrics for the simulation runs identified as 'Run03' through 'Run08A' are plotted in Figure 130 along with the simulation runs 'Run07J' through 'Run11J' that were discussed in Chapter and are represented by the square symbols.

Runs 03, 04, and 05 constitute a group based on the common power-based weighting scheme with different forcing functions. All three simulations also have the same payload starting position and initial hoist-fall angle offset, ρ . The power metric values fall between 2.0 KW and 3.25 KW and the rate metric has a range from 0.45 m/s for the heave input, to 1.05 m/s for the surge input, and 2.4 m/s for the pitch input, but the discriminating factor is $J_{L+\theta}$, which an order of magnitude lower for Run04 (0.0016 m) the heave case, compared to Run03 (0.0192 m, surge input) and

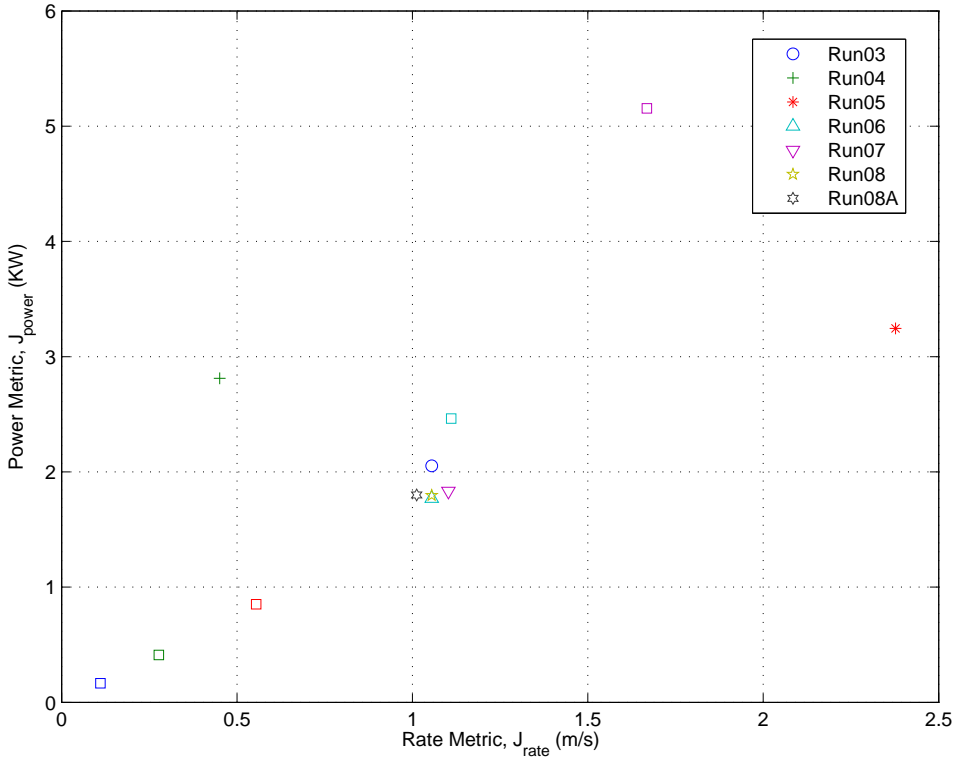


Figure 130. Cross-plot of the performance metrics J_{rate} and J_{power} for a range of conditions. Conditions are identified by run number in Table 4.

Run05 (0.0121 m, pitch input).

On the same figure, Runs 06 and 07 both used an inverse kinematic control solution obtained with $\mathbf{W} = \mathbf{I}$ and had the same surge forcing function. The difference is that for Run06, $\rho = 10^\circ$, and for Run07, $\rho = 0^\circ$. Again, the values of J_{rate} (1.06 m/s, 1.10 m/s respectively) and J_{power} (1.77 KW, 1.83 KW respectively) are very similar for the cases, and with the difference in $J_{L+\theta}$ being between 0.02 m and 0.03 m indicating that the non-zero ρ may have a positive effect on reducing the motion.

The last two data points presented on this plot are Runs 08 and 08A. They used the balanced coordinate weighting scheme and a hoist-fall offset angle of 10 degrees. The difference between Run 08 and Run 08A is the time constant in the model representing the actuator dynamics. The baseline time constant was set to

0.002 seconds, in part because derivatives of the actuator rates were required for the solution and this value produced smooth trajectories¹. As a quick look at the effect of the actuator dynamics, Run08A was executed with a actuator-model time constant of 0.05 seconds or 25 times slower. Interestingly, the values of J_{rate} (1.06 m/s, 1.01 m/s) and J_{power} (1.80 KW for both) did not show any significant effect; however, the value of $J_{L+\theta}$ for the slower actuator response was increased by a factor of 48, from 0.0191 m to 0.9379 m. So roughly twice the change in $J_{L+\theta}$ respective to the change in the time constant.

Figure 131 shows a 3-dimensional plot of the performance metrics (note that Run08A is omitted because of the large scale difference in $J_{L+\theta}$). Run04 has clearly the lowest $J_{L+\theta}$ for this group of runs.

The next figure (Figure 132) shows the results for run numbers 12 through 30. A short description of the similarities and differences between the data presented follows. A 3-dimensional presentation of the performance metrics is also provided to help distinguish between sets of results. This is shown in Figure 133.

We will examine clusters of runs where the trend in the results appear to give insight into the effect of the hoist-fall offset angle, ρ , the length of the hoist cables, and the type of ship motion input.

In the lower left corner of Figure 132 lies the group of runs 20,21, and 22. The hoist-fall angle was varied between -10, 0, and 10 degrees with an input in heave. As all the metric values are virtually the same it appears that the ρ angle does not have much influence on these conditions.

The next group of runs consists of Run 15 through 19, which are similar to the previous runs with a range of ρ angles (-10,-5,0,5,10 degrees), but with a surge input. Here we see that while the rate and power metrics are virtually the same, there is a

¹The integration time step used was 0.05 seconds with a 5th order Dormand-Prince integration method. Using the analysis developed by Howe [65], it was assessed that the error introduced in the dynamic response by this integration method was about 5% of the root value, so the effective time constant was ≈ 0.0021 seconds.

positive effect of the magnitude of the angle on the displacement metric. Thus, the results for both -10 deg. and 10 deg. show a lower displacement than 0 degrees. The $J_{L+\theta}$ for this group overall is higher than the heave group. The average value for the heave-group was 0.0016 m and 0.0239 m for the surge-group - more than an order of magnitude.

The next grouping of runs includes Run 12, 13, and 14. Here the input is surge motion, there are two different ρ angles (0, 10 deg.), and two different payload heights-above-deck (5 meters above, 10 meters below). Again, from Figure 133 we can determine that the longer hoist cable lengths for the payload below deck level have a positive effect on motion reduction for either of the ρ angle settings.

The runs for which pitch was the input (Runs 23, 24, and 25) show that negative ($\rho = -10^\circ$) angles have a lower rate and power metric and a slightly increased displacement metric compared to $\rho = 0^\circ$ or $\rho = 10^\circ$.

The remaining runs included on this plot have combinations of surge, heave, and pitch inputs (Runs 26, 27, 28, 29, and 30). As expected, most of these runs appear to have larger values of rate, power, and displacement. The interesting exception is Run 26 (combined surge and heave input), which has a relatively larger $J_{L+\theta}$, but has rate and power metrics equivalent to the single input (surge) runs.

The next figures summarize the results for Run 31 through 38, which with the exception of Run 31 are all combined (surge, heave, and pitch) motion inputs. Figure 134 and Figure 135 show the cross-plot and 3-dimensional plot of the performance metrics.

Again looking for groupings of results, we see that Runs 36, 37, and 38 show that the negative to zero to positive progression of ρ angle also yields an increasing progression in rate, power, and displacement metrics. I believe that the distinction here between negative and positive ρ angles is the result of the cross product between the jib and the hoist-fall unit vector in the jib torque calculation. Negative ρ angles mean that the hoist-falls are more parallel to the jib, while larger positive angles

will increase the result of this vector product resulting in higher torque and therefore higher J_{power} values.

Run 35 used the modified weighting matrix after the method of Franklin and Powell [64] in the minimum norm solution. The relative values of the metrics do not distinguish this run from any of the others that employed the Identity matrix as the weights.

Runs 31, 32, 33, and 34 all had manipulations of the solution weighting matrix that resulted in slowing or shutting-down one of the actuators. Run 31 (surge input only) has the luffing on the left jib shutdown, yet the value of $J_{L+\theta}$ is relatively low as are the rate and power values. Runs 32, 33, and 34 do have combined inputs that result in increases in all three metrics, but only the loss of the hoist in Run 33 causes a fivefold increase (from 0.04 m to 0.20 m) in the resulting displacement. Putting this in perspective, a value of $J_{L+\theta}$ of 0.20 m is equivalent to a surge motion of 0.3 m at a period of 8.75 seconds, which is well within the 1.0 m goal stated earlier for the motion compensation. The relationship between the surge input magnitude and the displacement metric values can be seen in Figure 136, which can be referred to as the "input calibration curve" for surge motion. This curve was generated by calculating the displacement metric for the input forcing signal - treating it as if the payload exactly followed the input motion. For completeness, the value of the metric for a heave input of 1.0 m at a period of 10.0 seconds is 0.6207 m, the value for 5° of pitch at 12.0 seconds is 0.0227 m, and the value for the combination of surge, heave, and pitch is 0.9412 m. So these values should be kept in mind when assessing the effectiveness of the motion compensation. This may also be a method to quantify the effectiveness of the motion-compensated controlled response the uncontrolled response. All the simulations for the uncontrolled system used a fairly small 0.1 m surge amplitude forcing function to avoid overly large magnitude oscillations that could induce numerical problems in the simulation. Of the controlled cases, Run 07J also had a 0.1 m surge input and the resulting displacement metric value was

0.0318 m. The comparable uncontrolled simulation ($\rho = 0$, 0.1 m at 8.75 s surge, $\vec{P}_{8/1,z} = -5$ m in Chapter VI) had a calculated $J_{L+\theta}$ metric value of 3.3036 m. As we saw from the input calibration curve, the change in the metric values are linear with the change in motion. This means that the motion compensation using the inverse kinematic controller was demonstrated in simulation to reduce the resulting motion by 99% relative to the uncontrolled system.

To summarize the results of the analysis conducted in this section -

The inverse kinematic control appears to be very effective in response to heave motion and with lower rate and power required than for surge or pitch motion.

With the payload below the level of the deck, the longer hoist cable lengths have a beneficial effect on the actuation rates required.

Negative hoist-fall offset angles (ρ) appear to reduce the power required relative to zero or positive angles as a result of the reduced jib torque when the hoist cables become more parallel to the jib.

The operationally desirable feature of actuator selectivity may not impose a large penalty in terms of rate, power, or motion compensation effectiveness for some scenarios.

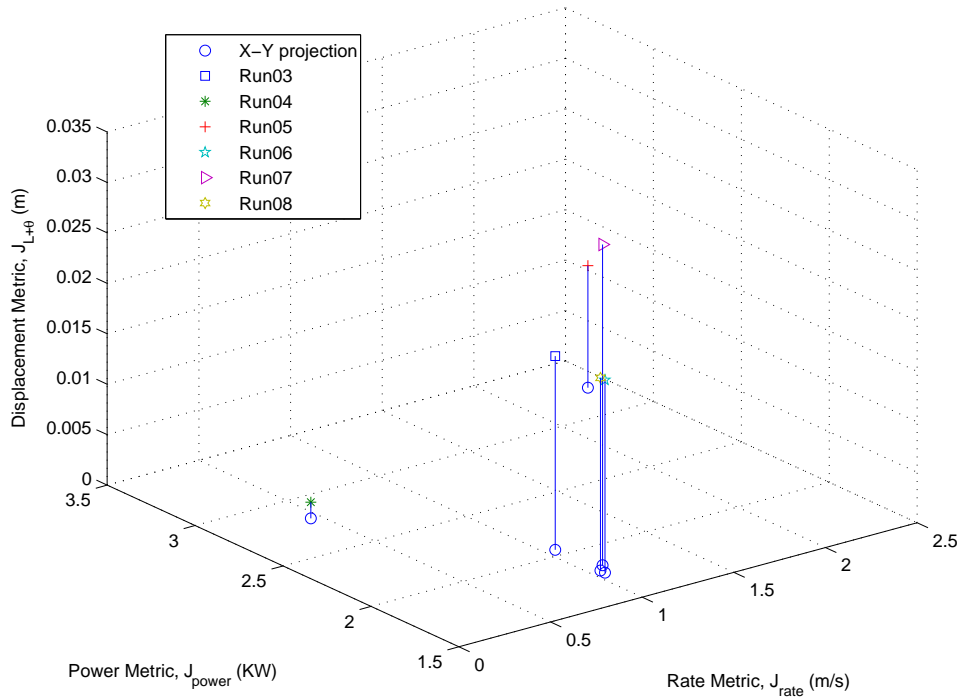


Figure 131. 3-Dimensional plot of the performance metrics J_{rate} , J_{power} , and $J_{L+\theta}$ for simulation runs 03 through 08. The relative value of $J_{L+\theta}$ can be discerned from the vertical line projected down to the J_{rate} - J_{power} plane. Simulation conditions are identified by run number in Table 4.

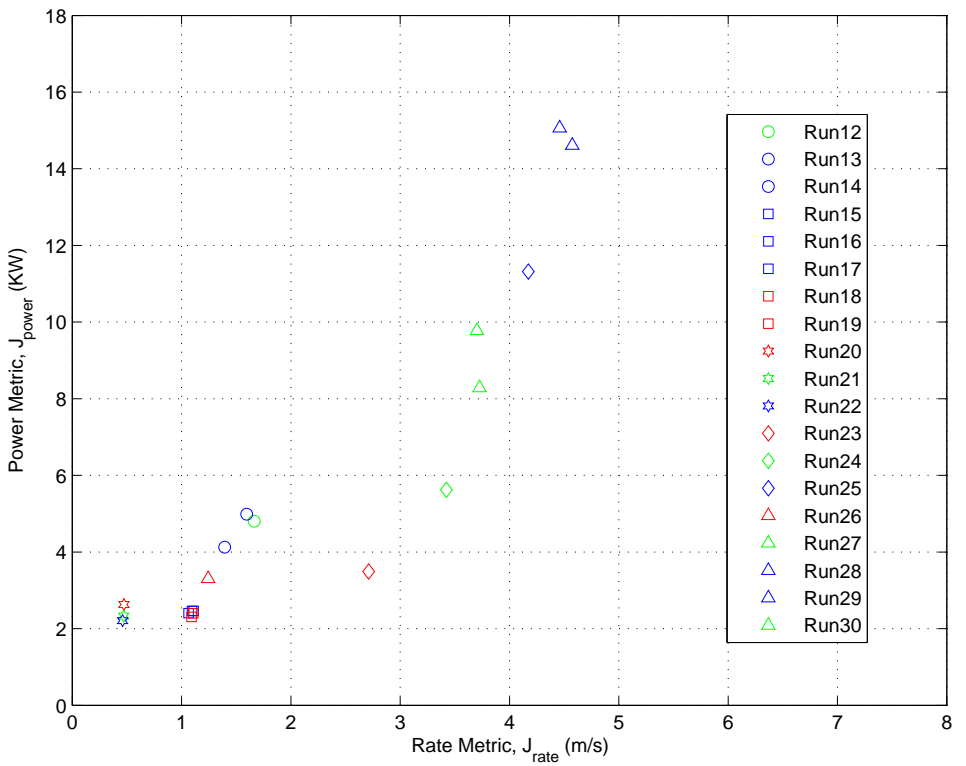


Figure 132. Cross-plot of the performance metrics J_{rate} and J_{power} for simulation runs 12J through 30J. Simulation conditions are identified by run number in Table 4.

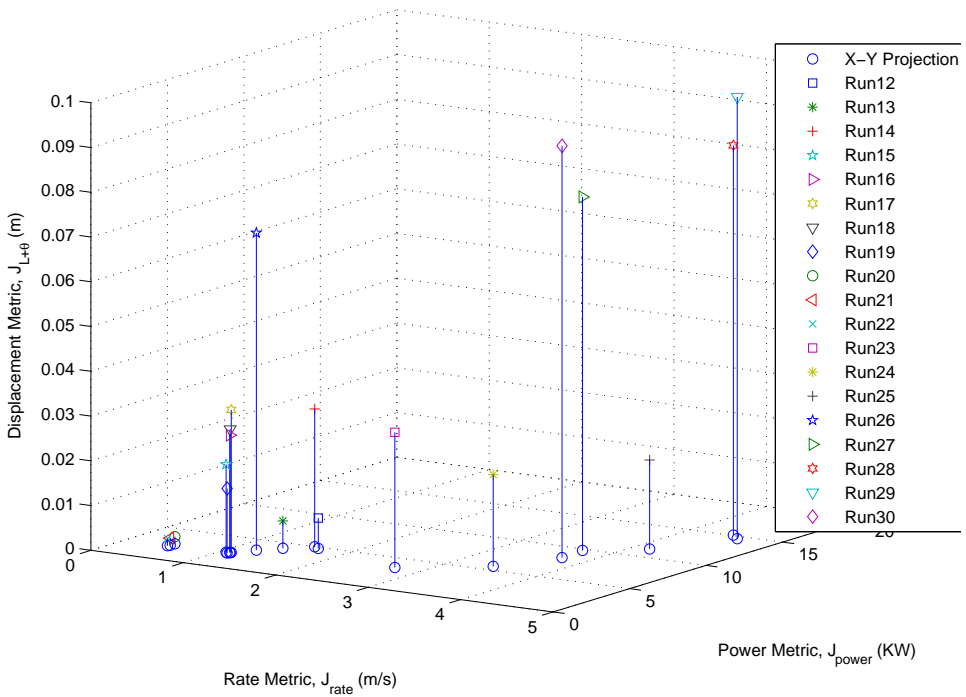


Figure 133. 3-Dimensional plot of the performance metrics J_{rate} , J_{power} , and $J_{L+\theta}$ for simulation runs 12J through 30J. The relative value of $J_{L+\theta}$ can be discerned from the vertical line projected down to the J_{rate} - J_{power} plane. Simulation conditions are identified by run number in Table 4.

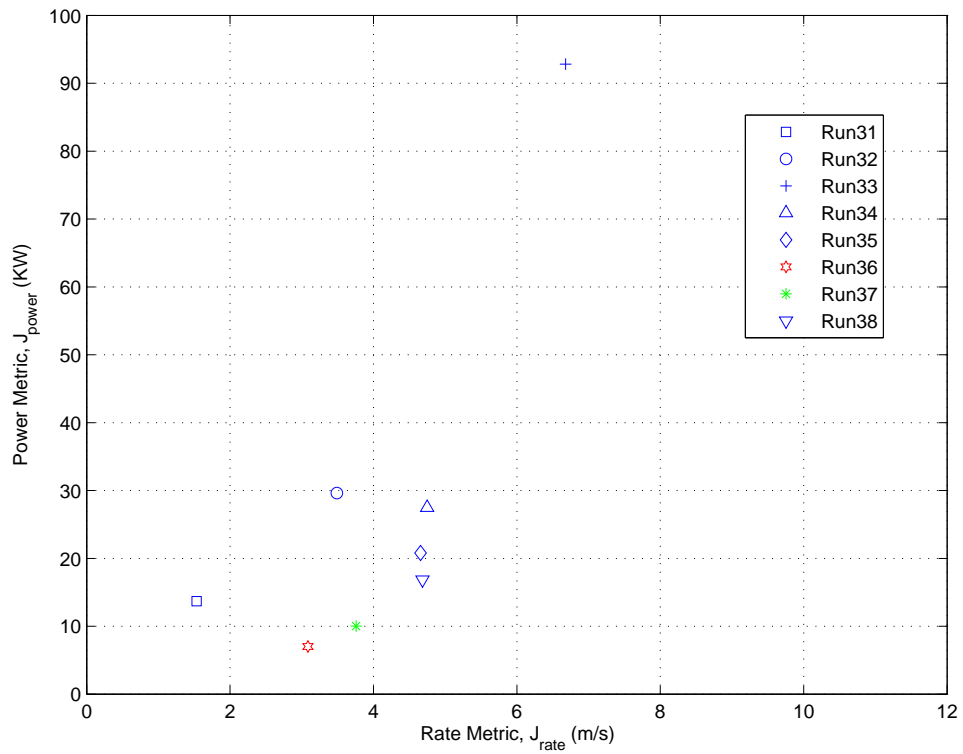


Figure 134. Cross-plot of the performance metrics J_{rate} and J_{power} for simulation runs 31 through 38. Simulation conditions are identified by run number in Table 4.

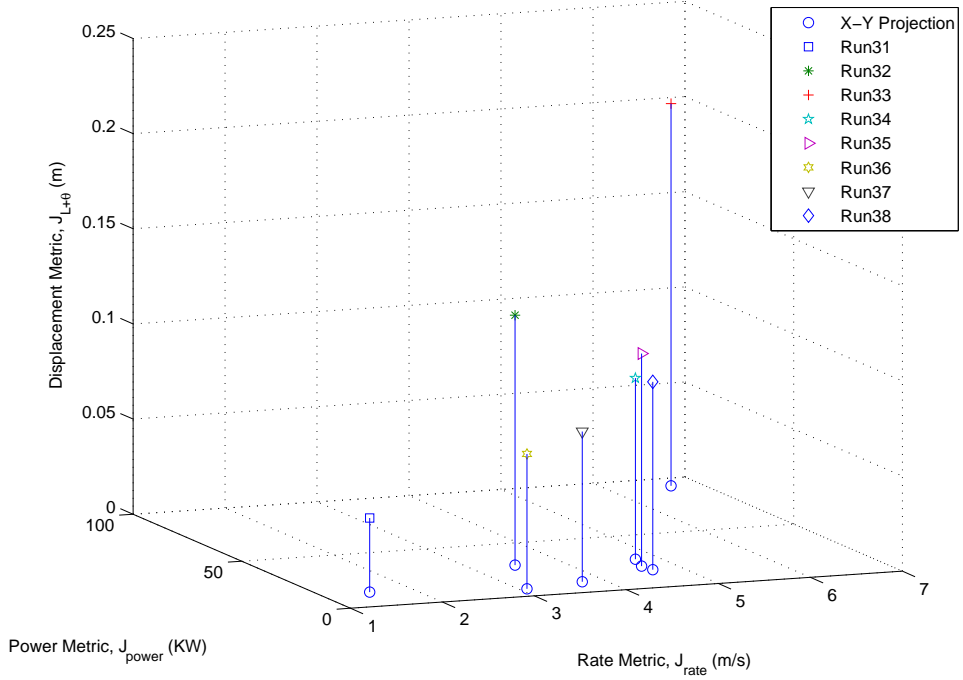


Figure 135. 3-Dimensional plot of the performance metrics J_{rate} , J_{power} , and $J_{L+\theta}$ for simulation runs 31 through 38. The relative value of $J_{L+\theta}$ can be discerned from the vertical line projected down to the J_{rate} - J_{power} plane. Simulation conditions are identified by run number in Table 4.

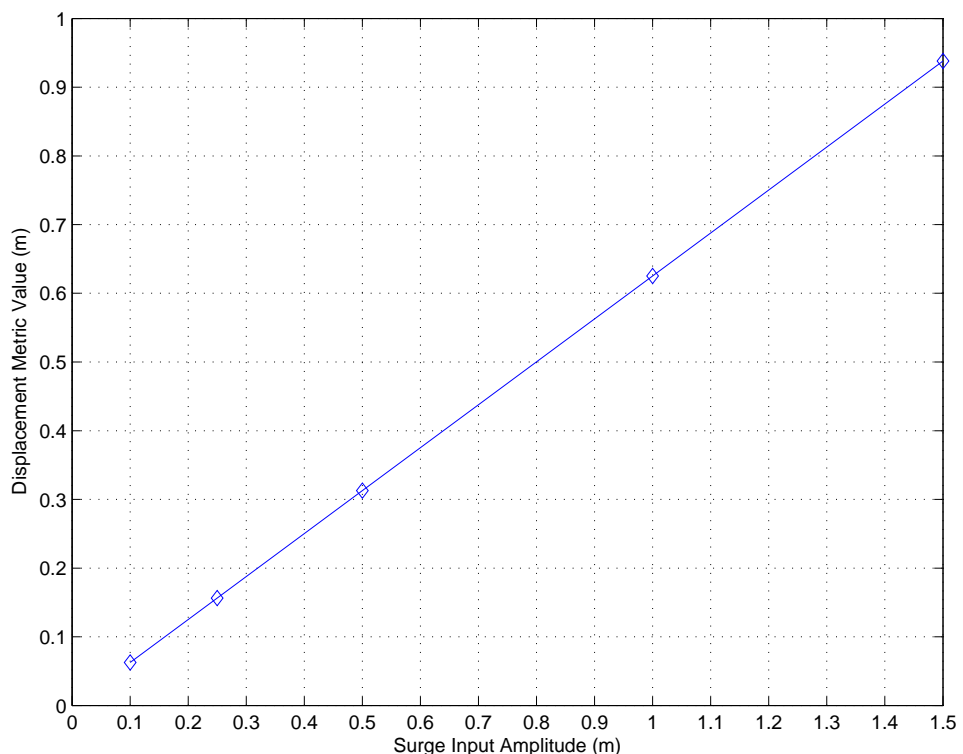


Figure 136. Calibration curve relating surge input amplitude for a 8.75 second period sinusoidal input to the calculated displacement metric values, $J_{L+\theta}$.

Identifier	\mathbf{W} Scheme	ρ_I Offset (deg)	$\vec{P}_{8/1,z}$ Deck(m)	Excitation (Amp,Period)	Cable Ten (max) (MT)
Run03	Power	10	5	Surge(1m,8.75s)	9.9715
Run04	Power	10	5	Heave(1m,10.0s)	10.031
Run05	Power	10	5	Pitch(5° ,12.0s)	9.9668
Run06	Identity	10	5	Surge(1m,8.75s)	9.9737
Run07	Identity	0	5	Surge(1m,8.75s)	9.8112
Run08	Coord. Balance	10	5	Surge(1m,8.75s)	9.9735
Run08A	Coord. Balance	10	5	Surge(1m,8.75s)	10.43
Run07J	Identity	0	5	Surge(0.1m,8.75s)	9.81
Run08J	Identity	0	5	Surge(0.25m,8.75s)	9.8101
Run09J	Identity	0	5	Surge(0.5m,8.75s)	9.8104
Run10J	Identity	0	5	Surge(1.0m,8.75s)	9.8116
Run11J	Identity	0	5	Surge(1.5m,8.75s)	9.8138
Run12J	Identity	0	-10	Surge(1.5m,8.75s)	9.8128
Run13J	Identity	10	-10	Surge(1.5m,8.75s)	9.9757
Run14J	Identity	10	5	Surge(1.5m,8.75s)	9.9962
Run15J	Identity	10	5	Surge(1m,8.75s)	9.9802
Run16J	Identity	5	5	Surge(1m,8.75s)	9.8593
Run17J	Identity	0	5	Surge(1m,8.75s)	9.8116
Run18J	Identity	-5	5	Surge(1m,8.75s)	9.8588
Run19J	Identity	-10	5	Surge(1m,8.75s)	9.9781
Run20J	Identity	-10	5	Heave(1m,10.0s)	9.9985
Run21J	Identity	0	5	Heave(1m,10.0s)	9.856
Run22J	Identity	10	5	Heave(1m,10.0s)	10.034
Run23J	Identity	-10	5	Pitch(5° ,7.0s)	10.033
Run24J	Identity	0	5	Pitch(5° ,7.0s)	9.8572
Run25J	Identity	10	5	Pitch(5° ,7.0s)	10.001
Run26J	Identity	-10	5	Combined(S,H)	10.014
Run27J	Identity	0	5	Combined(S,P)	9.8726
Run28J	Identity	10	5	Combined(S,H,P)	10.157
Run29J	Identity	20	-10	Combined(H,P)	10.583
Run30J	Identity	0	-10	Combined(S,H,P)	9.8924
Run31	Jib1-off	10	5	Surge(1m,8.75s)	10.046
					10.049
Run32	Jib1-off	10	5	Combined(S,H,P)	10.483
					10.487
Run33	Hoist2-off	10	5	Combined(S,H,P)	10.662
					10.641
Run34	Jib2-slo	10	5	Combined(S,H,P)	10.293
					10.282
Run35	FP	10	5	Combined(S,H,P)	10.302
Run36	Identity	-10	5	Combined(S,H,P)	10.053
Run37	Identity	0	5	Combined(S,H,P)	9.8926
Run38	Identity	20	5	Combined(S,H,P)	10.704

Table 4. Summary table of simulation results for the forced response of the planar dual-crane system.

Jib Torq max ($N \cdot M \times 10^5$)	Hoist Rate (max) (m/s)	Luff Rate max (deg/s)	Power (max) (KW)	J_{rate} (m/s)	J_{power} (KW) (m)	$J_{L+\theta}$
2.8959	0.6144	1.7311	5.6329	1.0551	2.052	0.0192
1.5364	0.3568	0.6126	4.6213	0.4509	2.8123	0.0016
1.8942	1.9320	3.3470	6.3666	2.3773	3.2447	0.0121
2.8502	0.6152	1.736	5.3049	1.0553	1.7697	0.0191
2.8056	0.7186	1.7191	5.3046	1.1025	1.8321	0.0318
2.8543	0.615	1.7354	5.3344	1.0553	1.7951	0.0191
2.822	0.6573	1.9013	4.8704	1.0122	1.7995	0.9379
1.3264	0.0808	0.1929	0.2751	0.1109	0.165	0.0032
1.5493	0.202	0.4822	0.7761	0.2773	0.4111	0.0079
1.9182	0.404	0.9645	1.9341	0.5548	0.8511	0.0159
2.6472	0.8082	1.9296	5.5466	1.1106	2.4631	0.0319
3.3658	1.2127	2.8961	10.902	1.6684	5.1543	0.0481
3.2886	1.2123	2.8995	10.257	1.6651	4.8017	0.0068
2.9982	0.8307	2.6662	8.9325	1.3938	4.1267	0.0061
3.3859	1.0571	2.9172	10.69	1.5966	4.9856	0.0308
2.6849	0.7046	1.9419	5.4743	1.0639	2.406	0.0196
2.6765	0.766	1.9555	5.5825	1.0963	2.4593	0.0262
2.6472	0.8082	1.9296	5.5466	1.1106	2.4631	0.0319
2.5982	0.8381	1.8902	5.3777	1.1078	2.3997	0.0276
2.5314	0.8495	1.8234	5.1765	1.0909	2.307	0.0144
1.5043	0.3472	0.6834	4.4318	0.4725	2.6308	0.0016
1.5465	0.3362	0.6974	3.9837	0.4719	2.3285	0.0016
1.5768	0.3247	0.6877	3.7861	0.4615	2.2094	0.0016
4.0459	2.5668	3.974	9.1535	2.711	3.4909	0.0302
2.9436	3.106	5.1799	18.865	3.423	5.621	0.0205
3.9231	3.6257	6.4734	36.66	4.1725	11.317	0.0199
2.6429	1.1946	2.5012	9.0305	1.2429	3.306	0.0709
3.5466	4.0103	7.3853	35.878	3.7013	9.7744	0.0790
4.24	4.5996	8.8878	53.81	4.459	15.061	0.0871
4.6067	4.0027	8.0896	49.469	4.5746	14.612	0.0987
3.436	4.0991	7.4766	31.816	3.7261	8.2852	0.0920
1.2811	0.1276	0.0022	25.601	1.5328	13.703	0.0389
3.3953	1.3607	3.4549				
3.042	1.2182	0.0082	98.093	3.4892	29.61	0.1313
4.5936	4.8177	10.5221				
11.725	8.1575	18.1554	300.07	6.6789	92.809	0.2009
7.328	0	3.8158				
5.3324	5.5521	11.2214	95.658	4.7478	27.486	0.0952
3.9379	2.8336	5.0522				
4.8591	4.9578	10.5699	7.3244	4.6566	20.784	0.1117
4.3839	3.7393	6.3655	29.313	3.0854	7.0242	0.0709
3.627	4.2092	7.6314	37.599	3.7576	10.015	0.0790
4.1588	4.1689	9.4508	50.542	4.6846	16.83	0.0987

Table 5. Continuation of Table 4, summary of simulation results for the forced response of the planar dual-crane system.

VII. PHYSICAL SCALE-MODEL RESULTS

To complement the analytical modeling and simulation results presented in the previous sections, a physical model of the dual-crane system was produced in 1/32-scale. The two crane models were mounted on a custom-designed hexapod motion platform with the capacity, range-of-motion, and velocity capability to accurately represent the appropriate ship motion environment. The details of the design of the crane models and the motion platform are found in Appendices E and F respectively. A photograph of the laboratory setup is shown in Figure 137.

For a better sense of scale, Figure 138 shows a dimensioned schematic of the same configuration.

The 1/32-scale factor was chosen based on the existence of drawings for a 1/16-scale crane of the same design. Because the dual-crane configuration would not fit within the available laboratory space at 1/16-scale, all the dimensions on the drawings were divided in half to produce a 1/32-scale design. The hexapod motion platform was designed and fabricated specifically to support the dual-crane apparatus and produce the motions representative of a ship at the appropriate scale.

A high-speed, 3D Digital Motion Analysis System (DMAS6, Spica Technology Corporation, Figure 139) was used to capture the payload motion data in the laboratory. The motion capturing system supports 3D real-time (up to 20 Hz) automatic tracking with autolabeling to subpixel accuracy, including simultaneous recording of synchronized video, and offers users a choice of either static or dynamic calibration.

DMAS6 supports capture and tracking with any number of progressive scan cameras. In this experiment, three high-speed video cameras, Imperx IPX-VGA210-L (Figure 140), are used to provide three channels of 12-bit digital image data. The camera provides 640 x 480 resolution and delivers 210 frames per second at full resolution. The camera image processing is based on a 1 million gate FPGA and 32



Figure 137. Photograph of the 1/32-scale dual-crane configuration mounted on the motion platform. Note the reference target on the payload for use with the motion capture system.

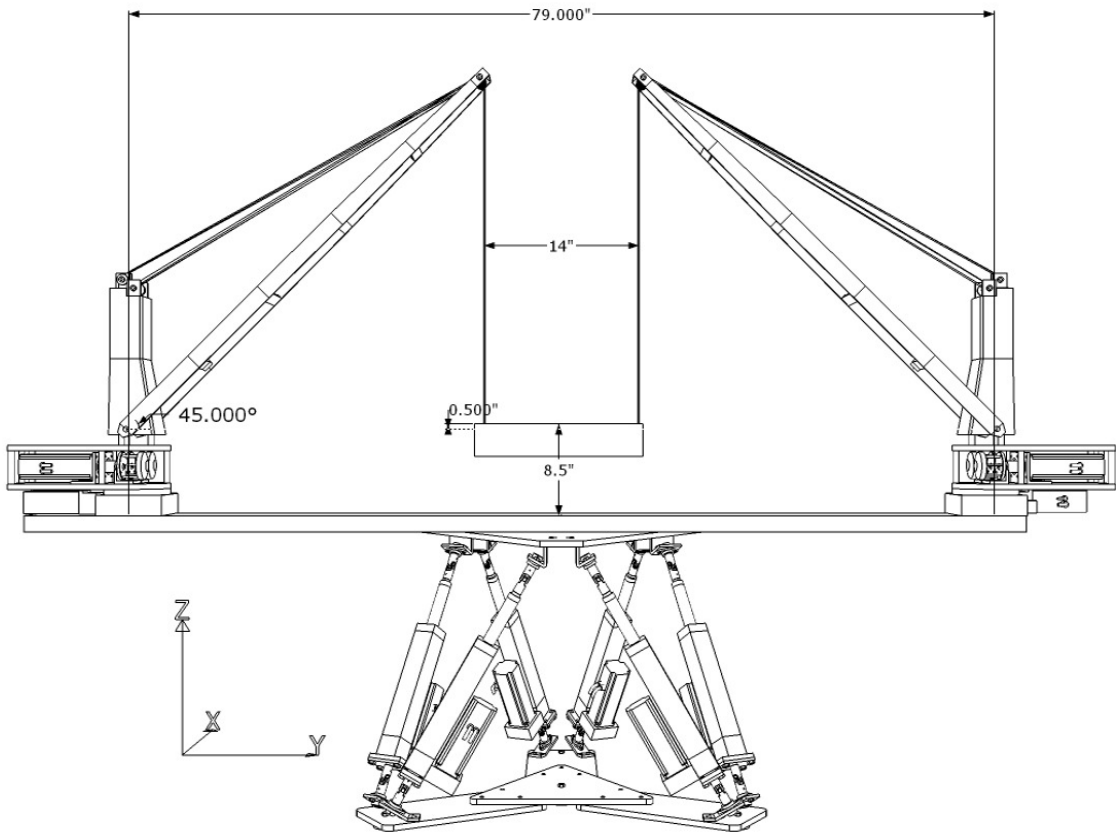


Figure 138. Photograph of the 1/32-scale dual-crane configuration mounted on the motion platform. Note the reference target on the payload for use with the motion capture system.

bit RISC processor.

The system provides an accuracy of less than 0.5 mm for a calibration volume of 3000 x 3000 x 3000 (mm) space and less than 0.05 degree orientation angles of yaw, pitch, and roll. The real time latency between three cameras and DMAS6 is less than 5 ms. The computer used in the DMAS6 is a dual CPU Intel XEON 2.8 GHZ with a Tyan S2676 motherboard (Figure 141).

A global reference frame is fixed to the floor to as the absolute position reference established during calibration of the system. A three-marker reference is attached to the payload on the surface facing the three cameras. While not used here, the system is capable of tracking multiple independent targets, which could have been used to verify jib positions and platform motion relative to the commanded values.

Using the DMAS-6 system both digital time history data and video of the payload motion were obtained for both uncontrolled and controlled (inverse kinematics) response to the applied platform motion.

There were five distinct scenarios executed with the scale-model apparatus and replicated in the MATLAB simulation. The descriptions of the scenarios and the results based on the displacement metric, $J_{L+\theta}$, computed from the captured motion data are compared to computed values from the simulation as shown in Table . Because only payload motion data were captured, it was not possible to compute J_{rate} or J_{power} for the scale model. The simulations were setup using the dimensions of the scale crane and payload and the same input function was used for both the simulation and to drive the motion platform. The amplitudes of the input forcing were scaled by $\frac{1}{32}$ and the period was scaled by $\frac{1}{\sqrt{32}}$ in accordance with the geometric scaling conventions. The displacements in the output of the simulation were converted to mm to be consistent with the captured data and thus the units of $J_{L+\theta}$ are in mm.

Time histories of payload motion (surge, heave, and pitch) for each scenario were over-plotted and presented in the following figures. The out-of-plane motion (sway) is also plotted, although there is no simulation data for comparison.

DMAS6

MOTION CAPTURE SUITE



SPICA Technology Corporation's 3D Digital Motion Analysis System – DMAS6™, supports 3D Real Time and Automatic tracking with autolabeling to subpixel accuracy, including simultaneous recording of synchronized video, and offers users a choice of either static or dynamic calibration.

DMAS6™ supports capture and tracking with any number of CameraLink, LVDS EIA-644 and all Firewire IEEE-1394a(b) DCAM progressive scan cameras.

DMAS6™ is also capable of importing video from external file formats such as AVI, MPEG and of any size without restrictions. Simultaneous capture and synchronization of audio, analog and digital data, GPS, IRIG-B, Forceplatforms, EMG etc. are also supported.



DMAS6 FastTraq™ 3D tracking application.



DMAS6™ dynamic calibration procedure

Fiber Optics DMAS6™ is now available with fiber optics cables to maximize distance between cameras and imaging stations.

Copyright ©2005 Spica Technology Corporation. Trademarks are the property of their owners.

No Proprietary Hardware DMAS6™ uses only standard commercial off the shelf (COTS) hardware including cameras, framegrabbers and processing hardware.

Digital Technology The DMAS6™ system is designed around the very latest in digital imaging technologies to fully take advantage of the recent advances in cameras, processing and networking. We are therefore able to offer digital image processing previously not available in the motion capture industry and can bring more advanced tracking algorithms with subpixel marker centroid calculations and autolabeling.



<http://www.spicatek.com>
spicatek@spicatek.com
3400 Kehala Dr., Kihei
HI 96753. Phone (808) 879.0343

Figure 139. Digital Motion Analysis System-6 (DMAS6) brochure.

CAMERAS | FRAME GRABBERS | ADAPTERS | UAV | LAW ENFORCEMENT | ACCESSORIES
[HOME](#) | [CORPORATE](#) | [NEWS](#) | [DISTRIBUTORS](#) | [SUPPORT](#) | [CONTACT US](#) | [MEMBERS](#)

Programmable CCD Area Scan - IPX-VGA210-L

LYNX IPX-VGA210-G, IPX-VGA210-GC

Features

- 640 x 480 @ 210 fps
- Mono or Color, 8/10/12-bit data
- Gig E (Gigabit Ethernet), Single or Dual Tap
- 32-bit Risc Processor
- Horizontal and Vertical binning
- Programmable Resolution and Frame Rate
- Programmable External Trigger
- Dynamic Transfer Function Correction
- Dynamic S/N Correction
- Temperature Monitor
- Field upgradable software, firmware, LUT
- 802.3, Ethernet v2.0, IP, ICMP, UDP, and PING support
- Automatic Iris Control - optional

LYNX IPX-VGA210-L, IPX-VGA210-LC

Features

- 640 x 480 @ 210 fps
- Mono or Color, 8/10/12-bit data
- Base Camera Link, Single or Dual Tap
- RS232 Serial Communication
- 32-bit Risc Processor
- Horizontal and Vertical binning
- Programmable Resolution and Frame Rate
- Programmable External Trigger
- Dynamic Transfer Function Correction
- Dynamic S/N Correction
- Temperature Monitor
- Field upgradable software, firmware, LUT
- Automatic Iris Control - optional

Description

The IPX-VGA210-L is an advanced, high-resolution progressive scan, fully programmable and field upgradable CCD camera, build around KODAK's KAI-0340 interline transfer CCD. The camera provides 640 x 480 resolution and delivers 210 frames per second at full resolution. The camera image processing engine is based on a 1 million gate FPGA and 32 bit RISC processor, featuring programmable resolution, AOI, binning, triggering, shutter, long integration, transfer function correction and temperature monitor.

Downloads

- Lynx IPX-VGA210-L Spec
- Lynx IPX-VGA210-L Manual*
- Lynx IPX-VGA210-G Spec
- Lynx IPX-VGA210-G Manual
- Downloads*

* Members only may download







Imperx Incorporated • 6421 Congress Avenue • Boca Raton, FL 33487 • USA
 Phone: (561) 989-0006 • 1-866-849-1662 • Fax: (561) 989-0045
www.imperx.com • sales@imperx.com

http://www.imperx.com/cameras/high_speed_digital/vga_210fps/index.html

9/19/2008

Figure 140. Motion capture system - camera brochure.



Spica Technology Corporation
3400 Kehala, Kihei, Maui
HI, 96773 USA
1-808-879-0343 www.spicatek.com

Specifications
DMAS6 Motion Capture Suite with Qty 2 Pulnix TM6740 200Hz

Real Time Latency	5 [ms]
Accuracy	<0.5 mm for 3000 x 3000 x 3000 [mm] X,Y,Z <0.05 degree Yaw Pitch Roll
Max Targets	Unlimited
DMAS6 SDK	Customer definable GUI and C++ Plugin facility
Inputs	2 or more Pulnix TM6740 digital cameras (or similar) Camera Link data transmission interfaces, resolution of 640x480 pixels at 200 frames per second.
Cable length	10 [m] Optional Fiber optics to 500[m]
Tracking Volume	Variable, no theoretical limits
Optics	C-Mount 12.5 [mm] standard Linearized or per customer specification
Calibration	Static or Dynamic
Real Time Output	<ul style="list-style-type: none">• 3D Display Schematics• Ethernet TCP and/or UDP *• RS232C *
	Note: Possible to have a user defined data transmission protocol.
External Triggers	<ul style="list-style-type: none">• TTL Signal• Network TCP/UDP*• RS232C*
	Note: Possible to have a user defined data transmission protocol.
Targets	<ul style="list-style-type: none">• Passive Retroreflective• Active LEDs 470 - 850 [nm]• 6DOF Trajectories• Uncompressed or compressed Video
Recording	
Computer	Tyan S2676 Motherboard, dual CPU Intel XEON 2.8 GHz 1MB , Dual Channel SCSI-320, Gigabit Ethernet, 2GB DDR-2, 4U rackmount chassis
Warranty	Software - 3 Years Hardware - 3 Years Cameras - Original manufacturer's warranty
Delivery	Approx 4 weeks ARO

Figure 141. Digital Motion Analysis System-6 (DMAS6) Specification sheet.

Figures 142, 143, 144, and 145 show the results for the uncontrolled pure surge-input case. For each figure, the input time history is included as a reference along with the simulation and model data.

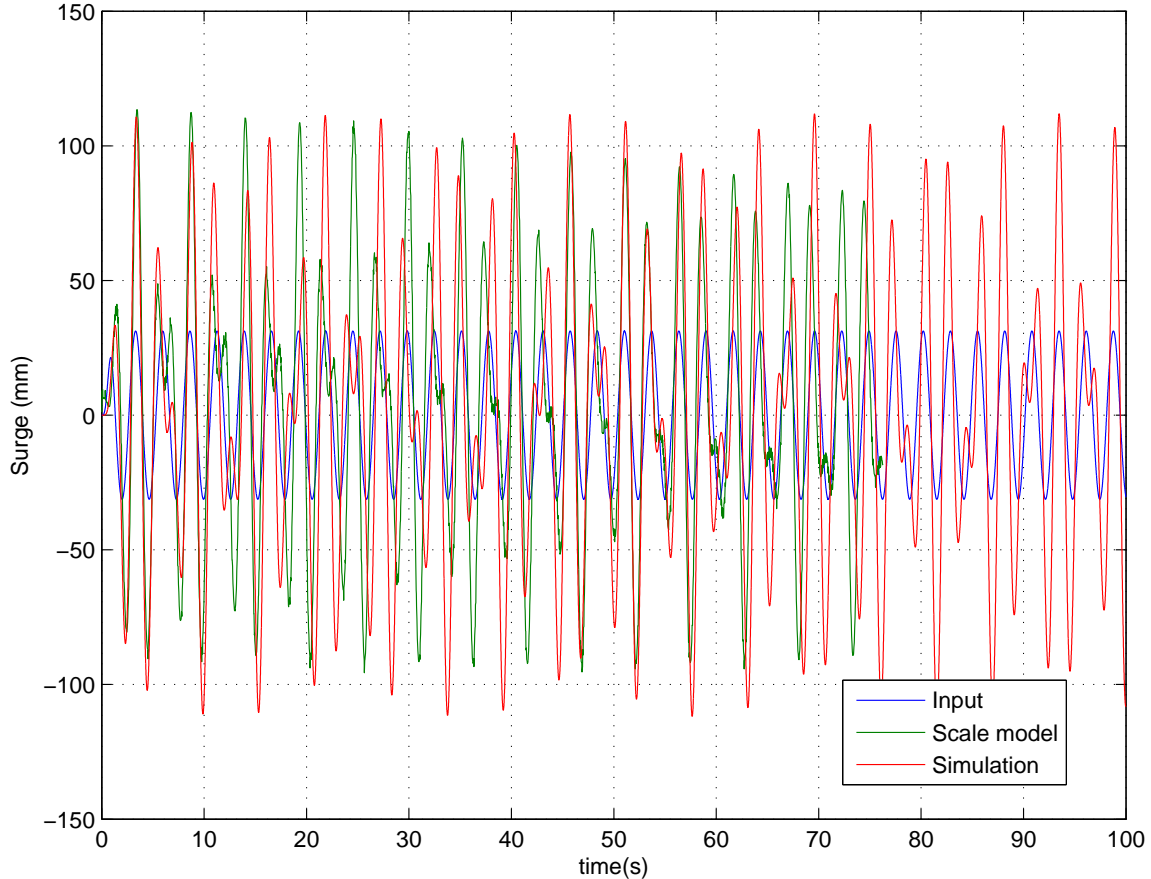


Figure 142. Surge time histories for simulated, scale-model, and input data for the uncontrolled case. (Simulation parameters: $\rho = 0$ degrees, $\vec{P}_{8/1,z} = 12.7$ mm, with a sinusoidal forcing function of $x_s = 31.25$ mm at a period of 2.65 seconds.)

Figures 146, 147, 148, and 149 show the results for the controlled pure surge-input case.

Figures 150, 151, 152, and 153 show the results for the uncontrolled pure surge-input case with the hoist-fall offset angle, $\rho = 10^\circ$.

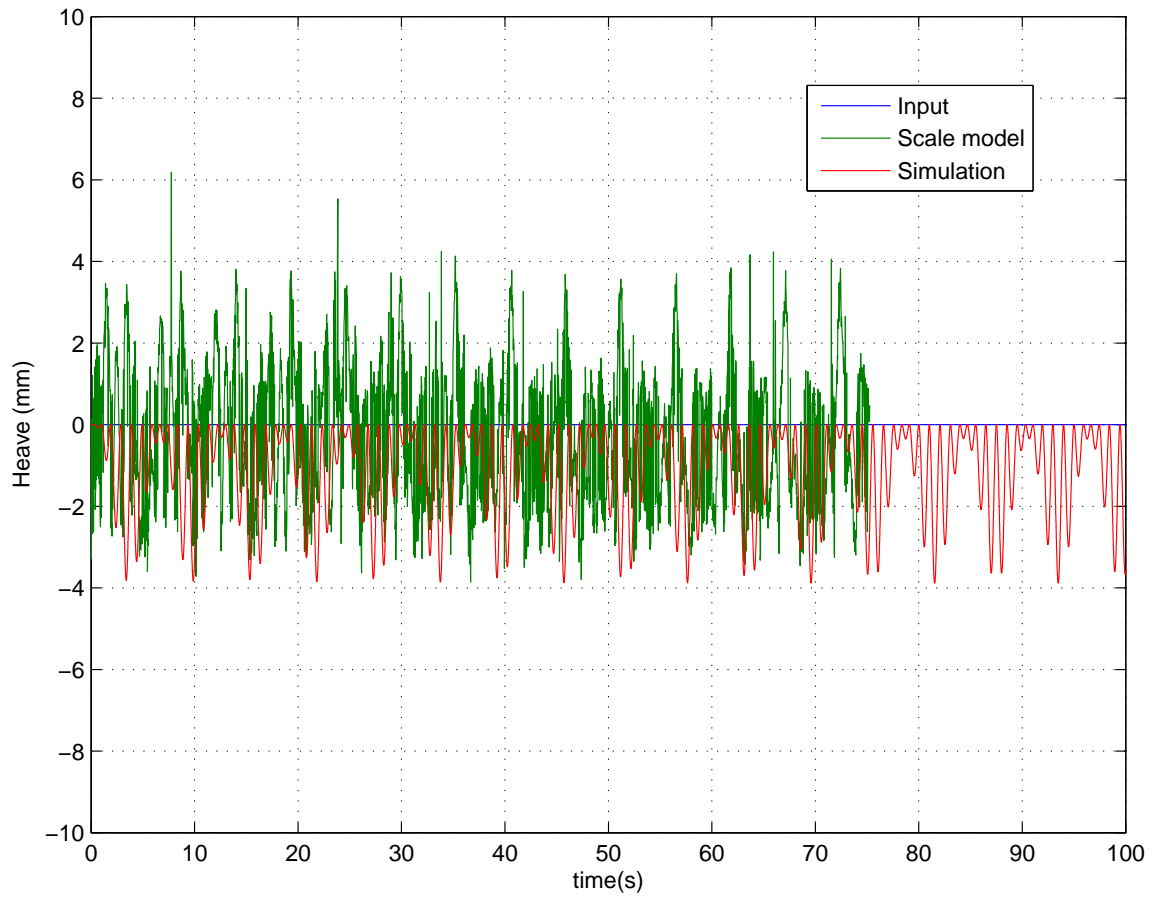


Figure 143. Heave time histories for simulated, scale-model, and input data for the uncontrolled case. (Simulation parameters: $\rho = 0$ degrees, $\vec{P}_{8/1,z} = 12.7$ mm, with a sinusoidal forcing function of $x_s = 31.25$ mm at a period of 2.65 seconds.)

Figures 154, 155, 156, and 157 show the results for the controlled pure surge-input case with the hoist-fall offset angle, $\rho = 10^\circ$.

Figures 158, 159, 160, and 161 show the results for the uncontrolled pure heave-input case. Because the payload is restrained in heave by the two hoist cables it is expected that the uncontrolled motion for both the simulation and the model should follow closely to the input signal. The slight differences in the model response (3-5 mm) from the simulation shown in Figure 159 do not appear to be measurement noise and may be attributable to either cable stretch or compliance in the model

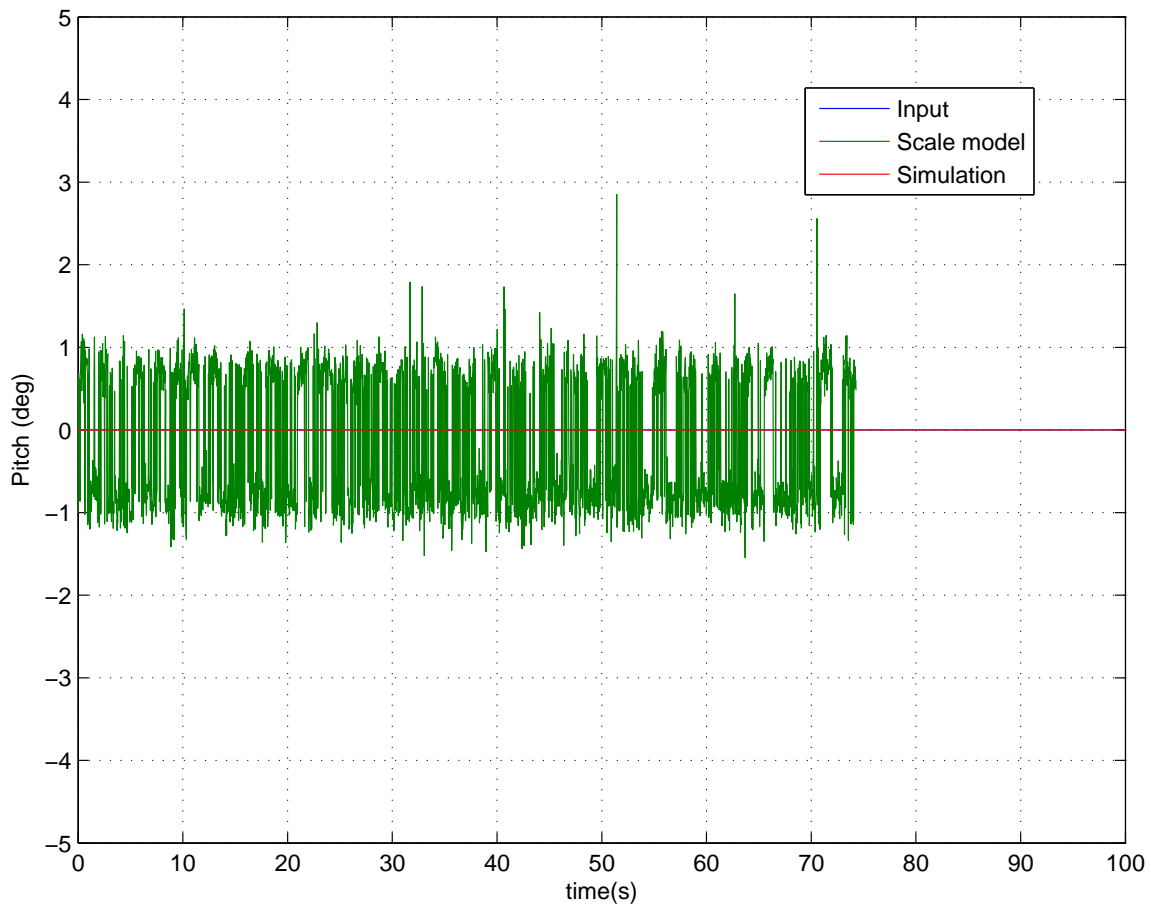


Figure 144. Pitch angle time histories for simulated, scale-model, and input data for the uncontrolled case. (Simulation parameters: $\rho = 0$ degrees, $\vec{P}_{8/1,z} = 12.7$ mm, with a sinusoidal forcing function of $x_s = 31.25$ mm at a period of 2.65 seconds.)

crane structure.

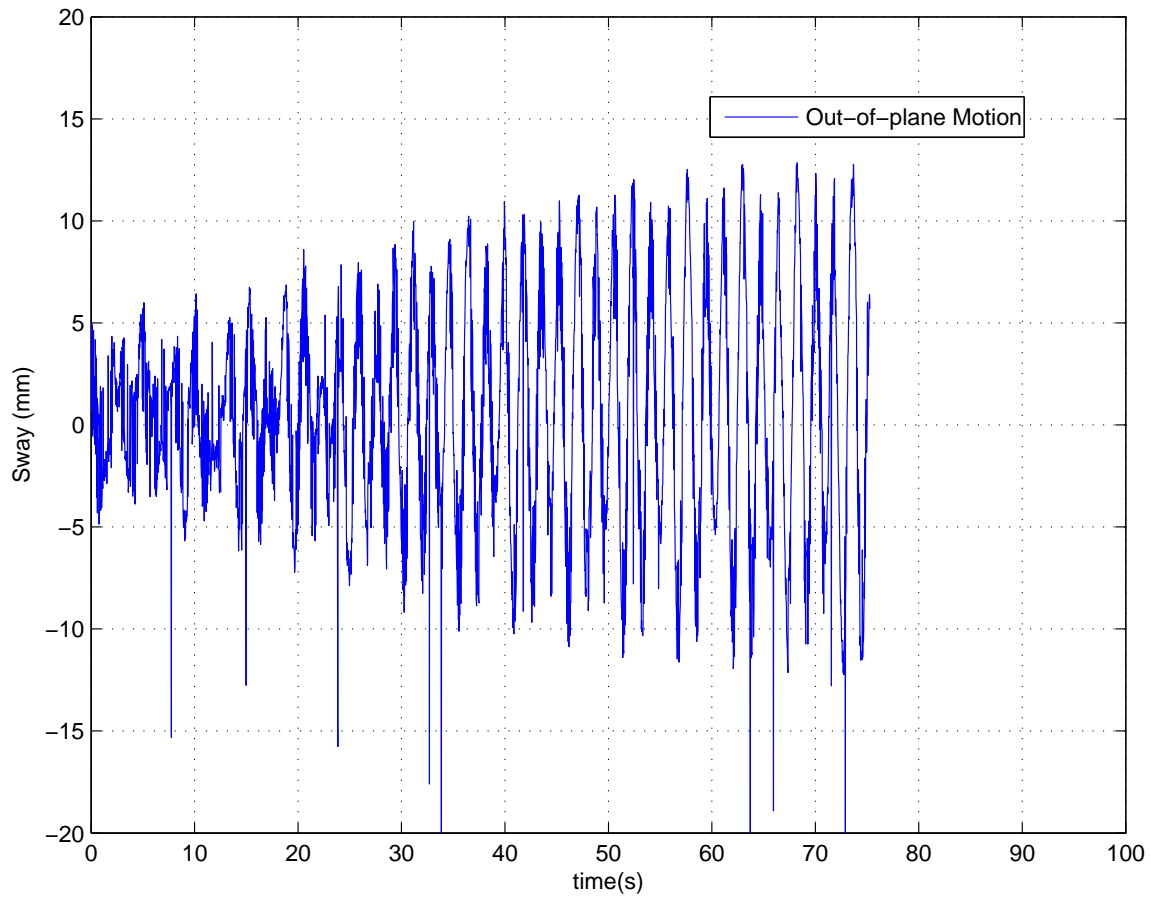


Figure 145. Out-of-plane (sway) time histories for simulated, scale-model, and input data for the uncontrolled case. The magnitude of the out-of-plane motion is about 10% of the primary forced response in surge. (Simulation parameters: $\rho = 0$ degrees, $\vec{P}_{8/1,z} = 12.7$ mm, with a sinusoidal forcing function of $x_s = 31.25$ mm at a period of 2.65 seconds.)

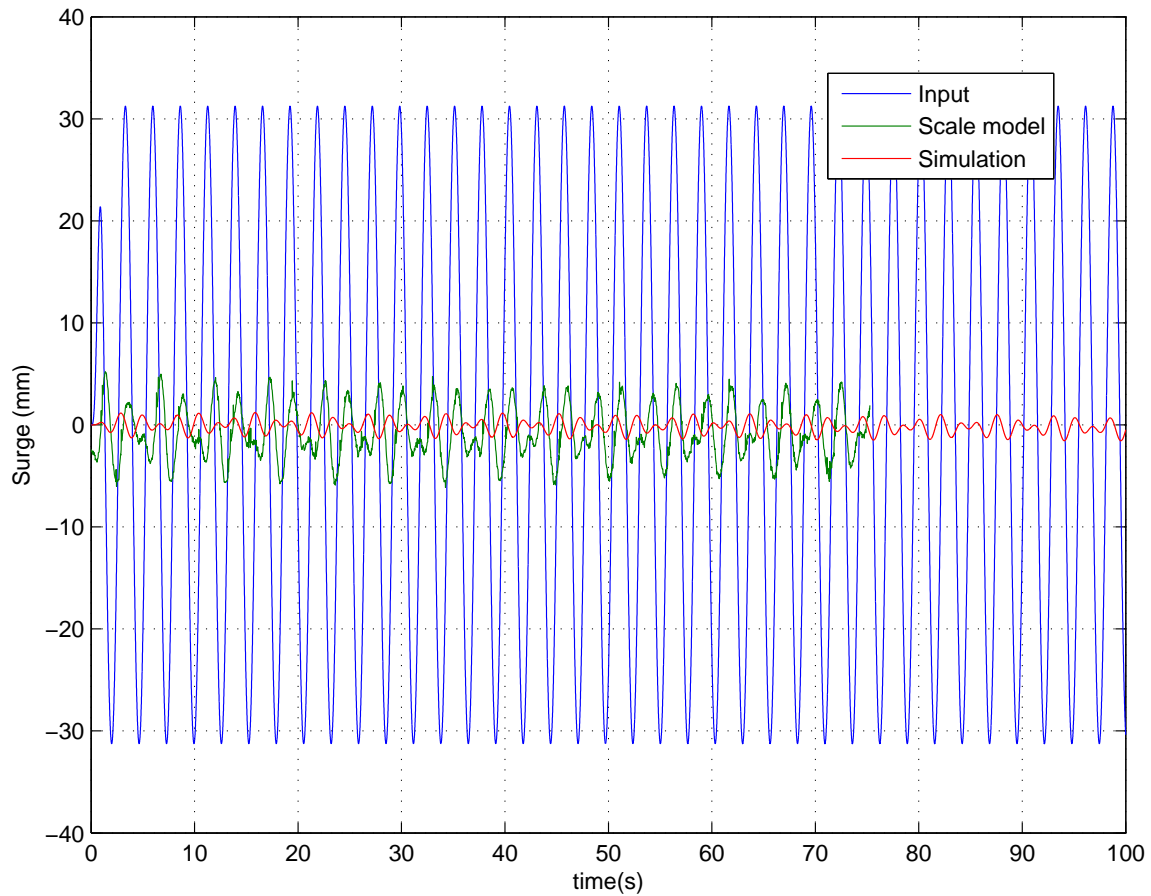


Figure 146. Surge time histories for simulated, scale-model, and input data for the controlled case. (Simulation parameters: $\rho = 0$ degrees, $\vec{P}_{8/1,z} = 12.7$ mm, with a sinusoidal forcing function of $x_s = 31.25$ mm at a period of 2.65 seconds.)

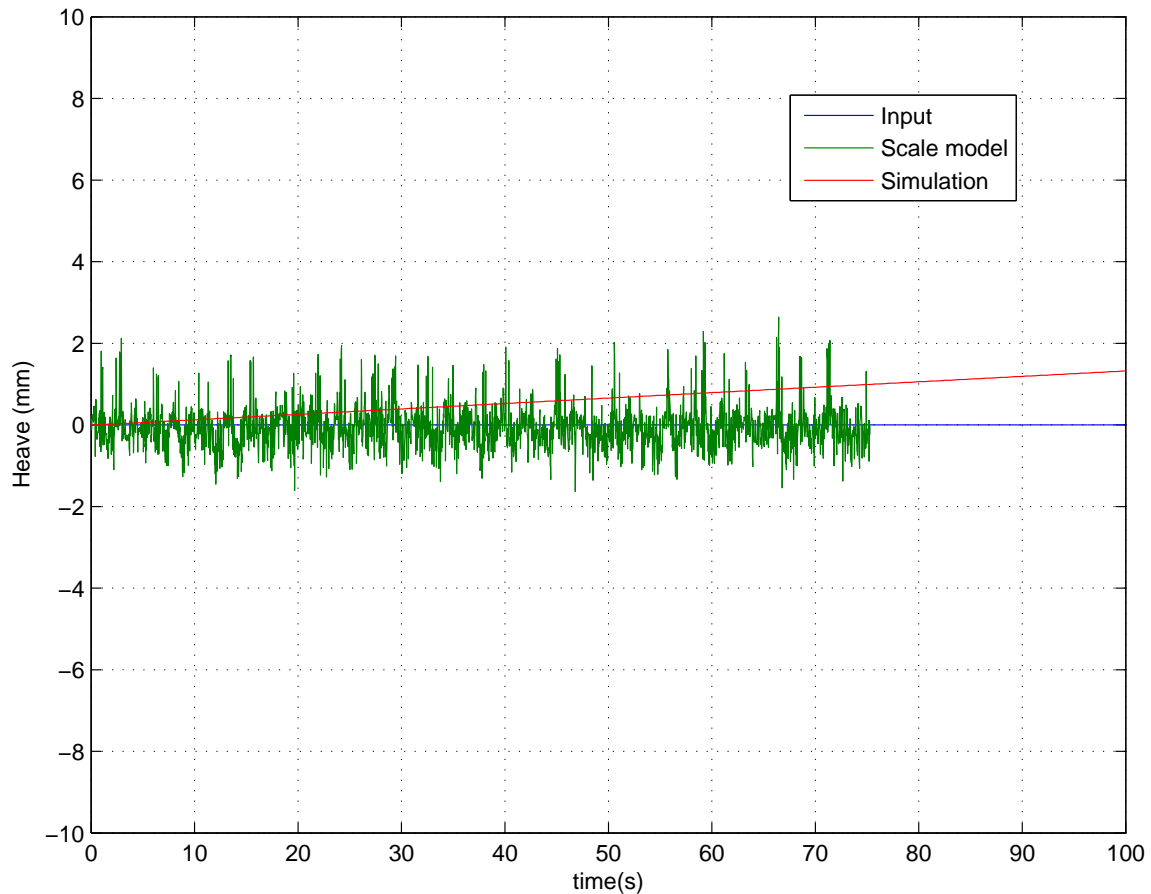


Figure 147. Heave time histories for simulated, scale-model, and input data for the controlled case. (Simulation parameters: $\rho = 0$ degrees, $\vec{P}_{8/1,z} = 12.7$ mm, with a sinusoidal forcing function of $x_s = 31.25$ mm at a period of 2.65 seconds.)

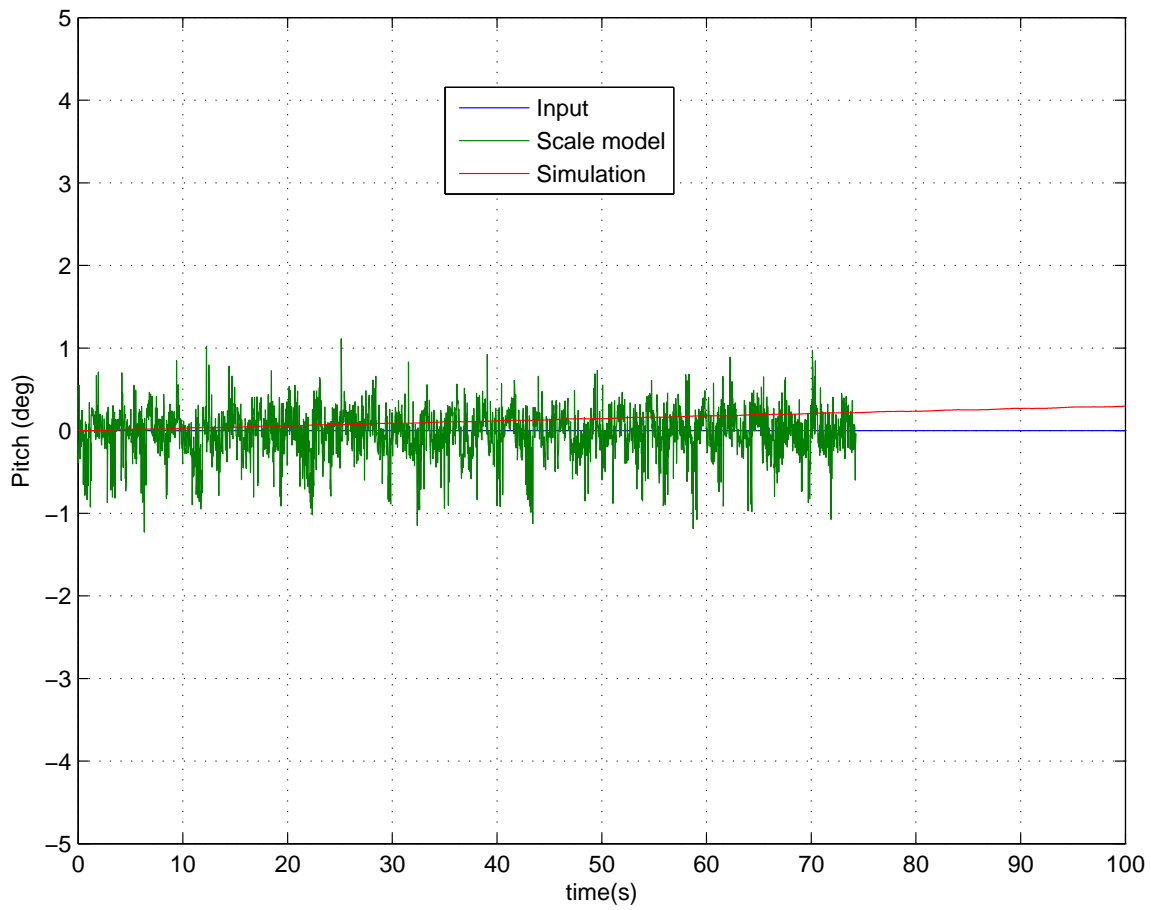


Figure 148. Pitch angle time histories for simulated, scale-model, and input data for the controlled case. (Simulation parameters: $\rho = 0$ degrees, $\bar{P}_{8/1,z} = 12.7$ mm, with a sinusoidal forcing function of $x_s = 31.25$ mm at a period of 2.65 seconds.)

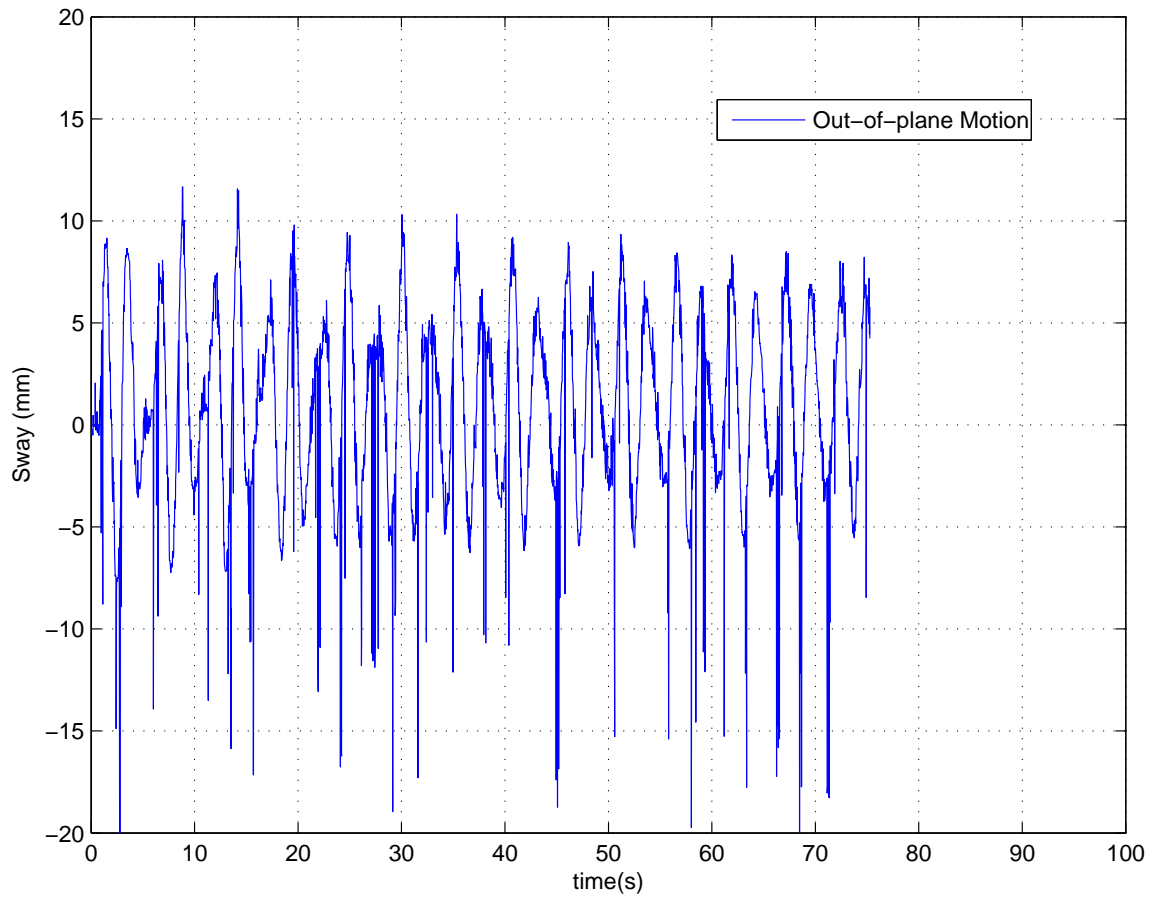


Figure 149. Out-of-plane (sway) time histories for simulated, scale-model, and input data for the controlled case. The magnitude of the peaks of the out-of-plane motion is about 20% of the primary forced response in surge. (Simulation parameters: $\rho = 0$ degrees, $\vec{P}_{8/1,z} = 12.7$ mm, with a sinusoidal forcing function of $x_s = 31.25$ mm at a period of 2.65 seconds.)

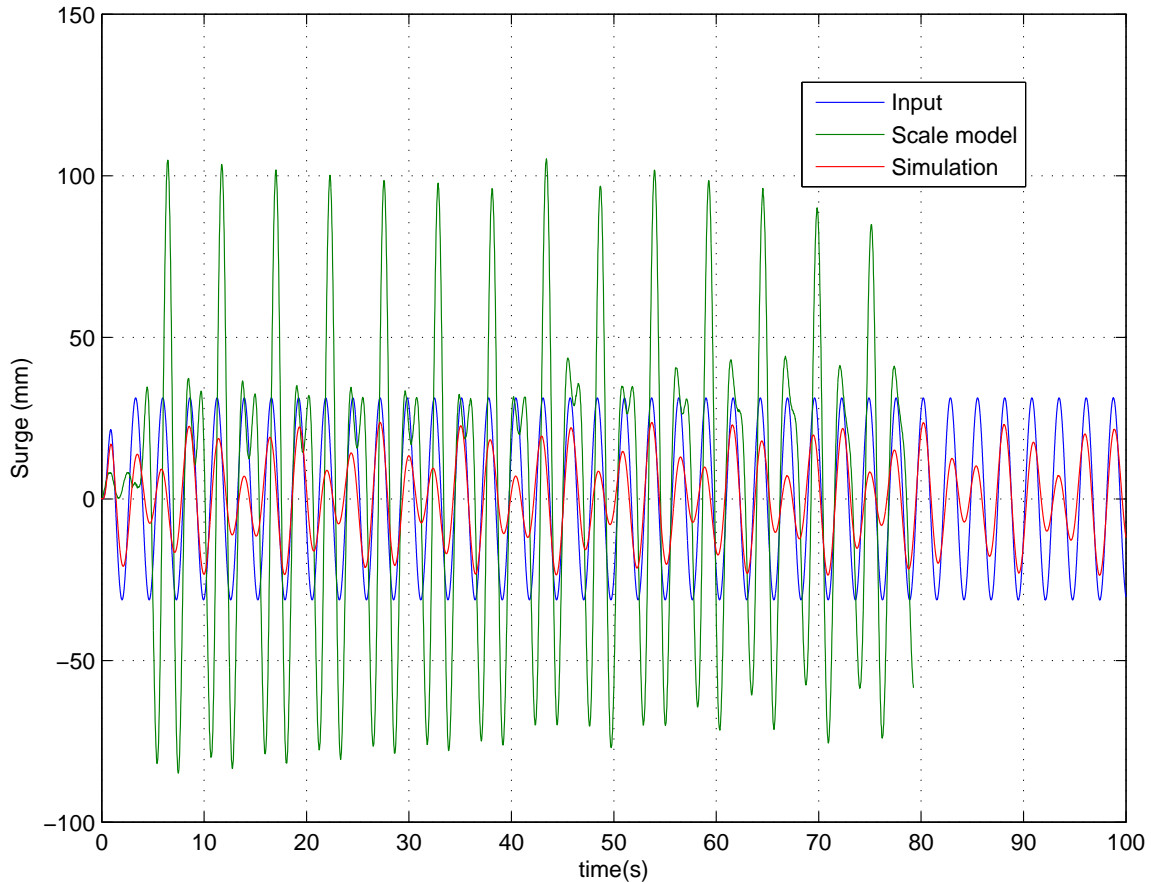


Figure 150. Surge time histories for simulated, scale-model, and input data for the uncontrolled case. (Simulation parameters: $\rho = 10$ degrees, $\vec{P}_{8/1,z} = 12.7$ mm, with a sinusoidal forcing function of $x_s = 31.25$ mm at a period of 2.65 seconds.)

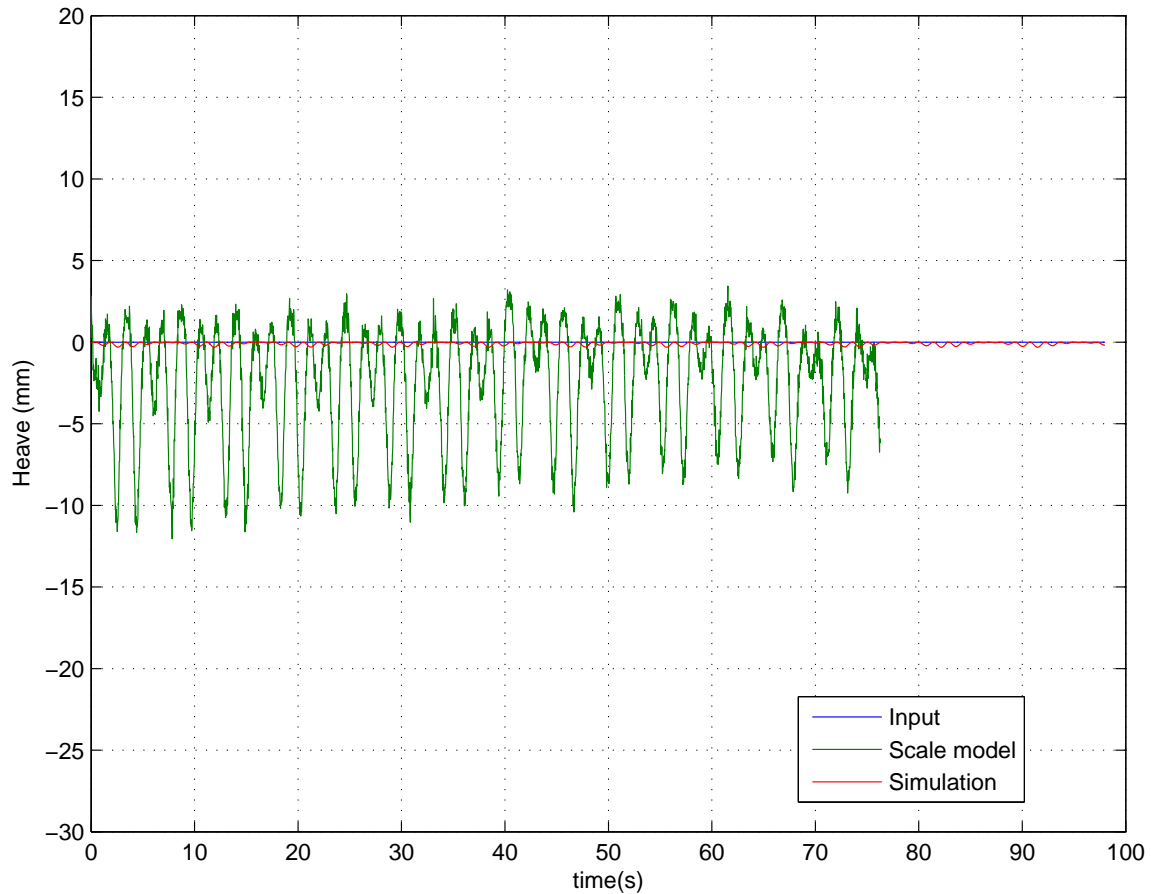


Figure 151. Heave time histories for simulated, scale-model, and input data for the uncontrolled case. (Simulation parameters: $\rho = 10$ degrees, $\vec{P}_{8/1,z} = 12.7$ mm, with a sinusoidal forcing function of $x_s = 31.25$ mm at a period of 2.65 seconds.)

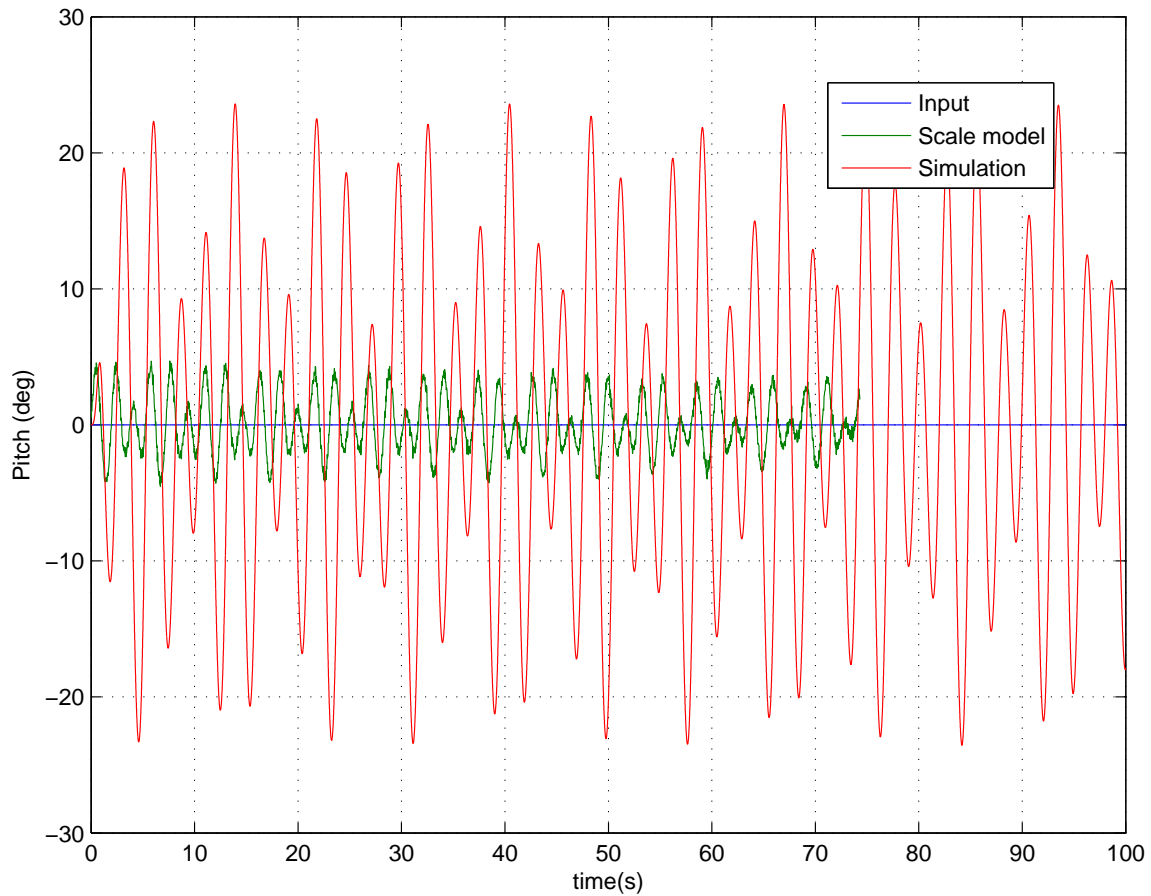


Figure 152. Pitch angle time histories for simulated, scale-model, and input data for the uncontrolled case. (Simulation parameters: $\rho = 10$ degrees, $\vec{P}_{8/1,z} = 12.7$ mm, with a sinusoidal forcing function of $x_s = 31.25$ mm at a period of 2.65 seconds.)

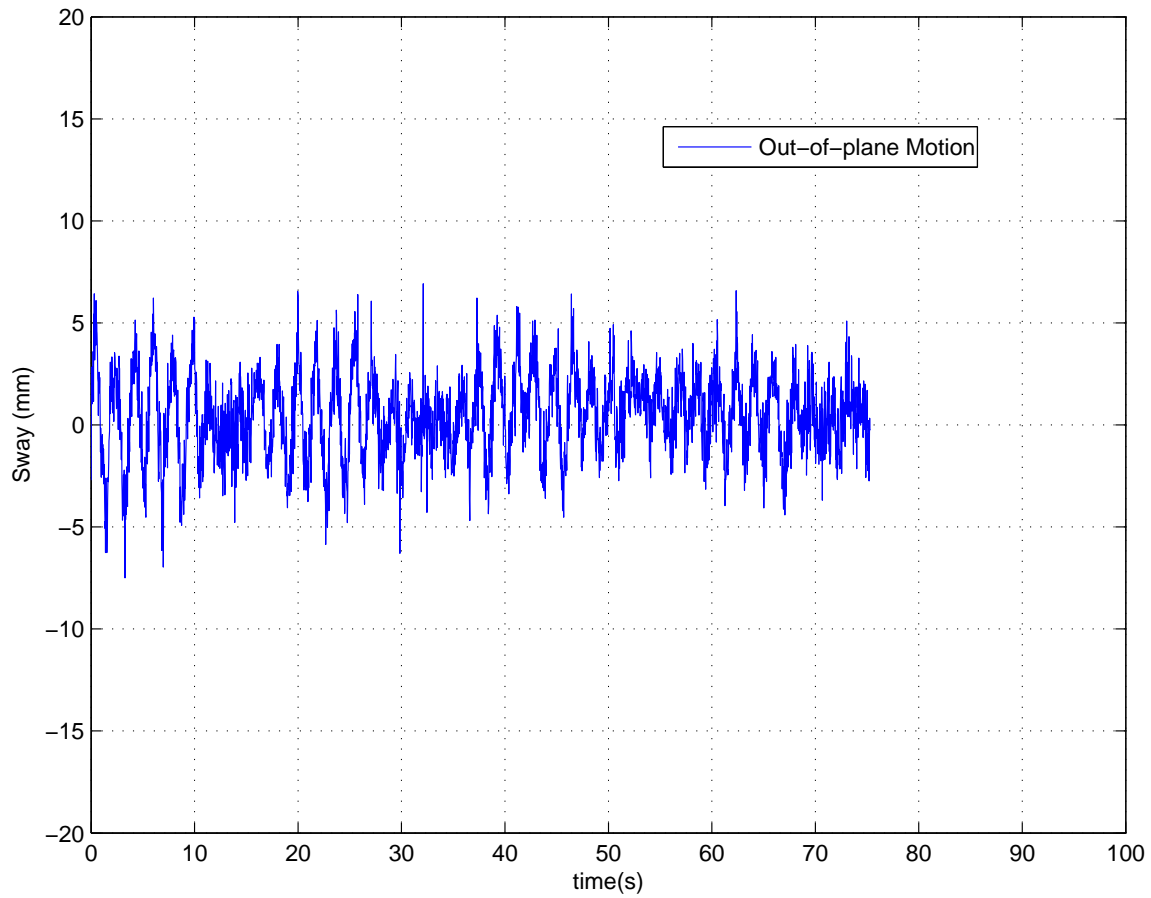


Figure 153. Out-of-plane (sway) time histories for simulated, scale-model, and input data for the uncontrolled case. The magnitude of the out-of-plane motion is about 5% of the primary forced response in surge. (Simulation parameters: $\rho = 10$ degrees, $\vec{P}_{8/1,z} = 12.7$ mm, with a sinusoidal forcing function of $x_s = 31.25$ mm at a period of 2.65 seconds.)

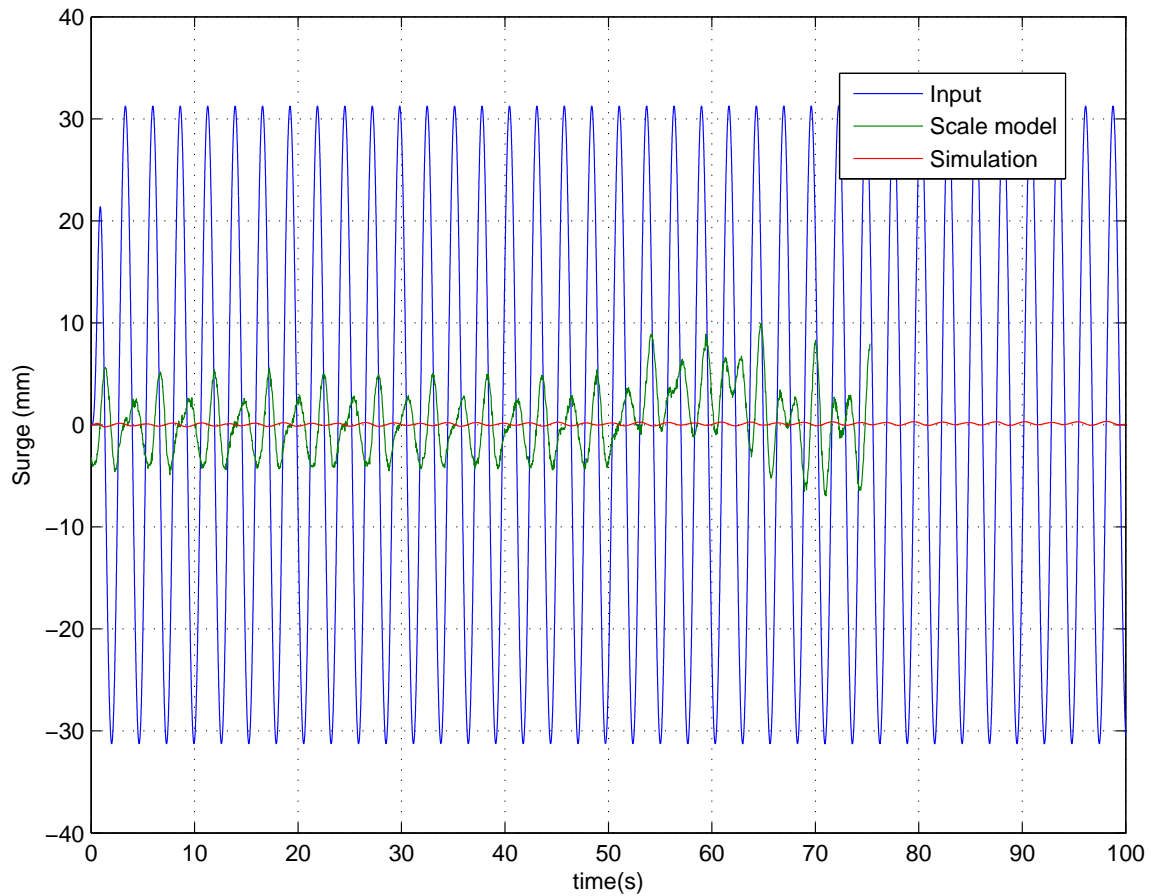


Figure 154. Surge time histories for simulated, scale-model, and input data for the controlled case. (Simulation parameters: $\rho = 10$ degrees, $\vec{P}_{8/1,z} = 12.7$ mm, with a sinusoidal forcing function of $x_s = 31.25$ mm at a period of 2.65 seconds.)

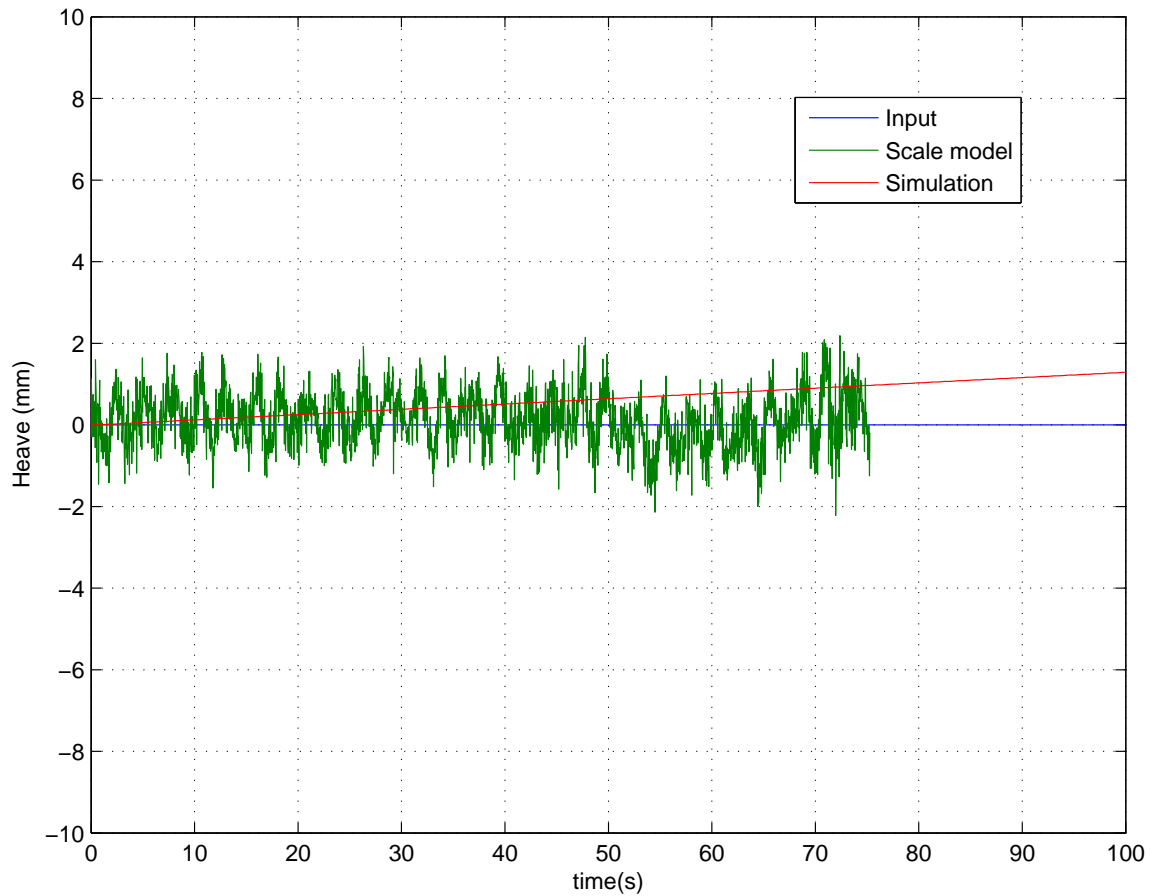


Figure 155. Heave time histories for simulated, scale-model, and input data for the controlled case. (Simulation parameters: $\rho = 10$ degrees, $\vec{P}_{8/1,z} = 12.7$ mm, with a sinusoidal forcing function of $x_s = 31.25$ mm at a period of 2.65 seconds.)

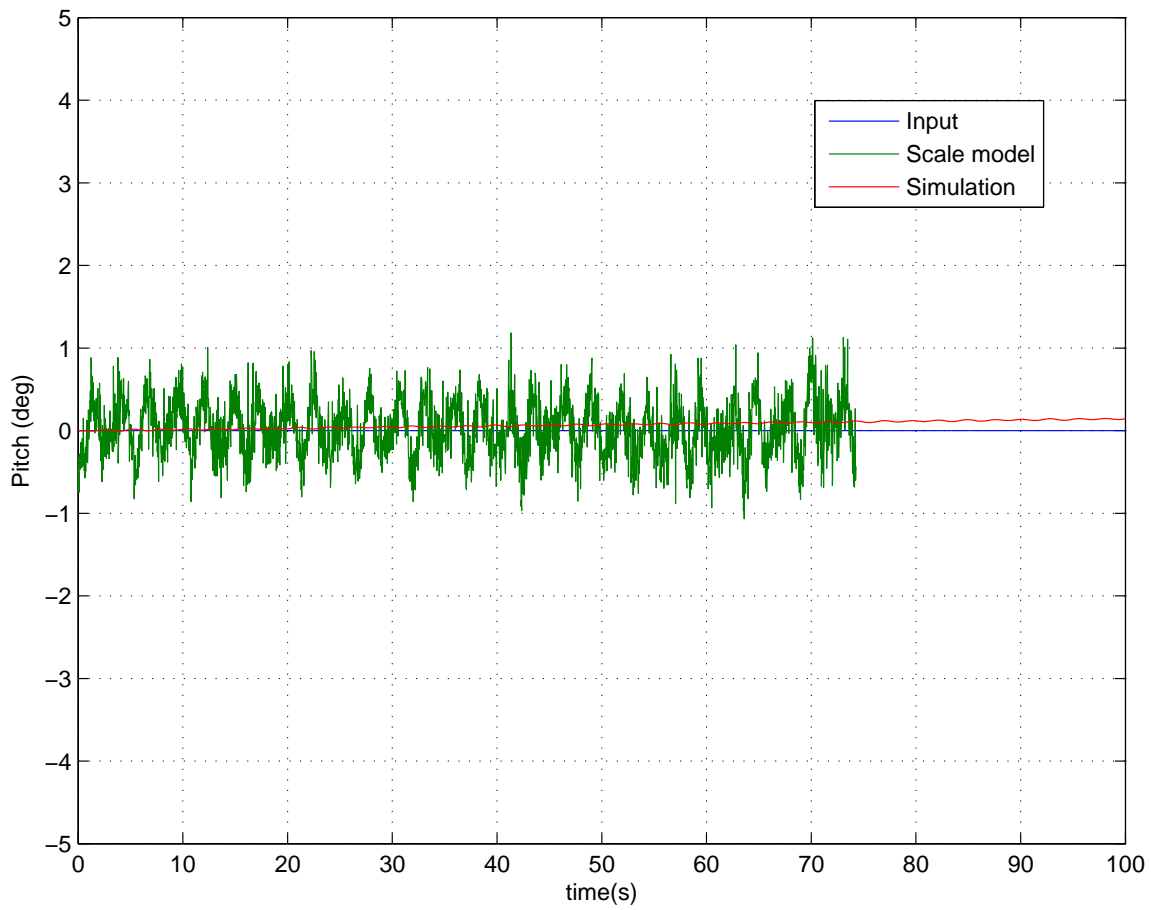


Figure 156. Pitch angle time histories for simulated, scale-model, and input data for the controlled case. (Simulation parameters: $\rho = 10$ degrees, $\bar{P}_{8/1,z} = 12.7$ mm, with a sinusoidal forcing function of $x_s = 31.25$ mm at a period of 2.65 seconds.)

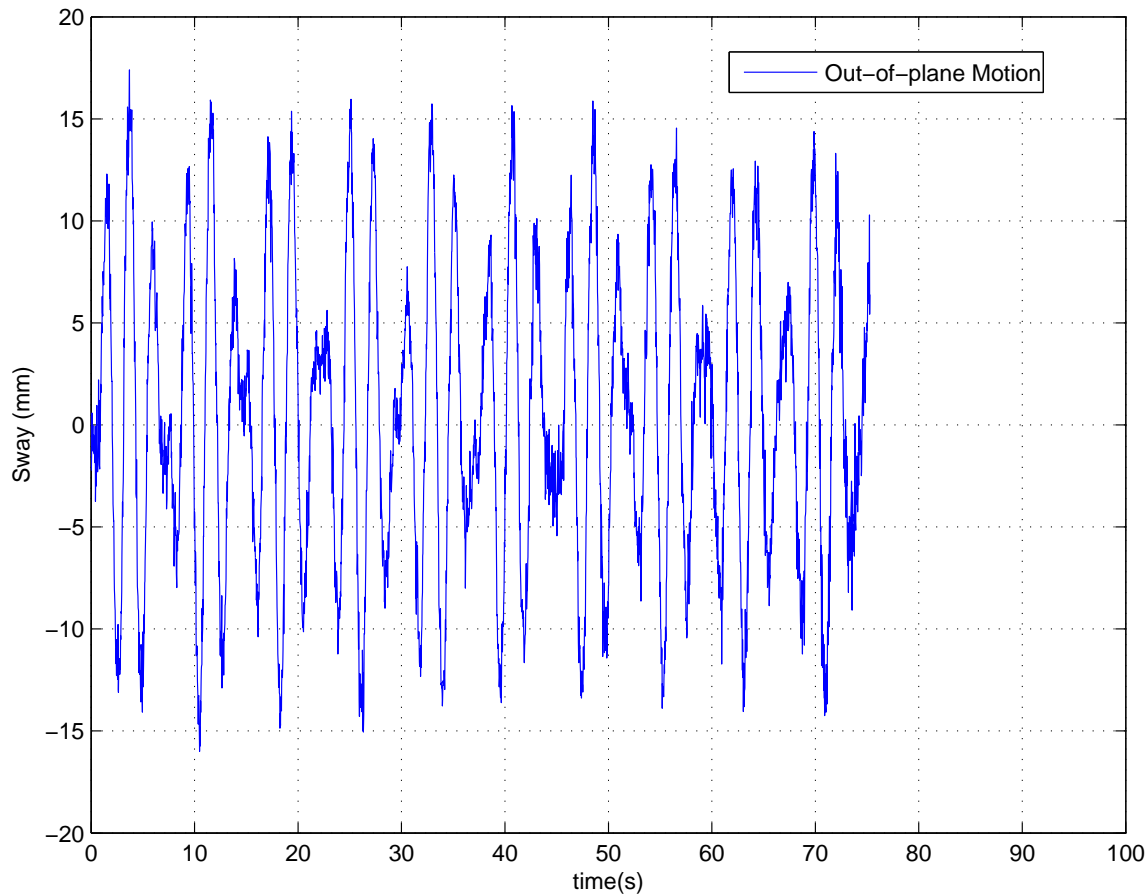


Figure 157. Out-of-plane (sway) time histories for simulated, scale-model, and input data for the controlled case. The magnitude of the peaks of the out-of-plane motion is about 15% of the primary forced response in surge. (Simulation parameters: $\rho = 10$ degrees, $\vec{P}_{8/1,z} = 12.7$ mm, with a sinusoidal forcing function of $x_s = 31.25$ mm at a period of 2.65 seconds.)

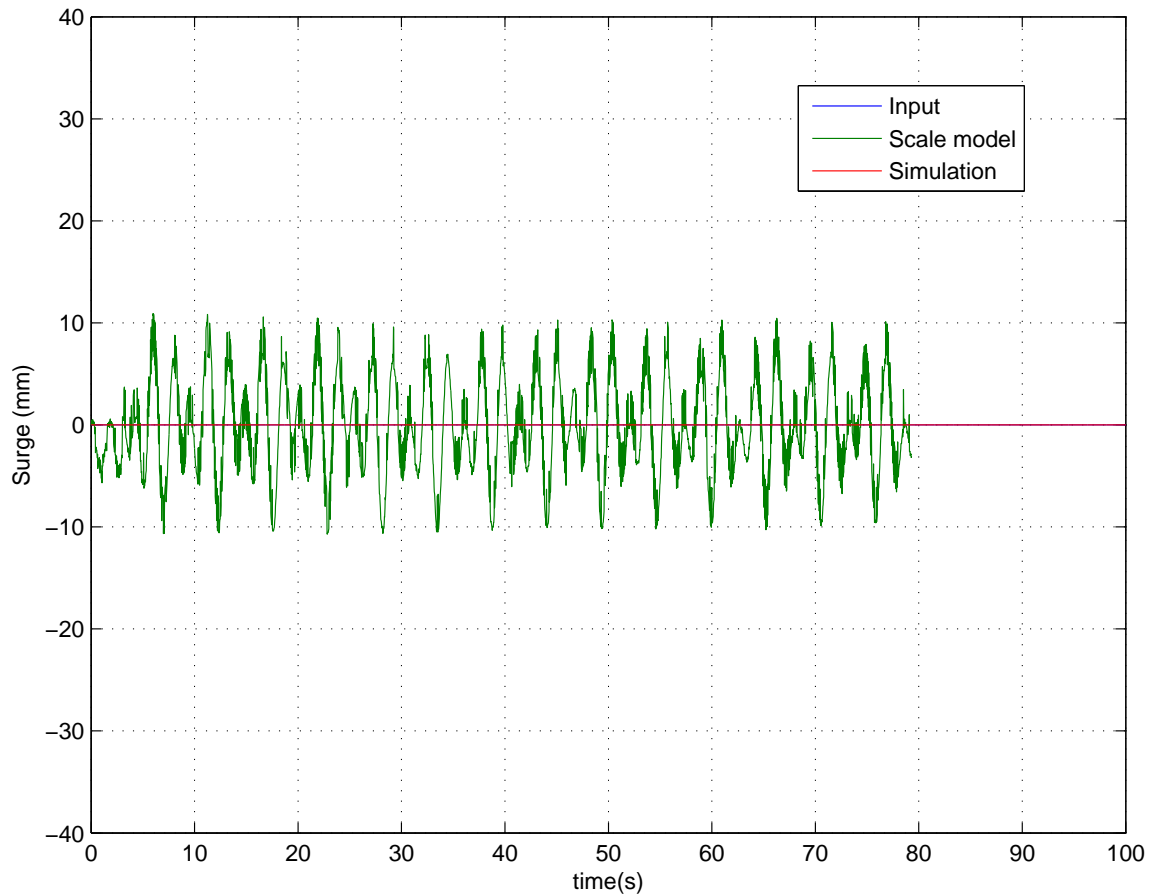


Figure 158. Surge time histories for simulated, scale-model, and input data for the uncontrolled case. (Simulation parameters: $\rho = 0$ degrees, $\vec{P}_{8/1,z} = 12.7$ mm, with a sinusoidal forcing function of $z_s = 31.25$ mm at a period of 2.65 seconds.)

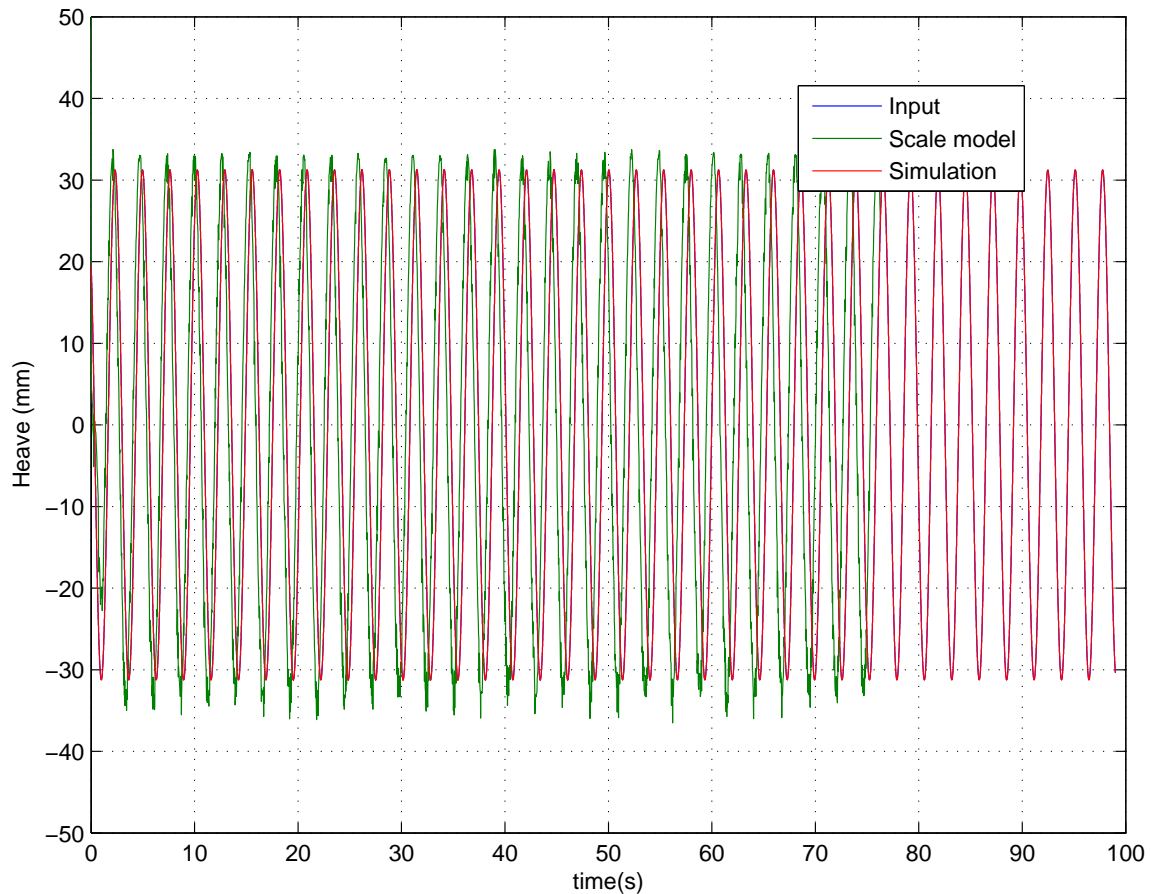


Figure 159. Heave time histories for simulated, scale-model, and input data for the uncontrolled case. (Simulation parameters: $\rho = 0$ degrees, $\vec{P}_{8/1,z} = 12.7$ mm, with a sinusoidal forcing function of $z_s = 31.25$ mm at a period of 2.65 seconds.)

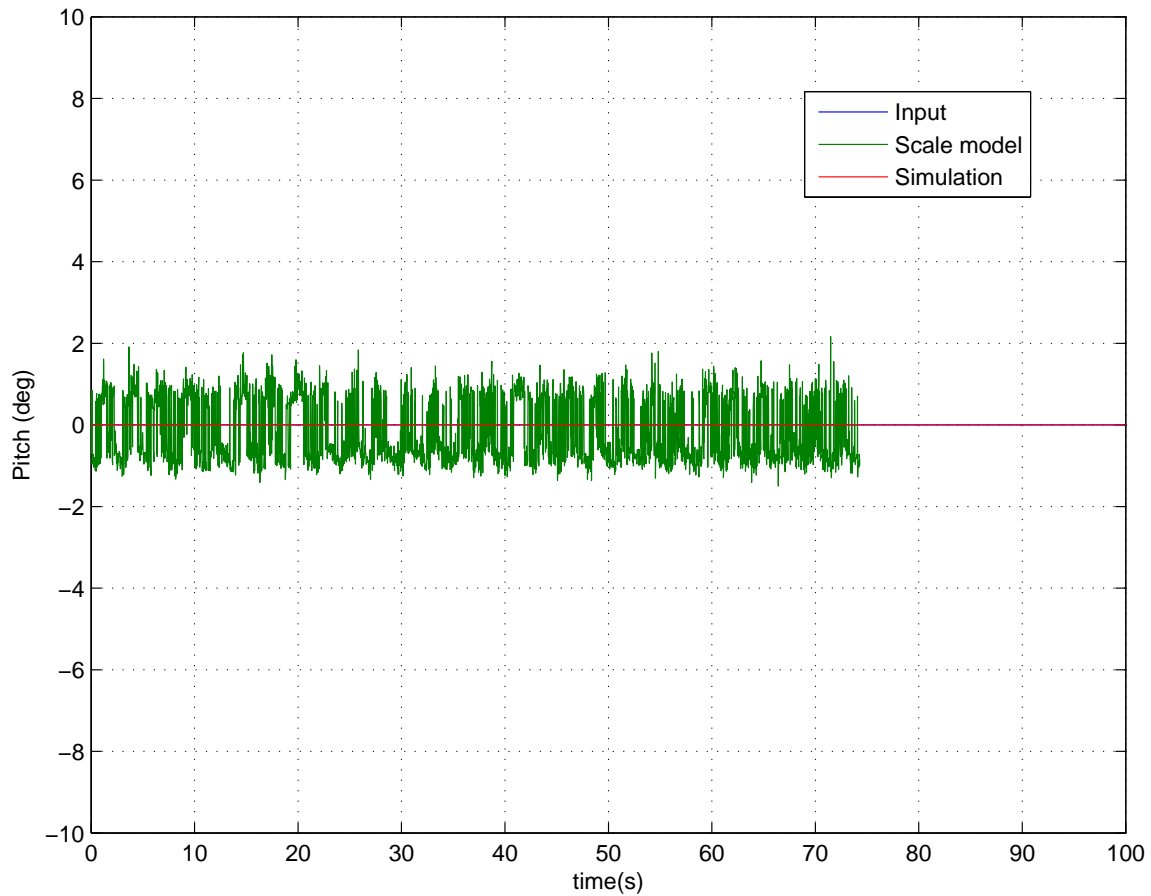


Figure 160. Pitch angle time histories for simulated, scale-model, and input data for the uncontrolled case. (Simulation parameters: $\rho = 0$ degrees, $\vec{P}_{8/1,z} = 12.7$ mm, with a sinusoidal forcing function of $x_s = 31.25$ mm at a period of 2.65 seconds.)

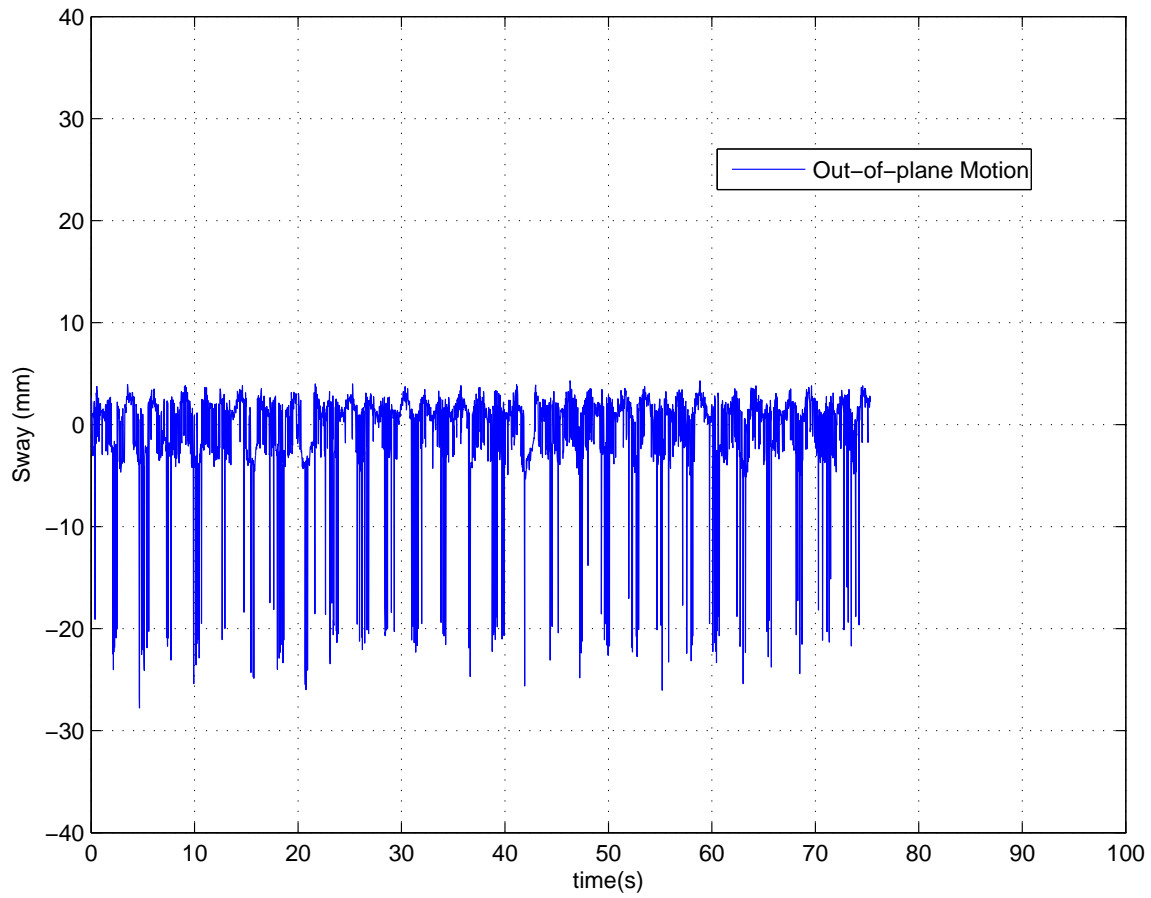


Figure 161. Out-of-plane (sway) time histories for simulated, scale-model, and input data for the uncontrolled case. The magnitude of the out-of-plane motion is about 33% of the primary forced response in heave. (Simulation parameters: $\rho = 0$ degrees, $\vec{P}_{8/1,z} = 12.7$ mm, with a sinusoidal forcing function of $x_s = 31.25$ mm at a period of 2.65 seconds.)

Figures 162, 163, 164, and 165 show the results for the controlled pure heave-input case. The range of the out-of-plane motion is $\approx \pm 10$ mm, typical of the other cases; however this amplitude is much larger than the residual motion in the primary heave axis. The surge motion is of similar magnitude to sway.

Figures 166, 167, 168, and 169 show the results for the uncontrolled pure pitch-input case. Because the payload is restrained in pitch by the two hoist cables

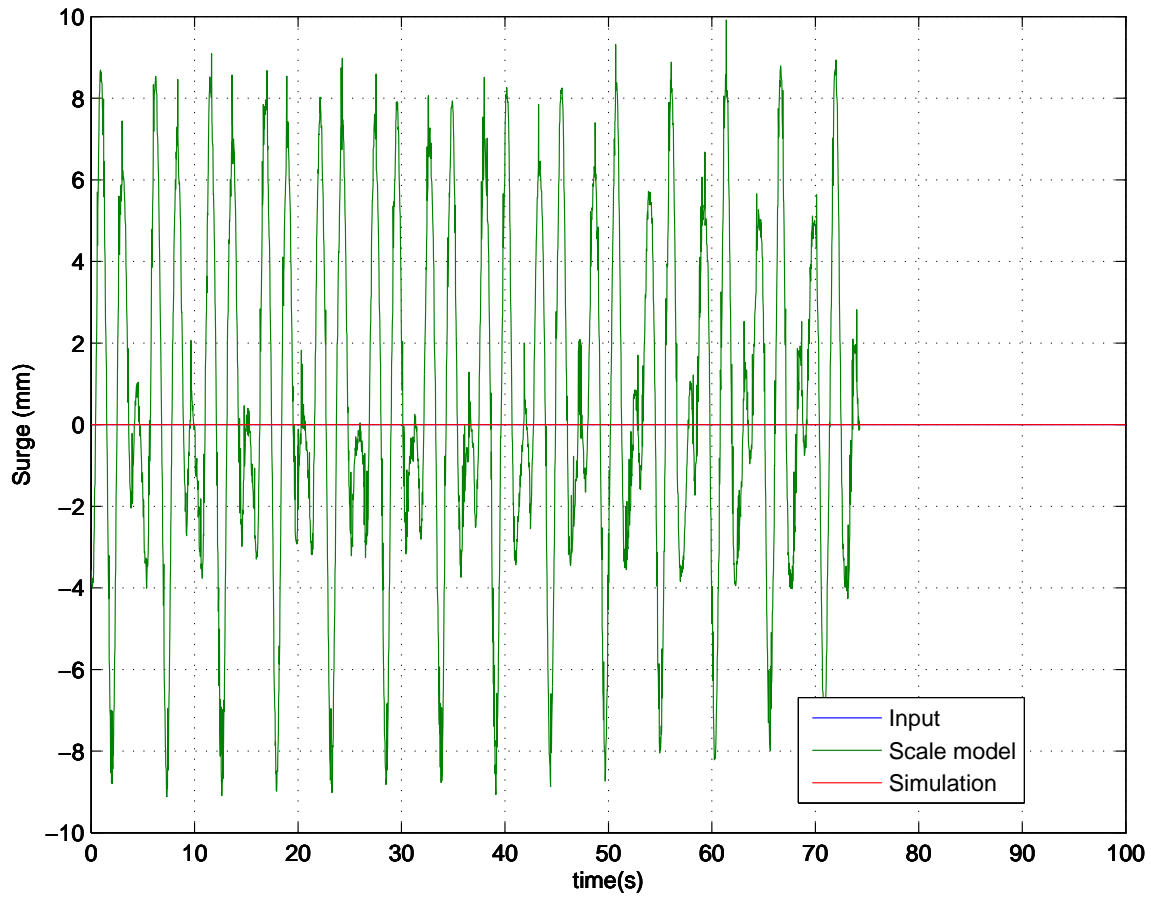


Figure 162. Surge time histories for simulated, scale-model, and input data for the controlled case. (Simulation parameters: $\rho = 0$ degrees, $\vec{P}_{8/1,z} = 12.7$ mm, with a sinusoidal forcing function of $z_s = 31.25$ mm at a period of 2.65 seconds.)

it is expected that the uncontrolled motion for both the simulation and the model should follow closely to the input signal. The slight differences in the model response (1-2 mm) from the simulation shown in Figure 168 do not appear to be measurement noise and may be attributable to either cable stretch or compliance in the model crane structure.

Figures 170, 171, 172, and 173 show the results for the controlled pure pitch-input case. With the control on, the pitch response is reduced from 5° to less than 2° for the model - the simulation results have a non-zero mean drift.

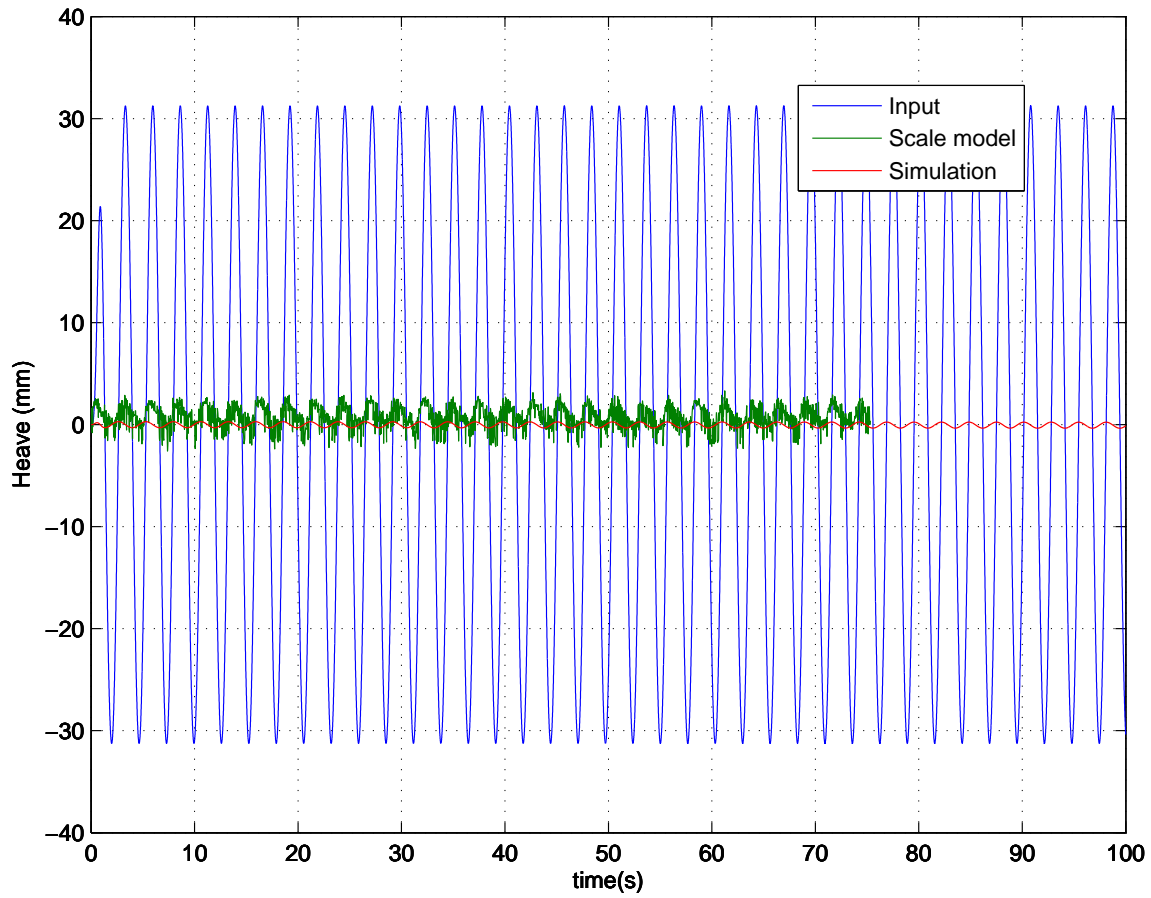


Figure 163. Heave time histories for simulated, scale-model, and input data for the controlled case. (Simulation parameters: $\rho = 0$ degrees, $\vec{P}_{8/1,z} = 12.7$ mm, with a sinusoidal forcing function of $z_s = 31.25$ mm at a period of 2.65 seconds.)

Figures 174, 175, 176, and 177 show the results for the uncontrolled combined-input case. The combined inputs are simultaneous surge, heave, and pitch using the same amplitude and period as in the single axis cases. The most dramatic example is Figure 174 where the simulation predicts (and the model also shows) that the peak surge is on the order of 500 mm, over 10 times the surge input alone - obviously the pitch input is also driving this motion.

Figures 178, 179, 180, and 181 show the results for the controlled combined-input case. With the control on, the model surge motion is larger than is predicted

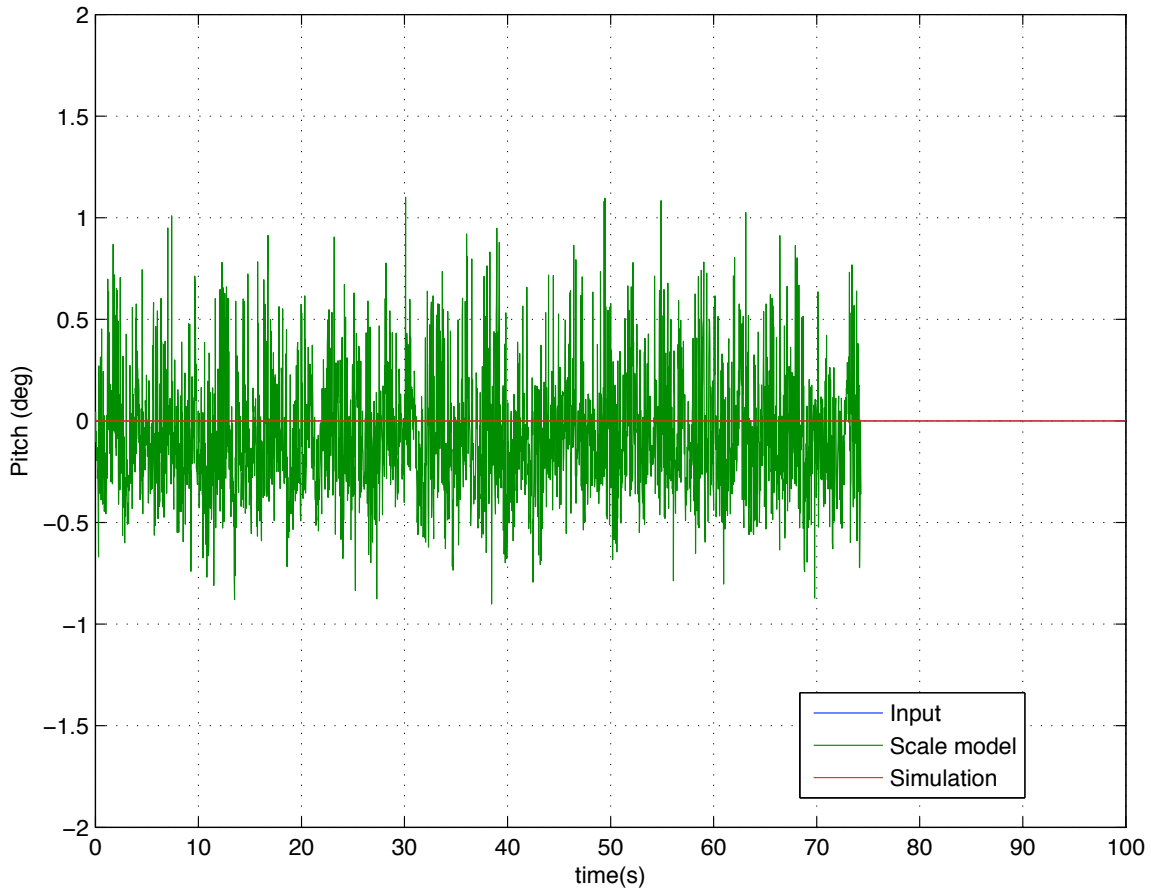


Figure 164. Pitch angle time histories for simulated, scale-model, and input data for the controlled case. (Simulation parameters: $\rho = 0$ degrees, $\vec{P}_{8/1,z} = 12.7$ mm, with a sinusoidal forcing function of $z_s = 31.25$ mm at a period of 2.65 seconds.)

by the simulation, but has been reduced by 80% compared to the uncontrolled case.

As Table 6 shows, the controlled cases have significantly lower calculated values of $J_{L+\theta}$ compared to the uncontrolled cases. The smallest reduction was 78.1% and the largest was 99% reduction. The comparison to the input was based on computing $J_{L+\theta}$ for the input motion - treating the input as if the payload motion followed the input exactly. In many of the uncontrolled cases the response exceeded the input, thereby producing negative motion reductions as denoted by the values in parentheses.

The calculation of $J_{L+\theta}$ did not include the out-of-plane (sway) motion. The

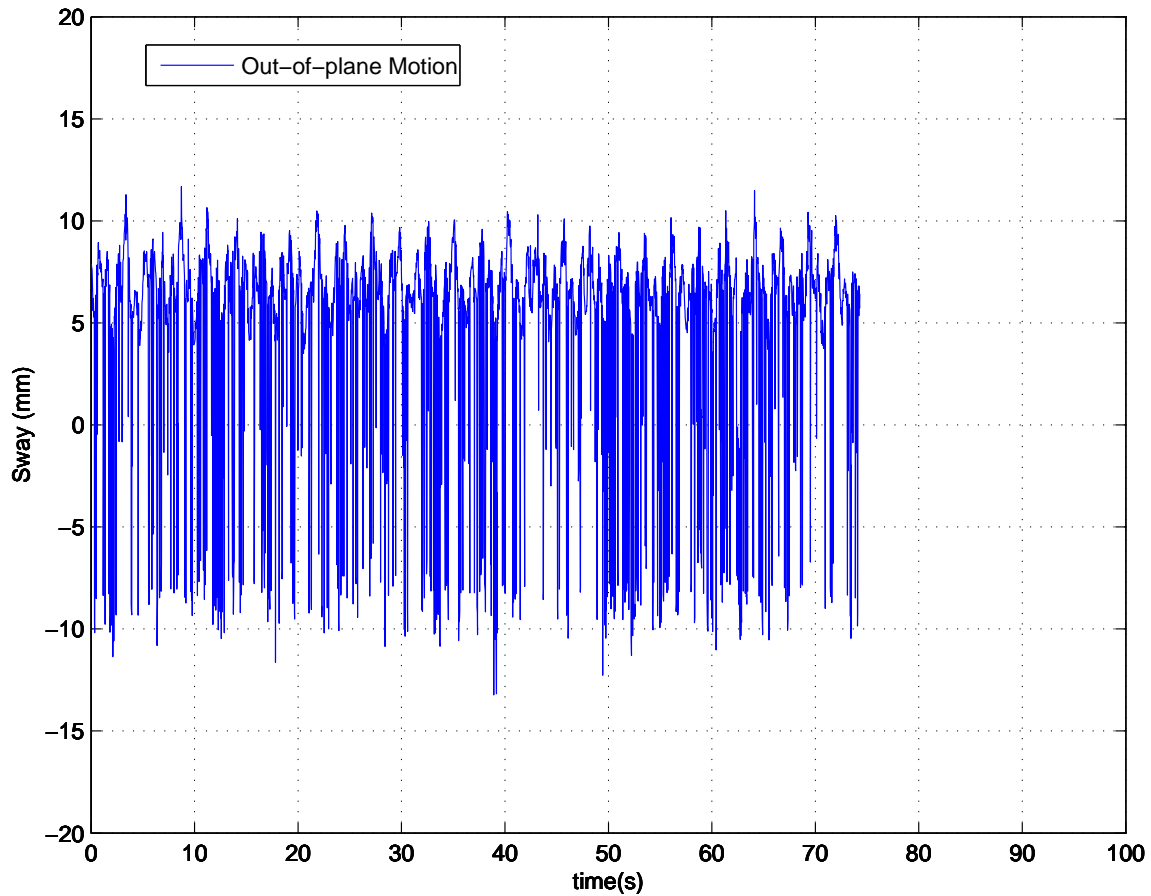


Figure 165. Out-of-plane (sway) time histories for simulated, scale-model, and input data for the controlled case. The magnitude of the peaks of the out-of-plane motion is about $\pm 10\text{mm}$ about 5 times the magnitude of the primary forced response in heave. (Simulation parameters: $\rho = 0$ degrees, $\vec{P}_{8/1,z} = 12.7 \text{ mm}$, with a sinusoidal forcing function of $z_s = 31.25 \text{ mm}$ at a period of 2.65 seconds.)

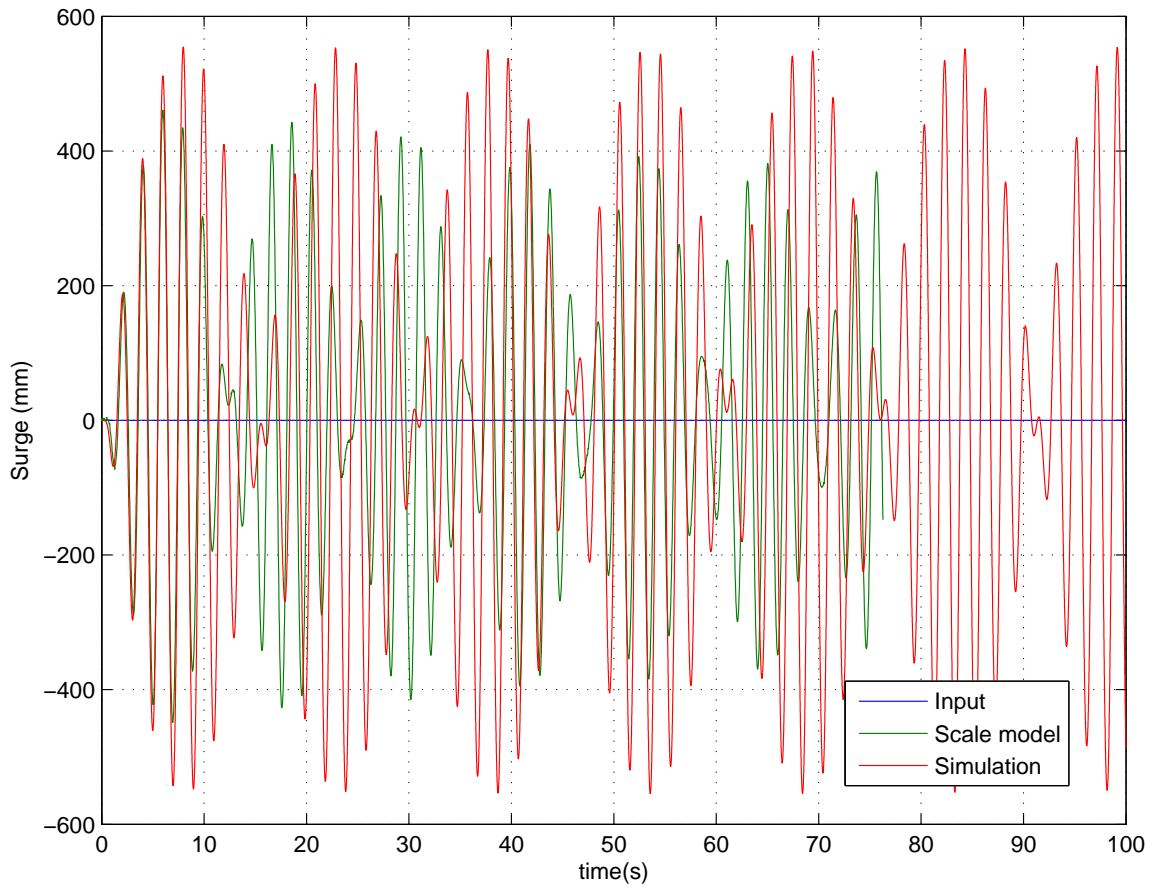


Figure 166. Surge time histories for simulated, scale-model, and input data for the uncontrolled case. (Simulation parameters: $\rho = 0$ degrees, $\bar{P}_{8/1,z} = 12.7$ mm, with a sinusoidal forcing function of $\theta_s = 5^\circ$ at a period of 2.12 seconds.)

amount of sway was fairly consistent across the cases, with the controlled cases involving significant luffing having more sway than the uncontrolled cases. One explanation for this is a physical imperfection in the model - twist in the sheave-block at the tip of the jib. This can be seen in a photograph of the jib top shown in Figure 182. Another source of out-of-plane motion could be the motion platform. If all the actuators are not perfectly synchronized, then slight tilt angles could result that would generate harmonic forcing throughout the run - this effect also would be present in the uncontrolled runs. The presence of a non-zero ρ angle appeared to slightly reduce

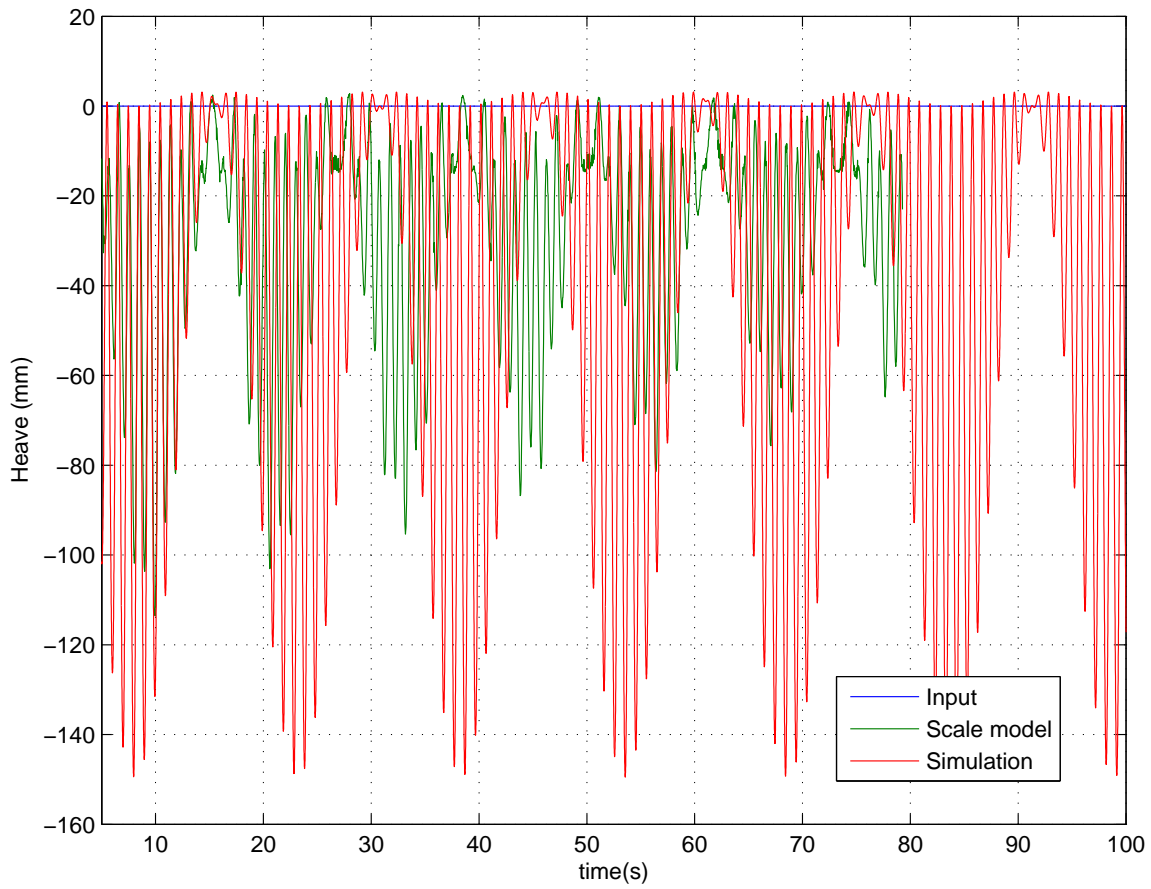


Figure 167. Heave time histories for simulated, scale-model, and input data for the uncontrolled case. (Simulation parameters: $\rho = 0$ degrees, $\bar{P}_{8/1,z} = 12.7$ mm, with a sinusoidal forcing function of $\theta_s = 5^\circ$ at a period of 2.12 seconds.)

the out-of-plane motion, but only one case was examined so more data are necessary to validate that observation.

In spite of the imperfections in the construction of the crane model and the unmodeled dynamics of the crane actuators and the motion platform and in the absence of any feedback of the payload motion, the feedforward structure of the inverse kinematic control was able to substantially reduce the response of the planar dual-crane system to a range of motion inputs.

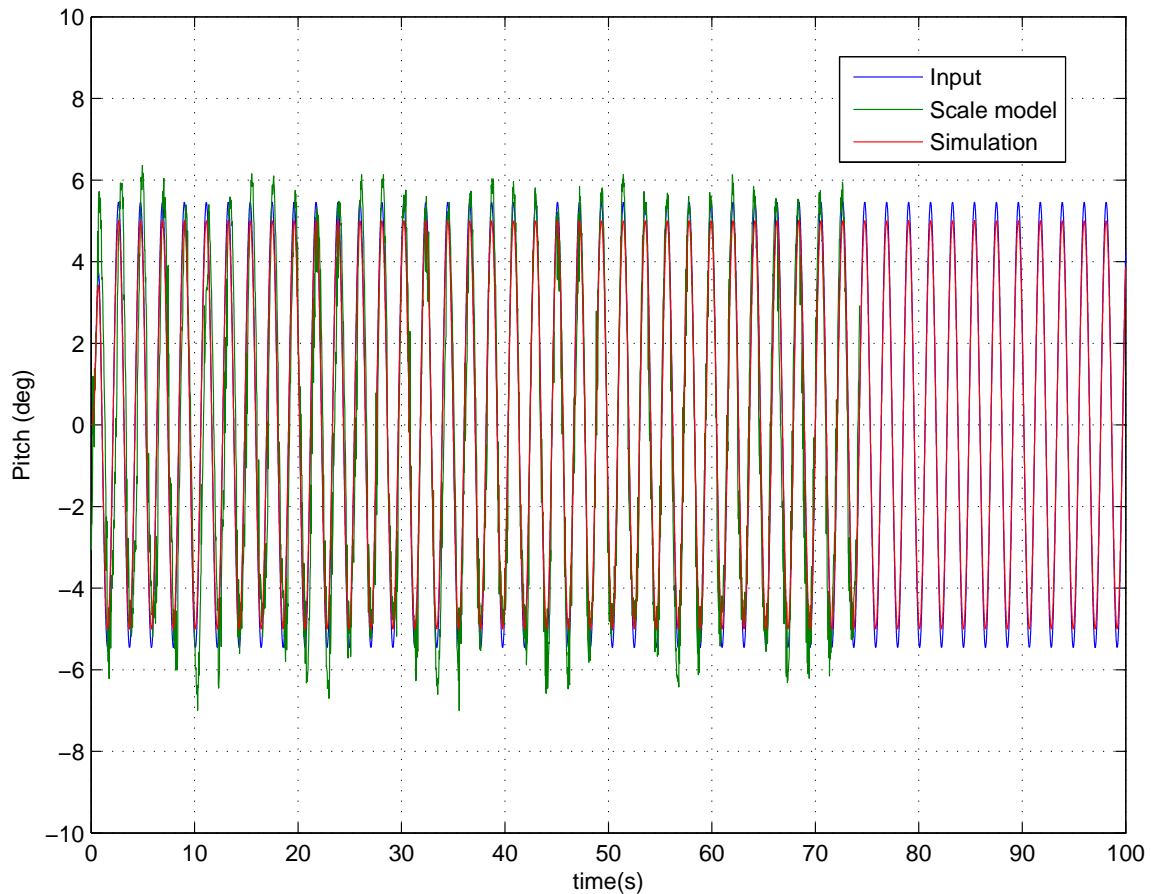


Figure 168. Pitch angle time histories for simulated, scale-model, and input data for the uncontrolled case. (Simulation parameters: $\rho = 0$ degrees, $\vec{P}_{8/1,z} = 12.7$ mm, with a sinusoidal forcing function of $\theta_s = 5^\circ$ at a period of 2.12 seconds.)

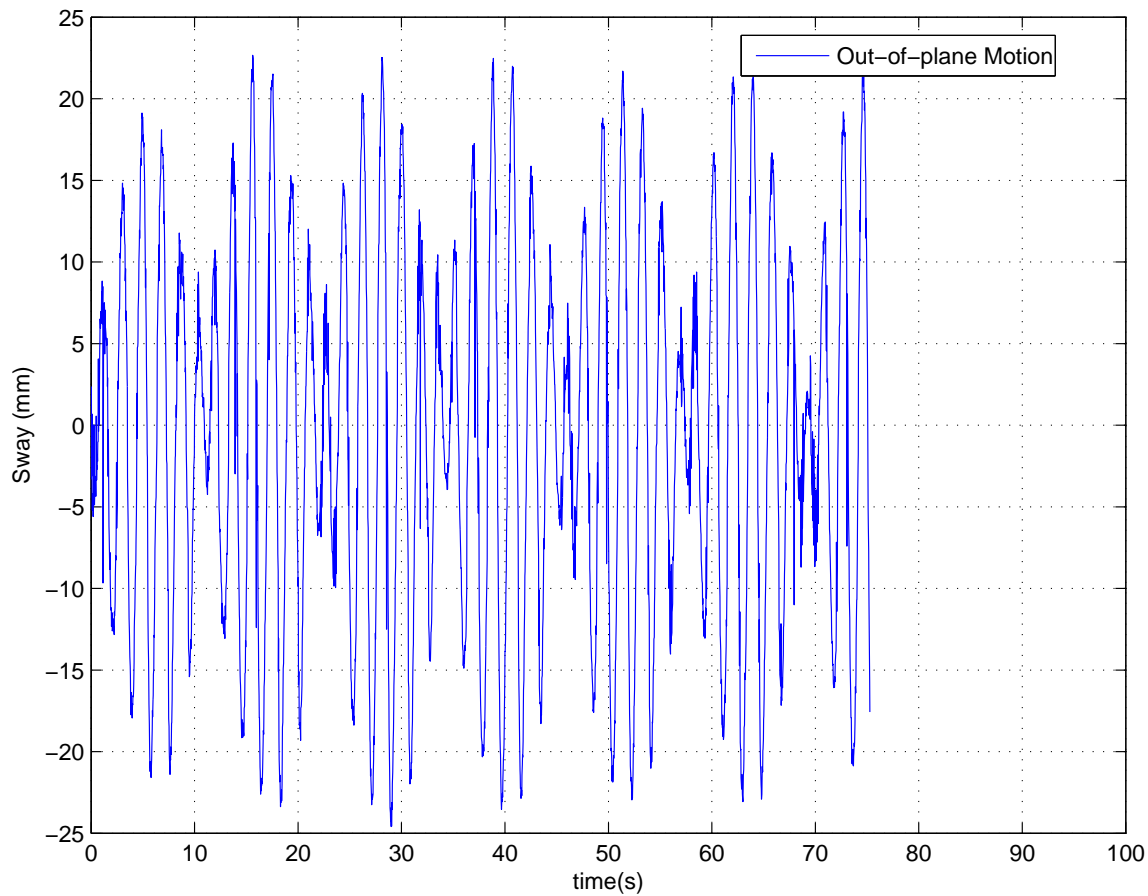


Figure 169. Out-of-plane (sway) time histories for simulated, scale-model, and input data for the uncontrolled case. The magnitude of the out-of-plane motion is about +/- 20 mm. (Simulation parameters: $\rho = 0$ degrees, $\vec{P}_{8/1,z} = 12.7$ mm, with a sinusoidal forcing function of $\theta_s = 5^\circ$ at a period of 2.12 seconds.)

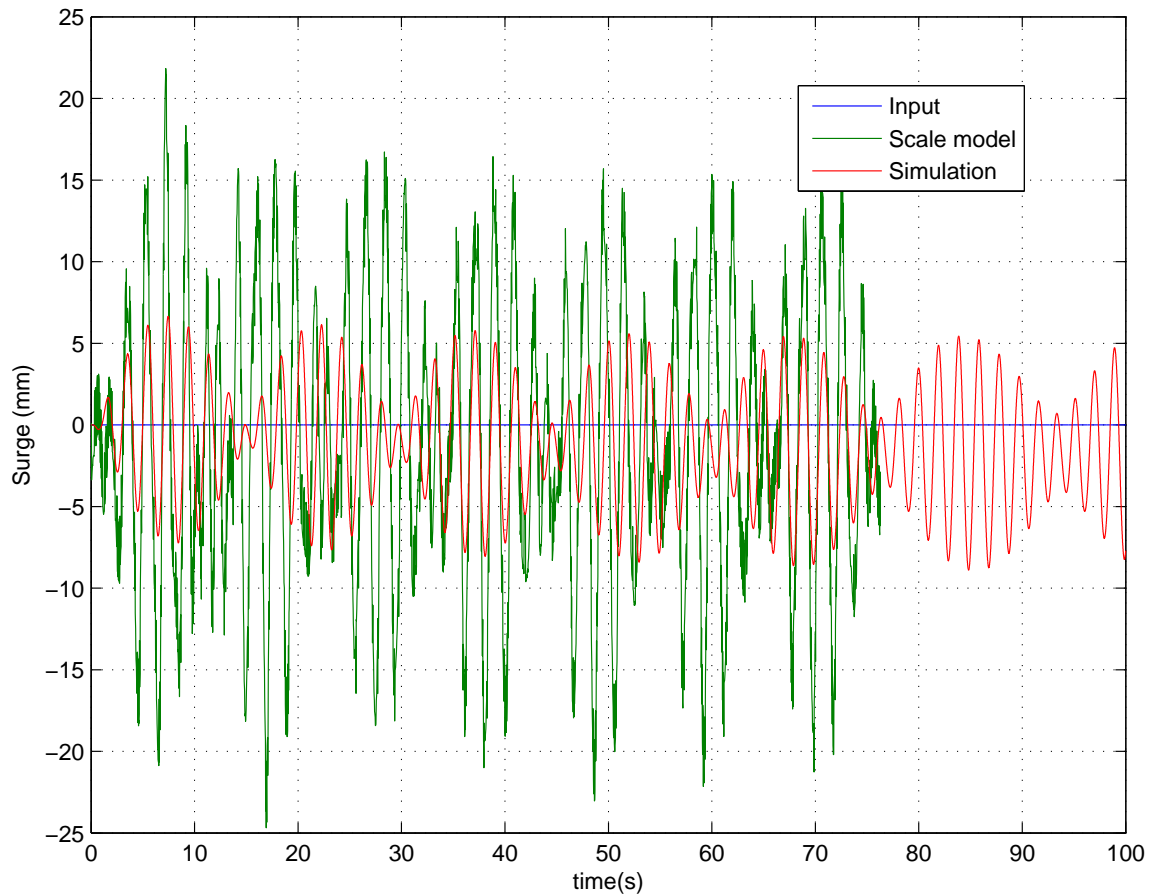


Figure 170. Surge time histories for simulated, scale-model, and input data for the controlled case. (Simulation parameters: $\rho = 0$ degrees, $\vec{P}_{8/1,z} = 12.7$ mm, with a sinusoidal forcing function of $\theta_s = 5^\circ$ at a period of 2.12 seconds.)

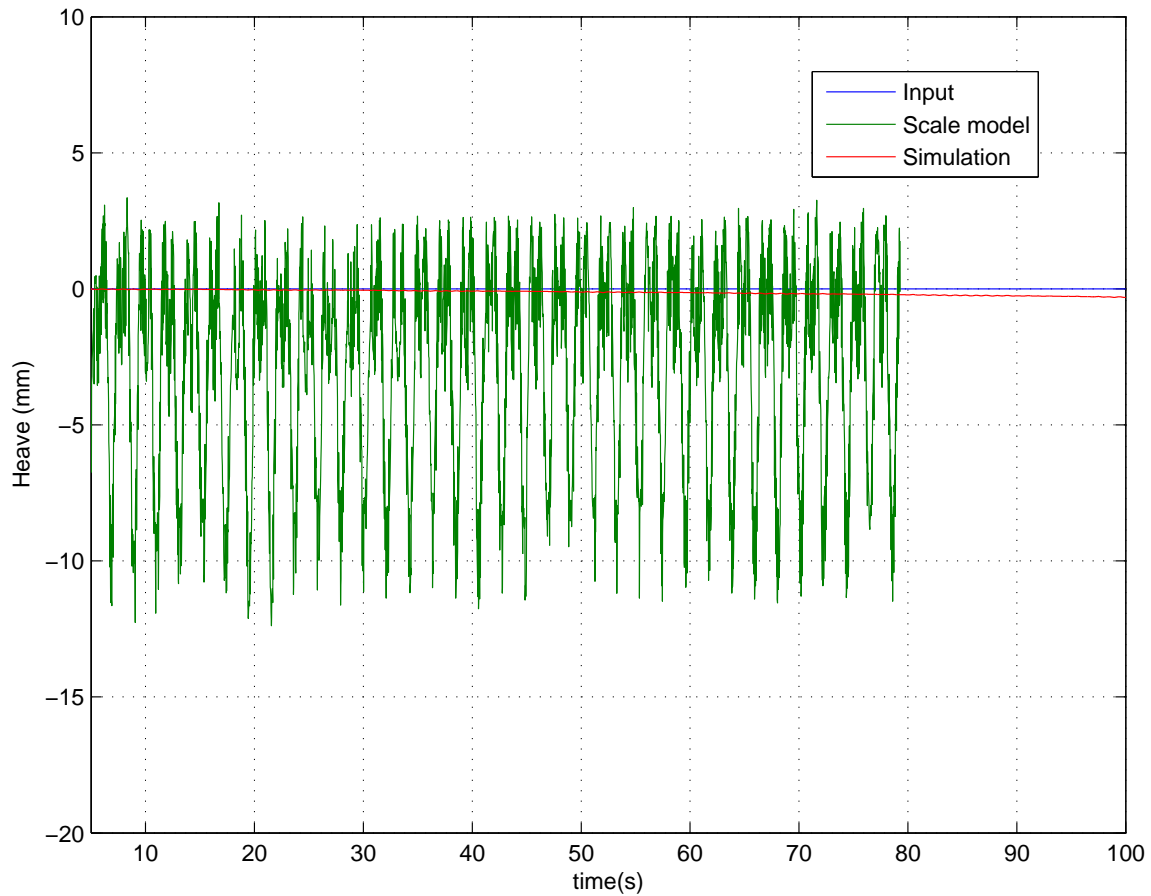


Figure 171. Heave time histories for simulated, scale-model, and input data for the controlled case. (Simulation parameters: $\rho = 0$ degrees, $\vec{P}_{8/1,z} = 12.7$ mm, with a sinusoidal forcing function of $\theta_s = 5^\circ$ at a period of 2.12 seconds.)

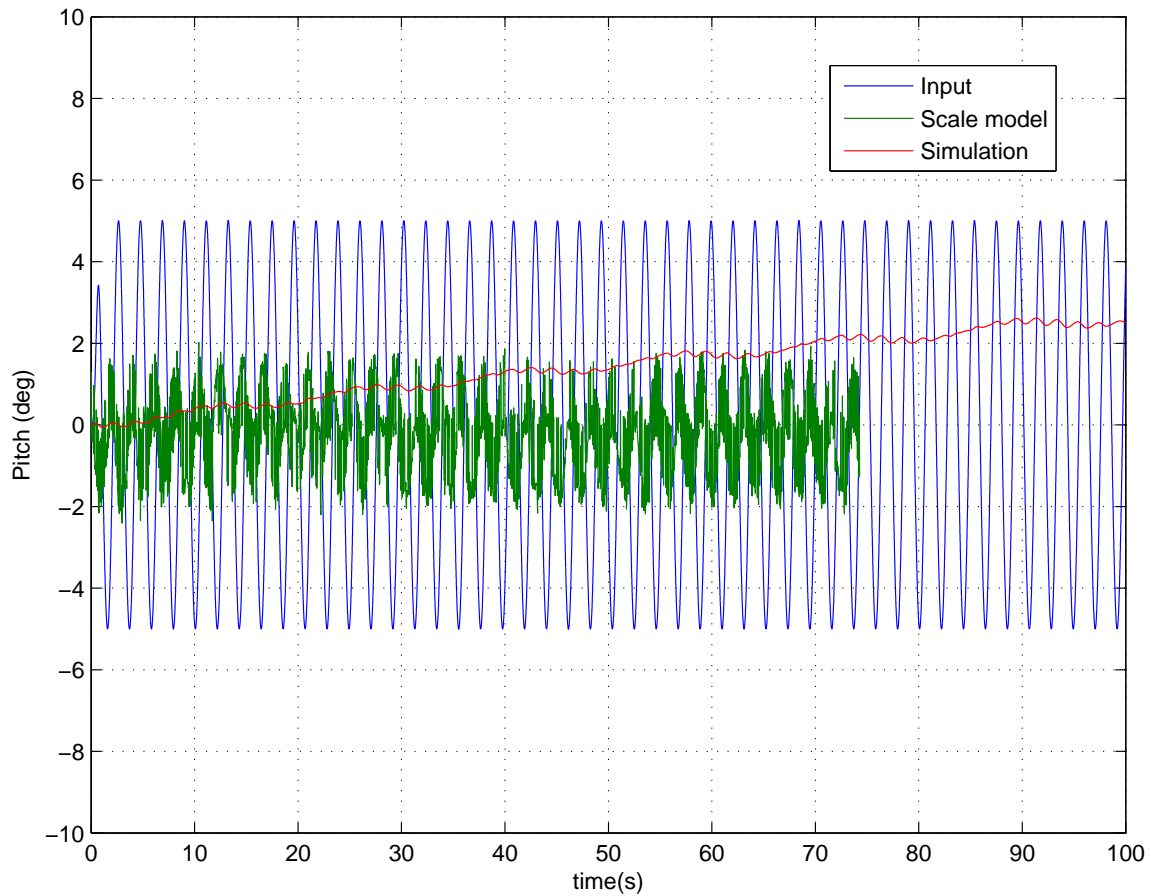


Figure 172. Pitch angle time histories for simulated, scale-model, and input data for the controlled case. (Simulation parameters: $\rho = 0$ degrees, $\vec{P}_{8/1,z} = 12.7$ mm, with a sinusoidal forcing function of $\theta_s = 5^\circ$ at a period of 2.12 seconds.)

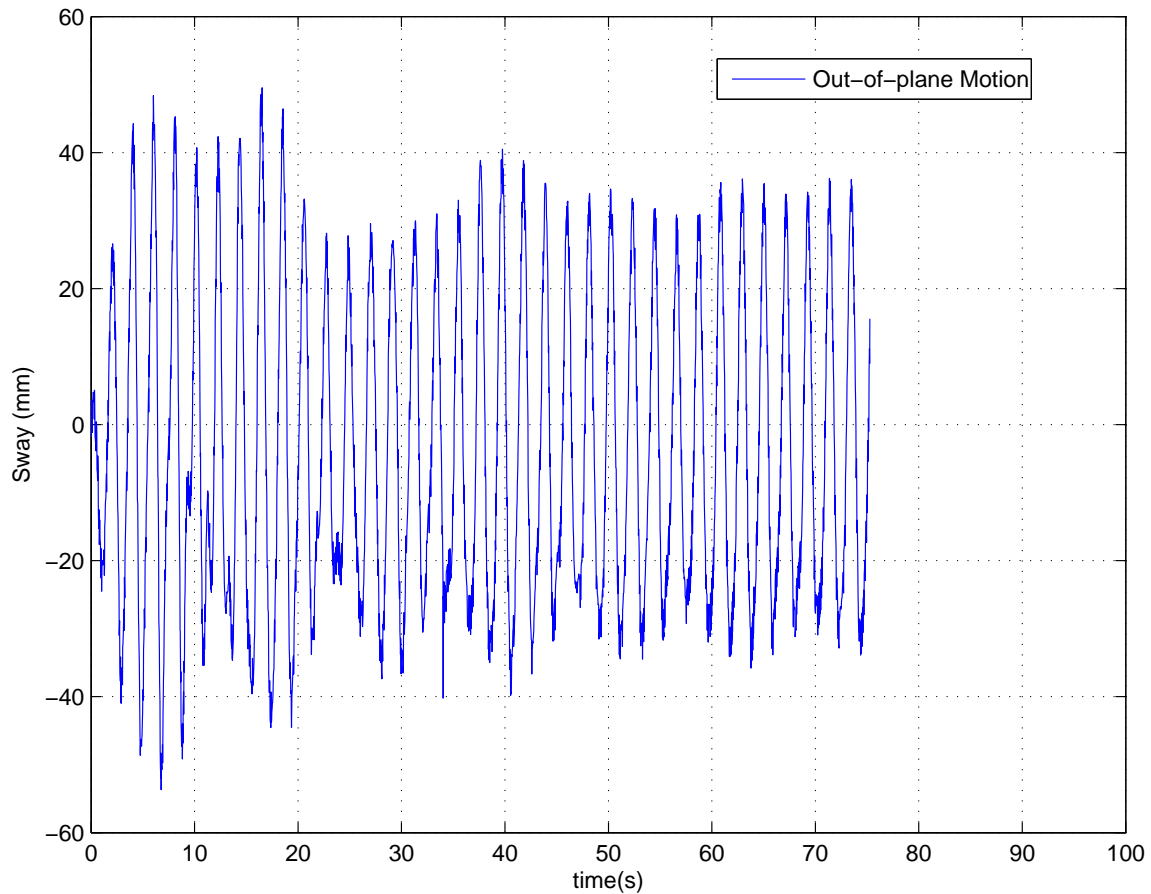


Figure 173. Out-of-plane (sway) time histories for simulated, scale-model, and input data for the controlled case. The magnitude of the peaks of the out-of-plane motion is about +/-40mm. (Simulation parameters: $\rho = 0$ degrees, $\bar{P}_{8/1,z} = 12.7$ mm, with a sinusoidal forcing function of $\theta_s = 5^\circ$ at a period of 2.12 seconds.)

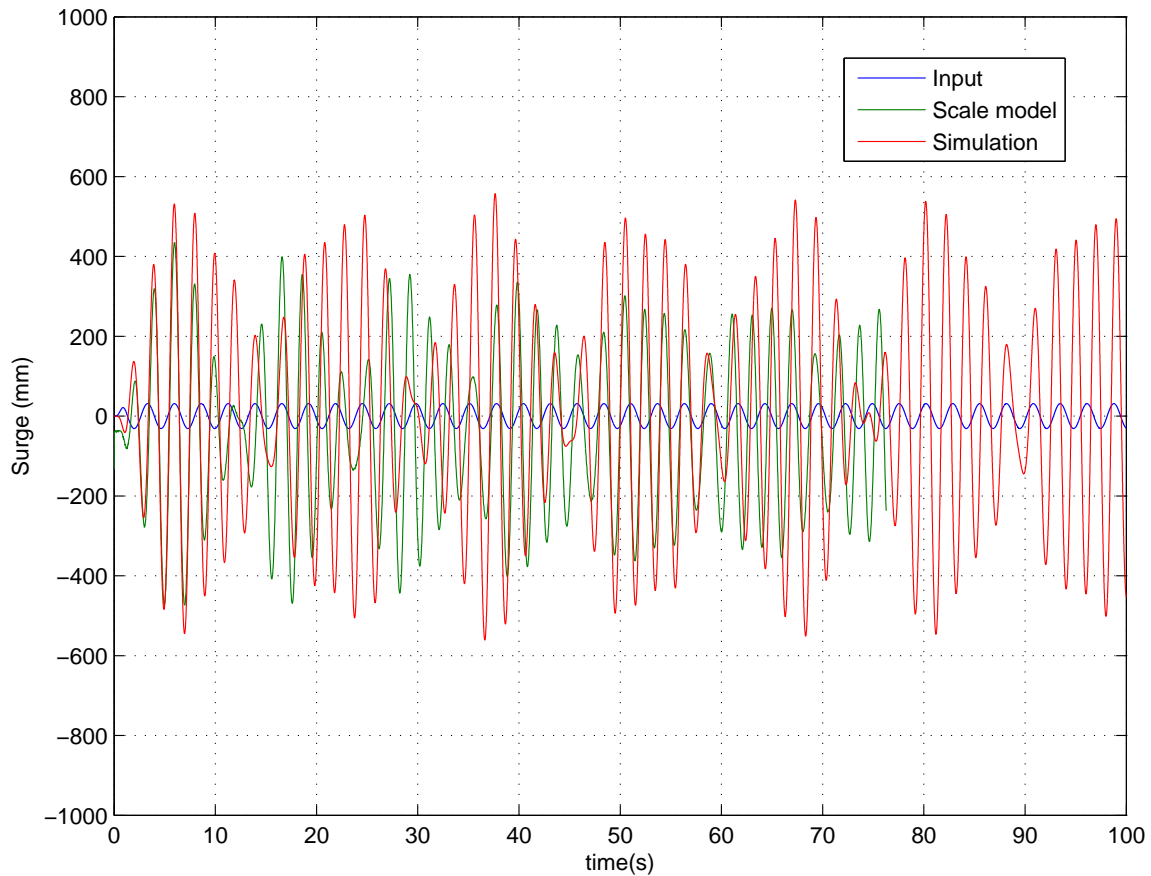


Figure 174. Surge time histories for simulated, scale-model, and input data for the uncontrolled case. (Simulation parameters: $\rho = 0$ degrees, $\vec{P}_{8/1,z} = 12.7$ mm, with a sinusoidal forcing function of $x_s = 31.25$ mm at a period of 2.65 seconds, $z_s = 31.25$ mm at a period of 2.65 seconds, and $\theta_s = 5^\circ$ at a period of 2.12 seconds.)

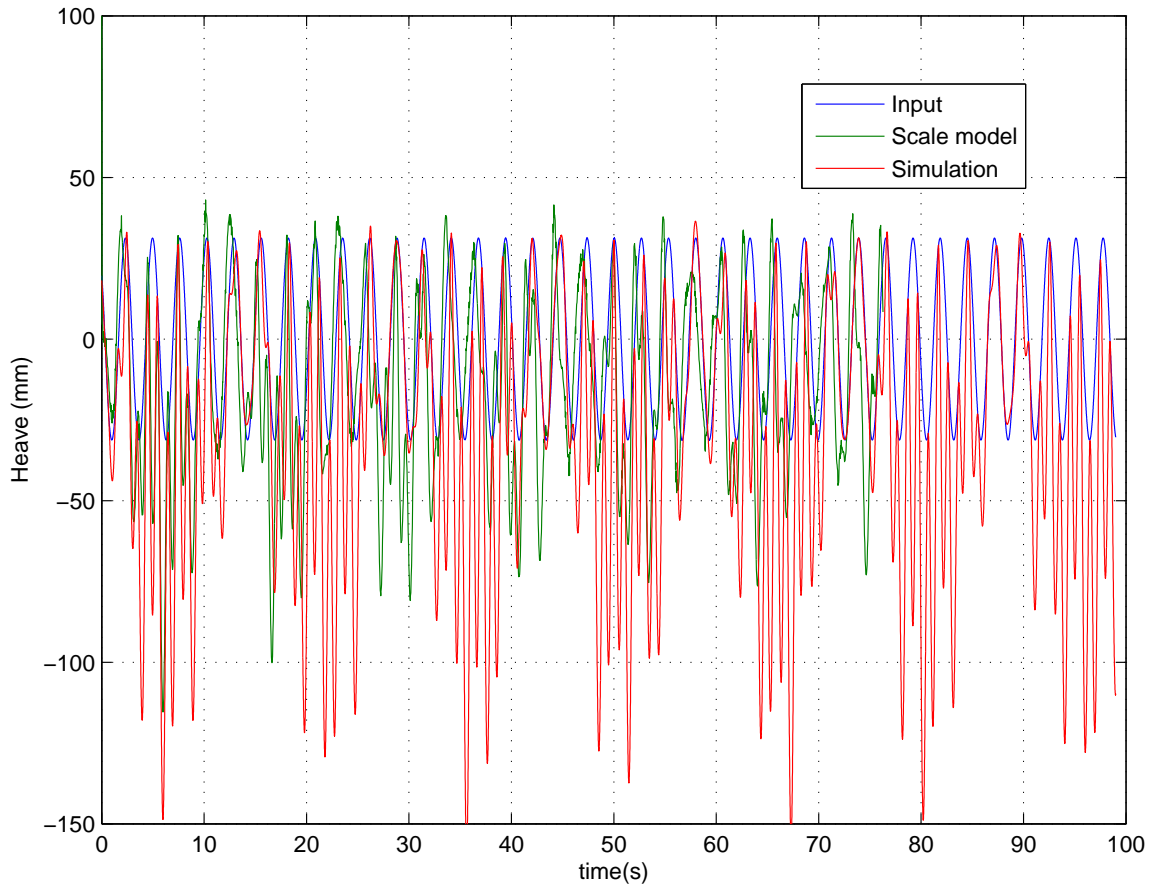


Figure 175. Heave time histories for simulated, scale-model, and input data for the uncontrolled case. (Simulation parameters: $\rho = 0$ degrees, $\vec{P}_{8/1,z} = 12.7$ mm, with a sinusoidal forcing function of $x_s = 31.25$ mm at a period of 2.65 seconds, $z_s = 31.25$ mm at a period of 2.65 seconds, and $\theta_s = 5^\circ$ at a period of 2.12 seconds.)

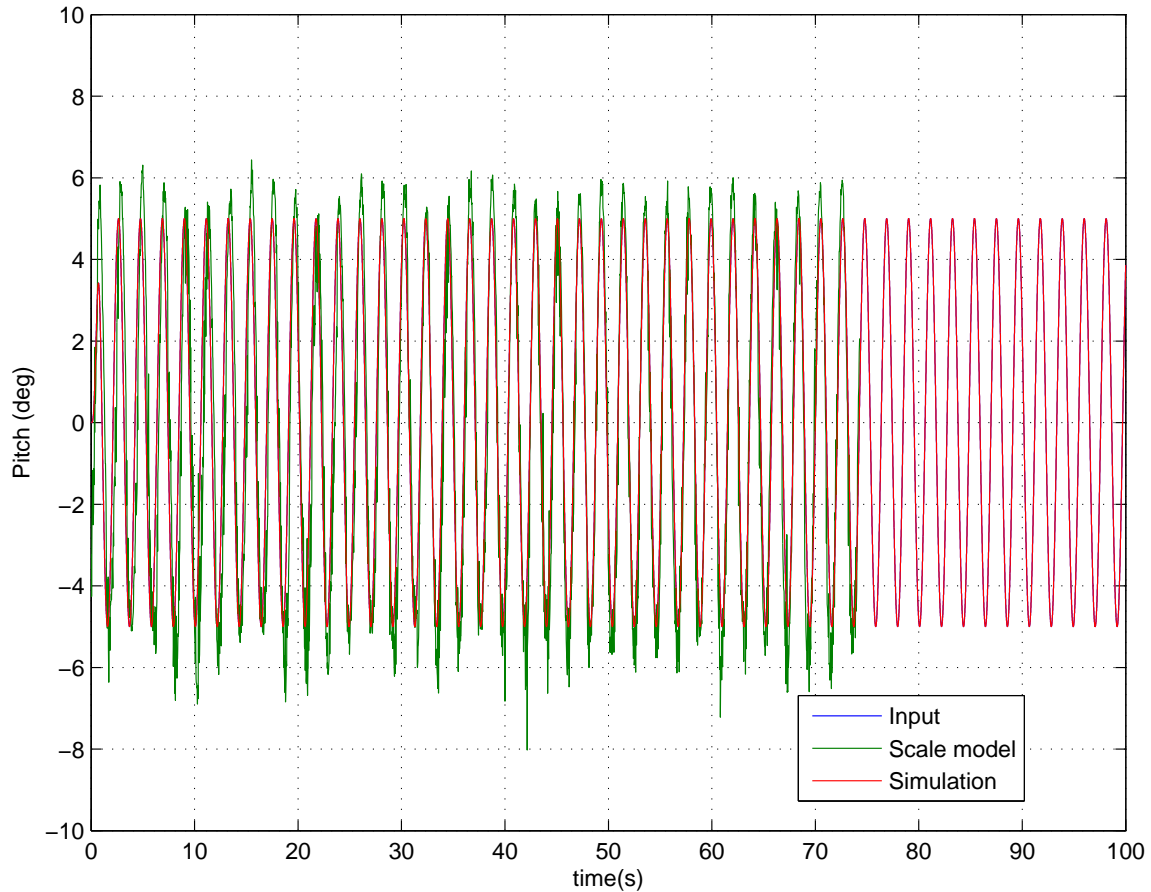


Figure 176. Pitch angle time histories for simulated, scale-model, and input data for the uncontrolled case. (Simulation parameters: $\rho = 0$ degrees, $\vec{P}_{8/1,z} = 12.7$ mm, with a sinusoidal forcing function of $x_s = 31.25$ mm at a period of 2.65 seconds, $z_s = 31.25$ mm at a period of 2.65 seconds, and $\theta_s = 5^\circ$ at a period of 2.12 seconds.)

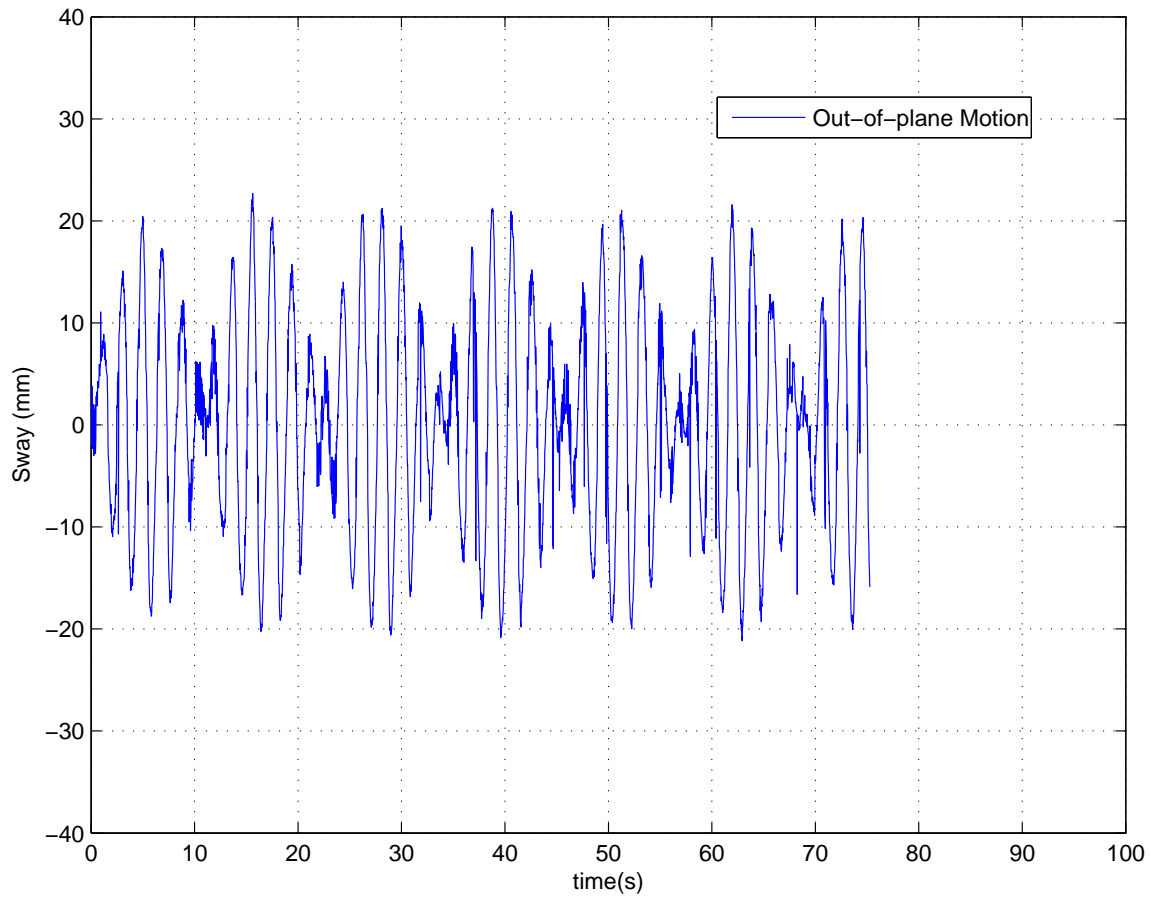


Figure 177. Out-of-plane (sway) time histories for simulated, scale-model, and input data for the uncontrolled case. The magnitude of the out-of-plane motion is about +/- 20 mm. (Simulation parameters: $\rho = 0$ degrees, $\vec{P}_{8/1,z} = 12.7$ mm, with a sinusoidal forcing function of $x_s = 31.25$ mm at a period of 2.65 seconds, $z_s = 31.25$ mm at a period of 2.65 seconds, and $\theta_s = 5^\circ$ at a period of 2.12 seconds.)

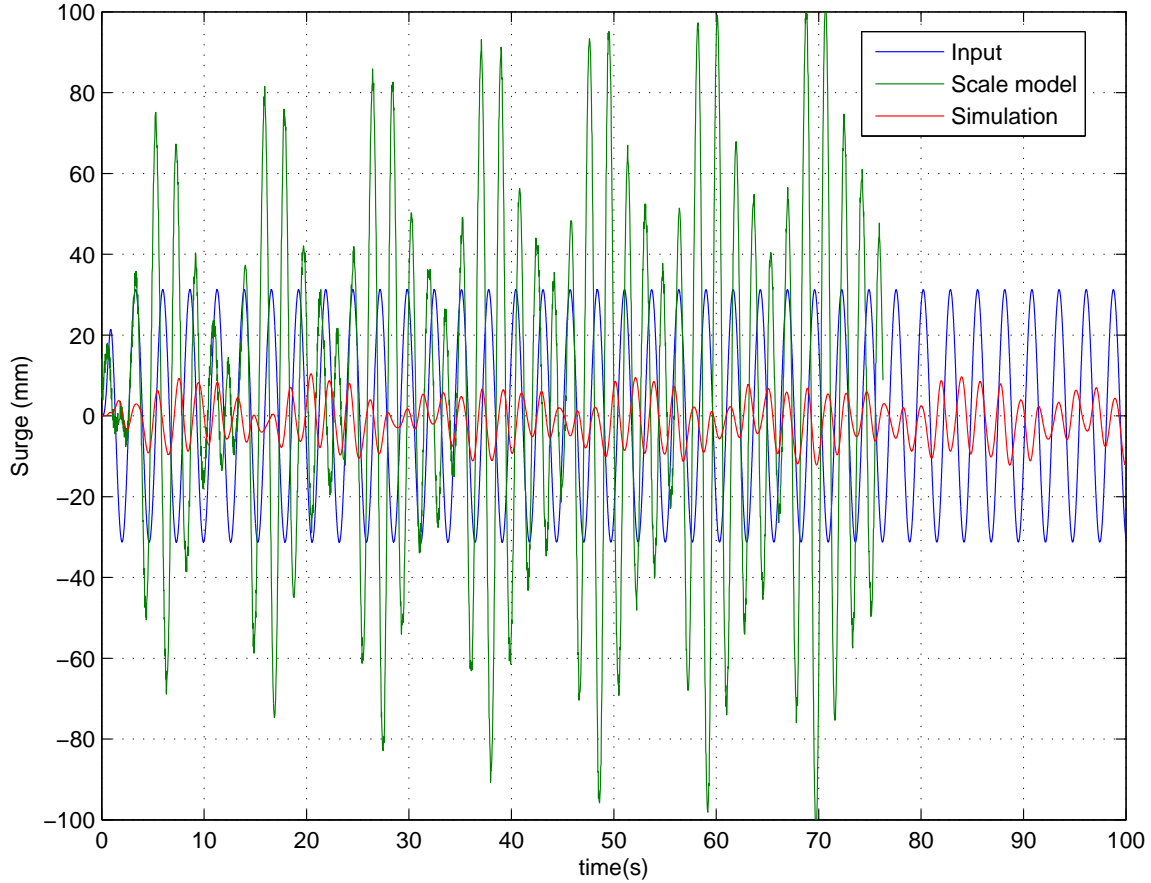


Figure 178. Surge time histories for simulated, scale-model, and input data for the controlled case. (Simulation parameters: $\rho = 0$ degrees, $\bar{P}_{8/1,z} = 12.7$ mm, with a sinusoidal forcing function of $x_s = 31.25$ mm at a period of 2.65 seconds, $z_s = 31.25$ mm at a period of 2.65 seconds, and $\theta_s = 5^\circ$ at a period of 2.12 seconds.)

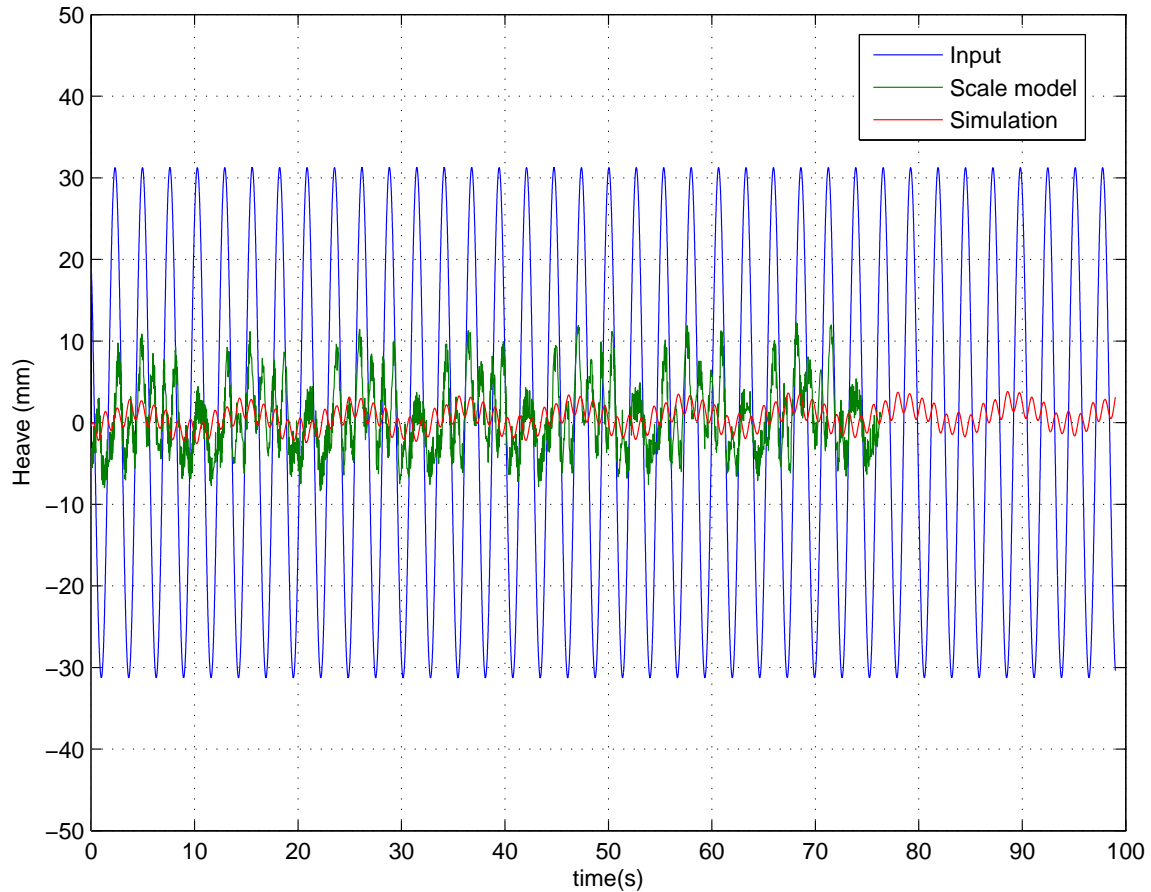


Figure 179. Heave time histories for simulated, scale-model, and input data for the controlled case. (Simulation parameters: $\rho = 0$ degrees, $\vec{P}_{8/1,z} = 12.7$ mm, with a sinusoidal forcing function of $x_s = 31.25$ mm at a period of 2.65 seconds, $z_s = 31.25$ mm at a period of 2.65 seconds, and $\theta_s = 5^\circ$ at a period of 2.12 seconds.)

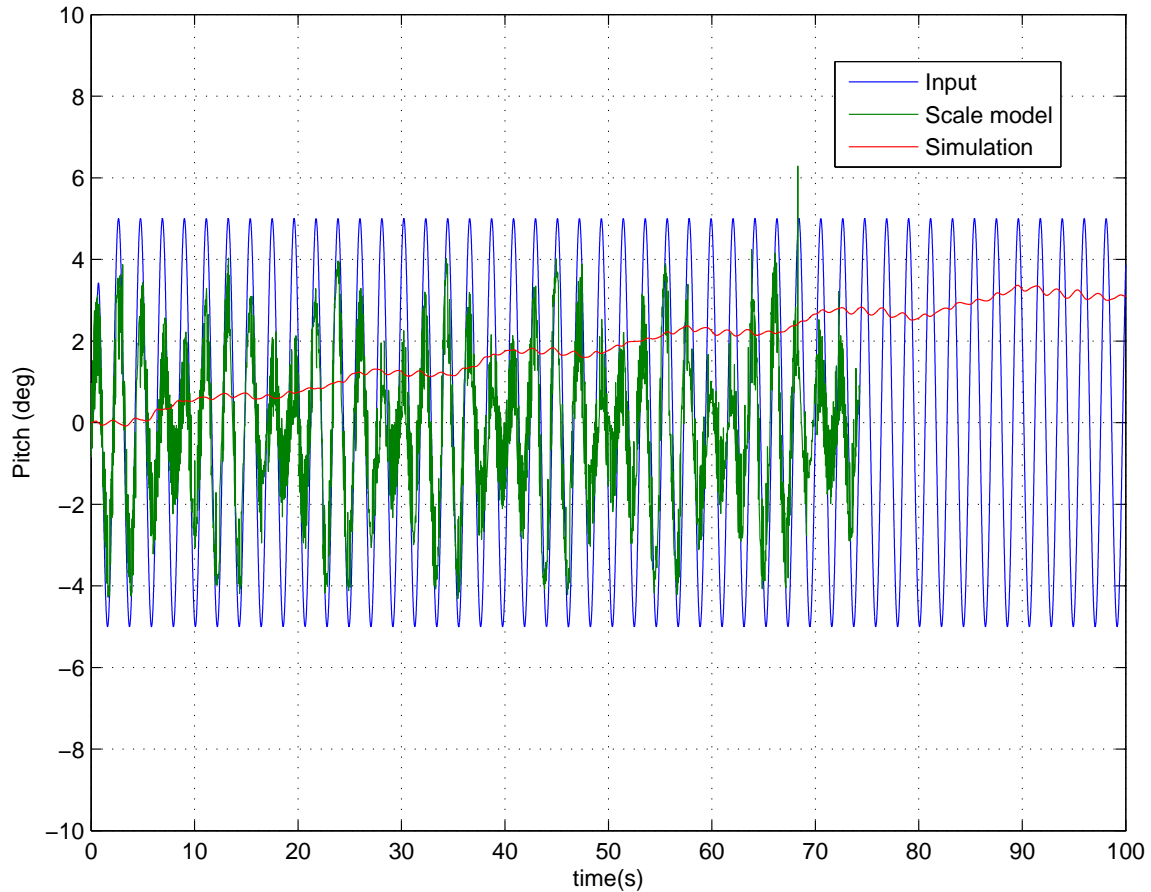


Figure 180. Pitch angle time histories for simulated, scale-model, and input data for the controlled case. (Simulation parameters: $\rho = 0$ degrees, $\vec{F}_{8/1,z} = 12.7$ mm, with a sinusoidal forcing function of $x_s = 31.25$ mm at a period of 2.65 seconds, $z_s = 31.25$ mm at a period of 2.65 seconds, and $\theta_s = 5^\circ$ at a period of 2.12 seconds.)

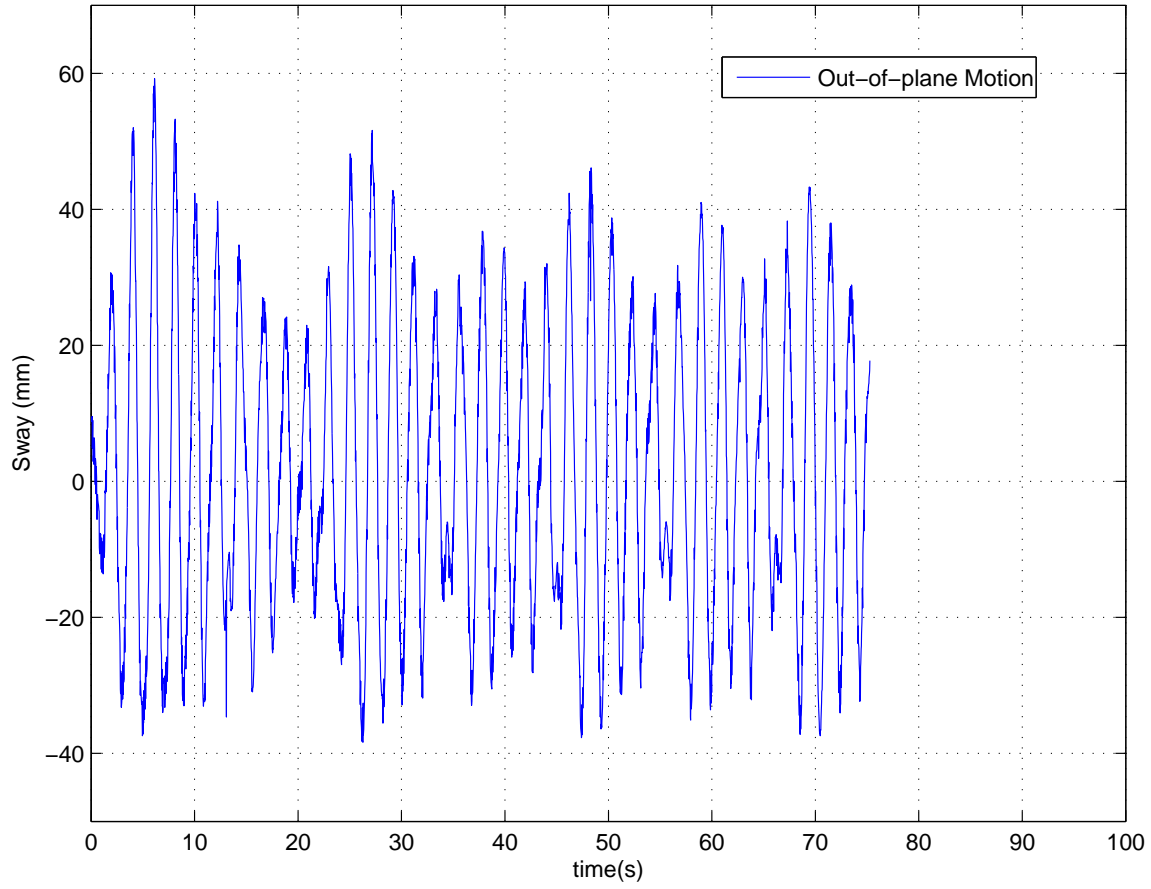


Figure 181. Out-of-plane (sway) time histories for simulated, scale-model, and input data for the controlled case. The magnitude of the peaks of the out-of-plane motion is about ± 40 mm. (Simulation parameters: $\rho = 0$ degrees, $\vec{P}_{8/1,z} = 12.7$ mm, with a sinusoidal forcing function of $x_s = 31.25$ mm at a period of 2.65 seconds, $z_s = 31.25$ mm at a period of 2.65 seconds, and $\theta_s = 5^\circ$ at a period of 2.12 seconds.)



Figure 182. Photograph of jib top of scale crane model showing warping. This warping may produce out-of-plane motion during controlled cases with significant luffing and hoisting motion.

Run ID	I-K Control Condition	Displacement Metrics			Motion Reduction (%)		
		Simulation (mm)	Scale Model (mm)	Input (mm)	Relative to Input Simulation Model	Relative to Input Model	Relative to Uncontrolled Model
Surge	Uncontrolled	45.7	38.9	19.8	(130.8)	(96.5)	-
	Controlled	1.3	5.1	19.8	93.4	74.2	97.2
Surge, rho=10	Uncontrolled	11.8	38.8	19.8	40.4	(96.0)	-
	Controlled	0.8	5.3	19.8	96.0	73.2	93.2
Surge, rho=11	Uncontrolled	19.8	20.6	19.8	0.0	(4.0)	-
	Controlled	0.2	0.6	19.8	99.0	97.0	99.0
Heave	Uncontrolled	243.1	165.4	20.0	(1115.5)	(727.0)	-
	Controlled	9.9	10.9	20.0	50.5	45.5	95.9
Combined	Uncontrolled	230.3	162.3	36.4	(532.7)	(345.9)	-
	Controlled	12.9	35.5	36.4	64.6	2.5	94.4
							78.1

Table 6. Comparison of simulated and scale-model results using the displacement metric, $J_{L+\theta}$.

THIS PAGE INTENTIONALLY LEFT BLANK

VIII. CONCLUSIONS & FUTURE WORK

In this final chapter the results discussed earlier in this dissertation will be restated, the contribution that this work embodies will be assessed, and areas for future work identified.

A. CONCLUSIONS

To first summarize the results, the motion compensation controller based on an inverse kinematic feed-forward structure was up to 99% effective in reducing the motion response in simulation, when compared to the uncontrolled system (Chapter VI).

This result was supported by the physical scale-model results with the motion compensation effectiveness measured to be between 78% and 99% relative to the uncontrolled system (Chapter VII).

The use of a weighted norm formulation for the inverse of the Jacobian to generate the actuator commands offered the opportunity to investigate various schemes to influence the control solution. While it was determined that a straightforward application of a consumed-power based approach did not yield any significant results, the ability to reduce or eliminate specific actuator participation in the solution does appear to be feasible and have operational relevance (Chapter IV).

This solution technique could not have been used without the introduction of the hoist-fall angle, ρ as a dynamic quantity into the formulation. The ρ -angle offset was also found to have beneficial properties for passive motion reduction through the influence on the natural frequency of the planar system, which could also serve to separate in frequency the in-plane and out-of-plane dynamics (Chapter III).

Engineers designing new capabilities for shipboard cranes have benefited from advancements in machinery control technology and the accumulated experience of logistics operations over the past thirty years. Several single crane solutions exist

that show promise towards a safe and efficient at-sea capability to transfer cargo up to the safe working load of a single jib. The dual crane solution presented here is an attempt to progress to active motion compensation for multiple crane lifts. This capability has potential utility to both the military and commercial sectors. In particular, the ability to deploy large structures such as vehicle discharge ramps or barge sections from a vessel while underway or at anchor could support current and future sustainment paradigms for expeditionary operations. Multiple crane control appears feasible, but much work remains to develop this approach into a fielded capability.

B. CONTRIBUTION

This work has provided additional insight into the control of multiple manipulators (cranes) that do not completely restrain the payload in an environment where base motion disturbances are present. The literature review that was conducted as part of this dissertation disclosed a paucity of work in this area. Related areas such as multiple manipulators in an industrial setting and motion compensation for single cranes exist separately, but have not been brought together such as was done in this dissertation. It is the hope of the author, that a contribution of this dissertation will be the stimulation of interest in this area, both for additional fundamental research and for development leading to implementation and operation in the Fleet. The author is looking forward to collaborating with other researchers that can apply more sophisticated analysis and synthesis techniques than were attempted herein.

C. FUTURE WORK

Many topics for future work were identified during the course of the development of this dissertation - several were attractive to pursue, but were beyond the scope of this effort either by departing too far from the central focus of this effort or by offering no solution within the time frame allotted for completion.

A natural extension of this research is a complete model that includes both the in-plane and out-of-plane dynamics. Developing a full three-dimensional model will provide a definitive confirmation or refutation of the supposition that the in-plane and out-of-plane dynamics are naturally decoupled.

The dynamic model should be expanded to include more realistic representations of sensor and actuator dynamics and non-linear effects such as rate saturation.

The development of a complete model also facilitates the application of payload trajectory control. The inverse kinematic control derivation included the provision for commanded rate terms beyond the commands attributable to the ship motion inputs - these terms could be exploited along with path planning algorithms to implement a fully automated manipulation of large payloads such as the causeway sections or ship sideport ramps.

Within the framework of a numerical simulation and even in the physical model, the motion compensation was shown to be effective. However, as further development progresses towards full-scale implementation the accumulation of unmodeled dynamics and the presence of disturbances uncorrelated with ship motion are going to dictate that some form of feedback control be added. The inverse kinematic control may simplify the design of the feedback control system by reducing the residual motion to a magnitude that is amenable to a linear rate-based approach.

Much more time could have been devoted to the properties of the weighted norm solution, including a more thorough investigation into the appropriate selection of weights for specific configurations defined by the hoist-fall offset, ρ , the jib angle, β , and the hoist cable length, L_h . It is certainly intuitive to recognize that there are preferred actuators for basic motions; e.g. hoisting for changing the payload height and translation of the load by luffing the jib , which may mean that a hoist-optimized scheme be employed when the ship motion is predominately heave. Of course this presupposes that a guaranteed stable algorithm for dynamically altering the weighting matrix exists or can be developed. Certainly the capability to change the weighting

matrix in response to machinery diagnostic inputs on the health and performance of the crane actuation system would be beneficial to a fielded system for reliable performance and robustness in the advent of an actuator failure.

APPENDIX A. PLANAR DUAL-CRANE DYNAMIC MODEL RESULTS

A. TIME HISTORY DATA FOR PLANAR DUAL-CRANE SYSTEM

An extensive set of time history data was generated from simulation of the planar dual-crane system for various values of the hoist-fall angle ρ and two surge ship-motion excitation conditions. The data set for each simulation run consists of plots of the x , z , and θ_p displacements, the inertial hoist-fall angle ρ_I , the hoist cable tensions, F_1 and F_2 and the calculation of the displacement metrics, J_l , J_θ , and $J_{l+\theta}$.

The data is presented here, organized first by the excitation condition and then by the value of the angle, ρ .

1. Surge Motion - 0.1 meter amplitude, 8.05 second period
 - i. $\rho = -10.0$ degrees
 - ii. $\rho = -7.5$ degrees
 - iii. $\rho = -5.0$ degrees

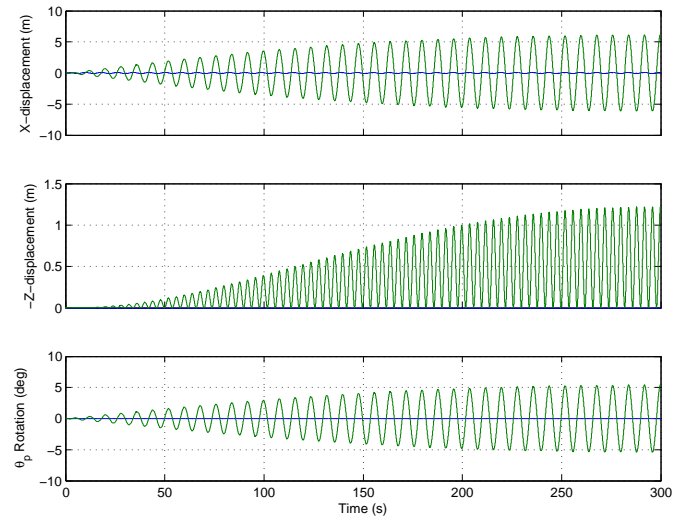


Figure 183. Time history of the payload motion for a 0.1 meter, 8.05 second period surge motion excitation with initial $\rho = -10.0$ degree. The blue trace is the ship motion and the payload response is shown in green. The maximum x and z displacements are reduced slightly. The payload rotation, θ_p is no longer small.

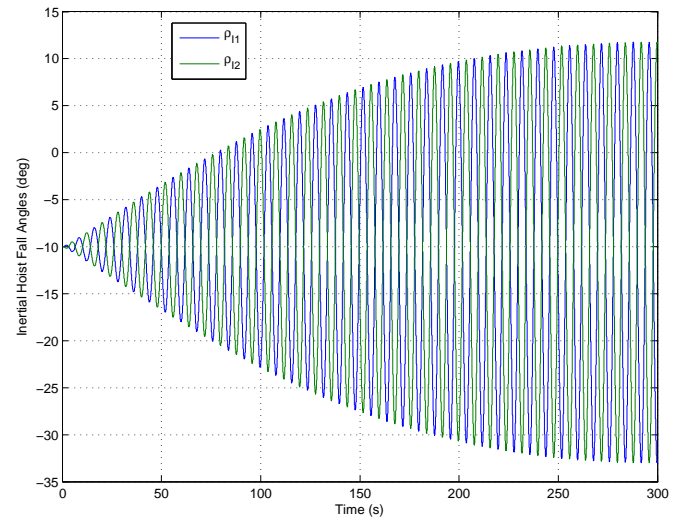


Figure 184. Time history of the inertial hoist fall angles, ρ_{I1} and ρ_{I2} for a 0.1 meter, 8.05 second period surge motion excitation with initial $\rho = -10$ degrees. The peak ρ angle response is more than 20 degrees on either side of the initial offset.

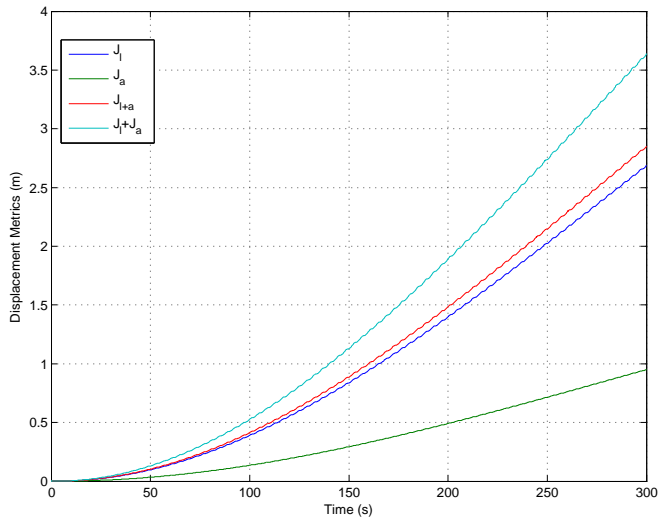


Figure 185. Time history of the calculation of the displacement metrics for a 0.1 meter, 8.05 second period surge motion excitation with initial $\rho = -10.0$ degree. Note that payload rotation is no longer zero, so J_θ is nonzero and there is a separation between J_l and $J_{l+\theta}$ and the sum of J_l and J_θ .

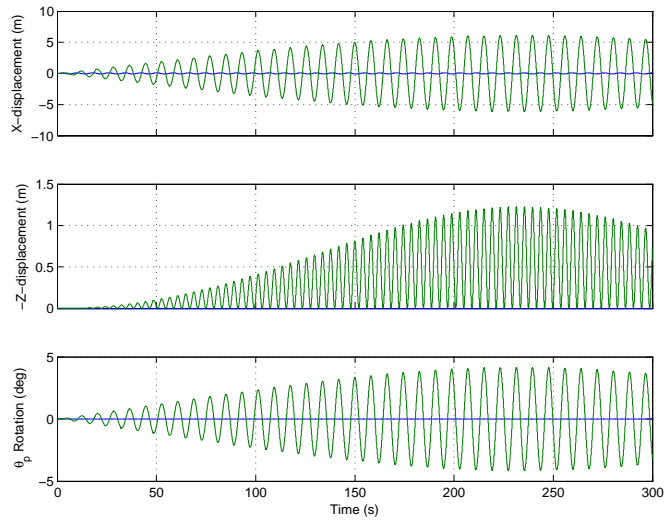


Figure 186. Time history of the payload motion for a 0.1 meter, 8.05 second period surge motion excitation with initial $\rho = -7.5$ degree. The blue trace is the ship motion and the payload response is shown in green.

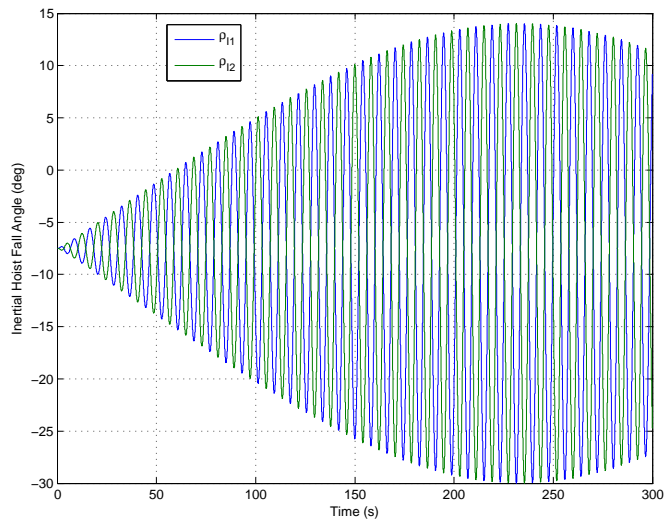


Figure 187. Time history of the inertial hoist fall angles, ρ_{I1} and ρ_{I2} for a 0.1 meter, 8.05 second period surge motion excitation with initial $\rho = -7.5$ degrees.

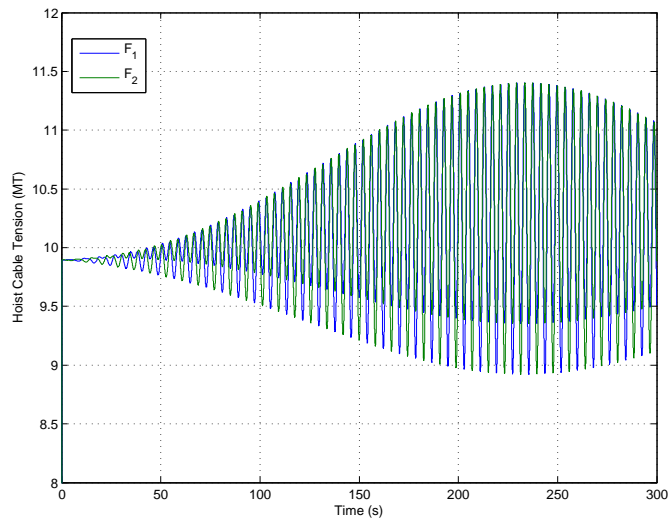


Figure 188. Time history of the hoist cable tensions, F_1 and F_2 in metric tons for a 0.1 meter, 8.05 second period surge motion excitation with initial $\rho = -7.5$ degrees.

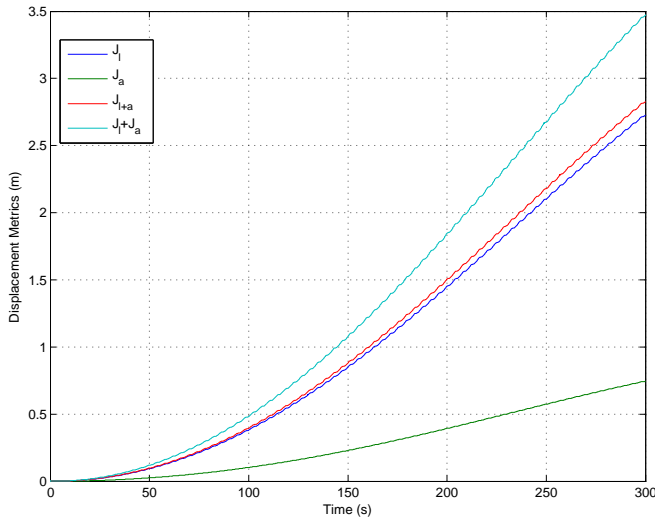


Figure 189. Time history of the calculation of the displacement metrics for a 0.1 meter, 8.05 second period surge motion excitation with initial $\rho = -7.5$ degree. Note that payload rotation is no longer zero, so J_θ is nonzero and there is a separation between J_l and $J_{l+\theta}$ and the sum of J_l and J_θ .

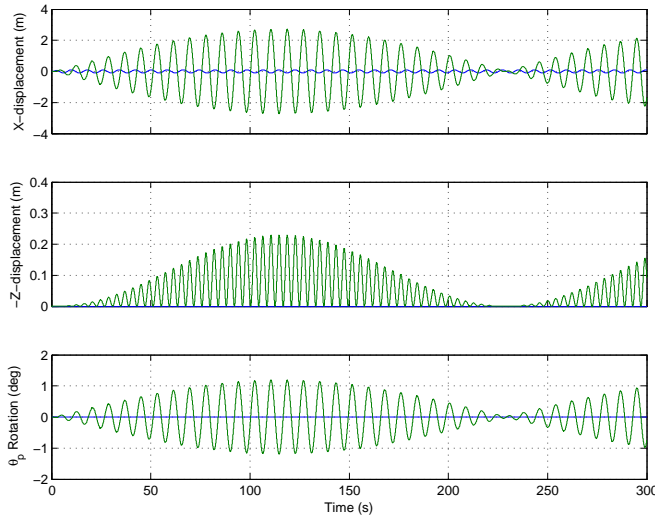


Figure 190. Time history of the payload motion for a 0.1 meter, 8.05 second period surge motion excitation with initial $\rho = -5.0$ degree. The blue trace is the ship motion and the payload response is shown in green.

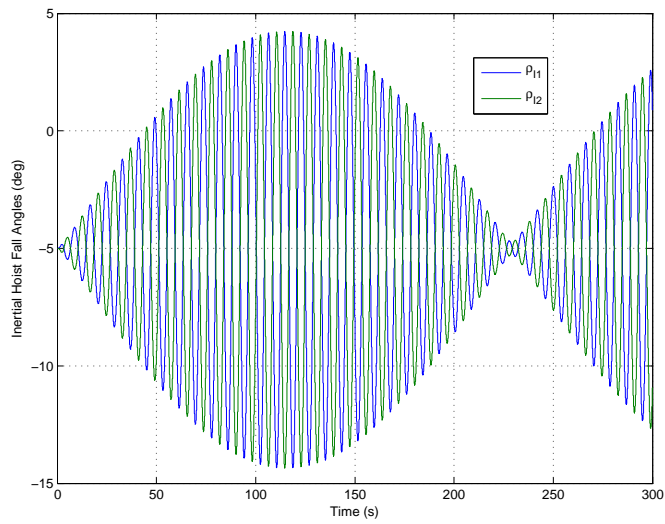


Figure 191. Time history of the inertial hoist fall angles, ρ_{I1} and ρ_{I2} for a 0.1 meter, 8.05 second period surge motion excitation with initial $\rho = -5.0$ degrees.

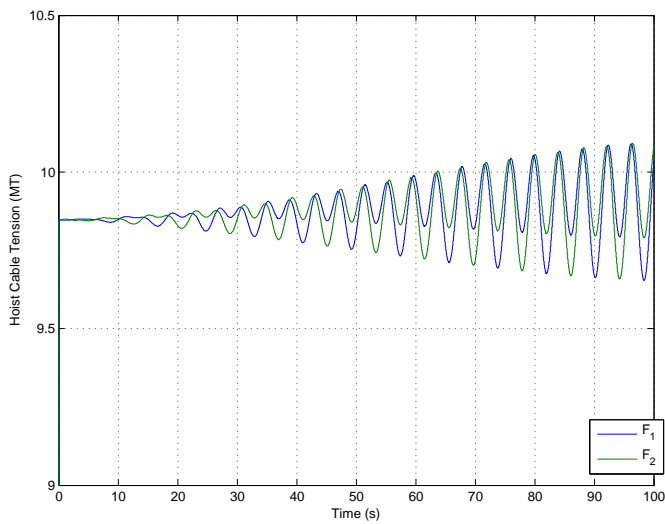


Figure 192. Time history of the hoist cable tensions, F_1 and F_2 in metric tons for a 0.1 meter, 8.05 second period surge motion excitation with initial $\rho = -5.0$ degrees.

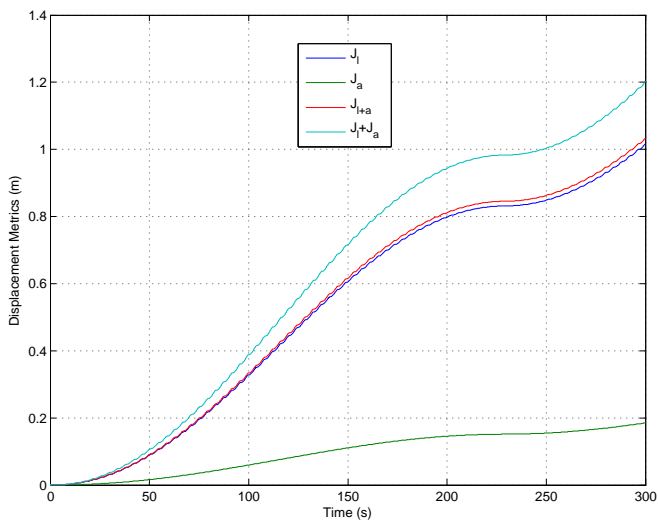


Figure 193. Time history of the calculation of the displacement metrics for a 0.1 meter, 8.05 second period surge motion excitation with initial $\rho = -5.0$ degree. Note that payload rotation is no longer zero, so J_θ is nonzero and there is a separation between J_l and $J_{l+\theta}$ and the sum of J_l and J_θ .

iv. $\rho = -2.5$ *degrees*

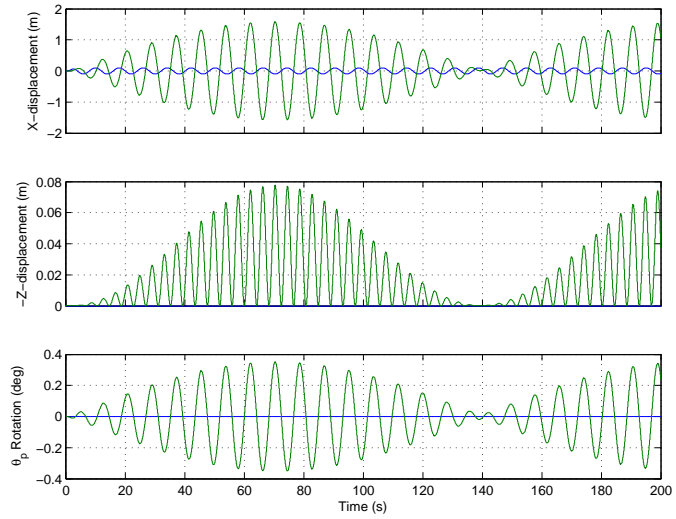


Figure 194. Time history of the payload motion for a 0.1 meter, 8.05 second period surge motion excitation with initial $\rho = -2.5$ degree. The blue trace is the ship motion and the payload response is shown in green.

v. $\rho = -1.0$ *degrees*

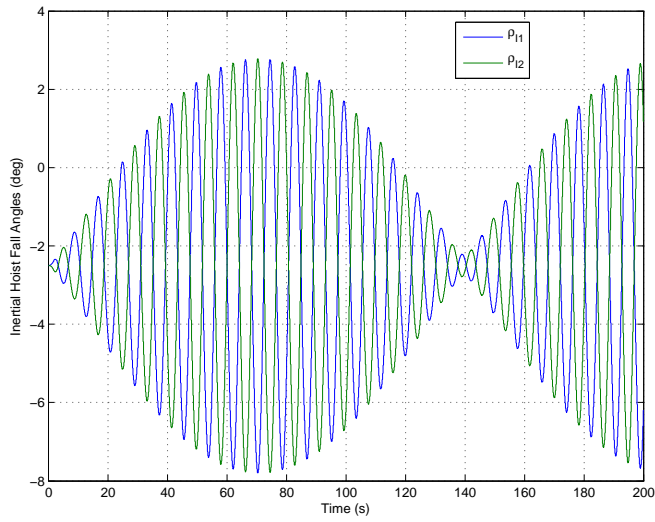


Figure 195. Time history of the inertial hoist fall angles, ρ_{I1} and ρ_{I2} for a 0.1 meter, 8.05 second period surge motion excitation with initial $\rho = -2.5$ degrees.

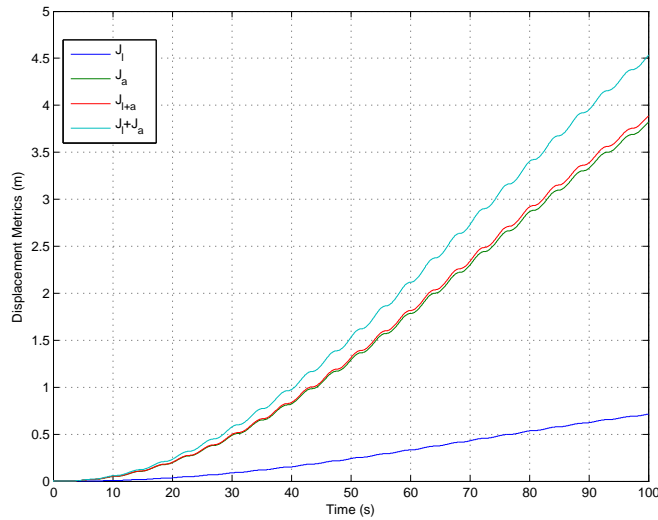


Figure 196. Time history of the calculation of the displacement metrics for a 0.1 meter, 8.05 second period surge motion excitation with initial $\rho = -5.0$ degree. Note that payload rotation is no longer zero, so J_θ is nonzero and there is a separation between J_l and $J_{l+\theta}$ and the sum of J_l and J_θ .

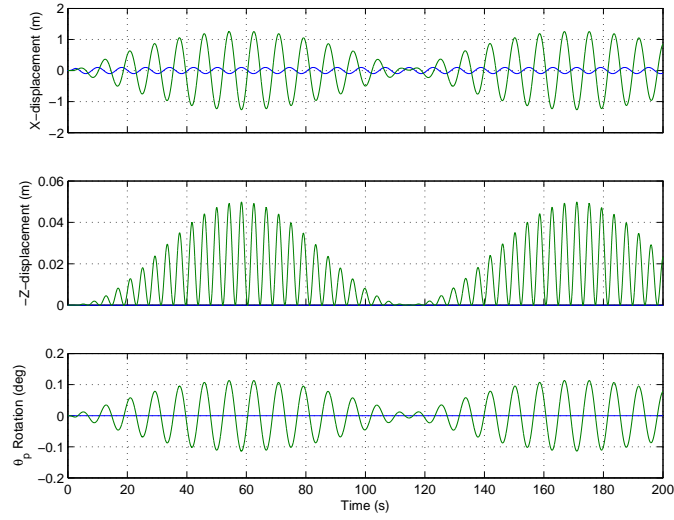


Figure 197. Time history of the payload motion for a 0.1 meter, 8.05 second period surge motion excitation with initial $\rho = -1.0$ degree. The blue trace is the ship motion and the payload response is shown in green. The maximum x and z displacements are reduced slightly. Note that the payload rotation, θ_p is small, but not zero as was the case for $\rho = 0$.

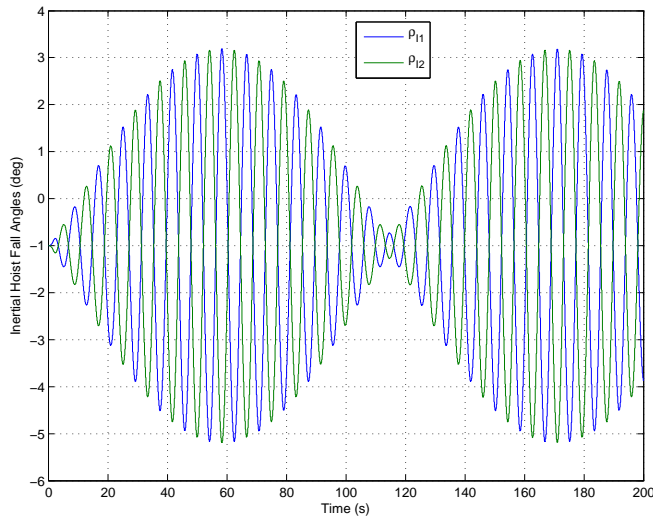


Figure 198. Time history of the inertial hoist fall angles, ρ_{I1} and ρ_{I2} for a 0.1 meter, 8.05 second period surge motion excitation with initial $\rho = -1$ degree. The peak ρ angle response is slightly more than 3.5 degrees for the given input.

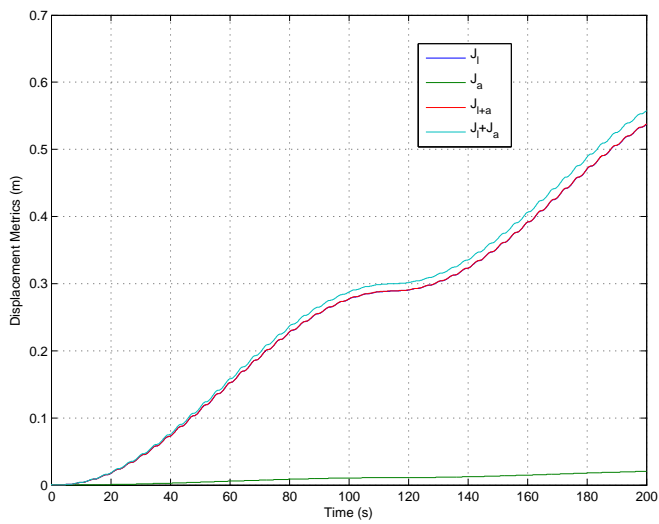


Figure 199. Time history of the calculation of the displacement metrics for a 0.1 meter, 8.05 second period surge motion excitation with initial $\rho = -1.0$ degree. Note that since the payload rotation is no longer zero, J_θ is nonzero and there is a separation between J_l and $J_{l+\theta}$ and the sum of J_l and J_θ .

vi. $\rho = 0.0$ degrees

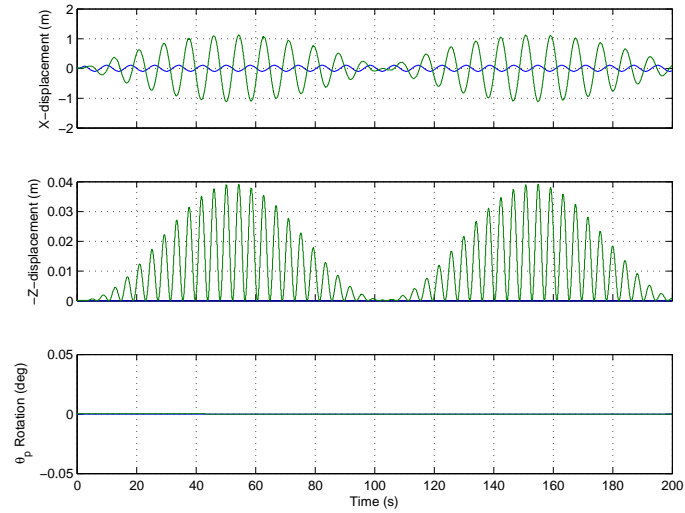


Figure 200. Time history of the payload motion for a 0.1 meter, 8.05 second period surge motion excitation with initial $\rho = 0$ degrees. The blue trace is the ship motion and the payload response is shown in green. Note that the payload rotation, θ_p about its pitch axis is essentially zero.

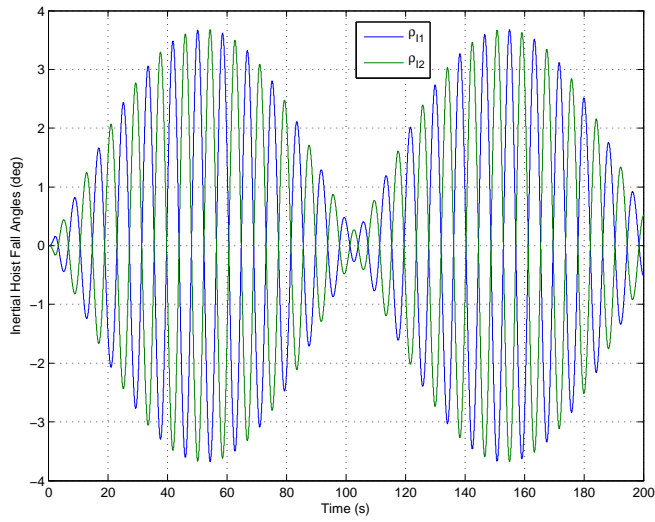


Figure 201. Time history of the inertial hoist fall angles, ρ_{I1} and ρ_{I2} for a 0.1 meter, 8.05 second period surge motion excitation with initial $\rho = 0$ degrees. The peak ρ angle response is slightly more than 3.5 degrees for the given input.

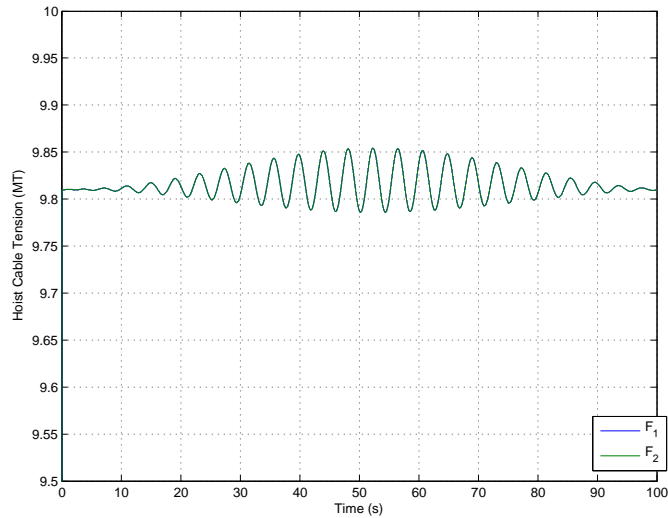


Figure 202. Time history of the hoist cable tensions, F_1 and F_2 in metric tons for a 0.1 meter, 8.05 second period surge motion excitation with initial $\rho = 0$ degrees. The peak response is approximately 0.5 percent above the initial (static) tension.

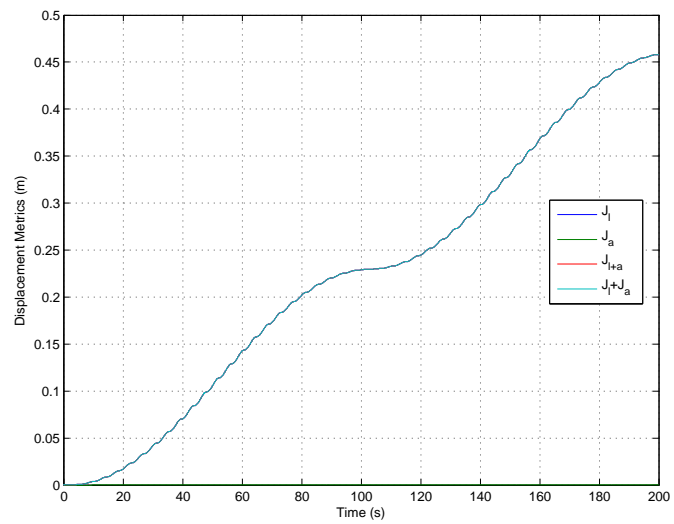


Figure 203. Time history of the calculation of the displacement metrics for a 0.1 meter, 8.05 second period surge motion excitation with initial $\rho = 0$ degrees. Note that since the payload rotation is essentially zero, there is no difference between J_l and $J_{l+\theta}$ and the sum of J_l and J_θ .

vii. $\rho = 1.0$ *degrees*

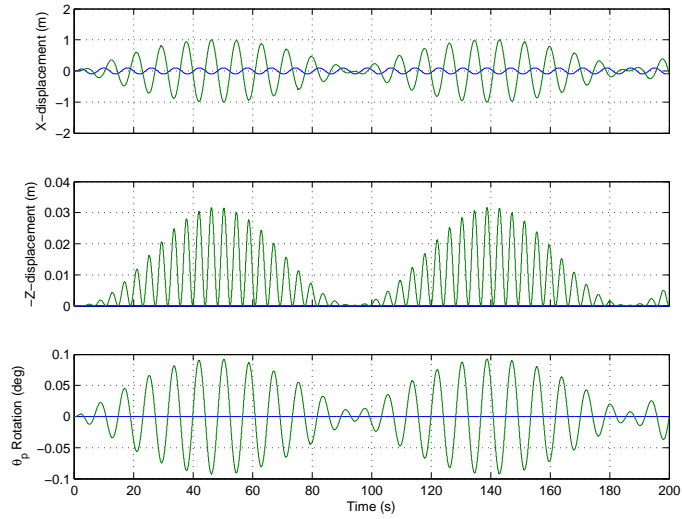


Figure 204. Time history of the payload motion for a 0.1 meter, 8.05 second period surge motion excitation with initial $\rho = 1.0$ degree. The blue trace is the ship motion and the payload response is shown in green. The maximum x and z displacements are reduced slightly. Note that the payload rotation, θ_p is small, but not zero as was the case for $\rho = 0$.

viii. $\rho = 2.5$ *degrees*

ix. $\rho = 5.0$ *degrees*

x. $\rho = 10.0$ *degrees*

xi. $\rho = 15.0$ *degrees*

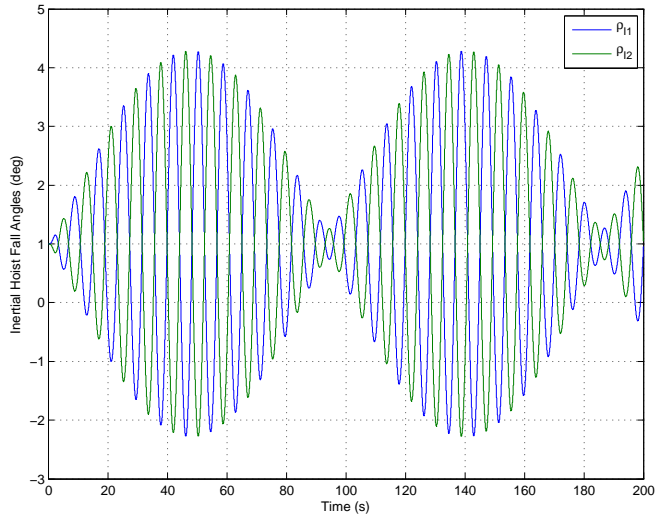


Figure 205. Time history of the inertial hoist fall angles, ρ_{I1} and ρ_{I2} for a 0.1 meter, 8.05 second period surge motion excitation with initial $\rho = 1.0$ degrees.

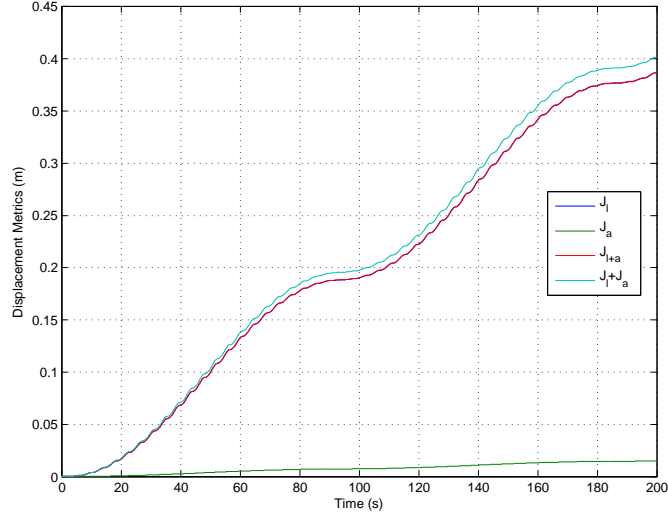


Figure 206. Time history of the calculation of the displacement metrics for a 0.1 meter, 8.05 second period surge motion excitation with initial $\rho = 1.0$ degree. Note that since the payload rotation is no longer zero, J_θ is nonzero and there is a separation between J_l and $J_{l+\theta}$ and the sum of J_l and J_θ .

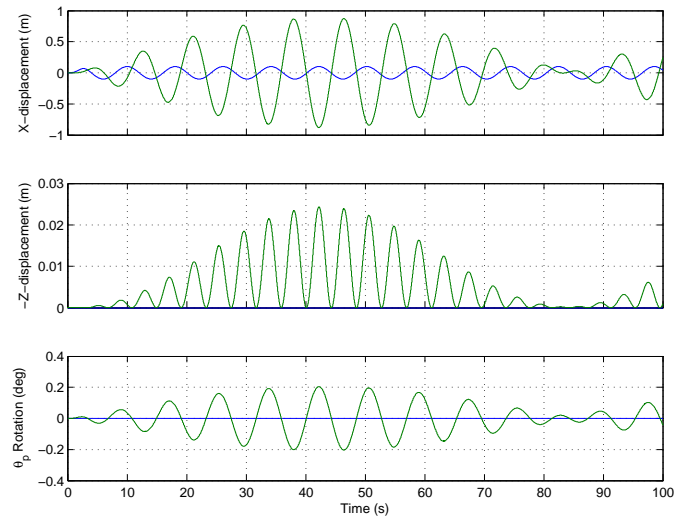


Figure 207. Time history of the payload motion for a 0.1 meter, 8.05 second period surge motion excitation with initial $\rho = 2.5$ degree. The blue trace is the ship motion and the payload response is shown in green.

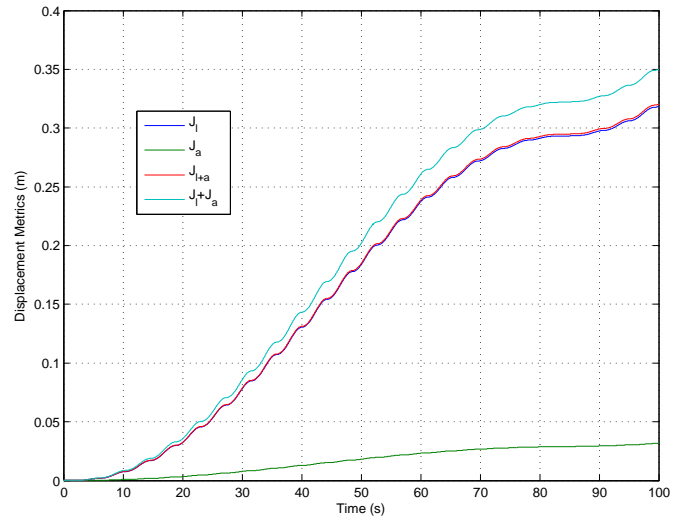


Figure 208. Time history of the calculation of the displacement metrics for a 0.1 meter, 8.05 second period surge motion excitation with initial $\rho = 2.5$ degree. Note that payload rotation is no longer zero, so J_θ is nonzero and there is a separation between J_l and $J_{l+\theta}$ and the sum of J_l and J_θ .

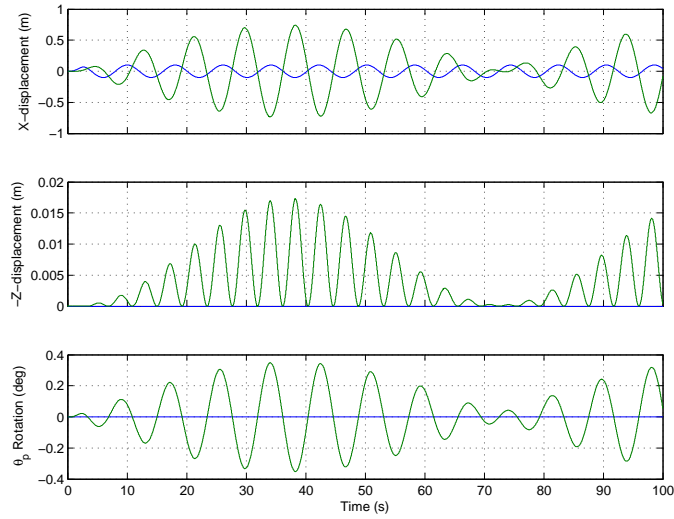


Figure 209. Time history of the payload motion for a 0.1 meter, 8.05 second period surge motion excitation with initial $\rho = 5.0$ degree. The blue trace is the ship motion and the payload response is shown in green.

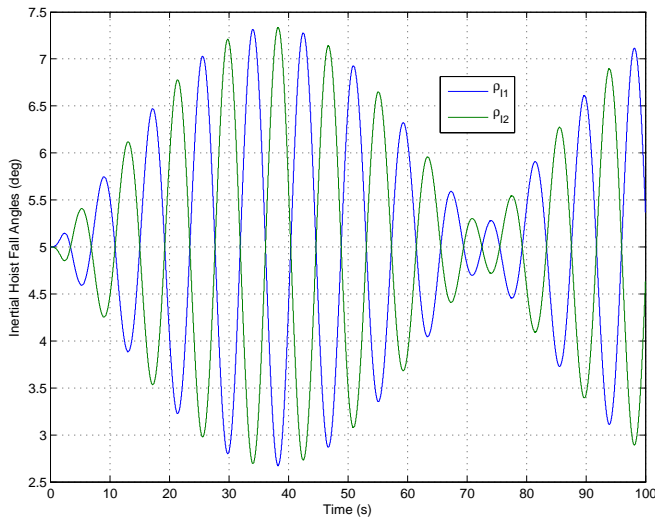


Figure 210. Time history of the inertial hoist fall angles, ρ_{I1} and ρ_{I2} for a 0.1 meter, 8.05 second period surge motion excitation with initial $\rho = 5.0$ degrees.

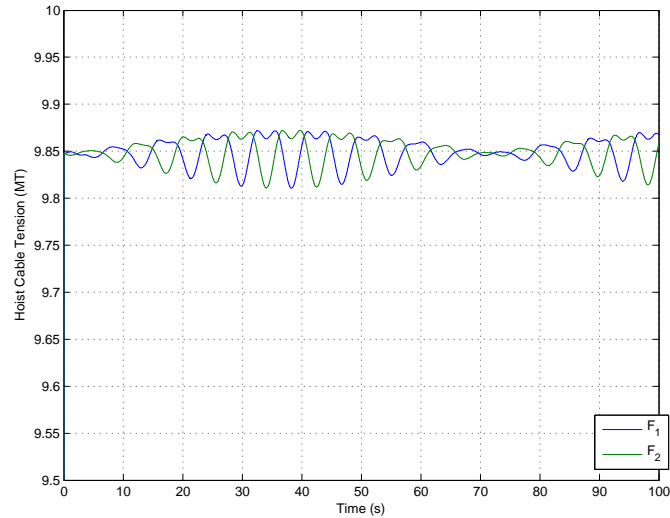


Figure 211. Time history of the hoist cable tensions, F_1 and F_2 in metric tons for a 0.1 meter, 8.05 second period surge motion excitation with initial $\rho = 5.0$ degrees.

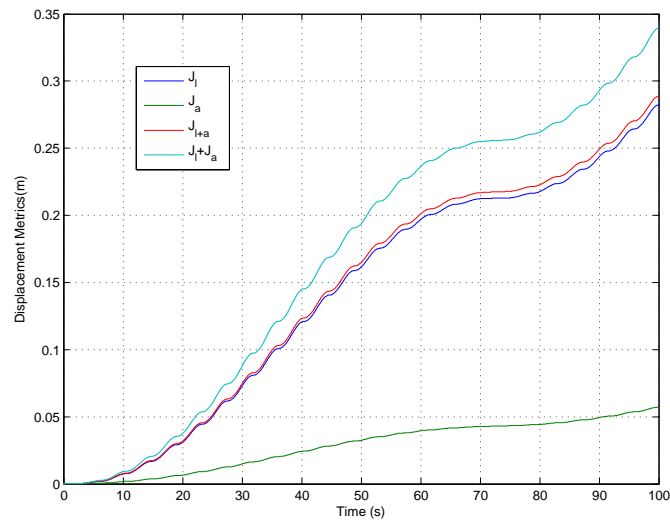


Figure 212. Time history of the calculation of the displacement metrics for a 0.1 meter, 8.05 second period surge motion excitation with initial $\rho = -5.0$ degree. Note that payload rotation is no longer zero, so J_θ is nonzero and there is a separation between J_l and $J_{l+\theta}$ and the sum of J_l and J_θ .

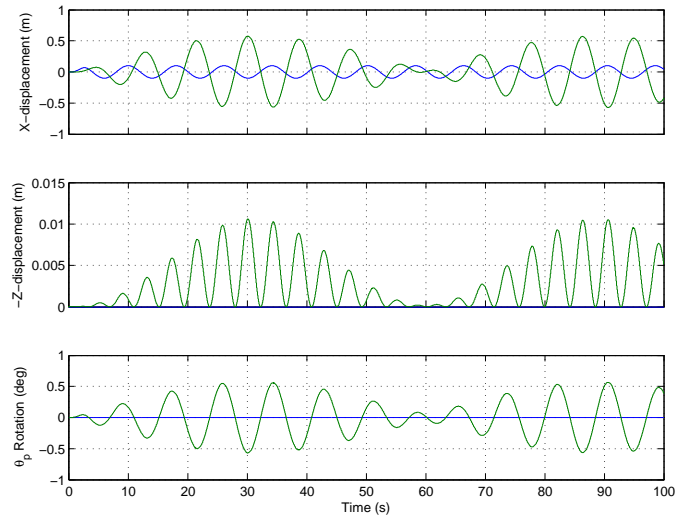


Figure 213. Time history of the payload motion for a 0.1 meter, 8.05 second period surge motion excitation with initial $\rho = 10.0$ degree. The blue trace is the ship motion and the payload response is shown in green.

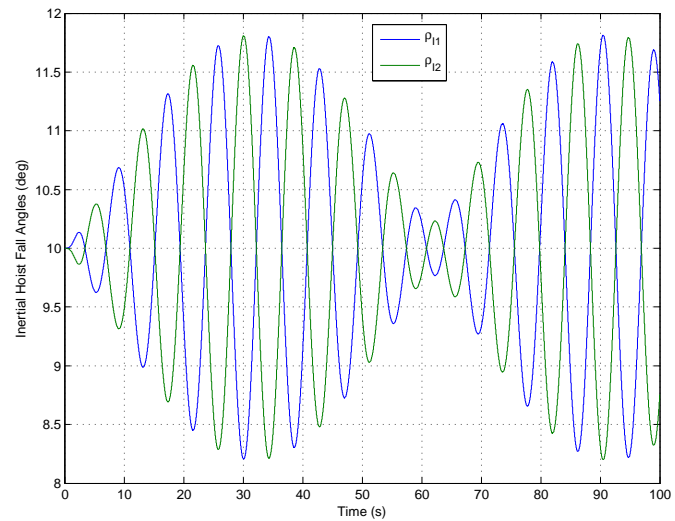


Figure 214. Time history of the inertial hoist fall angles, ρ_{I1} and ρ_{I2} for a 0.1 meter, 8.05 second period surge motion excitation with initial $\rho = 10.0$ degrees.

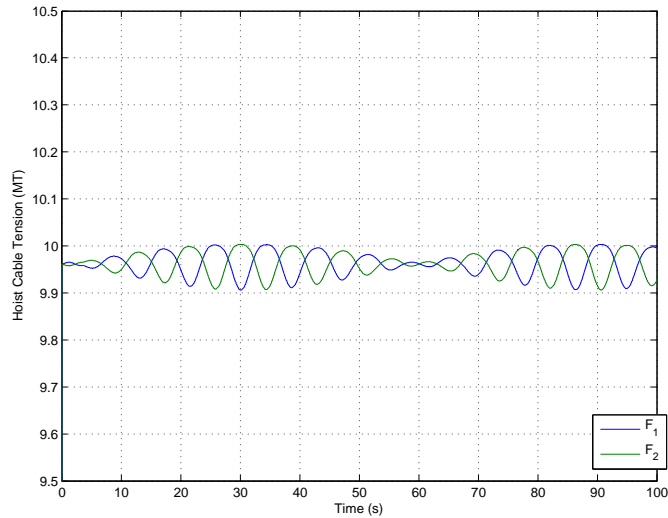


Figure 215. Time history of the hoist cable tensions, F_1 and F_2 in metric tons for a 0.1 meter, 8.05 second period surge motion excitation with initial $\rho = 10.0$ degrees.

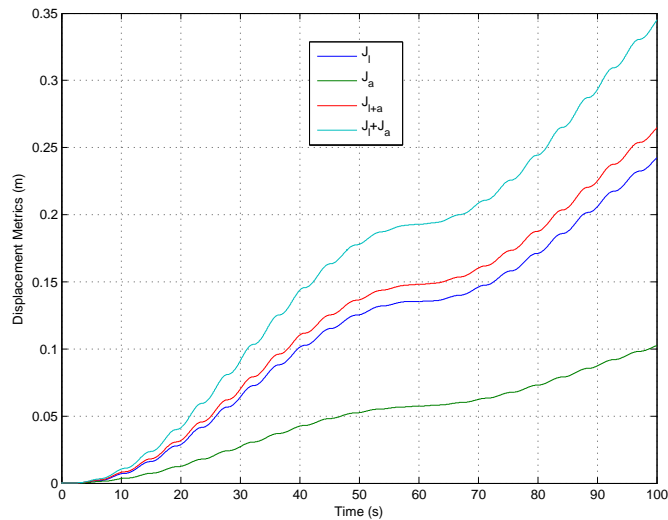


Figure 216. Time history of the calculation of the displacement metrics for a 0.1 meter, 8.05 second period surge motion excitation with initial $\rho = 10.0$ degree. Note that payload rotation is no longer zero, so J_θ is nonzero and there is a separation between J_l and $J_{l+\theta}$ and the sum of J_l and J_θ .

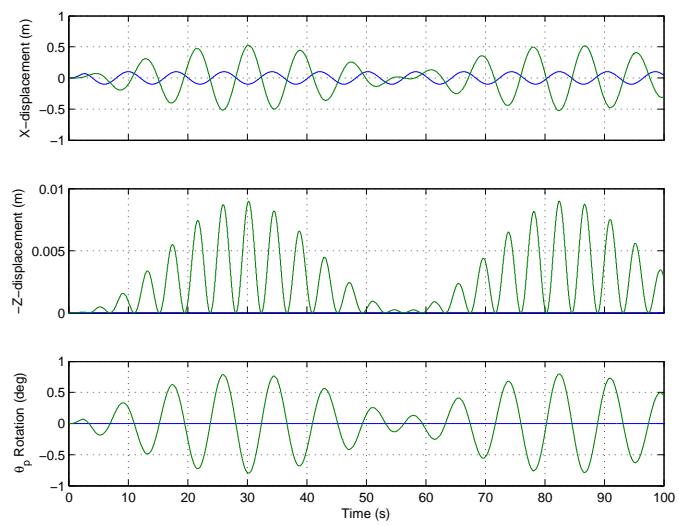


Figure 217. Time history of the payload motion for a 0.1 meter, 8.05 second period surge motion excitation with initial $\rho = 15.0$ degree. The blue trace is the ship motion and the payload response is shown in green.

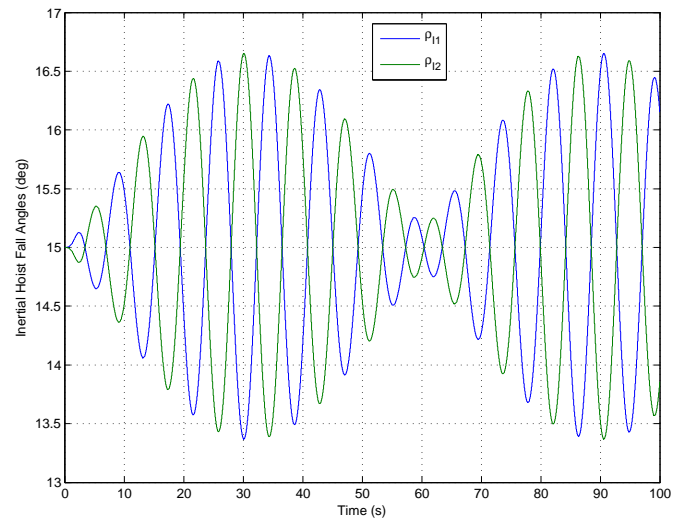


Figure 218. Time history of the inertial hoist fall angles, ρ_{I1} and ρ_{I2} for a 0.1 meter, 8.05 second period surge motion excitation with initial $\rho = 15.0$ degrees.

- xii.* $\rho = 20.0$ **degrees**
- xiii.* $\rho = 25.0$ **degrees**
- xiv.* $\rho = 30.0$ **degrees**
- xv.* $\rho = 35.0$ **degrees**

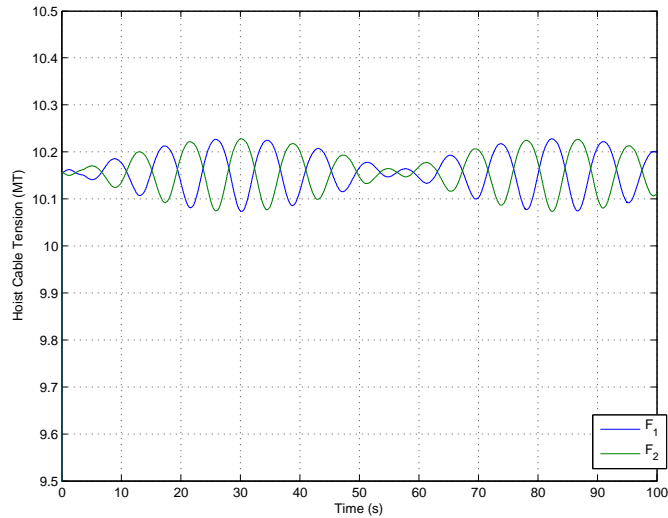


Figure 219. Time history of the hoist cable tensions, F_1 and F_2 in metric tons for a 0.1 meter, 8.05 second period surge motion excitation with initial $\rho = 15.0$ degrees.

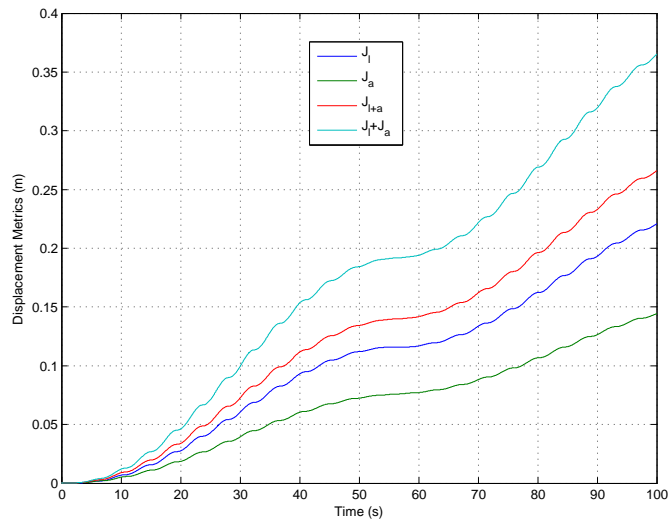


Figure 220. Time history of the calculation of the displacement metrics for a 0.1 meter, 8.05 second period surge motion excitation with initial $\rho = 15.0$ degree. Note that payload rotation is no longer zero, so J_θ is nonzero and there is a separation between J_l and $J_{l+\theta}$ and the sum of J_l and J_θ .

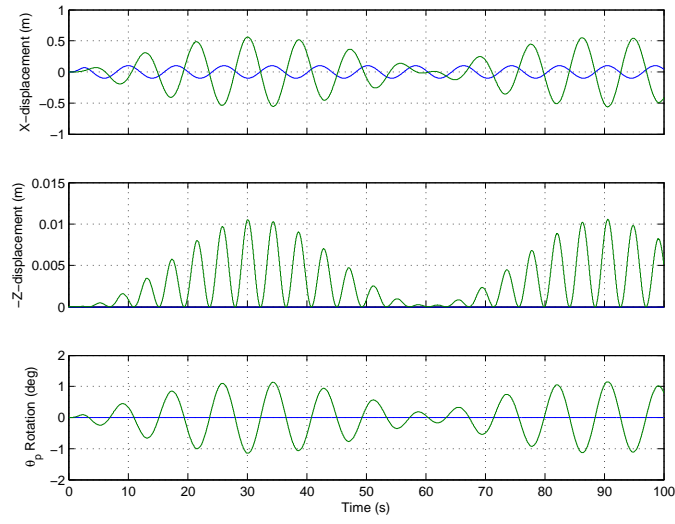


Figure 221. Time history of the payload motion for a 0.1 meter, 8.05 second period surge motion excitation with initial $\rho = 20.0$ degree. The blue trace is the ship motion and the payload response is shown in green.

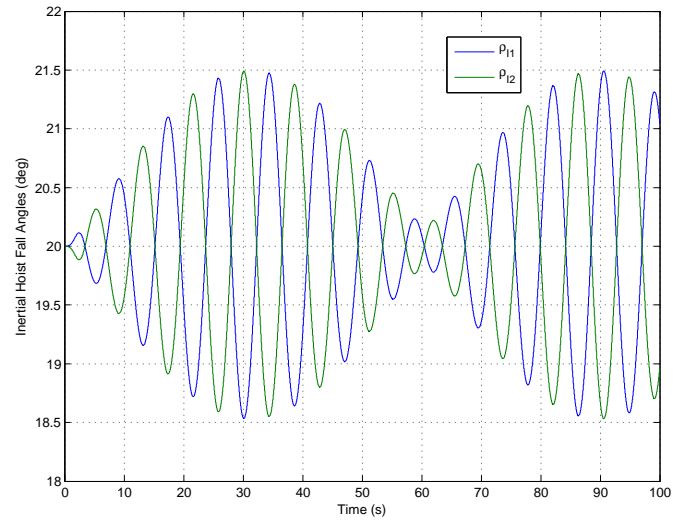


Figure 222. Time history of the inertial hoist fall angles, ρ_{I1} and ρ_{I2} for a 0.1 meter, 8.05 second period surge motion excitation with initial $\rho = 20.0$ degrees.

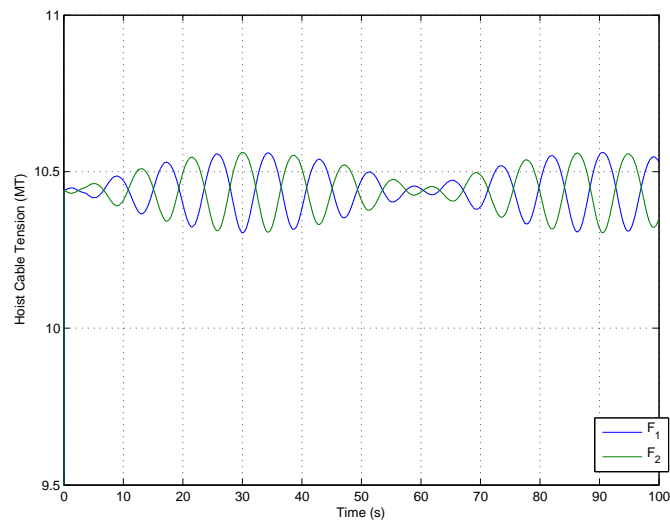


Figure 223. Time history of the hoist cable tensions, F_1 and F_2 in metric tons for a 0.1 meter, 8.05 second period surge motion excitation with initial $\rho = 20.0$ degrees.

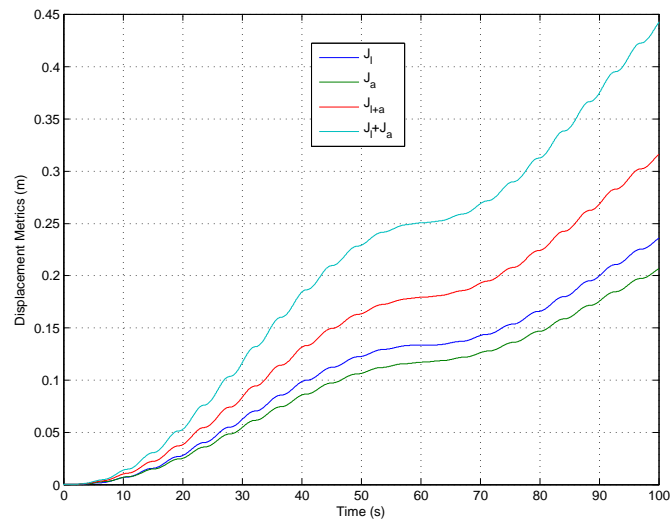


Figure 224. Time history of the calculation of the displacement metrics for a 0.1 meter, 8.05 second period surge motion excitation with initial $\rho = 20.0$ degree. Note that payload rotation is no longer zero, so J_θ is nonzero and there is a separation between J_l and $J_{l+\theta}$ and the sum of J_l and J_θ .

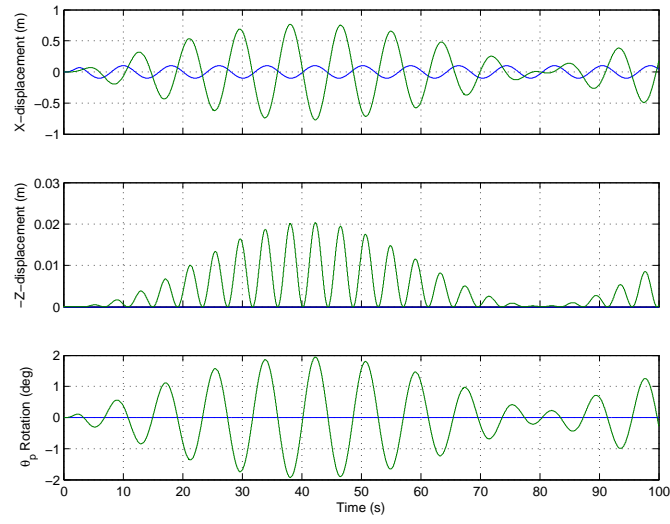


Figure 225. Time history of the payload motion for a 0.1 meter, 8.05 second period surge motion excitation with initial $\rho = 25.0$ degree. The blue trace is the ship motion and the payload response is shown in green.

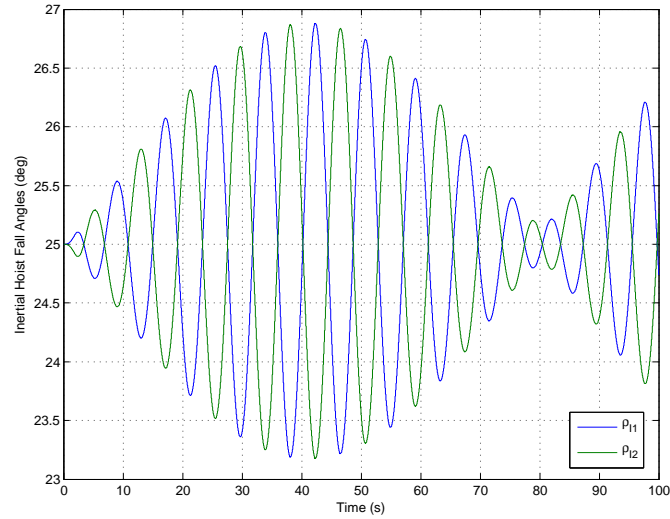


Figure 226. Time history of the inertial hoist fall angles, ρ_{I1} and ρ_{I2} for a 0.1 meter, 8.05 second period surge motion excitation with initial $\rho = 25.0$ degrees.

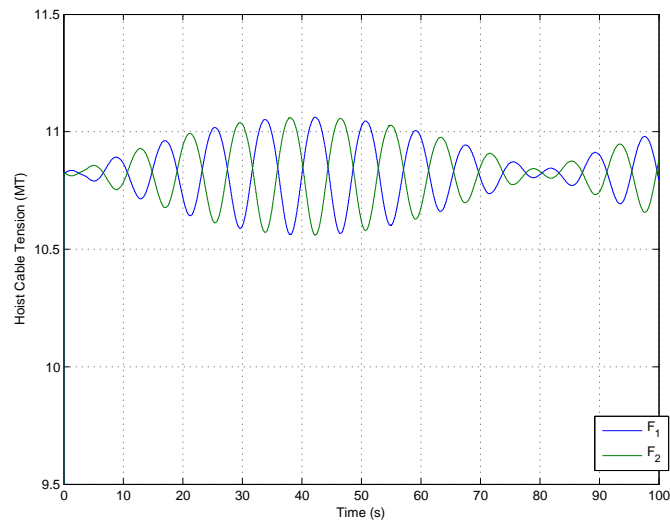


Figure 227. Time history of the hoist cable tensions, F_1 and F_2 in metric tons for a 0.1 meter, 8.05 second period surge motion excitation with initial $\rho = 25.0$ degrees.

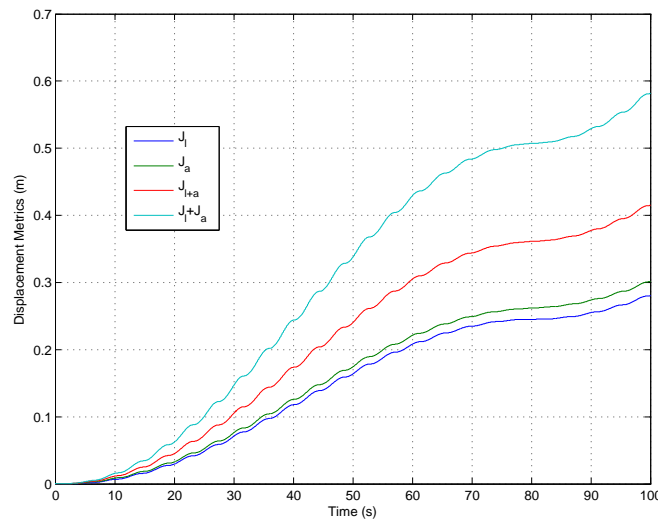


Figure 228. Time history of the calculation of the displacement metrics for a 0.1 meter, 8.05 second period surge motion excitation with initial $\rho = 25.0$ degree. Note that payload rotation is no longer zero, so J_θ is nonzero and there is a separation between J_l and $J_{l+\theta}$ and the sum of J_l and J_θ .

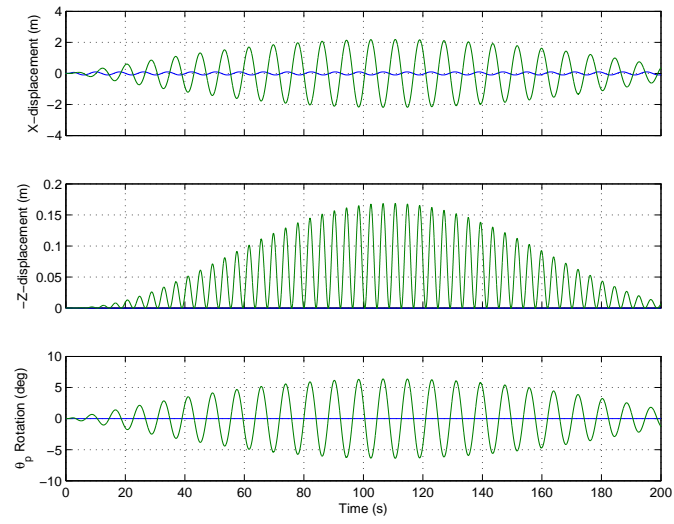


Figure 229. Time history of the payload motion for a 0.1 meter, 8.05 second period surge motion excitation with initial $\rho = 30.0$ degree. The blue trace is the ship motion and the payload response is shown in green.

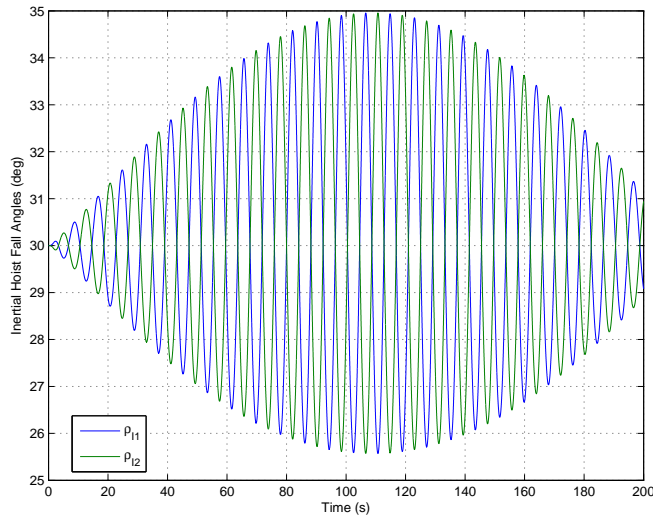


Figure 230. Time history of the inertial hoist fall angles, ρ_{I1} and ρ_{I2} for a 0.1 meter, 8.05 second period surge motion excitation with initial $\rho = 30.0$ degrees.

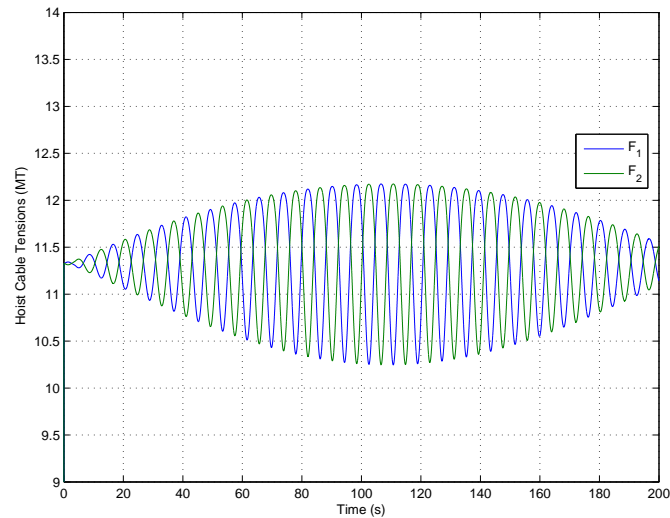


Figure 231. Time history of the hoist cable tensions, F_1 and F_2 in metric tons for a 0.1 meter, 8.05 second period surge motion excitation with initial $\rho = 30.0$ degrees.

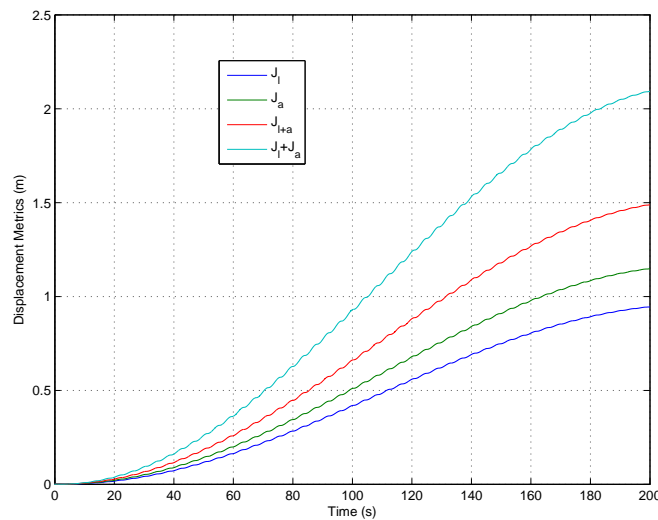


Figure 232. Time history of the calculation of the displacement metrics for a 0.1 meter, 8.05 second period surge motion excitation with initial $\rho = 30.0$ degree. Note that payload rotation is no longer zero, so J_θ is nonzero and there is a separation between J_l and $J_{l+\theta}$ and the sum of J_l and J_θ .

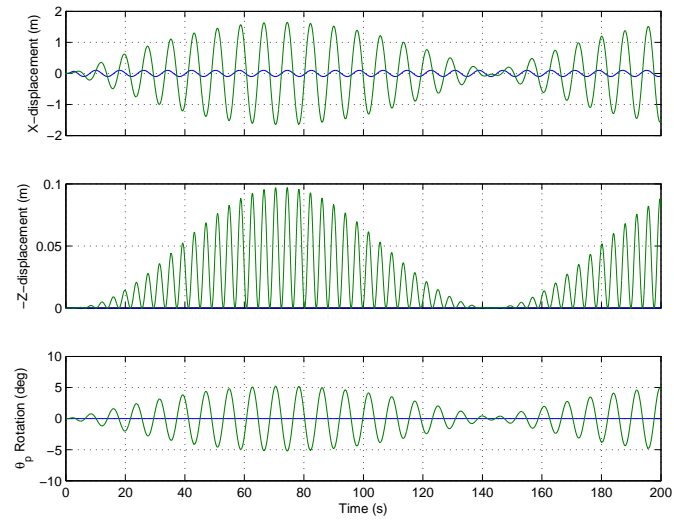


Figure 233. Time history of the payload motion for a 0.1 meter, 8.05 second period surge motion excitation with initial $\rho = 35.0$ degree. The blue trace is the ship motion and the payload response is shown in green.

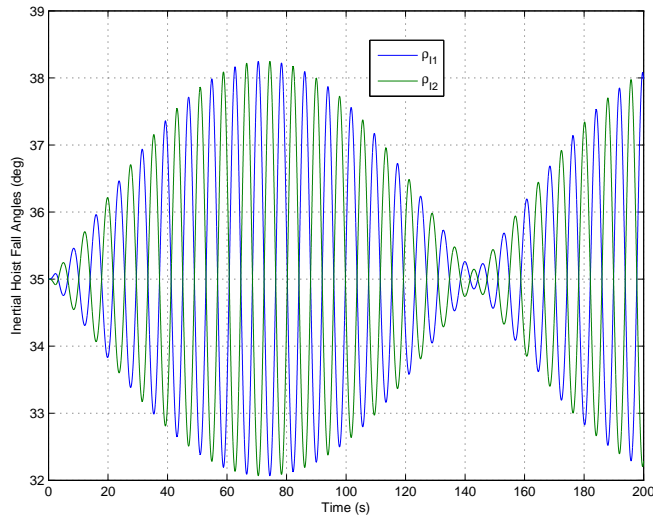


Figure 234. Time history of the inertial hoist fall angles, ρ_{I1} and ρ_{I2} for a 0.1 meter, 8.05 second period surge motion excitation with initial $\rho = 35.0$ degrees.

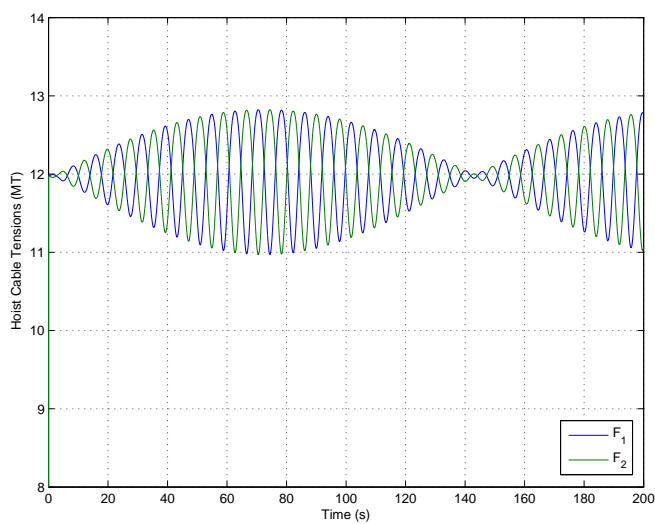


Figure 235. Time history of the hoist cable tensions, F_1 and F_2 in metric tons for a 0.1 meter, 8.05 second period surge motion excitation with initial $\rho = 35.0$ degrees.

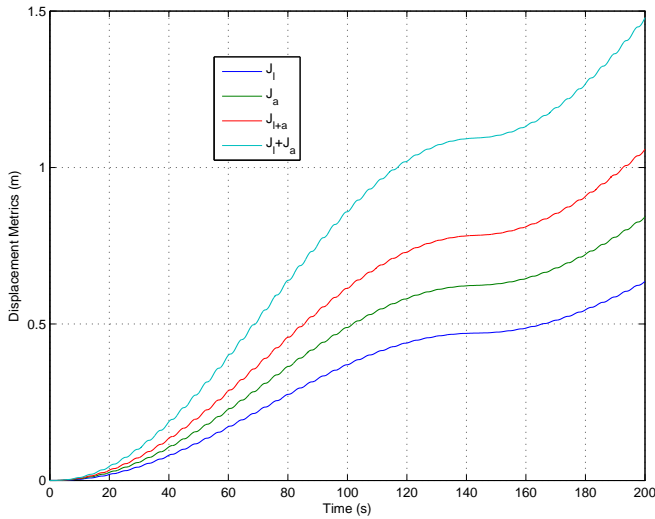


Figure 236. Time history of the calculation of the displacement metrics for a 0.1 meter, 8.05 second period surge motion excitation with initial $\rho = 35.0$ degree. Note that payload rotation is no longer zero, so J_θ is nonzero and there is a separation between J_l and $J_{l+\theta}$ and the sum of J_l and J_θ .

xvi. $\rho = 40.0$ degrees

xvii. $\rho = 45.0$ degrees

xviii. $\rho = 50.0$ degrees

2. Surge Motion - 0.1 meter amplitude, 8.75 second period

i. $\rho = -15.0$ degrees

ii. $\rho = -10.0$ degrees

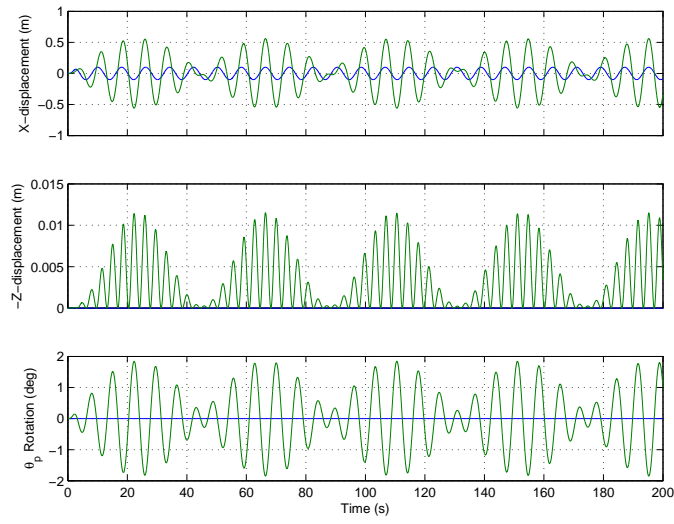


Figure 237. Time history of the payload motion for a 0.1 meter, 8.05 second period surge motion excitation with initial $\rho = 40.0$ degree. The blue trace is the ship motion and the payload response is shown in green.

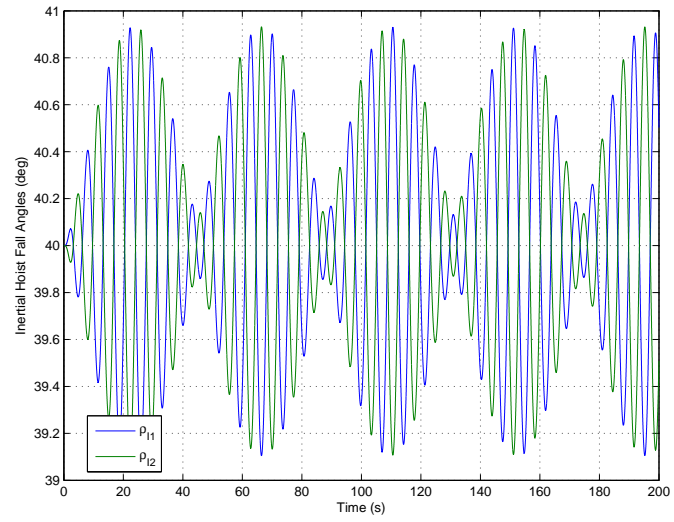


Figure 238. Time history of the inertial hoist fall angles, ρ_{I1} and ρ_{I2} for a 0.1 meter, 8.05 second period surge motion excitation with initial $\rho = 40.0$ degrees.

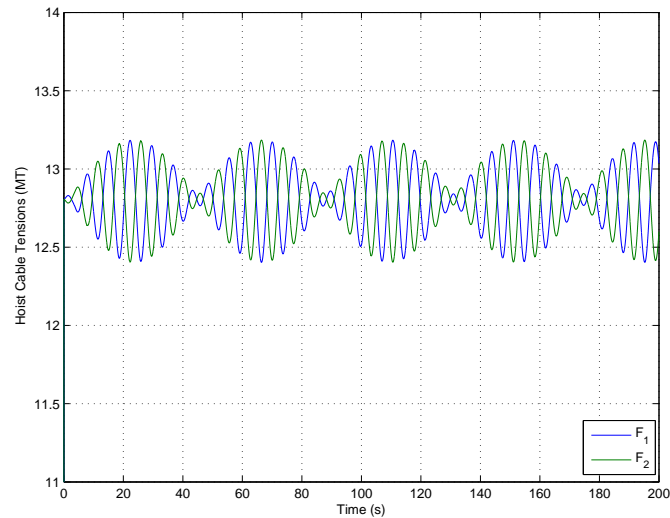


Figure 239. Time history of the hoist cable tensions, F_1 and F_2 in metric tons for a 0.1 meter, 8.05 second period surge motion excitation with initial $\rho = 40.0$ degrees.

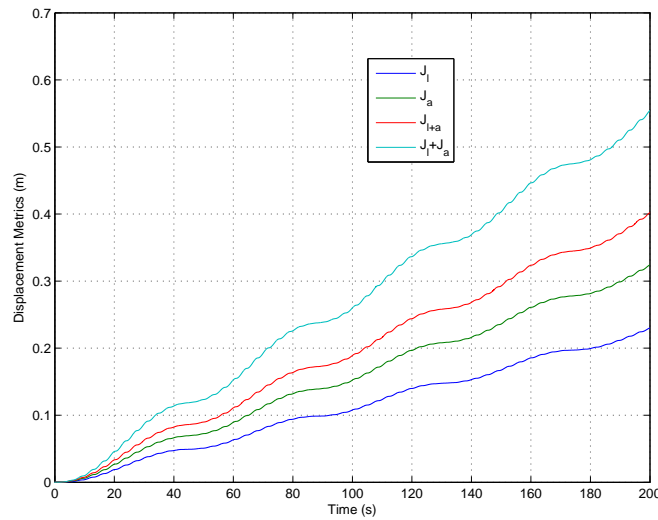


Figure 240. Time history of the calculation of the displacement metrics for a 0.1 meter, 8.05 second period surge motion excitation with initial $\rho = 40.0$ degree. Note that payload rotation is no longer zero, so J_θ is nonzero and there is a separation between J_l and $J_{l+\theta}$ and the sum of J_l and J_θ .

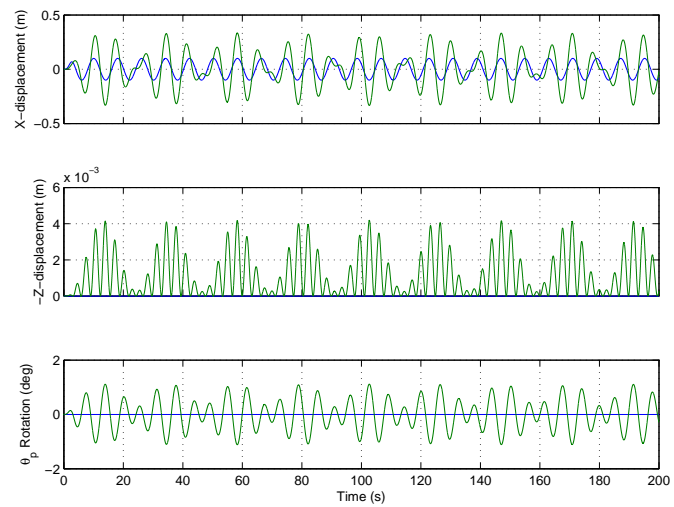


Figure 241. Time history of the payload motion for a 0.1 meter, 8.05 second period surge motion excitation with initial $\rho = 45.0$ degree. The blue trace is the ship motion and the payload response is shown in green.

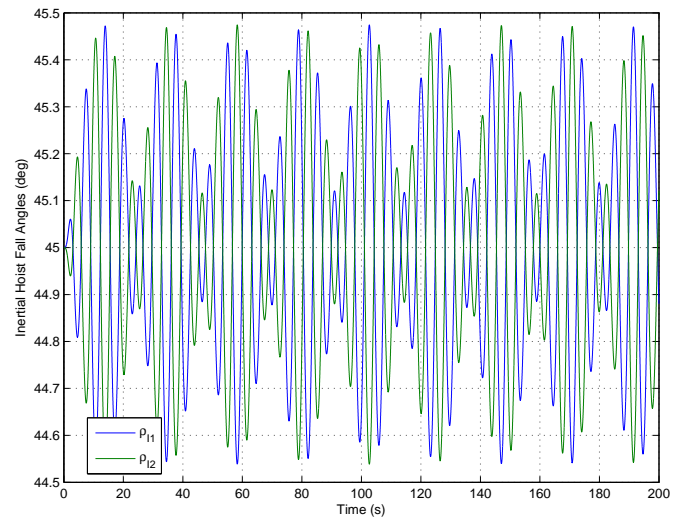


Figure 242. Time history of the inertial hoist fall angles, ρ_{I1} and ρ_{I2} for a 0.1 meter, 8.05 second period surge motion excitation with initial $\rho = 45.0$ degrees.

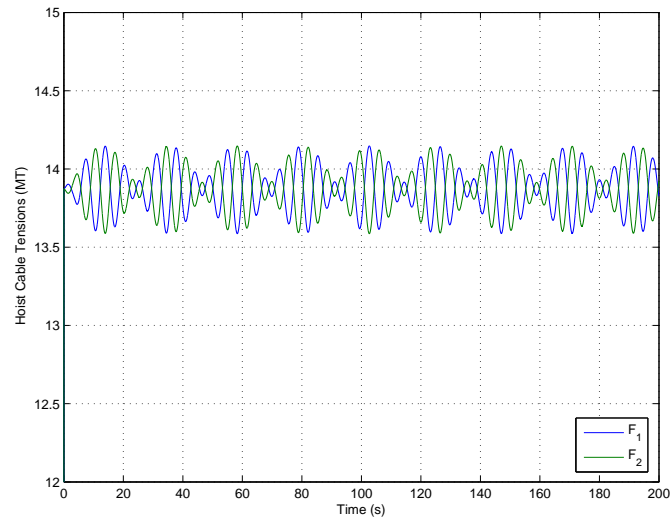


Figure 243. Time history of the hoist cable tensions, F_1 and F_2 in metric tons for a 0.1 meter, 8.05 second period surge motion excitation with initial $\rho = 45.0$ degrees.

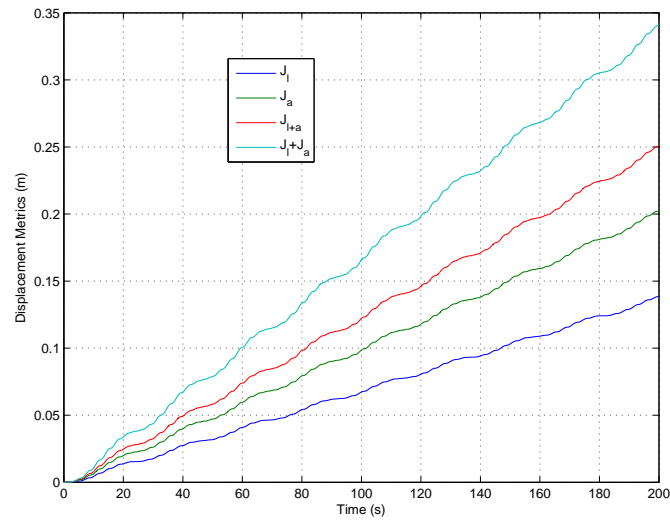


Figure 244. Time history of the calculation of the displacement metrics for a 0.1 meter, 8.05 second period surge motion excitation with initial $\rho = 30.0$ degree. Note that payload rotation is no longer zero, so J_θ is nonzero and there is a separation between J_l and $J_{l+\theta}$ and the sum of J_l and J_θ .

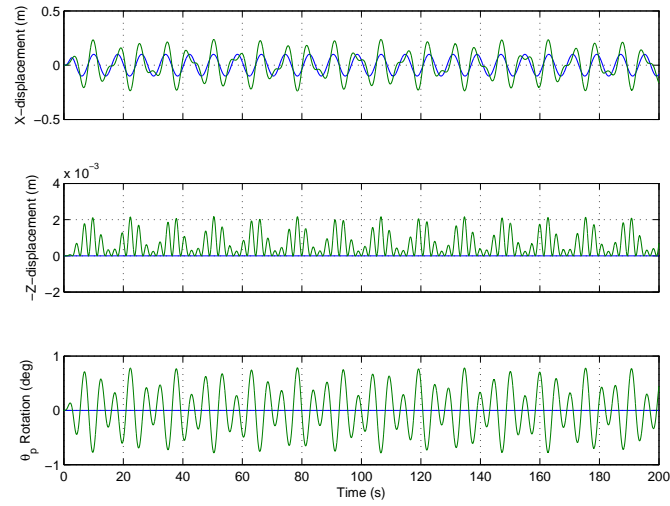


Figure 245. Time history of the payload motion for a 0.1 meter, 8.05 second period surge motion excitation with initial $\rho = 50.0$ degree. The blue trace is the ship motion and the payload response is shown in green.

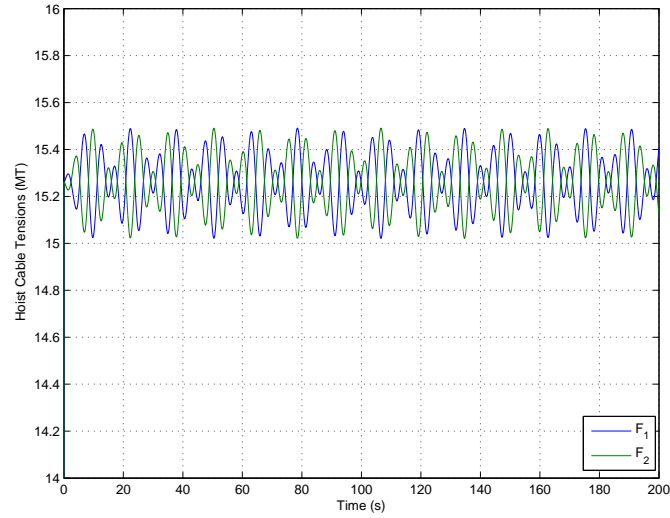


Figure 246. Time history of the hoist cable tensions, F_1 and F_2 in metric tons for a 0.1 meter, 8.05 second period surge motion excitation with initial $\rho = 50$ degrees. The peak response is approximately 1.5 percent above the initial (static) tension.

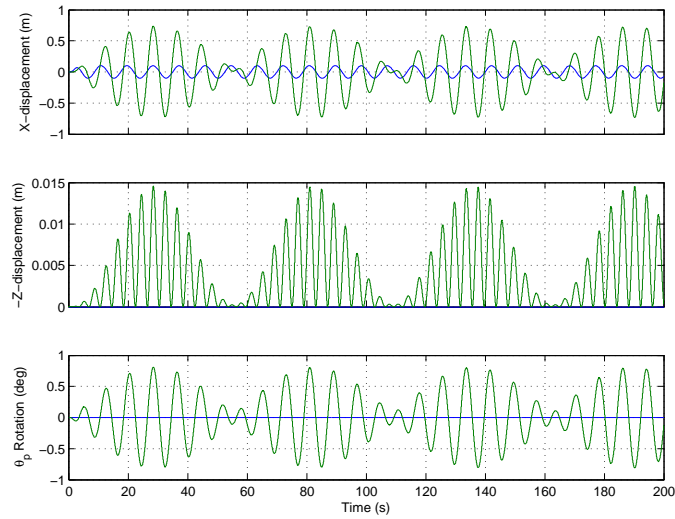


Figure 247. Time history of the payload motion for a 0.1 meter, 8.75 second period surge motion excitation with initial $\rho = -15.0$ degree. The blue trace is the ship motion and the payload response is shown in green.

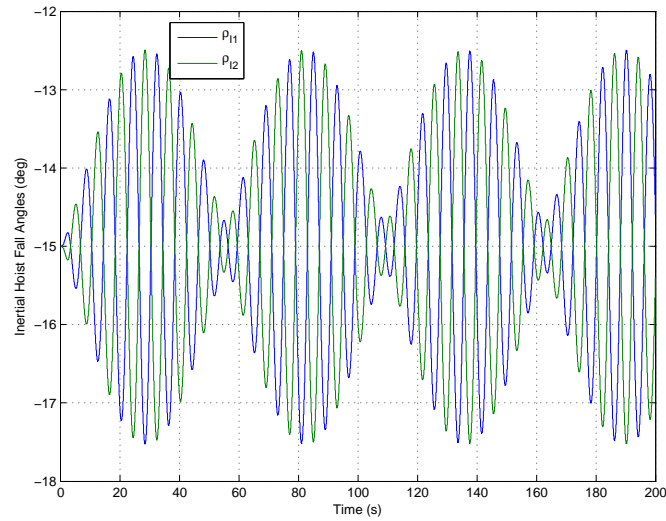


Figure 248. Time history of the inertial hoist fall angles, ρ_{I1} and ρ_{I2} for a 0.1 meter, 8.75 second period surge motion excitation with initial $\rho = -15.0$ degrees.

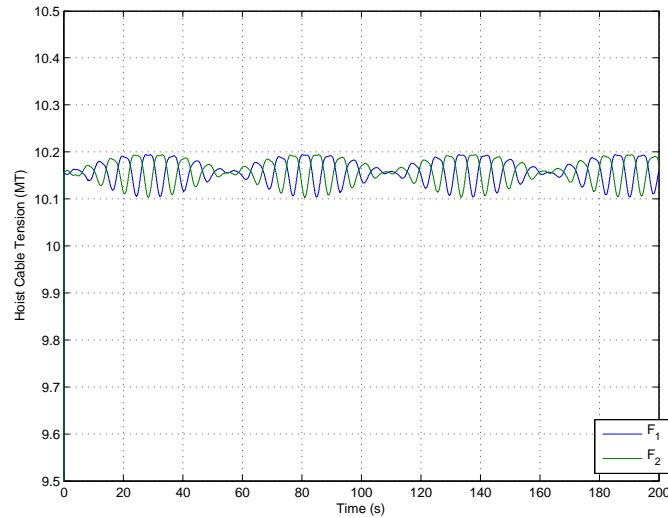


Figure 249. Time history of the hoist cable tensions, F_1 and F_2 in metric tons for a 0.1 meter, 8.75 second period surge motion excitation with initial $\rho = -15.0$ degrees.

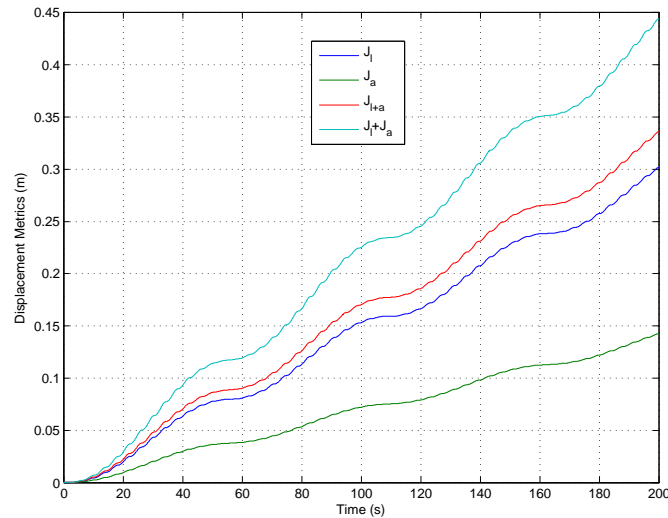


Figure 250. Time history of the calculation of the displacement metrics for a 0.1 meter, 8.75 second period surge motion excitation with initial $\rho = -15.0$ degree. Note that payload rotation is no longer zero, so J_θ is nonzero and there is a separation between J_l and $J_{l+\theta}$ and the sum of J_l and J_θ .

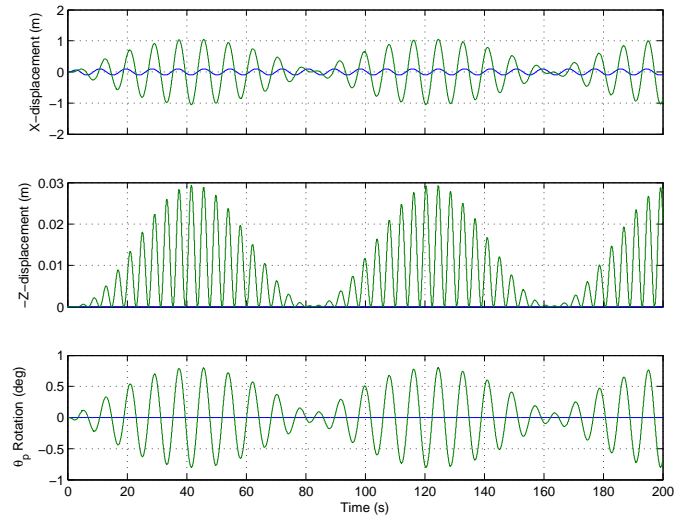


Figure 251. Time history of the payload motion for a 0.1 meter, 8.75 second period surge motion excitation with initial $\rho = -10.0$ degree. The blue trace is the ship motion and the payload response is shown in green.

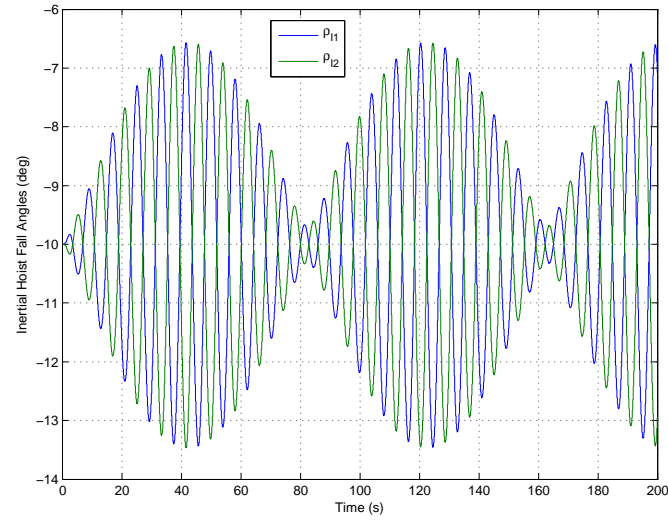


Figure 252. Time history of the inertial hoist fall angles, ρ_{I1} and ρ_{I2} for a 0.1 meter, 8.75 second period surge motion excitation with initial $\rho = -10.0$ degrees.

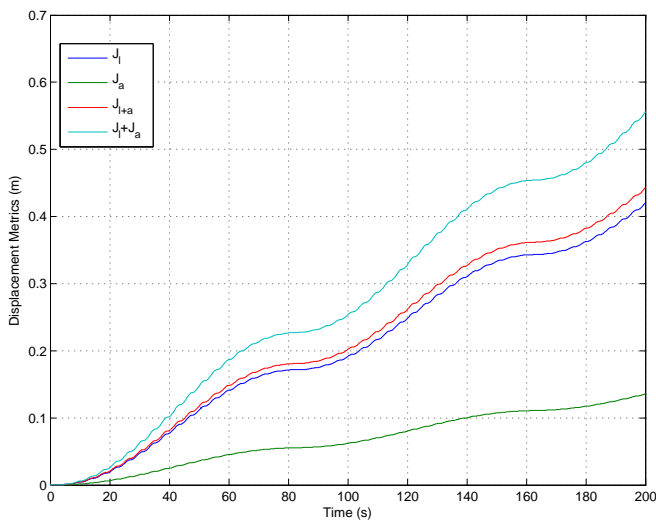


Figure 253. Time history of the calculation of the displacement metrics for a 0.1 meter, 8.75 second period surge motion excitation with initial $\rho = -10.0$ degree. Note that payload rotation is no longer zero, so J_θ is nonzero and there is a separation between J_l and $J_{l+\theta}$ and the sum of J_l and J_θ .

iii. $\rho = -5.0$ *degrees*

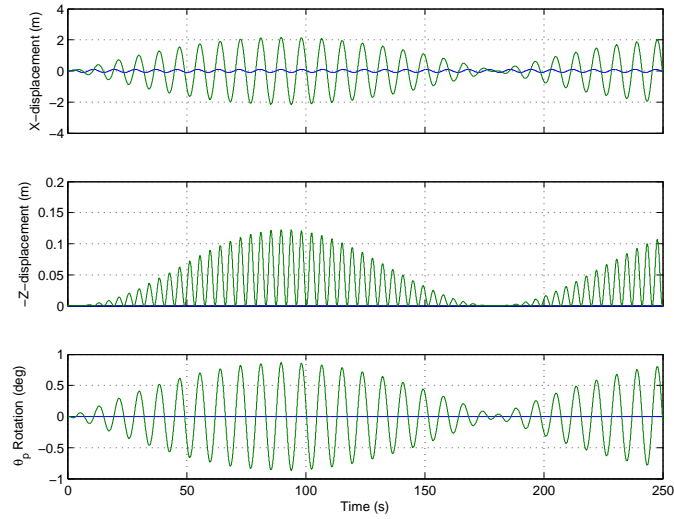


Figure 254. Time history of the payload motion for a 0.1 meter, 8.75 second period surge motion excitation with initial $\rho = -5.0$ degree. The blue trace is the ship motion and the payload response is shown in green.

iv. $\rho = 0.0$ *degrees*

v. $\rho = 5.0$ *degrees*

vi. $\rho = 10.0$ *degrees*

vii. $\rho = 15.0$ *degrees*

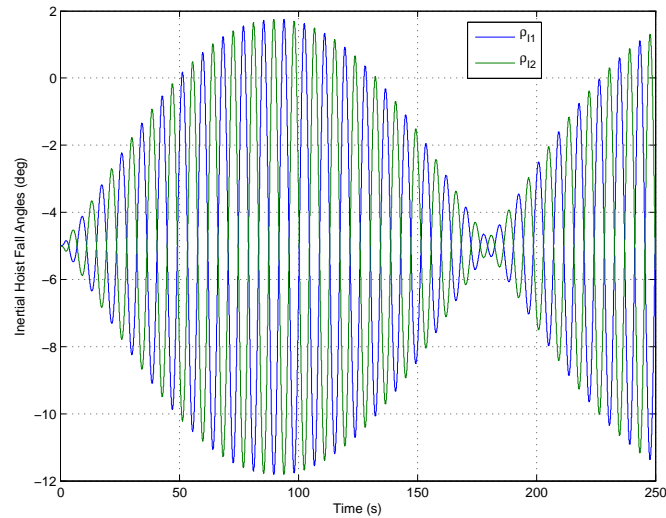


Figure 255. Time history of the inertial hoist fall angles, ρ_{I1} and ρ_{I2} for a 0.1 meter, 8.75 second period surge motion excitation with initial $\rho = -5.0$ degrees.

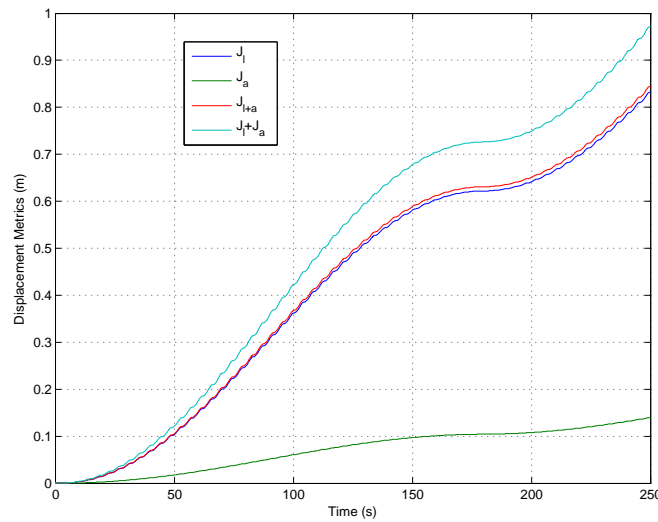


Figure 256. Time history of the calculation of the displacement metrics for a 0.1 meter, 8.75 second period surge motion excitation with initial $\rho = -5.0$ degree. Note that payload rotation is no longer zero, so J_θ is nonzero and there is a separation between J_l and $J_{l+\theta}$ and the sum of J_l and J_θ .

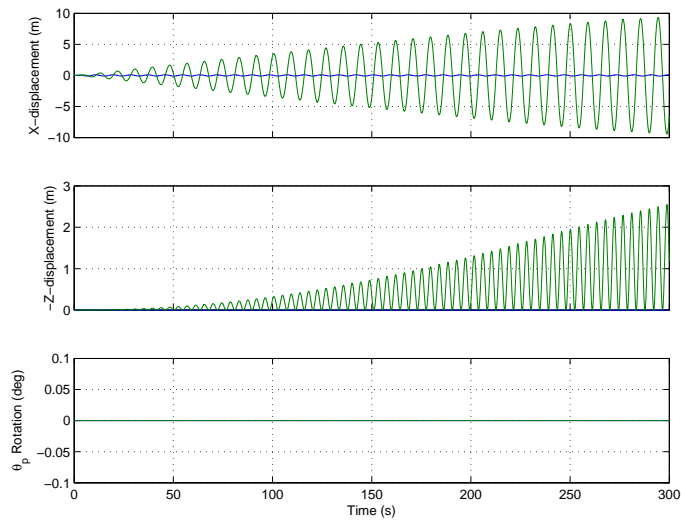


Figure 257. Time history of the payload motion for a 0.1 meter, 8.75 second period surge motion excitation with initial $\rho = 0.0$ degree. The blue trace is the ship motion and the payload response is shown in green.

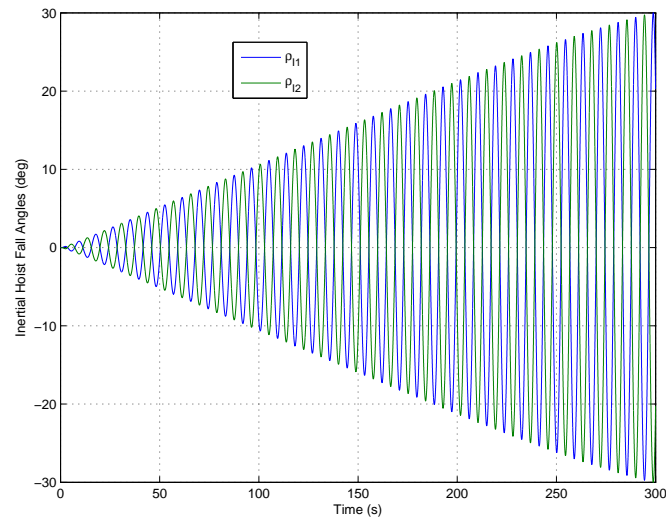


Figure 258. Time history of the inertial hoist fall angles, ρ_{I1} and ρ_{I2} for a 0.1 meter, 8.75 second period surge motion excitation with initial $\rho = 0.0$ degrees.

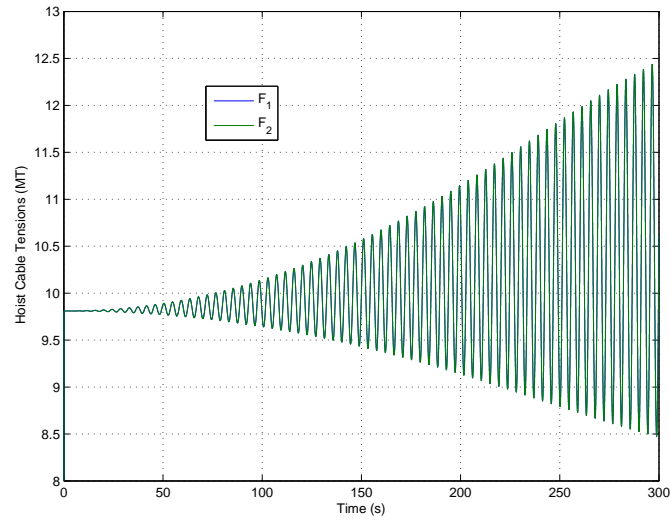


Figure 259. Time history of the hoist cable tensions, F_1 and F_2 in metric tons for a 0.1 meter, 8.75 second period surge motion excitation with initial $\rho = 0.0$ degrees.

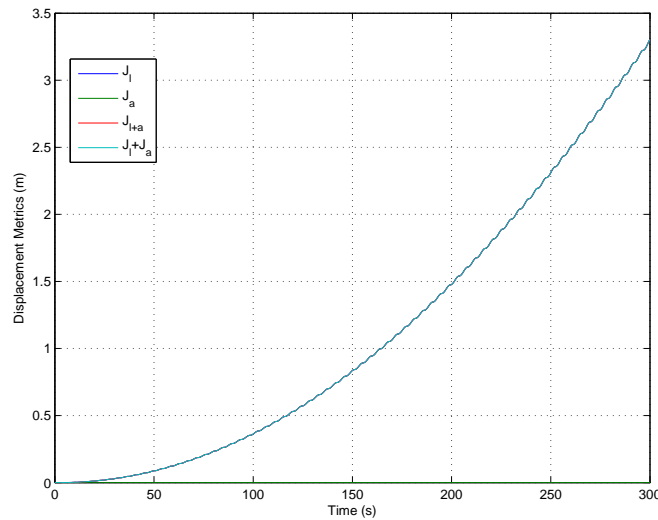


Figure 260. Time history of the calculation of the displacement metrics for a 0.1 meter, 8.75 second period surge motion excitation with initial $\rho = 0.0$ degree. Note that payload rotation is no longer zero, so J_θ is nonzero and there is a separation between J_l and $J_{l+\theta}$ and the sum of J_l and J_θ .

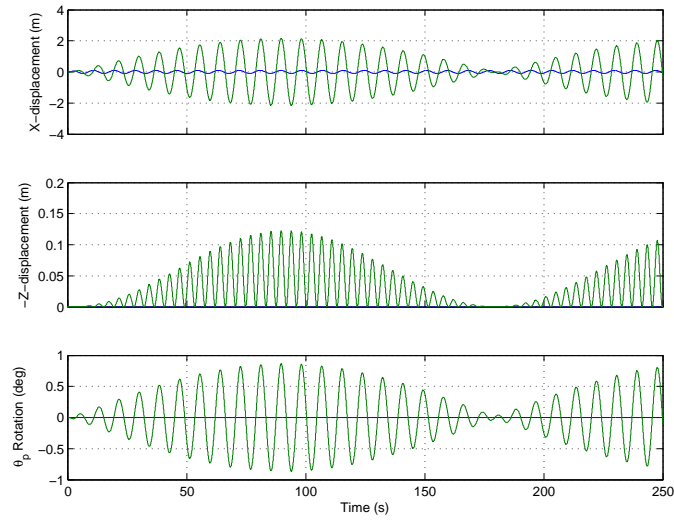


Figure 261. Time history of the payload motion for a 0.1 meter, 8.75 second period surge motion excitation with initial $\rho = 5.0$ degree. The blue trace is the ship motion and the payload response is shown in green.

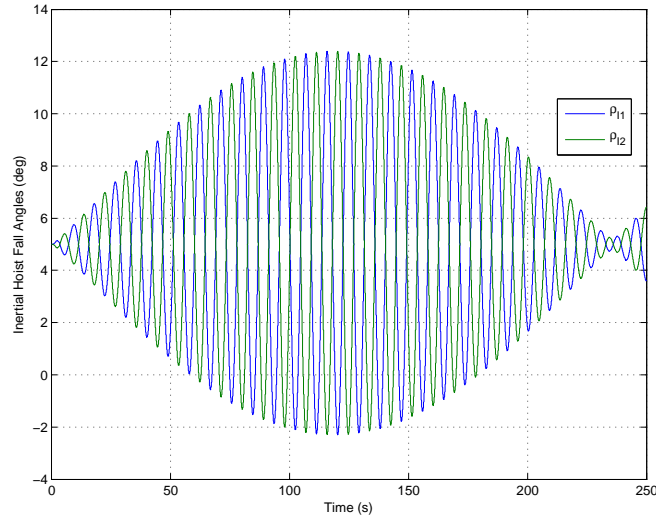


Figure 262. Time history of the inertial hoist fall angles, ρ_{I1} and ρ_{I2} for a 0.1 meter, 8.75 second period surge motion excitation with initial $\rho = 5.0$ degrees.

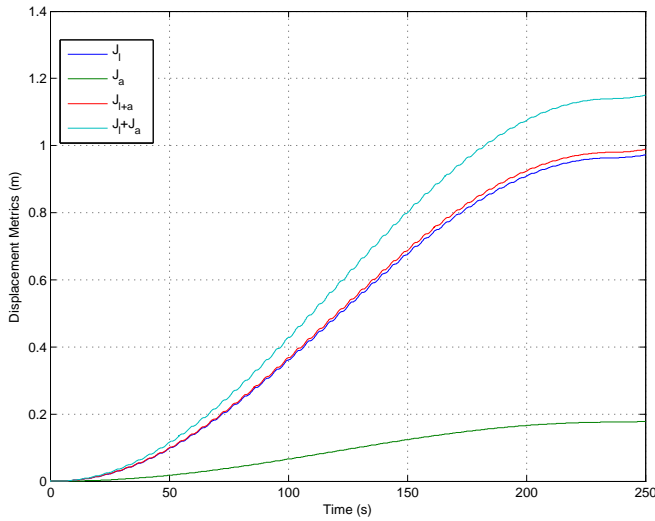


Figure 263. Time history of the calculation of the displacement metrics for a 0.1 meter, 8.75 second period surge motion excitation with initial $\rho = 5.0$ degree. Note that payload rotation is no longer zero, so J_θ is nonzero and there is a separation between J_l and $J_{l+\theta}$ and the sum of J_l and J_θ .

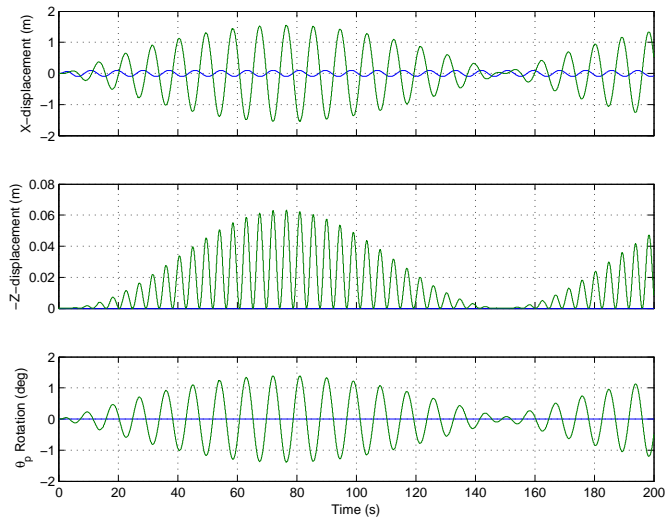


Figure 264. Time history of the payload motion for a 0.1 meter, 8.75 second period surge motion excitation with initial $\rho = 10.0$ degree. The blue trace is the ship motion and the payload response is shown in green.

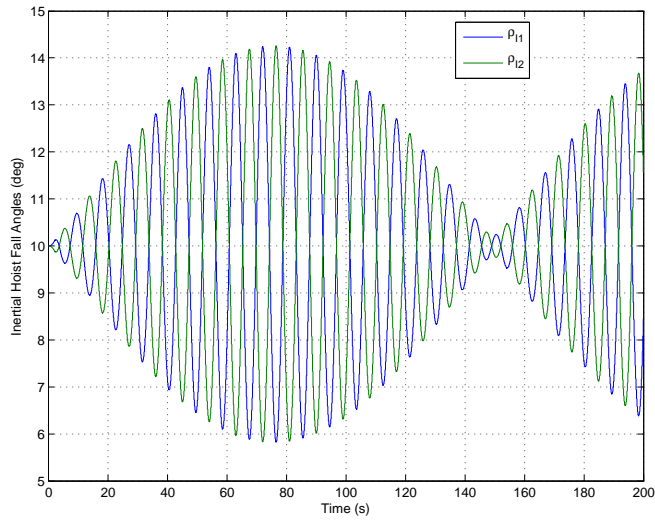


Figure 265. Time history of the inertial hoist fall angles, ρ_{I1} and ρ_{I2} for a 0.1 meter, 8.75 second period surge motion excitation with initial $\rho = 10.0$ degrees.

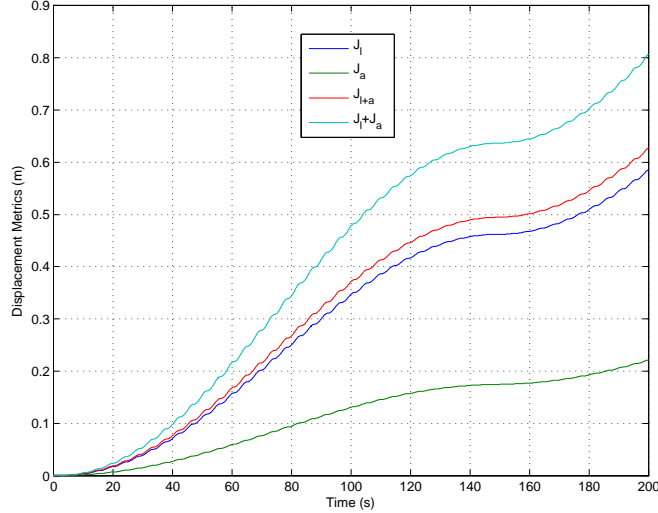


Figure 266. Time history of the calculation of the displacement metrics for a 0.1 meter, 8.75 second period surge motion excitation with initial $\rho = 10.0$ degree. Note that payload rotation is no longer zero, so J_θ is nonzero and there is a separation between J_l and $J_{l+\theta}$ and the sum of J_l and J_θ .

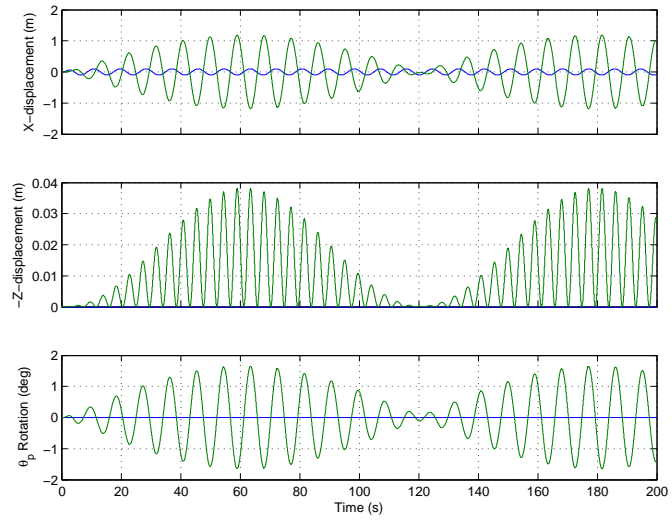


Figure 267. Time history of the payload motion for a 0.1 meter, 8.75 second period surge motion excitation with initial $\rho = 15.0$ degree. The blue trace is the ship motion and the payload response is shown in green.

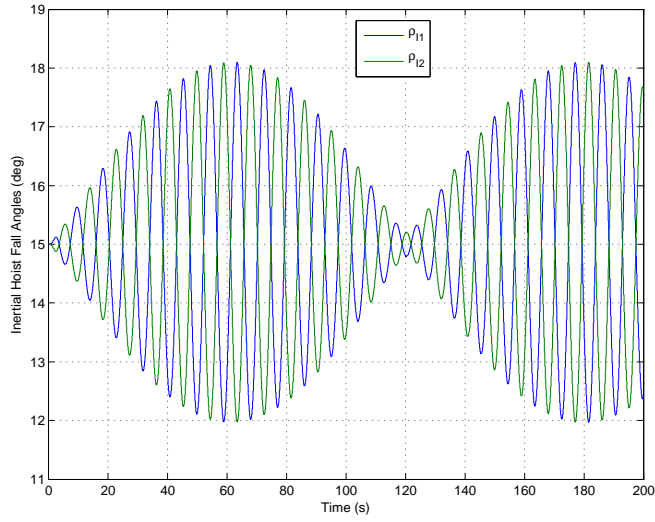


Figure 268. Time history of the inertial hoist fall angles, ρ_{I1} and ρ_{I2} for a 0.1 meter, 8.75 second period surge motion excitation with initial $\rho = 15.0$ degrees.

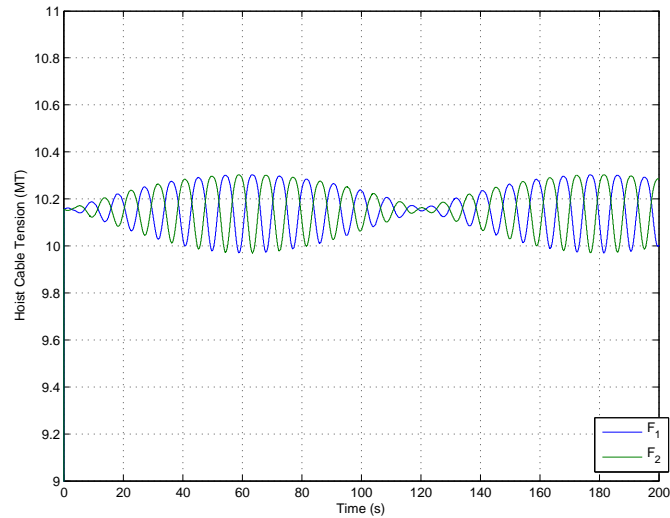


Figure 269. Time history of the hoist cable tensions, F_1 and F_2 in metric tons for a 0.1 meter, 8.75 second period surge motion excitation with initial $\rho = 15.0$ degrees.

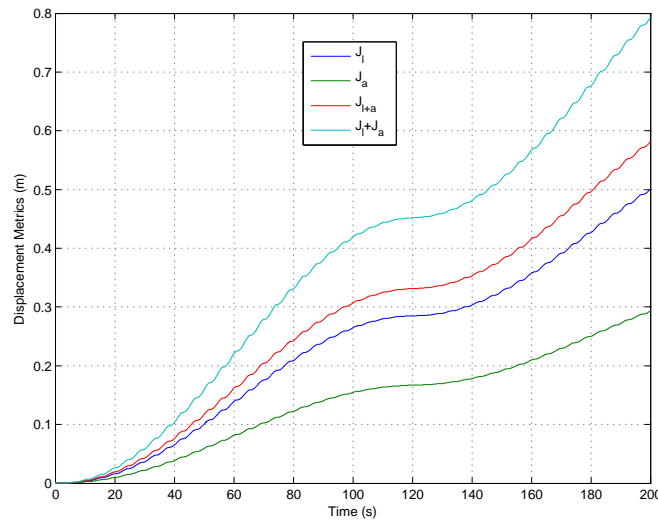


Figure 270. Time history of the calculation of the displacement metrics for a 0.1 meter, 8.75 second period surge motion excitation with initial $\rho = 15.0$ degree. Note that payload rotation is no longer zero, so J_θ is nonzero and there is a separation between J_l and $J_{l+\theta}$ and the sum of J_l and J_θ .

THIS PAGE INTENTIONALLY LEFT BLANK

APPENDIX B. MINIMUM NORM SOLUTION

A. DERIVATION

The minimum norm solution introduced in Chapter IV, can be easily derived for the system of equations $\mathbf{y} = \mathbf{A}\mathbf{x}$ where \mathbf{A} is a matrix $A(m \times n)$, $n > m$ and $\text{rank}(\mathbf{A}) = m$.

First define a cost function, J of the following form (Eqn. B.1), where W must be invertible and in this form of the solution, symmetric as well.

$$J = \mathbf{x}^T \mathbf{W} \mathbf{x} \quad (\text{B.1})$$

Now constructing the Hamiltonian function as shown in Eqn. B.2 and taking the derivative, we can then apply the necessary condition shown in Eqn. B.3 (Bryson & Ho, [66]).

$$H = \mathbf{x}^T \mathbf{W} \mathbf{x} + \boldsymbol{\lambda} (\mathbf{A}\mathbf{x} - \mathbf{y}) \quad (\text{B.2})$$

$$\frac{\partial H}{\partial \mathbf{x}} = 2\mathbf{x}^T \mathbf{W} + \boldsymbol{\lambda}^T \mathbf{A} = 0 \quad (\text{B.3})$$

(assuming \mathbf{W} is symmetric)

From Eqn. B.3, we can solve for \mathbf{x}^T and thus \mathbf{x} as shown in Eqn. B.5. Substituting for \mathbf{x} in the original system yields the following expression for \mathbf{y} (Eqn. B.6). This expression can then be solved for $\boldsymbol{\lambda}$ (Eqn. B.7) and substituted back into Eqn. B.5. Thus the final result (Eqn B.8) is obtained, Q.E.D.

$$\mathbf{x}^T = -\frac{1}{2} \boldsymbol{\lambda}^T \mathbf{A} \mathbf{W}^{-1} \quad (\text{B.4})$$

$$\mathbf{x} = -\frac{1}{2} \mathbf{W}^{-1} \mathbf{A}^T \boldsymbol{\lambda} \quad (\text{B.5})$$

$$\mathbf{y} = -\frac{1}{2} \mathbf{W}^{-1} \mathbf{A}^T \boldsymbol{\lambda} \quad (\text{B.6})$$

$$\boldsymbol{\lambda} = -2 \left(\mathbf{A} \mathbf{W}^{-1} \mathbf{A}^T \right)^{-1} \mathbf{y} \quad (\text{B.7})$$

$$\mathbf{x} = \mathbf{W}^{-1} \mathbf{A}^T \left(\mathbf{A} \mathbf{W}^{-1} \mathbf{A}^T \right)^{-1} \mathbf{y} \quad (\text{B.8})$$

APPENDIX C. INVERSE KINEMATIC CONTROL MODEL RESULTS

A. TIME HISTORY DATA FOR INVERSE-KINEMATIC SHIP MOTION COMPENSATOR

An extensive set of time history data was generated from simulation of the planar dual-crane system with the inverse kinematic control in the loop.

The data set for each simulation run consists of plots of the x , z , and θ_p displacements, the displacements and rate response of the jib and hoist actuators, the inertial hoist-fall angle ρ_I , the hoist cable tensions, F_1 and F_2 , the instantaneous power, and the calculation of the rate-based and power-based performance metrics, J_{rate} and J_{power} .

The data is presented here, organized by the run number assigned in the Table in Chapter VI

1. Power-based Weighting

- i. *Dynamic Weighting*
- ii. *Run #3 - Constant (Maximum) Torque & Tension Weights, Surge*
- iii. *Run #4 - Constant (Maximum) Torque & Tension Weights, Heave*
- iv. *Run #5 - Constant (Maximum) Torque & Tension Weights, Pitch*

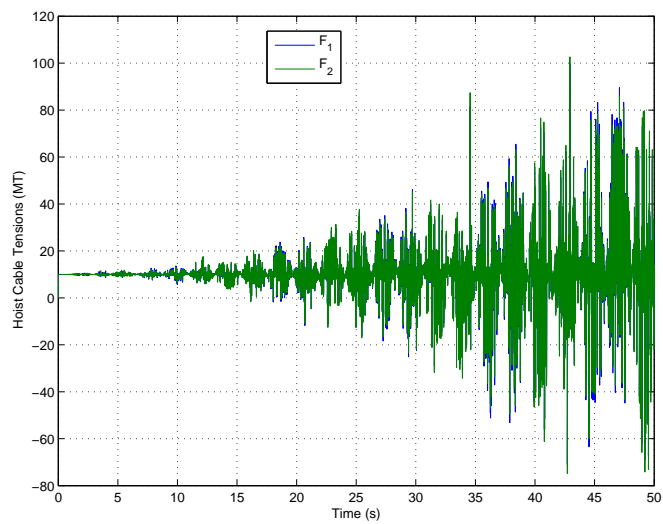


Figure 271. Plot of hoist cable tensions, F_1 and F_2 , for the inverse kinematic control case with dynamically changing torques and cable tension values used as the weights in the minimum norm solution. (Simulation parameters: $\rho = 10$ degrees, $\vec{P}_{8/1,z} = 5$ meters, and $\dot{x}_s = 1$ meter at a period of 8.75 seconds.)

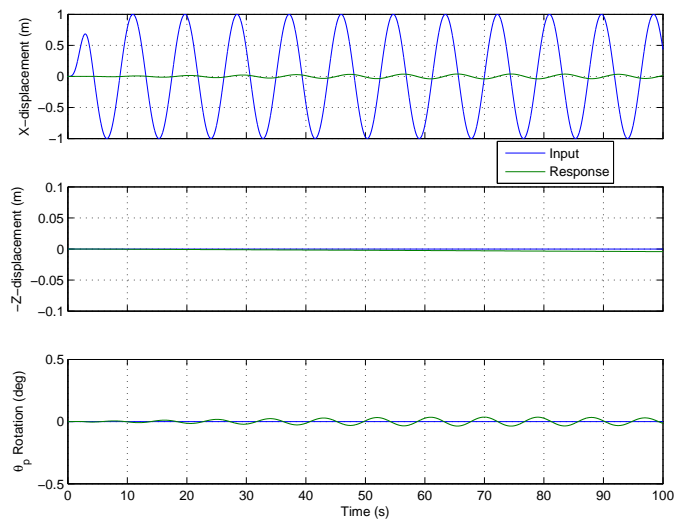


Figure 272. Plot of x , z , and θ time histories for the inverse kinematic control case with constant torques and cable tension values used as the weights in the minimum norm solution. The constant values chosen were the maximums observed during a simulation of the same conditions using the identity matrix as the weighting elements. (Simulation parameters: $\rho = 10$ degrees, $\bar{P}_{8/1,z} = 5$ meters, and $\dot{x}_s = 1$ meter at a period of 8.75 seconds.)

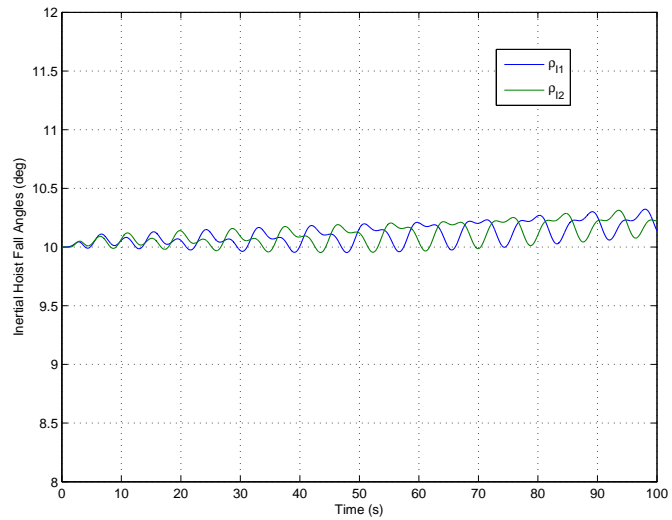


Figure 273. Plot of time histories for the inertial hoist-fall angle, ρ , for the inverse kinematic control case with constant torques and cable tension values used as the weights in the minimum norm solution. The constant values chosen were the maximums observed during a simulation of the same conditions using the identity matrix as the weighting elements. (Simulation parameters: $\rho = 10$ degrees, $\bar{P}_{8/1,z} = 5$ meters, and $\dot{x}_s = 1$ meter at a period of 8.75 seconds.)

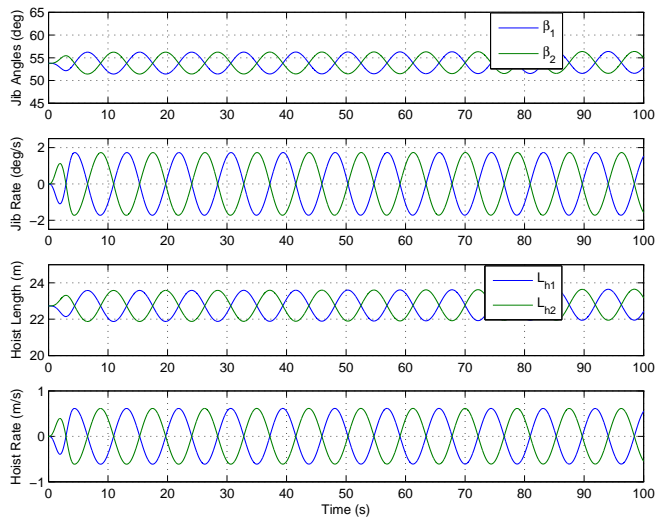


Figure 274. Plots of β , $\dot{\beta}$, L_h , and \dot{L}_h for the inverse kinematic control case with constant torques and cable tension values used as the weights in the minimum norm solution. The constant values chosen were the maximums observed during a simulation of the same conditions using the identity matrix as the weighting elements. (Simulation parameters: $\rho = 10$ degrees, $\vec{P}_{8/1,z} = 5$ meters, and $\dot{x}_s = 1$ meter at a period of 8.75 seconds.)

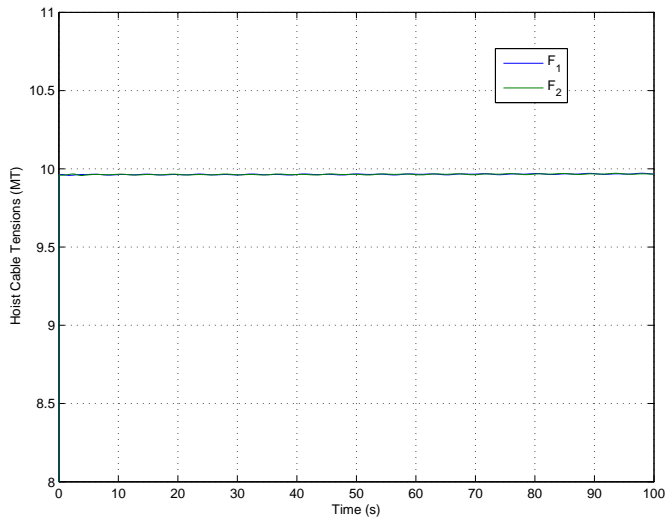


Figure 275. Plot of hoist cable tensions, F_1 and F_2 , for the inverse kinematic control case with constant torques and cable tension values used as the weights in the minimum norm solution. The constant values chosen were the maximums observed during a simulation of the same conditions using the identity matrix as the weighting elements. (Simulation parameters: $\rho = 10$ degrees, $\bar{P}_{8/1,z} = 5$ meters, and $\dot{x}_s = 1$ meter at a period of 8.75 seconds.)

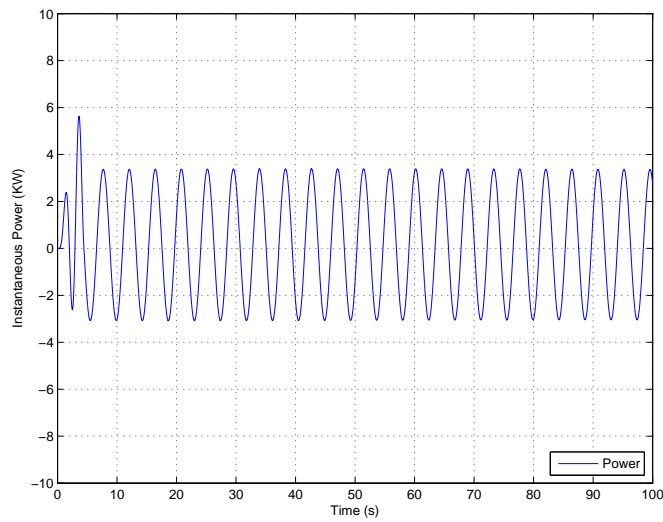


Figure 276. Plot of instantaneous power for the inverse kinematic control case with constant torques and cable tension values used as the weights in the minimum norm solution. The constant values chosen were the maximums observed during a simulation of the same conditions using the identity matrix as the weighting elements. (Simulation parameters: $\rho = 10$ degrees, $\vec{P}_{8/1,z} = 5$ meters, and $\dot{x}_s = 1$ meter at a period of 8.75 seconds.)

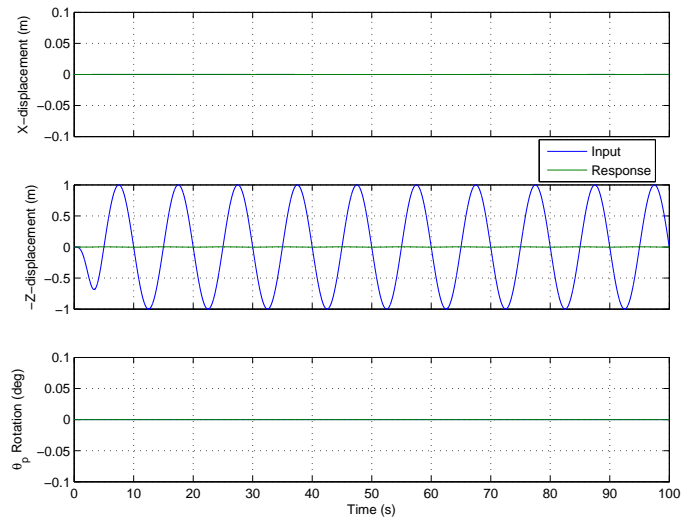


Figure 277. Plot of x , z , and θ time histories for the inverse kinematic control case with constant torques and cable tension values used as the weights in the minimum norm solution. The constant values chosen were the maximums observed during a simulation of the same conditions using the identity matrix as the weighting elements. (Simulation parameters: $\rho = 10$ degrees, $\vec{P}_{8/1,z} = 5$ meters, and $\dot{z}_s = 1$ meter at a period of 10.0 seconds.)

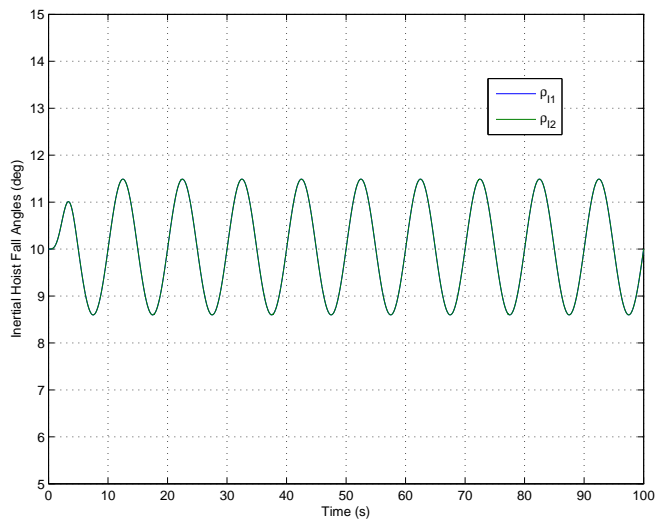


Figure 278. Plot of time histories for the inertial hoist-fall angle, ρ , for the inverse kinematic control case with constant torques and cable tension values used as the weights in the minimum norm solution. The constant values chosen were the maximums observed during a simulation of the same conditions using the identity matrix as the weighting elements. (Simulation parameters: $\rho = 10$ degrees, $\bar{P}_{8/1,z} = 5$ meters, and $\dot{z}_s = 1$ meter at a period of 10.0 seconds.)

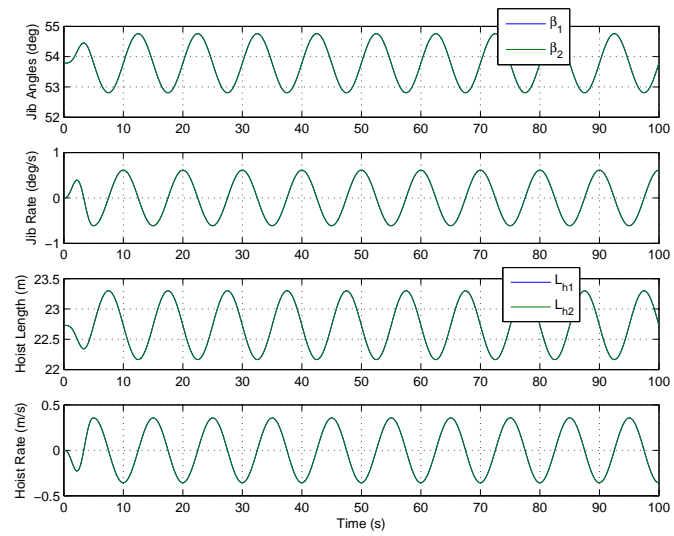


Figure 279. Plots of β , $\dot{\beta}$, L_h , and \dot{L}_h for the inverse kinematic control case with constant torques and cable tension values used as the weights in the minimum norm solution. The constant values chosen were the maximums observed during a simulation of the same conditions using the identity matrix as the weighting elements. (Simulation parameters: $\rho = 10$ degrees, $\vec{P}_{8/1,z} = 5$ meters, and $\dot{z}_s = 1$ meter at a period of 10 seconds.)

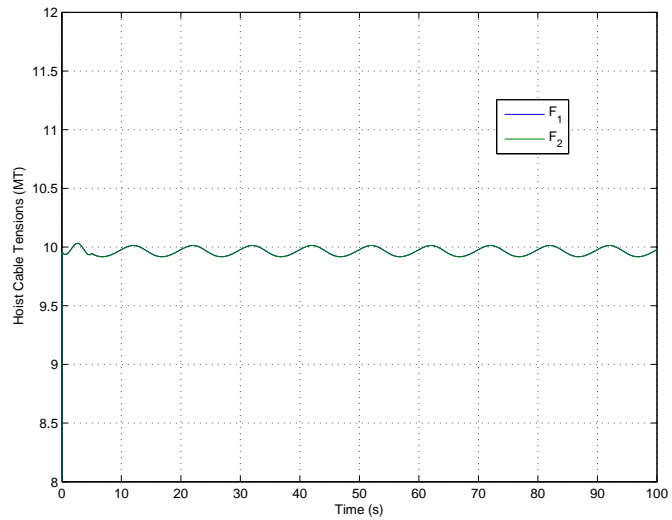


Figure 280. Plot of hoist cable tensions, F_1 and F_2 , for the inverse kinematic control case with constant torques and cable tension values used as the weights in the minimum norm solution. The constant values chosen were the maximums observed during a simulation of the same conditions using the identity matrix as the weighting elements. (Simulation parameters: $\rho = 10$ degrees, $\vec{P}_{8/1,z} = 5$ meters, and $\dot{z}_s = 1$ meter at a period of 10.0 seconds.)

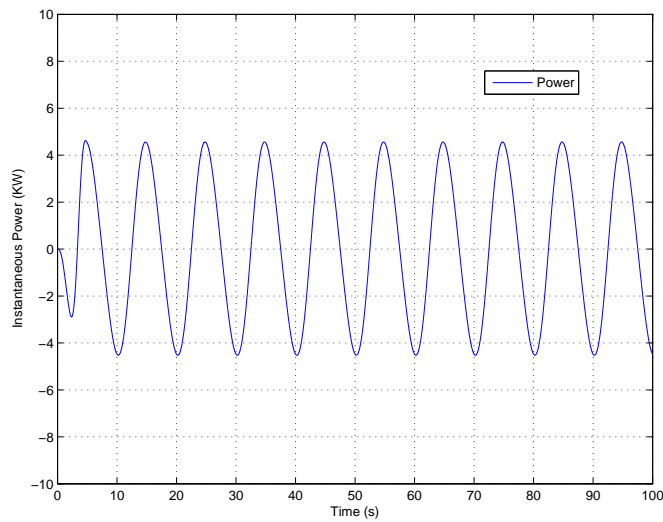


Figure 281. Plot of instantaneous power for the inverse kinematic control case with constant torques and cable tension values used as the weights in the minimum norm solution. The constant values chosen were the maximums observed during a simulation of the same conditions using the identity matrix as the weighting elements. (Simulation parameters: $\rho = 10$ degrees, $\vec{P}_{8/1,z} = 5$ meters, and $\dot{z}_s = 1$ meter at a period of 10.0 seconds.)

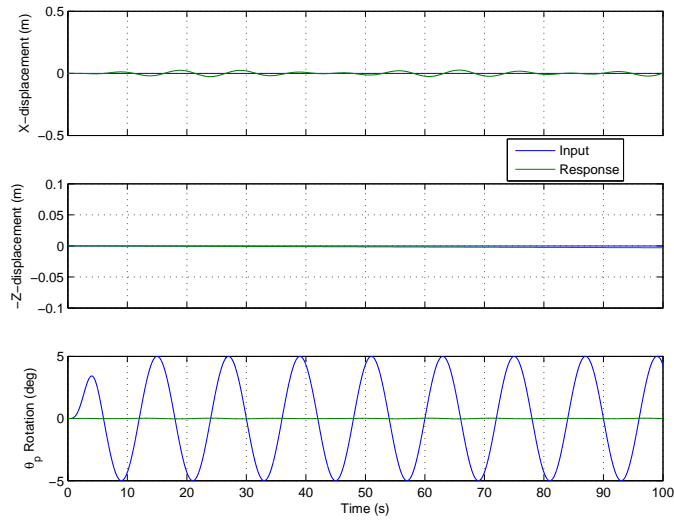


Figure 282. Plot of x , z , and θ time histories for the inverse kinematic control case with constant torques and cable tension values used as the weights in the minimum norm solution.. (Simulation parameters: $\rho = 10$ degrees, $\vec{P}_{8/1,z} = 5$ meters, and $\theta_s = 5$ degrees at a period of 12 seconds.)

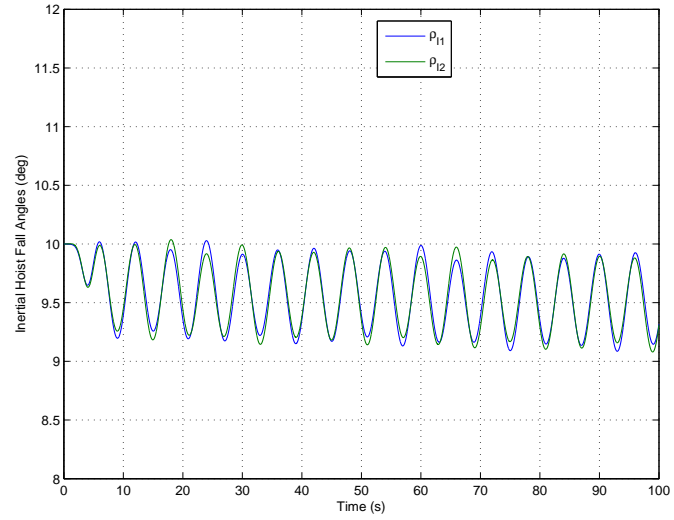


Figure 283. Plot of time histories for the inertial hoist-fall angle, ρ , for the inverse kinematic control case with constant torques and cable tension values used as the weights in the minimum norm solution. (Simulation parameters: $\rho = 10$ degrees, $\vec{P}_{8/1,z} = 5$ meters, and $\theta_s = 5$ degrees at a period of 12 seconds.)

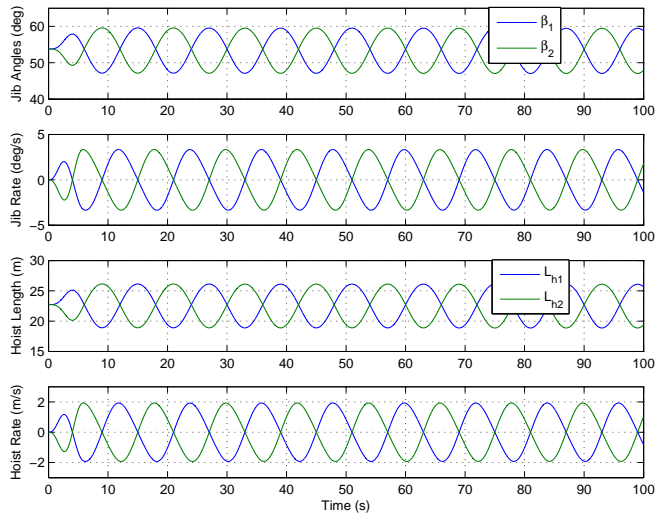


Figure 284. Plots of β , $\dot{\beta}$, L_h , and \dot{L}_h for the inverse kinematic control case with constant torques and cable tension values used as the weights in the minimum norm solution. (Simulation parameters: $\rho = 10$ degrees, $\vec{P}_{8/1,z} = 5$ meters, and $\theta_s = 5$ degrees at a period of 12 seconds.)

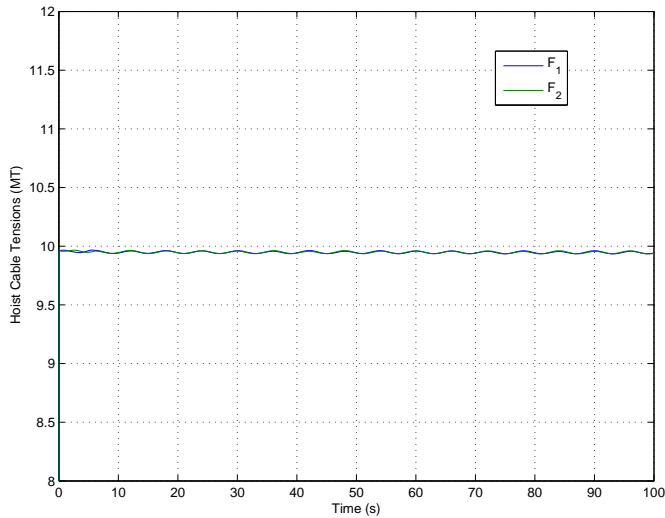


Figure 285. Plot of hoist cable tensions, F_1 and F_2 , for the inverse kinematic control case with constant torques and cable tension values used as the weights in the minimum norm solution. (Simulation parameters: $\rho = 10$ degrees, $\vec{P}_{8/1,z} = 5$ meters, and $\theta_s = 5$ degrees at a period of 12 seconds.)

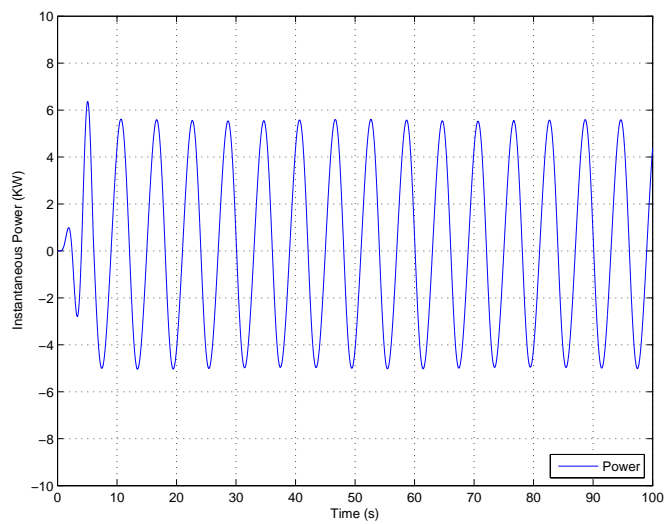


Figure 286. Plot of instantaneous power for the inverse kinematic control case with constant torques and cable tension values used as the weights in the minimum norm solution. (Simulation parameters: $\rho = 10$ degrees, $\vec{P}_{8/1,z} = 5$ meters, and $\theta_s = 5$ degrees at a period of 12 seconds.)

v. **Run #6 - Unity Weights, Surge**

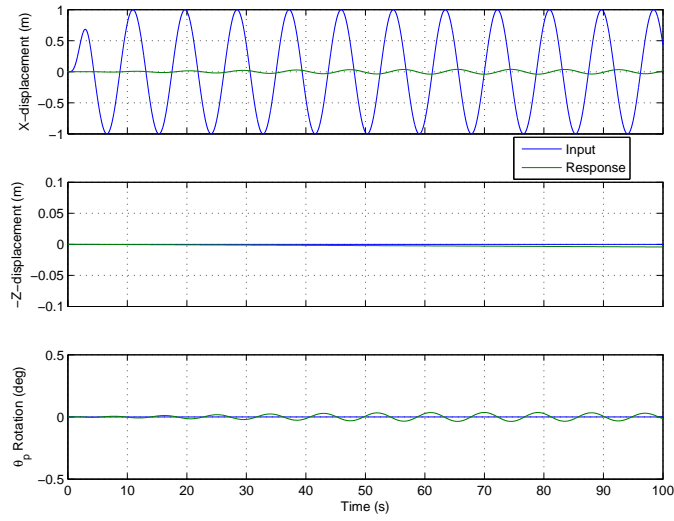


Figure 287. Plot of x , z , and θ time histories for the inverse kinematic control case with the identity matrix used as the weights in the minimum norm solution. (Simulation parameters: $\rho = 10$ degrees, $\vec{P}_{8/1,z} = 5$ meters, and $\dot{x}_s = 1$ meter at a period of 8.75 seconds.)

vi. **Run #7 - Unity Weights, Surge, $\rho = 0$**

vii. **Run #8 - Balanced Coordinate Weights, Surge**

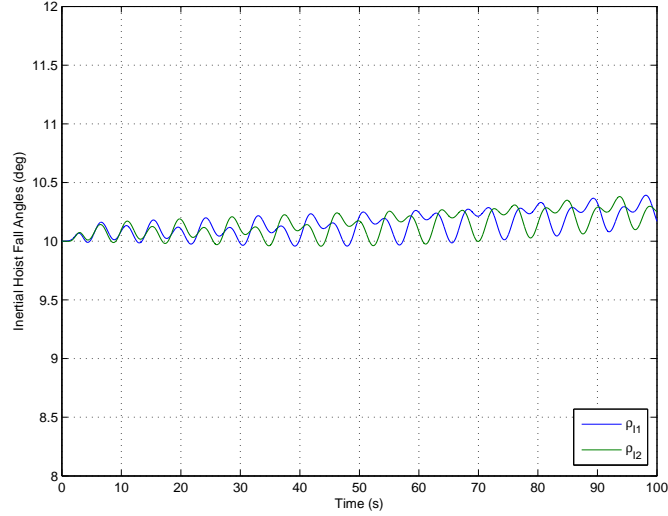


Figure 288. Plot of time histories for the inertial hoist-fall angle, ρ , for the inverse kinematic control case with the identity matrix used as the weights in the minimum norm solution. (Simulation parameters: $\rho = 10$ degrees, $\vec{P}_{8/1,z} = 5$ meters, and $\dot{x}_s = 1$ meter at a period of 8.75 seconds.)

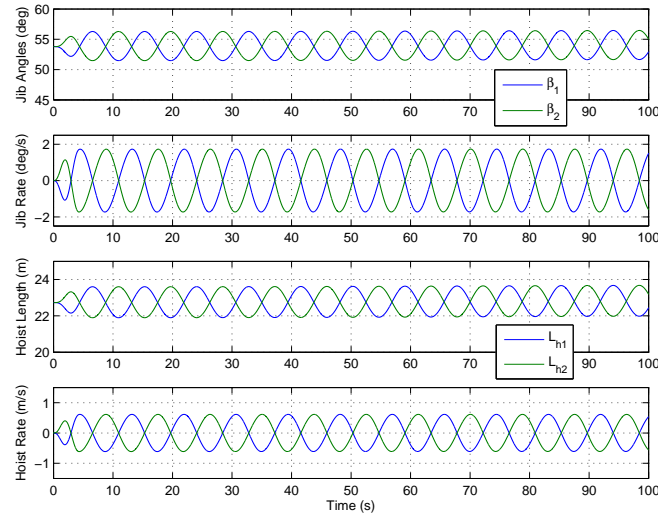


Figure 289. Plots of β , $\dot{\beta}$, L_h , and \dot{L}_h for the inverse kinematic control case with the identity matrix used as the weights in the minimum norm solution. (Simulation parameters: $\rho = 10$ degrees, $\vec{P}_{8/1,z} = 5$ meters, and $\dot{x}_s = 1$ meter at a period of 8.75 seconds.)

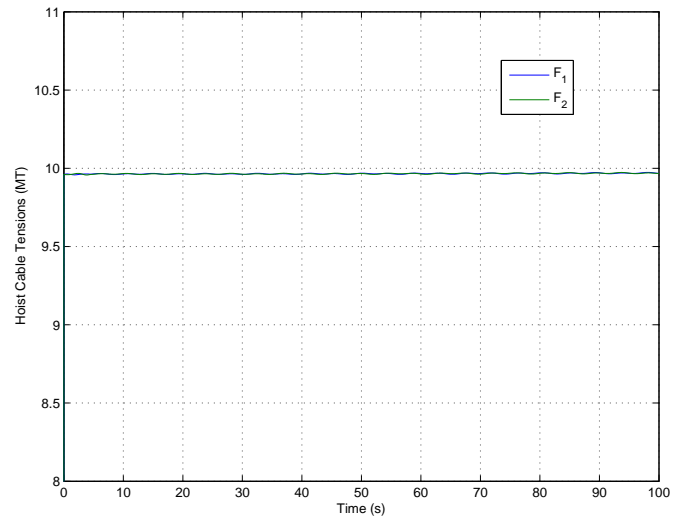


Figure 290. Plot of hoist cable tensions, F_1 and F_2 , for the inverse kinematic control case with the identity matrix used as the weights in the minimum norm solution. (Simulation parameters: $\rho = 10$ degrees, $\vec{P}_{8/1,z} = 5$ meters, and $\dot{x}_s = 1$ meter at a period of 8.75 seconds.)

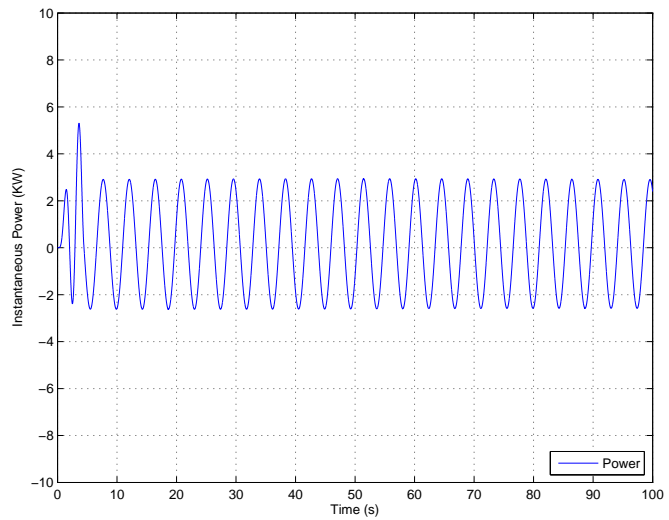


Figure 291. Plot of instantaneous power for the inverse kinematic control case with the identity matrix used as the weights in the minimum norm solution. (Simulation parameters: $\rho = 10$ degrees, $\vec{P}_{8/1,z} = 5$ meters, and $\dot{x}_s = 1$ meter at a period of 8.75 seconds.)

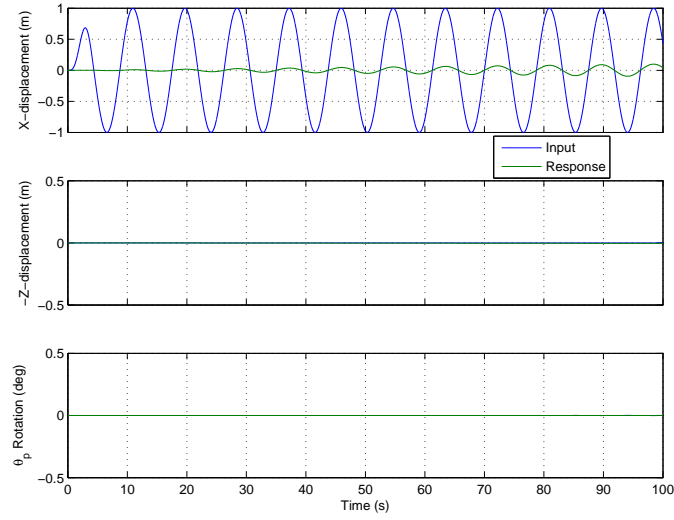


Figure 292. Plot of x , z , and θ time histories for the inverse kinematic control case with the identity matrix used as the weights in the minimum norm solution. (Simulation parameters: $\rho = 0$ degrees, $\vec{P}_{8/1,z} = 5$ meters, and $\dot{x}_s = 1$ meter at a period of 8.75 seconds.)

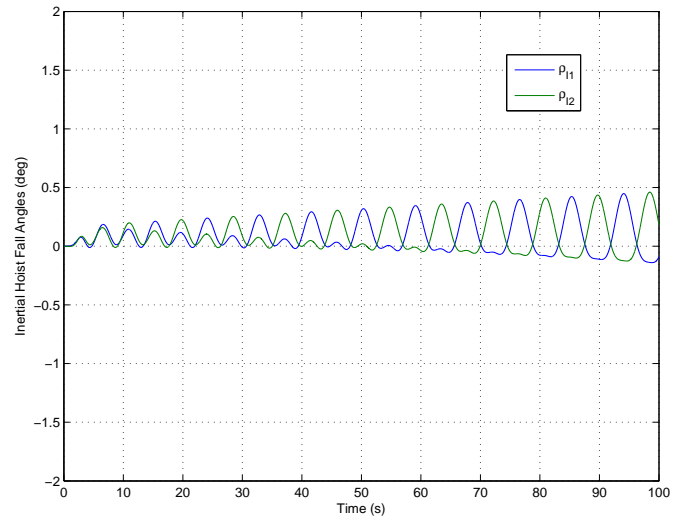


Figure 293. Plot of time histories for the inertial hoist-fall angle, ρ , for the inverse kinematic control case with the identity matrix used as the weights in the minimum norm solution. (Simulation parameters: $\rho = 0$ degrees, $\vec{P}_{8/1,z} = 5$ meters, and $\dot{x}_s = 1$ meter at a period of 8.75 seconds.)

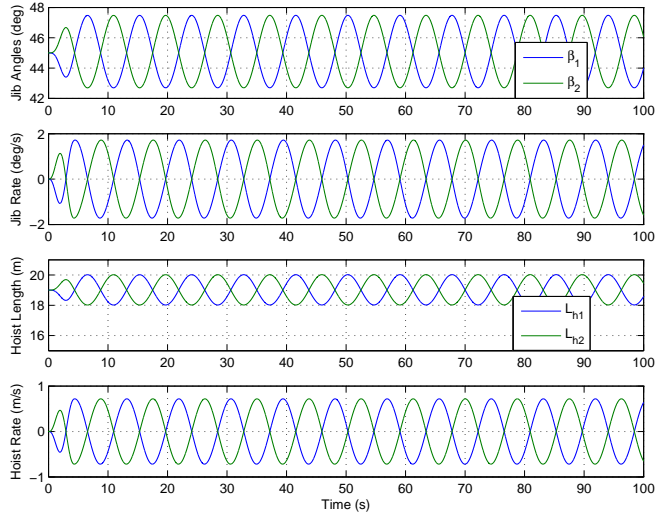


Figure 294. Plots of β , $\dot{\beta}$, L_h , and \dot{L}_h for the inverse kinematic control case with the identity matrix used as the weights in the minimum norm solution. (Simulation parameters: $\rho = 0$ degrees, $\vec{P}_{8/1,z} = 5$ meters, and $\dot{x}_s = 1$ meter at a period of 8.75 seconds.)

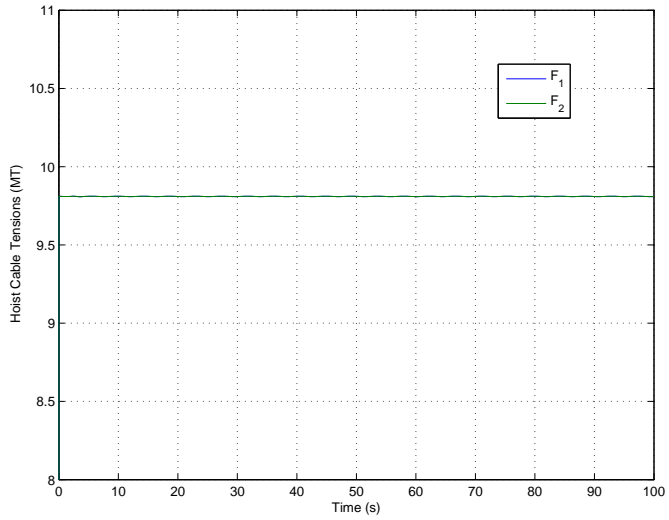


Figure 295. Plot of hoist cable tensions, F_1 and F_2 , for the inverse kinematic control case with the identity matrix used as the weights in the minimum norm solution. (Simulation parameters: $\rho = 0$ degrees, $\vec{P}_{8/1,z} = 5$ meters, and $\dot{x}_s = 1$ meter at a period of 8.75 seconds.)

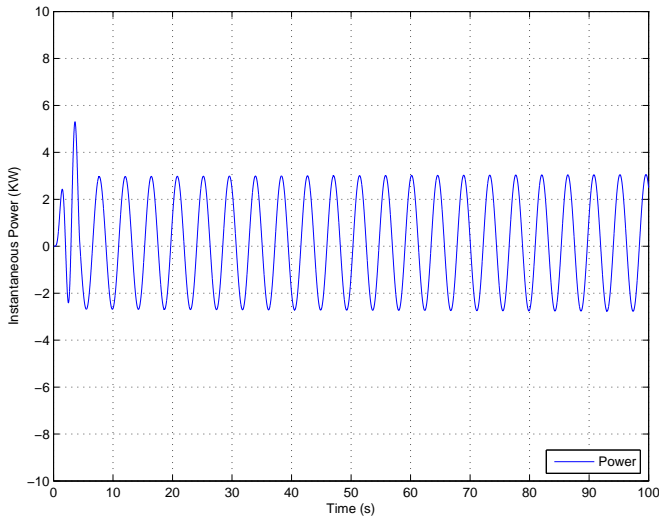


Figure 296. Plot of instantaneous power for the inverse kinematic control case with the identity matrix used as the weights in the minimum norm solution. (Simulation parameters: $\rho = 10$ degrees, $\vec{P}_{8/1,z} = 5$ meters, and $\dot{x}_s = 1$ meter at a period of 8.75 seconds.)

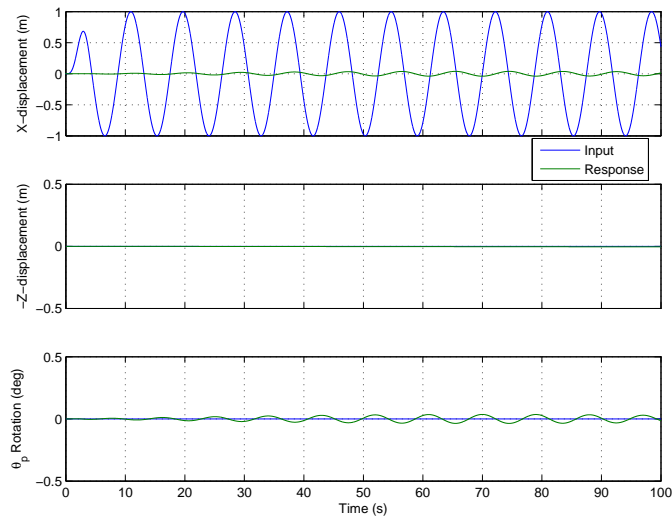


Figure 297. Plot of x , z , and θ time histories for the inverse kinematic control case with the jib length used as the weights on the luffing rates and unity on the hoist rates so that the actuation rates are in equivalent units of m/s. (Simulation parameters: $\rho = 10$ degrees, $\vec{P}_{8/1,z} = 5$ meters, and $\dot{x}_s = 1$ meter at a period of 8.75 seconds.)

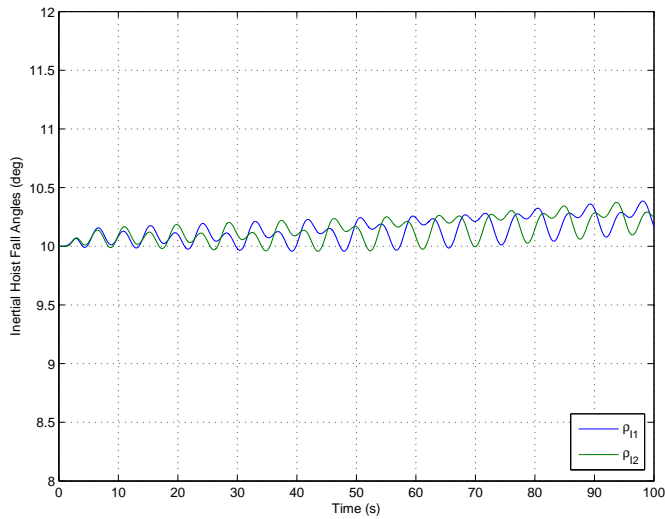


Figure 298. Plot of time histories for the inertial hoist-fall angle, ρ , for the inverse kinematic control case with the jib length used as the weights on the luffing rates and unity on the hoist rates so that the actuation rates are in equivalent units of m/s. (Simulation parameters: $\rho = 10$ degrees, $\vec{P}_{8/1,z} = 5$ meters, and $\dot{x}_s = 1$ meter at a period of 8.75 seconds.)

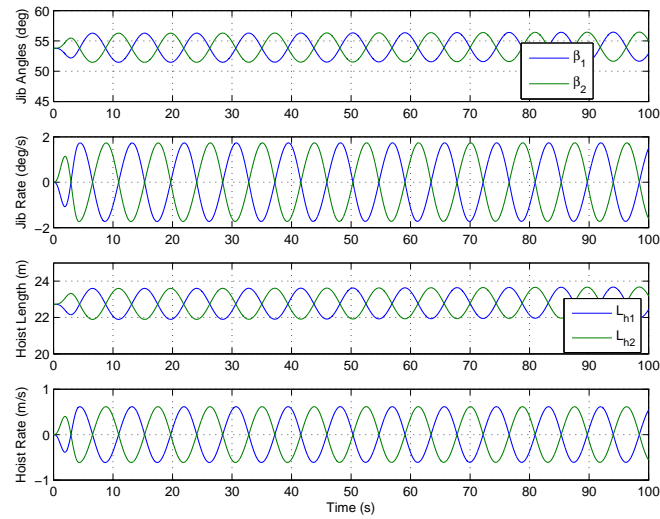


Figure 299. Plots of β , $\dot{\beta}$, L_h , and \dot{L}_h for the inverse kinematic control case with the jib length used as the weights on the luffing rates and unity on the hoist rates so that the actuation rates are in equivalent units of m/s. (Simulation parameters: $\rho = 10$ degrees, $\vec{P}_{8/1,z} = 5$ meters, and $\dot{x}_s = 1$ meter at a period of 8.75 seconds.)

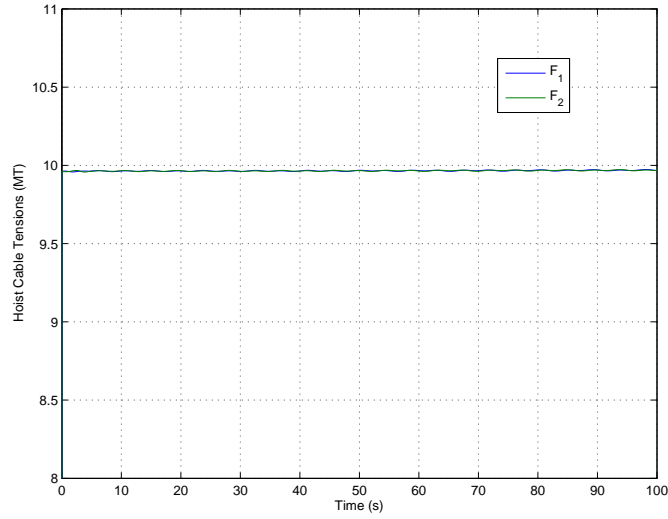


Figure 300. Plot of hoist cable tensions, F_1 and F_2 , for the inverse kinematic control case with the jib length used as the weights on the luffing rates and unity on the hoist rates so that the actuation rates are in equivalent units of m/s. (Simulation parameters: $\rho = 10$ degrees, $\vec{P}_{8/1,z} = 5$ meters, and $\dot{x}_s = 1$ meter at a period of 8.75 seconds.)

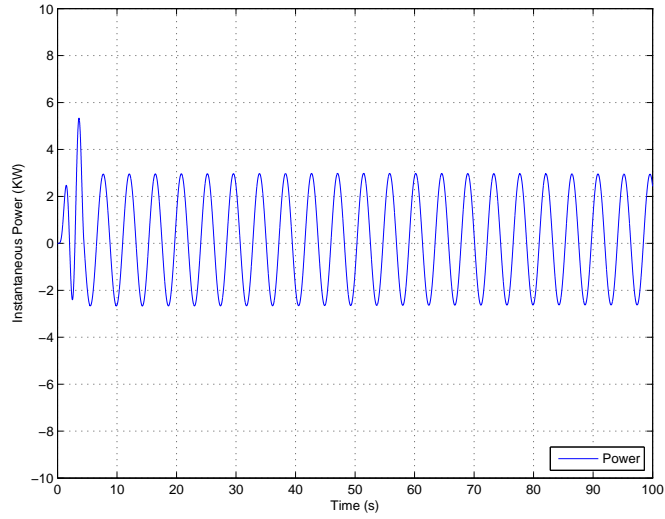


Figure 301. Plot of instantaneous power for the inverse kinematic control case with the jib length used as the weights on the luffing rates and unity on the hoist rates so that the actuation rates are in equivalent units of m/s. (Simulation parameters: $\rho = 10$ degrees, $\vec{P}_{8/1,z} = 5$ meters, and $\dot{x}_s = 1$ meter at a period of 8.75 seconds.)

THIS PAGE INTENTIONALLY LEFT BLANK

APPENDIX D. INVERSE KINEMATIC CONTROL ALGORITHM - MATLAB CODE

A. INVERSE KINEMATIC CONTROL ALGORITHM- MATLAB M-FILE

This appendix contains a listing of the inverse kinematic control algorithm for the planar dual-crane system as implemented as a MATLAB m-file.

```
function [sys,x0,str,ts] = ik(t,x,u,flag,dp)
%
% Inverse Kinematic Control Algorithm m-file S-function
%
% Section near end of file sets the weighting matrix
% used in the minimum norm solution
%
% General M-file S-function template comments below
% With M-file S-functions, you can define your own ordinary differential
% equations (ODEs), discrete system equations, and/or just about
% any type of algorithm to be used within a Simulink block diagram.
%

switch flag,
    case 0,
        [sys,x0,str,ts]=mdlInitializeSizes;
    case 1,
        sys=mdlDerivatives(t,x,u);
    case 2,
        sys=mdlUpdate(t,x,u);
    case 3,
        sys=mdlOutputs(t,x,u,dp);
    case 4,
        sys=mdlGetTimeOfNextVarHit(t,x,u);
    case 9,
        sys=mdlTerminate(t,x,u);
    otherwise
        error(['Unhandled flag = ',num2str(flag)]);
end

function [sys,x0,str,ts]=mdlInitializeSizes
```

```

sizes = simsizes;

sizes.NumContStates  = 0;
sizes.NumDiscStates = 0;
sizes.NumOutputs     = 6+5+3+3;
sizes.NumInputs      = 36+2+4;
sizes.DirFeedthrough = 1;
sizes.NumSampleTimes = 1;    % at least one sample time is needed

sys = simsizes(sizes);

% initialize the initial conditions

% str is always an empty matrix
str = [];
x0 = [];

% initialize the array of sample times
ts = [0 0];

% end mdlInitializeSizes

function sys=mdlDerivatives(t,x,u,dp)
sys=[];
% end mdlDerivatives

function sys=mdlUpdate(t,x,u)
sys = [];
% end mdlUpdate

function sys=mdlOutputs(t,x,u,dp)

tp = u(3);
xsd = u(8);
zsd = u(14);
ts = u(19);
%tht = u(22)
tsd = u(20);
%thtd = u(23)
b1 = u(25);
b2 = u(28);

```

```

Lh1 = u(31);
Lh2 = u(34);

Tension1 = u(41);
Tension2 = u(42);
Torque1 = u(39);
Torque2 = u(40);

ds1 = dp(1);
ds2 = dp(2);
Lb = dp(3);
%Lb2 = dp(4);
dp1 = dp(5);
dp2 = dp(6);
mp = dp(7);
Jp = dp(8);
ztx = dp(9);
ztz = dp(10);
ztp = dp(11);

mg = mp*9.81;

p8r1_s = [u(1) 0 u(2)]';
p1_s = [u(7) u(10) u(13)]';
p8_s = p1_s+p8r1_s;

p2r1_s = [ds1 0 0]';
p4r2_s = Lb*[-cos(b1) 0-sin(b1)]';
p6r8_s = dp1*[cos(tp-ts) 0-sin(tp-ts)]';
p4_s = p1_s+p2r1_s+p4r2_s;
p6_s = p8_s+p6r8_s;
p4r6_s = p4_s- p6_s;

% ship to boom frame xfr
Rsb = [cos(b1) 0 sin(b1);0 1 0;-sin(b1) 0 cos(b1)];
p4r6_b = Rsb*p4r6_s;
rho1 = atan2(p4r6_b(1),-p4r6_b(3));
%[p8r1_s p4r6_s p4r6_b]

p3r1_s = [-ds2 0 0]';
p5r3_s = Lb*[cos(b2) 0-sin(b2)]';
p7r8_s = dp2*[-cos(tp-ts) 0 sin(tp-ts)]';

```

```

p5_s    = p1_s+p3r1_s+p5r3_s;
p7_s    = p8_s+p7r8_s;
p5r7_s = p5_s- p7_s;
Rsb = [cos(b2) 0-sin(b2);0 1 0;sin(b2) 0 cos(b2)];
p5r7_b = Rsb*p5r7_s;
rho2 = atan2(-p5r7_b(1),-p5r7_b(3));
%[rho1*180/pi rho2*180/pi]

% We are sure this is now, 3/30/08
rI1 = b1- ts+rho1;
rI2 = b2+ts+rho2;
Jac = zeros(3,4);
RHS = zeros(3,1);

t1 = mg*dp1;
t2 = tp+rI1;
t3 = sin(t2);
t4 = cos(t2);
t6 = cos(rI2);
t8 = cos(rI1);
t11 = cos(tp+rI2);
t13 = dp1*t4*t6+dp2*t8*t11;
t14 = 0.1e1/t13;
t16 = sin(rI1);
t20 = t13*t13;
t21 = 0.1e1/t20;
t27 = -dp1*t3*t6- dp2*t16*t11;
t35 = sin(rI2);
J55 = -t1*t3*t14*t16- t1*t4*t21*t16*t27+t1*t4...
      ...* t14*t8+t21*dp2*mg*t11*t35*t27;
t3 = cos(tp+rI1);
t5 = dp1*t3;
t6 = cos(rI2);
t8 = cos(rI1);
t9 = dp2*t8;
t10 = tp+rI2;
t11 = cos(t10);
t13 = t5*t6+t9*t11;
t14 = t13*t13;
t15 = 0.1e1/t14;
t16 = sin(rI1);
t18 = sin(rI2);

```

```

t20 = sin(t10);
t22 ==-t5*t18- t9*t20;
t31 = 0.1e1/t13*dp2;
J56 ==-mg*dp1*t3*t15*t16*t22+t15*dp2*mg*t11*t18 ...
    ...*t22+t31*mg*t20*t18- t31*mg*t11*t6;
t2 = cos(-ts- rI1+b1);
t4 = cos(rI1);
Jac11 ==-Lb*t2/t4;
Jac12 = 0;
t1 = cos(rI1);
Jac13 = 0.1e1/t1;
Jac14 = 0;
Jac21 = 0;
t2 = cos(ts- rI2+b2);
t4 = cos(rI2);
Jac22 ==-Lb*t2/t4;
Jac23 = 0;
t1 = cos(rI2);
Jac24 = 0.1e1/t1;
t3 = sin(b1- ts);
t6 = cos(rI1);
Jac31 = J55*Lb*t3/Lh1/t6;
t3 = sin(b2+ts);
t6 = cos(rI2);
Jac32 = J56*Lb*t3/Lh2/t6;
t1 = sin(rI1);
t4 = cos(rI1);
Jac33 ==-J55*t1/Lh1/t4;
t1 = sin(rI2);
t4 = cos(rI2);
Jac34 ==-J56*t1/Lh2/t4;
t1 = cos(rI1);
t5 = cos(rI1+ts);
t9 = cos(-ts- rI1+b1);
t11 = sin(rI1);
rhs1 = (-zsd*t1+ds1*tsd*t5- Lb*tsd*t9+t11*xsd)/t1;
t1 = cos(rI2);
t5 = cos(rI2- ts);
t9 = cos(ts- rI2+b2);
t11 = sin(rI2);
rhs2 = (-zsd*t1- ds2*tsd*t5+Lb*tsd*t9- t11*xsd)/t1;
t2 = cos(rI2);

```

```

t6 = J55*ds1;
t7 = tsd*Lh2;
t9 = sin(rI2+ts);
t13 = sin(rI2- ts);
t16 = J55*Lb;
t18 = sin(rI2+b1- ts);
t22 = sin(-rI2+b1- ts);
t26 = cos(rI1);
t30 = J56*ds2;
t31 = tsd*Lh1;
t33 = sin(rI1+ts);
t37 = sin(-rI1+ts);
t40 = J56*Lb;
t42 = sin(rI1+b2+ts);
t46 = sin(-rI1+b2+ts);
t50 = Lh1*Lh2;
t52 = cos(-rI1+rI2);
t55 = cos(rI1+rI2);
rhs3 = (-0.2e1*J55*xsd*Lh2*t2+t6*t7*t9- t6*t7*t13...
...+t16*t7*t18+t16*t7*t22+0.2e1*J56*xsd*Lh1...
...*t26+t30*t31*t33+t30*t31*t37- t40*t31*t42...
...- t40*t31*t46)/(t50*t52+t50*t55);

```

Jac(1,1) = Jac11;

Jac(1,2) = Jac12;

Jac(1,3) = Jac13;

Jac(1,4) = Jac14;

Jac(2,1) = Jac21;

Jac(2,2) = Jac22;

Jac(2,3) = Jac23;

Jac(2,4) = Jac24;

Jac(3,1) = Jac31;

Jac(3,2) = Jac32;

Jac(3,3) = Jac33;

Jac(3,4) = Jac34;

RHS(1) = rhs1;

RHS(2) = rhs2;

```

RHS(3) = rhs3;

%if t>0
%   rho1*180/pi
%   rI1*180/pi
%disp(p3r1_s);
%disp(p5r3_s);
%disp(p7r8_s);
%disp(p5_s);
%disp(p7_s);
%disp(p5r7_s);
%disp(Rsb);
%disp(p5r7_b);
%   rho2*180/pi
%   rI2*180/pi
%end

%sys = inv(Jac)*RHS;
%sys = Jac\RHS;
W = eye(4);

% Construct weighting matrix
% A_wt = [Torque1 Torque2 Tension1 Tension2] '
%
% W = A_wt*A_wt'
%
% temp = eig(W)
% if min(temp) < .0001
%     W = eye(4);
% end

W = eye(4);
% W(1,1) = 1.0+(Torque1*Torque1); % Power weighting scheme #1
% W(2,2) = 1.0+(Torque2*Torque2);
% W(1,2)= Torque1*Torque2;
% W(2,1)= W(1,2);
% W(3,3) = (Tension1*Tension1);
% W(4,4) = (Tension2*Tension2);
% W(3,4) = Tension1*Tension2;
% W(4,3) = W(3,4);
%% Power weighting scheme #1A upper diagonal
% W(1,1) = 1.0+(Torque1*Torque1);

```

```

% W(1,2) = Torque1*Torque2;
% W(1,3) = Torque1*Tension1;
% W(1,4) = Torque1*Tension2;
% W(2,1) = 0.0;
% W(2,2) = 1.0+(Torque2*Torque2);
% W(2,3) = Torque2*Tension1;
% W(2,4) = Torque2*Tension2;
% W(3,3) = (Tension1*Tension1);
% W(3,4) = Tension1*Tension2;
% W(4,3) = 0.0;
% W(4,4) = (Tension2*Tension2);

%% Power weighting scheme #2 Diagonal terms only
% W(1,1) = 1.0+(Torque1*Torque1);
%
% W(2,2) = 1.0+(Torque2*Torque2);
% W(1,2)= 0.0;
% W(2,1)= W(1,2);
% W(3,3) = (Tension1*Tension1);
% W(4,4) = (Tension2*Tension2);
% W(3,4) = 0.0;
% W(4,3) = W(3,4);

%% Power weighting scheme #3 constant max torque,tension values
W(1,1) = (2.8056e+05)^2;
%
W(2,2) = (2.2112e+05)^2;
W(3,3) = (9.8112e+03)^2;
W(4,4) = (9.8113e+03)^2;

W(1,2) = 0.0;
W(1,3) = 0.0;
W(1,4) = 0.0;
W(2,1) = W(1,2);

W(3,4) = 0.0;
W(4,3) = W(3,4);

temp = eig(W);
% if t <= 0.01
%     eigen_vals = eig(W)
% end

```

```

if min(temp) < .0001
    W = eye(4);
end

%W= eye(4);
%W(2,2) = 9600;
%W(1,1) = 9600;

%W(1,1) = 1000; % do not use luff
%W(2,2) = 1000; % do not use luff
%W(1,1) = 1;
%W(2,2) = 1;
% W(1,1) = 1E6; % do not use luff
% W(2,2) = 1E6; % do not use luff
%eig(Jac*Jac')
%
% Minimum Norm Solution
temp = inv(W)*Jac'*inv(Jac*inv(W)*Jac')*RHS;
if t>2
%Jac
%RHS
%temp
end

sys(1:4) = temp;
sys(5) = rI1;
sys(6) = rI2;

b1d = temp(1);
b2d = temp(2);
Lh1d = temp(3);
Lh2d = temp(4);

tpd = 0;
x8d = 0;
z8d = 0;

rI1d = (xsd- ds1*sin(ts)*tsd+Lb*sin(b1-ts)*(b1d- tsd)-...
...Lh1d*sin(rI1)+dp1*sin(tp)*tpd- x8d)/Lh1/cos(rI1);

```

```

rI2d = (-xsd- ds2*sin(ts)*tsd+Lb*sin(b2+ts)*(b2d+tsd)-...
...Lh2d*sin(rI2)+dp2*sin(tp)*tpd+x8d)/Lh2/cos(rI2);

sys(7) = xsd- ds1*sin(ts)*tsd+Lb*sin(b1-ts)*(b1d-tsd)-...
... Lh1d*sin(rI1)-Lh1*cos(rI1)*rI1d+dp1*sin(tp)*tpd-x8d;

sys(8) = zsd- ds1*cos(ts)*tsd- Lb*cos(b1-ts)*(b1d-tsd)+...
...Lh1d*cos(rI1)-Lh1*sin(rI1)*rI1d+dp1*cos(tp)*tpd-z8d;

sys(9) = xsd+ds2*sin(ts)*tsd- Lb*sin(b2+ts)*(b2d+tsd)+...
...Lh2d*sin(rI2)+Lh2*cos(rI2)*rI2d-dp2*sin(tp)*tpd-x8d;

sys(10) = zsd+ds2*cos(ts)*tsd-Lb*cos(b2+ts)*(b2d+tsd)+...
...Lh2d*cos(rI2)-Lh2*sin(rI2)*rI2d-dp2*cos(tp)*tpd-z8d;
sys(7) = 0;
sys(8) = 0;
sys(9) = 0;
sys(10)=0;

sys(11) =-mg*dp2*sin(tp+rI2)*(tpd+rI2d)/(dp1*cos(rI2)*cos(tp+rI1)...
...+dp2*cos(tp+rI2)*cos(rI1))*sin(rI1)-mg*dp2*cos(tp+rI2)*...
...pow(dp1*cos(rI2)*cos(tp+rI1)+dp2*cos(tp+rI2)*cos(rI1),...
...-0.2e1)*sin(rI1)*(-dp1*sin(rI2)*rI2d*cos(tp+rI1)-
...dp1*cos(rI2)*sin(tp+rI1)*(tpd+rI1d)- dp2*sin(tp+rI2)*...
...(tpd+rI2d)*cos(rI1)-dp2*cos(tp+rI2)*sin(rI1)*rI1d)+mg*dp2*...
...cos(tp+rI2)/(dp1*cos(rI2)*cos(tp+rI1)+dp2*cos(tp+rI2)*...
...cos(rI1))*cos(rI1)*rI1d+pow(dp1*cos(rI2)*cos(tp+rI1)+...
...dp2*cos(tp+rI2)*cos(rI1),-0.2e1)*dp1*mg*cos(tp+rI1)*...
...sin(rI2)*(-dp1*sin(rI2)*rI2d*cos(tp+rI1)-dp1*cos(rI2)*...
...sin(tp+rI1)*(tpd+rI1d)- dp2*sin(tp+rI2)*(tpd+rI2d)*cos(rI1)-...
...dp2*cos(tp+rI2)*sin(rI1)*rI1d)+0.1e1/(dp1*cos(rI2)*cos(tp+rI1)...
...+dp2*cos(tp+rI2)*cos(rI1))*dp1*mg*sin(tp+rI1)*(tpd+rI1d)*...
...sin(rI2)- 0.1e1/(dp1*cos(rI2)*cos(tp+rI1)+dp2*cos(tp+rI2)*...
...cos(rI1))*dp1*mg*cos(tp+rI1)*cos(rI2)*rI2d;
sys(11) = 0;

sys(12) = zsd- ds1*cos(ts)*tsd- Lb*cos(b1- ts)*(b1d- tsd)+Lh1d*cos(rI1)-...
... sin(rI1)*(xsd-ds1*sin(ts)*tsd+Lb*sin(b1-ts)*b1d-Lb*sin(b1-ts)*...
...tsd-Lh1d*sin(rI1))/cos(rI1);

sys(13) = zsd+ds2*cos(ts)*tsd- Lb*cos(b2+ts)*(b2d+tsd)+Lh2d*cos(rI2)-...

```

```

...sin(rI2)*(-xsd- ds2*sin(ts)*tsd+Lb*sin(b2+ts)*b2d+Lb*...
...sin(b2+ts)*tsd-Lh2d*sin(rI2))/cos(rI2);

sys(14) = J55*(xsd- ds1*sin(ts)*tsd+Lb*sin(b1-ts)*b1d-Lb*sin(b1-ts)*tsd-...
...Lh1d*sin(rI1))/Lh1/cos(rI1)+J56*(-xsd- ds2*sin(ts)*tsd+Lb*...
...sin(b2+ts)*b2d+Lb*sin(b2+ts)*tsd- Lh2d*sin(rI2))/Lh2/cos(rI2);

sys(12)=0;
sys(13)=0;
sys(14)=0;

F1 = u(37);
F2 = u(38);

mtx1 = [-cos(rI1)-cos(rI2);dp1*cos(tp+rI1)-dp2*cos(tp+rI2)];
sde = [-mg;0];

Fest = inv(mtx1)*sde;

sys(15)=-F1*cos(rI1)-F2*cos(rI2)+mg;
sys(15)=0;
sys(16)=1*(F1-Fest(1));
sys(17)=0*(F2-Fest(2));
%sys(16)=F1;
%sys(17)=F2;
%sys(16)=Fest(1);
%sys(17)=Fest(2);

% end mdlOutputs

function sys=mdlGetTimeOfNextVarHit(t,x,u)

sampleTime = 1;% Example, set the next hit to be one second later.
sys = t+sampleTime;

% end mdlGetTimeOfNextVarHit

function sys=mdlTerminate(t,x,u)
sys = [];

% end mdlTerminate

```

THIS PAGE INTENTIONALLY LEFT BLANK

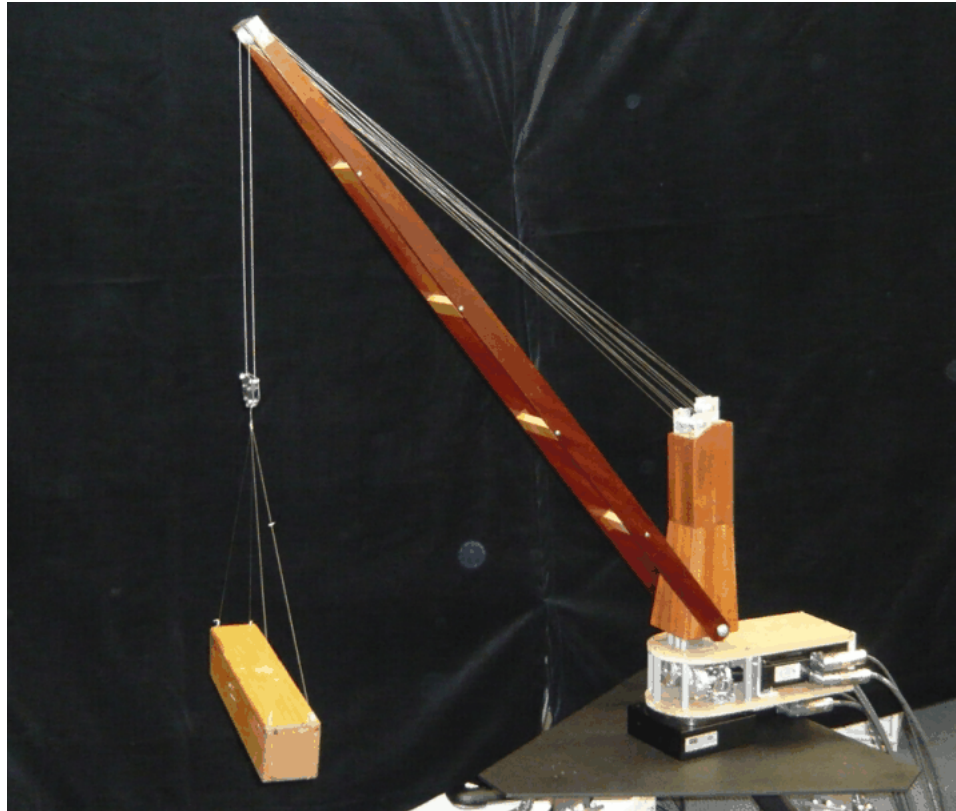
APPENDIX E. DEVELOPMENT OF THE PHYSICAL CRANE MODEL

A. CRANE DESIGN REPORT

This appendix contains the technical report that describes the design and development of the 1/32nd-scale crane models of the MacGREGOR TG3637 crane used for verification of the dual crane simulation model and inverse kinematic motion compensation.

The report is unpublished and so is included in its entirety.

REPORT ON
1/32nd Scale Crane Testbed Development



Prepared for
NSWC Carderock Division, Code 2120

Prepared by
BMT Designers & Planners, Inc.
2120 Washington Blvd., Ste. 200
Arlington, VA 22204

B. PURPOSE

The purpose of this document is to document the development of a high-fidelity testbed consisting of two 1/32nd scale crane models. The scale crane represents a Hagglunds TG3637 pedestal crane installed at the SS Flickertail State. It is mobilized by three servo motors, handling hoist, luff, and slew axes, allowing it to be operated in a way that can create a scaled version of the crane and cargo dynamics found on a full-size TAC-S ship.

C. BACKGROUND

The selection of the scale factor was based on the requirement to operate the model in a typical office-sized laboratory space. Previous 1/16th-scale single crane models had been constructed by the Sandia National Laboratory and Craft Engineering Associates (under contract to Daniel Wagner Associates). At this scale the jib is slightly over 2 meters long and an arrangement of two cranes would not fit the space requirement. A 1/36th-scale crane with a jib of slightly more than 1 meter in length would have been ideal, but would have required the development of new design drawings. For a slight increase in size, the decision was made to construct a 1/32nd-scale model by halving all the dimensions on the drawings used by Craft Engineering to construct their 1/16th-scale model. Craft Engineering's design was selected over Sandia's 1/16th-scale design, because the construction material was wood instead of machined and extruded metal, which was less expensive and could be more easily worked at the smaller scale. Craft Engineering constructed a total of four identical crane models of which two were mechanized for use in this testbed.

D. ASSEMBLY OVERVIEW

This section will detail the structure of the crane as well as the components used to make it into a fully motorized system. The objective is to give enough information here to allow for identical crane systems to be built in the future.

1. Crane Structure

The crane structures used for this project were pre-built by Dexter Bird of Craft Engineering. The supporting materials are primarily composed of wood, aluminum and brass and are held together with wood screws and glue.

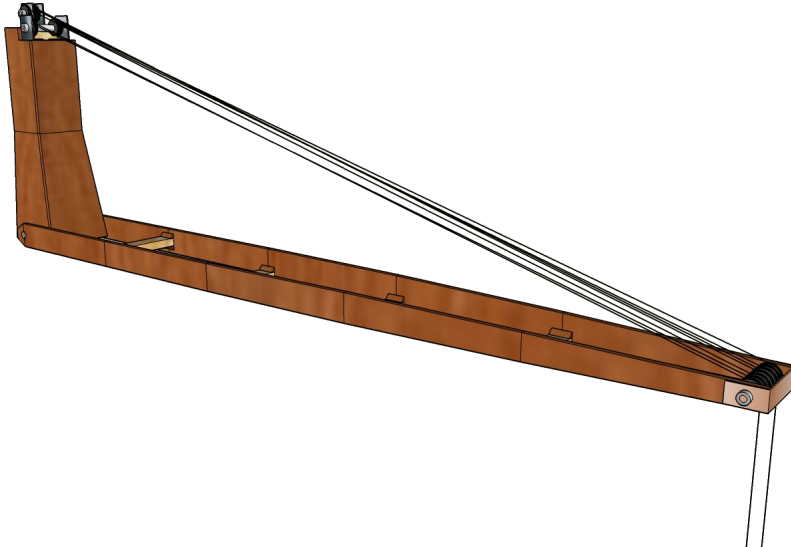


Figure 302. Drawing of crane model provided by Craft Engineering.

2. Winch & Motor Housing

For this project, an electro-mechanical approach was taken in order to control the linear displacement of the hoist and luff lines and simulate the line-leveling winches used on the full-size cranes. Each line is secured and rotated by a modified fishing reel that allows for approximately $\pm 1\frac{1}{4}$ " linear line displacement per spool revolution. Nylon-coated stainless steel wire rope was used for the hoist and luff lines due to its 40 lb breaking strength and its 7x7 strand core construction, allowing for very good flexibility.

In order to apply rotational force to the reel spool, a modification similar to the one demonstrated by Michigan Technological University (MTU)¹ was used. This

¹Bulgakov, Parker and Wheeler, 2005

involved removing the reel cover assembly, grounding off the obstructions and attaching a custom-made aluminum reel drive shaft and winch adapter plate to complete the winch design.

Each winch is then coupled to a high-performance servo motor shaft by means of a clamp-style flexible shaft coupling. The motors selected for this task were manufactured by Danaher Motion, part number AKM23C-BNC2C-00. They were chosen due to their ability of providing high torque at a wide range of speeds. The torque rating for these motors is 9.8 lb-in while offering a rated speed of 1000 rpm. It was estimated that the maximum torque needed for the winches would be approximately 3 lb-in and the maximum speed approximately 75 rpm, so the motors selected can allow for a wide range of system configurations and winch loads.

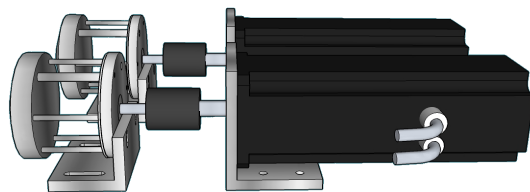


Figure 303. Drawing of the motor and winch bracket design.

As shown in Figure 303, the motors and winches are held in place with the use of custom-made aluminum mounting brackets. These brackets allow the components to be tightly secured and easily removed if necessary. They were designed to ensure that the shafts of each component remain properly aligned. Drawings for the brackets were made in-house and sent to ShortRunPro for fabrication and machining.

The structure which holds the crane, motors and winches in place consists of two MDF fiberboard plates, one below the crane and one below the motors and winches, which serve as mounting pieces for all of the system components. These plates are kept rigidly in place by attaching several 3" aluminum hex standoffs between the two plates.

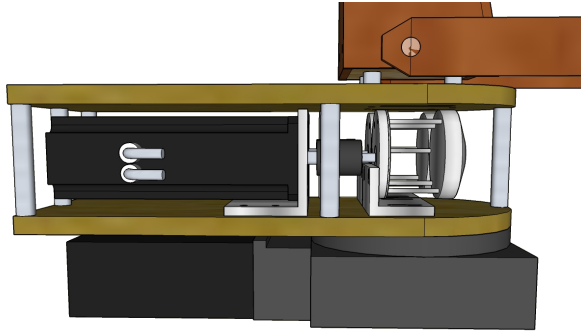


Figure 304. Side view of crane model, motor/winch structure and rotary table.

In addition to hoist and luff axes, the crane model also features a slewing axis. A 6" crossed roller bearing rotary table is attached to the bottom mounting plate and rotates the system around the center of crane. The table utilizes an anti-backlash worm assembly with a worm/gear ratio of 36:1. Therefore, one shaft revolution of the slew servo motor provides 10° of angular movement from the table, with high-resolution performance that is only limited by the resolution of the servo encoder. With the current servo configuration, the maximum encoder resolution is 131,072 quadrature counts per revolution, making the maximum resolution of the rotary table approximately 0.000076° , or 3.64 arcseconds.

E. DYNAMIC SCALING

1. Motor Drive Characteristics

In order for the scale cranes to exhibit the same behaviors caused by external events as the full scale TAC-S cranes, dynamic scaling laws must be applied to the geometry and motion of the scale cranes. These relationships are based on the assumption that gravity will remain constant regardless of scaling, therefore the linear acceleration ratio between scale model and full scale is 1. All other dynamic scaling relationships can be derived from this assumption, as is shown in Table 7. One may assume that λ is equal to 1/32.

Table 7. Electro-mechanical Parts List

Quality	$\lambda = \frac{\text{model size}}{\text{full-scale size}}$
Length	λ
Time	$\sqrt{\lambda}$
Displacement	λ
Linear Velocity	$\sqrt{\lambda}$
Linear Acceleration	1
Angular Velocity	$\frac{1}{\sqrt{\lambda}}$
Angular Acceleration	$\frac{1}{\lambda}$
Frequency	$\frac{1}{\sqrt{\lambda}}$

2. Characterization of Crane Winches

Since each scale crane was custom-assembled by hand, the relationship between the rotation of the winches and the luffing and hoisting behavior will be unique to each crane. Due to this non-uniformity, it was necessary to characterize the performance of each crane to ensure accurate and repeatable behavior for all axes of motion. Slew characterization was ignored because of the direct relationship between servo motor shaft rotation and rotary table angle.

The method chosen for this characterization process involved individual data collection runs for each luff and hoist axis on both cranes, resulting in four runs. A marker triangle was attached to either the side of the boom or the hook block depending on which axis was being measured. Once the video tracking system correctly and continuously began tracking the markers, translation and rotation data for the virtual 2-D object created by the markers was broadcast over UDP to the LabVIEW computer controlling the cranes. Depending on which axis was being measured, a timed loop running at 40 Hz logged the pitch angle or Z-axis displacement along with the absolute encoder count for the corresponding servo axis.

During each characterization run, the luff angle or hoist displacement was positioned to its maximum angle or height where the video tracking system could still detect the markers. At this point, the LabVIEW program operating the cranes

and logging the data would begin and the crane operator would slowly lower the boom or hook block to the minimum trackable angle or displacement. The operator would then raise the boom or hook block back to its maximum position and stop the LabVIEW program. If all went according to plan, a log file would be generated that included rows of tab-separated data containing each timestep's encoder count and luff angle or hook block displacement. This data was then imported into Microsoft Excel, graphed and given a fitted trendline. The slope of this trendline determined the average relationship between servo/winch rotation and luff/hoist movement. The results are plotted below.

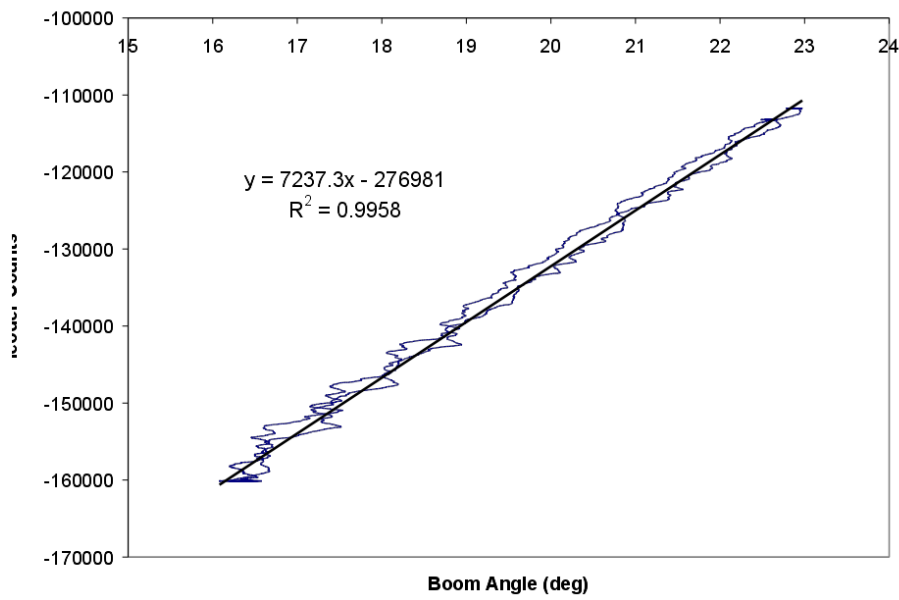


Figure 305. Graph plotting encoder counts versus boom angle for crane 1.

F. SOFTWARE

The cranes are currently controlled using LabVIEW, a graphical programming environment developed by National Instruments, which easily communicates with the motion control system using National Instruments hardware.

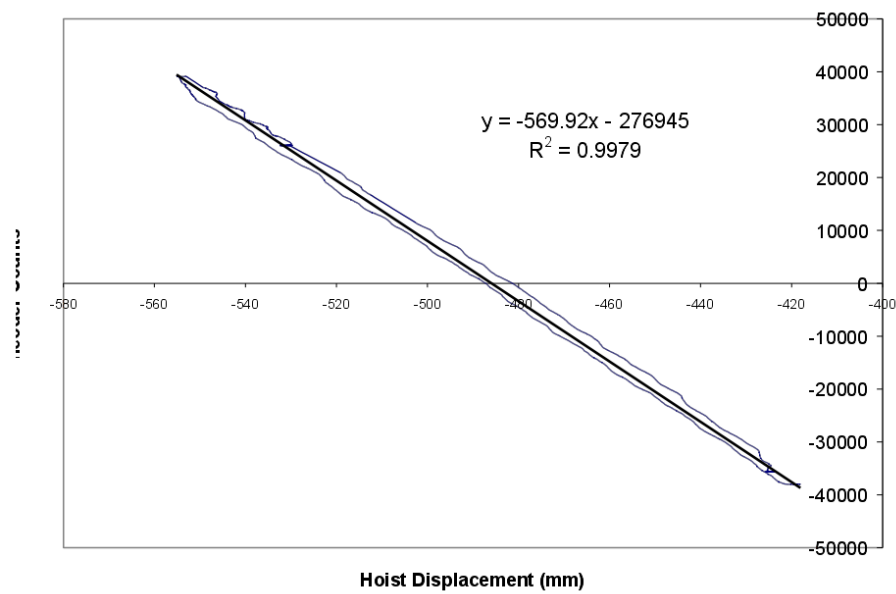


Figure 306. Graph plotting encoder counts versus hoist displacement for crane 1.

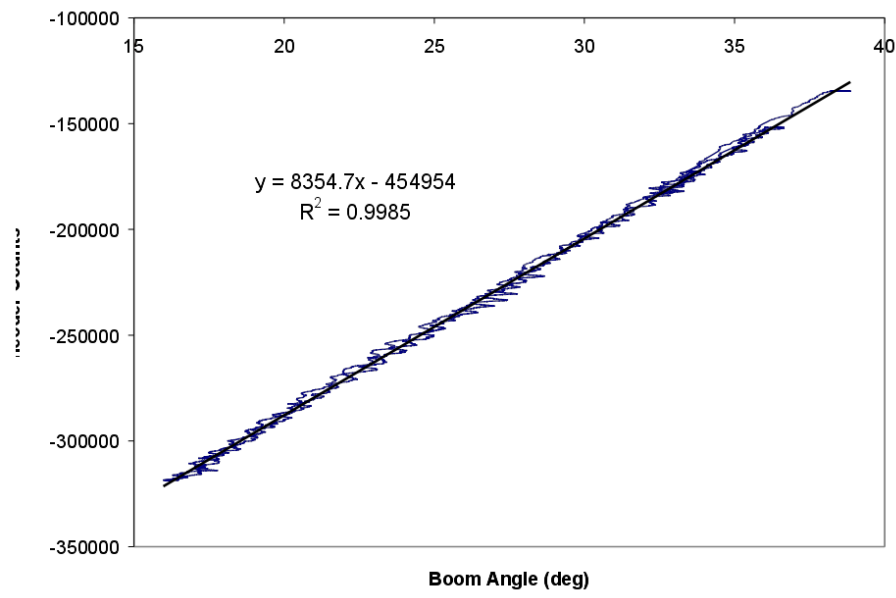


Figure 307. Graph plotting encoder counts versus boom angle for crane 2.

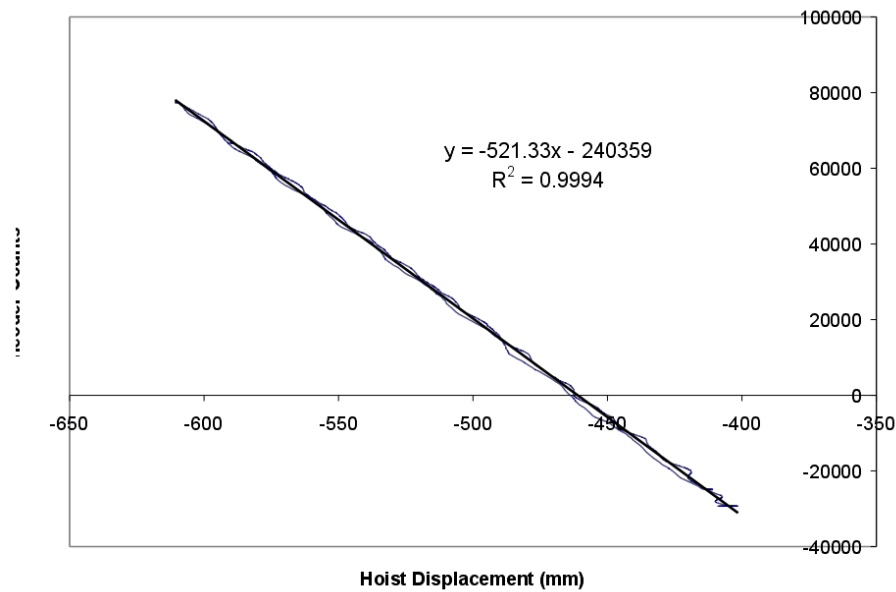


Figure 308. Graph plotting encoder counts versus hoist displacement for crane 2.

1. LabVIEW

In order to issue motion commands to the servo drives and receive encoder feedback from the motors, the NI-Motion virtual instrumentation (VI) set was used in creating the crane model program. NI-Motion is a feature-rich collection of tools allowing you develop a comprehensive motion control system. You are given total control over the trajectory settings of each axis, with configurable settings for absolute/relative position, velocity, acceleration, position limits and home reference points. This section will go into detail on how these features were utilized in creating a basic team crane motion control program using two wireless operating joysticks.

Before any motion commands are issued, both joysticks must be initialized using the Initialize Joystick VI. Each joystick has a unique Device ID, and in this case those IDs are 0 and 1. Both initialized joysticks are passed on to a While Loop where LabVIEW acquires the joystick commands using the Acquire Input Data VI and converts them into velocity (rpm) commands for each axis of motion. The joysticks feature two 2-axis analog sticks that are used to issue the motion commands.

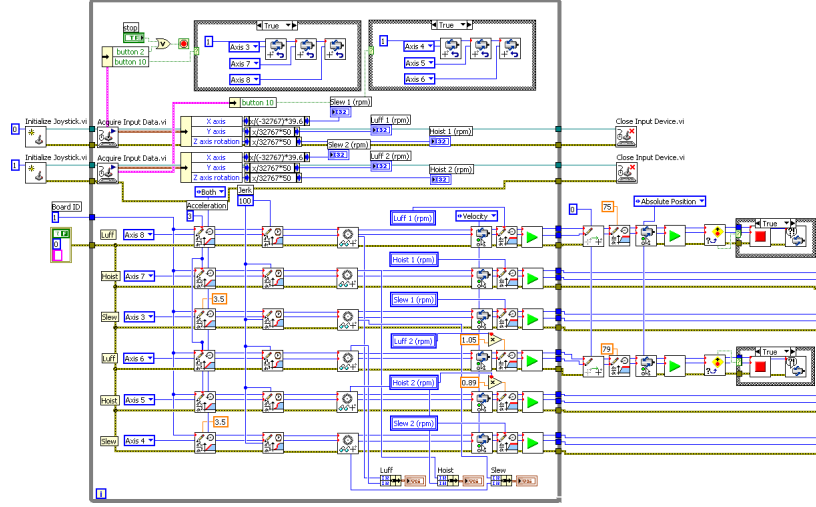


Figure 309. Acquiring joystick inputs for controlling luff, hoist and slew axes.

Each analog stick returns a 16-bit ($\pm 32,768$ counts) signed integer value for each axis which is then computed as a percentage of the maximum rpm set for each axis of motion. This process is shown in Figure 310.

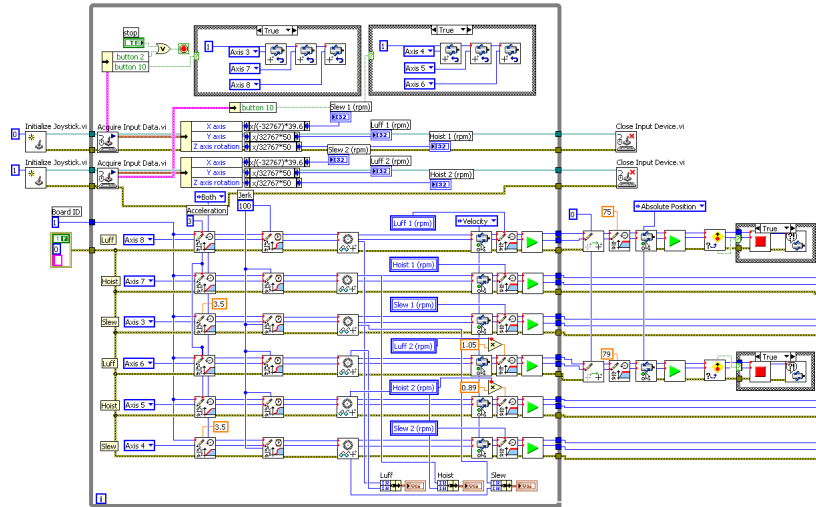


Figure 310. Axes of motion being configured and given velocity commands.

Once the motion commands have been calculated, their values are passed on to the Load Velocity in RPM functions followed by the Start Motion command. This updates the analog velocity command signal given to each servo drive and continues

to update within the While loop until the user manually stops the program.

While the parameters for each axis are being updated, the quadrature encoder counts are being read and displayed on a graph on the front screen of the program. This allows the user to ensure that each motor is exhibiting the correct behavior and diagnoses any potential problems such as faulty code, applying too much torque to the motor, etc.

G. APPENDIX: PARTS LIST

Table 8. Parts list of all significant components to build a single scale crane model.

Part Number	Description	Qty	Total Cost
2938578	Power Supply, 24VDC, 2.5A	1	\$168.00
5500C3	Right-handed Abu Garcia Reel	1	\$79.99
5501C3	Left-handed Abu Garcia Reel	1	\$79.99
BT000100-C.375-C.250	Flexible Shaft Coupling	2	\$63.30
AKM23C-BNB2C-00	Servo Motor (Luff/Hoist)	2	\$1,610.00
S20260-VT	Servo Drive	3	\$2,040.00
AKM21C-BNBNC-00	Servo Motor (Slew)	1	\$520.00
RTR-6	Rotary Table	1	\$2,763.00
CP-102ABAN	3-Meter Power Cable	3	\$459.00
CF-DA0111N	3-Meter Feedback Cable	3	\$396.00
A 7Y55-FSS6225	Ball Bearings	2	\$17.19
N/A	Motor Mount	2	\$78.40
N/A	Reel Drive Shaft	2	\$142.00
N/A	Winch Adapter Plate	2	\$138.60
N/A	Winch Mount	2	\$86.88
		Total	\$8,642.35

H. APPENDIX: INTERFACE CONNECTIONS

Table 9. Motion Command and Feedback Connections.

S200 [High-Density DB26]		UMI-7774 [DB15]		
Pin	Signal	Pin	Signal	S200
1	Digital IN COM	C1	Analog Output (+)	24
2	Digital IN 1 (Enable)	C2		
3		C3		
4		C4		
5		C5		
6	Digital OUT 1 -	C6	Enable (Isolated) (+)	2
7	Digital OUT 1 + (Fault)	C7	Fault +	7
8		C8		
9		C9	Analog Output Ground (-)	25
10		C10		
11		C11		
12		C12		
13		C13		
14		C14	Fault -	6
15		C15	Isolated Common (-)	1
16		Encoder Splitter		
17	Channel Z OUT	Pin	Signal	S200
18	Channel Z-bar OUT	P2-3	Encoder Phase A IN	19
19	Channel A OUT	P2-5	Encoder Phase B IN	21
20	Channel A-bar OUT	P2-7	Encoder Phase Z IN	17
21	Channel B OUT	P2-4	Encoder Phase A-bar IN	20
22	Chanel B-bar OUT	P2-6	Encoder Phase B-bar IN	22
23		P2-8	Encoder Phase Z-bar IN	18
24	Analog Command +			
25	Analog Command -			
26				

I. APPENDIX: ALUMINUM PARTS DRAWINGS

Mechanical drawings are provided below for the following encoder emulation system components:

- Motor Mounting Bracket
- Winch Mounting Bracket
- Winch Adapter Plate
- Reel Drive Shaft

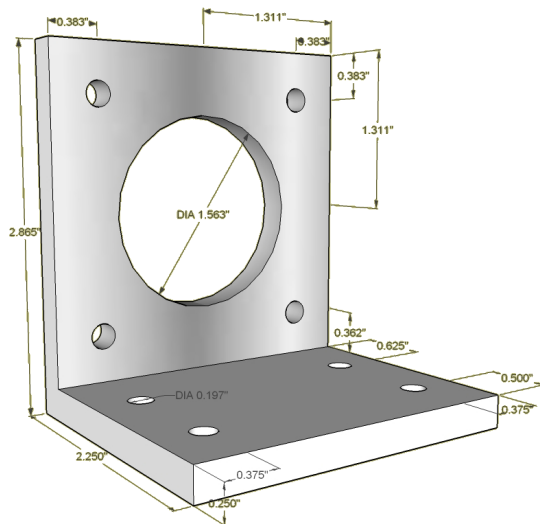


Figure 311. 3D Drawing of Motor Mounting Bracket Dimensions (in inches).

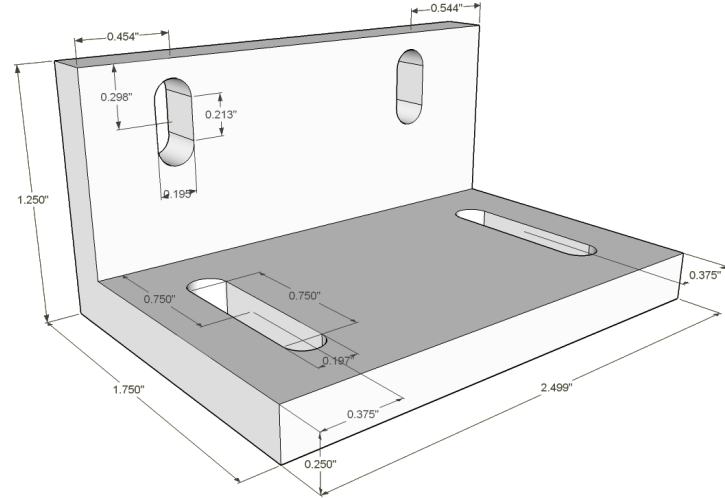


Figure 312. 3D Drawing of Winch Motor Bracket Dimensions (in inches).

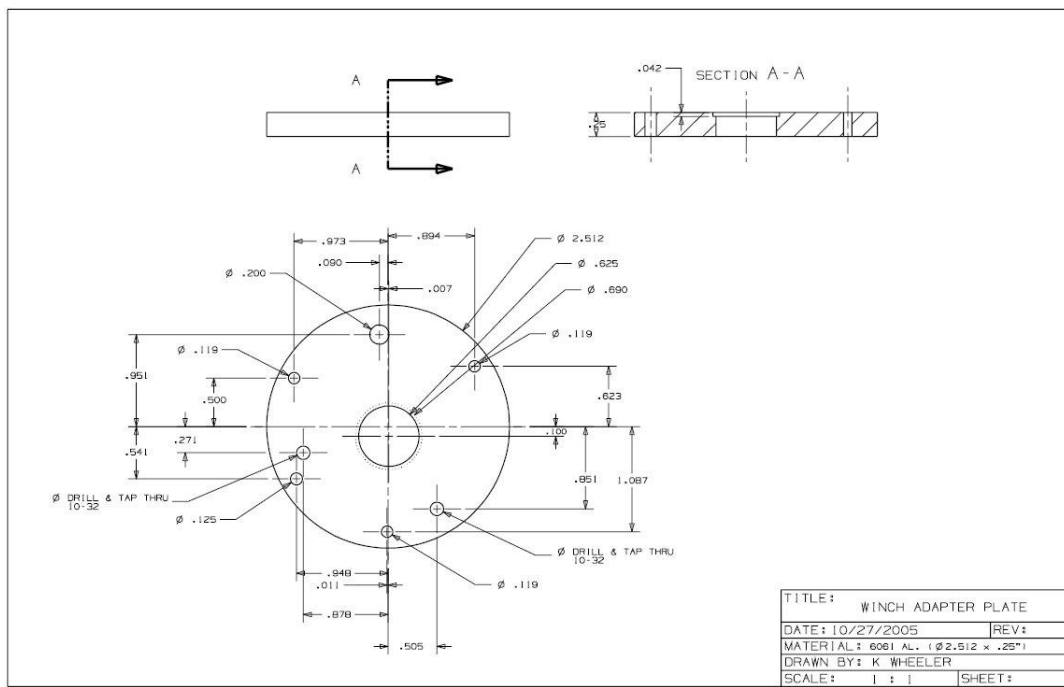


Figure 313. CAD Drawing of Winch Adapter Plate Dimensions (in inches).

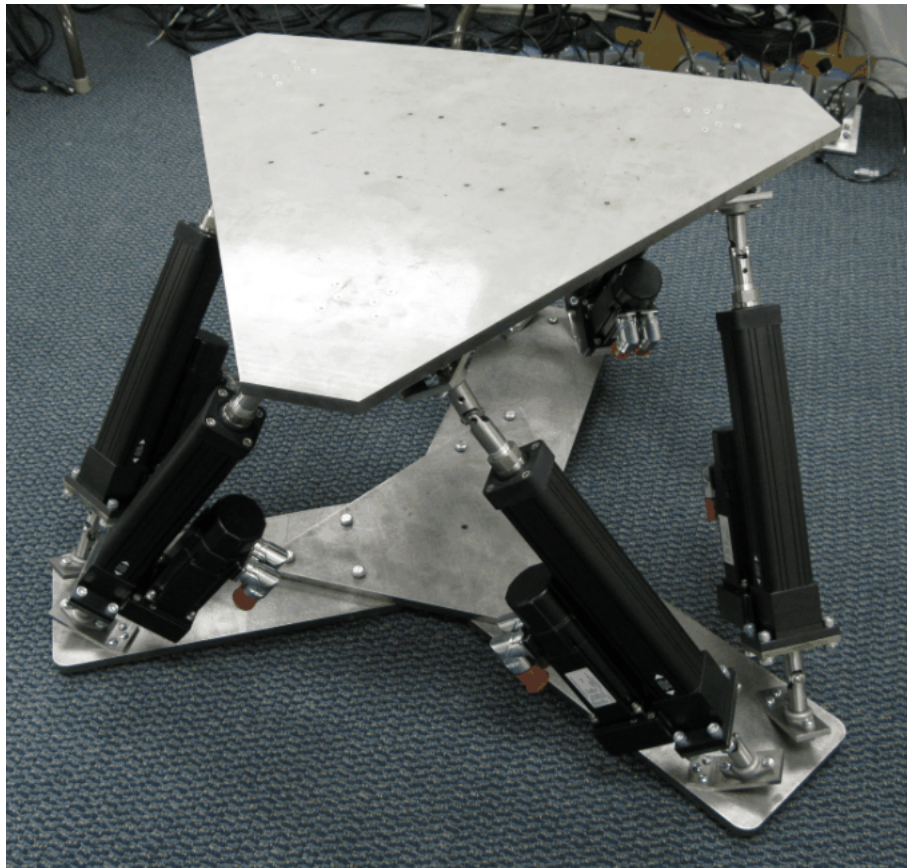
APPENDIX F. DEVELOPMENT OF THE MOTION PLATFORM APPARATUS

A. MOTION PLATFORM DESIGN REPORT

This appendix contains the technical report that describes the design and development of the motion platform that simulated the ship motion input for the dual-crane model apparatus used for verification of the dual crane simulation model and inverse kinematic motion compensation.

The report is unpublished and so is included in its entirety.

REPORT ON
6-DOF Portable Motion Base Testbed Development



Prepared for
NSWC Carderock Division, Code 2120

Prepared by
BMT Designers & Planners, Inc.
2120 Washington Blvd., Ste. 200
Arlington, VA 22204

B. PURPOSE

The purpose of this report is to document the development of a high-precision 6-DOF portable motion base testbed, which is capable of simulating the ship motion of the SS Flickertail State (T-ACS5) up to sea state 4 with a scaling factor of $1/32^{nd}$. The motion base is a spatial Stewart mechanism. It is powered by six linear electrical actuators and servo motors, which provide six degrees-of-freedom, i.e., surge, sway, heave, roll, pitch, and yaw. The linear actuators and servo motors are controlled via high-performance, 12-axis stepper/servo controllers. A graphical user interface is developed in Labview for setting up control parameters and monitoring the performance of the motion base. This report provides design, fabrication, and testing details of the hardware and software components of the motion base testbed.

C. BACKGROUND

The 6-DOF portable motion base is intended to precisely simulate the ship motion of the SS Flickertail State (T-ACS 5) in a laboratory environment. One or two $1/32^{nd}$ scale pedestal cranes will be mounted onto the motion base. Under this contract, Prof. Gordon Parker and his students at Michigan Technological University did a preliminary design (Reference [?]). BMT Designers & Planners refined the structural design, fabricated two sets of the motion base, and mobilized them with a new control system approach.

This refined version of the 6-DOF portable motion base shares the same set of specifications with slight modifications. That is,

- Base footprint no larger than 160" diameter
- Each subassembly including case weighs no more than 100 lbs
- Powered by 120v power
- Assemble the entire platform and calibrate it in no longer than 2 hours
- System has a safety braking system

- Each subassembly fits inside a hard case no larger than 29" by 29" by 8"
- Have at least $\pm 10^\circ$ of pitch, roll, and yaw motion
- Have at least $\pm 3"$ travel for heave
- Have at least $\pm 1.5"$ travel for surge and sway
- System has a simple user interface with at least the following parameters: sine wave amplitude and frequency input for all motions and individual motion control for roll, pitch, yaw, surge, sway, and heave
- Support a static load of 300 lb
- Reproduce sinusoidal motion for all six motions both independently and simultaneously with a period of no more than 3 seconds
- Less than 39" tall
- Use "clean" actuators like electric or pneumatic
- Platform has a resolution of 0.5° in all directions

1. Structure

The structure of the motion base can be divided into three parts: platform, actuator legs, and supporting base. The platform is simply an aluminum or steel plate which allows for the load to be attached on top and actuator legs below. The actuator legs include the linear actuators themselves, several custom components used for linking the actuators to universal joints as well as the platform and base. The supporting base consists of four custom-machined steel parts bolted together to create a sturdy and easy-to-disassemble foundation for the motion base.

2. Components

Much of the motion base was constructed using high-quality steel and aluminum parts, most of which were custom-designed to allow for a specific range of motion and load capacity expected of the scenarios that were devised for this machine. In total, the base is comprised of seven unique custom parts that all serve as linking or load-bearing pieces throughout the system. Supporting base legs, actuator

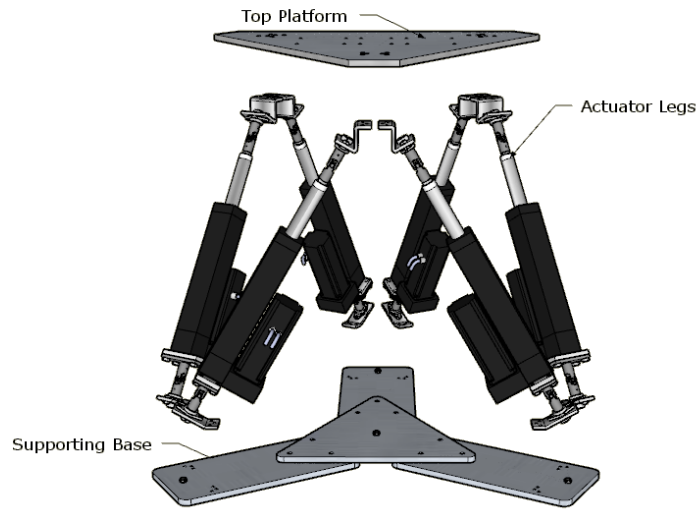


Figure 314. Exploded view of three main motion base components.

leg brackets and connecting shafts were all cut from $\frac{1}{4}$ " to $\frac{1}{2}$ " cold-rolled steel to ensure minimum deflection and plasticity while under loading stress. The top platform piece was made from $\frac{1}{4}$ " aluminum and electrostatically powder painted to minimize corrosion and provide an aesthetically pleasing surface. Dimension drawings of all components can be found in the Appendix.

Danaher Motion TN-B23 series ball screw actuators are selected to provide linear motion for six legs. Each actuator is equipped with an AKM23D servo motor. This combination of the actuator and servo motor provides each leg with a load capacity of 600lb and a max thrust of 275 lbs. The max velocity and acceleration of the actuator is 30 in/sec and 700 in/sec^2 , respectively. The ball screw provides the actuator an excellent repeatability of $\pm - 0.001\text{in}$.

3. Kinematic

Because the Stewart platform employs the use of six rigidly coupled actuator legs, a set of kinematic equations must be determined to calculate the displacement of each actuator for each given platform orientation. This is done by first setting an

inertial reference frame with respect to the motion of the platform. The platform is capable of moving with six degrees of freedom, which is made up of translational and rotational motions. The translational motion consists of three displacements: heave, surge and sway. The rotational motion is made up of three angles: roll, pitch and yaw.

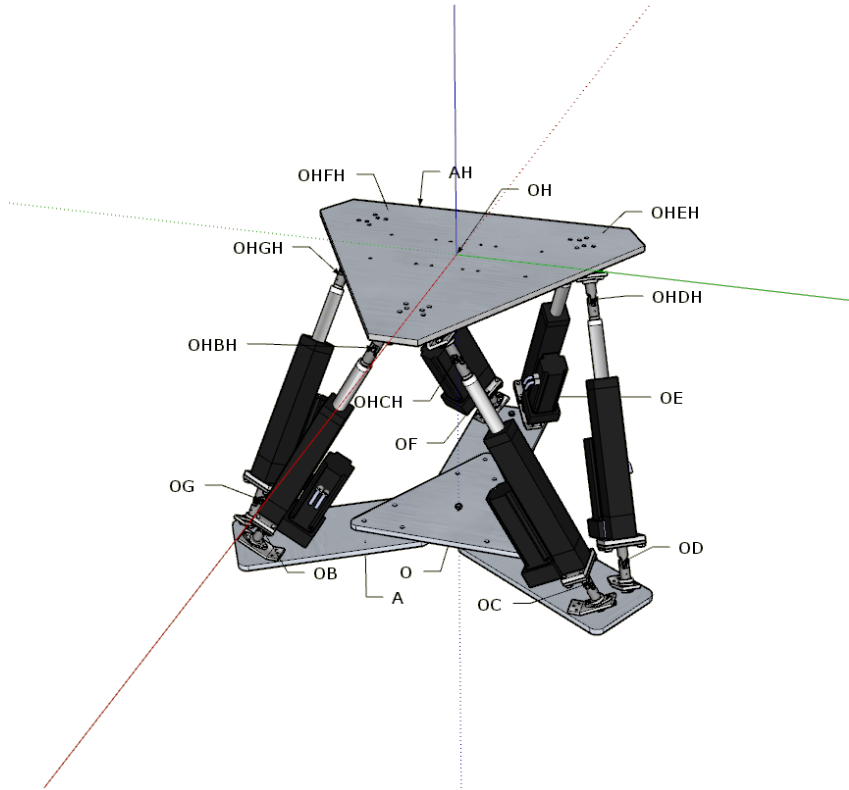


Figure 315. Base-fixed coordinate system.

As described earlier and shown in Figure 315, an inertial reference frame **A** is used in conjunction with the moving platform frame **AH** to calculate the displacements of each actuator. In addition, each frame is given six points to indicate the end of each actuator leg, which is located at the center of each legs two respective Universal joints. A vector is created between each corresponding point pair (e.g. **OB** → **OHBH**) and its magnitude is calculated to give the total distance between the actuator joints. Using the known initial distance of each actuator leg, the calculated

vector magnitudes can be used to determine the change in stroke length of each leg. As it follows, when the linear actuators are all fully retracted this constitutes the initial condition for all legs before the motion base is run. However, before a simulation is run the motion base is extended to its mid-point to allow ± 4 inches of travel for each actuator.

The six linear and rotational motions are mapped to the red, green and blue axis lines shown above. Surge is along the red axis while roll rotates around it. Sway moves along the green axis while pitch rotates around it. Finally, heave rotates along the blue axis while yaw rotates around it. It is these six parameters which make up the rows of input data to the kinematic equations which determine the stroke lengths of each actuator. These equations were developed using Autolev software (Reference [?]) and, given the correct Cartesian coordinates for each of the joints in the system, are able to determine the positions and velocities for any six-legged parallel-link system configuration.

Figure 316. Example DAT file containing 6-DOF data for motion base simulation.

D. SOFTWARE

1. Motion Base Simulation in Processing

Due to its ease of use, graphics support and open-source license, the Processing programming environment was used to model and simulate the motion base test cases. Code is written in the Java programming language and uses its own graphics and utility API to support OpenGL and native Processing functions.

The main components of the simulation can be broken down into four parts:

1. Read 6-DOF data file
2. Calculate stroke lengths of each actuator leg
3. Update drawing of motion base using new stroke lengths and direction cosine matrix
4. Dump stroke length and 6-DOF data into a DAT file

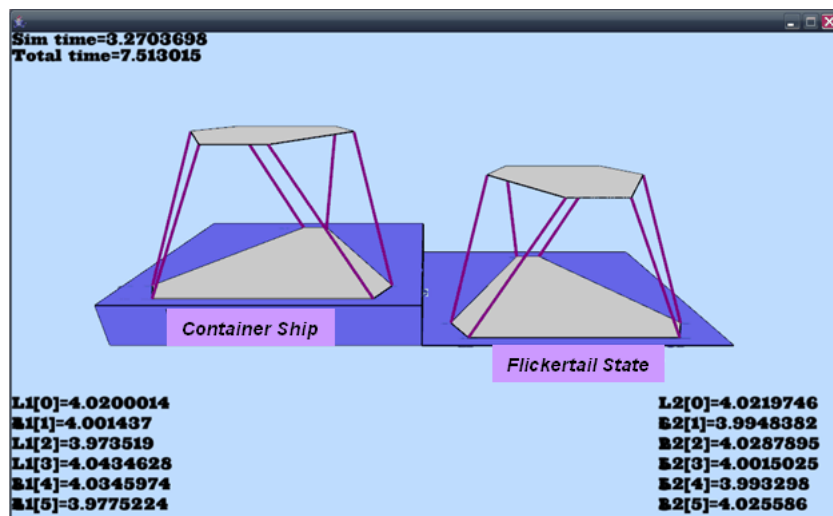


Figure 317. Screenshot of Processing motion base simulator.

As shown in Figure 317, the simulator produces a simple line and polygon 3D representation of the motion base(s). In the top-left the elapsed simulation time (number of seconds elapsed using input data) and total time (number of seconds elapsed including ramping up and down time) are shown. The bottom corners show

the current stroke lengths of each actuator in inches. Actuator velocities can be seen by pressing ‘V’, while pressing ‘P’ will return to position view. When the user has enough simulation data, the motion base(s) must be ramped down back to their original position. This can be accomplished using the ‘Z’ button. Once the actuators have reached their minimum position, the user can press ‘X’ to exit the program and store the data to a text file.

2. LabVIEW

In order to issue motion commands to the servo drives and receive encoder feedback from the motors, the National Instruments NI-Motion virtual instrumentation (VI) set was used in creating the crane model program. NI-Motion is a feature-rich collection of tools allowing development of a comprehensive motion control system. The user has total control over the trajectory settings of each axis, with configurable settings for absolute/relative position, velocity, acceleration, position limits and home reference points. This section will go into detail on how these features were utilized in creating a tightly-coupled six-axis motion control system.

All software used to control the motion base, as well as other components, can be found in the Project Explorer window for the “Motion Base (Contouring).lvproj”. Within this window is a hierarchical file viewer which separates all projects files into two lists: local and networked. Local files are run on the machine itself and can communicate with networked programs directly through LabVIEW shared network variables or serial, TCP or UDP protocols.

Motion Base (Contouring).lvproj.

Main project file containing all local and remote VIs for operation of motion base, scale crane and PCS.

Send Actuator Commands.

Waits for RT Motion Base... to ping for a line of data from the user-specified motion base data file over UDP. Also sends and receives Program Status updates to/from RT Motion Base during operation.

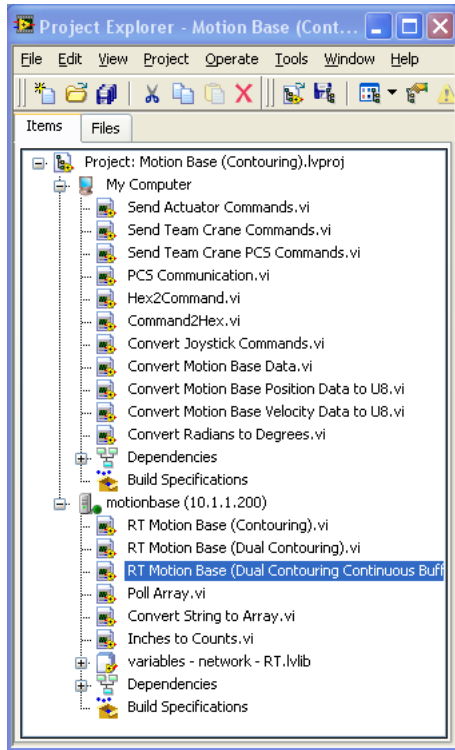


Figure 318. Project Explorer window showing Local and Networked files.

RT Motion Base (Dual Contouring Continuous Buffer) v2.

Initializes motion cards and pings Send Actuator Commands line by line for all stroke length and 6-DOF position and velocity data. Stroke length data is stored in a buffer where data points are cubic spline interpolated to smooth motion. Program waits for both buffers (motion card 1 & 2) to fill up then synchronizes the execution of the buffers. As buffer data is read old data is replaced by new commands until all data has been read.

Poll Array.

Pings the Send Actuator Commands program for data at a specified line in the user data file and passes the incoming packet string to Convert String to Array to create floating point arrays of stroke length and 6-DOF position and velocity data.

Convert String to Array.

Receives comma and forward-slash separated data and converts it into three arrays: stroke length commands, 6-DOF position data and 6-DOF velocity data.

Inches to Counts.

Converts stroke length commands into encoder count target positions based on the resolution of the linear actuator encoders.

E. APPENDIX: PARTS LIST

List of electro-mechanical parts necessary to construct one motion base.

Table 10. Electro-mechanical Parts List

Part No.	Description	Unit Price	Qty	Total Price
TN-X-10-2B-8- MF2-FT1E-23-C AKM23D-EFB2C-00	Linear actuators and servo motors	\$2,345.00	6	\$14,070.00
S20360-VTS	Servo drives	\$650.00	6	\$3,900.00
CK-S200-IP-AC-TB	Servo drive connection kit	\$80.00	6	\$480.00
CP-102ABAN-03	3 meter power/feedback cables	\$422.00	6	\$2,532.00
PSP-1Q	PNP (open) limit switch, 4 meter quick disconnect cable	\$120.00	6	\$720.00
	Bottom Bracket	\$16.13	6	\$96.78
	Flange Mount	\$43.36	6	\$260.16
	Coupling Shaft	\$101.19	6	\$607.14
	Top Bracket	\$26.99	6	\$161.94
	Top Platform	\$233.56	1	\$233.56
	Center Leg Connector	\$116.57	1	\$116.57
	Platform Leg	\$50.38	3	\$151.14
CJ644BKW1SS	Universal Joints	\$42.26	12	\$507.12
	Misc. Parts (screws, nuts, mounting feet, etc)	\$350.00	1	\$350.00
		Total		\$24,186.41

LIST OF REFERENCES

- [1] Operations of the Service Force U. S. Pacific Fleet, Fiscal Year 1964. Technical report, Commander Service Force, U. S. Pacific Fleet, 1964.
- [2] CNET. Seaman - navedtra 14067. Technical report, U.S. Navy, Chief of Naval Education and Training, 1993.
- [3] Operations of the Service Force U. S. Pacific Fleet, Fiscal Year 1967. Technical report, Commander Service Force, U. S. Pacific Fleet, 1967.
- [4] Vice Admiral Edwin Bickford Hooper, USN (Retired). *Mobility, Support, Endurance - A Story of Naval Operational Logistics in the Vietnam War, 1965-1968.* U.S. Government Printing Office, Washington, DC, USA, 1972.
- [5] Operations of the Service Force U. S. Pacific Fleet, Fiscal Year 1969. Technical report, Commander Service Force, U. S. Pacific Fleet, 1969.
- [6] Operations of the Service Force U. S. Pacific Fleet, Fiscal Year 1968. Technical report, Commander Service Force, U. S. Pacific Fleet, 1968.
- [7] Edward J. Marolda and Oscar P. Fitzgerald. *The United States Navy and the Vietnam Conflict, Vol. II, From Military Assistance to Combat, 1959-1965.* Naval Historical Center, Department of the Navy, Washington, D.C., USA, 1986.
- [8] Dexter Bird. Preliminary report joint army navy rider block tagline system test. Technical report, EG and G Washington Analytical Services Center, Inc., December 1977.
- [9] Intelligent Systems Division. Survey of cargo handling research relative to the mobile offshore base (mob) needs. Technical report, National Institute of Standards and Technology, July 1998.
- [10] Real-Time Innovations, October 2007. [online]
<http://www.rti.com/corporate/news/seicor.html>.
- [11] Operations of the Service Force U. S. Pacific Fleet, Fiscal Year 1966. Technical report, Commander Service Force, U. S. Pacific Fleet, 1966.
- [12] U. S. Military, August 2008. [online]
<http://www.transchool.eustis.army.mil/MUSEUM/DeLongFloatingPier.htm>.

- [13] Military Traffic Management Command Transportation Engineering Agency. Vessel characteristics for shiploading. MTMCTEA Pamphlet 700-4, 720 Thimble Shoals Boulevard, Suite 130, Newport News, VA 23606-4537, August 2001.
- [14] U. S. Army Transportation Museum, August 2008.
[online]<http://usmilitary.about.com/od/glossarytermsm/g/m3895.htm>.
- [15] National Academy of Sciences. Shipboard cranes and burtoning gear - evaluation of cargo handling equipment in the liberty ship modernization program. Technical Report NAS-NRC-1, Maritime Administration, Washington, D.C., USA, 1957.
- [16] George R. Cottingham. Offshore discharge of containership. Technical report, Military Traffic Management Command Transportation Engineering Agency, June 1971.
- [17] Weigel R.L. *Oceanographical Engineering*. Prentice Hall, Englewood Cliffs, New Jersey, 1964.
- [18] Steven R. Gunderson and Lawrence C. Ruth. An investigation of the relative and absolute ship motions of ships involved in the 'offshore discharge of containerships' (osdoc ii) sea trials. Technical Report SPD-515-01, David W. Taylor Naval Ship R&D Center, November 1976.
- [19] Robert D. Pierce. Compilation of motion data obtained on voyageur acv during osdoc ii exercise in october 1972. Technical Report CID-29-1, David W. Taylor Naval Ship R&D Center, February 1973.
- [20] M. J. Wolfe and S. K. Wang. Impact and operational tests of the container hopper. Technical Report NCEL-TN-1313, Naval Civil Engineering Laboratory, November 1973.
- [21] Richard C. Towne, James J. Traffalis, Duane A. Davis, Jones Don B., and Billie R. Karrh. Osdock ii engineering tests - coronado. Technical note, 1 sep 71-31 may 72, Naval Civil Engineering Laboratory, Port Hueneme, CA, December 1972.
- [22] Michael Agostini, Gordon Parker, Kenneth Groom, and Hanspeter Schaub. Command shaping and closed-loop control interactions for a ship crane. In *Proceedings of the American Control Conference*, pages 2298–2304, 2002.
- [23] N. C. Singer and W. P. Seering. Preshaping command inputs to reduce system vibration. *ASME Journal of Dynamic Systems, Measurement, and Control*, 112:76–82, March 1990.

- [24] L. Bonde and D. Dillon. A concept for improved crane performance in offshore operations. Industrial/Commercial EG/G-HCG-TR-4694-0001, EG&G Washington Analytical Services Center, August 1976.
- [25] Dr. John Dexter Bird III. *A Methodology for the Evaluation of Alternative Amphibious Material Handling Systems*. PhD thesis, University of Virginia, 1979.
- [26] Naval Sea Systems Command. T-ac 4 class mission operations handbook (t-ac 4,5,6). Washington, D.C., USA, December 2000.
- [27] Analysis and evaluation report - jlots ii throughput test. Technical report, Department of Defense, August 1985.
- [28] W. J. Pierson and L. Moskowitz. A proposed spectral form for full-developed wind sea based on the similarity law of s.a. kitaigorodoski, 1964.
- [29] STANAG 4194. Standardized wave and wind conditions and shipboard reporting of sea conditions. Technical report, North Atlantic Treaty Organization, April 1983.
- [30] Beaufort_scale, September 2008.
http://en.wikipedia.org/wiki/Beaufort_scale.
- [31] D. Bird III and Lucero L. Integrated rbts control system for t-ac crane - a preliminary design study for the coastal system station nswc, dahlgren division. Technical report, Craft Engineering Associates, Inc., 1997.
- [32] Joint Test Director. JLOTS II Operational Test Report-Throughput Phase. Technical report, Department of Defense, March 1985.
- [33] M. Yamamoto, N. Yanai, and A. Mohri. Trajectory control of incompletely restrained parallel-wire-suspended mechanism based on inverse dynamics. *IEEE Transactions on Robotics and Automation*, 20, October 2004.
- [34] R. J. Henry, Z. N. Masoud, A. H. Nayfeh, and D. T. Mook. Cargo pendulation reduction on ship-mounted cranes via boom-luff angle actuation. *Journal of Vibration and Control*, 7:1253–1264, 2001.
- [35] Virginia Polytechnic Institute. *Dynamics, Stability, and Control of Cranes - Third Semi-Annual MURI Meeting Nonlinear Active Control of Dynamical Systems*, Blacksburg, VA, April 1998.
- [36] P. Dadone and H. VanLandingham. Intelligent control methods for ship-mounted cranes, third semi-annual muri meeting nonlinear active control of dynamical systems. Technical report, Virginia Polytechnic Institute, Blacksburg, VA, April 1998.

- [37] E. Abdel-Rahman and A. H. Nayfeh. Pendulation reduction in boom cranes using cable length manipulation. *Nonlinear Dynamics*, 2002.
- [38] E. M. Abdel-Rahman and A. H. Nayfeh. Pendulation reduction in boom cranes using cable length manipulation. *Nonlinear Dynamics*, 27:255–269, 2002.
- [39] M. Todd, S. Vohra, C Vandette, and J. Nichols. Analysis of pendulated load response and t-acs/lighter interaction in a 1:24 scale model jlots cargo transfer operation at the david taylor model basin in 1997. Technical Report NRL/MR/5673-98-8310, Naval Research Laboratory, Fiberoptics Smart Structures Section, Washington, D.C., USA, October 1998.
- [40] H. Schaub and K. Groom. Performance review of the tg3637 hägglunds crane operating with the sandia swing-free control. Technical report, Sandia National Laboratories, October 2000.
- [41] NUCLEAR SHIP SAVANNAH, October 2007.
[online]<http://nuclearshipsavannah.com>.
- [42] International Conference on Robotics and Automation. *Dynamic Analysis of the Cable Array Robotic Crane*, volume 2495–2500, 1999.
- [43] J. J. Gorman, K.W. Jablokow, and D.J. Cannon. The cable array robot: theory and experiment. In *Proceedings of the 1999 IEEE International Conference on Robotics and Automation*, pages 2804–2810, 1999.
- [44] James Albus, Roger Bostelman, and Adam Jacoff. Robocrane final report, mobile offshore base project, vol. 1, 2. Technical report, National Institute of Standards and Technology, 1997.
- [45] J. Albus, R. Bostelman, and N. Dagalakis. The nist robocrane. In *Journal of Robotic Systems*, volume 10, pages 709–724, 1993.
- [46] S. Kery, G. Hughes, E. May, P. Kjolseth, M. Pang, W. Thomas, T. Treakle, and D. Liut. Achieving high container through-put rates, between vessels in high seas (a vision of HiCASS). In *OCEANS , 2005 Proceedings of MTS/IEEE*, volume 1, pages 454–459, 2005.
- [47] Gordon Parker, Michael Graziano, Frank Leban, Jeffrey Green, and Dexter Bird III. Reducing crane payload swing using a rider block tagline control system. In *IEEE Oceans '07*, June 2007.
- [48] S. Kawamura, W. Choe, S. Tanaka, and S.R. Pandian. Development of an ultrahigh speed robot falcon using wire driven system. In *IEEE Transactions on Robotics and Automation*, pages 215–220, 1995.

- [49] K. Maeda and S Tadokoro. On design of a redundant wire-driven parallel robot warp manipulator. In *Proceedings of the 1999 IEEE International Conference on Robotics and Automation*, pages 895–900, 1999.
- [50] Smith, R. and Starr, G. and Lumia, R. and Wood J. Preshaped trajectories for residual vibration suppression in payloads suspended from multiple robot manipulators. In *Robotics and Automation, 2004. Proceedings. ICRA '04, 2004 IEEE International Conference on*, volume 2, pages 1599–1603, 2004.
- [51] M.J. McDonald, D.E. Small, C.C. Graves, and D. Cannon. Virtual collaborative control to improve intelligent robotic system efficiency and quality. pages 418–424. International Conference on Robotics and Automation, 1997.
- [52] D.G. Wilson, R. D. Robinett, and G.R. Eisler. Discrete dynamic programming for optimized path planning of flexible robots. In *Proceedings of the IEEE/RSJ International Conference on Robotics and Systems*, pages 2918–2923, October 2004.
- [53] M. Galicki. Path following by the end-effector of a redundant manipulator operating in a dynamic environment. In *IEEE Transactions on Robotics*, page 7, 2004.
- [54] J. Agirrebeitia, R. Aviles, I. F. de Bustos, and G. Ajuria. A method for the study of position in highly redundant multibody systems in environments with obstacles. In *IEEE Transactions on Robotics and Automation*, volume 18, April 2002.
- [55] P. Ogren, M. Egerstedt, and X. Hu. A control lyapunov function approach to multiagent coordination. In *IEEE Transactions on Robotics and Automation*, volume 18, October 2002.
- [56] M. Yamamoto and A. Mohri. Inverse kinematics analysis for incompletely restrained parallel wire mechanisms. In *Proceedings of the 2000 IEEE/RSJ International Conference on Intelligent Robots and Systems*, pages 504–509, 2000.
- [57] John J. Craig. *Introduction to Robotics: Mechanics and Control*. Addison-Wesley Longman Publishing Co., Inc., Boston, MA, USA, 1989.
- [58] Michael Graziano. Reducing crane payload swing using a rider block tagline control system. Master's thesis, Michigan Technological University, 2007.
- [59] Thomas D. Rossing and Neville H. Fletcher. *Principles of Vibration and Sound*. ISBN 0387405569. Springer, 2nd edition, 2004.

- [60] William T. Thomson and Marie D. Dahleh. *Theory of Vibration with Applications*. Number ISBN 013651068. Prentice Hall, Upper Saddle River, New Jersey, 5th edition, 1998.
- [61] Pierson - moskowitz sea spectrum, August 2008.
http://www.eustis.army.mil/WEATHER/Weather_Products/seastate.htm.
- [62] Institute of Electrical and Electronics Engineers. *A Constraint Oriented Approach to Inverse Problems for Kinematically Redundant Manipulators*, 1987.
- [63] John L. Junkins. *An Introduction to Optimal Estimation of Dynamical Systems*. Sijthoff & Noordhoff, 1978.
- [64] Gene F. Franklin, David J. Powell, and Michael L. Workman. *Digital Control of Dynamic Systems*. Addison-Wesley Longman Publishing Co., Inc., Menlo Park, CA 94025, 3rd edition edition, 1998.
- [65] R. M. Howe. *Dynamics of Real-Time Digital Simulation*. Applied Dynamics International, 3800 Stone School Road, Ann Arbor, Michigan, June 1987.
- [66] Arthur E. Jr Bryson and Yu-Chi Ho. *Applied Optimal Control: Optimization, Estimation, and Control*. Taylor & Francis, January 1975.

INITIAL DISTRIBUTION LIST

- | | |
|--|---|
| 1. Defense Technical Information Center
Ft. Belvoir, VA | |
| 2. Dudley Knox Library
Naval Postgraduate School
Monterey, CA | |
| 3. Professor Anthony Healey
Naval Postgraduate School
Monterey, CA | 1 |
| 4. Professor Fotis Papoulias
Naval Postgraduate School
Monterey, CA | 1 |
| 5. Professor Roberto Cristi
Naval Postgraduate School
Monterey, CA | 1 |
| 6. Professor Wei Kang
Naval Postgraduate School
Monterey, CA | 1 |
| 7. Dr. Gordon G. Parker
Michigan Technological University
Houghton, MI | 1 |
| 8. Dr. W. Thomas Zhao
BMT Designers & Planners
Arlington, VA | 1 |
| 9. Dr. J Dexter Bird, III
Craft Engineering Associates, Inc.
Hampton, VA | 1 |